
Description of the NCAR Community Atmosphere Model (CAM 5.0)

Richard B. Neale Chih-Chieh Chen
Andrew Gettelman Peter H. Lauritzen
Sungsu Park David L. Williamson

Climate And Global Dynamics Division
National Center For Atmospheric Research
Boulder, Colorado, USA

Andrew J. Conley Rolando Garcia
Doug Kinnison Jean-Francois Lamarque
Dan Marsh Mike Mills
Anne K. Smith Simone Tilmes
Francis Vitt

Atmospheric Chemistry Division
National Center For Atmospheric Research
Boulder, Colorado, USA

² Hugh Morrison

Mesoscale and Microscale Meteorology
National Center For Atmospheric Research
Boulder, Colorado, USA

Philip Cameron-Smith

Lawrence Livermore National Lab
Livermore, California

William D. Collins

UC Berkeley/Lawrence Berkeley National Laboratory
Berkeley, California

Michael J. Iacono

Atmospheric and Environmental Research, Inc.
Lexington, Massachusetts

Richard C. Easter Steven J. Ghan
Xiaohong Liu Philip J. Rasch

Pacific Northwest National Laboratory
Richland, Washington

Mark A. Taylor

Sandia National Laboratories
Albuquerque, New Mexico

NCAR TECHNICAL NOTES

4 The Technical Note series provides an outlet for a variety of NCAR manuscripts that contribute
5 in specialized ways to the body of scientific knowledge but which are not suitable for journal,
6 monograph, or book publication. Reports in this series are issued by the NCAR Scientific Di-
7 visions; copies may be obtained on request from the Publications Office of NCAR. Designation
8 symbols for the series include:

9

EDD: *Engineering, Design, or Development Reports*

Equipment descriptions, test results, instrumentation,
and operating and maintenance manuals.

IA: *Instructional Aids*

Instruction manuals, bibliographies, film supplements,
and other research or instructional aids.

PPR: *Program Progress Reports*

Field program reports, interim and working reports,
survey reports, and plans for experiments.

PROC: *Proceedings*

Documentation of symposia, colloquia, conferences, workshops,
and lectures. (Distribution may be limited to attendees.)

STR: *Scientific and Technical Reports*

Data compilations, theoretical and numerical
investigations, and experimental results.

10 *The National Center for Atmospheric Research (NCAR) is operated by the University Corpora-*
11 *tion for Atmospheric Research (UCAR) and is sponsored by the National Science Foundation.*
12 *Any opinions, findings, conclusions, or recommendations expressed in this publication are those*
13 *of the author(s) and do not necessarily reflect the views of the National Science Foundation.*

14 Contents

15	Acknowledgments	xi
16	1 Introduction	1
17	1.1 Brief History	1
18	1.1.1 CCM0 and CCM1	1
19	1.1.2 CCM2	2
20	1.1.3 CCM3	3
21	1.1.4 CAM3	4
22	1.1.5 CAM4	6
23	1.1.6 Overview of CAM 5.0	7
24	2 Coupling of Dynamical Core and Parameterization Suite	11
25	3 Dynamics	15
26	3.1 Finite Volume Dynamical Core	15
27	3.1.1 Overview	15
28	3.1.2 The governing equations for the hydrostatic atmosphere	15
29	3.1.3 Horizontal discretization of the transport process on the sphere	17
30	3.1.4 A <i>vertically Lagrangian</i> and <i>horizontally Eulerian</i> control-volume discretization of the hy	
31	3.1.5 Optional diffusion operators in CAM5	24
32	3.1.6 A mass, momentum, and total energy conserving mapping algorithm	26
33	3.1.7 A geopotential conserving mapping algorithm	28
34	3.1.8 Adjustment of pressure to include change in mass of water vapor	29
35	3.1.9 Negative Tracer Fixer	30
36	3.1.10 Global Energy Fixer	30
37	3.1.11 Further discussion	32
38	3.2 Spectral Element Dynamical Core	33
39	3.2.1 Continuum Formulation of the Equations	34
40	3.2.2 Conserved Quantities	35
41	3.2.3 Horizontal Discretization: Functional Spaces	36
42	3.2.4 Horizontal Discretization: Differential Operators	38
43	3.2.5 Horizontal Discretization: Discrete Inner-Product	39
44	3.2.6 Horizontal Discretization: The Projection Operators	40
45	3.2.7 Horizontal Discretization: Galerkin Formulation	40
46	3.2.8 Vertical Discretization	41
47	3.2.9 Discrete formulation: Dynamics	42

48	3.2.10 Consistency	43
49	3.2.11 Time Stepping	44
50	3.2.12 Dissipation	44
51	3.2.13 Discrete formulation: Tracer Advection	45
52	3.2.14 Conservation and Compatibility	46
53	3.3 Eulerian Dynamical Core	47
54	3.3.1 Generalized terrain-following vertical coordinates	47
55	3.3.2 Conversion to final form	49
56	3.3.3 Continuous equations using $\partial \ln(\pi)/\partial t$	50
57	3.3.4 Semi-implicit formulation	51
58	3.3.5 Energy conservation	53
59	3.3.6 Horizontal diffusion	56
60	3.3.7 Finite difference equations	58
61	3.3.8 Time filter	60
62	3.3.9 Spectral transform	61
63	3.3.10 Spectral algorithm overview	61
64	3.3.11 Combination of terms	64
65	3.3.12 Transformation to spectral space	65
66	3.3.13 Solution of semi-implicit equations	66
67	3.3.14 Horizontal diffusion	67
68	3.3.15 Initial divergence damping	68
69	3.3.16 Transformation from spectral to physical space	69
70	3.3.17 Horizontal diffusion correction	70
71	3.3.18 Semi-Lagrangian Tracer Transport	71
72	3.3.19 Mass fixers	75
73	3.3.20 Energy Fixer	77
74	3.3.21 Statistics Calculations	78
75	3.3.22 Reduced grid	78
76	3.4 Semi-Lagrangian Dynamical Core	78
77	3.4.1 Introduction	78
78	3.4.2 Vertical coordinate and hydrostatic equation	79
79	3.4.3 Semi-implicit reference state	79
80	3.4.4 Perturbation surface pressure prognostic variable	79
81	3.4.5 Extrapolated variables	80
82	3.4.6 Interpolants	80
83	3.4.7 Continuity Equation	80
84	3.4.8 Thermodynamic Equation	82
85	3.4.9 Momentum equations	84
86	3.4.10 Development of semi-implicit system equations	85
87	3.4.11 Trajectory Calculation	91
88	3.4.12 Mass and energy fixers and statistics calculations	91

89	4 Model Physics	93
90	4.1 Conversion to and from dry and wet mixing ratios for trace constituents in the model	95
91	4.2 Moist Turbulence Scheme	97
92	4.2.1 Bulk Moist Richardson Number	98
93	4.2.2 Identification of Convective, Stably Turbulent, and Stable Layers	100
94	4.2.3 Turbulent Length Scale	101
95	4.2.4 Steady-State Turbulent Kinetic Energy	101
96	4.2.5 Stability Functions	102
97	4.2.6 CL Extension-Merging Procedure	103
98	4.2.7 Entrainment Rates at the CL Top and Base Interfaces	104
99	4.2.8 Implicit Diffusion with Implicit Diffusivity	104
100	4.2.9 Implicit Surface Stress	106
101	4.3 Shallow Convection Scheme	108
102	4.3.1 Reconstruction of Mean Profiles and Cloud Condensate Partitioning	108
103	4.3.2 Source Air Properties of Convective Updraft	110
104	4.3.3 Closures at the Cloud Base	111
105	4.3.4 Vertical Evolution of A Single Updraft Plume	112
106	4.3.5 Penetrative Entrainment	113
107	4.3.6 Convective Fluxes at and below the PBL top interface	114
108	4.3.7 Grid-Mean Tendency of Conservative Scalars	115
109	4.3.8 Grid-Mean Tendency of Non-Conservative Scalars	116
110	4.4 Deep Convection	118
111	4.4.1 Updraft Ensemble	118
112	4.4.2 Downdraft Ensemble	121
113	4.4.3 Closure	122
114	4.4.4 Numerical Approximations	122
115	4.4.5 Deep Convective Momentum Transports	125
116	4.4.6 Deep Convective Tracer Transport	125
117	4.5 Evaporation of convective precipitation	127
118	4.6 Cloud Microphysics	128
119	4.6.1 Overview of the microphysics scheme	128
120	4.6.2 Radiative Treatment of Ice	133
121	4.6.3 Formulations for the microphysical processes	133
122	4.7 Cloud Macrophysics	141
123	4.7.1 Cloud Fractions	141
124	4.7.2 Cloud Overlaps	144
125	4.7.3 Condensation Processes	146
126	4.8 Aerosols	151
127	4.8.1 Emissions	152
128	4.8.2 Chemistry	153
129	4.8.3 Secondary Organic Aerosol	154
130	4.8.4 Nucleation	154
131	4.8.5 Condensation	154
132	4.8.6 Coagulation	155
133	4.8.7 Water Uptake	155

134	4.8.8	Subgrid Vertical Transport and Activation/Resuspension	157
135	4.8.9	Wet Deposition	157
136	4.8.10	Dry Deposition	158
137	4.9	Condensed Phase Optics	160
138	4.9.1	Tropospheric Aerosol Optics	160
139	4.9.2	Stratospheric Volcanic Aerosol Optics	160
140	4.9.3	Liquid Cloud Optics	162
141	4.9.4	Ice Cloud Optics	162
142	4.9.5	Snow Cloud Optics	164
143	4.10	Radiative Transfer	165
144	4.10.1	Combination of Aerosol Radiative Properties	165
145	4.10.2	Combination of Cloud Optics	165
146	4.10.3	Radiative Fluxes and Heating Rates	166
147	4.10.4	Surface Radiative Properties	169
148	4.10.5	Time Sampling	169
149	4.10.6	Diurnal Cycle and Earth Orbit	169
150	4.10.7	Solar Spectral Irradiance	171
151	4.11	Surface Exchange Formulations	176
152	4.11.1	Land	176
153	4.11.2	Ocean	180
154	4.11.3	Sea Ice	181
155	4.12	Dry Adiabatic Adjustment	182
156	4.13	Prognostic Greenhouse Gases	183
157	5	Extensions to CAM	185
158	5.1	Chemistry	186
159	5.1.1	Introduction	186
160	5.1.2	Emissions	186
161	5.1.3	Lower boundary conditions	186
162	5.1.4	Lightning	187
163	5.1.5	Dry deposition	187
164	5.1.6	Wet removal	187
165	5.1.7	Photolytic Approach (Neutral Species)	188
166	5.1.8	Numerical Solution Approach	188
167	5.2	Superfast Chemistry	190
168	5.2.1	Chemical mechanism	190
169	5.2.2	LINOZ	190
170	5.2.3	PSC ozone loss	191
171	5.2.4	Upper boundary condition	191
172	5.3	WACCM4.0 Physical Parameterizations	192
173	5.3.1	WACCM4.0 Domain and Resolution	192
174	5.3.2	Molecular Diffusion and Constituent Separation	193
175	5.3.3	Gravity Wave Drag	196
176	5.3.4	Turbulent Mountain Stress	203
177	5.3.5	QBO Forcing	204

178	5.3.6	Radiation	205
179	5.3.7	WACCM4.0 chemistry	207
180	5.3.8	Electric Field	222
181	5.3.9	Boundary Conditions	231
182	6	Initial and Boundary Data	233
183	6.1	Initial Data	233
184	6.2	Boundary Data	234

Appendices

185	A	Physical Constants	237
186	B	Acronyms	239
187	C	Resolution and dycore-dependent parameters	241
188		References	242

List of Figures

189

190

3.1 A graphical illustration of the different levels of sub-cycling in CAM5. 24

191

3.2 Tiling the surface of the sphere with quadrilaterals. An inscribed cube is projected to the surface

192

3.3 A 4×4 tensor product grid of GLL nodes used within each element, for a degree $d = 3$ discretization

193

3.4 Vertical level structure of CAM 5.0 53

194

3.5 Pentagonal truncation parameters 62

195

4.1 Schematic structure of moist turbulence scheme 99

196

4.2 Schematic structure of shallow cumulus scheme 109

197

4.3 Predicted species for interstitial and cloud-borne component of each aerosol mode in MAM-7. St

198

4.4 Predicted species for interstitial and cloud-borne component of each aerosol mode in MAM-3. St

199

4.5 Kurucz spectrum. ssf in $\text{W}/\text{m}^2/\text{nm}$. Source Data: AER. Range from $[20, 20000]$ nm. 173

200

4.6 Lean spectrum. Average over 1 solar cycle, May 1, 1996 to Dec 31, 2006. Source Data: Marsh. s

201

4.7 Relative difference, $\frac{\text{Lean}-\text{Kurucz}}{.5(\text{Lean}+\text{Kurucz})}$ between spectra. RRTMG band boundaries are marked with ve

202

5.1 Global mean distribution of charged constituents during July solar minimum conditions. 211

203

5.2 a) Global distribution of ionization rates at 7.3×10^{-5} hPa, July 1, UT0100 HRS. Contour interv

List of Tables

205	4.1	Size distributions of primary emissions.	156
206	4.2	Assumed SOA (gas) yields	156
207	4.3	Hygroscopicity of aerosol components	156
208	4.4	Density (kg/m ³) of aerosol material.	160
209	4.5	Hygroscopicity of aerosol components.	160
210	4.6	RRTMG_SW spectral band boundaries and the solar irradiance in each band.	167
211	4.7	RRTMG_LW spectral band boundaries.	168
212	4.8	Band-level ratio of Solar Irradiances, based on average of one solar cycle	172
213	5.1	Surface fluxes for CAM4 superfast chemistry.	186
214	5.2	WACCM4.0 Neutral Chemical Species (51 computed species + N ₂)	213
215	5.1	(continued) WACCM4.0 Neutral Chemical Species (51 computed species + N ₂)	214
216	5.2	WACCM4.0 Gas-phase Reactions.	215
217	5.2	(continued) WACCM4.0 Gas-phase Reactions.	216
218	5.2	(continued) WACCM4.0 Gas-phase Reactions.	217
219	5.2	(continued) WACCM4.0 Gas-phase Reactions.	218
220	5.2	(continued) WACCM4.0 Gas-phase Reactions.	219
221	5.3	WACCM4.0 Heterogeneous Reactions on liquid and solid aerosols.	219
222	5.4	WACCM4.0 Photolytic Reactions.	220
223	5.4	(continued) WACCM4.0 Photolytic Reactions.	221
224	5.5	Ion-neutral and recombination reactions and exothermicities.	222
225	5.6	Ionization reactions.	223
226	5.7	EUVAC model parameters.	223
227	C.1	Resolution-dependent parameters	241

228 Acknowledgments

229 The authors wish to acknowledge members of NCAR's Atmospheric Modeling and Predictability
230 Section (AMP), Computer Software and Engineering Group (CSEG), and Computation and
231 Information Systems Laboratory (CISL) for their contributions to the development of CAM 5.0.

232 The new model would not exist without the significant input from members of the CESM
233 Atmospheric Model Working Group ([AMWG](#)) too numerous to mention. Leo Donner (GFDL),
234 Minghua Zhang (SUNY) and Phil Rasch (PNNL) were the co-chairs of the AMWG during the
235 development of CAM 5.0.

236 We would like to acknowledge the substantial contributions to the CAM 5.0 effort from the
237 National Science Foundation, Department of Energy, the National Oceanic and Atmospheric
238 Administration, and the National Aeronautics and Space Administration.

Chapter 1

Introduction

This report presents the details of the governing equations, physical parameterizations, and numerical algorithms defining the version of the NCAR Community Atmosphere Model designated CAM 5.0. The material provides an overview of the major model components, and the way in which they interact as the numerical integration proceeds. Details on the coding implementation, along with in-depth information on running the CAM 5.0 code, are given in a separate technical report entitled ‘ ‘User’s Guide to Community Atmosphere ModelCAM 5.0” [Eaton, 2010]. As before, it is our objective that this model provide NCAR and the university research community with a reliable, well documented atmospheric general circulation model. This version of the CAM 5.0 incorporates a number enhancements to the physics package (*e.g.* adjustments to the deep convection algorithm including the addition of Convective Momentum Transports (CMT), a transition to the finite volume dynamical core as default and the option to run a computationally highly scaleable dynamical core). The ability to transition between CAM-standalone and fully coupled experiment frameworks is much improved in CAM 5.0. We believe that collectively these improvements provide the research community with a significantly improved atmospheric modeling capability.

1.1 Brief History

1.1.1 CCM0 and CCM1

Over the last twenty years, the NCAR Climate and Global Dynamics (CGD) Division has provided a comprehensive, three-dimensional global atmospheric model to university and NCAR scientists for use in the analysis and understanding of global climate. Because of its widespread use, the model was designated a community tool and given the name Community Climate Model (CCM). The original versions of the NCAR Community Climate Model, CCM0A [Washington, 1982] and CCM0B [Williamson, 1983], were based on the Australian spectral model [Bourke et al., 1977; McAvaney et al., 1978] and an adiabatic, inviscid version of the ECMWF spectral model [Baede et al., 1979]. The CCM0B implementation was constructed so that its simulated climate would match the earlier CCM0A model to within natural variability (*e.g.* incorporated the same set of physical parameterizations and numerical approximations), but also provided a more flexible infrastructure for conducting medium- and long-range global forecast studies. The major strength of this latter effort was that all aspects of the model were described

270 in a series of technical notes, which included a Users' Guide [Sato et al., 1983], a subroutine guide
271 which provided a detailed description of the code [Williamson et al., 1983] a detailed description
272 of the algorithms [Williamson, 1983], and a compilation of the simulated circulation statistics
273 [Williamson and Williamson, 1984]. This development activity firmly established NCAR's com-
274 mitment to provide a versatile, modular, and well-documented atmospheric general circulation
275 model that would be suitable for climate and forecast studies by NCAR and university scien-
276 tists. A more detailed discussion of the early history and philosophy of the Community Climate
277 Model can be found in Anthes [1986].

278 The second generation community model, CCM1, was introduced in July of 1987, and in-
279 cluded a number of significant changes to the model formulation which were manifested in
280 changes to the simulated climate. Principal changes to the model included major modifica-
281 tions to the parameterization of radiation, a revised vertical finite-differencing technique for the
282 dynamical core, modifications to vertical and horizontal diffusion processes, and modifications
283 to the formulation of surface energy exchange. A number of new modeling capabilities were
284 also introduced, including a seasonal mode in which the specified surface conditions vary with
285 time, and an optional interactive surface hydrology that followed the formulation presented by
286 Manabe [1969]. A detailed series of technical documentation was also made available for this ver-
287 sion [Williamson et al., 1987; Bath et al., 1987; Williamson and Williamson, 1987; Hack et al.,
288 1989] and more completely describe this version of the CCM.

289 1.1.2 CCM2

290 The most ambitious set of model improvements occurred with the introduction of the third
291 generation of the Community Climate Model, CCM2, which was released in October of 1992.
292 This version was the product of a major effort to improve the physical representation of a wide
293 range of key climate processes, including clouds and radiation, moist convection, the planetary
294 boundary layer, and transport. The introduction of this model also marked a new philosophy
295 with respect to implementation. The CCM2 code was entirely restructured so as to satisfy three
296 major objectives: much greater ease of use, which included portability across a wide range of
297 computational platforms; conformance to a plug-compatible physics interface standard; and the
298 incorporation of single-job multitasking capabilities.

299 The standard CCM2 model configuration was significantly different from its predecessor in
300 almost every way, starting with resolution where the CCM2 employed a horizontal T42 spectral
301 resolution (approximately 2.8 x 2.8 degree transform grid), with 18 vertical levels and a rigid lid
302 at 2.917 mb. Principal algorithmic approaches shared with CCM1 were the use of a semi-implicit,
303 leap frog time integration scheme; the use of the spectral transform method for treating the dry
304 dynamics; and the use of a bi-harmonic horizontal diffusion operator. Major changes to the
305 dynamical formalism included the use of a terrain-following hybrid vertical coordinate, and the
306 incorporation of a shape-preserving semi-Lagrangian transport scheme [Williamson and Olson,
307 1994a] for advecting water vapor, as well as an arbitrary number of other scalar fields (*e.g.* cloud
308 water variables, chemical constituents, etc.). Principal changes to the physics included the use
309 of a δ -Eddington approximation to calculate solar absorption [Briegleb, 1992]; the use of a Voigt
310 line shape to more accurately treat infrared radiative cooling in the stratosphere; the inclusion
311 of a diurnal cycle to properly account for the interactions between the radiative effects of the
312 diurnal cycle and the surface fluxes of sensible and latent heat; the incorporation of a finite heat

313 capacity soil/sea ice model; a more sophisticated cloud fraction parameterization and treatment
314 of cloud optical properties [Kiehl et al., 1994]; the incorporation of a sophisticated non-local
315 treatment of boundary-layer processes [Holtzlag and Boville, 1993a]; the use of a simple mass
316 flux representation of moist convection [Hack, 1994a], and the optional incorporation of the
317 Biosphere-Atmosphere Transfer Scheme (BATS) of Dickinson et al. [1987]. As with previous
318 versions of the model, a User’s Guide [Bath et al., 1992] and model description [Hack et al.,
319 1993] were provided to completely document the model formalism and implementation. Control
320 simulation data sets were documented in Williamson [1993].

321 1.1.3 CCM3

322 The CCM3 was the fourth generation in the series of NCAR’s Community Climate Model. Many
323 aspects of the model formulation and implementation were identical to the CCM2, although there
324 were a number of important changes that were incorporated into the collection of parameterized
325 physics, along with some modest changes to the dynamical formalism. Modifications to the
326 physical representation of specific climate processes in the CCM3 were motivated by the need
327 to address the more serious systematic errors apparent in CCM2 simulations, as well as to make
328 the atmospheric model more suitable for coupling to land, ocean, and sea-ice component models.
329 Thus, an important aspect of the changes to the model atmosphere was that they address well
330 known systematic biases in the top-of-atmosphere and surface (to the extent that they were
331 known) energy budgets. When compared to the CCM2, changes to the model formulation fell
332 into five major categories: modifications to the representation of radiative transfer through both
333 clear and cloudy atmospheric columns, modifications to hydrological processes (i.e., in the form
334 of changes to the atmospheric boundary layer, moist convection, and surface energy exchange),
335 the incorporation of a sophisticated land surface model, the incorporation of an optional slab
336 mixed-layer ocean/thermodynamic sea-ice component, and a collection of other changes to the
337 formalism which did not introduce significant changes to the model climate.

338 Changes to the clear-sky radiation formalism included the incorporation of minor CO₂ bands
339 trace gases (*CH₄*, *N₂O*, *CFC11*, *CFC12*) in the longwave parameterization, and the incorpo-
340 ration of a background aerosol (0.14 optical depth) in the shortwave parameterization. All-sky
341 changes included improvements to the way in which cloud optical properties (effective radius and
342 liquid water path) were diagnosed, the incorporation of the radiative properties of ice clouds,
343 and a number of minor modifications to the diagnosis of convective and layered cloud amount.
344 Collectively these modification substantially reduced systematic biases in the global annually
345 averaged clear-sky and all-sky outgoing longwave radiation and absorbed solar radiation to well
346 within observational uncertainty, while maintaining very good agreement with global observa-
347 tional estimates of cloud forcing. Additionally, the large warm bias in simulated July surface
348 temperature over the Northern Hemisphere, the systematic over-prediction of precipitation over
349 warm land areas, and a large component of the stationary-wave error in CCM2, were also reduced
350 as a result of cloud-radiation improvements.

351 Modifications to hydrological processes included revisions to the major contributing param-
352 eterizations. The formulation of the atmospheric boundary layer parameterization was revised
353 (in collaboration with Dr. A. A. M. Holtzlag of KNMI), resulting in significantly improved
354 estimates of boundary layer height, and a substantial reduction in the overall magnitude of the
355 hydrological cycle. Parameterized convection was also modified where this process was repre-

356 sented using the deep moist convection formalism of [Zhang and McFarlane \[1995\]](#) in conjunction
357 with the scheme developed by [Hack \[1994a\]](#) for CCM2. This change resulted in an additional
358 reduction in the magnitude of the hydrological cycle and a smoother distribution of tropical pre-
359 cipitation. Surface roughness over oceans was also diagnosed as a function of surface wind speed
360 and stability, resulting in more realistic surface flux estimates for low wind speed conditions.
361 The combination of these changes to hydrological components resulted in a 13% reduction in
362 the annually averaged global latent heat flux and the associated precipitation rate. It should
363 be pointed out that the improvements in the radiative and hydrological cycle characteristics of
364 the model climate were achieved without compromising the quality of the simulated equilibrium
365 thermodynamic structures (one of the major strengths of the CCM2) thanks in part to the
366 incorporation of a [Sundqvist \[1988\]](#) style evaporation of stratiform precipitation.

367 The CCM3 incorporated version 1 of the Land Surface Model (LSM) developed by [Bonan](#)
368 [\[1996\]](#) which provided for the comprehensive treatment of land surface processes. This was a
369 one-dimensional model of energy, momentum, water, and CO₂ exchange between the atmosphere
370 and land, accounting for ecological differences among vegetation types, hydraulic and thermal
371 differences among soil types, and allowing for multiple surface types including lakes and wetlands
372 within a grid cell. LSM replaced the prescribed surface wetness, prescribed snow cover, and
373 prescribed surface albedos in CCM2. It also replaced the land surface fluxes in CCM2, using
374 instead flux parameterizations that included hydrological and ecological processes (*e.g.* soil
375 water, phenology, stomatal physiology, interception of water by plants).

376 The fourth class of changes to the CCM2 included the option to run CCM3 with a simple
377 slab ocean-thermodynamic sea ice model. The model employs a spatially and temporally pre-
378 scribed ocean heat flux and mixed layer depth, which ensures replication of realistic sea surface
379 temperatures and ice distributions for the present climate. The model allowed for the simplest
380 interactive surface for the ocean and sea ice components of the climate system.

381 The final class of model modifications included a change to the form of the hydrostatic matrix
382 which ensures consistency between ω and the discrete continuity equation, and a more general-
383 ized form of the gravity wave drag parameterization. In the latter case, the parameterization
384 was configured to behave in the same way as the CCM2 parameterization of wave drag, but
385 included the capability to exploit more sophisticated descriptions of this process.

386 One of the more significant implementation differences with the earlier model was that CCM3
387 included an optional message-passing configuration, allowing the model to be executed as a
388 parallel task in distributed-memory environments. This was an example of how the Climate
389 and Global Dynamics Division continued to invest in technical improvements to the CCM in
390 the interest of making it easier to acquire and use in evolving computational environments. As
391 was the case for CCM2, the code was internally documented, obviating the need for a separate
392 technical note that describes each subroutine and common block in the model library. Thus,
393 the Users' Guide, the land surface technical note, the CCM3 technical note [\[Kiehl et al., 1996\]](#),
394 the actual code and a series of reviewed scientific publications (including a special issue of the
395 Journal of Climate, Volume 11, Number 6) were designed to completely document CCM3.

396 **1.1.4 CAM3**

397 The CAM3 was the fifth generation of the NCAR atmospheric GCM. The name of the model
398 series was changed from Community Climate Model to Community Atmosphere Model to reflect

399 the role of CAM3 in the fully coupled climate system. In contrast to previous generations of
400 the atmospheric model, CAM3 had been designed through a collaborative process with users
401 and developers in the Atmospheric Model Working Group (AMWG). The AMWG includes
402 scientists from NCAR, the university community, and government laboratories. For CAM3,
403 the consensus of the AMWG was to retain the spectral Eulerian dynamical core for the first
404 official release although the code includes the option to run with semi-Lagrange dynamics or
405 with finite-volume dynamics (FV). The addition of FV was a major extension to the model
406 provided through a collaboration between NCAR and NASA Goddard’s Data Assimilation Office
407 (DAO). The major changes in the physics included treatment of cloud condensed water using a
408 prognostic formulation with a bulk microphysical component following [Rasch and Kristjánsson](#)
409 [\[1998a\]](#) and a macroscale component following [Zhang et al. \[2003b\]](#). The [Zhang and McFarlane](#)
410 [\[1995\]](#) parameterization for deep convection was retained from CCM3.

411 A new treatment of geometrical cloud overlap in the radiation calculations computed the
412 shortwave and longwave fluxes and heating rates for random overlap, maximum overlap, or
413 an arbitrary combination of maximum and random overlap. The calculation was completely
414 separated from the radiative parameterizations. The introduction of the generalized overlap
415 assumptions permitted more realistic treatments of cloud-radiative interactions. The method-
416 ology was designed and validated against calculations based upon the independent column ap-
417 proximation (ICA). A new parameterization for the longwave absorptivity and emissivity of
418 water vapor preserved the formulation of the radiative transfer equations using the absorptiv-
419 ity/emissivity method. The components of the method related to water vapor were replaced with
420 new terms calculated with the General Line-by-line Atmospheric Transmittance and Radiance
421 Model (GENLN3). The mean absolute errors in the surface and top-of-atmosphere clear-sky
422 longwave fluxes for standard atmospheres were reduced to less than 1 W/m². The near-infrared
423 absorption by water vapor was also updated to a parameterization based upon the HITRAN2k
424 line database [\[Rothman et al., 2003\]](#) that incorporated the CKD 2.4 prescription for the con-
425 tinuum. The magnitude of errors in flux divergences and heating rates relative to modern LBL
426 calculations were reduced by approximately seven times compared to the previous CCM3 pa-
427 rameterization. The uniform background aerosol was replaced with a present-day climatology
428 of sulfate, sea-salt, carbonaceous, and soil-dust aerosols. The climatology was obtained from a
429 chemical transport model forced with meteorological analysis and constrained by assimilation of
430 satellite aerosol retrievals. These aerosols affect the shortwave energy budget of the atmosphere.
431 CAM3 also included a mechanism for treating the shortwave and longwave effects of volcanic
432 aerosols. Evaporation of convective precipitation following [Sundqvist \[1988\]](#) was implemented
433 and enhancement of atmospheric moisture through this mechanism was offset by drying intro-
434 duced by changes in the longwave absorptivity and emissivity. A careful formulation of vertical
435 diffusion of dry static energy was also implemented.

436 Additional capabilities included a new thermodynamic package for sea ice in order to mimic
437 the major non-dynamical aspects of CSIM; including snow depth, brine pockets, internal short-
438 wave radiative transfer, surface albedo, ice-atmosphere drag, and surface exchange fluxes. CAM3
439 also allowed for an explicit representation of fractional land and sea-ice coverage that gave a
440 much more accurate representation of flux exchanges from coastal boundaries, island regions,
441 and ice edges. This fractional specification provided a mechanism to account for flux differences
442 due to sub-grid inhomogeneity of surface types. A new, extensible climatological and time-mean
443 sea-surface temperature boundary data was made available from a blended product using the

444 global HadISST OI dataset prior to 1981 and the Smith/Reynolds EOF dataset post-1981. Cou-
445 pling was upgraded in order to couple the dynamical core with the parameterization suite in a
446 purely time split or process split manner. The distinction is that in the process split approx-
447 imation the physics and dynamics are both calculated from the same past state, while in the
448 time split approximations the dynamics and physics are calculated sequentially, each based on
449 the state produced by the other.

450 1.1.5 CAM4

451 The CAM4 was the sixth generation of the NCAR atmospheric GCM and had again been devel-
452 oped through a collaborative process of users and developers in the Atmosphere Model Working
453 Group (AMWG) with significant input from the Chemistry Climate Working Group (Chem-Clim
454 WG) and the Whole Atmosphere Model Working Group (WAMWG). The model had science en-
455 hancements from CAM3 and represented an intermediate release version as part of a staged and
456 parallel process in atmospheric model development. In the CAM4 changes to the moist phys-
457 ical representations centered on enhancements to the existing Zhang and McFarlane [1995] deep
458 convection parameterization. The calculation of Convective Available Potential Energy (CAPE)
459 assumed an entraining plume to provide the in-cloud temperature and humidity profiles used
460 to determine buoyancy and related cloud closure properties (chapter 4.4). The modification is
461 based on the conservation of moist entropy and mixing methods of Raymond and Blyth [1986,
462 1992]. It replaced the standard undilute non-entraining plume method used in CAM3 and was
463 employed to increase convection sensitivity to tropospheric moisture and reduce the amplitude
464 of the diurnal cycle of precipitation over land. Sub-grid scale Convective Momentum Trans-
465 ports (CMT) were added to the deep convection scheme following Richter and Rasch [2008] and
466 the methodology of Gregory et al. [1997b] (chapter 4.4.5). CMT affects tropospheric climate
467 mainly through changes to the Coriolis torque. These changes resulted in improvement of the
468 Hadley circulation during northern Winter and it reduced many of the model biases. In an
469 annual mean, the tropical easterly bias, subtropical westerly bias, and the excessive southern
470 hemisphere mid-latitude jet were improved.

471 In combination these modifications to the deep-convection lead to significant improvements
472 in the phase, amplitude and spacial anomaly patterns of the modeled El Niño, as documented
473 in Neale et al. [2008]. The calculation of cloud fraction in polar climates was also modified for
474 the CAM4.0. Due to the combination of a diagnostic cloud fraction and prognostic cloud water
475 representation it was possible to model unphysical extensive cloud decks with near zero in-cloud
476 water in the CAM3. This was particularly pervasive in polar climates in Winter. These calcula-
477 tion inconsistencies and large cloud fractions are significantly reduced with modifications to the
478 calculation of stratiform cloud following Vavrus and Waliser [2008]. In the lower troposphere a
479 'freeze-drying' process is performed whereby cloud fractions were systematically reduced for very
480 low water vapor amounts. The low cloud reduction caused an Arctic-wide drop of 15 W m^{-2} in
481 surface cloud radiative forcing (CRF) during winter and about a 50% decrease in mean annual
482 Arctic CRF. Consequently, wintertime surface temperatures fell by up to 4 K on land and 2 K
483 over the Arctic Ocean, thus significantly reducing the CAM3 pronounced warm bias. More gen-
484 erally the radiation calculation was performed using inconsistent cloud fraction and condensate
485 quantities in the CAM3. In CAM4 this was remedied with an updated cloud fraction calcula-
486 tion prior to the radiation call at each physics timestep. The coupled climate performance with

487 the CAM4.0 physics changes was summarized in the horizontal resolution comparison study of
488 [Gent et al. \[2009\]](#).

489 For the dynamical core component of CAM4 the finite volume (FV) scheme was made the
490 default due to its superior transport properties [[Lin and Rood, 1996](#)]. Modifications were made
491 that upgraded the code version to a more recent NASA Goddard supported version. Other
492 changes provided new horizontal grid discretizations (e.g., 1.9x2.5 deg and 0.9x1.25 deg) for
493 optimal computational processor decomposition and polar filtering changes for noise reductions
494 and more continuous (in latitude) filtering. In addition to the existing finite volume and spectral-
495 based dynamical core a new option was also made available that represents the first scheme
496 released with CAM that removes the computational scalability restrictions associated with a
497 pole convergent latitude-longitude grid and the associated polar filtering requirements.

498 Funded in part by the Department of Energy (DOE) Climate Change Prediction Program the
499 scalable and efficient spectral-element-based atmospheric dynamical core uses the High Order
500 Method Modeling Environment (HOMME) on a cubed sphere grid and was developed by mem-
501 bers of the Computational Science Section and the Computational Numerics Group of NCAR's
502 Computational and Information Systems Laboratory (CISL). The finite element dynamical core
503 (commonly referred to as the HOMME core) is fully integrated into CCSM coupling architecture
504 and is invaluable for high resolution climate integrations on existing and upcoming massively
505 parallel computing platforms.

506 Model flexibility was increased significantly from the CAM3, both within CAM and the
507 CCSM system as a whole. The method for running thermodynamic sea-ice in CAM-only mode
508 was moved to be maintained entirely within the CICE model of the CCSM4. The single-column
509 version of CAM was given the flexibility to be built and run using the same infrastructure as
510 the CAM build and run mechanism. The SCAM GUI run method was no longer supported.
511 The increased coupling flexibility also allowed the introduction of a more consistent method
512 for performing slab-ocean model (SOM) experiments. SOM experiments were, by default, now
513 performed using forcing data from an existing CCSM coupled run. This had the advantage of
514 having a closed temperature budget for both the ice and the ocean mixed layer from a coupled
515 run. The methodology was therefore configured to reproduce the fully coupled CCSM climate as
516 opposed to a reproduction of a pseudo-observed climate available with the CAM3-specific SOM
517 method. The CAM3-specific SOM method was no longer made available. For more information
518 regarding updated run methods see the CAM4.0 users guide of [Eaton \[2010\]](#).

519 **1.1.6 Overview of CAM 5.0**

520 *The Community Atmosphere Model*

521 CAM has been modified substantially with a range of enhancements and improvements in the
522 representation of physical processes since version 4 (CAM4). In particular, the combination of
523 physical parameterization enhancements makes it possible to simulate full aerosol cloud inter-
524 actions including cloud droplet activation by aerosols, precipitation processes due to particle
525 size dependant behavior and explicit radiative interaction of cloud particles. As such the CAM
526 5.0 represents the first version of CAM that is able to simulate the cloud-aerosol indirect radia-
527 tive effects. More generally CAM 5.0 forms the main atmosphere component of the Community

528 Earth System Model, version 1 (CESM1). The extensive list of physical parameterization im-
529 provements are described below:

530 A new moist turbulence scheme (Section 4.2) is included that explicitly simulates stratus-
531 radiation-turbulence interactions, making it possible to simulate full aerosol indirect effects
532 within stratus. It is based on a diagnostic Turbulent Kinetic Energy (TKE) formulation and
533 uses a 1st order K-diffusion scheme with entrainment [Bretherton and Park, 2009a] originally
534 developed at the University of Washington.. The scheme operates in any layer of the atmosphere
535 when the moist Ri (Richardson number) is larger than its critical value.

536 A new shallow convection scheme (Section 4.3) uses a realistic plume dilution equation
537 and closure that accurately simulates the spatial distribution of shallow convective activity
538 [Park and Bretherton, 2009]. A steady state convective updraft plume and small fractional
539 area are assumed. An explicit computation of the convective updraft vertical velocity and up-
540 draft fraction is performed using an updraft vertical momentum equation, and thus provides
541 a representation of convective momentum transports. The scheme is specifically designed to
542 interact with the new moist turbulence scheme in order to prevent double counting seen in pre-
543 vious CAM parameterizations. The deep convection parameterization is retained from CAM4.0
544 (Section 4.4).

545 Stratiform microphysical processes (Section 4.6) are represented by a prognostic, two-moment
546 formulation for cloud droplet and cloud ice with mass and number concentrations following
547 the original parameterization of Morrison and Gettelman [2008]. The implementation in CAM
548 5.0 [Gettelman et al., 2008] determines liquid and ice particle sizes from gamma functions and
549 their evolution in time is subject to grid-scale advection, convective detrainment, turbulent
550 diffusion and several microphysical processes. Activation of cloud droplets occurs on an aerosol
551 size distribution based on aerosol chemistry, temperature and vertical velocity. A sub-grid
552 scale vertical velocity is provided through a turbulent kinetic energy approximation. A number
553 of mechanisms are calculated for ice crystal nucleation [Liu et al., 2007] and combined with
554 modifications to allow ice supersaturation [Gettelman et al., 2010b].

555 The revised cloud macrophysics scheme (Section 4.7, Park et al. [2010]) provides a more
556 transparent treatment of cloud processes and imposes full consistency between cloud fraction
557 and cloud condensate. Separate calculations are performed for liquid and ice stratiform cloud
558 fractions which are assumed to be maximally overlapped. Liquid cloud fraction is based on
559 an assumed triangular distribution of total relative humidity. Ice cloud fraction is based on
560 Gettelman et al. [2010a] and allows supersaturation via a modified relative humidity over ice
561 and the inclusion of ice condensate amount.

562 A new 3-mode modal aerosol scheme (MAM3, Section 4.8, Liu and Ghan [2010]) provides
563 internally mixed representations of number concentrations and mass for Aitkin, accumulation
564 and coarse aerosol modes which are merged characterizations of the more complex 7-mode ver-
565 sion of the scheme. Anthropogenic emissions, defined as originating from industrial, domestic
566 and agriculture activity sectors, are provided from the Lamarque et al. [2010a] IPCC AR5 emis-
567 sion data set. Emissions of black carbon and organic carbon represent an update of Bond et al.
568 [2007] and Junker and Liousse [2008]. Emissions of sulfur dioxide are an update of Smith et al.
569 [2001, 2004]. Injection heights, and size distribution of emissions data are not provided with the
570 raw datasets so the protocols of [Dentener et al., 2006a] are followed for CAM 5.0. AEROCOM
571 emission datasets are used for natural aerosol sources. All emission datasets required to run
572 MAM for pre-industrial or 20th century scenarios are available for download. A full inventory of

573 observationally based aerosol emission mass and size is provided in standard available datasets.
574 The 7-mode version of the scheme is also available.

575 Calculations and specifications for the condensed phase optics (aerosols, liquid cloud droplets,
576 hydrometeors and ice crystals) are taken from the microphysics and aerosol parameteriza-
577 tion quantities and provided as input to the radiation scheme (Section 4.9). The radiation
578 scheme (Section 4.10) has been updated to the Rapid Radiative Transfer Method for GCMs
579 (RRTMG, Iacono et al. [2008]; Mlawer et al. [1997]). It employs an efficient and accurate mod-
580 ified correlated-k method for calculating radiative fluxes and heating rates in the clear sky and
581 for the condensed phase species. For each short-wave band calculation extinction optical depth,
582 single scattering albedo and asymmetry properties are specified. For each long-wave band mass-
583 specific absorption is specified. The aerosol optical properties are defined for each mode of the
584 MAM as described by [Ghan and Zaveri, 2007]. Hygroscopicity characteristics are specified for
585 soluble species. For volcanic aerosols a geometric mean radius is used. Optical properties of
586 aerosols are combined prior to the radiative calculation. Liquid-cloud optics are calculated fol-
587 lowing Wiscombe [1996] and ice-cloud optics are calculated following Mitchell [2002]. Ice-cloud
588 size optics are extended to allow for radiatively active falling snow. Optical properties of clouds
589 (including separate fractions and in-cloud water contents) are combined prior to the radiative cal-
590 culation. RRTM separates the short-wave spectrum into 14 bands extending from 0.2 μm to 12.2
591 μm , and models sources of extinction for H_2O , O_3 , CO_2 , O_2 , CH_4 , N_2 and Rayleigh scattering.
592 Solar irradiance is now specified for the short-wave bands from the Lean dataset [Wang et al.,
593 2005]. The long-wave spectrum is separated into 16 bands extending from 3.1 μm to 1000 μm
594 with molecular sources of absorption for the same species, in addition to CFC-11 (containing
595 multiple CFC species) and CFC-12. RRTMG has extensive modifications from the original
596 RRTM in order to provide significant speed-up for long climate integrations. Chief amongst
597 these is the Monte-Carlo Independent Column Approximation (McICA, Pincus and Morcrette
598 [2003]) that represents sub-grid scale cloud variability. With these modifications RRTMG still
599 retains superior offline agreement with line-by-line calculations when compared to the previous
600 CAM radiation package (CAM-RT).

601 *The CAM Chemistry Model (CAM-CHEM)*

602 Chemistry in CAM is now fully interactive and implemented in CESM (Section 5.1); in particu-
603 lar, emissions of biogenic compounds and deposition of aerosols to snow, ice, ocean and vegeta-
604 tion are handled through the coupler. The released version of CAM-chem in CESM is using the
605 recently-developed superfast chemistry (Section 5.2), in collaboration with P. Cameron-Smith
606 from LLNL and M. Prather from UCI) to perform centennial scale simulations at a minor cost
607 increase over the base CAM4. These simulations use the recently developed 1850-2005 emissions
608 created in support of CMIP5.

609 *The Whole Atmosphere Community Climate Model (WACCM)*

610 WACCM4 (Section 5.3), incorporates several improvements and enhancements over the previous
611 version (3.1.9). It can be run coupled to the POP2 and CICE CESM model components. The
612 model's chemistry module (Section 5.1) has been updated according to the latest JPL-2006 rec-
613 ommendations; a quasi-biennial oscillation may be imposed (as an option) by relaxing the winds

614 to observations in the Tropics; heating from stratospheric volcanic aerosols is now computed ex-
615 plicitly; the effects of solar proton events are now included; the effect of unresolved orography is
616 parameterized as a surface stress (turbulent mountain stress) leading to an improvement in the
617 frequency of sudden stratospheric warmings; and gravity waves due to convective and frontal
618 sources are parameterized based upon the occurrence of convection and the diagnosis of regions
619 of frontogenesis in the model.

Chapter 2

Coupling of Dynamical Core and Parameterization Suite

The CAM 5.0 cleanly separates the parameterization suite from the dynamical core, and makes it easier to replace or modify each in isolation. The dynamical core can be coupled to the parameterization suite in a purely time split manner or in a purely process split one, as described below.

Consider the general prediction equation for a generic variable ψ ,

$$\frac{\partial\psi}{\partial t} = D(\psi) + P(\psi) , \quad (2.1)$$

where ψ denotes a prognostic variable such as temperature or horizontal wind component. The dynamical core component is denoted D and the physical parameterization suite P .

A three-time-level notation is employed which is appropriate for the semi-implicit Eulerian spectral transform dynamical core. However, the numerical characteristics of the physical parameterizations are more like those of diffusive processes rather than advective ones. They are therefore approximated with forward or backward differences, rather than centered three-time-level forms.

The *Process Split* coupling is approximated by

$$\psi^{n+1} = \psi^{n-1} + 2\Delta t D(\psi^{n+1}, \psi^n, \psi^{n-1}) + 2\Delta t P(\psi^*, \psi^{n-1}) , \quad (2.2)$$

where $P(\psi^*, \psi^{n-1})$ is calculated first from

$$\psi^* = \psi^{n-1} + 2\Delta t P(\psi^*, \psi^{n-1}) . \quad (2.3)$$

The *Time Split* coupling is approximated by

$$\psi^* = \psi^{n-1} + 2\Delta t D(\psi^*, \psi^n, \psi^{n-1}) , \quad (2.4)$$

$$\psi^{n+1} = \psi^* + 2\Delta t P(\psi^{n+1}, \psi^*) . \quad (2.5)$$

The distinction is that in the *Process Split* approximation the calculations of D and P are both based on the same past state, ψ^{n-1} , while in the *Time Split* approximations D and P are calculated sequentially, each based on the state produced by the other.

637 As mentioned above, the Eulerian core employs the three-time-level notation in (2.2)-(2.5).
 638 Eqns. (2.2)-(2.5) also apply to two-time-level finite volume, semi-Lagrangian and spectral ele-
 639 ment (HOMME) cores by dropping centered n term dependencies, and replacing $n-1$ by n and
 640 $2\Delta t$ by Δt .

The parameterization package can be applied to produce an updated field as indicated in (2.3) and (2.5). Thus (2.5) can be written with an operator notation

$$\psi^{n+1} = \mathbf{P}(\psi^*) , \quad (2.6)$$

where only the past state is included in the operator dependency for notational convenience. The implicit predicted state dependency is understood. The *Process Split* equation (2.2) can also be written in operator notation as

$$\psi^{n+1} = \mathbf{D} \left(\psi^{n-1}, \frac{\mathbf{P}(\psi^{n-1}) - \psi^{n-1}}{2\Delta t} \right) , \quad (2.7)$$

where the first argument of \mathbf{D} denotes the prognostic variable input to the dynamical core and the second denotes the forcing rate from the parameterization package, e.g. the heating rate in the thermodynamic equation. Again only the past state is included in the operator dependency, with the implicit predicted state dependency left understood. With this notation the *Time Split* system (2.5) and (2.5) can be written

$$\psi^{n+1} = \mathbf{P}(\mathbf{D}(\psi^{n-1}, 0)) . \quad (2.8)$$

The total parameterization package in CAM 5.0 consists of a sequence of components, indicated by

$$P = \{M, R, S, T\} , \quad (2.9)$$

641 where M denotes (Moist) precipitation processes, R denotes clouds and Radiation, S denotes the
 642 Surface model, and T denotes Turbulent mixing. Each of these in turn is subdivided into various
 643 components: M includes an optional dry adiabatic adjustment (normally applied only in the
 644 stratosphere), moist penetrative convection, shallow convection, and large-scale stable conden-
 645 sation; R first calculates the cloud parameterization followed by the radiation parameterization;
 646 S provides the surface fluxes obtained from land, ocean and sea ice models, or calculates them
 647 based on specified surface conditions such as sea surface temperatures and sea ice distribution.
 648 These surface fluxes provide lower flux boundary conditions for the turbulent mixing T which
 649 is comprised of the planetary boundary layer parameterization, vertical diffusion, and gravity
 650 wave drag.

651 Defining operators following (2.6) for each of the parameterization components, the couplings
 652 in CAM 5.0 are summarized as:

TIME SPLIT

$$\psi^{n+1} = \mathbf{T}(\mathbf{S}(\mathbf{R}(\mathbf{M}(\mathbf{D}(\psi^{n-1}, 0)))))) \quad (2.10)$$

PROCESS SPLIT

$$\psi^{n+1} = \mathbf{D} \left(\psi^{n-1}, \frac{\mathbf{T}(\mathbf{S}(\mathbf{R}(\mathbf{M}(\psi^{n-1})))) - \psi^{n-1}}{2\Delta t} \right) \quad (2.11)$$

653 The labels *Time Split* and *Process Split* refer to the coupling of the dynamical core with the
654 complete parameterization suite. The components within the parameterization suite are coupled
655 via time splitting in both forms.

656 The *Process Split* form is convenient for spectral transform models. With *Time Split* approx-
657 imations extra spectral transforms are required to convert the updated momentum variables
658 provided by the parameterizations to vorticity and divergence for the Eulerian spectral core, or
659 to recalculate the temperature gradient for the semi-Lagrangian spectral core. The *Time Split*
660 form is convenient for the finite-volume core which adopts a Lagrangian vertical coordinate.
661 Since the scheme is explicit and restricted to small time-steps by its non-advective component,
662 it sub-steps the dynamics multiple times during a longer parameterization time step. With
663 *Process Split* approximations the forcing terms must be interpolated to an evolving Lagrangian
664 vertical coordinate every sub-step of the dynamical core. Besides the expense involved, it is not
665 completely obvious how to interpolate the parameterized forcing, which can have a vertical grid
666 scale component arising from vertical grid scale clouds, to a different vertical grid. [Williamson,
667 2002] compares simulations with the Eulerian spectral transform dynamical core coupled to the
668 CCM3 parameterization suite via *Process Split* and *Time Split* approximations.

Chapter 3

Dynamics

3.1 Finite Volume Dynamical Core

3.1.1 Overview

This document describes the Finite-Volume (FV) dynamical core that was initially developed and used at the NASA Data Assimilation Office (DAO) for data assimilation, numerical weather predictions, and climate simulations. The finite-volume discretization is local and entirely in physical space. The horizontal discretization is based on a conservative “flux-form semi-Lagrangian” scheme described by Lin and Rood [1996] (hereafter LR96) and Lin and Rood [1997] (hereafter LR97). The vertical discretization can be best described as *Lagrangian* with a conservative re-mapping, which essentially makes it *quasi-Lagrangian*. The *quasi-Lagrangian* aspect of the vertical coordinate is transparent to model users or physical parameterization developers, and it functions exactly like the η – coordinate (a hybrid $\sigma - p$ coordinate) used by other dynamical cores within CAM.

In the current implementation for use in CAM, the FV dynamics and physics are “time split” in the sense that all prognostic variables are updated sequentially by the “dynamics” and then the “physics”. The time integration within the FV dynamics is fully explicit, with sub-cycling within the 2D Lagrangian dynamics to stabilize the fastest wave (see section 3.1.4). The transport for tracers, however, can take a much larger time step (*e.g.*, 30 minutes as for the physics).

3.1.2 The governing equations for the hydrostatic atmosphere

For reference purposes, we present the continuous differential equations for the hydrostatic 3D atmospheric flow on the sphere for a general vertical coordinate ζ (*e.g.*, Kasahara [1974]). Using standard notations, the hydrostatic balance equation is given as follows:

$$\frac{1}{\rho} \frac{\partial p}{\partial \zeta} + g = 0, \quad (3.1)$$

where ρ is the density of the air, p the pressure, and g the gravitational constant. Introducing the “pseudo-density” $\pi = \frac{\partial p}{\partial \zeta}$ (*i.e.*, the vertical pressure gradient in the general coordinate), from the hydrostatic balance equation the *pseudo-density* and the true density are related as follows:

$$\pi = -\frac{\partial\Phi}{\partial\zeta}\rho, \quad (3.2)$$

696 where $\Phi = gz$ is the geopotential. Note that π reduces to the “true density” if $\zeta = -gz$, and
 697 the “surface pressure” P_s if $\zeta = \sigma$ ($\sigma = \frac{p}{P_s}$). The conservation of total air mass using π as the
 698 prognostic variable can be written as

$$\frac{\partial}{\partial t}\pi + \nabla \cdot (\vec{V}\pi) = 0, \quad (3.3)$$

699 where $\vec{V} = (u, v, \frac{d\zeta}{dt})$. Similarly, the mass conservation law for tracer species (or water vapor)
 700 can be written as

$$\frac{\partial}{\partial t}(\pi q) + \nabla \cdot (\vec{V}\pi q) = 0, \quad (3.4)$$

701 where q is the mass mixing ratio (or specific humidity) of the tracers (or water vapor).

702 Choosing the (virtual) potential temperature Θ as the thermodynamic variable, the first law
 703 of thermodynamics is written as

$$\frac{\partial}{\partial t}(\pi\Theta) + \nabla \cdot (\vec{V}\pi\Theta) = 0. \quad (3.5)$$

704 Letting (λ, θ) denote the (longitude, latitude) coordinate, the momentum equations can be
 705 written in the “vector-invariant form” as follows:

$$\frac{\partial}{\partial t}u = \Omega v - \frac{1}{A\cos\theta} \left[\frac{\partial}{\partial\lambda} (\kappa + \Phi - \nu D) + \frac{1}{\rho} \frac{\partial}{\partial\lambda} p \right] - \frac{d\zeta}{dt} \frac{\partial u}{\partial\zeta}, \quad (3.6)$$

$$\frac{\partial}{\partial t}v = -\Omega u - \frac{1}{A} \left[\frac{\partial}{\partial\theta} (\kappa + \Phi - \nu D) + \frac{1}{\rho} \frac{\partial}{\partial\theta} p \right] - \frac{d\zeta}{dt} \frac{\partial v}{\partial\zeta}, \quad (3.7)$$

where A is the radius of the earth, ν is the coefficient for the optional divergence damping, D
 is the horizontal divergence

$$D = \frac{1}{A\cos\theta} \left[\frac{\partial}{\partial\lambda}(u) + \frac{\partial}{\partial\theta}(v\cos\theta) \right],$$

$$\kappa = \frac{1}{2} (u^2 + v^2),$$

706 and Ω , the vertical component of the absolute vorticity, is defined as follows:

$$\Omega = 2\omega \sin\theta + \frac{1}{A\cos\theta} \left[\frac{\partial}{\partial\lambda}v - \frac{\partial}{\partial\theta}(u\cos\theta) \right],$$

707 where ω is the angular velocity of the earth. Note that the last term in (3.6) and (3.7) vanishes
 708 if the vertical coordinate ζ is a conservative quantity (*e.g.*, entropy under adiabatic conditions
 709 [Hsu and Arakawa, 1990] or an imaginary conservative tracer), and the 3D divergence opera-
 710 tor becomes 2D along constant ζ surfaces. The discretization of the 2D horizontal transport
 711 process is described in section 3.1.3. The complete dynamical system using the Lagrangian
 712 control-volume vertical discretization is described in section 3.1.4 and section 3.1.5 describes

713 the explicit diffusion operators available in CAM5. A mass, momentum, and total energy con-
 714 servative mapping algorithm is described in section 3.1.6 and in section 3.1.7 an alternative
 715 geopotential conserving vertical remapping method is described. Sections 3.1.8 and 3.1.9 are on
 716 the adjustment of pressure to include the change in mass of water vapor and on the negative
 717 tracer fixer in CAM, respectively. Last the global energy fixer is described (section 3.1.10).

718 3.1.3 Horizontal discretization of the transport process on the sphere

719 Since the vertical transport term would vanish after the introduction of the vertical Lagrangian
 720 control-volume discretization (see section 3.1.4), we shall present here only the 2D (horizontal)
 721 forms of the FFSL transport algorithm for the transport of density (3.3) and mixing ratio-like
 722 quantities (3.4) on the sphere. The governing equation for the pseudo-density (3.3) becomes

$$\frac{\partial}{\partial t} \pi + \frac{1}{A \cos \theta} \left[\frac{\partial}{\partial \lambda} (u \pi) + \frac{\partial}{\partial \theta} (v \pi \cos \theta) \right] = 0. \quad (3.8)$$

723 The finite-volume (*integral*) representation of the continuous π field is defined as follows:

$$\tilde{\pi}(t) \equiv \frac{1}{A^2 \Delta \theta \Delta \lambda \cos \theta} \iint \pi(t; \lambda, \theta) A^2 \cos \theta \, d\theta \, d\lambda. \quad (3.9)$$

724 Given the *exact* 2D wind field $\vec{V}(t; \lambda, \theta) = (U, V)$ the 2D integral representation of the conser-
 725 vation law for $\tilde{\pi}$ can be obtained by integrating (3.8) in time and in space

$$\tilde{\pi}^{n+1} = \tilde{\pi}^n - \frac{1}{A^2 \Delta \theta \Delta \lambda \cos \theta} \int_t^{t+\Delta t} \left[\oint \pi(t; \lambda, \theta) \vec{V} \cdot \vec{n} \, dl \right] dt. \quad (3.10)$$

726

727 The above 2D transport equation is still *exact for the finite-volume under consideration*. To
 728 carry out the contour integral, certain approximations must be made. LR96 essentially decom-
 729 posed the flux integral using two orthogonal 1D flux-form transport operators. Introducing the
 730 following difference operator

$$\delta_x q = q\left(x + \frac{\Delta x}{2}\right) - q\left(x - \frac{\Delta x}{2}\right),$$

731 and assuming (u^*, v^*) is the time-averaged (from time t to time $t + \Delta t$) \vec{V} on the C-grid (*e.g.*,
 732 Fig. 1 in LR96), the 1-D finite-volume flux-form transport operator F in the λ -direction is

$$F(u^*, \Delta t, \tilde{\pi}) = -\frac{1}{A \Delta \lambda \cos \theta} \delta_\lambda \left[\int_t^{t+\Delta t} \pi U \, dt \right] = -\frac{\Delta t}{A \Delta \lambda \cos \theta} \delta_\lambda [\chi(u^*, \Delta t; \pi)], \quad (3.11)$$

733 where χ , the time-accumulated (from t to $t + \Delta t$) mass flux across the cell wall, is defined as
 734 follows,

$$\chi(u^*, \Delta t; \pi) = \frac{1}{\Delta t} \int_t^{t+\Delta t} \pi U \, dt \equiv u^* \pi^*(u^*, \Delta t, \tilde{\pi}), \quad (3.12)$$

and

$$\pi^*(u^*, \Delta t; \tilde{\pi}) \approx \frac{1}{\Delta t} \int_t^{t+\Delta t} \pi dt \quad (3.13)$$

735 can be interpreted as a time mean (from time t to time $t + \Delta t$) pseudo-density value of all
 736 material that passed through the cell edge from the upwind direction.

737 Note that the above *time integration* is to be carried out along the *backward-in-time* trajec-
 738 tory of the cell edge position from $t = t + \Delta t$ (the arrival point; *e.g.*, point B in Fig. 3 of LR96)
 739 back to time t (the departure point; *e.g.*, point B' in Fig. 3 of LR96). The very essence of the
 740 1D finite-volume algorithm is to construct, based on the given initial cell-mean values of $\tilde{\pi}$, an
 741 approximated subgrid distribution of the true π field, to enable an analytic integration of (3.13).
 742 Assuming there is no error in obtaining the time-mean wind (u^*), the only error produced by the
 743 1D transport scheme would be solely due to the approximation to the continuous distribution
 744 of π within the subgrid under consideration (this is not the case in 2D; Lauritzen et al. [2010]).
 745 From this perspective, it can be said that the 1D finite-volume transport algorithm combines
 746 the time-space discretization in the approximation of the time-mean cell-edge values π^* . The
 747 physically correct way of approximating the integral (3.13) must be “upwind”, in the sense that
 748 it is integrated along the backward trajectory of the cell edges. For example, a center difference
 749 approximation to (3.13) would be physically incorrect, and consequently numerically unstable
 750 unless artificial numerical diffusion is added.

751 Central to the accuracy and computational efficiency of the finite-volume algorithms is the
 752 degrees of freedom that describe the subgrid distribution. The first order upwind scheme, for
 753 example, has zero degrees of freedom within the volume as it is assumed that the subgrid distri-
 754 bution is piecewise constant having the same value as the given volume-mean. The second order
 755 finite-volume scheme (*e.g.*, Lin et al. [1994]) assumes a piece-wise linear subgrid distribution,
 756 which allows one degree of freedom for the specification of the “slope” of the linear distribu-
 757 tion to improve the accuracy of integrating (3.13). The Piecewise Parabolic Method (PPM,
 758 Colella and Woodward [1984]) has two degrees of freedom in the construction of the second or-
 759 der polynomial within the volume, and as a result, the accuracy is significantly enhanced. The
 760 PPM appears to strike a good balance between computational efficiency and accuracy. There-
 761 fore, the PPM is the basic 1D scheme we chose (see, *e.g.*, Machenhauer [1998]). Note that the
 762 subgrid PPM distributions are compact, and do not extend beyond the volume under consider-
 763 ation. The accuracy is therefore significantly better than the order of the chosen polynomials
 764 implies. While the PPM scheme possesses all the desirable attributes (mass conserving, mono-
 765 tonicity preserving, and high-order accuracy) in 1D, it is important that a solution be found to
 766 avoid the directional splitting in the multi-dimensional problem of modeling the dynamics and
 767 transport processes of the Earth’s atmosphere.

768 The first step for reducing the splitting error is to apply the two orthogonal 1D flux-form
 769 operators in a directionally symmetric way. After symmetry is achieved, the “inner operators”
 770 are then replaced with corresponding advective-form operators (in CAM5 the “inner operators”
 771 are based on constant cell-average values and not the PPM). A stability analysis of the conse-
 772 quences of using different inner and outer operators in the LR96 scheme is given in Lauritzen
 773 [2007]. A consistent advective-form operator in the λ -direction can be derived from its flux-form
 774 counterpart (F) as follows:

$$f(u^*, \Delta t, \tilde{\pi}) = F(u^*, \Delta t, \tilde{\pi}) + \tilde{\rho} F(u^*, \Delta t, \tilde{\pi} \equiv 1) = F(u^*, \Delta t, \tilde{\pi}) + \tilde{\pi} C_{def}^\lambda, \quad (3.14)$$

$$C_{def}^\lambda = \frac{\Delta t \delta_\lambda u^*}{A \Delta \lambda \cos \theta}, \quad (3.15)$$

775 where C_{def}^λ is a dimensionless number indicating the degree of the flow deformation in the λ -
 776 direction. The above derivation of f is slightly different from LR96's approach, which adopted
 777 the traditional 1D advective-form semi-Lagrangian scheme. The advantage of using (3.14) is
 778 that computation of winds at cell centers (Eq. 2.25 in LR96) are avoided.

Analogously, the 1D flux-form transport operator G in the latitudinal (θ) direction is derived as follows:

$$G(v^*, \Delta t, \tilde{\pi}) = -\frac{1}{A \Delta \theta \cos \theta} \delta_\theta \left[\int_t^{t+\Delta t} \pi V \cos \theta dt \right] = -\frac{\Delta t}{A \Delta \theta \cos \theta} \delta_\theta [v^* \cos \theta \pi^*], \quad (3.16)$$

and likewise the advective-form operator,

$$g(v^*, \Delta t, \tilde{\pi}) = G(v^*, \Delta t, \tilde{\pi}) + \tilde{\pi} C_{def}^\theta, \quad (3.17)$$

where

$$C_{def}^\theta = \frac{\Delta t \delta_\theta [v^* \cos \theta]}{A \Delta \theta \cos \theta}. \quad (3.18)$$

779 To complete the construction of the 2D algorithm on the sphere, we introduce the following
 780 short hand notations:

$$()^\theta = ()^n + \frac{1}{2} g[v^*, \Delta t, ()^n], \quad (3.19)$$

$$()^\lambda = ()^n + \frac{1}{2} f[u^*, \Delta t, ()^n]. \quad (3.20)$$

The 2D transport algorithm (*cf.* Eq. 2.24 in LR96) can then be written as

$$\tilde{\pi}^{n+1} = \tilde{\pi}^n + F[u^*, \Delta t, \tilde{\pi}^\theta] + G[v^*, \Delta t, \tilde{\pi}^\lambda]. \quad (3.21)$$

Using explicitly the mass fluxes (χ, Y), (3.21) is rewritten as

$$\tilde{\pi}^{n+1} = \tilde{\pi}^n - \frac{\Delta t}{A \cos \theta} \left\{ \frac{1}{\Delta \lambda} \delta_\lambda [\chi(u^*, \Delta t; \tilde{\pi}^\theta)] + \frac{1}{\Delta \theta} \delta_\theta [\cos \theta Y(v^*, \Delta t; \tilde{\pi}^\lambda)] \right\}, \quad (3.22)$$

781 where Y , the mass flux in the meridional direction, is defined in a similar fashion as χ (3.12). The
 782 ability of the LR96 scheme to approximate the exact geometry of the fluxes for deformational
 783 flows is discussed in Machenhauer et al. [2009] and Lauritzen et al. [2010].

It can be verified that in the special case of constant density flow ($\tilde{\pi} = \text{constant}$) the above equation degenerates to the finite-difference representation of the *incompressibility condition* of the “time mean” wind field (u^*, v^*), *i.e.*,

$$\frac{1}{\Delta \lambda} \delta_\lambda u^* + \frac{1}{\Delta \theta} \delta_\theta (v^* \cos \theta) = 0. \quad (3.23)$$

The fulfillment of the above *incompressibility condition* for constant density flows is crucial to the accuracy of the 2D flux-form formulation. For transport of volume mean mixing ratio-like quantities (\tilde{q}) the mass fluxes (χ, Y) as defined previously should be used as follows

$$\tilde{q}^{n+1} = \frac{1}{\tilde{\pi}^{n+1}} [\tilde{\pi}^n \tilde{q}^n + F(\chi, \Delta t, \tilde{q}^\theta) + G(Y, \Delta t, \tilde{q}^\lambda)]. \quad (3.24)$$

784 Note that the above form of the tracer transport equation consistently degenerates to (3.21) if
 785 $\tilde{q} \equiv 1$ (*i.e.*, the tracer density equals to the background air density), which is another important
 786 condition for a flux-form transport algorithm to be able to avoid generation of noise (*e.g.*,
 787 creation of artificial gradients) and to maintain mass conservation.

788 **3.1.4 A vertically Lagrangian and horizontally Eulerian control-** 789 **volume discretization of the hydrodynamics**

790 The very idea of using Lagrangian vertical coordinate for formulating governing equations for
 791 the atmosphere is not entirely new. Starr [1945]) is likely the first to have formulated, in the
 792 *continuous differential form*, the governing equations using a Lagrangian coordinate. Starr did
 793 not make use of the *discrete* Lagrangian control-volume concept for discretization nor did he
 794 present a solution to the problem of computing the pressure gradient forces. In the *finite-volume*
 795 *discretization* to be described here, the Lagrangian surfaces are treated as the bounding material
 796 surfaces of the Lagrangian control-volumes within which the finite-volume algorithms developed
 797 in LR96, LR97, and L97 will be directly applied.

798 To use a vertical Lagrangian coordinate system to reduce the 3D governing equations to the
 799 2D forms, one must first address the issue of whether it is an inertial coordinate or not. For
 800 hydrostatic flows, it is. This is because both the right-hand-side and the left-hand-side of the
 801 vertical momentum equation vanish for purely hydrostatic flows.

802 Realizing that the earth’s surface, for all practical modeling purposes, can be regarded as
 803 a non-penetrable material surface, it becomes straightforward to construct a terrain-following
 804 Lagrangian control-volume coordinate system. In fact, any commonly used terrain-following
 805 coordinates can be used as the starting reference (*i.e.*, fixed, Eulerian coordinate) of the floating
 806 Lagrangian coordinate system. To close the coordinate system, the model top (at a prescribed
 807 constant pressure) is also assumed to be a Lagrangian surface, which is the same assumption
 808 being used by practically all global hydrostatic models.

809 The basic idea is to start the time marching from the chosen terrain-following Eulerian coordi-
 810 nate (*e.g.*, pure σ or hybrid σ - p), *treating the initial coordinate surfaces as material surfaces*,
 811 the finite-volumes bounded by two coordinate surfaces, *i.e.*, the Lagrangian control-volumes,
 812 are free vertically, to float, compress, or expand with the flow as dictated by the hydrostatic
 813 dynamics.

By choosing an imaginary conservative tracer ζ that is a monotonic function of height and constant on the initial reference coordinate surfaces (*e.g.*, the value of “ η ” in the hybrid $\sigma - p$ coordinate used in CAM), the 3D governing equations written for the general vertical coordinate in section 1.2 can be reduced to 2D forms. After factoring out the constant $\delta\zeta$, (3.3), the conservation law for the pseudo-density ($\pi = \frac{\delta p}{\delta\zeta}$), becomes

$$\frac{\partial}{\partial t} \delta p + \frac{1}{A \cos \theta} \left[\frac{\partial}{\partial \lambda} (u \delta p) + \frac{\partial}{\partial \theta} (v \delta p \cos \theta) \right] = 0, \quad (3.25)$$

814 where the symbol δ represents the vertical difference between the two neighboring Lagrangian
815 surfaces that bound the finite control-volume. From (3.1), the pressure thickness δp of that
816 control-volume is proportional to the total mass, *i.e.*, $\delta p = -\rho g \delta z$. Therefore, it can be said
817 that the Lagrangian control-volume vertical discretization has the hydrostatic balance built-in,
818 and δp can be regarded as the “pseudo-density” for the discretized Lagrangian vertical coordinate
819 system.

Similarly, (3.4), the mass conservation law for all tracer species, is

$$\frac{\partial}{\partial t}(q\delta p) + \frac{1}{A\cos\theta} \left[\frac{\partial}{\partial\lambda}(uq\delta p) + \frac{\partial}{\partial\theta}(vq\delta p \cos\theta) \right] = 0, \quad (3.26)$$

820 the thermodynamic equation, (3.5), becomes

$$\frac{\partial}{\partial t}(\Theta\delta p) + \frac{1}{A\cos\theta} \left[\frac{\partial}{\partial\lambda}(u\Theta\delta p) + \frac{\partial}{\partial\theta}(v\Theta\delta p \cos\theta) \right] = 0, \quad (3.27)$$

and (3.6) and (3.7), the momentum equations, are reduced to

$$\frac{\partial}{\partial t}u = \Omega v - \frac{1}{A\cos\theta} \left[\frac{\partial}{\partial\lambda}(\kappa + \Phi - \nu D) + \frac{1}{\rho} \frac{\partial}{\partial\lambda}p \right], \quad (3.28)$$

$$\frac{\partial}{\partial t}v = -\Omega u - \frac{1}{A} \left[\frac{\partial}{\partial\theta}(\kappa + \Phi - \nu D) + \frac{1}{\rho} \frac{\partial}{\partial\theta}p \right]. \quad (3.29)$$

Given the prescribed pressure at the model top P_∞ , the position of each Lagrangian surface P_l (horizontal subscripts omitted) is determined in terms of the hydrostatic pressure as follows:

$$P_l = P_\infty + \sum_{k=1}^l \delta P_k, \quad (\text{for } l = 1, 2, 3, \dots, N), \quad (3.30)$$

821 where the subscript l is the vertical index ranging from 1 at the lower bounding Lagrangian
822 surface of the first (the highest) layer to N at the Earth’s surface. There are $N+1$ Lagrangian
823 surfaces to define a total number of N Lagrangian layers. The surface pressure, which is the
824 pressure at the lowest Lagrangian surface, is easily computed as P_N using (3.30). The sur-
825 face pressure is needed for the physical parameterizations and to define the reference Eulerian
826 coordinate for the mapping procedure (to be described in section 3.1.6).

827 With the exception of the pressure-gradient terms and the addition of a thermodynamic
828 equation, the above 2D Lagrangian dynamical system is the same as the shallow water system
829 described in LR97. The conservation law for the depth of fluid h in the shallow water system of
830 LR97 is replaced by (3.25) for the pressure thickness δp . The ideal gas law, the mass conservation
831 law for air mass, the conservation law for the potential temperature (3.27), together with the
832 modified momentum equations (3.28) and (3.29) close the 2D Lagrangian dynamical system,
833 which are vertically coupled only by the hydrostatic relation (see (3.54), section 3.1.6).

834 The time marching procedure for the 2D Lagrangian dynamics follows closely that of the
835 shallow water dynamics fully described in LR97. For computational efficiency, we shall take
836 advantage of the stability of the FFSL transport algorithm by using a much larger time step
837 (Δt) for the transport of all tracer species (including water vapor). As in the shallow water

838 system, the Lagrangian dynamics uses a relatively small time step, $\Delta\tau = \Delta t/m$, where m is
 839 the number of the sub-cycling needed to stabilize the fastest wave in the system. We shall
 840 describe here this time-split procedure for the *prognostic variables* $[\delta p, \Theta, u, v; q]$ on the D-grid.
 841 Discretization on the C-grid for obtaining the *diagnostic variables*, the time-averaged winds
 842 (u^*, v^*) , is analogous to that of the D-grid (see also LR97).

Introducing the following short hand notations (*cf.* (3.19) and (3.20)):

$$\begin{aligned} ()_i^\theta &= ()^{n+\frac{i-1}{m}} + \frac{1}{2}g[v_i^*, \Delta\tau, ()^{n+\frac{i-1}{m}}], \\ ()_i^\lambda &= ()^{n+\frac{i-1}{m}} + \frac{1}{2}f[u_i^*, \Delta\tau, ()^{n+\frac{i-1}{m}}], \end{aligned}$$

and applying directly (3.22), the update of “pressure thickness” δp , using the fractional time step $\Delta\tau = \Delta t/m$, can be written as

$$\delta p^{n+\frac{i}{m}} = \delta p^{n+\frac{i-1}{m}} - \frac{\Delta\tau}{A\cos\theta} \left\{ \frac{1}{\Delta\lambda}\delta_\lambda [x_i^*(u_i^*, \Delta\tau; \delta p_i^\theta)] + \frac{1}{\Delta\theta}\delta_\theta [\cos\theta y_i^*(v_i^*, \Delta\tau; \delta p_i^\lambda)] \right\} \quad (3.31)$$

(*for* $i = 1, \dots, m$),

where $[x_i^*, y_i^*]$ are the background air mass fluxes, which are then used as input to Eq. 24 for transport of the potential temperature Θ :

$$\Theta^{n+\frac{i}{m}} = \frac{1}{\delta p^{n+\frac{i}{m}}} \left[\delta p^{n+\frac{i-1}{m}} \Theta^{n+\frac{i-1}{m}} + F(x_i^*, \Delta\tau; \Theta_i^\theta) + G(y_i^*, \Delta\tau, \Theta_i^\lambda) \right]. \quad (3.32)$$

The discretized momentum equations for the shallow water system (*cf.* Eq. 16 and Eq. 17 in LR97) are modified for the pressure gradient terms as follows:

$$u^{n+\frac{i}{m}} = u^{n+\frac{i-1}{m}} + \Delta\tau \left[y_i^*(v_i^*, \Delta\tau; \Omega^\lambda) - \frac{1}{A\Delta\lambda\cos\theta}\delta_\lambda(\kappa^* - \nu D^*) + \widehat{P}_\lambda \right], \quad (3.33)$$

$$v^{n+\frac{i}{m}} = v^{n+\frac{i-1}{m}} - \Delta\tau \left[x_i^*(u_i^*, \Delta\tau; \Omega^\theta) + \frac{1}{A\Delta\theta}\delta_\theta(\kappa^* - \nu D^*) - \widehat{P}_\theta \right], \quad (3.34)$$

where κ^* is the upwind-biased “kinetic energy” (as defined by Eq. 18 in LR97), and D^* , the horizontal divergence on the D-grid, is discretized as follows:

$$D^* = \frac{1}{A\cos\theta} \left[\frac{1}{\Delta\lambda}\delta_\lambda u^{n+\frac{i-1}{m}} + \frac{1}{\Delta\theta}\delta_\theta \left(v^{n+\frac{i-1}{m}} \cos\theta \right) \right].$$

The finite-volume mean pressure-gradient terms in (3.33) and (3.34) are computed as follows:

$$\widehat{P}_\lambda = \frac{\oint_{\Pi=\lambda} \phi d\Pi}{A\cos\theta \oint_{\Pi=\lambda} \Pi d\lambda}, \quad (3.35)$$

$$\widehat{P}_\theta = \frac{\oint_{\Pi=\theta} \phi d\Pi}{A \oint_{\Pi=\theta} \Pi d\theta}, \quad (3.36)$$

843 where $\Pi = p^\kappa$ ($\kappa = R/C_p$), and the symbols “ $\Pi \rightleftharpoons \lambda$ ” and “ $\Pi \rightleftharpoons \theta$ ” indicate that the contour
 844 integrations are to be carried out, using the finite-volume algorithm described in L97, in the
 845 (Π, λ) and (Π, θ) space, respectively.

846 To complete one time step, equations (3.31-3.34), together with their counterparts on the
 847 C-grid are cycled m times using the fractional time step $\Delta\tau$, which are followed by the tracer
 848 transport using (3.26) with the large-time-step Δt .

Mass fluxes (x^*, y^*) and the winds (u^*, v^*) on the C-grid are accumulated for the large-time-
 step transport of tracer species (including water vapor) q as

$$q^{n+1} = \frac{1}{\delta p^{n+1}} [q^n \delta p^n + F(X^*, \Delta t, q^\theta) + G(Y^*, \Delta t, q^\lambda)], \quad (3.37)$$

where the time-accumulated mass fluxes (X^*, Y^*) are computed as

$$X^* = \sum_{i=1}^m x_i^*(u_i^*, \Delta\tau, \delta p_i^\theta), \quad (3.38)$$

$$Y^* = \sum_{i=1}^m y_i^*(v_i^*, \Delta\tau, \delta p_i^\lambda). \quad (3.39)$$

849 The time-averaged winds (U^*, V^*) , defined as follows, are to be used as input for the com-
 850 putations of q^λ and q^θ :

$$U^* = \frac{1}{m} \sum_{i=1}^m u_i^*, \quad (3.40)$$

$$V^* = \frac{1}{m} \sum_{i=1}^m v_i^*. \quad (3.41)$$

851 The use of the time accumulated mass fluxes and the time-averaged winds for the large-
 852 time-step tracer transport in the manner described above ensures the conservation of the tracer
 853 mass and maintains the highest degree of consistency possible given the time split integration
 854 procedure. A graphical illustration of the different levels of sub-cycling in CAM5 is given on
 855 Figure 3.1.

856 The algorithm described here can be readily applied to a regional model if appropriate bound-
 857 ary conditions are supplied. There is formally no Courant number related time step restriction
 858 associated with the transport processes. There is, however, a stability condition imposed by the
 859 gravity-wave processes. For application on the whole sphere, it is computationally advantageous
 860 to apply a polar filter to allow a dramatic increase of the size of the small time step $\Delta\tau$. The
 861 effect of the polar filter is to stabilize the short-in-wavelength (and high-in-frequency) gravity
 862 waves that are being unnecessarily and unidirectionally resolved at very high latitudes in the
 863 zonal direction. To minimize the impact to meteorologically significant larger scale waves, the
 864 polar filter is highly scale selective and is applied only to the diagnostic variables on the auxiliary
 865 C-grid and the tendency terms in the D-grid momentum equations. No polar filter is applied
 866 directly to any of the prognostic variables.

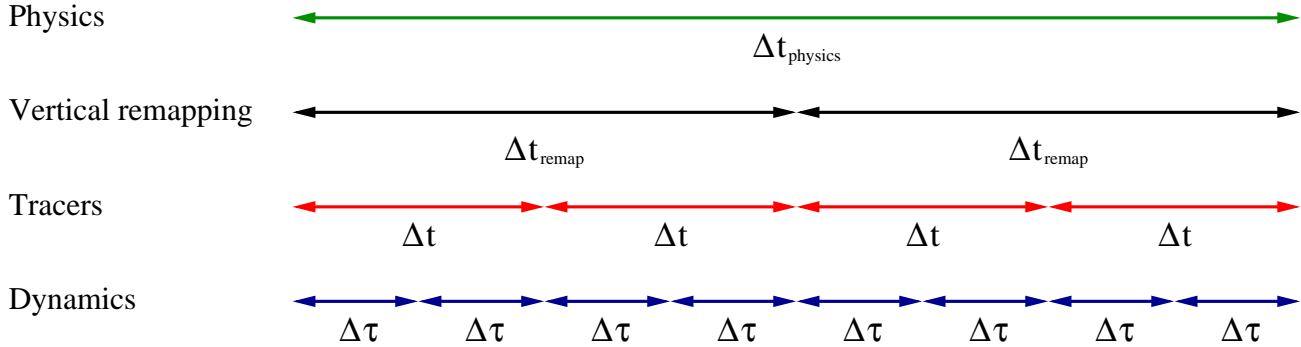


Figure 3.1: A graphical illustration of the different levels of sub-cycling in CAM5.

867 The design of the polar filter follows closely that of [Suarez and Takacs \[1995\]](#) for the C-grid
 868 Arakawa type dynamical core (*e.g.*, [Arakawa and Lamb \[1981\]](#)). For the CAM 5.0 the fast-
 869 fourier transform component of the polar filtering has replaced the algebraic form at all filtering
 870 latitudes. Because our prognostic variables are computed on the D-grid and the fact that the
 871 FFSL transport scheme is stable for Courant number greater than one, in realistic test cases
 872 the maximum size of the time step is about two to three times larger than a model based on
 873 Arakawa and Lamb’s C-grid differencing scheme. It is possible to avoid the use of the polar
 874 filter if, for example, the “Cubed grid” is chosen, instead of the current latitude-longitude grid.
 875 rewrite of the rest of the model codes including physics parameterizations, the land model, and
 876 most of the post processing packages.

877 The size of the small time step for the Lagrangian dynamics is only a function of the horizontal
 878 resolution. Applying the polar filter, for the 2-degree horizontal resolution, a small-time-step size
 879 of 450 seconds can be used for the Lagrangian dynamics. From the large-time-step transport
 880 perspective, the small-time-step integration of the 2D Lagrangian dynamics can be regarded
 881 as a very accurate iterative solver, with m iterations, for computing the time mean winds
 882 and the mass fluxes, analogous in functionality to a semi-implicit algorithm’s elliptic solver
 883 (*e.g.*, [Ringler et al. \[2000\]](#)). Besides accuracy, the merit of an “explicit” versus “semi-implicit”
 884 algorithm ultimately depends on the computational efficiency of each approach. In light of the
 885 advantage of the explicit algorithm in parallelization, we do not regard the explicit algorithm for
 886 the Lagrangian dynamics as an impedance to computational efficiency, particularly on modern
 887 parallel computing platforms.

888 3.1.5 Optional diffusion operators in CAM5

The ‘CD’-grid discretization method used in the CAM finite-volume dynamical core provides explicit control over the rotational modes at the grid scale, due to monotonicity constraint in the PPM-based advection, but there is no explicit control over the divergent modes at the grid scale [see, *e.g.*, [Skamarock, 2010](#)]. Therefore divergence damping terms appear on the right-hand side of the momentum equations ((3.28) and (3.29)):

$$-\frac{1}{A \cos \theta} \left[\frac{\partial}{\partial \lambda} (-\nu D) \right] \quad (3.42)$$

and

$$-\frac{1}{A} \left[\frac{\partial}{\partial \theta} (-\nu D) \right], \quad (3.43)$$

respectively, where the strength of the divergence damping is controlled by the coefficient ν given by

$$\nu = \frac{\nu_2 (A^2 \Delta \lambda \Delta \theta)}{\Delta t}, \quad (3.44)$$

889 where $\nu_2 = 1/128$ throughout the atmosphere except in the top model levels where it monoton-
 890 ically increases to approximately $4/128$ at the top of the atmosphere. The divergence damping
 891 described above is referred to as ‘second-order’ divergence damping as it effectively damps di-
 892 vergence with a ∇^2 operator.

In CAM5 optional ‘fourth-order’ divergence damping has been implemented where the di-
 vergence is effectively damped with a ∇^4 -operator which is usually more scale selective than
 ‘second-order’ damping operators. For ‘fourth-order’ divergence damping the terms

$$-\frac{1}{A \cos \theta} \left[\frac{\partial}{\partial \lambda} (-\nu_4 \nabla^2 D) \right] \quad (3.45)$$

and

$$-\frac{1}{A} \left[\frac{\partial}{\partial \theta} (-\nu_4 \nabla^2 D) \right], \quad (3.46)$$

are added to the right-hand side of (3.28) and (3.29), respectively. The horizontal Laplacian
 ∇^2 -operator in spherical coordinates for a scalar ψ is given by

$$\nabla^2 \psi = \frac{1}{A^2 \cos^2 \theta} \frac{\partial^2 \psi}{\partial^2 \lambda} + \frac{1}{A^2 \cos \theta} \frac{\partial}{\partial \theta} \left(\cos \theta \frac{\partial \psi}{\partial \theta} \right). \quad (3.47)$$

The fourth-order divergence damping coefficient is given by

$$\nu_4 = 0.01 (A^2 \cos(\theta) \Delta \lambda \Delta \theta)^2 / \Delta t. \quad (3.48)$$

893 Since divergence damping is added explicitly to the equations of motion it is unstable if the
 894 time-step is too large or the damping coefficients (ν or ν_4) are too large. To stabilize the fourth-
 895 order divergence damping the winds used to compute the divergence are filtered using the same
 896 FFT filtering which is applied to stabilize the gravity waves.

To control potentially excessive polar night jets in high-resolution configurations of CAM,
 Laplacian damping of the wind components has been added as an option in CAM5. That is,
 the terms

$$\nu_{del2} \nabla^2 u \quad (3.49)$$

and

$$\nu_{del2} \nabla^2 v \quad (3.50)$$

897 are added to the right-hand side of the momentum equations (3.28) and (3.29), respectively.
 898 The damping coefficient ν_{del2} is zero throughout the atmosphere except in the top layers where
 899 it increases monotonically and smoothly from zero to approximately four times a user-specified
 900 damping coefficient at the top of the atmosphere (the user-specified damping coefficient is typ-
 901 ically on the order of $2.5 \times 10^5 \text{ m}^2 \text{ sec}^{-1}$).

902 **3.1.6 A mass, momentum, and total energy conserving mapping al-**
 903 **gorithm**

904 The Lagrangian surfaces that bound the finite-volume will eventually deform, particularly in
 905 the presence of persistent diabatic heating/cooling, in a time scale of a few hours to a day
 906 depending on the strength of the heating and cooling, to a degree that it will negatively impact
 907 the accuracy of the horizontal-to-Lagrangian-coordinate transport and the computation of the
 908 pressure gradient forces. Therefore, a key to the success of the Lagrangian control-volume
 909 discretization is an accurate and conservative algorithm for mapping the deformed Lagrangian
 910 coordinate back to a fixed reference Eulerian coordinate.

911 There are some degrees of freedom in the design of the vertical mapping algorithm. To ensure
 912 conservation, our current (and recommended) mapping algorithm is based on the reconstruction
 913 of the “mass” (pressure thickness δp), zonal and meridional “winds”, “tracer mixing ratios”, and
 914 “total energy” (volume integrated sum of the internal, potential, and kinetic energy), using the
 915 monotonic Piecewise Parabolic sub-grid distributions with the hydrostatic pressure (as defined
 916 by (3.30)) as the mapping coordinate. We outline the mapping procedure as follows.

917 **Step 1:** Define a suitable Eulerian reference coordinate as a target coordinate. The
 918 mass in each layer (δp) is then distributed vertically according to the chosen
 919 Eulerian coordinate. The surface pressure typically plays an “anchoring” role
 920 in defining the terrain following Eulerian vertical coordinate. The hybrid η –
 921 *coordinate* used in the NCAR CCM3 [Kiehl et al., 1996] is adopted in the current
 922 model setup.

Step 2: Construct the piece-wise continuous vertical subgrid profiles of tracer mixing
 ratios (q), zonal and meridional winds (u and v), and total energy (Γ) in the
 Lagrangian control-volume coordinate, or the source coordinate. The total energy
 Γ is computed as the sum of the finite-volume integrated geopotential ϕ , internal
 energy ($C_v T_v$), and the kinetic energy (K) as follows:

$$\Gamma = \frac{1}{\delta p} \int \left[C_v T_v + \phi + \frac{1}{2} (u^2 + v^2) \right] dp. \quad (3.51)$$

Applying integration by parts and the ideal gas law, the above integral can be
 rewritten as

$$\begin{aligned} \Gamma &= \frac{1}{\delta p} \left\{ \int \left[C_p T_v + \frac{1}{2} (u^2 + v^2) \right] dp + \int d(p\phi) \right\} \\ &= C_p \overline{T_v} + \frac{1}{\delta p} \delta(p\phi) + K, \end{aligned} \quad (3.52)$$

where $\overline{T_v}$ is the layer mean virtual temperature, K is the layer mean kinetic
 energy, p is the pressure at layer edges, and C_v and C_p are the specific heat of the
 air at constant volume and at constant pressure, respectively. The total energy

in each grid cell is calculated as

$$\Gamma_{i,j,k} = C_p T_{v_{i,j,k}} + \frac{1}{\delta p_{i,j,k}} \left(p_{i,j,k+\frac{1}{2}} \phi_{i,j,k+\frac{1}{2}} - p_{i,j,k-\frac{1}{2}} \phi_{i,j,k-\frac{1}{2}} \right) + \frac{1}{2} \left(\frac{u_{i,j-\frac{1}{2},k}^2 + u_{i,j+\frac{1}{2},k}^2}{2} + \frac{v_{i-\frac{1}{2},j,k}^2 + v_{i+\frac{1}{2},j,k}^2}{2} \right)$$

923
924
925
926

The method employed to create subgrid profiles is set by the flag *te_method*. For *te_method* = 0 (default), the Piece-wise Parabolic Method (PPM, [Colella and Woodward \[1984\]](#)) over a pressure coordinate is used and for *te_method* = 1 a cubic spline over a logarithmic pressure coordinate is used.

Step 3: Layer mean values of q , (u, v) , and Γ in the Eulerian coordinate system are obtained by integrating analytically the sub-grid distributions, in the vertical direction, from model top to the surface, layer by layer. Since the hydrostatic pressure is chosen as the mapping coordinate, tracer mass, momentum, and total energy are locally and globally conserved. In mapping a variable from the source coordinate to the target coordinate, different limiter constraints may be used and they are controlled by two flags, *iv* and *kord*. For winds on D-grid, *iv* should be set to -1. For tracers, *iv* should be set to 0. For all others, *iv* = 1. *kord* directly controls which limiter constraint is used. For $kord \geq 7$, Huynh's 2nd constraint is used. If $kord = 7$, the original quasi-monotonic constraint is used. If $kord > 7$, a full monotonic constraint is used. If *kord* is less than 7, the variable, *lmt*, is determined by the following:

$$\begin{aligned} lmt &= kord - 3, \\ lmt &= \max(0, lmt), \\ \text{if}(iv = 0) \quad lmt &= \min(2, lmt). \end{aligned}$$

927
928
929

If *lmt* = 0, a standard PPM constraint is used. If *lmt* = 1, an improved full monotonicity constraint is used. If *lmt* = 2, a positive definite constraint is used. If *lmt* = 3, the algorithm will do nothing.

930
931
932
933
934
935

Step 4: Retrieve virtual temperature in the Eulerian (target) coordinate. Start by computing kinetic energy in the Eulerian coordinate system for each layer. Then substitute kinetic energy and the hydrostatic relationship into (3.52). The layer mean temperature \overline{T}_{v_k} for layer k in the Eulerian coordinate is then retrieved from the reconstructed total energy (done in Step 3) by a fully explicit integration procedure starting from the surface up to the model top as follows:

$$\overline{T}_{v_k} = \frac{\Gamma_k - K_k - \phi_{k+\frac{1}{2}}}{C_p \left[1 - \kappa p_{k-\frac{1}{2}} \frac{\ln p_{k+\frac{1}{2}} - \ln p_{k-\frac{1}{2}}}{p_{k+\frac{1}{2}} - p_{k-\frac{1}{2}}} \right]}, \quad (3.53)$$

936

where $\kappa = R_d/C_p$ and R_d is the gas constant for dry air.

To convert the potential virtual temperature Θ_v to the layer mean temperature the conversion factor is obtained by equating the following two equivalent forms of the hydrostatic relation for Θ and $\overline{T_v}$:

$$\delta\phi = -C_p\Theta_v \delta\Pi, \quad (3.54)$$

$$\delta\phi = -R_d\overline{T_v} \delta\ln p, \quad (3.55)$$

where $\Pi = p^\kappa$. The conversion formula between layer mean temperature and layer mean potential temperature is obtained as follows:

$$\Theta_v = \kappa \frac{\delta\ln p}{\delta\Pi} \overline{T_v}. \quad (3.56)$$

937 The physical implication of retrieving the layer mean temperature from the total energy as
 938 described in Step 3 is that the dissipated kinetic energy, if any, is locally converted into internal
 939 energy via the vertically sub-grid mixing (dissipation) processes. Due to the monotonicity
 940 preserving nature of the sub-grid reconstruction the column-integrated kinetic energy inevitably
 941 decreases (dissipates), which leads to local frictional heating. The frictional heating is a physical
 942 process that maintains the conservation of the total energy in a closed system.

943 As viewed by an observer riding on the Lagrangian surfaces, the mapping procedure essen-
 944 tially performs the physical function of the relative-to-the-Eulerian-coordinate vertical trans-
 945 port, by vertically redistributing (air and tracer) mass, momentum, and total energy from the
 946 Lagrangian control-volume back to the Eulerian framework.

947 As described in section 3.1.4, the model time integration cycle consists of m small time steps
 948 for the 2D Lagrangian dynamics and one large time step for tracer transport. The mapping time
 949 step can be much larger than that used for the large-time-step tracer transport. In tests using
 950 the Held-Suarez forcing [Held and Suarez, 1994], a three-hour mapping time interval is found
 951 to be adequate. In the full model integration, one may choose the same time step used for the
 952 physical parameterizations so as to ensure the input state variables to physical parameterizations
 953 are in the usual ‘‘Eulerian’’ vertical coordinate. In CAM5, vertical remapping takes place at
 954 each physics time step.

955 3.1.7 A geopotential conserving mapping algorithm

An alternative vertical mapping approach is available in CAM5. Instead of retrieving tem-
 perature by remapped total energy in the Eulerian coordinate, the alternative approach maps
 temperature directly from the Lagrangian coordinate to the Eulerian coordinate. Since geopo-
 tential is defined as

$$\delta\phi = -C_p\Theta_v\delta\Pi = -R_dT_v\delta\ln p,$$

956 mapping Θ_v over Π or T_v over $\ln p$ preserves the geopotential at the model lid. This approach
 957 prevents the mapping procedure from generating spurious pressure gradient forces at the model
 958 lid. Unlike the energy-conserving algorithm which could produce substantial temperature fluc-
 959 tuations at the model lid, the geopotential conserving approach guarantees a smooth (potential)
 960 temperature profile. However, the geopotential conserving does not conserve total energy in the
 961 remapping procedure. This may be resolved by a global energy fixer already implemented in
 962 the model (see section 3.1.10).

963 3.1.8 Adjustment of pressure to include change in mass of water 964 vapor

965 The physics parameterizations operate on a model state provided by the dynamics, and are
966 allowed to update specific humidity. However, the surface pressure remains fixed throughout
967 the physics updates, and since there is an explicit relationship between the surface pressure and
968 the air mass within each layer, the total air mass must remain fixed as well throughout the
969 physics updates. If no further correction were made, this would imply that the dry air mass
970 changed if the water vapor mass changed in the physics updates. Therefore the pressure field is
971 changed to include the change in water vapor mass due to the physics updates. We impose the
972 restrictions that dry air mass and water mass are conserved as follows:

The total pressure p is

$$p = d + e. \quad (3.57)$$

with dry pressure d , water vapor pressure e . The specific humidity is

$$q = \frac{e}{p} = \frac{e}{d + e}, \quad d = (1 - q)p. \quad (3.58)$$

We define a layer thickness as $\delta^k p \equiv p^{k+1/2} - p^{k-1/2}$, so

$$\delta^k d = (1 - q^k)\delta^k p. \quad (3.59)$$

973 We are concerned about 3 time levels: q_n is input to physics, q_{n^*} is output from physics, q_{n+1} is
974 the adjusted value for dynamics.

Dry mass is the same at n and $n + 1$ but not at n^* . To conserve dry mass, we require that

$$\delta^k d_n = \delta^k d_{n+1} \quad (3.60)$$

or

$$(1 - q_n^k)\delta^k p_n = (1 - q_{n+1}^k)\delta^k p_{n+1}. \quad (3.61)$$

Water mass is the same at n^* and $n + 1$, but not at n . To conserve water mass, we require that

$$q_{n^*}^k \delta^k p_n = q_{n+1}^k \delta^k p_{n+1}. \quad (3.62)$$

Substituting (3.62) into (3.61),

$$(1 - q_n^k)\delta^k p_n = \delta^k p_{n+1} - q_{n^*}^k \delta^k p_n \quad (3.63)$$

$$\delta^k p_{n+1} = (1 - q_n^k + q_{n^*}^k)\delta^k p_n \quad (3.64)$$

which yields a modified specific humidity for the dynamics:

$$q_{n+1}^k = q_n^k \frac{\delta^k p_n}{\delta^k p_{n+1}} = \frac{q_{n^*}^k}{1 - q_n^k + q_{n^*}^k}. \quad (3.65)$$

975 We note that this correction as implemented makes a small change to the water vapor as well.
976 The pressure correction could be formulated to leave the water vapor unchanged.

977 3.1.9 Negative Tracer Fixer

978 In the Finite Volume dynamical core, neither the monotonic transport nor the conservative ver-
979 tical remapping guarantee that tracers will remain positive definite. Thus the Finite Volume
980 dynamical core includes a negative tracer fixer applied before the parameterizations are calcu-
981 lated. For negative mixing ratios produced by horizontal transport, the model will attempt to
982 borrow mass from the east and west neighboring cells. In practice, most negative values are
983 introduced by the vertical remapping which does not guarantee positive definiteness in the first
984 and last layer of the vertical column.

985 A minimum value q_{min} is defined for each tracer. If the tracer falls below that minimum value,
986 it is set to that minimum value. If there is enough mass of the tracer in the layer immediately
987 above, tracer mass is removed from that layer to conserve the total mass in the column. If
988 there is not enough mass in the layer immediately above, no compensation is applied, violating
989 conservation. Usually such computational sources are very small.

The amount of tracer needed from the layer above to bring q_k up to q_{min} is

$$q_{fill} = (q_{min} - q_k) \frac{\Delta p_k}{\Delta p_{k-1}} \quad (3.66)$$

where k is the vertical index, increasing downward. After the filling

$$q_{k_{FILLED}} = q_{min} \quad (3.67)$$

$$q_{k-1_{FILLED}} = q_{k-1} - q_{fill} \quad (3.68)$$

990 Currently $q_{min} = 1.0 \times 10^{-12}$ for water vapor, $q_{min} = 0.0$ for CLDLIQ, CLDICE, NUMLIQ and
991 NUMICE, and $q_{min} = 1.0 \times 10^{-36}$ for the remaining constituents.

992 3.1.10 Global Energy Fixer

993 The finite-volume dynamical core as implemented in CAM and described here conserves the dry
994 air and all other tracer mass exactly without a “mass fixer”. The vertical Lagrangian discretiza-
995 tion and the associated remapping conserves the total energy exactly. The only remaining issue
996 regarding conservation of the total energy is the horizontal discretization and the use of the
997 “diffusive” transport scheme with monotonicity constraint. To compensate for the loss of total
998 energy due to horizontal discretization, we apply a global fixer to add the loss in kinetic energy
999 due to “diffusion” back to the thermodynamic equation so that the total energy is conserved.
1000 The loss in total energy (in flux unit) is found to be around 2 (W/m^2) with the 2 degrees
1001 resolution.

1002 The energy fixer is applied following the negative tracer fixer. The fixer is applied on the
1003 unstaggered physics grid rather than on the staggered dynamics grid. The energies on these
1004 two grids are difficult to relate because of the nonlinear terms in the energy definition and
1005 the interpolation of the state variables between the grids. The energy is calculated in the
1006 parameterization suite before the state is passed to the finite volume core as described in the
1007 beginning of Chapter 4. The fixer is applied just before the parameterizations are calculated.
1008 The fixer is a simplification of the fixer in the Eulerian dynamical core described in section
1009 3.3.20.

Let minus sign superscript $()^-$ denote the values at the beginning of the dynamics time step, i.e. after the parameterizations are applied, let a plus sign superscript $()^+$ denote the values after fixer is applied, and let a hat $(\hat{})^+$ denote the provisional value before adjustment. The total energy over the entire computational domain after the fixer is

$$E^+ = \int_{p_t}^{p_s} \int_0^{2\pi} \int_{-\frac{\pi}{2}}^{\frac{\pi}{2}} \frac{1}{g} \left[C_p T^+ + \Phi + \frac{1}{2} (u^{+2} + v^{+2}) + (L_v + L_i) q_v^+ + L_i q_\ell^+ \right] A^2 \cos \theta d\theta d\lambda dp, \quad (3.69)$$

where L_v is the latent heat of vaporation, L_i is the latent heat of fusion, q_v is water vapor mixing ratio, and q_ℓ is cloud water mixing ratio. E^+ should equal the energy at the beginning of the dynamics time step

$$E^- = \int_{p_t}^{p_s} \int_0^{2\pi} \int_{-\frac{\pi}{2}}^{\frac{\pi}{2}} \frac{1}{g} \left[c_p T^- + \Phi + \frac{1}{2} (u^{-2} + v^{-2}) + (L_v + L_i) q_v^- + L_i q_\ell^- \right] A^2 \cos \theta d\theta d\lambda dp. \quad (3.70)$$

Let \hat{E}^+ denote the energy of the provisional state provided by the dynamical core before the adjustment.

$$\hat{E}^+ = \int_{p_t}^{p_s} \int_0^{2\pi} \int_{-\frac{\pi}{2}}^{\frac{\pi}{2}} \frac{1}{g} \left[c_p \hat{T}^+ + \hat{\Phi} + \frac{1}{2} (\hat{u}^{+2} + \hat{v}^{+2}) + (L_v + L_i) \hat{q}_v^+ + L_i \hat{q}_\ell^+ \right] A^2 \cos \theta d\theta d\lambda dp. \quad (3.71)$$

Thus, the total energy added into the system by the dynamical core is $\hat{E}^+ - E^-$. The energy fixer then changes dry static energy ($s = C_p T + \Phi$) by a constant amount over each grid cell to conserve total energy in the entire computational domain. The dry static energy added to each grid cell may be expressed as

$$\Delta s = \frac{E^- - \hat{E}^+}{\int_{p_t}^{p_s} \int_0^{2\pi} \int_{-\frac{\pi}{2}}^{\frac{\pi}{2}} A^2 \cos \theta d\theta d\lambda \frac{dp}{g}}. \quad (3.72)$$

Therefore,

$$s^+ = \hat{s}^+ + \Delta s, \quad (3.73)$$

or

$$C_p T^+ + \Phi^+ = \hat{s}^+ + \Delta s. \quad (3.74)$$

1010 This will ensure $E^+ = E^-$.

By hydrostatic approximation, the geopotential equation is

$$d\Phi = -R_d T_v d \ln p, \quad (3.75)$$

and for any arbitrary point between $p_{k+\frac{1}{2}}$ and $p_{k-\frac{1}{2}}$ the geopotential may be written as

$$\int_{\Phi_{k+\frac{1}{2}}}^{\Phi} d\Phi' = -R_d T_v \int_{p_{k+\frac{1}{2}}}^p d \ln p', \quad (3.76)$$

$$\Phi = \Phi_{k+\frac{1}{2}} + R_d T_v (\ln p_{k+\frac{1}{2}} - \ln p). \quad (3.77)$$

The geopotential at the mid point of a model layer between $p_{k+\frac{1}{2}}$ and $p_{k-\frac{1}{2}}$, or the layer mean, is

$$\begin{aligned}
\Phi_k &= \frac{\int_{p_{k-\frac{1}{2}}}^{p_{k+\frac{1}{2}}} \Phi dp}{\int_{p_{k-\frac{1}{2}}}^{p_{k+\frac{1}{2}}} dp} \\
&= \frac{\int_{p_{k-\frac{1}{2}}}^{p_{k+\frac{1}{2}}} \left[\Phi_{k+\frac{1}{2}} + R_d T_v \left(\ln p_{k+\frac{1}{2}} - \ln p \right) \right] dp}{\int_{p_{k-\frac{1}{2}}}^{p_{k+\frac{1}{2}}} dp} \\
&= \Phi_{k+\frac{1}{2}} + R_d T_v \ln p_{k+\frac{1}{2}} - \frac{\int_{p_{k-\frac{1}{2}}}^{p_{k+\frac{1}{2}}} \ln p dp}{p_{k+\frac{1}{2}} - p_{k-\frac{1}{2}}} \\
&= \Phi_{k+\frac{1}{2}} + R_d T_v \left(1 - p_{k-\frac{1}{2}} \frac{\ln p_{k+\frac{1}{2}} - \ln p_{k-\frac{1}{2}}}{p_{k+\frac{1}{2}} - p_{k-\frac{1}{2}}} \right) \tag{3.78}
\end{aligned}$$

For layer k , the energy fixer will solve the following equation based on (3.74),

$$C_p T_k^+ + \Phi_{k+\frac{1}{2}}^+ + R_d T_k^+ \left(1 + \epsilon q_{v_k}^+ \right) \left(1 - p_{k-\frac{1}{2}}^+ \frac{\ln p_{k+\frac{1}{2}}^+ - \ln p_{k-\frac{1}{2}}^+}{p_{k+\frac{1}{2}}^+ - p_{k-\frac{1}{2}}^+} \right) = \hat{s}^+ + \Delta s. \tag{3.79}$$

Since the energy fixer will not alter the water vapor mixing ratio and the pressure field,

$$q_v^+ = \hat{q}_v^+, \tag{3.80}$$

$$p^+ = \hat{p}^+. \tag{3.81}$$

Therefore,

$$T_k^+ = \frac{(\hat{s}^+ + \Delta s) - \Phi_{k+\frac{1}{2}}^+}{C_p + R_d \left(1 + \epsilon \hat{q}_{v_k}^+ \right) \left(1 - \hat{p}_{k-\frac{1}{2}}^+ \frac{\ln \hat{p}_{k+\frac{1}{2}}^+ - \ln \hat{p}_{k-\frac{1}{2}}^+}{\hat{p}_{k+\frac{1}{2}}^+ - \hat{p}_{k-\frac{1}{2}}^+} \right)}. \tag{3.82}$$

1011 The energy fixer starts from the Earth's surface and works its way up to the model top in
1012 adjusting the temperature field. At the surface layer, $\Phi_{k+\frac{1}{2}}^+ = \Phi_s$. After the temperature is
1013 adjusted in a grid cell, the geopotential at the upper interface of the cell is updated which is
1014 needed for the temperature adjustment in the grid cell above.

1015 3.1.11 Further discussion

1016 There are still aspects of the numerical formulation in the finite volume dynamical core that can
1017 be further improved. For example, the choice of the horizontal grid, the computational efficiency
1018 of the split-explicit time marching scheme, the choice of the various monotonicity constraints,
1019 and how the conservation of total energy is achieved.

1020 The impact of the non-linear diffusion associated with the monotonicity constraint is dif-
1021 ficult to assess. All discrete schemes must address the problem of subgrid-scale mixing. The
1022 finite-volume algorithm contains a non-linear diffusion that mixes strongly when monotonicity

1023 principles are locally violated. However, the effect of nonlinear diffusion due to the imposed
1024 monotonicity constraint diminishes quickly as the resolution matches better to the spatial struc-
1025 ture of the flow. In other numerical schemes, however, an explicit (and tunable) linear diffusion
1026 is often added to the equations to provide the subgrid-scale mixing as well as to smooth and/or
1027 stabilize the time marching.

1028 **3.2 Spectral Element Dynamical Core**

1029 The CAM includes an optional dynamical core from HOMME, NCAR’s High-Order Method
1030 Modeling Environment [Dennis et al., 2005]. The stand-alone HOMME is used for re-
1031 search in several different types of dynamical cores. The dynamical core incorporated into
1032 CAM4 uses HOMME’s continuous Galerkin spectral finite element method [Taylor et al., 1997;
1033 Fournier et al., 2004; Thomas and Loft, 2005; Wang et al., 2007; Taylor and Fournier, 2010],
1034 here abbreviated to the spectral element method (SEM). This method is designed for fully
1035 unstructured quadrilateral meshes. The current configurations in the CAM are based on the
1036 cubed-sphere grid. The main motivation for the inclusion of HOMME is to improve the scalabil-
1037 ity of the CAM by introducing quasi-uniform grids which require no polar filters [Taylor et al.,
1038 2008]. HOMME is also the first dynamical core in the CAM which locally conserves energy in
1039 addition to mass and two-dimensional potential vorticity [Taylor, 2010].

1040 HOMME represents a large change in the horizontal grid as compared to the other dynamical
1041 cores in CAM. Almost all other aspects of HOMME are based on a combination of well-tested ap-
1042 proaches from the Eulerian and FV dynamical cores. For tracer advection, HOMME is modeled
1043 as closely as possible on the FV core. It uses the same conservation form of the transport equa-
1044 tion and the same vertically Lagrangian discretization [Lin, 2004]. The HOMME dynamics are
1045 modeled as closely as possible on Eulerian core. They share the same vertical coordinate, vertical
1046 discretization, hyper-viscosity based horizontal diffusion, top-of-model dissipation, and solve the
1047 same moist hydrostatic equations. The main differences are that HOMME advects the surface
1048 pressure instead of its logarithm (in order to conserve mass and energy), and HOMME uses the
1049 vector-invariant form of the momentum equation instead of the vorticity-divergence formulation.
1050 Several dry dynamical cores including HOMME are evaluated in Lauritzen et al. [2010] using a
1051 grid-rotated version of the baroclinic instability test case [Jablonowski and Williamson, 2006].

1052 The timestepping in HOMME is a form of dynamics/tracer/physics subcycling, achieved
1053 through the use of multi-stage 2nd order accurate Runge-Kutta methods. The tracers and
1054 dynamics use the same timestep which is controlled by the maximum anticipated wind speed,
1055 but the dynamics uses more stages than the tracers in order to maintain stability in the presence
1056 of gravity waves. The forcing is applied using a time-split approach. The optimal forcing
1057 strategy in HOMME has not yet been determined, so HOMME supports several options. The
1058 first option is modeled after the FV dynamical core and the forcing is applied as an adjustment
1059 at each physics timestep. The second option is to convert all forcings into tendencies which are
1060 applied at the end of each dynamics/tracer timestep. If the physics timestep is larger than the
1061 tracer timestep, then the tendencies are held fixed and only updated at each physics timestep.
1062 Finally, a hybrid approach can be used where the tracer tendencies are applied as in the first
1063 option and the dynamics tendencies are applied as in the second option.

1064 **3.2.1 Continuum Formulation of the Equations**

1065 HOMME uses a conventional vector-invariant form of the moist primitive equations. For the
 1066 vertical discretization it uses the hybrid η pressure vertical coordinate system modeled after
 1067 **3.3.1** The formulation here differs only in that surface pressure is used as a prognostic variable
 1068 as opposed to its logarithm.

In the η -coordinate system, the pressure is given by

$$p(\eta) = A(\eta)p_0 + B(\eta)p_s.$$

The hydrostatic approximation $\partial p/\partial z = -g\rho$ is used to replace the mass density ρ by an η -coordinate pseudo-density $\partial p/\partial\eta$. The material derivative in η -coordinates can be written (e.g. Satoh [2004], Sec.3.3),

$$\frac{DX}{Dt} = \frac{\partial X}{\partial t} + \vec{u} \cdot \nabla X + \dot{\eta} \frac{\partial X}{\partial \eta}$$

1069 where the $\nabla()$ operator (as well as $\nabla \cdot ()$ and $\nabla \times ()$ below) is the two-dimensional gradient on
 1070 constant η -surfaces, $\partial/\partial\eta$ is the vertical derivative, $\dot{\eta} = D\eta/Dt$ is a vertical flow velocity and \vec{u}
 1071 is the horizontal velocity component (tangent to constant z -surfaces, not η -surfaces).

The η -coordinate atmospheric primitive equations, neglecting dissipation and forcing terms can then be written as

$$\frac{\partial \vec{u}}{\partial t} + (\zeta + f) \hat{k} \times \vec{u} + \nabla \left(\frac{1}{2} \vec{u}^2 + \Phi \right) + \dot{\eta} \frac{\partial \vec{u}}{\partial \eta} + \frac{RT_v}{p} \nabla p = 0 \tag{3.83}$$

$$\frac{\partial T}{\partial t} + \vec{u} \cdot \nabla T + \dot{\eta} \frac{\partial T}{\partial \eta} - \frac{RT_v}{c_p^* p} \omega = 0 \tag{3.84}$$

$$\frac{\partial}{\partial t} \left(\frac{\partial p}{\partial \eta} \right) + \nabla \cdot \left(\frac{\partial p}{\partial \eta} \vec{u} \right) + \frac{\partial}{\partial \eta} \left(\dot{\eta} \frac{\partial p}{\partial \eta} \right) = 0 \tag{3.85}$$

$$\frac{\partial}{\partial t} \left(\frac{\partial p}{\partial \eta} q \right) + \nabla \cdot \left(\frac{\partial p}{\partial \eta} q \vec{u} \right) + \frac{\partial}{\partial \eta} \left(\dot{\eta} \frac{\partial p}{\partial \eta} q \right) = 0. \tag{3.86}$$

1072 These are prognostic equations for \vec{u} , the temperature T , density $\frac{\partial p}{\partial \eta}$, and $\frac{\partial p}{\partial \eta} q$ where q is the
 1073 specific humidity. The prognostic variables are functions of time t , vertical coordinate η and
 1074 two coordinates describing the surface of the sphere. The unit vector normal to the surface of
 1075 the sphere is denoted by \hat{k} . This formulation has already incorporated the hydrostatic equation
 1076 and the ideal gas law, $p = \rho RT_v$. There is a no-flux ($\dot{\eta} = 0$) boundary condition at $\eta = 1$ and
 1077 $\eta = \eta_{\text{top}}$. The vorticity is denoted by $\zeta = \hat{k} \cdot \nabla \times \vec{u}$, f is a Coriolis term and $\omega = Dp/Dt$ is the
 1078 pressure vertical velocity. The virtual temperature T_v and variable-of-convenience c_p^* are defined
 1079 as in **3.3.1**.

The diagnostic equations for the geopotential height field Φ is

$$\Phi = \Phi_s + \int_{\eta}^1 \frac{RT_v}{p} \frac{\partial p}{\partial \eta} d\eta \tag{3.87}$$

where Φ_s is the prescribed surface geopotential height (given at $\eta = 1$). To complete the system, we need diagnostic equations for $\dot{\eta}$ and ω , which come from integrating (3.85) with respect to

η . In fact, (3.85) can be replaced by a diagnostic equation for $\dot{\eta} \frac{\partial p}{\partial \eta}$ and a prognostic equation for surface pressure p_s

$$\frac{\partial}{\partial t} p_s + \int_{\eta_{\text{top}}}^1 \nabla \cdot \left(\frac{\partial p}{\partial \eta} \vec{u} \right) d\eta = 0 \quad (3.88)$$

$$\dot{\eta} \frac{\partial p}{\partial \eta} = -\frac{\partial p}{\partial t} - \int_{\eta_{\text{top}}}^{\eta} \nabla \cdot \left(\frac{\partial p}{\partial \eta'} \vec{u} \right) d\eta', \quad (3.89)$$

where (3.88) is (3.89) evaluated at the model bottom ($\eta = 1$) after using that $\partial p / \partial t = B(\eta) \partial p_s / \partial t$ and $\dot{\eta}(1) = 0, B(1) = 1$. Using Eq 3.89, we can derive a diagnostic equation for the pressure vertical velocity $\omega = Dp/Dt$,

$$\omega = \frac{\partial p}{\partial t} + \vec{u} \cdot \nabla p + \dot{\eta} \frac{\partial p}{\partial \eta} = \vec{u} \cdot \nabla p - \int_{\eta_{\text{top}}}^{\eta} \nabla \cdot \left(\frac{\partial p}{\partial \eta'} \vec{u} \right) d\eta'$$

Finally, we rewrite (3.89) as

$$\dot{\eta} \frac{\partial p}{\partial \eta} = B(\eta) \int_{\eta_{\text{top}}}^1 \nabla \cdot \left(\frac{\partial p}{\partial \eta} \vec{u} \right) d\eta - \int_{\eta_{\text{top}}}^{\eta} \nabla \cdot \left(\frac{\partial p}{\partial \eta'} \vec{u} \right) d\eta', \quad (3.90)$$

1080 3.2.2 Conserved Quantities

The equations have infinitely many conserved quantities, including mass, tracer mass, potential temperature defined by

$$M_X = \iint \frac{\partial p}{\partial \eta} X d\eta d\mathcal{A}$$

with ($X = 1, q$ or $(p/p_0)^{-\kappa} T$) and the total moist energy E defined by

$$E = \iint \frac{\partial p}{\partial \eta} \left(\frac{1}{2} \vec{u}^2 + c_p^* T \right) d\eta d\mathcal{A} + \int p_s \Phi_s d\mathcal{A} \quad (3.91)$$

1081 where $d\mathcal{A}$ is the spherical area measure. To compute these quantities in their traditional units
 1082 they should be divided by the constant of gravity g . We have omitted this scaling since g
 1083 has also been scaled out from (3.83)–(3.86). We note that in this formulation of the primitive
 1084 equations, the pressure p is a moist pressure, representing the effects of both dry air and water
 1085 vapor. The unforced equations conserve both the moist air mass ($X = 1$ above) and the dry air
 1086 mass ($X = 1 - q$). However, in the presence of a forcing term in (3.86) (representing sources
 1087 and sinks of water vapor as would be present in a full model) a corresponding forcing term must
 1088 be added to (3.85) to ensure that dry air mass is conserved.

The energy (3.91) is specific to the hydrostatic equations. We have omitted terms from the physical total energy which are constant under the evolution of the unforced hydrostatic equations [Staniforth et al., 2003]. It can be converted into a more universal form involving $\frac{1}{2} \vec{u}^2 + c_v^* T + \Phi$, with c_v^* defined similarly to c_p^* , so that $c_v^* = c_v + (c_{vv} - c_v)q$ where c_v and c_{vv} are the specific heats of dry air and water vapor defined at constant volume. We note that $c_p = R + c_v$ and $c_{pv} = R_v + c_{vv}$ so that $c_p^* T = c_v^* T + RT_v$. Expanding $c_p^* T$ with this expression,

integrating by parts with respect to η and making use of the fact that the model top is at a constant pressure

$$\int \frac{\partial p}{\partial \eta} RT_v d\eta = - \int p \frac{\partial \Phi}{\partial \eta} d\eta = \int \frac{\partial p}{\partial \eta} \Phi d\eta - (p\Phi) \Big|_{\eta=\eta_{\text{top}}}^{\eta=1}$$

and thus

$$E = \iint \frac{\partial p}{\partial \eta} \left(\frac{1}{2} \vec{u}^2 + c_v^* T + \Phi \right) d\eta dA + \int p_{\text{top}} \Phi(\eta_{\text{top}}) dA. \quad (3.92)$$

1089 The model top boundary term in (3.92) vanishes if $p_{\text{top}} = 0$. Otherwise it must be included to
 1090 be consistent with the hydrostatic equations. It is present due to the fact that the hydrostatic
 1091 momentum equation (3.83) neglects the vertical pressure gradient.

1092 3.2.3 Horizontal Discretization: Functional Spaces

1093 In the finite element method, instead of constructing discrete approximations to derivative
 1094 operators, one constructs a discrete functional space, and then finds the function in this space
 1095 which solves the equations of interest in a minimum residual sense. As compared to finite
 1096 volume methods, there is less choice in how one constructs the discrete derivative operators
 1097 in this setting, since functions in the discrete space are represented in terms of known basis
 1098 functions whose derivatives are known, often analytically.

Let x^α and $\vec{x} = x^1 \vec{e}_1 + x^2 \vec{e}_2$ be the Cartesian coordinates and position vector of a point in the reference square $[-1, 1]^2$ and let r^α and \vec{r} be the coordinates and position vector of a point on the surface of the sphere, denoted by Ω . We mesh Ω using the cubed-sphere grid (Fig. 3.2) first used in Sadourny [1972]. Each cube face is mapped to the surface of the sphere with the equal-angle gnomonic projection [Rančić et al., 1996]. The map from the reference element $[-1, 1]^2$ to the cube face is a translation and scaling. The composition of these two maps defines a \mathcal{C}^1 map from the spherical elements to the reference element $[-1, 1]^2$. We denote this map and its inverse by

$$\vec{r} = \vec{r}(\vec{x}; m), \quad \vec{x} = \vec{x}(\vec{r}; m). \quad (3.93)$$



Figure 3.2: Tiling the surface of the sphere with quadrilaterals. An inscribed cube is projected to the surface of the sphere. The faces of the cubed sphere are further subdivided to form a quadrilateral grid of the desired resolution. Coordinate lines from the gnomonic equal-angle projection are shown.

We now define the discrete space used by the SEM. First we denote the space of polynomials up to degree d in $[-1, 1]^2$ by

$$\mathcal{P}_d = \text{span}_{i,j=0}^d (x^1)^i (x^2)^j = \text{span}_{\vec{i} \in \mathbb{I}} \phi_{\vec{i}}(\vec{x}),$$

where $\mathbb{I} = \{0, \dots, d\}^2$ contains all the degrees and $\phi_{\vec{i}}(\vec{x}) = \varphi_{i^1}(x^1)\varphi_{i^2}(x^2)$, $i^\alpha = 0, \dots, d$, are the cardinal functions, namely polynomials that interpolate the tensor-product of degree- d Gauss-Lobatto-Legendre (GLL) nodes $\vec{\xi}_{\vec{i}} = \xi_{i^1}\vec{e}_1 + \xi_{i^2}\vec{e}_2$. The GLL nodes used within an element for $d = 3$ are shown in Fig. 3.3. The cardinal-function expansion coefficients of a function g are its GLL nodal values, so we have

$$g(\vec{x}) = \sum_{\vec{i} \in \mathbb{I}} g(\vec{\xi}_{\vec{i}}) \phi_{\vec{i}}(\vec{x}). \quad (3.94)$$

We can now define the piecewise-polynomial SEM spaces \mathcal{V}^0 and \mathcal{V}^1 as

$$\mathcal{V}^0 = \{f \in \mathcal{L}^2(\Omega) : f(\vec{r}(\cdot; m)) \in \mathcal{P}_d, \forall m\} = \text{span}_{m=1}^M \{\phi_{\vec{i}}(\vec{x}(\cdot; m))\}_{\vec{i} \in \mathbb{I}} \quad (3.95)$$

$$\text{and } \mathcal{V}^1 = \mathcal{C}^0(\Omega) \cap \mathcal{V}^0.$$

Functions in \mathcal{V}^0 are polynomial within each element but may be discontinuous at element boundaries and \mathcal{V}^1 is the subspace of continuous function in \mathcal{V}^0 . We take $M_d = \dim \mathcal{V}^0 = (d+1)^2 M$, and $L = \dim \mathcal{V}^1 < M_d$. We then construct a set of L unique points by

$$\{\vec{r}_\ell\}_{\ell=1}^L = \bigcup_{m=1}^M \vec{r}(\{\vec{\xi}_{\vec{i}}\}_{\vec{i} \in \mathbb{I}}; m), \quad (3.96)$$

1100 For every point \vec{r}_ℓ , there exists at least one element Ω_m and at least one GLL node $\vec{\xi}_{\vec{i}} = \vec{x}(\vec{r}_\ell; m)$.
 1101 In 2D, if \vec{r}_ℓ belongs to exactly one Ω_m it is an element-interior node. If it belongs to exactly two Ω_m s, it is an element-edge interior node. Otherwise it is a vertex node.

Figure 3.3: A 4×4 tensor product grid of GLL nodes used within each element, for a degree $d = 3$ discretization. Nodes on the boundary are shared by neighboring elements.

1102

We also define similar spaces for 2D vectors. We introduce two families of spaces, with a subscript of either *con* or *cov*, denoting if the contravariant or covariant components of the vectors are piecewise polynomial, respectively.

$$\mathcal{V}_{\text{con}}^0 = \{\vec{u} \in \mathcal{L}^2(\Omega)^2 : u^\alpha \in \mathcal{V}^0, \alpha = 1, 2\}$$

$$\text{and } \mathcal{V}_{\text{con}}^1 = \mathcal{C}^0(\Omega)^2 \cap \mathcal{V}_{\text{con}}^0,$$

where u^1, u^2 are the contravariant components of \vec{u} defined below. Vectors in $\mathcal{V}_{\text{con}}^1$ are globally continuous and their contravariant components are polynomials in each element. Similarly,

$$\mathcal{V}_{\text{cov}}^0 = \{\vec{u} \in \mathcal{L}^2(\Omega)^2 : u_\beta \in \mathcal{V}^0, \beta = 1, 2\}$$

$$\text{and } \mathcal{V}_{\text{cov}}^1 = \mathcal{C}^0(\Omega)^2 \cap \mathcal{V}_{\text{cov}}^0.$$

The SEM is a Galerkin method with respect to the \mathcal{V}^1 subspace and it can be formulated solely in terms of functions in \mathcal{V}^1 . In CAM-HOMME, the typical configuration is to run with $d = 3$ which achieves a 4th order accurate horizontal discretization [Taylor and Fournier, 2010]. All variables in the CAM-HOMME initial condition and history files as well as variables passed to the physics routines are represented by their grid point values at the points $\{\vec{r}_\ell\}_{\ell=1}^L$. However, for some intermediate quantities and internally in the dynamical core it is useful to consider the larger \mathcal{V}^0 space, where variables are represented by their grid point values at the M_d mapped GLL nodes. This later representation can also be considered as the cardinal-function (3.94) expansion of a function f local to each element,

$$f(\vec{r}) = \sum_{\vec{r} \in \mathbb{I}} f(\vec{r}(\vec{\xi}_i; m)) \phi_{\vec{r}}(\vec{x}(\vec{r}; m)) \quad (3.97)$$

1103 since the expansion coefficients are the function values at the mapped GLL nodes. Functions f
 1104 in \mathcal{V}^0 can be multiple-valued at GLL nodes that are *redundant* (i.e., shared by more than one
 1105 element), while for $f \in \mathcal{V}^1$, the values at any redundant points must all be the same.

1106 3.2.4 Horizontal Discretization: Differential Operators

We use the standard curvilinear coordinate formulas for vector operators following Heinbockel [2001]. Given the 2×2 Jacobian of the the mapping (3.93) from $[-1, 1]^2$ to Ω_m , we denote its determinant-magnitude by

$$J = \left| \frac{\partial \vec{r}}{\partial \vec{x}} \right|. \quad (3.98)$$

A vector \vec{v} may be written in terms of physical or covariant or contravariant components, $v[\gamma]$ or v_β or v^α ,

$$\vec{v} = \sum_{\gamma=1}^3 v[\gamma] \frac{\partial \vec{r}}{\partial r^\gamma} = \sum_{\beta=1}^3 v_\beta \vec{g}^\beta = \sum_{\alpha=1}^3 v^\alpha \vec{g}_\alpha, \quad (3.99)$$

1107 that are related by $v_\beta = \vec{v} \cdot \vec{g}_\beta$ and $v^\alpha = \vec{v} \cdot \vec{g}^\alpha$, where $\vec{g}^\alpha = \nabla x^\alpha$ is a contravariant basis vector
 1108 and $\vec{g}_\beta = \frac{\partial \vec{r}}{\partial x^\beta}$ is a covariant basis vector.

The dot product and contravariant components of the cross product are Heinbockel [2001, Table 1]

$$\vec{u} \cdot \vec{v} = \sum_{\alpha=1}^3 u_\alpha v^\alpha \quad \text{and} \quad (\vec{u} \times \vec{v})^\alpha = \frac{1}{J} \sum_{\beta, \gamma=1}^3 \epsilon^{\alpha\beta\gamma} u_\beta v_\gamma \quad (3.100)$$

where $\epsilon^{\alpha\beta\gamma} \in \{0, \pm 1\}$ is the Levi-Civita symbol. The divergence, covariant coordinates of the gradient and contravariant coordinates of the curl are Heinbockel [2001, eqs. 2.1.1, 2.1.4 & 2.1.6]

$$\nabla \cdot \vec{v} = \frac{1}{J} \sum_{\alpha} \frac{\partial}{\partial x^\alpha} (J v^\alpha), \quad (\nabla f)_\alpha = \frac{\partial f}{\partial x^\alpha} \quad \text{and} \quad (\nabla \times \vec{v})^\alpha = \frac{1}{J} \sum_{\beta, \gamma} \epsilon^{\alpha\beta\gamma} \frac{\partial v_\gamma}{\partial x^\beta}. \quad (3.101)$$

1109 In the SEM, these operators are all computed in terms of the derivatives with respect to \vec{x} in the
 1110 reference element, computed exactly (to machine precision) by differentiating the local element
 1111 expansion (3.97). For the gradient, the covariant coordinates of $\nabla f, f \in \mathcal{V}^0$ are thus computed

1112 exactly within each element. Note that $\nabla f \in \mathcal{V}_{\text{cov}}^0$, but may not be in $\mathcal{V}_{\text{cov}}^1$ even for $f \in \mathcal{V}^1$
 1113 due to the fact that its components will be multi-valued at element boundaries because ∇f
 1114 computed in adjacent elements will not necessarily agree along their shared boundary. In the
 1115 case where J is constant within each element, the SEM curl of $\vec{v} \in \mathcal{V}_{\text{cov}}^0$ and the divergence of
 1116 $\vec{u} \in \mathcal{V}_{\text{con}}^0$ will also be exact, but as with the gradient, multiple-valued at element boundaries.

For non-constant J , these operators may not be computed exactly by the SEM due to the Jacobian factors in the operators and the Jacobian factors that appear when converting between covariant and contravariant coordinates. We follow [Thomas and Loft \[2000\]](#) and evaluate these operators in the form shown in (3.101). The quadratic terms that appear are first projected into \mathcal{V}^0 via interpolation at the GLL nodes and then this interpolant is differentiated exactly using (3.97). For example, to compute the divergence of $\vec{v} \in \mathcal{V}_{\text{con}}^0$, we first compute the interpolant $\mathcal{I}(Jv^\alpha) \in \mathcal{V}^0$ of Jv^α , where the GLL interpolant of a product fg derives simply from the product of the GLL nodal values of f and g . This operation is just a reinterpretation of the nodal values and is essentially free in the SEM. The derivatives of this interpolant are then computed exactly from (3.97). The sum of partial derivatives are then divided by J at the GLL nodal values and thus the SEM divergence operator $\nabla_{\text{h}} \cdot ()$ is given by

$$\nabla \cdot \vec{v} \approx \nabla_{\text{h}} \cdot \vec{v} = \mathcal{I} \left(\frac{1}{J} \sum_{\alpha} \frac{\partial \mathcal{I}(Jv^\alpha)}{\partial x^\alpha} \right) \in \mathcal{V}^0. \quad (3.102)$$

Similarly, the gradient and curl are approximated by

$$(\nabla f)_{\alpha} \approx (\nabla_{\text{h}} f)_{\alpha} = \frac{\partial f}{\partial x^\alpha} \quad (3.103)$$

$$\text{and} \quad (\nabla \times \vec{v})^{\alpha} \approx (\nabla_{\text{h}} \times \vec{v})^{\alpha} = \sum_{\beta, \gamma} \epsilon^{\alpha\beta\gamma} \mathcal{I} \left(\frac{1}{J} \frac{\partial v_{\gamma}}{\partial x^{\beta}} \right) \quad (3.104)$$

1117 with $\nabla_{\text{h}} f \in \mathcal{V}_{\text{cov}}^0$ and $\nabla_{\text{h}} \times \vec{v} \in \mathcal{V}_{\text{con}}^0$. The SEM is well known for being quite efficient in computing
 1118 these types of operations. The SEM divergence, gradient and curl can all be evaluated at the
 1119 $(d+1)^3$ GLL nodes within each element in $\mathcal{O}(d)$ operations per node using the tensor-product
 1120 property of these points [[Deville et al., 2002](#); [Karniadakis and Sherwin, 2005](#)].

1121 3.2.5 Horizontal Discretization: Discrete Inner-Product

Instead of using exact integration of the basis functions as in a traditional finite-element method, the SEM uses a GLL quadrature approximation for the integral over Ω , that we denote by $\langle \cdot \rangle$. We can write this integral as a sum of area-weighted integrals over the set of elements $\{\Omega_m\}_{m=1}^M$ used to decompose the domain,

$$\int fg \, dA = \sum_{m=1}^M \int_{\Omega_m} fg \, dA.$$

The integral over a single element Ω_m is written as an integral over $[-1, 1]^2$ by

$$\int_{\Omega_m} fg \, dA = \iint_{[-1, 1]^2} f(\vec{r}(\cdot; m))g(\vec{r}(\cdot; m))J_m \, dx^1 \, dx^2 \approx \langle fg \rangle_{\Omega_m},$$

where we approximate the integral over $[-1, 1]^2$ by GLL quadrature,

$$\langle fg \rangle_{\Omega_m} = \sum_{\vec{i} \in \mathbb{I}} w_{i^1} w_{i^2} J_m(\vec{\xi}_{\vec{i}}) f(\vec{r}(\vec{\xi}_{\vec{i}}; m)) g(\vec{r}(\vec{\xi}_{\vec{i}}; m)) \quad (3.105)$$

The SEM approximation to the global integral is then naturally defined as

$$\int fg dA \approx \sum_{m=1}^M \langle fg \rangle_{\Omega_m} = \langle fg \rangle \quad (3.106)$$

1122 When applied to the product of functions $f, g \in \mathcal{V}^0$, the quadrature approximation $\langle fg \rangle$ defines
 1123 a discrete inner-product in the usual manner.

1124 3.2.6 Horizontal Discretization: The Projection Operators

1125 Let $P : \mathcal{V}^0 \rightarrow \mathcal{V}^1$ be the unique orthogonal (self-adjoint) projection operator from \mathcal{V}^0 onto \mathcal{V}^1
 1126 w.r.t. the SEM discrete inner product (3.106). The operation P is essentially the same as the
 1127 common procedure in the SEM described as *assembly* [Karniadakis and Sherwin, 2005, p. 7], or
 1128 *direct stiffness summation* [Deville et al., 2002, eq. 4.5.8]. Thus the SEM assembly procedure
 1129 is not an ad-hoc way to remove the redundant degrees of freedom in \mathcal{V}^0 , but is in fact the
 1130 natural projection operator P . Applying the projection operator in a finite element method
 1131 requires inverting the finite element mass matrix. A remarkable fact about the SEM is that
 1132 with the GLL based discrete inner product and the careful choice of global basis functions, the
 1133 mass matrix is diagonal [Maday and Patera, 1987]. The resulting projection operator then has
 1134 a very simple form: at element interior points, it leaves the nodal values unchanged, while at
 1135 element boundary points shared by multiple elements it is a Jacobian-weighted average over all
 1136 redundant values [Taylor and Fournier, 2010].

To apply the projection $P : \mathcal{V}_{\text{cov}}^0 \rightarrow \mathcal{V}_{\text{cov}}^1$ to vectors \vec{u} , one cannot project the covariant components since the corresponding basis vectors \vec{g}_β and \vec{g}^α do not necessarily agree along element faces. Instead we must define the projection as acting on the components using a globally continuous basis such as the latitude-longitude unit vectors $\hat{\theta}$ and $\hat{\lambda}$,

$$P(\vec{u}) = P(\vec{u} \cdot \hat{\lambda}) \hat{\lambda} + P(\vec{u} \cdot \hat{\theta}) \hat{\theta}.$$

1137 3.2.7 Horizontal Discretization: Galerkin Formulation

The SEM solves a Galerkin formulation of the equations of interest. Given the discrete differential operators described above, the primitive equations can be written as an ODE for a generic prognostic variable U and right-hand-side (RHS) terms

$$\frac{\partial U}{\partial t} = \text{RHS}.$$

The SEM solves this equation in integral form with respect to the SEM inner product. That is, for a $\text{RHS} \in \mathcal{V}^0$, the SEM finds the unique $\frac{\partial U}{\partial t} \in \mathcal{V}^1$ such that

$$\left\langle \phi \frac{\partial U}{\partial t} \right\rangle = \langle \phi \text{RHS} \rangle \quad \forall \phi \in \mathcal{V}^1.$$

As the prognostic variable is assumed to belong to \mathcal{V}^1 , the RHS will in general belong to \mathcal{V}^0 since it contains derivatives of the prognostic variables, resulting in the loss of continuity at the element boundaries. If one picks a suitable basis for \mathcal{V}^1 , this discrete integral equation results in a system of L equations for the L expansion coefficients of $\frac{\partial U}{\partial t}$. The SEM solves these equations exactly, and the solution can be written in terms of the SEM projection operator as

$$\frac{\partial U}{\partial t} = P(\text{RHS}).$$

1138 The projection operator commutes with any time-stepping scheme, so the equations can be
1139 solved in a two step process, illustrated here for simplicity with the forward Euler method

- Step 1:

$$U^* = U^t + \Delta t \text{ RHS} \quad U^* \in \mathcal{V}^0$$

- Step 2:

$$U^{t+1} = P(U^*) \quad U^{t+1} \in \mathcal{V}^1$$

For compactness of notation, we will denote this two step procedure in what follows by

$$P^{-1} \frac{\partial U}{\partial t} = \text{RHS}.$$

1140 Note that P maps a M_d dimensional space \mathcal{V}^0 into a L dimensional space \mathcal{V}^1 , so here P^{-1} denotes
1141 the left inverse of P . This inverse will never be computed, it is only applied as in step 2 above.

1142 This two step Galerkin solution process represents a natural separation between computation
1143 and communication for the implementation of the SEM on a parallel computer. The computa-
1144 tions in step 1 are all local to the data contained in a single element. Assuming an element-based
1145 decomposition so that each processor contains at least one element, no inter-processor commu-
1146 nication is required in step 1. All inter-processor communication in HOMME is isolated to the
1147 projection operator step, in which element boundary data must be exchanged between adjacent
1148 elements.

1149 3.2.8 Vertical Discretization

The vertical coordinate system uses a Lorenz staggering of the variables as shown in 3.4. Let K be the total number of layers, with variables $\bar{u}, T, q, \omega, \Phi$ at layer mid points denoted by $k = 1, 2, \dots, K$. We denote layer interfaces by $k + \frac{1}{2}, k = 0, 1, \dots, K$, so that $\eta_{1/2} = \eta_{\text{top}}$ and $\eta_{K+1/2} = 1$. The η -integrals will be replaced by sums. We will use δ_η to denote the discrete $\partial/\partial\eta$ operator. The δ_η operator uses centered differences to compute derivatives with respect to η at layer mid point from layer interface values, $\delta_\eta(X)_k = (X_{k+1/2} - X_{k-1/2})/(\eta_{k+1/2} - \eta_{k-1/2})$. We will use the over-bar notation for vertical averaging, $\bar{q}_{k+1/2} = (q_{k+1} + q_k)/2$. We also introduce the symbol π to denote the discrete pseudo-density $\frac{\partial p}{\partial \eta}$ given by

$$\pi_k = \delta_\eta(p)_k$$

We will use $\overline{\dot{\eta}\delta_\eta}$ to denote the discrete form of the $\dot{\eta}\partial/\partial\eta$ operator. We use the discretization given in 3.3.5. This operator acts on quantities defined at layer mid-points and returns a result also at layer mid-points,

$$\overline{\dot{\eta}\delta_\eta}(X)_k = \frac{1}{2\pi_k\Delta\eta_k} [(\dot{\eta}\pi)_{k+1/2}(X_{k+1} - X_k) + (\dot{\eta}\pi)_{k-1/2}(X_k - X_{k-1})] \quad (3.107)$$

where $\Delta\eta_k = \eta_{k+1/2} - \eta_{k-1/2}$. We use the over-bar notation since the formula can be seen as a π -weighted average of a layer interface centered difference approximation to $\dot{\eta}\partial/\partial\eta$. This formulation was constructed in Simmons and Burridge [1981] in order to ensure mass and energy conservation. Here we will use an equivalent expression that can be written in terms of δ_η ,

$$\overline{\dot{\eta}\delta_\eta}(X)_k = \frac{1}{\pi_k} \left[\delta_\eta (\dot{\eta}\pi\overline{X})_k - X \delta_\eta (\dot{\eta}\pi)_k \right]. \quad (3.108)$$

1151 3.2.9 Discrete formulation: Dynamics

We discretize the equations exactly in the form shown in (3.83), (3.84), (3.88) and (3.90), obtaining

$$P^{-1}\frac{\partial\vec{u}}{\partial t} = -(\zeta + f)\hat{k}\times\vec{u} + \nabla_h \left(\frac{1}{2}\vec{u}^2 + \Phi \right) - \overline{\dot{\eta}\delta_\eta}(\vec{u}) - \frac{RT_v}{p}\nabla_h(p) \quad (3.109)$$

$$P^{-1}\frac{\partial T}{\partial t} = -\vec{u} \cdot \nabla_h(T) - \overline{\dot{\eta}\delta_\eta}(T) + \frac{RT_v}{c_p^*p}\omega \quad (3.110)$$

$$P^{-1}\frac{\partial p_s}{\partial t} = -\sum_{j=1}^K \nabla_h \cdot (\pi\vec{u})_j \Delta\eta_j \quad (3.111)$$

$$(\dot{\eta}\pi)_{i+1/2} = B(\eta_{i+1/2}) \sum_{j=1}^K \nabla_h \cdot (\pi\vec{u})_j \Delta\eta_j - \sum_{j=1}^i \nabla_h \cdot (\pi\vec{u})_j \Delta\eta_j. \quad (3.112)$$

1152 We consider $(\dot{\eta}\pi)$ a single quantity given at layer interfaces and defined by (3.112). The no-flux
 1153 boundary condition is $(\dot{\eta}\pi)_{1/2} = (\dot{\eta}\pi)_{K+1/2} = 0$. In (3.112), we used a midpoint quadrature
 1154 rule to evaluate the indefinite integral from (3.90). In practice $\Delta\eta$ can be eliminated from the
 1155 discrete equations by scaling π , but here we retain them so as to have a direct correspondence
 1156 with the continuum form of the equations written in terms of $\frac{\partial p}{\partial \eta}$.

Finally we give the approximations for the diagnostic equations. We first integrate to layer interface $i - \frac{1}{2}$ using the same mid-point rule as used to derive (3.112), and then add an additional term representing the integral from $i - \frac{1}{2}$ to i :

$$\omega_i = (\vec{u} \cdot \nabla_h p)_i - \sum_{j=1}^{i-1} \nabla_h \cdot (\pi\vec{u})_j \Delta\eta_j + \nabla_h \cdot (\pi\vec{u})_i \frac{\Delta\eta_i}{2} \quad (3.113)$$

$$= (\vec{u} \cdot \nabla_h p)_i - \sum_{j=1}^K C_{ij} \nabla_h \cdot (\pi\vec{u})_j \quad (3.114)$$

where

$$C_{ij} = \begin{cases} \Delta\eta_j & i > j \\ \Delta\eta_j/2 & i = j \\ 0 & i < j \end{cases}$$

and similar for Φ ,

$$(\Phi - \Phi_s)_i = \left(\frac{RT_v}{p}\pi\right)_i \frac{\Delta\eta_i}{2} + \sum_{j=i+1}^K \left(\frac{RT_v}{p}\pi\right)_j \Delta\eta_j \quad (3.115)$$

$$= \sum_{j=1}^K H_{ij} \left(\frac{RT_v}{p}\pi\right)_j \quad (3.116)$$

where

$$H_{ij} = \begin{cases} \Delta\eta_j & i < j \\ \Delta\eta_j/2 & i = j \\ 0 & i > j \end{cases}$$

Similar to 3.3.5, we note that

$$\Delta\eta_i C_{ij} = \Delta\eta_j H_{ji} \quad (3.117)$$

1157 which ensures energy conservation [Taylor, 2010].

1158 3.2.10 Consistency

It is important that the discrete equations be as consistent as possible. In particular, we need a discrete version of (3.85), the non-vertically averaged continuity equation. Equation (3.112) implicitly implies such an equation. To see this, apply δ_η to (3.112) and using that $\partial p/\partial t = B(\eta)\partial p_s/\partial t$ then we can derive, at layer mid-points,

$$P^{-1}\frac{\partial\pi}{\partial t} = -\nabla_{\mathbf{h}} \cdot (\pi\vec{u}) - \delta_\eta(\dot{\eta}\pi). \quad (3.118)$$

A second type of consistency that has been identified as important is that (3.113), the discrete equation for ω , be consistent with (3.112), the discrete continuity equation [Williamson and Olson, 1994b]. The two discrete equations should imply a reasonable discretization of $\omega = Dp/Dt$. To show this, we take the average of (3.112) at layers $i-1/2$ and $i+1/2$ and combine this with (3.113) (at layer mid-points i) and assuming that $B(\eta_i) = B(\eta_{i-1/2}) + B(\eta_{i+1/2})$ we obtain

$$P^{-1}\frac{\partial p}{\partial t} = \omega_i - (\vec{u} \cdot \nabla_{\mathbf{h}} p)_i - \frac{1}{2}((\dot{\eta}\delta_\eta)_{i-1/2} + (\dot{\eta}\delta_\eta)_{i+1/2}).$$

1159 which, since $\vec{u} \cdot \nabla_{\mathbf{h}} p$ is given at layer mid-points and $\dot{\eta}\pi$ at layer interfaces, is the SEM discretiza-
1160 tion of $w = \partial p/\partial t + \vec{u} \cdot \nabla_{\mathbf{h}} p + \dot{\eta}\pi$.

1161 3.2.11 Time Stepping

Applying the SEM discretization to (3.109)-(3.112) results in a system of ODEs. These are solved with an N -stage Runge-Kutta method. This method allows for a gravity-wave based CFL number close to $N - 1$, (normalized so that the largest stable timestep of the Robert filtered Leapfrog method has a CFL number of 1.0). The value of N is chosen large enough so that the dynamics will be stable at the same timestep used by the tracer advection scheme. To determine N , we first note that the tracer advection scheme uses a less efficient (in terms of maximum CFL) strong stability preserving Runge-Kutta method described below. It is stable at an advective CFL number of 1.4. Let u_0 be a maximum wind speed and c_0 be the maximum gravity wave speed. The gravity wave and advective CFL conditions are

$$\Delta t \leq (N - 1)\Delta x/c_0, \quad \Delta t \leq 1.4\Delta x/u_0.$$

1162 In the case where Δt is chosen as the largest stable timestep for advection, then we require
 1163 $N \geq 1 + 1.4c_0/u_0$ for a stable dynamics timestep. Using a typical values $u_0 = 120$ m/s and
 1164 $c_0 = 340$ m/s gives $N = 5$. CAM places additional restrictions on the timestep (such as that the
 1165 physics timestep must be an integer multiple of Δt) which also influence the choice of Δt and
 1166 N .

1167 3.2.12 Dissipation

A horizontal hyper-viscosity operator, modeled after 3.3.6 is applied to the momentum and temperature equations. It is applied in a time-split manor after each dynamics timestep. The hyper-viscosity step for vectors can be written as

$$\frac{\partial \vec{u}}{\partial t} = -\nu \Delta^2 \vec{u}.$$

An integral form of this equation suitable for the SEM is obtained using a mixed finite element formulation (following Giraldo [1999]) which writes the equation as a system of equations involving only first derivatives. We start by introduced an auxiliary vector \vec{f} and using the identity $\Delta \vec{u} = \nabla(\nabla \cdot \vec{u}) - \nabla \times (\nabla \times \vec{u})$,

$$\frac{\partial \vec{u}}{\partial t} = -\nu \left(\nabla(\nabla \cdot \vec{f}) - \nabla \times \hat{k}(\nabla \times \vec{f}) \right) \quad (3.119)$$

$$\vec{f} = \nabla(\nabla \cdot \vec{u}) - \nabla \times (\nabla \times \vec{u}) \hat{k}. \quad (3.120)$$

Integrating the gradient and curl operators by parts gives

$$\iint \vec{\phi} \cdot \frac{\partial \vec{u}}{\partial t} dA = \nu \iint \left[(\nabla \cdot \vec{\phi})(\nabla \cdot \vec{f}) + (\nabla \times \vec{\phi}) \cdot \hat{k}(\nabla \times \vec{f}) \right] dA \quad (3.121)$$

$$\iint \vec{\phi} \cdot \vec{f} dA = - \iint \left[(\nabla \cdot \vec{\phi})(\nabla \cdot \vec{u}) + (\nabla \times \vec{\phi}) \cdot \hat{k}(\nabla \times \vec{u}) \right] dA. \quad (3.122)$$

$$(3.123)$$

The SEM Galerkin solution of this integral equation is most naturally written in terms of an inverse mass matrix instead of the projection operator. It can be written in terms of the SEM

projection operator by first testing with the product of the element cardinal functions and the contravariant basis vector $\vec{\phi} = \phi_{\bar{i}}\vec{g}_{\alpha}$. With this type of test function, the RHS of (3.122) can be defined as a weak Laplacian operator $\vec{f} = D(\vec{u}) \in \mathcal{V}_{\text{cov}}^0$. The covariant components of \vec{f} given by $f_{\alpha} = \vec{f} \cdot \vec{g}_{\alpha}$ are then

$$f_{\alpha}(\vec{r}(\vec{\xi}_{\bar{i}}; m)) = \frac{-1}{w_{i1}w_{i2}J_m(\vec{\xi}_{\bar{i}})} \left\langle (\nabla_{\text{h}} \cdot \phi_{\bar{i}}\vec{g}_{\alpha})(\nabla_{\text{h}} \cdot \vec{u}) + (\nabla_{\text{h}} \times \phi_{\bar{i}}\vec{g}_{\alpha}) \cdot \hat{k}(\nabla_{\text{h}} \times \vec{u}) \right\rangle$$

Then the SEM solution to (3.121) and (3.122) is given by

$$\vec{u}(t + \Delta t) = \vec{u}(t) - \nu \Delta t P \left(D \left(P(D(\vec{u})) \right) \right).$$

1168 Because of the SEM tensor product decomposition, the expression for D can be evaluated in
1169 only $O(d)$ operations per grid point, and in CAM-HOMME typically $d = 3$.

1170 Following 3.3.6, a correction term is added so the hyper-viscosity does not damp rigid rota-
1171 tion. The hyper-viscosity formulation used for scalars such as T is much simpler, since instead
1172 of the vector Laplacian identity we use $\Delta T = \nabla \cdot \nabla T$. Otherwise the approach is identical to
1173 that used above so we omit the details. The correction for terrain following coordinates given
1174 in 3.3.6 is not yet implemented in CAM-HOMME.

1175 3.2.13 Discrete formulation: Tracer Advection

1176 All tracers, including specific humidity, are advected with a discretized version of (3.86).
1177 HOMME uses the vertically Lagrangian approach (see 3.1.4) from Lin [2004]. At the begin-
1178 ning of each timestep, the tracers are assumed to be given on the η -coordinate layer mid points.
1179 The tracers are advanced in time on a moving vertical coordinate system η' defined so that
1180 $\eta' = 0$. At the end of the timestep, the tracers are remapped back to the η -coordinate layer mid
1181 points using the monotone remap algorithm from Zerroukat et al. [2005].

The horizontal advection step consists of using the SEM to solve

$$\frac{\partial}{\partial t} (\pi q) = -\nabla_{\text{h}} \cdot \left(\overline{(\pi \vec{u})} q \right) \quad (3.124)$$

1182 on the surfaces defined by the η' layer mid points. The quantity $\overline{(\pi \vec{u})}$ is the mean flux computed
1183 during the dynamics update. The mean flux used in (3.124), combined with a suitable mean
1184 vertical flux used in the remap stage allows HOMME to preserve mass/tracer-mass consistency:
1185 The tracer advection of πq with $q = 1$ will be identical to the advection of π implied from
1186 (3.118). The mass/tracer-mass consistency capability is not in the version of HOMME included
1187 in CAM 4.0, but should be in all later versions.

The equation is discretized in time using the optimal 3 stage strong stability preserving (SSP) second order Runge-Kutta method from Spiteri and Ruuth [2002]. The RK-SSP method is chosen because it will preserve the monotonicity properties of the horizontal discretization. RK-SSP methods are convex combinations of forward-Euler timesteps, so each stage s of the RK-SSP timestep looks like

$$(\pi q)^{s+1} = (\pi q)^s - \Delta t \nabla_{\text{h}} \cdot \left(\overline{(\pi \vec{u})} q^s \right) \quad (3.125)$$

1188 Simply discretizing this equation with the SEM will result in locally conservative, high-order
 1189 accurate but oscillatory transport scheme. A limiter is added to reduce or eliminate these oscil-
 1190 lations [Taylor et al., 2009]. HOMME supports both monotone and sign-preserving limiters, but
 1191 the most effective limiter for HOMME has not yet been determined. The default configuration
 1192 in CAM4 is to use the sign-preserving limiter to prevent negative values of q coupled with a
 1193 sign-preserving hyper-viscosity operator which dissipates q^2 .

1194 3.2.14 Conservation and Compatibility

The SEM is compatible, meaning it has a discrete version of the divergence theorem, Stokes theorem and curl/gradients annihilator properties Taylor and Fournier [2010]. The divergence theorem is the key property of the horizontal discretization that is needed to show conservation. For an arbitrary scalar h and vector \vec{u} at layer mid-points, the divergence theorem (or the divergence/gradients adjoint relation) can be written

$$\int h \nabla \cdot \vec{u} dA + \int \vec{u} \nabla h dA = 0.$$

The discrete version obeyed by the SEM discretization, using (3.106), is given by

$$\langle h \nabla_h \cdot \vec{u} \rangle + \langle \vec{u} \cdot \nabla_h h \rangle = 0. \quad (3.126)$$

1195 The discrete divergence and Stokes theorem apply locally at the element with the addition of
 1196 an element boundary integral. The local form is used to show local conservation of mass and
 1197 that the horizontal advection operator locally conserves the two-dimensional potential vorticity
 1198 [Taylor and Fournier, 2010].

In the vertical, Simmons and Burridge [1981] showed that the δ_η and $\overline{\dot{\eta}\delta_\eta}$ operators needed to satisfy two integral identities to ensure conservation. For any $\dot{\eta}$ layer interface velocity which satisfies $\dot{\eta}_{1/2} = \dot{\eta}_{K+1/2} = 0$ and f, g arbitrary functions of layer mid points. The first identity is the adjoint property (compatibility) for δ_η and π ,

$$\sum_{i=1}^K \Delta\eta_i \pi_i \overline{\dot{\eta}\delta_\eta}(f) + \sum_{i=1}^K \Delta\eta_i f_i \delta_\eta(\dot{\eta}\pi) = 0 \quad (3.127)$$

which follows directly from the definition of the $\overline{\dot{\eta}\delta_\eta}$ difference operator given in (3.108). The second identity we write in terms of δ_η ,

$$\sum_{i=1}^K \Delta\eta_i f g \delta_\eta(\dot{\eta}\pi) = \sum_{i=1}^K \Delta\eta_i f \delta_\eta(\dot{\eta}\pi \bar{g}) + \sum_{i=1}^K \Delta\eta_i g \delta_\eta(\dot{\eta}\pi \bar{f}) \quad (3.128)$$

1199 which is a discrete integrated-by-parts analog of $\partial(fg) = f\partial g + g\partial f$. Construction of methods
 1200 with both properties on a staggered unequally spaced grid is the reason behind the complex
 1201 definition for $\overline{\dot{\eta}\delta_\eta}$ in (3.108).

The energy conservation properties of CAM-HOMME were studied in Taylor [2010] using the aqua planet test case [Neale and Hoskins, 2001a,b]. CAM-HOMME uses

$$E = \left\langle \sum_{i=1}^K \Delta\eta_i \pi_i \left(\frac{1}{2} \vec{u}^2 + c_p^* T \right)_i \right\rangle + \langle p_s \Phi_s \rangle$$

1202 as the discretization of the total moist energy (3.91). The conservation of E is *semi-discrete*,
 1203 meaning that the only error in conservation is the time truncation error. In the adiabatic case
 1204 (with no hyper-viscosity and no limiters), running from a fully spun up initial condition, the error
 1205 in conservation decreases to machine precision at a second-order rate with decreasing timestep.
 1206 In the full non-adiabatic case with a realistic timestep, $dE/dt \sim 0.013\text{W/m}^2$.

1207 The CAM physics conserve a dry energy E_{dry} from Boville and Bretherton [2003a] which is
 1208 not conserved by the moist primitive equations. Although $E - E_{\text{dry}}$ is small, adiabatic processes
 1209 in the primitive equations result in a net heating $dE_{\text{dry}}/dt \sim 0.5\text{W/m}^2$ [Taylor, 2010]. If it is
 1210 desired that the dynamical core conserve E_{dry} instead of E , HOMME uses the energy fixer from
 1211 3.3.20.

1212 3.3 Eulerian Dynamical Core

1213 The hybrid vertical coordinate that has been implemented in CAM 5.0 is described in this
 1214 section. The hybrid coordinate was developed by Simmons and Strüfing [1981] in order to
 1215 provide a general framework for a vertical coordinate which is terrain following at the Earth's
 1216 surface, but reduces to a pressure coordinate at some point above the surface. The hybrid
 1217 coordinate is more general in concept than the modified σ scheme of Sangster [1960], which is
 1218 used in the GFDL SKYHI model. However, the hybrid coordinate is normally specified in such
 1219 a way that the two coordinates are identical.

1220 The following description uses the same general development as Simmons and Strüfing [1981],
 1221 who based their development on the generalized vertical coordinate of Kasahara [1974]. A
 1222 specific form of the coordinate (the hybrid coordinate) is introduced at the latest possible point.
 1223 The description here differs from Simmons and Strüfing [1981] in allowing for an upper boundary
 1224 at finite height (nonzero pressure), as in the original development by Kasahara. Such an upper
 1225 boundary may be required when the equations are solved using vertical finite differences.

1226 3.3.1 Generalized terrain-following vertical coordinates

1227 Deriving the primitive equations in a generalized terrain-following vertical coordinate requires
 1228 only that certain basic properties of the coordinate be specified. If the surface pressure is π ,
 1229 then we require the generalized coordinate $\eta(p, \pi)$ to satisfy:

- 1230 1. $\eta(p, \pi)$ is a monotonic function of p .
- 1231 2. $\eta(\pi, \pi) = 1$
- 1232 3. $\eta(0, \pi) = 0$
- 1233 4. $\eta(p_t, \pi) = \eta_t$ where p_t is the top of the model.

The latter requirement provides that the top of the model will be a pressure surface, simplifying
 the specification of boundary conditions. In the case that $p_t = 0$, the last two requirements
 are identical and the system reduces to that described in Simmons and Strüfing [1981]. The
 boundary conditions that are required to close the system are:

$$\dot{\eta}(\pi, \pi) = 0, \tag{3.129}$$

$$\dot{\eta}(p_t, \pi) = \omega(p_t) = 0. \tag{3.130}$$

Given the above description of the coordinate, the continuous system of equations can be written following [Kasahara \[1974\]](#) and [Simmons and Strüfing \[1981\]](#). The prognostic equations are:

$$\frac{\partial \zeta}{\partial t} = \mathbf{k} \cdot \nabla \times (\mathbf{n} / \cos \phi) + F_{\zeta_H}, \quad (3.131)$$

$$\frac{\partial \delta}{\partial t} = \nabla \cdot (\mathbf{n} / \cos \phi) - \nabla^2 (E + \Phi) + F_{\delta_H}, \quad (3.132)$$

$$\begin{aligned} \frac{\partial T}{\partial t} = & \frac{-1}{a \cos^2 \phi} \left[\frac{\partial}{\partial \lambda} (UT) + \cos \phi \frac{\partial}{\partial \phi} (VT) \right] + T\delta - \dot{\eta} \frac{\partial T}{\partial \eta} + \frac{R}{c_p^*} T_v \frac{\omega}{p} \\ & + Q + F_{T_H} + F_{F_H}, \end{aligned} \quad (3.133)$$

$$\frac{\partial q}{\partial t} = \frac{-1}{a \cos^2 \phi} \left[\frac{\partial}{\partial \lambda} (Uq) + \cos \phi \frac{\partial}{\partial \phi} (Vq) \right] + q\delta - \dot{\eta} \frac{\partial q}{\partial \eta} + S, \quad (3.134)$$

$$\frac{\partial \pi}{\partial t} = \int_1^{\eta_t} \nabla \cdot \left(\frac{\partial p}{\partial \eta} \mathbf{V} \right) d\eta. \quad (3.135)$$

The notation follows standard conventions, and the following terms have been introduced with $\mathbf{n} = (n_U, n_V)$:

$$n_U = +(\zeta + f)V - \dot{\eta} \frac{\partial U}{\partial \eta} R \frac{T_v}{p} \frac{1}{a} - \frac{\partial p}{\partial \lambda} + F_U, \quad (3.136)$$

$$n_V = -(\zeta + f)U - \dot{\eta} \frac{\partial V}{\partial \eta} - R \frac{T_v \cos \phi}{p} \frac{\partial p}{\partial \phi} + F_V, \quad (3.137)$$

$$E = \frac{U^2 + V^2}{2 \cos^2 \phi}, \quad (3.138)$$

$$(U, V) = (u, v) \cos \phi, \quad (3.139)$$

$$T_v = \left[1 + \left(\frac{R_v}{R} - 1 \right) q \right] T, \quad (3.140)$$

$$c_p^* = \left[1 + \left(\frac{c_{p_v}}{c_p} - 1 \right) q \right] c_p. \quad (3.141)$$

1234 The terms F_U, F_V, Q , and S represent the sources and sinks from the parameterizations for
 1235 momentum (in terms of U and V), temperature, and moisture, respectively. The terms F_{ζ_H} and
 1236 F_{δ_H} represent sources due to horizontal diffusion of momentum, while F_{T_H} and F_{F_H} represent
 1237 sources attributable to horizontal diffusion of temperature and a contribution from frictional
 1238 heating (see sections on horizontal diffusion and horizontal diffusion correction).

In addition to the prognostic equations, three diagnostic equations are required:

$$\Phi = \Phi_s + R \int_{p(\eta)}^{p(1)} T_v d \ln p, \quad (3.142)$$

$$\dot{\eta} \frac{\partial p}{\partial \eta} = -\frac{\partial p}{\partial t} - \int_{\eta_t}^{\eta} \nabla \cdot \left(\frac{\partial p}{\partial \eta} \mathbf{V} \right) d\eta, \quad (3.143)$$

$$\omega = \mathbf{V} \cdot \nabla p - \int_{\eta_t}^{\eta} \nabla \cdot \left(\frac{\partial p}{\partial \eta} \mathbf{V} \right) d\eta. \quad (3.144)$$

1239 Note that the bounds on the vertical integrals are specified as values of η (*e.g.* $\eta_t, 1$) or as
 1240 functions of p (*e.g.* $p(1)$, which is the pressure at $\eta = 1$).

1241 3.3.2 Conversion to final form

1242 Equations (3.129)-(3.144) are the complete set which must be solved by a GCM. However, in
 1243 order to solve them, the function $\eta(p, \pi)$ must be specified. In advance of actually specifying
 1244 $\eta(p, \pi)$, the equations will be cast in a more convenient form. Most of the changes to the
 1245 equations involve simple applications of the chain rule for derivatives, in order to obtain terms
 1246 that will be easy to evaluate using the predicted variables in the model. For example, terms
 1247 involving horizontal derivatives of p must be converted to terms involving only $\partial p/\partial\pi$ and
 1248 horizontal derivatives of π . The former can be evaluated once the function $\eta(p, \pi)$ is specified.

The vertical advection terms in (3.133), (3.134), (3.136), and (3.137) may be rewritten as:

$$\dot{\eta} \frac{\partial \psi}{\partial \eta} = \dot{\eta} \frac{\partial p}{\partial \eta} \frac{\partial \psi}{\partial p}, \quad (3.145)$$

since $\dot{\eta} \partial p/\partial \eta$ is given by (3.143). Similarly, the first term on the right-hand side of (3.143) can be expanded as

$$\frac{\partial p}{\partial t} = \frac{\partial p}{\partial \pi} \frac{\partial \pi}{\partial t}, \quad (3.146)$$

1249 and (3.135) invoked to specify $\partial \pi/\partial t$.

The integrals which appear in (3.135), (3.143), and (3.144) can be written more conveniently by expanding the kernel as

$$\nabla \cdot \left(\frac{\partial p}{\partial \eta} \mathbf{V} \right) = \mathbf{V} \cdot \nabla \left(\frac{\partial p}{\partial \eta} \right) + \frac{\partial p}{\partial \eta} \nabla \cdot \mathbf{V}. \quad (3.147)$$

The second term in (3.147) is easily treated in vertical integrals, since it reduces to an integral in pressure. The first term is expanded to:

$$\begin{aligned} \mathbf{V} \cdot \nabla \left(\frac{\partial p}{\partial \eta} \right) &= \mathbf{V} \cdot \frac{\partial}{\partial \eta} (\nabla p) \\ &= \mathbf{V} \cdot \frac{\partial}{\partial \eta} \left(\frac{\partial p}{\partial \pi} \nabla \pi \right) \\ &= \mathbf{V} \cdot \frac{\partial}{\partial \eta} \left(\frac{\partial p}{\partial \pi} \right) \nabla \pi + \mathbf{V} \cdot \frac{\partial p}{\partial \pi} \nabla \left(\frac{\partial \pi}{\partial \eta} \right). \end{aligned} \quad (3.148)$$

1250 The second term in (3.148) vanishes because $\partial \pi/\partial \eta = 0$, while the first term is easily treated
 1251 once $\eta(p, \pi)$ is specified. Substituting (3.148) into (3.147), one obtains:

$$\nabla \cdot \left(\frac{\partial p}{\partial \eta} \mathbf{V} \right) = \frac{\partial}{\partial \eta} \left(\frac{\partial p}{\partial \pi} \right) \mathbf{V} \cdot \nabla \pi + \frac{\partial p}{\partial \eta} \nabla \cdot \mathbf{V}. \quad (3.149)$$

1252 Using (3.149) as the kernel of the integral in (3.135), (3.143), and (3.144), one obtains integrals
 1253 of the form

$$\begin{aligned} \int \nabla \cdot \left(\frac{\partial p}{\partial \eta} \mathbf{V} \right) d\eta &= \int \left[\frac{\partial}{\partial \eta} \left(\frac{\partial p}{\partial \pi} \right) \mathbf{V} \cdot \nabla \pi + \frac{\partial p}{\partial \eta} \nabla \cdot \mathbf{V} \right] d\eta \\ &= \int \mathbf{V} \cdot \nabla \pi d \left(\frac{\partial p}{\partial \pi} \right) + \int \delta dp. \end{aligned} \quad (3.150)$$

The original primitive equations (3.131)-(3.135), together with (3.136), (3.137), and (3.142)-(3.144) can now be rewritten with the aid of (3.145), (3.146), and (3.150).

$$\frac{\partial \zeta}{\partial t} = \mathbf{k} \cdot \nabla \times (\mathbf{n} / \cos \phi) + F_{\zeta_H}, \quad (3.151)$$

$$\frac{\partial \delta}{\partial t} = \nabla \cdot (\mathbf{n} / \cos \phi) - \nabla^2 (E + \Phi) + F_{\delta_H}, \quad (3.152)$$

$$\begin{aligned} \frac{\partial T}{\partial t} = & \frac{-1}{a \cos^2 \phi} \left[\frac{\partial}{\partial \lambda} (UT) + \cos \phi \frac{\partial}{\partial \phi} (VT) \right] + T\delta - \dot{\eta} \frac{\partial p}{\partial \eta} \frac{\partial T}{\partial p} + \frac{R}{c_p^*} T_v \frac{\omega}{p} \\ & + Q + F_{T_H} + F_{F_H} \end{aligned} \quad (3.153)$$

$$\frac{\partial q}{\partial t} = \frac{-1}{a \cos^2 \phi} \left[\frac{\partial}{\partial \lambda} (Uq) + \cos \phi \frac{\partial}{\partial \phi} (Vq) \right] + q\delta - \dot{\eta} \frac{\partial p}{\partial \eta} \frac{\partial q}{\partial p} + S, \quad (3.154)$$

$$\frac{\partial \pi}{\partial t} = - \int_{(\eta_t)}^{(1)} \mathbf{V} \cdot \nabla \pi d \left(\frac{\partial p}{\partial \pi} \right) - \int_{p(\eta_t)}^{p(1)} \delta dp, \quad (3.155)$$

$$n_U = +(\zeta + f)V - \dot{\eta} \frac{\partial p}{\partial \eta} \frac{\partial -U}{\partial p} - R \frac{T_v}{a} \frac{1}{p} \frac{\partial p}{\partial \pi} \frac{\partial \pi}{\partial \lambda} + F_U, \quad (3.156)$$

$$n_V = -(\zeta + f)U - \dot{\eta} \frac{\partial p}{\partial \eta} \frac{\partial -V}{\partial p} - R \frac{T_v \cos \phi}{a} \frac{1}{p} \frac{\partial p}{\partial \pi} \frac{\partial \pi}{\partial \phi} + F_V, \quad (3.157)$$

$$\Phi = \Phi_s + R \int_{p(\eta)}^{p(1)} T_v d \ln p, \quad (3.158)$$

$$\begin{aligned} \dot{\eta} \frac{\partial p}{\partial \eta} = & \frac{\partial p}{\partial \pi} \left[\int_{(\eta_t)}^{(1)} \mathbf{V} \cdot \nabla \pi d \left(\frac{\partial p}{\partial \pi} \right) + \int_{p(\eta_t)}^{p(1)} \delta dp \right] \\ & - \int_{(\eta_t)}^{(\eta)} \mathbf{V} \cdot \nabla \pi d \left(\frac{\partial p}{\partial \pi} \right) - \int_{p(\eta_t)}^{p(\eta)} \delta dp, \end{aligned} \quad (3.159)$$

$$\omega = \frac{\partial p}{\partial \pi} \mathbf{V} \cdot \nabla \pi - \int_{(\eta_t)}^{(\eta)} \mathbf{V} \cdot \nabla \pi d \left(\frac{\partial p}{\partial \pi} \right) - \int_{p(\eta_t)}^{p(\eta)} \delta dp. \quad (3.160)$$

1254 Once $\eta(p, \pi)$ is specified, then $\partial p / \partial \pi$ can be determined and (3.151)-(3.160) can be solved in a
1255 GCM.

1256 In the actual definition of the hybrid coordinate, it is not necessary to specify $\eta(p, \pi)$ ex-
1257 plicitly, since (3.151)-(3.160) only requires that p and $\partial p / \partial \pi$ be determined. It is sufficient to
1258 specify $p(\eta, \pi)$ and to let η be defined implicitly. This will be done in section 3.3.7. In the case
1259 that $p(\eta, \pi) = \sigma \pi$ and $\eta_t = 0$, (3.151)-(3.160) can be reduced to the set of equations solved by
1260 CCM1.

1261 3.3.3 Continuous equations using $\partial \ln(\pi) / \partial t$

1262 In practice, the solutions generated by solving the above equations are excessively noisy. This
1263 problem appears to arise from aliasing problems in the hydrostatic equation (3.158). The $\ln p$
1264 integral introduces a high order nonlinearity which enters directly into the divergence equation
1265 (3.152). Large gravity waves are generated in the vicinity of steep orography, such as in the
1266 Pacific Ocean west of the Andes.

1267 The noise problem is solved by converting the equations given above, which use π as a
1268 prognostic variable, to equations using $\Pi = \ln(\pi)$. This results in the hydrostatic equation
1269 becoming only quadratically nonlinear except for moisture contributions to virtual temperature.
1270 Since the spectral transform method will be used to solve the equations, gradients will be
1271 obtained during the transform from wave to grid space. Outside of the prognostic equation for
1272 Π , all terms involving $\nabla\pi$ will then appear as $\pi\nabla\Pi$.

Equations (3.151)-(3.160) become:

$$\frac{\partial\zeta}{\partial t} = \mathbf{k} \cdot \nabla \times (\mathbf{n}/\cos\phi) + F_{\zeta_H}, \quad (3.161)$$

$$\frac{\partial\delta}{\partial t} = \nabla \cdot (\mathbf{n}/\cos\phi) - \nabla^2 (E + \Phi) + F_{\delta_H}, \quad (3.162)$$

$$\begin{aligned} \frac{\partial T}{\partial t} = & \frac{-1}{a \cos^2 \phi} \left[\frac{\partial}{\partial \lambda} (UT) + \cos \phi \frac{\partial}{\partial \phi} (VT) \right] + T\delta - \dot{\eta} \frac{\partial p}{\partial \eta} \frac{\partial T}{\partial p} + \frac{R}{c_p^*} T_v \frac{\omega}{p} \\ & + Q + F_{T_H} + F_{F_H}, \end{aligned} \quad (3.163)$$

$$\frac{\partial q}{\partial t} = \frac{-1}{a \cos^2 \phi} \left[\frac{\partial}{\partial \lambda} (Uq) + \cos \phi \frac{\partial}{\partial \phi} (Vq) \right] + q\delta - \dot{\eta} \frac{\partial p}{\partial \eta} \frac{\partial q}{\partial p} + S, \quad (3.164)$$

$$\frac{\partial \Pi}{\partial t} = - \int_{(\eta_t)}^{(1)} \mathbf{V} \cdot \nabla \Pi d \left(\frac{\partial p}{\partial \pi} \right) - \frac{1}{\pi} \int_{p(\eta_t)}^{p(1)} \delta dp, \quad (3.165)$$

$$n_U = +(\zeta + f)V - \dot{\eta} \frac{\partial p}{\partial \eta} \frac{\partial -U}{\partial p} R \frac{T_v}{a} \frac{\pi}{p} \frac{\partial p}{\partial \pi} \frac{\partial \Pi}{\partial \lambda} + F_U, \quad (3.166)$$

$$n_V = -(\zeta + f)U - \dot{\eta} \frac{\partial p}{\partial \eta} \frac{\partial -V}{\partial p} R \frac{T_v \cos \phi}{a} \frac{\pi}{p} \frac{\partial p}{\partial \pi} \frac{\partial \Pi}{\partial \phi} + F_V, \quad (3.167)$$

$$\Phi = \Phi_s + R \int_{p(\eta)}^{p(1)} T_v d \ln p, \quad (3.168)$$

$$\begin{aligned} \dot{\eta} \frac{\partial p}{\partial \eta} = & \frac{\partial p}{\partial \pi} \left[\int_{(\eta_t)}^{(1)} \pi \mathbf{V} \cdot \nabla \Pi d \left(\frac{\partial p}{\partial \pi} \right) + \int_{p(\eta_t)}^{p(1)} \delta dp \right] \\ & - \int_{(\eta_t)}^{(\eta)} \pi \mathbf{V} \cdot \nabla \Pi d \left(\frac{\partial p}{\partial \pi} \right) - \int_{p(\eta_t)}^{p(\eta)} \delta dp, \end{aligned} \quad (3.169)$$

$$\omega = \frac{\partial p}{\partial \pi} \pi \mathbf{V} \cdot \nabla \Pi - \int_{(\eta_t)}^{(\eta)} \pi \mathbf{V} \cdot \nabla \Pi d \left(\frac{\partial p}{\partial \pi} \right) - \int_{p(\eta_t)}^{p(\eta)} \delta dp. \quad (3.170)$$

1273 The above equations reduce to the standard σ equations used in CCM1 if $\eta = \sigma$ and $\eta_t = 0$.
1274 (Note that in this case $\partial p/\partial \pi = p/\pi = \sigma$.)

1275 3.3.4 Semi-implicit formulation

The model described by (3.161)-(3.170), without the horizontal diffusion terms, together with boundary conditions (3.129) and (3.130), is integrated in time using the semi-implicit leapfrog scheme described below. The semi-implicit form of the time differencing will be applied to (3.162) and (3.164) without the horizontal diffusion sources, and to (3.165). In order to derive the semi-implicit form, one must linearize these equations about a reference state. Isolating

the terms that will have their linear parts treated implicitly, the prognostic equations (3.161), (3.162), and (3.165) may be rewritten as:

$$\frac{\partial \delta}{\partial t} = -RT_v \nabla^2 \ln p - \nabla^2 \Phi + X_1, \quad (3.171)$$

$$\frac{\partial T}{\partial t} = +\frac{R}{c_p^*} T_v \frac{\omega}{p} - \dot{\eta} \frac{\partial p}{\partial \eta} \frac{\partial T}{\partial p} + Y_1, \quad (3.172)$$

$$\frac{\partial \Pi}{\partial t} = -\frac{1}{\pi} \int_{p(\eta_t)}^{p(1)} \delta dp + Z_1, \quad (3.173)$$

where X_1, Y_1, Z_1 are the remaining nonlinear terms not explicitly written in (3.171)-(3.173). The terms involving Φ and ω may be expanded into vertical integrals using (3.168) and (3.170), while the $\nabla^2 \ln p$ term can be converted to $\nabla^2 \Pi$, giving:

$$\frac{\partial \delta}{\partial t} = -RT \frac{\pi}{p} \frac{\partial p}{\partial \pi} \nabla^2 \Pi - R \nabla^2 \int_{p(\eta)}^{p(1)} T d \ln p + X_2, \quad (3.174)$$

$$\frac{\partial T}{\partial t} = -\frac{R T}{c_p p} \int_{p(\eta_t)}^{p(\eta)} \delta dp - \left[\frac{\partial p}{\partial \pi} \int_{p(\eta_t)}^{p(1)} \delta dp - \int_{p(\eta_t)}^{p(\eta)} \delta dp \right] \frac{\partial T}{\partial p} + Y_2, \quad (3.175)$$

$$\frac{\partial \Pi}{\partial t} = -\frac{1}{p_i} \int_{p(\eta_t)}^{p(1)} \delta dp + Z_2. \quad (3.176)$$

1276 Once again, only terms that will be linearized have been explicitly represented in (3.174)-(3.176),
 1277 and the remaining terms are included in $X_2, Y_2,$ and Z_2 . Anticipating the linearization, T_v and
 1278 c_p^* have been replaced by T and c_p in (3.174) and (3.175). Furthermore, the virtual temperature
 1279 corrections are included with the other nonlinear terms.

In order to linearize (3.174)-(3.176), one specifies a reference state for temperature and pressure, then expands the equations about the reference state:

$$T = T^r + T', \quad (3.177)$$

$$\pi = \pi^r + \pi', \quad (3.178)$$

$$p = p^r(\eta, \pi^r) + p'. \quad (3.179)$$

1280 In the special case that $p(\eta, \pi) = \sigma \pi$, (3.174)-(3.176) can be converted into equations involving
 1281 only $\Pi = \ln \pi$ instead of p , and (3.178) and (3.179) are not required. This is a major difference
 1282 between the hybrid coordinate scheme being developed here and the σ coordinate scheme in
 1283 CCM1.

Expanding (3.174)-(3.176) about the reference state (3.177)-(3.179) and retaining only the linear terms explicitly, one obtains:

$$\frac{\partial \delta}{\partial t} = -R \nabla^2 \left[T^r \frac{\pi^r}{p^r} \left(\frac{\partial p}{\partial \pi} \right)^r \Pi + \int_{p^r(\eta)}^{p^r(1)} T' d \ln p^r + \int_{p^r(\eta)}^{p^r(1)} \frac{T^r}{p^r} dp^r \right] + X_3, \quad (3.180)$$

$$\frac{\partial T}{\partial t} = -\frac{R T^r}{c_p p^r} \int_{p^r(\eta_t)}^{p^r(\eta)} \delta dp^r - \left[\left(\frac{\partial p}{\partial \pi} \right)^r \int_{p^r(\eta_t)}^{p^r(1)} \delta dp^r - \int_{p^r(\eta_t)}^{p^r(\eta)} \delta dp^r \right] \frac{\partial T^r}{\partial p^r} + Y_3, \quad (3.181)$$

$$\frac{\partial \Pi}{\partial t} = -\frac{1}{\pi^r} \int_{p^r(\eta_t)}^{p^r(1)} \delta dp^r + Z_3. \quad (3.182)$$

Figure 3.4: Vertical level structure of CAM 5.0

The semi-implicit time differencing scheme treats the linear terms in (3.180)-(3.182) by averaging in time. The last integral in (3.180) is reduced to purely linear form by the relation

$$dp' = \pi' d \left(\frac{\partial p}{\partial \pi} \right)^r + x. \quad (3.183)$$

1284 In the hybrid coordinate described below, p is a linear function of π , so x above is zero.

We will assume that centered differences are to be used for the nonlinear terms, and the linear terms are to be treated implicitly by averaging the previous and next time steps. Finite differences are used in the vertical, and are described in the following sections. At this stage only some very general properties of the finite difference representation must be specified. A layering structure is assumed in which field values are predicted on K layer midpoints denoted by an integer index, η_k (see Figure 3.4). The interface between η_k and η_{k+1} is denoted by a half-integer index, $\eta_{k+1/2}$. The model top is at $\eta_{1/2} = \eta_t$, and the Earth's surface is at $\eta_{K+1/2} = 1$. It is further assumed that vertical integrals may be written as a matrix (of order K) times a column vector representing the values of a field at the η_k grid points in the vertical. The column vectors representing a vertical column of grid points will be denoted by underbars, the matrices will be denoted by bold-faced capital letters, and superscript T will denote the vector transpose. The finite difference forms of (3.180)-(3.182) may then be written down as:

$$\begin{aligned} \underline{\delta}^{n+1} &= \underline{\delta}^{n-1} + 2\Delta t \underline{X}^n \\ &\quad - 2\Delta t R \underline{b}^r \nabla^2 \left(\frac{\Pi^{n-1} + \Pi^{n+1}}{2} - \Pi^n \right) \\ &\quad - 2\Delta t R \underline{H}^r \nabla^2 \left(\frac{(\underline{T}')^{n-1} + (\underline{T}')^{n+1}}{2} - (\underline{T}')^n \right) \\ &\quad - 2\Delta t R \underline{h}^r \nabla^2 \left(\frac{\Pi^{n-1} + \Pi^{n+1}}{2} - \Pi^n \right), \end{aligned} \quad (3.184)$$

$$\underline{T}^{n+1} = \underline{T}^{n-1} + 2\Delta t \underline{Y}^n - 2\Delta t \underline{D}^r \left(\frac{\underline{\delta}^{n-1} + \underline{\delta}^{n+1}}{2} - \underline{\delta}^n \right), \quad (3.185)$$

$$\Pi^{n+1} = \Pi^{n-1} + 2\Delta t Z^n - 2\Delta t \left(\frac{\underline{\delta}^{n-1} + \underline{\delta}^{n+1}}{2} - \underline{\delta}^n \right)^T \frac{1}{\Pi^r} \underline{\Delta p}^r, \quad (3.186)$$

1285 where $()^n$ denotes a time varying value at time step n . The quantities $\underline{X}^n, \underline{Y}^n$, and Z^n are
 1286 defined so as to complete the right-hand sides of (3.171)-(3.173). The components of $\underline{\Delta p}^r$
 1287 are given by $\Delta p_k^r = p_{k+\frac{1}{2}}^r - p_{k-\frac{1}{2}}^r$. This definition of the vertical difference operator Δ will be used in
 1288 subsequent equations. The reference matrices \underline{H}^r and \underline{D}^r , and the reference column vectors \underline{b}^r
 1289 and \underline{h}^r , depend on the precise specification of the vertical coordinate and will be defined later.

1290 3.3.5 Energy conservation

We shall impose a requirement on the vertical finite differences of the model that they conserve the global integral of total energy *in the absence of sources and sinks*. We need to derive

equations for kinetic and internal energy in order to impose this constraint. The momentum equations (more painfully, the vorticity and divergence equations) without the F_U, F_V, F_{ζ_H} and F_{δ_H} contributions, can be combined with the continuity equation

$$\frac{\partial}{\partial t} \left(\frac{\partial p}{\partial \eta} \right) + \nabla \cdot \left(\frac{\partial p}{\partial \eta} \mathbf{V} \right) + \frac{\partial}{\partial \eta} \left(\frac{\partial p}{\partial \eta} \dot{\eta} \right) = 0 \quad (3.187)$$

to give an equation for the rate of change of kinetic energy:

$$\begin{aligned} \frac{\partial}{\partial t} \left(\frac{\partial p}{\partial \eta} E \right) &= -\nabla \cdot \left(\frac{\partial p}{\partial \eta} E \mathbf{V} \right) - \frac{\partial}{\partial \eta} \left(\frac{\partial p}{\partial \eta} E \dot{\eta} \right) \\ &\quad - \frac{RT_v}{p} \frac{\partial p}{\partial \eta} \mathbf{V} \cdot \nabla p - \frac{\partial p}{\partial \eta} \mathbf{V} \cdot \nabla \Phi - . \end{aligned} \quad (3.188)$$

1291 The first two terms on the right-hand side of (3.188) are transport terms. The horizontal integral
 1292 of the first (horizontal) transport term should be zero, and it is relatively straightforward to
 1293 construct horizontal finite difference schemes that ensure this. For spectral models, the integral
 1294 of the horizontal transport term will not vanish in general, but we shall ignore this problem.

1295 The vertical integral of the second (vertical) transport term on the right-hand side of (3.188)
 1296 should vanish. Since this term is obtained from the vertical advection terms for momentum,
 1297 which will be finite differenced, we can construct a finite difference operator that will ensure
 1298 that the vertical integral vanishes.

The vertical advection terms are the product of a vertical velocity ($\dot{\eta} \partial p / \partial \eta$) and the vertical derivative of a field ($\partial \psi / \partial p$). The vertical velocity is defined in terms of vertical integrals of fields (3.170), which are naturally taken to interfaces. The vertical derivatives are also naturally taken to interfaces, so the product is formed there, and then adjacent interface values of the products are averaged to give a midpoint value. It is the definition of the average that must be correct in order to conserve kinetic energy under vertical advection in (3.188). The derivation will be omitted here, the resulting vertical advection terms are of the form:

$$\left(\dot{\eta} \frac{\partial p}{\partial \eta} \frac{\partial \psi}{\partial p} \right)_k = \frac{1}{2\Delta p_k} \left[\left(\dot{\eta} \frac{\partial p}{\partial \eta} \right)_{k+1/2} (\psi_{k+1} - \psi_k) + \left(\dot{\eta} \frac{\partial p}{\partial \eta} \right)_{k-1/2} (\psi_k - \psi_{k-1}) \right], \quad (3.189)$$

$$\Delta p_k = p_{k+1/2} - p_{k-1/2}. \quad (3.190)$$

1299 The choice of definitions for the vertical velocity at interfaces is not crucial to the energy con-
 1300 servation (although not completely arbitrary), and we shall defer its definition until later. The
 1301 vertical advection of temperature is not required to use (3.189) in order to conserve mass or en-
 1302 ergy. Other constraints can be imposed that result in different forms for temperature advection,
 1303 but we will simply use (3.189) in the system described below.

The last two terms in (3.188) contain the conversion between kinetic and internal (potential) energy and the form drag. Neglecting the transport terms, under assumption that global integrals will be taken, noting that $\nabla p / p = \frac{\pi}{p} \frac{\partial p}{\partial \pi} \nabla \Pi$, and substituting for the geopotential using (3.168), (3.188) can be written as:

$$\begin{aligned} \frac{\partial}{\partial t} \left(\frac{\partial p}{\partial \eta} E \right) &= -RT_v \frac{\partial p}{\partial \eta} \mathbf{V} \cdot \left(\frac{\pi}{p} \frac{\partial p}{\partial \pi} \nabla \Pi \right) \\ &\quad - \frac{\partial p}{\partial \eta} \mathbf{V} \cdot \nabla \Phi_s - \frac{\partial p}{\partial \eta} \mathbf{V} \cdot \nabla \int_{p(\eta)}^{p(1)} RT_v d \ln p + \dots \end{aligned} \quad (3.191)$$

The second term on the right-hand side of (3.192) is a source (form drag) term that can be neglected as we are only interested in internal conservation properties. The last term on the right-hand side of (3.192) can be rewritten as

$$\frac{\partial p}{\partial \eta} \mathbf{V} \cdot \nabla \int_{p(\eta)}^{p(1)} RT_v d \ln p = \nabla \cdot \left\{ \frac{\partial p}{\partial \eta} \mathbf{V} \int_{p(\eta)}^{p(1)} RT_v d \ln p \right\} - \nabla \cdot \left(\frac{\partial p}{\partial \eta} \mathbf{V} \right) \int_{p(\eta)}^{p(1)} RT_v d \ln p. \quad (3.192)$$

The global integral of the first term on the right-hand side of (3.192) is obviously zero, so that (3.192) can now be written as:

$$\frac{\partial}{\partial t} \left(\frac{\partial p}{\partial \eta} E \right) = -RT_v \frac{\partial p}{\partial \eta} \mathbf{V} \cdot \left(\frac{\pi}{p} \frac{\partial p}{\partial \pi} \nabla \Pi \right) + \nabla \cdot \left(\frac{\partial p}{\partial \eta} \mathbf{V} \right) \int_{p(\eta)}^{p(1)} RT_v d \ln p + \dots \quad (3.193)$$

We now turn to the internal energy equation, obtained by combining the thermodynamic equation (3.164), without the Q , F_{T_H} , and F_{F_H} terms, and the continuity equation (3.187):

$$\frac{\partial}{\partial t} \left(\frac{\partial p}{\partial \eta} c_p^* T \right) = -\nabla \cdot \left(\frac{\partial p}{\partial \eta} c_p^* T \mathbf{V} \right) - \frac{\partial}{\partial \eta} \left(\frac{\partial p}{\partial \eta} c_p^* T \dot{\eta} \right) + RT_v \frac{\partial p}{\partial \eta} \frac{\omega}{p}. \quad (3.194)$$

As in (3.188), the first two terms on the right-hand side are advection terms that can be neglected under global integrals. Using (3.144), (3.194) can be written as:

$$\frac{\partial}{\partial t} \left(\frac{\partial p}{\partial \eta} c_p^* T \right) = RT_v \frac{\partial p}{\partial \eta} \mathbf{V} \cdot \left(\frac{\pi}{p} \frac{\partial p}{\partial \pi} \nabla \Pi \right) - RT_v \frac{\partial p}{\partial \eta} \frac{1}{p} \int_{\eta_t}^{\eta} \nabla \cdot \left(\frac{\partial p}{\partial \eta} \mathbf{V} \right) d\eta + \dots \quad (3.195)$$

1304 The rate of change of total energy due to internal processes is obtained by adding (3.193) and
 1305 (3.195) and must vanish. The first terms on the right-hand side of (3.193) and (3.195) obviously
 1306 cancel in the continuous form. When the equations are discretized in the vertical, the terms will
 1307 still cancel, providing that the same definition is used for $(1/p \partial p / \partial \pi)_k$ in the nonlinear terms
 1308 of the vorticity and divergence equations (3.166) and (3.167), and in the ω term of (3.164) and
 1309 (3.170).

The second terms on the right-hand side of (3.193) and (3.195) must also cancel in the global mean. This cancellation is enforced locally in the horizontal on the column integrals of (3.193) and (3.195), so that we require:

$$\int_{\eta_t}^1 \left\{ \nabla \cdot \left(\frac{\partial p}{\partial \eta} \mathbf{V} \right) \int_{p(\eta)}^{p(1)} RT_v d \ln p \right\} d\eta = \int_{\eta_t}^1 \left\{ RT_v \frac{\partial p}{\partial \eta} \frac{1}{p} \int_{\eta_t}^{\eta} \nabla \cdot \left(\frac{\partial p}{\partial \eta'} \mathbf{V} \right) d\eta' \right\} d\eta. \quad (3.196)$$

The inner integral on the left-hand side of (3.196) is derived from the hydrostatic equation (3.168), which we shall approximate as

$$\begin{aligned} \Phi_k &= \Phi_s + R \sum_{\ell=k}^K H_{k\ell} T_{v\ell}, \\ &= \Phi_s + R \sum_{\ell=1}^K H_{k\ell} T_{v\ell}, \end{aligned} \quad (3.197)$$

$$\underline{\Phi} = \Phi_s \underline{1} + R \underline{H} \underline{T}_v, \quad (3.198)$$

where $H_{k\ell} = 0$ for $\ell < k$. The quantity $\underline{1}$ is defined to be the unit vector. The inner integral on the right-hand side of (3.196) is derived from the vertical velocity equation (3.170), which we shall approximate as

$$\left(\frac{\omega}{p}\right)_k = \left(\frac{\pi}{p} \frac{\partial p}{\partial \pi}\right)_k \mathbf{V}_k \cdot \nabla \Pi - \sum_{\ell=1}^K C_{k\ell} \left[\delta_\ell \Delta p_\ell + \pi (\mathbf{V}_\ell \cdot \nabla \Pi) \Delta \left(\frac{\partial p}{\partial \pi} \right)_\ell \right], \quad (3.199)$$

where $C_{k\ell} = 0$ for $\ell > k$, and $C_{k\ell}$ is included as an approximation to $1/p_k$ for $\ell \leq k$ and the symbol Δ is similarly defined as in (3.190). $C_{k\ell}$ will be determined so that ω is consistent with the discrete continuity equation following Williamson and Olson [1994a]. Using (3.197) and (3.199), the finite difference analog of (3.196) is

$$\begin{aligned} & \sum_{k=1}^K \left\{ \frac{1}{\Delta \eta_k} \left[\delta_k \Delta p_k + \pi (\mathbf{V}_k \cdot \nabla \Pi) \Delta \left(\frac{\partial p}{\partial \pi} \right)_k \right] R \sum_{\ell=1}^K H_{k\ell} T_{v\ell} \right\} \Delta \eta_k \\ &= \sum_{k=1}^K \left\{ RT_{vk} \frac{\Delta p_k}{\Delta \eta_k} \sum_{\ell=1}^K C_{k\ell} \left[\delta_\ell \Delta p_\ell + \pi (\mathbf{V}_\ell \cdot \nabla \Pi) \Delta \left(\frac{\partial p}{\partial \pi} \right)_\ell \right] \right\} \Delta \eta_k, \end{aligned} \quad (3.200)$$

where we have used the relation

$$\nabla \cdot \mathbf{V} (\partial p / \partial \eta)_k = [\delta_k \Delta p_k + \pi (\mathbf{V}_k \cdot \nabla \Pi) \Delta (\partial p / \partial \pi)_k] / \Delta \eta_k \quad (3.201)$$

(see 3.150). We can now combine the sums in (3.200) and simplify to give

$$\begin{aligned} & \sum_{k=1}^K \sum_{\ell=1}^K \left\{ \left[\delta_k \Delta p_k + \pi (\mathbf{V}_k \cdot \nabla \Pi) \Delta \left(\frac{\partial p}{\partial \pi} \right)_k \right] H_{k\ell} T_{v\ell} \right\} \\ &= \sum_{k=1}^K \sum_{\ell=1}^K \left\{ \left[\delta_\ell \Delta p_\ell + \pi (\mathbf{V}_\ell \cdot \nabla \Pi) \Delta \left(\frac{\partial p}{\partial \pi} \right)_\ell \right] \Delta p_k C_{k\ell} T_{vk} \right\}. \end{aligned} \quad (3.202)$$

Interchanging the indexes on the left-hand side of (3.202) will obviously result in identical expressions if we require that

$$H_{k\ell} = C_{\ell k} \Delta p_\ell. \quad (3.203)$$

1310 Given the definitions of vertical integrals in (3.198) and (3.199) and of vertical advection in
 1311 (3.189) and (3.190) the model will conserve energy as long as we require that \mathbf{C} and \mathbf{H} satisfy
 1312 (3.203). We are, of course, still neglecting lack of conservation due to the truncation of the
 1313 horizontal spherical harmonic expansions.

1314 3.3.6 Horizontal diffusion

1315 CAM 5.0 contains a horizontal diffusion term for T, ζ , and δ to prevent spectral blocking and
 1316 to provide reasonable kinetic energy spectra. The horizontal diffusion operator in CAM 5.0 is
 1317 also used to ensure that the CFL condition is not violated in the upper layers of the model.
 1318 The horizontal diffusion is a linear ∇^2 form on η surfaces in the top three levels of the model
 1319 and a linear ∇^4 form with a partial correction to pressure surfaces for temperature elsewhere.

1320 The ∇^2 diffusion near the model top is used as a simple sponge to absorb vertically propagating
 1321 planetary wave energy and also to control the strength of the stratospheric winter jets. The ∇^2
 1322 diffusion coefficient has a vertical variation which has been tuned to give reasonable Northern
 1323 and Southern Hemisphere polar night jets.

In the top three model levels, the ∇^2 form of the horizontal diffusion is given by

$$F_{\zeta_H} = K^{(2)} [\nabla^2 (\zeta + f) + 2 (\zeta + f) / a^2], \quad (3.204)$$

$$F_{\delta_H} = K^{(2)} [\nabla^2 \delta + 2(\delta/a^2)], \quad (3.205)$$

$$F_{T_H} = K^{(2)} \nabla^2 T. \quad (3.206)$$

1324 Since these terms are linear, they are easily calculated in spectral space. The undifferentiated
 1325 correction term is added to the vorticity and divergence diffusion operators to prevent damping
 1326 of uniform ($n = 1$) rotations [Orszag, 1974; Bourke et al., 1977]. The ∇^2 form of the horizontal
 1327 diffusion is applied *only* to pressure surfaces in the standard model configuration.

The horizontal diffusion operator is better applied to pressure surfaces than to terrain-following surfaces (applying the operator on isentropic surfaces would be still better). Although the governing system of equations derived above is designed to reduce to pressure surfaces above some level, problems can still occur from diffusion along the lower surfaces. Partial correction to pressure surfaces of harmonic horizontal diffusion ($\partial\xi/\partial t = K\nabla^2\xi$) can be included using the relations:

$$\begin{aligned} \nabla_p \xi &= \nabla_\eta \xi - p \frac{\partial \xi}{\partial p} \nabla_\eta \ln p \\ \nabla_p^2 \xi &= \nabla_\eta^2 \xi - p \frac{\partial \xi}{\partial p} \nabla_\eta^2 \ln p - 2 \nabla_\eta \left(\frac{\partial \xi}{\partial p} \right) \cdot \nabla_\eta p + \frac{\partial^2 \xi}{\partial p^2} \nabla_\eta^2 p. \end{aligned} \quad (3.207)$$

Retaining only the first two terms above gives a correction to the η surface diffusion which involves only a vertical derivative and the Laplacian of log surface pressure,

$$\nabla_p^2 \xi = \nabla_\eta^2 \xi - \pi \frac{\partial \xi}{\partial p} \frac{\partial p}{\partial \pi} \nabla^2 \Pi + \dots \quad (3.208)$$

Similarly, biharmonic diffusion can be partially corrected to pressure surfaces as:

$$\nabla_p^4 \xi = \nabla_\eta^4 \xi - \pi \frac{\partial \xi}{\partial p} \frac{\partial p}{\partial \pi} \nabla^4 \Pi + \dots \quad (3.209)$$

The bi-harmonic ∇^4 form of the diffusion operator is applied at all other levels (generally throughout the troposphere) as

$$F_{\zeta_H} = -K^{(4)} [\nabla^4 (\zeta + f) - (\zeta + f) (2/a^2)^2], \quad (3.210)$$

$$F_{\delta_H} = -K^{(4)} [\nabla^4 \delta - \delta(2/a^2)^2], \quad (3.211)$$

$$F_{T_H} = -K^{(4)} \left[\nabla^4 T - \pi \frac{\partial T}{\partial p} \frac{\partial p}{\partial \pi} \nabla^4 \Pi \right]. \quad (3.212)$$

1328 The second term in F_{T_H} consists of the leading term in the transformation of the ∇^4 operator
 1329 to pressure surfaces. It is included to offset partially a spurious diffusion of T over mountains.

1330 As with the ∇^2 form, the ∇^4 operator can be conveniently calculated in spectral space. The
 1331 correction term is then completed after transformation of T and $\nabla^4\Pi$ back to grid-point space.
 1332 As with the ∇^2 form, an undifferentiated term is added to the vorticity and divergence diffusion
 1333 operators to prevent damping of uniform rotations.

1334 3.3.7 Finite difference equations

1335 The governing equations are solved using the spectral method in the horizontal, so that only the
 1336 vertical and time differences are presented here. The dynamics includes horizontal diffusion of
 1337 T , $(\zeta + f)$, and δ . Only T has the leading term correction to pressure surfaces. Thus, equations
 1338 that include the terms in this time split sub-step are of the form

$$\frac{\partial\psi}{\partial t} = \text{Dyn}(\psi) - (-1)^i K^{(2i)} \nabla_\eta^{2i} \psi, \quad (3.213)$$

for $(\zeta + f)$ and δ , and

$$\frac{\partial T}{\partial t} = \text{Dyn}(T) - (-1)^i K^{(2i)} \left\{ \nabla_\eta^{2i} T - \pi \frac{\partial T}{\partial p} \frac{\partial p}{\partial \pi} \nabla^{2i} \Pi \right\}, \quad (3.214)$$

where $i = 1$ in the top few model levels and $i = 2$ elsewhere (generally within the troposphere).
 These equations are further subdivided into time split components:

$$\psi^{n+1} = \psi^{n-1} + 2\Delta t \text{Dyn}(\psi^{n+1}, \psi^n, \psi^{n-1}), \quad (3.215)$$

$$\psi^* = \psi^{n+1} - 2\Delta t (-1)^i K^{(2i)} \nabla_\eta^{2i} (\psi^{*n+1}), \quad (3.216)$$

$$\hat{\psi}^{n+1} = \psi^*, \quad (3.217)$$

for $(\zeta + f)$ and δ , and

$$T^{n+1} = T^{n-1} + 2\Delta t \text{Dyn}(T^{n+1}, T^n, T^{n-1}) \quad (3.218)$$

$$T^* = T^{n+1} - 2\Delta t (-1)^i K^{(2i)} \nabla_\eta^{2i} \eta(T^*), \quad (3.219)$$

$$\hat{T}^{n+1} = T^* + 2\Delta t (-1)^i K^{(2i)} \pi \frac{\partial T^*}{\partial p} \frac{\partial p}{\partial \pi} \nabla^{2i} \Pi, \quad (3.220)$$

1339 for T , where in the standard model i only takes the value 2 in (3.220). The first step from $()^{n-1}$
 1340 to $()^{n+1}$ includes the transformation to spectral coefficients. The second step from $()^{n+1}$ to
 1341 $(\hat{\ })^{n+1}$ for δ and ζ , or $()^{n+1}$ to $()^*$ for T , is done on the spectral coefficients, and the final step
 1342 from $()^*$ to $(\hat{\ })^{n+1}$ for T is done after the inverse transform to the grid point representation.

The following finite-difference description details only the forecast given by (3.215) and (3.218). The finite-difference form of the forecast equation for water vapor will be presented later in Section 3c. The general structure of the complete finite difference equations is determined by the semi-implicit time differencing and the energy conservation properties described above. In order to complete the specification of the finite differencing, we require a definition of the vertical coordinate. The actual specification of the generalized vertical coordinate takes advantage of the structure of the equations (3.161)-(3.170). The equations can be finite-differenced in the vertical and, in time, without having to know the value of η anywhere. The quantities that must

be known are p and $\partial p/\partial\pi$ at the grid points. Therefore the coordinate is defined implicitly through the relation:

$$p(\eta, \pi) = A(\eta)p_0 + B(\eta)\pi, \quad (3.221)$$

which gives

$$\frac{\partial p}{\partial \pi} = B(\eta). \quad (3.222)$$

1343 A set of levels η_k may be specified by specifying A_k and B_k , such that $\eta_k \equiv A_k + B_k$, and
1344 difference forms of (3.161)-(3.170) may be derived.

The finite difference forms of the Dyn operator (3.161)-(3.170), including semi-implicit time integration are:

$$\underline{\zeta}^{n+1} = \underline{\zeta}^{n-1} + 2\Delta t \mathbf{k} \cdot \nabla \times (\underline{\mathbf{n}}^n / \cos \phi), \quad (3.223)$$

$$\begin{aligned} \underline{\delta}^{n+1} &= \underline{\delta}^{n-1} + 2\Delta t \left[\nabla \cdot (\underline{\mathbf{n}}^n / \cos \phi) - \nabla^2 \left(\underline{E}^n + \Phi_s \underline{\mathbf{1}} + R \mathbf{H}^n (\underline{T}'^n) \right) \right] \\ &\quad - 2\Delta t R \mathbf{H}^r \nabla^2 \left(\frac{(\underline{T}')^{n-1} + (\underline{T}')^{n+1}}{2} - (\underline{T}')^n \right) \\ &\quad - 2\Delta t R (\underline{b}^r + \underline{h}^r) \nabla^2 \left(\frac{\Pi^{n-1} + \Pi^{n+1}}{2} - \Pi^n \right), \end{aligned} \quad (3.224)$$

$$\begin{aligned} (\underline{T}')^{n+1} &= (\underline{T}')^{n-1} - 2\Delta t \left[\frac{1}{a \cos^2 \phi} \frac{\partial}{\partial \lambda} (\underline{U} \underline{T}')^n + \frac{1}{a \cos \phi} \frac{\partial}{\partial \phi} (\underline{V} \underline{T}')^n - \underline{\Gamma}^n \right] \\ &\quad - 2\Delta t \mathbf{D}^r \left(\frac{\underline{\delta}^{n-1} + \underline{\delta}^{n+1}}{2} - \underline{\delta}^n \right) \end{aligned} \quad (3.225)$$

$$\begin{aligned} \Pi^{n+1} &= \Pi^{n-1} - 2\Delta t \frac{1}{\pi^n} \left((\underline{\delta}^n)^T \underline{\Delta p}^n + (\underline{\mathbf{V}}^n)^T \cdot \nabla \Pi^n \pi^n \underline{\Delta B} \right) \\ &\quad - 2\Delta t \left(\frac{\underline{\delta}^{n-1} + \underline{\delta}^{n+1}}{2} - \underline{\delta}^n \right)^T \frac{1}{\pi^r} \underline{\Delta p}^r, \end{aligned} \quad (3.226)$$

$$\begin{aligned} (n_U)_k &= (\zeta_k + f) V_k - R T_{vk} \left(\frac{1}{p} \frac{\partial p}{\partial \pi} \right)_k \pi \frac{1}{a} \frac{\partial \Pi}{\partial \lambda} \\ &\quad - \frac{1}{2\Delta p_k} \left[\left(\dot{\eta} \frac{\partial p}{\partial \eta} \right)_{k+1/2} (U_{k+1} - U_k) + \left(\dot{\eta} \frac{\partial p}{\partial \eta} \right)_{k-1/2} (U_k - U_{k-1}) \right] \\ &\quad + (F_U)_k, \end{aligned} \quad (3.227)$$

$$\begin{aligned} (n_V)_k &= -(\zeta_k + f) U_k - R T_{vk} \left(\frac{1}{p} \frac{\partial p}{\partial \pi} \right)_k \pi \frac{\cos \phi}{a} \frac{\partial \Pi}{\partial \phi} \\ &\quad - \frac{1}{2\Delta p_k} \left[\left(\dot{\eta} \frac{\partial p}{\partial \eta} \right)_{k+1/2} (V_{k+1} - V_k) + \left(\dot{\eta} \frac{\partial p}{\partial \eta} \right)_{k-1/2} (V_k - V_{k-1}) \right] \\ &\quad + (F_V)_k, \end{aligned} \quad (3.228)$$

$$\begin{aligned} \Gamma_k &= T'_k \delta_k + \frac{R T_{vk}}{(c_p^*)_k} \left(\frac{\omega}{p} \right)_k - Q \\ &\quad - \frac{1}{2\Delta p_k} \left[\left(\dot{\eta} \frac{\partial p}{\partial \eta} \right)_{k+1/2} (T_{k+1} - T_k) + \left(\dot{\eta} \frac{\partial p}{\partial \eta} \right)_{k-1/2} (T_k - T_{k-1}) \right], \end{aligned} \quad (3.229)$$

$$E_k = (u_k)^2 + (v_k)^2, \quad (3.230)$$

$$\frac{RT_{vk}}{(c_p^*)_k} = \frac{R}{c_p} \left(\frac{T_k^r + T_{vk}'}{1 + \left(\frac{c_{pv}}{c_p} - 1 \right) q_k} \right), \quad (3.231)$$

$$\begin{aligned} \left(\dot{\eta} \frac{\partial p}{\partial \eta} \right)_{k+1/2} &= B_{k+1/2} \sum_{\ell=1}^K [\delta_\ell \Delta p_\ell + \mathbf{V}_\ell \cdot \pi \nabla \Pi \Delta B_\ell] \\ &\quad - \sum_{\ell=1}^k [\delta_\ell \Delta p_\ell + \mathbf{V}_\ell \cdot \pi \nabla \Pi \Delta B_\ell], \end{aligned} \quad (3.232)$$

$$\left(\frac{\omega}{p} \right)_k = \left(\frac{1}{p} \frac{\partial p}{\partial \pi} \right)_k \mathbf{V}_k \cdot \pi \nabla \Pi - \sum_{\ell=1}^k C_{k\ell} [\delta_\ell \Delta p_\ell + \mathbf{V}_\ell \cdot \pi \nabla \Pi \Delta B_\ell], \quad (3.233)$$

$$C_{k\ell} = \begin{cases} \frac{1}{p_k}, & \ell < k \\ \frac{1}{2p_k}, & \ell = k, \end{cases} \quad (3.234)$$

$$H_{k\ell} = C_{\ell k} \Delta p_\ell, \quad (3.235)$$

$$\begin{aligned} D_{k\ell}^r &= \Delta p_\ell^r \frac{R}{c_p} T_k^r C_{\ell k}^r + \frac{\Delta p_\ell^r}{2\Delta p_k^r} (T_k^r - T_{k-1}^r) (\epsilon_{k\ell+1} - B_{k-1/2}) \\ &\quad + \frac{\Delta p_\ell^r}{2\Delta p_k^r} (T_{k+1}^r - T_k^r) (\epsilon_{k\ell} - B_{k+1/2}), \end{aligned} \quad (3.236)$$

$$\frac{\epsilon_{k\ell}}{R} = \begin{cases} 1, & \ell \leq k \\ 0, & \ell > k, \end{cases} \quad (3.237)$$

where notation such as $(\underline{UT}')^n$ denotes a column vector with components $(U_k T_k')^n$. In order to complete the system, it remains to specify the reference vector \underline{h}^r , together with the term $(1/p \partial p / \partial \pi)$, which results from the pressure gradient terms and also appears in the semi-implicit reference vector \underline{b}^r :

$$\left(\frac{1}{p} \frac{\partial p}{\partial \pi} \right)_k = \left(\frac{1}{p} \right)_k \left(\frac{\partial p}{\partial \pi} \right)_k = \frac{B_k}{p_k}, \quad (3.238)$$

$$\underline{b}^r = \underline{T}^r, \quad (3.239)$$

$$\underline{h}^r = 0. \quad (3.240)$$

1345 The matrices \mathbf{C}^n and \mathbf{H}^n (*i.e.* with components $C_{k\ell}$ and $H_{k\ell}$) must be evaluated at each time
 1346 step and each point in the horizontal. It is more efficient computationally to substitute the
 1347 definitions of these matrices into (3.224) and (3.233) at the cost of some loss of generality in
 1348 the code. The finite difference equations have been written in the form (3.223)-(3.240) because
 1349 this form is quite general. For example, the equations solved by Simmons and Strüfing [1981]
 1350 at ECMWF can be obtained by changing only the vectors and hydrostatic matrix defined by
 1351 (3.237)-(3.240).

1352 3.3.8 Time filter

1353 The time step is completed by applying a recursive time filter originally designed by [Robert,
 1354 1966] and later studied by [Asselin, 1972].

$$\bar{\psi}^n = \psi^n + \alpha \left(\bar{\psi}^{n-1} - 2\psi^n + \psi^{n+1} \right) \quad (3.241)$$

1355 3.3.9 Spectral transform

1356 The spectral transform method is used in the horizontal exactly as in CCM1. As shown earlier,
 1357 the vertical and temporal aspects of the model are represented by finite-difference approxima-
 1358 tions. The horizontal aspects are treated by the spectral-transform method, which is described
 1359 in this section. Thus, at certain points in the integration, the prognostic variables $(\zeta + f)$, δ , T ,
 1360 and Π are represented in terms of coefficients of a truncated series of spherical harmonic func-
 1361 tions, while at other points they are given by grid-point values on a corresponding Gaussian
 1362 grid. In general, physical parameterizations and nonlinear operations are carried out in grid-
 1363 point space. Horizontal derivatives and linear operations are performed in spectral space. Ex-
 1364 ternally, the model appears to the user to be a grid-point model, as far as data required and
 1365 produced by it. Similarly, since all nonlinear parameterizations are developed and carried out in
 1366 grid-point space, the model also appears as a grid-point model for the incorporation of physical
 1367 parameterizations, and the user need not be too concerned with the spectral aspects. For users
 1368 interested in diagnosing the balance of terms in the evolution equations, however, the details are
 1369 important and care must be taken to understand which terms have been spectrally truncated
 1370 and which have not. The algebra involved in the spectral transformations has been presented in
 1371 several publications [Daley et al., 1976; Bourke et al., 1977; Machenhauer, 1979]. In this report,
 1372 we present only the details relevant to the model code; for more details and general philosophy,
 1373 the reader is referred to these earlier papers.

1374 3.3.10 Spectral algorithm overview

The horizontal representation of an arbitrary variable ψ consists of a truncated series of spherical harmonic functions,

$$\psi(\lambda, \mu) = \sum_{m=-M}^M \sum_{n=|m|}^{\mathcal{N}(m)} \psi_n^m P_n^m(\mu) e^{im\lambda}, \quad (3.242)$$

where $\mu = \sin \phi$, M is the highest Fourier wavenumber included in the east-west representa-
 tion, and $\mathcal{N}(m)$ is the highest degree of the associated Legendre polynomials for longitudinal
 wavenumber m . The properties of the spherical harmonic functions used in the representation
 can be found in the review by Machenhauer [1979]. The model is coded for a general pentagonal
 truncation, illustrated in Figure 3.5, defined by three parameters: M , K , and N , where M
 is defined above, K is the highest degree of the associated Legendre polynomials, and N is the
 highest degree of the Legendre polynomials for $m = 0$. The common truncations are subsets of
 this pentagonal case:

$$\begin{aligned} \text{Triangular} : & \quad M = N = K, \\ \text{Rhomboidal} : & \quad K = N + M, \\ \text{Trapezoidal} : & \quad N = K > M. \end{aligned} \quad (3.243)$$

Figure 3.5: Pentagonal truncation parameters

1375 The quantity $\mathcal{N}(m)$ in (3.242) represents an arbitrary limit on the two-dimensional wavenumber
 1376 n , and for the pentagonal truncation described above is simply given by
 1377 $\mathcal{N}(m) = \min(N + |m|, K)$.

The associated Legendre polynomials used in the model are normalized such that

$$\int_{-1}^1 [P_n^m(\mu)]^2 d\mu = 1. \quad (3.244)$$

With this normalization, the Coriolis parameter f is

$$f = \frac{\Omega}{\sqrt{0.375}} P_1^0, \quad (3.245)$$

1378 which is required for the absolute vorticity.

The coefficients of the spectral representation (3.242) are given by

$$\psi_n^m = \int_{-1}^1 \frac{1}{2\pi} \int_0^{2\pi} \psi(\lambda, \mu) e^{-im\lambda} d\lambda P_n^m(\mu) d\mu. \quad (3.246)$$

The inner integral represents a Fourier transform,

$$\psi^m(\mu) = \frac{1}{2\pi} \int_0^{2\pi} \psi(\lambda, \mu) e^{-im\lambda} d\lambda, \quad (3.247)$$

which is performed by a Fast Fourier Transform (FFT) subroutine. The outer integral is performed via Gaussian quadrature,

$$\psi_n^m = \sum_{j=1}^J \psi^m(\mu_j) P_n^m(\mu_j) w_j, \quad (3.248)$$

where μ_j denotes the Gaussian grid points in the meridional direction, w_j the Gaussian weight at point μ_j , and J the number of Gaussian grid points from pole to pole. The Gaussian grid points (μ_j) are given by the roots of the Legendre polynomial $P_J(\mu)$, and the corresponding weights are given by

$$w_j = \frac{2(1 - \mu_j^2)}{[J P_{J-1}(\mu_j)]^2}. \quad (3.249)$$

The weights themselves satisfy

$$\sum_{j=1}^J w_j = 2.0. \quad (3.250)$$

The Gaussian grid used for the north–south transformation is generally chosen to allow un-aliased computations of quadratic terms only. In this case, the number of Gaussian latitudes J must satisfy

$$J \geq (2N + K + M + 1)/2 \quad \text{for } M \leq 2(K - N), \quad (3.251)$$

$$J \geq (3K + 1)/2 \quad \text{for } M \geq 2(K - N). \quad (3.252)$$

For the common truncations, these become

$$J \geq (3K + 1)/2 \quad \text{for triangular and trapezoidal,} \quad (3.253)$$

$$J \geq (3N + 2M + 1)/2 \quad \text{for rhomboidal.} \quad (3.254)$$

In order to allow exact Fourier transform of quadratic terms, the number of points P in the east–west direction must satisfy

$$P \geq 3M + 1. \quad (3.255)$$

1379 The actual values of J and P are often not set equal to the lower limit in order to allow use of
1380 more efficient transform programs.

Although in the next section of this model description, we continue to indicate the Gaussian quadrature as a sum from pole to pole, the code actually deals with the symmetric and antisymmetric components of variables and accumulates the sums from equator to pole only. The model requires an even number of latitudes to easily use the symmetry conditions. This may be slightly inefficient for some spectral resolutions. We define a new index, which goes from $-I$ at the point next to the south pole to $+I$ at the point next to the north pole and not including 0 (there are no points at the equator or pole in the Gaussian grid), *i.e.*, let $I = J/2$ and $i = j - J/2$ for $j \geq J/2 + 1$ and $i = j - J/2 - 1$ for $j \leq J/2$; then the summation in (3.248) can be rewritten as

$$\psi_n^m = \sum_{i=-I, i \neq 0}^I \psi^m(\mu_i) P_n^m(\mu_i) w_i. \quad (3.256)$$

The symmetric (even) and antisymmetric (odd) components of ψ^m are defined by

$$\begin{aligned} (\psi_E)_i^m &= \frac{1}{2} (\psi_i^m + \psi_{-i}^m), \\ (\psi_O)_i^m &= \frac{1}{2} (\psi_i^m - \psi_{-i}^m). \end{aligned} \quad (3.257)$$

Since w_i is symmetric about the equator, (3.256) can be rewritten to give formulas for the coefficients of even and odd spherical harmonics:

$$\psi_n^m = \begin{cases} \sum_{i=1}^I (\psi_E)_i^m (\mu_i) P_n^m(\mu_i) 2w_i & \text{for } n - m \text{ even,} \\ \sum_{i=1}^I (\psi_O)_i^m (\mu_i) P_n^m(\mu_i) 2w_i & \text{for } n - m \text{ odd.} \end{cases} \quad (3.258)$$

1381 The model uses the spectral transform method [Machenhauer, 1979] for all nonlinear terms.
1382 However, the model can be thought of as starting from grid–point values at time t (consistent
1383 with the spectral representation) and producing a forecast of the grid–point values at time $t + \Delta t$
1384 (again, consistent with the spectral resolution). The forecast procedure involves computation
1385 of the nonlinear terms including physical parameterizations at grid points; transformation via
1386 Gaussian quadrature of the nonlinear terms from grid–point space to spectral space; computation
1387 of the spectral coefficients of the prognostic variables at time $t + \Delta t$ (with the implied spectral
1388 truncation to the model resolution); and transformation back to grid–point space. The details
1389 of the equations involved in the various transformations are given in the next section.

3.3.11 Combination of terms

In order to describe the transformation to spectral space, for each equation we first group together all undifferentiated explicit terms, all explicit terms with longitudinal derivatives, and all explicit terms with meridional derivatives appearing in the Dyn operator. Thus, the vorticity equation (3.223) is rewritten

$$\underline{(\zeta + f)}^{n+1} = \underline{V} + \frac{1}{a(1 - \mu^2)} \left[\frac{\partial}{\partial \lambda} (\underline{V}_\lambda) - (1 - \mu^2) \frac{\partial}{\partial \mu} (\underline{V}_\mu) \right], \quad (3.259)$$

where the explicit forms of the vectors \underline{V} , \underline{V}_λ , and \underline{V}_μ are given as

$$\underline{V} = \underline{(\zeta + f)}^{n-1}, \quad (3.260)$$

$$\underline{V}_\lambda = 2\Delta t \underline{n}_V^n, \quad (3.261)$$

$$\underline{V}_\mu = 2\Delta t \underline{n}_U^n. \quad (3.262)$$

The divergence equation (3.224) is

$$\begin{aligned} \underline{\delta}^{n+1} = \underline{D} + \frac{1}{a(1 - \mu^2)} \left[\frac{\partial}{\partial \lambda} (\underline{D}_\lambda) + (1 - \mu^2) \frac{\partial}{\partial \mu} (\underline{D}_\mu) \right] - \nabla^2 \underline{D}_\nabla \\ - \Delta t \nabla^2 (R \underline{H}^r \underline{T}'^{n+1} + R (\underline{b}^r + \underline{h}^r) \Pi^{n+1}). \end{aligned} \quad (3.263)$$

The mean component of the temperature is not included in the next-to-last term since the Laplacian of it is zero. The thermodynamic equation (3.226) is

$$\underline{T}'^{n+1} = \underline{T} - \frac{1}{a(1 - \mu^2)} \left[\frac{\partial}{\partial \lambda} (\underline{T}_\lambda) + (1 - \mu^2) \frac{\partial}{\partial \mu} (\underline{T}_\mu) \right] - \Delta t \underline{D}^r \underline{\delta}^{n+1}. \quad (3.264)$$

The surface-pressure tendency (3.226) is

$$\Pi^{n+1} = PS - \frac{\Delta t}{\pi^r} (\underline{\Delta p}^r)^T \underline{\delta}^{n+1}. \quad (3.265)$$

The grouped explicit terms in (3.263)–(3.265) are given as follows. The terms of (3.263) are

$$\underline{D} = \underline{\delta}^{n-1}, \quad (3.266)$$

$$\underline{D}_\lambda = 2\Delta t \underline{n}_V^n, \quad (3.267)$$

$$\underline{D}_\mu = 2\Delta t \underline{n}_U^n, \quad (3.268)$$

$$\begin{aligned} \underline{D}_\nabla = 2\Delta t \left[\underline{E}^n + \Phi_s \underline{1} + R \underline{H}^r \underline{T}'^n \right] \\ + \Delta t \left[R \underline{H}^r \left((\underline{T}')^{n-1} - 2(\underline{T}')^n \right) + R (\underline{b}^r + \underline{h}^r) (\Pi^{n-1} - 2\Pi^n) \right]. \end{aligned} \quad (3.269)$$

The terms of (3.264) are

$$\underline{T} = (\underline{T}')^{n-1} + 2\Delta t \underline{\Gamma}^n - \Delta t \underline{D}^r [\underline{\delta}^{n-1} - 2\underline{\delta}^n], \quad (3.270)$$

$$\underline{T}_\lambda = 2\Delta t \underline{(UT')^n}, \quad (3.271)$$

$$\underline{T}_\mu = 2\Delta t \underline{(VT')^n}. \quad (3.272)$$

The nonlinear term in (3.265) is

$$\begin{aligned}
PS = \Pi^{n-1} - 2\Delta t \frac{1}{\pi^n} \left[(\underline{\delta}^n)^T (\underline{\Delta p}^n) + (\underline{\mathbf{V}}^n)^T \nabla \Pi^n \pi^n \underline{\Delta B} \right] \\
- \Delta t \left[(\underline{\Delta p}^r)^T \frac{1}{\pi^r} \right] [\underline{\delta}^{n-1} - 2\underline{\delta}^n] .
\end{aligned} \tag{3.273}$$

1391 3.3.12 Transformation to spectral space

1392 Formally, Equations (3.259)-(3.265) are transformed to spectral space by performing the opera-
1393 tions indicated in (3.274) to each term. We see that the equations basically contain three types
1394 of terms, for example, in the vorticity equation the undifferentiated term $\underline{\mathbf{V}}$, the longitudinally
1395 differentiated term $\underline{\mathbf{V}}_\lambda$, and the meridionally differentiated term $\underline{\mathbf{V}}_\mu$. All terms in the original
1396 equations were grouped into one of these terms on the Gaussian grid so that they could be
1397 transformed at once.

Transformation of the undifferentiated term is obtained by straightforward application of (3.246)-(3.248),

$$\{\underline{\mathbf{V}}\}_n^m = \sum_{j=1}^J \underline{\mathbf{V}}^m(\mu_j) P_n^m(\mu_j) w_j, \tag{3.274}$$

where $\underline{\mathbf{V}}^m(\mu_j)$ is the Fourier coefficient of $\underline{\mathbf{V}}$ with wavenumber m at the Gaussian grid line μ_j . The longitudinally differentiated term is handled by integration by parts, using the cyclic boundary conditions,

$$\left\{ \frac{\partial}{\partial \lambda} (\underline{\mathbf{V}}_\lambda) \right\}_n^m = \frac{1}{2\pi} \int_0^{2\pi} \frac{\partial \underline{\mathbf{V}}_\lambda}{\partial \lambda} e^{-im\lambda} d\lambda, \tag{3.275}$$

$$= im \frac{1}{2\pi} \int_0^{2\pi} \underline{\mathbf{V}}_\lambda e^{-im\lambda} d\lambda, \tag{3.276}$$

$$\tag{3.277}$$

so that the Fourier transform is performed first, then the differentiation is carried out in spectral space. The transformation to spherical harmonic space then follows (3.280):

$$\left\{ \frac{1}{a(1-\mu^2)} \frac{\partial}{\partial \lambda} (\underline{\mathbf{V}}_\lambda) \right\}_n^m = im \sum_{j=1}^J \underline{\mathbf{V}}_\lambda^m(\mu_j) \frac{P_n^m(\mu_j)}{a(1-\mu_j^2)} w_j, \tag{3.278}$$

1398 where $\underline{\mathbf{V}}_\lambda^m(\mu_j)$ is the Fourier coefficient of $\underline{\mathbf{V}}_\lambda$ with wavenumber m at the Gaussian grid line μ_j .

The latitudinally differentiated term is handled by integration by parts using zero boundary conditions at the poles:

$$\left\{ \frac{1}{a(1-\mu^2)} (1-\mu^2) \frac{\partial}{\partial \mu} (\underline{\mathbf{V}}_\mu) \right\}_n^m = \int_{-1}^1 \frac{1}{a(1-\mu^2)} (1-\mu^2) \frac{\partial}{\partial \mu} (\underline{\mathbf{V}}_\mu)^m P_n^m d\mu, \tag{3.279}$$

$$= - \int_{-1}^1 \frac{1}{a(1-\mu^2)} (\underline{\mathbf{V}}_\mu)^m (1-\mu^2) \frac{dP_n^m}{d\mu} d\mu. \tag{3.280}$$

Defining the derivative of the associated Legendre polynomial by

$$H_n^m = (1 - \mu^2) \frac{dP_n^m}{d\mu}, \quad (3.281)$$

(3.283) can be written

$$\left\{ \frac{1}{a(1 - \mu^2)} (1 - \mu^2) \frac{\partial}{\partial \mu} (\underline{V}_\mu) \right\}_n^m = - \sum_{j=1}^J (\underline{V}_\mu)^m \frac{H_n^m(\mu_j)}{a(1 - \mu_j^2)} w_j. \quad (3.282)$$

Similarly, the ∇^2 operator in the divergence equation can be converted to spectral space by sequential integration by parts and then application of the relationship

$$\nabla^2 P_n^m(\mu) e^{im\lambda} = \frac{-n(n+1)}{a^2} P_n^m(\mu) e^{im\lambda}, \quad (3.283)$$

to each spherical harmonic function individually so that

$$\{\nabla^2 \underline{D}_\nabla\}_n^m = \frac{-n(n+1)}{a^2} \sum_{j=1}^J \underline{D}_\nabla^m(\mu_j) P_n^m(\mu_j) w_j, \quad (3.284)$$

1399 where $\underline{D}_\nabla^m(\mu)$ is the Fourier coefficient of the original grid variable \underline{D}_∇ .

1400 3.3.13 Solution of semi-implicit equations

The prognostic equations can be converted to spectral form by summation over the Gaussian grid using (3.274), (3.278), and (3.282). The resulting equation for absolute vorticity is

$$\underline{(\zeta + f)}_n^m = \underline{VS}_n^m, \quad (3.285)$$

where $\underline{(\zeta + f)}_n^m$ denotes a spherical harmonic coefficient of $(\zeta + f)^{n+1}$, and the form of \underline{VS}_n^m , as a summation over the Gaussian grid, is given as

$$\underline{VS}_n^m = \sum_{j=1}^J \left[\underline{V}^m(\mu_j) P_n^m(\mu_j) + im \underline{V}_\lambda^m(\mu_j) \frac{P_n^m(\mu_j)}{a(1 - \mu_j^2)} + \underline{V}_\mu^m(\mu_j) \frac{H_n^m(\mu_j)}{a(1 - \mu_j^2)} \right] w_j. \quad (3.286)$$

The spectral form of the divergence equation (3.263) becomes

$$\underline{\delta}_n^m = \underline{DS}_n^m + \Delta t \frac{n(n+1)}{a^2} [R \underline{H}^r \underline{T}'_n^m + R (\underline{b}^r + \underline{h}^r) \Pi_n^m], \quad (3.287)$$

where $\underline{\delta}_n^m$, \underline{T}'_n^m , and Π_n^m are spectral coefficients of δ^{n+1} , T'^{n+1} , and Π^{n+1} . The Laplacian of the total temperature in (3.263) is replaced by the equivalent Laplacian of the perturbation temperature in (3.287). \underline{DS}_n^m is given by

$$\begin{aligned} \underline{DS}_n^m = \sum_{j=1}^J \left\{ \left[\underline{D}^m(\mu_j) + \frac{n(n+1)}{a^2} \underline{D}_\nabla^m(\mu_j) \right] P_n^m(\mu_j) \right. \\ \left. + im \underline{D}_\lambda^m(\mu_j) \frac{P_n^m(\mu_j)}{a(1 - \mu_j^2)} - \underline{D}_\mu^m(\mu_j) \frac{H_n^m(\mu_j)}{a(1 - \mu_j^2)} \right\} w_j. \end{aligned} \quad (3.288)$$

The spectral thermodynamic equation is

$$\underline{T}'^m = \underline{TS}_n^m - \Delta t \underline{D}^r \underline{\delta}_n^m, \quad (3.289)$$

with \underline{TS}_n^m defined as

$$\underline{TS}_n^m = \sum_{j=1}^J \left[\underline{T}^m(\mu_j) P_n^m(\mu_j) - im \underline{T}_\lambda^m(\mu_j) \frac{P_n^m(\mu_j)}{a(1-\mu_j^2)} + \underline{T}_\mu^m(\mu_j) \frac{H_n^m(\mu_j)}{a(1-\mu_j^2)} \right] w_j, \quad (3.290)$$

while the surface pressure equation is

$$\Pi_n^m = PS_n^m - \underline{\delta}_n^m (\underline{\Delta p}^r)^T \frac{\Delta t}{\pi^r}, \quad (3.291)$$

where PS_n^m is given by

$$PS_n^m = \sum_{j=1}^J PS^m(\mu_j) P_n^m(\mu_j) w_j. \quad (3.292)$$

Equation (3.285) for vorticity is explicit and complete at this point. However, the remaining equations (3.287)–(3.291) are coupled. They are solved by eliminating all variables except $\underline{\delta}_n^m$:

$$\mathbf{A}_n \underline{\delta}_n^m = \underline{DS}_n^m + \Delta t \frac{n(n+1)}{a^2} [R \underline{H}^r (\underline{TS}_n^m + R(\underline{b}^r + \underline{h}^r) (PS_n^m)], \quad (3.293)$$

where

$$\mathbf{A}_n = \mathbf{I} + \Delta t^2 \frac{n(n+1)}{a^2} \left[R \underline{H}^r \underline{D}^r + R(\underline{b}^r + \underline{h}^r) \left((\underline{\Delta p}^r)^T \frac{1}{\pi^r} \right) \right], \quad (3.294)$$

1401 which is simply a set of K simultaneous equations for the coefficients with given wavenumbers
 1402 (m, n) at each level and is solved by inverting \mathbf{A}_n . In order to prevent the accumulation of round-
 1403 off error in the global mean divergence (which if exactly zero initially, should remain exactly
 1404 zero) $(\mathbf{A}_o)^{-1}$ is set to the null matrix rather than the identity, and the formal application of
 1405 (3.293) then always guarantees $\underline{\delta}_o^o = 0$. Once $\underline{\delta}_n^m$ is known, \underline{T}'^m and Π_n^m can be computed
 1406 from (3.289) and (3.291), respectively, and all prognostic variables are known at time $n+1$ as
 1407 spherical harmonic coefficients. Note that the mean component \underline{T}'^o is not necessarily zero since
 1408 the perturbations are taken with respect to a specified \underline{T}^r .

1409 3.3.14 Horizontal diffusion

As mentioned earlier, the horizontal diffusion in (3.216) and (3.219) is computed implicitly via time splitting after the transformations into spectral space and solution of the semi-implicit equations. In the following, the ζ and δ equations have a similar form, so we write only the δ equation:

$$(\delta^*)^m_n = (\delta^{n+1})^m_n - (-1)^i 2\Delta t K^{(2i)} \left[\nabla^{2i} (\delta^*)^m_n - (-1)^i (\delta^*)^m_n (2/a^2)^i \right], \quad (3.295)$$

$$(T^*)^m_n = (T^{n+1})^m_n - (-1)^i 2\Delta t K^{(2i)} \left[\nabla^{2i} (T^*)^m_n \right]. \quad (3.296)$$

The extra term is present in (3.295), (3.299) and (3.301) to prevent damping of uniform rotations. The solutions are just

$$(\delta^*)_n^m = K_n^{(2i)}(\delta) (\delta^{n+1})_n^m, \quad (3.297)$$

$$(T^*)_n^m = K_n^{(2i)}(T) (T^{n+1})_n^m, \quad (3.298)$$

$$K_n^{(2)}(\delta) = \left\{ 1 + 2\Delta t D_n K^{(2)} \left[\left(\frac{n(n+1)}{a^2} \right) - \frac{2}{a^2} \right] \right\}^{-1}, \quad (3.299)$$

$$K_n^{(2)}(T) = \left\{ 1 + 2\Delta t D_n K^{(2)} \left(\frac{n(n+1)}{a^2} \right) \right\}^{-1}, \quad (3.300)$$

$$K_n^{(4)}(\delta) = \left\{ 1 + 2\Delta t D_n K^{(4)} \left[\left(\frac{n(n+1)}{a^2} \right)^2 - \frac{4}{a^4} \right] \right\}^{-1}, \quad (3.301)$$

$$K_n^{(4)}(T) = \left\{ 1 + 2\Delta t D_n K^{(4)} \left(\frac{n(n+1)}{a^2} \right)^2 \right\}^{-1}. \quad (3.302)$$

1410 $K_n^{(2)}(\delta)$ and $K_n^{(4)}(\delta)$ are both set to 1 for $n = 0$. The quantity D_n represents the “Courant
 1411 number limiter”, normally set to 1. However, D_n is modified to ensure that the CFL criterion
 1412 is not violated in selected upper levels of the model. If the maximum wind speed in any of
 1413 these upper levels is sufficiently large, then $D_n = 1000$ in that level for all $n > n_c$, where
 1414 $n_c = a\Delta t / \max |\mathbf{V}|$. This condition is applied whenever the wind speed is large enough that
 1415 $n_c < K$, the truncation parameter in (3.243), and temporarily reduces the effective resolution of
 1416 the model in the affected levels. The number of levels at which this “Courant number limiter”
 1417 may be applied is user-selectable, but it is only used in the top level of the 26 level CAM 5.0
 1418 control runs.

1419 The diffusion of T is not complete at this stage. In order to make the partial correction from
 1420 η to p in (3.210) local, it is not included until grid-point values are available. This requires
 1421 that $\nabla^4 \Pi$ also be transformed from spectral to grid-point space. The values of the coefficients
 1422 $K^{(2)}$ and $K^{(4)}$ for the standard T42 resolution are $2.5 \times 10^5 \text{m}^2 \text{sec}^{-1}$ and $1.0 \times 10^{16} \text{m}^4 \text{sec}^{-1}$,
 1423 respectively.

1424 3.3.15 Initial divergence damping

1425 Occasionally, with poorly balanced initial conditions, the model exhibits numerical instability
 1426 during the beginning of an integration because of excessive noise in the solution. Therefore, an
 1427 optional divergence damping is included in the model to be applied over the first few days. The
 1428 damping has an initial e-folding time of Δt and linearly decreases to 0 over a specified number
 1429 of days, t_D , usually set to be 2. The damping is computed implicitly via time splitting after the
 1430 horizontal diffusion.

$$r = \max \left[\frac{1}{\Delta t} (t_D - t) / t_D, 0 \right] \quad (3.303)$$

$$(\delta^*)_n^m = \frac{1}{1 + 2\Delta t r} (\delta^*)_n^m \quad (3.304)$$

3.3.16 Transformation from spectral to physical space

After the prognostic variables are completed at time $n + 1$ in spectral space $\left(\underline{(\zeta + f)}_n^*\right)^m$, $(\underline{\delta}^*)_n^m$, $(\underline{T}^*)_n^m$, $(\Pi^{n+1})_n^m$ they are transformed to grid space. For a variable ψ , the transformation is given by

$$\psi(\lambda, \mu) = \sum_{m=-M}^M \left[\sum_{n=|m|}^{\mathcal{N}(m)} \psi_n^m P_n^m(\mu) \right] e^{im\lambda}. \quad (3.305)$$

The inner sum is done essentially as a vector product over n , and the outer is again performed by an FFT subroutine. The term needed for the remainder of the diffusion terms, $\nabla^4 \Pi$, is calculated from

$$\nabla^4 \Pi^{n+1} = \sum_{m=-M}^M \left[\sum_{n=|m|}^{\mathcal{N}(m)} \left(\frac{n(n+1)}{a^2} \right)^2 (\Pi^{n+1})_n^m P_n^m(\mu) \right] e^{im\lambda}. \quad (3.306)$$

In addition, the derivatives of Π are needed on the grid for the terms involving $\nabla \Pi$ and $\mathbf{V} \cdot \nabla \Pi$,

$$\mathbf{V} \cdot \nabla \Pi = \frac{U}{a(1-\mu^2)} \frac{\partial \Pi}{\partial \lambda} + \frac{V}{a(1-\mu^2)} (1-\mu^2) \frac{\partial \Pi}{\partial \mu}. \quad (3.307)$$

These required derivatives are given by

$$\frac{\partial \Pi}{\partial \lambda} = \sum_{m=-M}^M im \left[\sum_{n=|m|}^{\mathcal{N}(m)} \Pi_n^m P_n^m(\mu) \right] e^{im\lambda}, \quad (3.308)$$

and using (3.281),

$$(1-\mu^2) \frac{\partial \Pi}{\partial \mu} = \sum_{m=-M}^M \left[\sum_{n=|m|}^{\mathcal{N}(m)} \Pi_n^m H_n^m(\mu) \right] e^{im\lambda}, \quad (3.309)$$

which involve basically the same operations as (3.306). The other variables needed on the grid are U and V . These can be computed directly from the absolute vorticity and divergence coefficients using the relations

$$(\zeta + f)_n^m = -\frac{n(n+1)}{a^2} \psi_n^m + f_n^m, \quad (3.310)$$

$$\delta_n^m = -\frac{n(n+1)}{a^2} \chi_n^m, \quad (3.311)$$

in which the only nonzero f_n^m is $f_1^o = \Omega/\sqrt{.375}$, and

$$U = \frac{1}{a} \frac{\partial \chi}{\partial \lambda} - \frac{(1-\mu^2)}{a} \frac{\partial \psi}{\partial \mu}, \quad (3.312)$$

$$V = \frac{1}{a} \frac{\partial \psi}{\partial \lambda} + \frac{(1-\mu^2)}{a} \frac{\partial \chi}{\partial \mu}. \quad (3.313)$$

Thus, the direct transformation is

$$U = - \sum_{m=-M}^M a \sum_{n=|m|}^{\mathcal{N}(m)} \left[\frac{im}{n(n+1)} \delta_n^m P_n^m(\mu) - \frac{1}{n(n+1)} (\zeta + f)_n^m H_n^m(\mu) \right] e^{im\lambda} - \frac{a}{2} \frac{\Omega}{\sqrt{0.375}} H_1^o, \quad (3.314)$$

$$V = - \sum_{m=-M}^M a \sum_{n=|m|}^{\mathcal{N}(m)} \left[\frac{im}{n(n+1)} (\zeta + f)_n^m P_n^m(\mu) + \frac{1}{n(n+1)} \delta_n^m H_n^m(\mu) \right] e^{im\lambda}. \quad (3.315)$$

The horizontal diffusion tendencies are also transformed back to grid space. The spectral coefficients for the horizontal diffusion tendencies follow from (3.295) and (3.296):

$$F_{T_H} (T^*)_n^m = (-1)^{i+1} K^{2i} [\nabla^{2i} (T^*)_n^m], \quad (3.316)$$

$$F_{\zeta_H} ((\zeta + f)^*)_n^m = (-1)^{i+1} K^{2i} \left\{ \nabla^{2i} (\zeta + f)^* - (-1)^i (\zeta + f)^* (2/a^2)^i \right\}, \quad (3.317)$$

$$F_{\delta_H} (\delta^*)_n^m = (-1) K^{2i} \left\{ \nabla^{2i} (\delta^*) - (-1)^i \delta^* (2/a^2)^i \right\}, \quad (3.318)$$

1432 using $i = 1$ or 2 as appropriate for the ∇^2 or ∇^4 forms. These coefficients are transformed to
 1433 grid space following (3.242) for the T term and (3.314) and (3.315) for vorticity and divergence.
 1434 Thus, the vorticity and divergence diffusion tendencies are converted to equivalent U and V
 1435 diffusion tendencies.

1436 3.3.17 Horizontal diffusion correction

After grid-point values are calculated, frictional heating rates are determined from the momentum diffusion tendencies and are added to the temperature, and the partial correction of the ∇^4 diffusion from η to p surfaces is applied to T . The frictional heating rate is calculated from the kinetic energy tendency produced by the momentum diffusion

$$F_{F_H} = -u^{n-1} F_{u_H}(u^*)/c_p^* - v^{n-1} F_{v_H}(v^*)/c_p^*, \quad (3.319)$$

where F_{u_H} , and F_{v_H} are the momentum equivalent diffusion tendencies, determined from F_{ζ_H} and F_{δ_H} just as U and V are determined from ζ and δ , and

$$c_p^* = c_p \left[1 + \left(\frac{c_{pv}}{c_p} - 1 \right) q^{n+1} \right]. \quad (3.320)$$

These heating rates are then combined with the correction,

$$\hat{T}_k^{n+1} = T_k^* + (2\Delta t F_{F_H})_k + 2\Delta t \left(\pi B \frac{\partial T^*}{\partial p} \right)_k K^{(4)} \nabla^4 \Pi^{n+1}. \quad (3.321)$$

The vertical derivatives of T^* (where the $*$ notation is dropped for convenience) are defined by

$$\left(\pi B \frac{\partial T}{\partial p}\right)_1 = \frac{\pi}{2\Delta p_1} \left[B_{1+\frac{1}{2}} (T_2 - T_1) \right], \quad (3.322)$$

$$\left(\pi B \frac{\partial T}{\partial p}\right)_k = \frac{\pi}{2\Delta p_k} \left[B_{k+\frac{1}{2}} (T_{k+1} - T_k) + B_{k-\frac{1}{2}} (T_k - T_{k-1}) \right], \quad (3.323)$$

$$\left(\pi B \frac{\partial T}{\partial p}\right)_K = \frac{\pi}{2\Delta p_K} \left[B_{K-\frac{1}{2}} (T_K - T_{K-1}) \right]. \quad (3.324)$$

The corrections are added to the diffusion tendencies calculated earlier (3.316) to give the total temperature tendency for diagnostic purposes:

$$\hat{F}_{T_H}(T^*)_k = F_{T_H}(T^*)_k + (2\Delta t F_{F_H})_k + 2\Delta t B_k \left(\pi \frac{\partial T^*}{\partial p} \right)_k K^{(4)} \nabla^4 \Pi^{n+1}. \quad (3.325)$$

1437 3.3.18 Semi-Lagrangian Tracer Transport

The forecast equation for water vapor specific humidity and constituent mixing ratio in the η system is from (3.164) excluding sources and sinks.

$$\frac{dq}{dt} = \frac{\partial q}{\partial t} + \mathbf{V} \cdot \nabla q + \dot{\eta} \frac{\partial p}{\partial \eta} \frac{\partial q}{\partial p} = 0 \quad (3.326)$$

or

$$\frac{dq}{dt} = \frac{\partial q}{\partial t} + \mathbf{V} \cdot \nabla q + \dot{\eta} \frac{\partial q}{\partial \eta} = 0. \quad (3.327)$$

1438 Equation (3.327) is more economical for the semi-Lagrangian vertical advection, as $\Delta\eta$ does not
1439 vary in the horizontal, while Δp does. Written in this form, the η advection equations look
1440 exactly like the σ equations.

The parameterizations are time-split in the moisture equation. The tendency sources have already been added to the time level $(n - 1)$. The semi-Lagrangian advection step is subdivided into horizontal and vertical advection sub-steps, which, in an Eulerian form, would be written

$$q^* = q^{n-1} + 2\Delta t (\mathbf{V} \cdot \nabla q)^n \quad (3.328)$$

and

$$q^{n+1} = q^* + 2\Delta t \left(\dot{\eta} \frac{\partial q}{\partial \eta} \right)^n. \quad (3.329)$$

In the semi-Lagrangian form used here, the general form is

$$q^* = L_{\lambda\varphi} (q^{n-1}), \quad (3.330)$$

$$q^{n+1} = L_{\eta} (q^*). \quad (3.331)$$

1441 Equation (3.330) represents the horizontal interpolation of q^{n-1} at the departure point calculated
1442 assuming $\dot{\eta} = 0$. Equation (3.331) represents the vertical interpolation of q^* at the departure
1443 point, assuming $\mathbf{V} = 0$.

The horizontal departure points are found by first iterating for the mid-point of the trajectory, using winds at time n , and a first guess as the location of the mid-point of the previous time step

$$\lambda_M^{k+1} = \lambda_A - \Delta t u^n (\lambda_M^k, \varphi_M^k) / a \cos \varphi_M^k, \quad (3.332)$$

$$\varphi_M^{k+1} = \varphi_A - \Delta t v^n (\lambda_M^k, \varphi_M^k) / a, \quad (3.333)$$

1444 where subscript A denotes the arrival (Gaussian grid) point and subscript M the midpoint of
 1445 the trajectory. The velocity components at $(\lambda_M^k, \varphi_M^k)$ are determined by Lagrange cubic inter-
 1446 polation. For economic reasons, the equivalent Hermite cubic interpolant with cubic derivative
 1447 estimates is used at some places in this code. The equations will be presented later.

Once the iteration of (3.332) and (3.333) is complete, the departure point is given by

$$\lambda_D = \lambda_A - 2\Delta t u^n (\lambda_M, \varphi_M) / a \cos \varphi_M, \quad (3.334)$$

$$\varphi_D = \lambda_A - 2\Delta t v^n (\lambda_M, \varphi_M) / a, \quad (3.335)$$

1448 where the subscript D denotes the departure point.

The form given by (3.332)-(3.335) is inaccurate near the poles and thus is only used for arrival points equatorward of 70° latitude. Poleward of 70° we transform to a local geodesic coordinate for the calculation at each arrival point. The local geodesic coordinate is essentially a rotated spherical coordinate system whose equator goes through the arrival point. Details are provided in Williamson and Rasch [1989]. The transformed system is rotated about the axis through $(\lambda_A - \frac{\pi}{2}, 0)$ and $(\lambda_A + \frac{\pi}{2}, 0)$, by an angle φ_A so the equator goes through (λ_A, φ_A) . The longitude of the transformed system is chosen to be zero at the arrival point. If the local geodesic system is denoted by (λ', φ') , with velocities (u', v') , the two systems are related by

$$\sin \phi' = \sin \phi \cos \phi_A - \cos \phi \sin \phi_A \cos (\lambda_A - \lambda), \quad (3.336)$$

$$\sin \phi = \sin \phi' \cos \phi_A + \cos \phi' \sin \phi_A \cos \lambda', \quad (3.337)$$

$$\sin \lambda' \cos \phi' = -\sin (\lambda_A - \lambda) \cos \phi, \quad (3.338)$$

$$\begin{aligned} v' \cos \phi' &= v [\cos \phi \cos \phi_A + \sin \phi \sin \phi_A \cos (\lambda_A - \lambda)] \\ &\quad - u \sin \phi_A \sin (\lambda_A - \lambda), \end{aligned} \quad (3.339)$$

$$u' \cos \lambda' - v' \sin \lambda' \sin \phi' = u \cos (\lambda_A - \lambda) + v \sin \phi \sin (\lambda_A - \lambda). \quad (3.340)$$

1449 The calculation of the departure point in the local geodesic system is identical to (3.332)-
 1450 (3.335) with all variables carrying a prime. The equations can be simplified by noting that
 1451 $(\lambda'_A, \varphi'_A) = (0, 0)$ by design and $u'(\lambda'_A, \varphi'_A) = u(\lambda_A, \varphi_A)$ and $v'(\lambda'_A, \varphi'_A) = v(\lambda_A, \varphi_A)$. The
 1452 interpolations are always done in global spherical coordinates.

The interpolants are most easily defined on the interval $0 \leq \theta \leq 1$. Define

$$\theta = (x_D - x_i) / (x_{i+1} - x_i), \quad (3.341)$$

where x is either λ or φ and the departure point x_D falls within the interval (x_i, x_{i+1}) . Following (23) of [Rasch and Williamson, 1990] with $r_i = 3$ the Hermite cubic interpolant is given by

$$\begin{aligned} q_D &= q_{i+1} [3 - 2\theta] \theta^2 - d_{i+1} [h_i \theta^2 (1 - \theta)] \\ &\quad + q_i [3 - 2(1 - \theta)] (1 - \theta)^2 + d_i [h_i \theta (1 - \theta)^2] \end{aligned} \quad (3.342)$$

1453 where q_i is the value at the grid point x_i , d_i is the derivative estimate given below, and $h_i =$
 1454 $x_{i+1} - x_i$.

Following (3.2.12) and (3.2.13) of Hildebrand [1956], the Lagrangian cubic polynomial interpolant used for the velocity interpolation, is given by

$$f_D = \sum_{j=-1}^2 \ell_j(x_D) f_{i+j} \quad (3.343)$$

where

$$\ell_j(x_D) = \frac{(x_D - x_{i-1}) \dots (x_D - x_{i+j-1})(x_D - x_{i+j+1}) \dots (x_D - x_{i+2})}{(x_{i+j} - x_{i-1}) \dots (x_{i+j} - x_{i+j-1})(x_{i+j} - x_{i+j+1}) \dots (x_{i+j} - x_{i+2})} \quad (3.344)$$

1455 where f can represent either u or v , or their counterparts in the geodesic coordinate system.

The derivative approximations used in (3.342) for q are obtained by differentiating (3.343) with respect to x_D , replacing f by q and evaluating the result at x_D equal x_i and x_{i+1} . With these derivative estimates, the Hermite cubic interpolant (3.342) is equivalent to the Lagrangian (3.343). If we denote the four point stencil $(x_{i-1}, x_i, x_{i+1}, x_{i+2})$ by (x_1, x_2, x_3, x_4) , the cubic derivative estimates are

$$d_2 = \left[\frac{(x_2 - x_3)(x_2 - x_4)}{(x_1 - x_2)(x_1 - x_3)(x_1 - x_4)} \right] q_1 \quad (3.345)$$

$$- \left[\frac{1}{(x_1 - x_2)} - \frac{1}{(x_2 - x_3)} - \frac{1}{(x_2 - x_4)} \right] q_2 \quad (3.346)$$

$$+ \left[\frac{(x_2 - x_1)(x_2 - x_4)}{(x_1 - x_3)(x_2 - x_3)(x_3 - x_4)} \right] q_3 \quad (3.347)$$

$$- \left[\frac{(x_2 - x_1)(x_2 - x_3)}{(x_1 - x_4)(x_2 - x_4)(x_3 - x_4)} \right] q_4 \quad (3.348)$$

and

$$d_3 = \left[\frac{(x_3 - x_2)(x_3 - x_4)}{(x_1 - x_2)(x_1 - x_3)(x_1 - x_4)} \right] q_1 \quad (3.349)$$

$$- \left[\frac{(x_3 - x_1)(x_3 - x_4)}{(x_1 - x_2)(x_2 - x_3)(x_2 - x_4)} \right] q_2 \quad (3.350)$$

$$- \left[\frac{1}{(x_1 - x_3)} + \frac{1}{(x_2 - x_3)} - \frac{1}{(x_3 - x_4)} \right] q_3 \quad (3.351)$$

$$- \left[\frac{(x_3 - x_1)(x_3 - x_2)}{(x_1 - x_4)(x_2 - x_4)(x_3 - x_4)} \right] q_4 \quad (3.352)$$

1456 The two dimensional (λ, φ) interpolant is obtained as a tensor product application of the
 1457 one-dimensional interpolants, with λ interpolations done first. Assume the departure point falls
 1458 in the grid box $(\lambda_i, \lambda_{i+1})$ and $(\varphi_i, \varphi_{i+1})$. Four λ interpolations are performed to find q values
 1459 at $(\lambda_D, \varphi_{j-1})$, (λ_D, φ_j) , $(\lambda_D, \varphi_{j+1})$, and $(\lambda_D, \varphi_{j+2})$. This is followed by one interpolation in φ
 1460 using these four values to obtain the value at (λ_D, φ_D) . Cyclic continuity is used in longitude.
 1461 In latitude, the grid is extended to include a pole point (row) and one row across the pole. The

1462 pole row is set equal to the average of the row next to the pole for q and to wavenumber 1
 1463 components for u and v . The row across the pole is filled with the values from the first row
 1464 below the pole shifted π in longitude for q and minus the value shifted by π in longitude for u
 1465 and v .

Once the departure point is known, the constituent value of $q^* = q_D^{n-1}$ is obtained as indicated in (3.330) by Hermite cubic interpolation (3.342), with cubic derivative estimates (3.343) and (3.344) modified to satisfy the Sufficient Condition for Monotonicity with C° continuity (SCMO) described below. Define $\Delta_i q$ by

$$\Delta_i q = \frac{q_{i+1} - q_i}{x_{i+1} - x_i}. \quad (3.353)$$

First, if $\Delta_i q = 0$ then

$$d_i = d_{i+1} = 0. \quad (3.354)$$

Then, if either

$$0 \leq \frac{d_i}{\Delta_i q} \leq 3 \quad (3.355)$$

or

$$0 \leq \frac{d_{i+1}}{\Delta_i q} \leq 3 \quad (3.356)$$

1466 is violated, d_i or d_{i+1} is brought to the appropriate bound of the relationship. These conditions
 1467 ensure that the Hermite cubic interpolant is monotonic in the interval $[x_i, x_{i+1}]$.

The horizontal semi-Lagrangian sub-step (3.330) is followed by the vertical step (3.331). The vertical velocity $\dot{\eta}$ is obtained from that diagnosed in the dynamical calculations (3.222) by

$$(\dot{\eta})_{k+\frac{1}{2}} = \left(\dot{\eta} \frac{\partial p}{\partial \eta} \right)_{k+\frac{1}{2}} \bigg/ \left(\frac{p_{k+1} - p_k}{\eta_{k+1} - \eta_k} \right), \quad (3.357)$$

with $\eta_k = A_k + B_k$. Note, this is the only place that the model actually requires an explicit specification of η . The mid-point of the vertical trajectory is found by iteration

$$\eta_M^{k+1} = \eta_A - \Delta t \dot{\eta}^n (\eta_M^k). \quad (3.358)$$

Note, the arrival point η_A is a mid-level point where q is carried, while the $\dot{\eta}$ used for the interpolation to mid-points is at interfaces. We restrict η_M by

$$\eta_1 \leq \eta_M \leq \eta_K, \quad (3.359)$$

which is equivalent to assuming that q is constant from the surface to the first model level and above the top q level. Once the mid-point is determined, the departure point is calculated from

$$\eta_D = \eta_A - 2\Delta t \dot{\eta}^n (\eta_M), \quad (3.360)$$

with the restriction

$$\eta_1 \leq \eta_D \leq \eta_K. \quad (3.361)$$

1468 The appropriate values of $\dot{\eta}$ and q are determined by interpolation (3.342), with the derivative
 1469 estimates given by (3.343) and (3.344) for $i = 2$ to $K - 1$. At the top and bottom we assume
 1470 a zero derivative (which is consistent with (3.359) and (3.361)), $d_i = 0$ for the interval $k = 1$,

1471 and $\delta_{i+1} = 0$ for the interval $k = K - 1$. The estimate at the interior end of the first and last
 1472 grid intervals is determined from an uncentered cubic approximation; that is d_{i+1} at the $k = 1$
 1473 interval is equal to d_i from the $k = 2$ interval, and d_i at the $k = K - 1$ interval is equal to d_{i+1}
 1474 at the $k = K - 2$ interval. The monotonic conditions (3.355) to (3.356) are applied to the q
 1475 derivative estimates.

1476 3.3.19 Mass fixers

1477 This section describes original and modified fixers used for the Eulerian and semi-Lagrangian
 1478 dynamical cores.

1479 Let π^0 , Δp^0 and q^0 denote the values of air mass, pressure intervals, and water vapor specific
 1480 humidity at the beginning of the time step (which are the same as the values at the end of the
 1481 previous time step.)

1482 π^+ , Δp^+ and q^+ are the values after fixers are applied at the end of the time step.

1483 π^- , Δp^- and q^- are the values after the parameterizations have updated the moisture field
 1484 and tracers.

1485 Since the physics parameterizations do not change the surface pressure, π^- and Δp^- are also
 1486 the values at the beginning of the time step.

The fixers which ensure conservation are applied to the dry atmospheric mass, water vapor specific humidity and constituent mixing ratios. For water vapor and atmospheric mass the desired discrete relations, following Williamson and Olson [1994a] are

$$\int_2 \pi^+ - \int_3 q^+ \Delta p^+ = \mathbf{P}, \quad (3.362)$$

$$\int_3 q^+ \Delta p^+ = \int_3 q^- \Delta p^-, \quad (3.363)$$

where \mathbf{P} is the dry mass of the atmosphere. From the definition of the vertical coordinate,

$$\Delta p = p_0 \Delta A + \pi \Delta B, \quad (3.364)$$

and the integral \int_2 denotes the normal Gaussian quadrature while \int_3 includes a vertical sum followed by Gaussian quadrature. The actual fixers are chosen to have the form

$$\pi^+ (\lambda, \varphi) = \mathbf{M} \hat{\pi}^+ (\lambda, \varphi), \quad (3.365)$$

preserving the horizontal gradient of Π , which was calculated earlier during the inverse spectral transform, and

$$q^+ (\lambda, \varphi, \eta) = \hat{q}^+ + \alpha \eta \hat{q}^+ |\hat{q}^+ - q^-|. \quad (3.366)$$

In (3.365) and (3.366) the $(\hat{\quad})$ denotes the provisional value before adjustment. The form (3.366) forces the arbitrary corrections to be small when the mixing ratio is small and when the change made to the mixing ratio by the advection is small. In addition, the η factor is included to make the changes approximately proportional to mass per unit volume [Rasch et al., 1995]. Satisfying

(3.362) and (3.363) gives

$$\alpha = \frac{\int_3 q^- \Delta p^- - \int_3 \hat{q}^+ p_0 \Delta A - M \int_3 \hat{q}^+ \hat{\pi}^+ \Delta B}{\int_3 \eta \hat{q}^+ |\hat{q}^+ - q^-| p_0 \Delta A + M \int_3 \eta \hat{q}^+ |\hat{q}^+ - q^-| \hat{\pi}^+ \Delta B} \quad (3.367)$$

and

$$M = \left(\mathbf{P} + \int_3 q^- \Delta p^- \right) \Big/ \int_2 \hat{\pi}^+ . \quad (3.368)$$

Note that water vapor and dry mass are corrected simultaneously. Additional advected constituents are treated as mixing ratios normalized by the mass of dry air. This choice was made so that as the water vapor of a parcel changed, the constituent mixing ratios would not change. Thus the fixers which ensure conservation involve the dry mass of the atmosphere rather than the moist mass as in the case of the specific humidity above. Let χ denote the mixing ratio of constituents. Historically we have used the following relationship for conservation:

$$\int_3 \chi^+ (1 - q^+) \Delta p^+ = \int_3 \chi^- (1 - q^-) \Delta p^- . \quad (3.369)$$

The term $(1 - q) \Delta p$ defines the dry air mass in a layer. Following [Rasch et al. \[1995\]](#) the change made by the fixer has the same form as (3.366)

$$\chi^+ (\lambda, \varphi, \eta) = \hat{\chi}^+ + \alpha_\chi \eta \hat{\chi}^+ |\hat{\chi}^+ - \chi^-| . \quad (3.370)$$

Substituting (3.370) into (3.369) and using (3.365) through (3.368) gives

$$\alpha_\chi = \frac{\int_3 \chi^- (1 - q^-) \Delta p^- - \int_{A,B} \hat{\chi}^+ (1 - \hat{q}^+) \Delta \hat{p}^+ + \alpha \int_{A,B} \hat{\chi}^+ \eta \hat{q}^+ |\hat{q}^+ - q^-| \Delta p}{\int_{A,B} \eta \hat{\chi}^+ |\hat{\chi}^+ - \chi^-| (1 - \hat{q}^+) \Delta p - \alpha \int_{A,B} \eta \hat{\chi}^+ |\hat{\chi}^+ - \chi^-| \eta \hat{q}^+ |\hat{q}^+ - q^-| \Delta p} , \quad (3.371)$$

where the following shorthand notation is adopted:

$$\int_{A,B} () \Delta p = \int_3 () p_0 \Delta A + M \int_3 () p_s \Delta B . \quad (3.372)$$

We note that there is a small error in (3.369). Consider a situation in which moisture is transported by a physical parameterization, but there is no source or sink of moisture. Under this circumstance $q^- \neq q^0$, but the surface pressure is not allowed to change. Since $(1 - q^-) \Delta p^- \neq (1 - q^0) \Delta p^0$, there is an implied change of dry mass of dry air in the layer, and even in circumstances where there is no change of dry mixing ratio χ there would be an implied change in mass of the tracer. The solution to this inconsistency is to define a dry air mass *only once* within the model time step, and use it consistently throughout the model. In this revision, we have chosen to fix the dry air mass in the model time step where the surface pressure is updated, e.g. at the end of the model time step. Therefore, we now replace (3.369) with

$$\int_3 \chi^+ (1 - q^+) \Delta p^+ = \int_3 \chi^- (1 - q^0) \Delta p^0 . \quad (3.373)$$

1487 There is a corresponding change in the first term of the numerator of (3.371) in which
 1488 q^- is replaced by q^0 . CAM 5.0 uses (3.371) for water substances and constituents affecting the
 1489 temperature field to prevent changes to the IPCC simulations. In the future, constituent fields
 1490 may use a *corrected* version of (3.371).

1491 3.3.20 Energy Fixer

Following notation in section 3.3.19, the total energy integrals are

$$\int_3 \frac{1}{g} \left[c_p T^+ + \Phi_s + \frac{1}{2} (u^{+2} + v^{+2}) \right] \Delta p^+ = \mathbf{E} \quad (3.374)$$

$$\mathbf{E} = \int_3 \frac{1}{g} \left[c_p T^- + \Phi_s + \frac{1}{2} (u^{-2} + v^{-2}) \right] \Delta p^- + \mathbf{S} \quad (3.375)$$

$$\mathbf{S} = \int_2 [(FSNT - FLNT) - (FSNS - FLNS - SHFLX - \rho_{H_2O} L_v PRECT) -] \Delta t \quad (3.376)$$

$$\mathbf{S} = \int_2 [(FSNT - FLNT) - (FSNS - FLNS - SHFLX)] \Delta t \quad (3.377)$$

$$+ \int_2 [\rho_{H_2O} L_v (PRECL + PRECC) + \rho_{H_2O} L_i (PRESL + PRESC)] \Delta t \quad (3.378)$$

where \mathbf{S} is the net source of energy from the parameterizations. $FSNT$ is the net downward solar flux at the model top, $FLNT$ is the net upward longwave flux at the model top, $FSNS$ is the net downward solar flux at the surface, $FLNS$ is the net upward longwave flux at the surface, $SHFLX$ is the surface sensible heat flux, and $PRECT$ is the total precipitation during the time step. From equation (3.365)

$$\pi^+ (\lambda, \varphi) = \mathbf{M} \hat{\pi}^+ (\lambda, \varphi) \quad (3.379)$$

and from (3.364)

$$\Delta p = p_0 \Delta A + \pi \Delta B \quad (3.380)$$

The energy fixer is chosen to have the form

$$T^+ (\lambda, \varphi, \eta) = \hat{T}^+ + \beta \quad (3.381)$$

$$u^+ (\lambda, \varphi, \eta) = \hat{u}^+ \quad (3.382)$$

$$v^+ (\lambda, \varphi, \eta) = \hat{v}^+ \quad (3.383)$$

Then

$$\beta = \frac{g \mathbf{E} - \int_3 \left[c_p \hat{T}^+ + \Phi_s + \frac{1}{2} (\hat{u}^{+2} + \hat{v}^{+2}) \right] p_0 \Delta A - \mathbf{M} \int_3 \left[c_p \hat{T}^+ + \Phi_s + \frac{1}{2} (\hat{u}^{+2} + \hat{v}^{+2}) \right] \hat{\pi}^+ \Delta B}{\int_3 c_p p_0 \Delta A + \mathbf{M} \int_3 c_p \hat{\pi}^+ \Delta B} \quad (3.384)$$

3.3.21 Statistics Calculations

At each time step, selected global average statistics are computed for diagnostic purposes when the model is integrated with the Eulerian and semi-Lagrangian dynamical cores. Let \int_3 denote a global and vertical average and \int_2 a horizontal global average. For an arbitrary variable ψ , these are defined by

$$\int_3 \psi dV = \sum_{k=1}^K \sum_{j=1}^J \sum_{i=1}^I \psi_{ijk} w_j \left(\frac{\Delta p_k}{\pi} \right) / 2I, \quad (3.385)$$

and

$$\int_2 \psi dA = \sum_{j=1}^J \sum_{i=1}^I \psi_{ijk} w_j / 2I, \quad (3.386)$$

where recall that

$$\sum_{j=1}^J w_j = 2. \quad (3.387)$$

The quantities monitored are:

$$\text{global rms } (\zeta + f)(\text{s}^{-1}) = \left[\int_3 (\zeta^n + f)^2 dV \right]^{1/2}, \quad (3.388)$$

$$\text{global rms } \delta(\text{s}^{-1}) = \left[\int_3 (\delta^n)^2 dV \right]^{1/2}, \quad (3.389)$$

$$\text{global rms } T \text{ (K)} = \left[\int_3 (T^r + T^n)^2 dV \right]^{1/2}, \quad (3.390)$$

$$\text{global average mass times } g \text{ (Pa)} = \int_2 \pi^n dA, \quad (3.391)$$

$$\text{global average mass of moisture (kg m}^{-2}\text{)} = \int_3 \pi^n q^n / g dV. \quad (3.392)$$

3.3.22 Reduced grid

The Eulerian core and semi-Lagrangian tracer transport can be run on reduced grids. The term reduced grid generally refers to a grid based on latitude and longitude circles in which the longitudinal grid increment increases at latitudes approaching the poles so that the longitudinal distance between grid points is reasonably constant. Details are provided in [Williamson and Rosinski, 2000]. This option provides a saving of computer time of up to 25%.

3.4 Semi-Lagrangian Dynamical Core

3.4.1 Introduction

The two-time-level semi-implicit semi-Lagrangian spectral transform dynamical core in CAM 5.0 evolved from the three-time-level CCM2 semi-Lagrangian version detailed in

1503 Williamson and Olson [1994a] hereafter referred to as W&O94. As a first approximation,
 1504 to convert from a three-time-level scheme to a two-time-level scheme, the time level index $n-1$
 1505 becomes n , the time level index n becomes $n+\frac{1}{2}$, and $2\Delta t$ becomes Δt . Terms needed at $n+\frac{1}{2}$
 1506 are extrapolated in time using time n and $n-1$ terms, except the Coriolis term which is implicit
 1507 as the average of time n and $n+1$. This leads to a more complex semi-implicit equation to solve.
 1508 Additional changes have been made in the scheme to incorporate advances in semi-Lagrangian
 1509 methods developed since W&O94. In the following, reference is made to changes from the
 1510 scheme developed in W&O94. The reader is referred to that paper for additional details of
 1511 the derivation of basic aspects of the semi-Lagrangian approximations. Only the details of the
 1512 two-time-level approximations are provided here.

1513 3.4.2 Vertical coordinate and hydrostatic equation

The semi-Lagrangian dynamical core adopts the same hybrid vertical coordinate (η) as the Eulerian core defined by

$$p(\eta, p_s) = A(\eta)p_o + B(\eta)p_s, \quad (3.393)$$

1514 where p is pressure, p_s is surface pressure, and p_o is a specified constant reference pressure. The
 1515 coefficients A and B specify the actual coordinate used. As mentioned by Simmons and Burridge
 1516 [1981] and implemented by Simmons and Strüfing [1981] and Simmons and Strüfing [1983], the
 1517 coefficients A and B are defined only at the discrete model levels. This has implications in the
 1518 continuity equation development which follows.

In the η system the hydrostatic equation is approximated in a general way by

$$\Phi_k = \Phi_s + R \sum_{l=k}^K H_{kl}(p) T_{vl} \quad (3.394)$$

1519 where k is the vertical grid index running from 1 at the top of the model to K at the first model
 1520 level above the surface, Φ_k is the geopotential at level k , Φ_s is the surface geopotential, T_v is the
 1521 virtual temperature, and R is the gas constant. The matrix H , referred to as the hydrostatic
 1522 matrix, represents the discrete approximation to the hydrostatic integral and is left unspecified
 1523 for now. It depends on pressure, which varies from horizontal point to point.

1524 3.4.3 Semi-implicit reference state

The semi-implicit equations are linearized about a reference state with constant T^r and p_s^r . We choose

$$T^r = 350\text{K}, \quad p_s^r = 10^5\text{Pa} \quad (3.395)$$

1525 3.4.4 Perturbation surface pressure prognostic variable

To ameliorate the mountain resonance problem, Ritchie and Tanguay [1996] introduce a perturbation $\ln p_s$ surface pressure prognostic variable

$$\ln p'_s = \ln p_s - \ln p_s^* \quad (3.396)$$

$$\ln p_s^* = -\frac{\Phi_s}{RT^r} \quad (3.397)$$

1526 The perturbation surface pressure, $\ln p'_s$, is never actually used as a grid point variable in the
 1527 CAM 5.0 code. It is only used for the semi-implicit development and solution. The total $\ln p_s$
 1528 is reclaimed in spectral space from the spectral coefficients of Φ_s immediately after the semi-
 1529 implicit equations are solved, and transformed back to spectral space along with its derivatives.
 1530 This is in part because $\nabla^4 \ln p_s$ is needed for the horizontal diffusion correction to pressure
 1531 surfaces. However the semi-Lagrangian CAM 5.0 default is to run with no horizontal diffusion.

1532 3.4.5 Extrapolated variables

Variables needed at time $(n + \frac{1}{2})$ are obtained by extrapolation

$$(\quad)^{n+\frac{1}{2}} = \frac{3}{2}(\quad)^n - \frac{1}{2}(\quad)^{n-1} \quad (3.398)$$

1533 3.4.6 Interpolants

1534 Lagrangian polynomial quasi-cubic interpolation is used in the prognostic equations for the
 1535 dynamical core. Monotonic Hermite quasi-cubic interpolation is used for tracers. Details are
 1536 provided in the Eulerian Dynamical Core description. The trajectory calculation uses tri-linear
 1537 interpolation of the wind field.

1538 3.4.7 Continuity Equation

The discrete semi-Lagrangian, semi-implicit continuity equation is obtained from (16) of W&O94 modified to be spatially uncentered by a fraction ϵ , and to predict $\ln p'_s$

$$\begin{aligned} \Delta B_l \left\{ (\ln p'_{s_l})_A^{n+1} - \left[(\ln p_{s_l})^n + \frac{\Phi_s}{RT^r} \right]_{D_2} \right\} / \Delta t = \\ - \frac{1}{2} \left\{ \left[(1 + \epsilon) \Delta \left(\frac{1}{p_s} \dot{\eta} \frac{\partial p}{\partial \eta} \right) \right]_{l_A}^{n+1} + \left[(1 - \epsilon) \Delta \left(\frac{1}{p_s} \dot{\eta} \frac{\partial p}{\partial \eta} \right) \right]_{l_{D_2}}^n \right\} \\ - \left(\frac{1}{p_s} \delta_l \Delta p_l \right)_{M_2}^{n+\frac{1}{2}} + \frac{\Delta B_l}{RT^r} (\mathbf{V}_l \cdot \nabla \Phi_s)_{M_2}^{n+\frac{1}{2}} \\ - \left\{ \frac{1}{2} \left[(1 + \epsilon) \left(\frac{1}{p'_s} \delta_l \Delta p'_l \right)_A^{n+1} + (1 - \epsilon) \left(\frac{1}{p'_s} \delta_l \Delta p'_l \right)_{D_2}^n \right] - \left(\frac{1}{p'_s} \delta_l \Delta p'_l \right)_{M_2}^{n+\frac{1}{2}} \right\} \end{aligned} \quad (3.399)$$

where

$$\Delta(\quad)_l = (\quad)_{l+\frac{1}{2}} - (\quad)_{l-\frac{1}{2}} \quad (3.400)$$

and

$$(\quad)_{M_2}^{n+\frac{1}{2}} = \frac{1}{2} \left[(1 + \epsilon) (\quad)_A^{n+\frac{1}{2}} + (1 - \epsilon) (\quad)_{D_2}^{n+\frac{1}{2}} \right] \quad (3.401)$$

1539 $\Delta(\quad)_l$ denotes a vertical difference, l denotes the vertical level, A denotes the arrival point, D_2
 1540 the departure point from horizontal (two-dimensional) advection, and M_2 the midpoint of that
 1541 trajectory.

The surface pressure forecast equation is obtained by summing over all levels and is related to (18) of W&O94 but is spatially uncentered and uses $\ln p'_s$

$$\begin{aligned}
(\ln p'_s)_A^{n+1} &= \sum_{l=1}^K \Delta B_l \left[(\ln p_{s_l})^n + \frac{\Phi_s}{RT^r} \right]_{D_2} - \frac{1}{2} \Delta t \sum_{l=1}^K \left[(1 - \epsilon) \Delta \left(\frac{1}{p_s} \dot{\eta} \frac{\partial p}{\partial \eta} \right)_l \right]_{D_2}^n \\
&\quad - \Delta t \sum_{l=1}^K \left(\frac{1}{p_s} \delta_l \Delta p_l \right)_{M_2}^{n+\frac{1}{2}} + \Delta t \sum_{l=1}^K \frac{\Delta B_l}{RT^r} (\mathbf{V}_l \cdot \nabla \Phi_s)_{M_2}^{n+\frac{1}{2}} \\
&\quad - \Delta t \sum_{l=1}^K \frac{1}{p_s^r} \left\{ \frac{1}{2} \left[(1 + \epsilon) (\delta_l)_A^{n+1} + (1 - \epsilon) (\delta_l)_{D_2}^n \right] - (\delta_l)_{M_2}^{n+\frac{1}{2}} \right\} \Delta p_l^r
\end{aligned} \tag{3.402}$$

1542 The corresponding $\left(\frac{1}{p_s} \dot{\eta} \frac{\partial p}{\partial \eta} \right)$ equation for the semi-implicit development follows and is related
1543 to (19) of W&O94, again spatially uncentered and using $\ln p'_s$.

$$\begin{aligned}
(1 + \epsilon) \left(\frac{1}{p_s} \dot{\eta} \frac{\partial p}{\partial \eta} \right)_{k+\frac{1}{2}}^{n+1} &= - \frac{2}{\Delta t} \left\{ B_{k+\frac{1}{2}} (\ln p'_s)_A^{n+1} - \sum_{l=1}^k \Delta B_l \left[(\ln p_{s_l})^n + \frac{\Phi_s}{RT^r} \right]_{D_2} \right\} \\
&\quad - \sum_{l=1}^k \left[(1 - \epsilon) \Delta \left(\frac{1}{p_s} \dot{\eta} \frac{\partial p}{\partial \eta} \right)_l \right]_{D_2}^n \\
&\quad - 2 \sum_{l=1}^k \left(\frac{1}{p_s} \delta_l \Delta p_l \right)_{M_2}^{n+\frac{1}{2}} + 2 \sum_{l=1}^k \frac{\Delta B_l}{RT^r} (\mathbf{V}_l \cdot \nabla \Phi_s)_{M_2}^{n+\frac{1}{2}} \\
&\quad - 2 \sum_{l=1}^k \frac{1}{p_s^r} \left\{ \frac{1}{2} \left[(1 + \epsilon) (\delta_l)_A^{n+1} + (1 - \epsilon) (\delta_l)_{D_2}^n \right] - (\delta_l)_{M_2}^{n+\frac{1}{2}} \right\} \Delta p_l^r
\end{aligned} \tag{3.403}$$

1544 This is not the actual equation used to determine $\left(\frac{1}{p_s} \dot{\eta} \frac{\partial p}{\partial \eta} \right)$ in the code. The equation actually
1545 used in the code to calculate $\left(\frac{1}{p_s} \dot{\eta} \frac{\partial p}{\partial \eta} \right)$ involves only the divergence at time $(n+1)$ with $(\ln p'_s)^{n+1}$
1546 eliminated.

$$\begin{aligned}
(1 + \epsilon) \left(\frac{1}{p_s} \dot{\eta} \frac{\partial p}{\partial \eta} \right)_{k+\frac{1}{2}}^{n+1} = & \\
\frac{2}{\Delta t} \left[\sum_{l=1}^k - B_{k+\frac{1}{2}} \sum_{l=1}^K \right] \Delta B_l \left[(\ln p_{s_l})^n + \frac{\Phi_s}{RT^r} \right]_{D_2} & \\
- \left[\sum_{l=1}^k - B_{k+\frac{1}{2}} \sum_{l=1}^K \right] \left[(1 - \epsilon) \Delta \left(\frac{1}{p_s} \dot{\eta} \frac{\partial p}{\partial \eta} \right)_l \right]_{D_2}^n & \\
- 2 \left[\sum_{l=1}^k - B_{k+\frac{1}{2}} \sum_{l=1}^K \right] \left(\frac{1}{p_s} \delta_l \Delta p_l \right)_{M_2}^{n+\frac{1}{2}} & \tag{3.404} \\
+ 2 \left[\sum_{l=1}^k - B_{k+\frac{1}{2}} \sum_{l=1}^K \right] \frac{\Delta B_l}{RT^r} (\mathbf{V}_l \cdot \nabla \Phi_s)_{M_2}^{n+\frac{1}{2}} & \\
- 2 \left[\sum_{l=1}^k - B_{k+\frac{1}{2}} \sum_{l=1}^K \right] \frac{1}{p_s^r} \left\{ \frac{1}{2} \left[(1 + \epsilon) (\delta_l)_A^{n+1} + (1 - \epsilon) (\delta_l)_{D_2}^n \right] - (\delta_l)_{M_2}^{n+\frac{1}{2}} \right\} \Delta p_l^r &
\end{aligned}$$

1547 The combination $\left[(\ln p_{s_l})^n + \frac{\Phi_s}{RT^r} + \frac{1}{2} \frac{\Delta t}{RT^r} (\mathbf{V} \cdot \nabla \Phi_s)^{n+\frac{1}{2}} \right]_{D_2}$ is treated as a unit, and follows from
1548 (3.401).

1549 3.4.8 Thermodynamic Equation

The thermodynamic equation is obtained from (25) of W&O94 modified to be spatially uncentered and to use $\ln p'_s$. In addition Hortal's modification [Temperton et al., 2001] is included, in which

$$\frac{d}{dt} \left[- \left(p_s B \frac{\partial T}{\partial p} \right)_{ref} \frac{\Phi_s}{RT^r} \right] \tag{3.405}$$

1550 is subtracted from both sides of the temperature equation. This is akin to horizontal diffusion
1551 which includes the first order term converting horizontal derivatives from eta to pressure co-
1552 ordinates, with $(\ln p_s)$ replaced by $-\frac{\Phi_s}{RT^r}$, and $\left(p_s B \frac{\partial T}{\partial p} \right)_{ref}$ taken as a global average so it is
1553 invariant with time and can commute with the differential operators.

$$\begin{aligned}
\frac{T_A^{n+1} - T_D^n}{\Delta t} = & \left\{ \left\{ \left[- \left(p_s B(\eta) \frac{\partial T}{\partial p} \right)_{ref} \frac{\Phi_s}{RT^r} \right]_A^{n+1} - \left[- \left(p_s B(\eta) \frac{\partial T}{\partial p} \right)_{ref} \frac{\Phi_s}{RT^r} \right]_D^n \right\} / \Delta t \right. \\
& + \left. \frac{1}{RT^r} \left[\left(p_s B(\eta) \frac{\partial T}{\partial p} \right)_{ref} \mathbf{V} \cdot \nabla \Phi_s + \Phi_s \dot{\eta} \frac{\partial}{\partial \eta} \left(p_s B(\eta) \frac{\partial T}{\partial p} \right)_{ref} \right]_M^{n+\frac{1}{2}} \right\} \\
& + \left(\frac{RT_v \omega}{c_p^* p} \right)_M^{n+\frac{1}{2}} + Q_M^n \\
& + \frac{RT^r p_s^r}{c_p p^r} \left[B(\eta) \frac{d_2 \ln p_s'}{dt} + \overline{\left(\frac{1}{p_s} \dot{\eta} \frac{\partial p}{\partial \eta} \right)^t} \right] \\
& - \frac{RT^r p_s^r}{c_p p^r} \left[\left(\frac{p}{p_s} \right) \left(\frac{\omega}{p} \right) \right]_M^{n+\frac{1}{2}} \\
& - \frac{RT^r p_s^r}{c_p p^r} B(\eta) \left[\frac{1}{RT^r} \mathbf{V} \cdot \nabla \Phi_s \right]_{M_2}^{n+\frac{1}{2}}
\end{aligned} \tag{3.406}$$

1554 Note that Q^n represents the heating calculated to advance from time n to time $n + 1$ and is
1555 valid over the interval.

1556 The calculation of $\left(p_s B \frac{\partial T}{\partial p} \right)_{ref}$ follows that of the ECMWF (Research Manual 3, ECMWF
1557 Forecast Model, Adiabatic Part, ECMWF Research Department, 2nd edition, 1/88, pp 2.25-
1558 2.26) Consider a constant lapse rate atmosphere

$$T = T_0 \left(\frac{p}{p_0} \right)^{R\gamma/g} \quad (3.407)$$

$$\frac{\partial T}{\partial p} = \frac{1}{p} \frac{R\gamma}{g} T_0 \left(\frac{p}{p_0} \right)^{R\gamma/g} \quad (3.408)$$

$$p_s B \frac{\partial T}{\partial p} = B \frac{p_s}{p} \frac{R\gamma}{g} T \quad (3.409)$$

$$\left(p_s B \frac{\partial T}{\partial p} \right)_{ref} = B_k \frac{(p_s)_{ref}}{(p_k)_{ref}} \frac{R\gamma}{g} (T_k)_{ref} \text{ for } (T_k)_{ref} > T_C \quad (3.410)$$

$$\left(p_s B \frac{\partial T}{\partial p} \right)_{ref} = 0 \text{ for } (T_k)_{ref} \leq T_C \quad (3.411)$$

$$(p_k)_{ref} = A_k p_0 + B_k (p_s)_{ref} \quad (3.412)$$

$$(T_k)_{ref} = T_0 \left(\frac{(p_k)_{ref}}{(p_s)_{ref}} \right)^{R\gamma/g} \quad (3.413)$$

$$(p_s)_{ref} = 1013.25 \text{mb} \quad (3.414)$$

$$T_0 = 288 \text{K} \quad (3.415)$$

$$p_0 = 1000 \text{mb} \quad (3.416)$$

$$\gamma = 6.5 \text{K/km} \quad (3.417)$$

$$T_C = 216.5 \text{K} \quad (3.418)$$

1559 3.4.9 Momentum equations

1560 The momentum equations follow from (3) of W&O94 modified to be spatially uncentered, to use
 1561 $\ln p'_s$, and with the Coriolis term implicit following [Côté and Staniforth \[1988\]](#) and [Temperton](#)
 1562 [\[1997\]](#). The semi-implicit, semi-Lagrangian momentum equation at level k (but with the level
 1563 subscript k suppressed) is

$$\begin{aligned}
\frac{\mathbf{V}_A^{n+1} - \mathbf{V}_D^n}{\Delta t} &= -\frac{1}{2} \left\{ (1 + \epsilon) \left[f \hat{\mathbf{k}} \times \mathbf{V} \right]_A^{n+1} + (1 - \epsilon) \left[f \hat{\mathbf{k}} \times \mathbf{V} \right]_D^n \right\} + \mathbf{F}_M^n \\
&\quad - \frac{1}{2} \left\{ (1 + \epsilon) \left[\nabla (\Phi_s + R \mathbf{H}_k \cdot \mathbf{T}_v) + RT_v \frac{B}{p} p_s \nabla \ln p_s \right]_A^{n+\frac{1}{2}} \right. \\
&\quad \left. + (1 - \epsilon) \left[\nabla (\Phi_s + R \mathbf{H}_k \cdot \mathbf{T}_v) + RT_v \frac{B}{p} p_s \nabla \ln p_s \right]_D^{n+\frac{1}{2}} \right\} \\
&\quad - \frac{1}{2} \left\{ (1 + \epsilon) \nabla [R \mathbf{H}_k^r \cdot \mathbf{T} + RT^r \ln p'_s]_A^{n+1} \right. \\
&\quad \quad - (1 + \epsilon) \nabla [\Phi_s + R \mathbf{H}_k^r \cdot \mathbf{T} + RT^r \ln p_s]_A^{n+\frac{1}{2}} \\
&\quad \quad + (1 - \epsilon) \nabla [\Phi_s + R \mathbf{H}_k^r \cdot \mathbf{T} + RT^r \ln p_s]_D^n \\
&\quad \quad \left. - (1 - \epsilon) \nabla [\Phi_s + R \mathbf{H}_k^r \cdot \mathbf{T} + RT^r \ln p_s]_D^{n+\frac{1}{2}} \right\} \quad (3.419)
\end{aligned}$$

1564 The gradient of the geopotential is more complex than in the σ system because the hydro-
1565 static matrix \mathbf{H} depends on the local pressure:

$$\nabla (\mathbf{H}_k \cdot \mathbf{T}_v) = \mathbf{H}_k \cdot [(1 + \epsilon_v \mathbf{q}) \nabla \mathbf{T} + \epsilon_v \mathbf{T} \nabla \mathbf{q}] + \mathbf{T}_v \cdot \nabla \mathbf{H}_k \quad (3.420)$$

where ϵ_v is $(R_v/R - 1)$ and R_v is the gas constant for water vapor. The gradient of T is calculated from the spectral representation and that of q from a discrete cubic approximation that is consistent with the interpolation used in the semi-Lagrangian water vapor advection. In general, the elements of \mathbf{H} are functions of pressure at adjacent discrete model levels

$$H_{kl} = f_{kl}(p_{l+1/2}, p_l, p_{l-1/2}) \quad (3.421)$$

The gradient is then a function of pressure and the pressure gradient

$$\nabla H_{kl} = g_{kl}(p_{l+1/2}, p_l, p_{l-1/2}, \nabla p_{l+1/2}, \nabla p_l, \nabla p_{l-1/2}) \quad (3.422)$$

The pressure gradient is available from (3.393) and the surface pressure gradient calculated from the spectral representation

$$\nabla p_l = B_l \nabla p_s = B_l p_s \nabla \ln p_s \quad (3.423)$$

1566 3.4.10 Development of semi-implicit system equations

The momentum equation can be written as

$$\begin{aligned}
\frac{\mathbf{V}_A^{n+1} - \mathbf{V}_D^n}{\Delta t} &= -\frac{1}{2} \left\{ (1 + \epsilon) \left[f \hat{\mathbf{k}} \times \mathbf{V} \right]_A^{n+1} + (1 - \epsilon) \left[f \hat{\mathbf{k}} \times \mathbf{V} \right]_D^n \right\} \\
&\quad - \frac{1}{2} \left\{ (1 + \epsilon) \nabla [R \mathbf{H}_k^r \cdot \mathbf{T} + RT^r \ln p'_s]_A^{n+1} \right\} + R H S_{\mathbf{V}}, \quad (3.424)
\end{aligned}$$

1567 where $RHS_{\mathbf{V}}$ contains known terms at times $(n + \frac{1}{2})$ and (n) .

By combining terms, 3.424 can be written in general as

$$\mathcal{U}_A^{n+1} \hat{\mathbf{i}}_A + \mathcal{V}_A^{n+1} \hat{\mathbf{j}}_A = \mathcal{U}_A \hat{\mathbf{i}}_A + \mathcal{V}_A \hat{\mathbf{j}}_A + \mathcal{U}_D \hat{\mathbf{i}}_D + \mathcal{V}_D \hat{\mathbf{j}}_D, \quad (3.425)$$

where $\hat{\mathbf{i}}$ and $\hat{\mathbf{j}}$ denote the spherical unit vectors in the longitudinal and latitudinal directions, respectively, at the points indicated by the subscripts, and \mathcal{U} and \mathcal{V} denote the appropriate combinations of terms in 3.424. Note that \mathcal{U}_A^{n+1} is distinct from the \mathcal{U}_A . Following Bates et al. [1990], equations for the individual components are obtained by relating the unit vectors at the departure points $(\hat{\mathbf{i}}_D, \hat{\mathbf{j}}_D)$ to those at the arrival points $(\hat{\mathbf{i}}_A, \hat{\mathbf{j}}_A)$:

$$\hat{\mathbf{i}}_D = \alpha_A^u \hat{\mathbf{i}}_A + \beta_A^u \hat{\mathbf{j}}_A \quad (3.426)$$

$$\hat{\mathbf{j}}_D = \alpha_A^v \hat{\mathbf{i}}_A + \beta_A^v \hat{\mathbf{j}}_A, \quad (3.427)$$

1568 in which the vertical components ($\hat{\mathbf{k}}$) are ignored. The dependence of α 's and β 's on the latitudes
1569 and longitudes of the arrival and departure points is given in the Appendix of Bates et al. [1990].

W&O94 followed Bates et al. [1990] which ignored rotating the vector to remain parallel to the earth's surface during translation. We include that factor by keeping the length of the vector written in terms of $(\hat{\mathbf{i}}_A, \hat{\mathbf{j}}_A)$ the same as the length of the vector written in terms of $(\hat{\mathbf{i}}_D, \hat{\mathbf{j}}_D)$. Thus, (10) of W&O94 becomes

$$\begin{aligned} \mathcal{U}_A^{n+1} &= \mathcal{U}_A + \gamma \alpha_A^u \mathcal{U}_D + \gamma \alpha_A^v \mathcal{V}_D \\ \mathcal{V}_A^{n+1} &= \mathcal{V}_A + \gamma \beta_A^u \mathcal{U}_D + \gamma \beta_A^v \mathcal{V}_D \end{aligned} \quad (3.428)$$

where

$$\gamma = \left[\frac{\mathcal{U}_D^2 + \mathcal{V}_D^2}{(\mathcal{U}_D \alpha_A^u + \mathcal{V}_D \alpha_A^v)^2 + (\mathcal{U}_D \beta_A^u + \mathcal{V}_D \beta_A^v)^2} \right]^{\frac{1}{2}} \quad (3.429)$$

After the momentum equation is written in a common set of unit vectors

$$\mathbf{V}_A^{n+1} + \left(\frac{1+\epsilon}{2} \right) \Delta t \left[f \hat{\mathbf{k}} \times \mathbf{V} \right]_A^{n+1} + \left(\frac{1+\epsilon}{2} \right) \Delta t \nabla [R \mathbf{H}_k^r \cdot \mathbf{T} + R T^r \ln p'_s]_A^{n+1} = \mathcal{R}_{\mathbf{V}}^* \quad (3.430)$$

Drop the $()_A^{n+1}$ from the notation, define

$$\alpha = (1 + \epsilon) \Delta t \Omega \quad (3.431)$$

and transform to vorticity and divergence

$$\zeta + \alpha \sin \varphi \delta + \frac{\alpha}{a} v \cos \varphi = \frac{1}{a \cos \varphi} \left[\frac{\partial \mathcal{R}_v^*}{\partial \lambda} - \frac{\partial}{\partial \varphi} (\mathcal{R}_u^* \cos \varphi) \right] \quad (3.432)$$

$$\begin{aligned} \delta - \alpha \sin \varphi \zeta + \frac{\alpha}{a} u \cos \varphi + \left(\frac{1+\epsilon}{2} \right) \Delta t \nabla^2 [R \mathbf{H}_k^r \cdot \mathbf{T} + R T^r \ln p'_s]_A^{n+1} \\ = \frac{1}{a \cos \varphi} \left[\frac{\partial \mathcal{R}_u^*}{\partial \lambda} + \frac{\partial}{\partial \varphi} (\mathcal{R}_v^* \cos \varphi) \right] \end{aligned} \quad (3.433)$$

Note that

$$u \cos \varphi = \frac{1}{a} \frac{\partial}{\partial \lambda} (\nabla^{-2} \delta) - \frac{\cos \varphi}{a} \frac{\partial}{\partial \varphi} (\nabla^{-2} \zeta) \quad (3.434)$$

$$v \cos \varphi = \frac{1}{a} \frac{\partial}{\partial \lambda} (\nabla^{-2} \zeta) + \frac{\cos \varphi}{a} \frac{\partial}{\partial \varphi} (\nabla^{-2} \delta) \quad (3.435)$$

Then the vorticity and divergence equations become

$$\begin{aligned} \zeta + \alpha \sin \varphi \delta + \frac{\alpha}{a^2} \frac{\partial}{\partial \lambda} (\nabla^{-2} \zeta) + \frac{\alpha \cos \varphi}{a^2} \frac{\partial}{\partial \varphi} (\nabla^{-2} \delta) \\ = \frac{1}{a \cos \varphi} \left[\frac{\partial \mathcal{R}_v^*}{\partial \lambda} - \frac{\partial}{\partial \varphi} (\mathcal{R}_u^* \cos \varphi) \right] = \mathcal{L} \end{aligned} \quad (3.436)$$

$$\begin{aligned} \delta - \alpha \sin \varphi \zeta + \frac{\alpha}{a^2} \frac{\partial}{\partial \lambda} (\nabla^{-2} \delta) - \frac{\alpha \cos \varphi}{a^2} \frac{\partial}{\partial \varphi} (\nabla^{-2} \zeta) + \left(\frac{1 + \epsilon}{2} \right) \Delta t \nabla^2 [R \mathbf{H}_k^r \cdot \mathbf{T} + RT^r \ln p'_s]^{n+1}_A \\ = \frac{1}{a \cos \varphi} \left[\frac{\partial \mathcal{R}_u^*}{\partial \lambda} + \frac{\partial}{\partial \varphi} (\mathcal{R}_v^* \cos \varphi) \right] = \mathcal{M} \end{aligned} \quad (3.437)$$

Transform to spectral space as described in the description of the Eulerian spectral transform dynamical core. Note, from (4.5b) and (4.6) on page 177 of [Machenhauer \[1979\]](#)

$$\mu P_n^m = D_{n+1}^m P_{n+1}^m + D_n^m P_{n-1}^m \quad (3.438)$$

$$D_n^m = \left(\frac{n^2 - m^2}{4n^2 - 1} \right)^{\frac{1}{2}} \quad (3.439)$$

and from (4.5a) on page 177 of [Machenhauer \[1979\]](#)

$$(1 - \mu^2) \frac{\partial}{\partial \mu} P_n^m = -n D_{n+1}^m P_{n+1}^m + (n + 1) D_n^m P_{n-1}^m \quad (3.440)$$

Then the equations for the spectral coefficients at time $n + 1$ at each vertical level are

$$\zeta_n^m \left(1 - \frac{im\alpha}{n(n+1)} \right) + \delta_{n+1}^m \alpha \left(\frac{n}{n+1} \right) D_{n+1}^m + \delta_{n-1}^m \alpha \left(\frac{n+1}{n} \right) D_n^m = \mathcal{L}_n^m \quad (3.441)$$

$$\begin{aligned} \delta_n^m \left(1 - \frac{im\alpha}{n(n+1)} \right) - \zeta_{n+1}^m \alpha \left(\frac{n}{n+1} \right) D_{n+1}^m - \zeta_{n-1}^m \alpha \left(\frac{n+1}{n} \right) D_n^m \\ - \left(\frac{1 + \epsilon}{2} \right) \Delta t \frac{n(n+1)}{a^2} [R \mathbf{H}_k^r \cdot \mathbf{T}_n^m + RT^r \ln p'_{sn}]^m = \mathcal{M}_n^m \end{aligned} \quad (3.442)$$

$$\ln p'_{sn}{}^m = \text{PS}_n^m - \left(\frac{1 + \epsilon}{2} \right) \frac{\Delta t}{p_s^r} (\underline{\Delta p}^r)^T \underline{\delta}_n^m \quad (3.443)$$

$$\underline{T}_n^m = \underline{\text{TS}}_n^m - \left(\frac{1 + \epsilon}{2} \right) \Delta t \mathbf{D}^r \underline{\delta}_n^m \quad (3.444)$$

The underbar denotes a vector over vertical levels. Rewrite the vorticity and divergence equations in terms of vectors over vertical levels.

$$\begin{aligned} \underline{\delta}_n^m \left(1 - \frac{im\alpha}{n(n+1)}\right) - \underline{\zeta}_{n+1}^m \alpha \left(\frac{n}{n+1}\right) - D_{n+1}^m \underline{\zeta}_{n-1}^m \alpha \left(\frac{n+1}{-n}\right) D_n^m \\ - \left(\frac{1+\epsilon}{2}\right) \Delta t \frac{n(n+1)}{a^2} [R\underline{H}^r \underline{T}_n^m + R\underline{T}^r \ln p'_{sn}] = \underline{D}\underline{S}_n^m \end{aligned} \quad (3.445)$$

$$\underline{\zeta}_n^m \left(1 - \frac{im\alpha}{n(n+1)}\right) + \underline{\delta}_{n+1}^m \alpha \left(\frac{n}{n+1}\right) D_{n+1}^m + \underline{\delta}_{n-1}^m \alpha \left(\frac{n+1}{n}\right) D_n^m = \underline{V}\underline{S}_n^m \quad (3.446)$$

Define \underline{h}_n^m by

$$g\underline{h}_n^m = R\underline{H}^r \underline{T}_n^m + R\underline{T}^r \ln p'_{sn} \quad (3.447)$$

and

$$\mathcal{A}_n^m = 1 - \frac{im\alpha}{n(n+1)} \quad (3.448)$$

$$\mathcal{B}_n^{+m} = \alpha \left(\frac{n}{n+1}\right) D_{n+1}^m \quad (3.449)$$

$$\mathcal{B}_n^{-m} = \alpha \left(\frac{n+1}{n}\right) D_n^m \quad (3.450)$$

Then the vorticity and divergence equations are

$$\mathcal{A}_n^m \underline{\zeta}_n^m + \mathcal{B}_n^{+m} \underline{\delta}_{n+1}^m + \mathcal{B}_n^{-m} \underline{\delta}_{n-1}^m = \underline{V}\underline{S}_n^m \quad (3.451)$$

$$\mathcal{A}_n^m \underline{\delta}_n^m - \mathcal{B}_n^{+m} \underline{\zeta}_{n+1}^m - \mathcal{B}_n^{-m} \underline{\zeta}_n^m - \underline{\zeta}_{n-1}^m - \left(\frac{1+\epsilon}{2}\right) \Delta t \frac{n(n+1)}{a^2} g\underline{h}_n^m = \underline{D}\underline{S}_n^m \quad (3.452)$$

1570 Note that these equations are uncoupled in the vertical, i.e. each vertical level involves variables
1571 at that level only. The equation for \underline{h}_n^m however couples all levels.

$$g\underline{h}_n^m = - \left(\frac{1+\epsilon}{2}\right) \Delta t \left[R\underline{H}^r \underline{D}^r + R\underline{T}^r \frac{(\Delta p^r)^T}{p_s^r} \right] \underline{\delta}_n^m + R\underline{H}^r \underline{T}\underline{S}_n^m + R\underline{T}^r \underline{P}\underline{S}_n^m \quad (3.453)$$

Define \underline{C}^r and $\underline{H}\underline{S}_n^m$ so that

$$g\underline{h}_n^m = - \left(\frac{1+\epsilon}{2}\right) \Delta t \underline{C}^r \underline{\delta}_n^m + \underline{H}\underline{S}_n^m \quad (3.454)$$

1572 Let gD_ℓ denote the eigenvalues of \underline{C}^r with corresponding eigenvectors $\underline{\Phi}_\ell$ and $\underline{\Phi}$ is the matrix
1573 with columns $\underline{\Phi}_\ell$

$$\underline{\Phi} = (\underline{\Phi}_1 \underline{\Phi}_2 \dots \underline{\Phi}_L) \quad (3.455)$$

1574 and $g\underline{D}$ the diagonal matrix of corresponding eigenvalues

$$g\mathbf{D} = g \begin{pmatrix} D_1 & 0 & \cdots & 0 \\ 0 & D_2 & \cdots & 0 \\ \vdots & \vdots & \ddots & \vdots \\ 0 & 0 & \cdots & D_L \end{pmatrix} \quad (3.456)$$

$$\mathbf{C}^r \Phi = \Phi g\mathbf{D} \quad (3.457)$$

$$\Phi^{-1} \mathbf{C}^r \Phi = g\mathbf{D} \quad (3.458)$$

Then transform

$$\tilde{\zeta}_n^m = \Phi^{-1} \zeta_n^m, \quad \widetilde{VS}_n^m = \Phi^{-1} VS_n^m \quad (3.459)$$

$$\tilde{\delta}_n^m = \Phi^{-1} \delta_n^m, \quad \widetilde{DS}_n^m = \Phi^{-1} DS_n^m \quad (3.460)$$

$$\tilde{h}_n^m = \Phi^{-1} h_n^m, \quad \widetilde{HS}_n^m = \Phi^{-1} HS_n^m \quad (3.461)$$

$$\mathcal{A}_n^m \tilde{\zeta}_n^m + \mathcal{B}_n^{+m} \tilde{\delta}_{n+1}^m + \mathcal{B}_n^{-m} \tilde{\delta}_{n-1}^m = \widetilde{VS}_n^m \quad (3.462)$$

$$\mathcal{A}_n^m \tilde{\delta}_n^m - \mathcal{B}_n^{+m} \tilde{\zeta}_{n+1}^m \mathcal{B}_n^{-m} - \tilde{\zeta}_{n-1}^m - \left(\frac{1+\epsilon}{2} \right) \Delta t \frac{n(n+1)}{a^2} g \tilde{h}_n^m = \widetilde{DS}_n^m \quad (3.463)$$

$$g \tilde{h}_n^m + \left(\frac{1+\epsilon}{2} \right) \Delta t \Phi^{-1} \mathbf{C}^r \Phi \Phi^{-1} \tilde{\delta}_n^m = \widetilde{HS}_n^m \quad (3.464)$$

$$\tilde{h}_n^m + \left(\frac{1+\epsilon}{2} \right) \Delta t \mathbf{D} \tilde{\delta}_n^m = \frac{1}{g} \widetilde{HS}_n^m \quad (3.465)$$

1575 Since \mathbf{D} is diagonal, all equations are now uncoupled in the vertical.

1576 For each vertical mode, i.e. element of $(\tilde{\zeta})_n^m$, and for each Fourier wavenumber m we have
 1577 a system of equations in n to solve. In following we drop the Fourier index m and the modal
 1578 element index $(\)_\ell$ from the notation.

$$\mathcal{A}_n \tilde{\zeta}_n + \mathcal{B}_n^+ \tilde{\delta}_{n+1} + \mathcal{B}_n^- \tilde{\delta}_{n-1} = \widetilde{VS}_n \quad (3.466)$$

$$\mathcal{A}_n \tilde{\delta}_n - \mathcal{B}_n^+ \tilde{\zeta}_{n+1} \mathcal{B}_n^- \tilde{\zeta}_{n-1} - \left(\frac{1+\epsilon}{2} \right) \Delta t \frac{n(n+1)}{a^2} g \tilde{h}_n = \widetilde{DS}_n \quad (3.467)$$

$$\tilde{h}_n + \left(\frac{1+\epsilon}{2} \right) \Delta t \mathbf{D}_\ell \tilde{\delta}_n = \frac{1}{g} \widetilde{HS}_n \quad (3.468)$$

1579 The modal index $(\)_\ell$ was included in the above equation on \mathbf{D} only as a reminder, but will also
 1580 be dropped in the following.

1581 Substitute $\tilde{\zeta}$ and \tilde{h} into the $\tilde{\delta}$ equation.

$$\begin{aligned} & \left[\mathcal{A}_n + \left(\frac{1+\epsilon}{2} \right)^2 (\Delta t)^2 \frac{n(n+1)}{a^2} g\mathbf{D} + \mathcal{B}_n^+ \mathcal{A}_{n+1}^{-1} \mathcal{B}_{n+1}^- + \mathcal{B}_n^- \mathcal{A}_{n-1}^{-1} \mathcal{B}_{n-1}^+ \right] \tilde{\delta}_n \\ & + (\mathcal{B}_n^+ \mathcal{A}_{n+1}^{-1} \mathcal{B}_{n+1}^+) \tilde{\delta}_{n+2} + (\mathcal{B}_n^- \mathcal{A}_{n-1}^{-1} \mathcal{B}_{n-1}^-) \tilde{\delta}_{n-2} \\ & = \widetilde{DS}_n + \left(\frac{1+\epsilon}{2} \right) \Delta t \frac{n(n+1)}{a^2} \widetilde{HS}_n + \mathcal{B}_n^+ \mathcal{A}_{n+1}^{-1} \widetilde{VS}_{n+1} + \mathcal{B}_n^- \mathcal{A}_{n-1}^{-1} \widetilde{VS}_{n-1} \end{aligned} \quad (3.469)$$

1582 which is just two tri-diagonal systems of equations, one for the even and one for the odd n 's,
 1583 and $m \leq n \leq N$

At the end of the system, the boundary conditions are

$$\begin{aligned} n = m, \quad \mathcal{B}^-_n &= \mathcal{B}^-_m = 0 \\ n = m + 1, \quad \mathcal{B}^-_{n-1} &= \mathcal{B}^-_m = \mathcal{B}^-_{(m+1)-1} = 0 \end{aligned} \quad (3.470)$$

the $\tilde{\delta}_{n-2}$ term is not present, and from the underlying truncation

$$\tilde{\delta}_{N+1}^m = \tilde{\delta}_{N+2}^m = 0 \quad (3.471)$$

For each m and ℓ we have the general systems of equations

$$-A_n \tilde{\delta}_{n+2} + B_n \tilde{\delta}_n - C_n - \tilde{\delta}_{n-2} = D_n, \quad \begin{cases} n = m, m+2, \dots, \begin{cases} N+1 \\ \text{or} \\ N+2 \end{cases} \\ n = m+1, m+3, \dots, \begin{cases} N+1 \\ \text{or} \\ N+2 \end{cases} \end{cases} \quad (3.472)$$

$$C_m = C_{m+1} = 0 \quad (3.473)$$

$$\tilde{\delta}_{N+1} = \tilde{\delta}_{N+2} = 0 \quad (3.474)$$

Assume solutions of the form

$$\tilde{\delta}_n = E_n \tilde{\delta}_{n+2} + F_n \quad (3.475)$$

then

$$E_m = \frac{A_m}{B_m} \quad (3.476)$$

$$F_M = \frac{D_M}{B_M} \quad (3.477)$$

$$E_n = \frac{A_n}{B_n - C_n E_{n-2}}, \quad n = m+2, m+4, \dots, \begin{cases} N-2 \\ \text{or} \\ N-3 \end{cases} \quad (3.478)$$

$$F_n = \frac{D_n + C_n F_{n-2}}{B_n - C_n E_{n-2}}, \quad n = m+2, m+4, \dots, \begin{cases} N \\ \text{or} \\ N-1 \end{cases} \quad (3.479)$$

$$\tilde{\delta}_N = F_N \quad \text{or} \quad \tilde{\delta}_{N-1} = F_{N-1}, \quad (3.480)$$

$$\tilde{\delta}_n = E_n \tilde{\delta}_{n+2} + F_n, \quad \begin{cases} n = N-2, N-4, \dots, \begin{cases} m \\ \text{or} \\ m+1 \end{cases} \\ n = N-3, N-5, \dots, \begin{cases} m+1 \\ \text{or} \\ m \end{cases} \end{cases} \quad (3.481)$$

Divergence in physical space is obtained from the vertical mode coefficients by

$$\underline{\delta}_n^m = \Phi \tilde{\delta}_n^m \quad (3.482)$$

The remaining variables are obtained in physical space by

$$\zeta_n^m \left(1 - \frac{im\alpha}{n(n+1)}\right) = \mathcal{L}_n^m - \delta_{n+1}^m \alpha \left(\frac{n}{n+1}\right) D_{n+1}^m - \delta_{n-1}^m \alpha \left(\frac{n+1}{n}\right) D_n^m \quad (3.483)$$

$$\underline{T}_n^m = \underline{\text{TS}}_n^m - \left(\frac{1+\epsilon}{2}\right) \Delta t \mathbf{D}^r \underline{\delta}_n^m \quad (3.484)$$

$$\ln p'_{sn}{}^m = \text{PS}_n^m - \left(\frac{1+\epsilon}{2}\right) \frac{\Delta t}{p_s^r} (\underline{\Delta p}^r)^T \underline{\delta}_n^m \quad (3.485)$$

3.4.11 Trajectory Calculation

The trajectory calculation follows Hortal [1999] Let \mathbf{R} denote the position vector of the parcel,

$$\frac{d\mathbf{R}}{dt} = \mathbf{V} \quad (3.486)$$

which can be approximated in general by

$$\mathbf{R}_D^n = \mathbf{R}_A^{n+1} - \Delta t \mathbf{V}_M^{n+\frac{1}{2}} \quad (3.487)$$

Hortal's method is based on a Taylor's series expansion

$$\mathbf{R}_A^{n+1} = \mathbf{R}_D^n + \Delta t \left(\frac{d\mathbf{R}}{dt}\right)_D^n + \frac{\Delta t^2}{2} \left(\frac{d^2\mathbf{R}}{dt^2}\right)_D^n + \dots \quad (3.488)$$

or substituting for $d\mathbf{R}/dt$

$$\mathbf{R}_A^{n+1} = \mathbf{R}_D^n + \Delta t \mathbf{V}_D^n + \frac{\Delta t^2}{2} \left(\frac{d\mathbf{V}}{dt}\right)_D^n + \dots \quad (3.489)$$

Approximate

$$\left(\frac{d\mathbf{V}}{dt}\right)_D^n \approx \frac{\mathbf{V}_A^n - \mathbf{V}_D^{n-1}}{\Delta t} \quad (3.490)$$

giving

$$\mathbf{V}_M^{n+\frac{1}{2}} = \frac{1}{2} [(2\mathbf{V}^n - \mathbf{V}^{n-1})_D + \mathbf{V}_A^n] \quad (3.491)$$

for the trajectory equation.

3.4.12 Mass and energy fixers and statistics calculations

The semi-Lagrangian dynamical core applies the same mass and energy fixers and statistical calculations as the Eulerian dynamical core. These are described in sections 3.3.19, 3.3.20, and

3.3.21.

Chapter 4

Model Physics

As stated in chapter 2, the total parameterization package in CAM 5.0 consists of a sequence of components, indicated by

$$P = \{M, R, S, T\}, \quad (4.1)$$

where M denotes (Moist) precipitation processes, R denotes clouds and Radiation, S denotes the Surface model, and T denotes Turbulent mixing. Each of these in turn is subdivided into various components: M includes an optional dry adiabatic adjustment normally applied only in the stratosphere, moist penetrative convection, shallow convection, and large-scale stable condensation; R first calculates the cloud parameterization followed by the radiation parameterization; S provides the surface fluxes obtained from land, ocean and sea ice models, or calculates them based on specified surface conditions such as sea surface temperatures and sea ice distribution. These surface fluxes provide lower flux boundary conditions for the turbulent mixing T which is comprised of the planetary boundary layer parameterization, vertical diffusion, and gravity wave drag.

The updating described in the preceding paragraph of all variable except temperature is straightforward. Temperature, however, is a little more complicated and follows the general procedure described by Boville and Bretherton [2003a] involving dry static energy. The state variable updated after each time-split parameterization component is the dry static energy s_i . Let i be the index in a sequence of I time-split processes. The dry static energy at the end of the i th process is s_i . The dry static energy is updated using the heating rate Q calculated by the i th process:

$$s_i = s_{i-1} + (\Delta t) Q_i(s_{i-1}, T_{i-1}, \Phi_{i-1}, q_{i-1}, \dots) \quad (4.2)$$

In processes not formulated in terms of dry static energy but rather in terms of a temperature tendency, the heating rate is given by $Q_i = (T_i - T_{i-1}) / (C_p \Delta t)$.

The temperature, T_i , and geopotential, Φ_i , are calculated from s_i by inverting the equation for s

$$s = C_p T + gz = C_p T + \Phi \quad (4.3)$$

with the hydrostatic equation

$$\Phi_k = \Phi_s + R \sum_{l=k}^K H_{kl} T_{vl} \quad (4.4)$$

substituted for Φ .

The temperature tendencies for each process are also accumulated over the processes. For processes formulated in terms of dry static energy the temperature tendencies are calculated from the dry static energy tendency. Let $\Delta T_i/\Delta t$ denote the total accumulation at the end of the i th process. Then

$$\frac{\Delta T_i}{\Delta t} = \frac{\Delta T_{i-1}}{\Delta t} + \frac{\Delta s_i}{\Delta t}/C_p \quad (4.5)$$

$$\frac{\Delta s_i}{\Delta t}/C_p = \frac{(s_i - s_{i-1})}{\Delta t}/C_p \quad (4.6)$$

1607 which assumes Φ is unchanged. Note that the inversion of s for T and Φ changes T and Φ .
 1608 This is not included in the $\Delta T_i/\Delta t$ above for processes formulated to give dry static energy
 1609 tendencies.. In processes not formulated in terms of dry static energy but rather in terms of a
 1610 temperature tendency, that tendency is simply accumulated.

After the last parameterization is completed, the dry static energy of the last update is saved. This final column energy is saved and used at the beginning of the next physics calculation following the Finite Volume dynamical update to calculate the global energy fixer associated with the dynamical core. The implication is that the energy inconsistency introduced by sending the T described above to the FV rather than the T returned by inverting the dry static energy is included in the fixer attributed to the dynamics. The accumulated physics temperature tendency is also available after the last parameterization is completed, $\Delta T_I/\Delta t$. An updated temperature is calculated from it by adding it to the temperature at the beginning of the physics.

$$T_I = T_0 + \frac{\Delta T_I}{\Delta t} * \Delta t \quad (4.7)$$

1611 This temperature is converted to virtual potential temperature and passed to the Finite Volume
 1612 dynamical core. The temperature tendency itself is passed to the spectral transform Eulerian
 1613 and semi-Lagrangian dynamical cores. The inconsistency in the use of temperature and dry
 1614 static energy apparent in the description above should be eliminated in future versions of the
 1615 model.

4.1 Conversion to and from dry and wet mixing ratios for trace constituents in the model

There are trade offs in the various options for the representation of trace constituents χ in any general circulation model:

1. When the air mass in a model layer is defined to include the water vapor, it is frequently convenient to represent the quantity of trace constituent as a “moist” mixing ratio χ^m , that is, the mass of tracer per mass of moist air in the layer. The advantage of the representation is that one need only multiply the moist mixing ratio by the moist air mass to determine the tracer air mass. It has the disadvantage of implicitly requiring a change in χ^m whenever the water vapor q changes within the layer, even if the mass of the trace constituent does not.
2. One can also utilize a “dry” mixing ratio χ^d to define the amount of constituent in a volume of air. This variable does not have the implicit dependence on water vapor, but does require that the mass of water vapor be factored out of the air mass itself in order to calculate the mass of tracer in a cell.

NCAR atmospheric models have historically used a combination of dry and moist mixing ratios. Physical parameterizations (including convective transport) have utilized moist mixing ratios. The resolved scale transport performed in the Eulerian (spectral), and semi-Lagrangian dynamics use dry mixing ratios, specifically to prevent oscillations associated with variations in water vapor requiring changes in tracer mixing ratios. The finite volume dynamics module utilizes moist mixing ratios, with an attempt to maintain internal consistency between transport of water vapor and other constituents.

There is no “right” way to resolve the requirements associated with the simultaneous treatment of water vapor, air mass in a layer and tracer mixing ratios. But the historical treatment significantly complicates the interpretation of model simulations, and in the latest version of CAM we have also provided an “alternate” representation. That is, we allow the user to specify whether any given trace constituent is interpreted as a “dry” or “wet” mixing ratio through the specification of an “attribute” to the constituent in the physics state structure. The details of the specification are described in the users manual, but we do identify the interaction between state quantities here.

At the end of the dynamics update to the model state, the surface pressure, specific humidity, and tracer mixing ratios are returned to the model. The physics update then is allowed to update specific humidity and tracer mixing ratios through a sequence of operator splitting updates *but the surface pressure is not allowed to evolve*. Because there is an explicit relationship between the surface pressure and the air mass within each layer we assume that water mass can change within the layer by physical parameterizations *but dry air mass cannot*. We have chosen to define the dry air mass in each layer at the beginning of the physics update as

$$\delta p_{i,k}^d = (1 - q_{i,k}^0) \delta p_{i,k}^m$$

for column i , level k . Note that the specific humidity used is the value defined at the beginning of the physics update. We define the transformation between dry and wet mixing ratios to be

$$\chi_{i,k}^d = (\delta p_{i,k}^d / \delta p_{i,k}^m) \chi_{i,k}^m$$

1646 We note that the various physical parameterizations that operate on tracers on the model
 1647 (convection, turbulent transport, scavenging, chemistry) will require a specification of the air
 1648 mass within each cell as well as the value of the mixing ratio in the cell. We have modified the
 1649 model so that it will use the correct value of δp depending on the attribute of the tracer, that
 1650 is, we use couplets of $(\chi^m, \delta p^m)$ or $(\chi^d, \delta p^d)$ in order to assure that the process conserves mass
 1651 appropriately.

We note further that there are a number of parameterizations (*e.g.* convection, vertical diffusion) that transport species using a continuity equation in a flux form that can be written generically as

$$\frac{\partial \chi}{\partial t} = \frac{\partial F(\chi)}{\partial p} \quad (4.8)$$

1652 where F indicates a flux of χ . For example, in convective transports $F(\chi)$ might correspond
 1653 to $M_u \chi$ where M_u is an updraft mass flux. In principle one should adjust M_u to reflect the fact
 1654 that it may be moving a mass of dry air or a mass of moist air. We assume these differences are
 1655 small, and well below the errors required to produce equation 4.8 in the first place. The same is
 1656 true for the diffusion coefficients involved in turbulent transport. All processes using equations
 1657 of such a form still satisfy a conservation relationship

$$\frac{\partial}{\partial t} \sum_k \chi_k \delta p_k = F_{kbot} - F_{ktop}$$

1658 provided the appropriate δp is used in the summation.

4.2 Moist Turbulence Scheme

Moist turbulence scheme in CAM5 is from Bretherton and Park [2009a] that is a replacement of dry turbulence scheme of Holtslag and Boville [1993b] in CAM3 and CAM4. The role of moist turbulence scheme is to vertically transport heat (dry static energy $s \equiv C_p \cdot T + g \cdot z$), moistures (q_v, q_l, q_i, n_l, n_i where n_l, n_i are number concentrations of cloud liquid droplets and ice crystals), horizontal momentum (u, v), and tracers (mass and number concentrations of aerosol and chemical species) by symmetric turbulences. In the symmetric turbulence, updraft and downdraft have similar vertical velocities, fractional areas, and degrees of saturation.

Compared to the dry PBL (Planetary Boundary Layer) scheme in CAM3 and CAM4, moist turbulence scheme in CAM5 has the following unique characteristics: (1) it is a diagnostic TKE-based (Turbulent Kinetic Energy, e) 1st order K-diffusion scheme with entrainment parameterization but without counter-gradient transport, (2) it simulates *cloud – radiation – turbulence* interactions in an explicit way, which makes it possible to simulate full aerosol indirect effects with direct interactions with cloud macro-microphysics and radiation schemes, (3) using a single set of consistent physical formula, it is operating in any layers above as well as within PBL as long as moist Ri (Richardson number) is larger than a critical value $Ri_c=0.19$. Thanks to explicit simulation of moist turbulences driven by LW (Longwave) radiative cooling at the cloud top, CAM5 does not need a separate formula for stability-based stratus fraction - stratus fraction is computed only using mean relative humidity. It performs much better in the cloud-topped PBL than CAM3/4's dry PBL scheme with similar or superior performance in dry stable and convective PBLs.

In order to illucidate conceptual background behind the CAM5's moist turbulence scheme, let's imagine a single symmetric turbulence being perturbed by a static vertical distance l from its equilibrium height. This symmetric turbulence is assumed to be imbedded in the environment without vertical discontinuity such as sharp inversion. If l is sufficiently smaller than the vertical length scale over which vertical gradient of environmental scalar ($\gamma_{\bar{\phi}} \equiv \partial\bar{\phi}/\partial z$) changes and if turbulent vertical velocity (w') is approximated to \sqrt{e} , we can easily derive that turbulent flux of any conservative scalar (ϕ) becomes $\overline{w'\phi'} = -l \cdot \sqrt{e} \cdot \gamma_{\bar{\phi}}$. In reality, however, atmospheric stability controls turbulent vertical velocity (i.e., w' will be a product of \sqrt{e} and an anisotropic factor of TKE, which is a function of atmospheric stability) and actual vertical perturbation distance of turbulent updraft and downdraft (i.e., turbulent *mixing* length will be a product of a *static* perturbation distance l and a certain atmospheric stability parameter). In addition, during vertical displacement, turbulent properties may be changed due to diabatic forcings or mixing with environment. All of these anomalous effects associated with atmospheric stability, diabatic forcings, and mixing are incorporated into a single stability function, S . As a result, turbulent flux of conservative scalar by symmetric turbulences embedded in the vertically-smooth-transitioning environment becomes

$$\overline{w'\phi'} = -l \cdot \sqrt{e} \cdot S \cdot \gamma_{\bar{\phi}} = -K \cdot \gamma_{\bar{\phi}} \quad (4.9)$$

Thus, computation of turbulent fluxes by symmetric turbulence is reduced to the computations of static turbulence length scale (l), turbulent kinetic energy (e), and stability function (S). The product of these 3 terms is so called eddy diffusivity, $K = l \cdot \sqrt{e} \cdot S$. Due to diabatic adjustment of turbulent horizontal momentum to the environment during vertical displacement,

1685 S for horizontal momentum (S_m) is likely to be smaller than the S for heat and moisture (S_h
 1686). This means that K_ϕ is a function of scalar, ϕ .

If turbulence is embedded in the environment with a sharp vertical transition of stability such as inversion layer at the top of convective PBL, Eqn.(4.9) is inappropriate since turbulent motion will be suppressed in the stable portion of the discontinuous interface. In this case, we use the following entrainment parameterization.

$$\overline{w'\phi'} = -w_e \cdot \Delta\bar{\phi} = -\Delta z_e \cdot w_e \cdot \gamma_{\bar{\phi}} = -K_e \cdot \gamma_{\bar{\phi}} \quad (4.10)$$

1687 where w_e is entrainment rate and Δz_e is the thickness of the entrainment interfacial layer. Above
 1688 entrainment parameterization is applied at the top and base interfaces of Convective Layer (
 1689 CL. See Fig.1) after finishing CL extension-merging procedures that will be explained later. In
 1690 this case, eddy diffusivity is simply a product of Δz_e and w_e , identical for all scalars.

1691 CAM5's moist turbulence scheme consists of 9 main processes: (1) Bulk Moist Richardson
 1692 number, (2) Initial identification of Convective (CL), Stably Turbulent (STL), and Stable (SL
 1693) Layers, (3) Turbulence Length Scale (l), (4) Steady-State TKE (e), (5) Stability Functions
 1694 (S_ϕ), (6) CL Extension-Merging Procedures, (7) Entrainment Rates at the CL Top and Base
 1695 Interfaces (w_e), (8) Implicit Diffusion with Implicit Eddy Diffusivity, and (9) Implicit Surface
 1696 Stress. Since many symmetric turbulences exist with different vertical length and velocity scales
 1697 at any interface, the quantities we are trying to parameterize (l, e, S_ϕ, w_e) should be understood
 1698 as the ensemble of all symmetric turbulences.

1699 4.2.1 Bulk Moist Richardson Number

1700
 1701 Richardson number (Ri) is used to diagnose the existence of turbulences. It is defined
 1702 as the ratio of buoyancy production ($P_b \equiv \overline{w'b'} = (g/\theta_v) \cdot \overline{w'\theta'_v}$) to shear production ($P_s \equiv$
 1703 $-\overline{w'u'} \cdot \partial\bar{u}/\partial z - \overline{w'v'} \cdot \partial\bar{v}/\partial z$) at the model interface. P_b represents energy conversion from mean
 1704 available potential energy (APE) to TKE, while P_s is conversion from mean kinetic energy to
 1705 TKE. If Ri is negative, turbulence is absolutely generated but if it is positive, turbulence can
 1706 be either generated or dissipated depending on the relative magnitude of $|P_b|$ and $|P_s|$.

Special treatment is necessary for saturated turbulences. If turbulence keeps its unsaturated state during vertical diaplacement, θ_v is a conserved quantity and Eqn.(4.9) can be directly used for computing $\overline{w'\theta'_v}$. However, if it is saturated, θ_v decreases within downdraft due to evaporative cooling of cloud droplet, while increases within updraft due to condensation heating of water vapor. The resulting $\overline{w'b'}$ including the effects of condensation and evaporation can be represented by the linear combinations of $\overline{w's'_c}$ and $\overline{w'q'_t}$ where $s_c \equiv C_p \cdot T + g \cdot z - L_v \cdot q_l - L_s \cdot q_i$ is *condensate static energy* and $q_t \equiv q_v + q_l + q_i$ is *total specific humidity*. Both s_c and q_t are conserved during vertical displacement and phase change. If we know saturated fractional area at the model interface (e.g., stratus fraction), we can write

$$\overline{w'b'} = c_h \cdot \overline{w's'_c} + c_q \cdot \overline{w'q'_t} \quad (4.11)$$

$$c_h = c_{h,s} \cdot a + c_{h,u} \cdot (1 - a), \quad c_q = c_{q,s} \cdot a + c_{q,u} \cdot (1 - a) \quad (4.12)$$

where c_h, c_m are buoyancy coefficients for heat (s_c) and moisture (q_t) which are complex functions of temperature and pressure (Schubert et al. [1979], Bretherton and Park [2009a]),

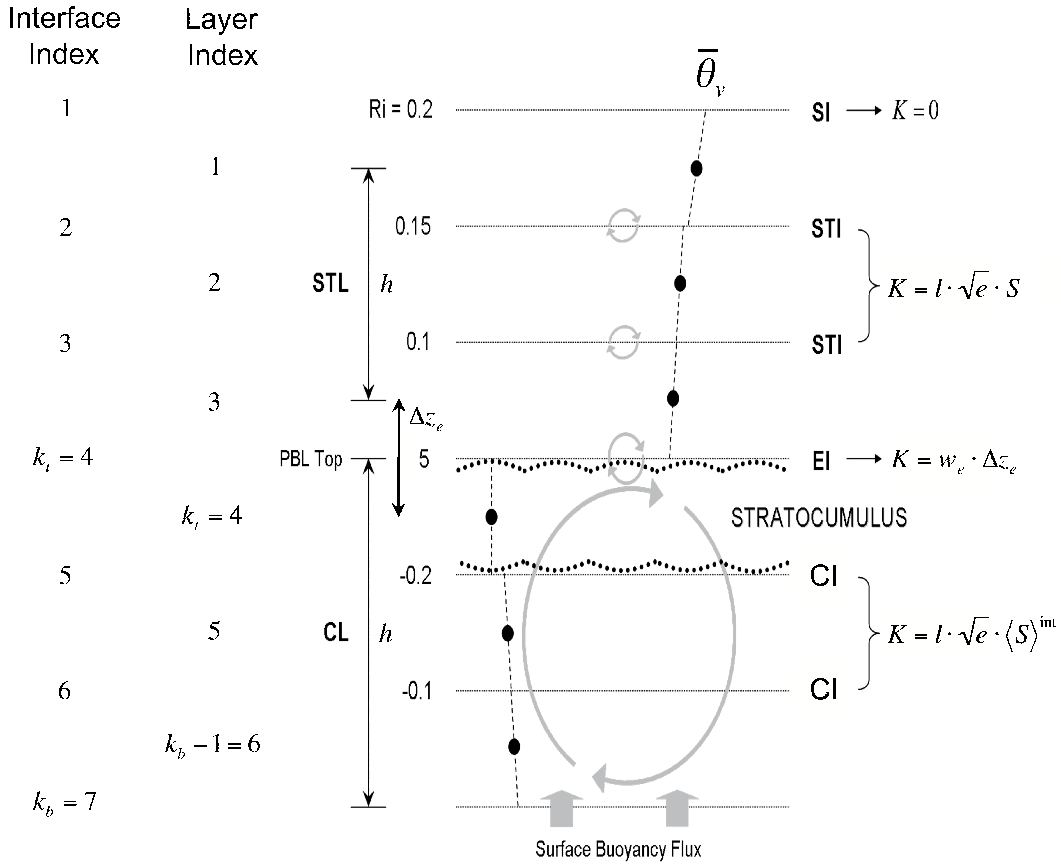


Figure 4.1: The indexing and example of turbulent layer structure in the bottom part of a typical column in the CAM5's moist turbulence scheme. Layer indexing used in CAM5 is shown at left. The bulk Richardson number Ri is used to locate a stable interface (SI) with $Ri > Ri_c$, stably turbulent interfaces (STI) with $0 < Ri < Ri_c$ comprising an STL, and unstable convective interfaces (CI) with $Ri < 0$ comprising a CL core. The CL is extended up to an entrainment interfaces (EI), at which the turbulent eddy diffusivity is computed from an explicitly predicted entrainment rate w_e . In the interior interfaces of the turbulent layers, the turbulent diffusivity K is conventionally using a length scale, diagnosed TKE, and stability function computed from local Ri in an STL and from layer-mean Ri in a CL. Thickness of STL and CL are denoted by h , and the thickness of entrainment interface is denoted by Δz_e . See text for further details.

subscripts s, u denotes saturated and unsaturated turbulences, and a is stratus fraction. Applying Eqn.(4.9) to each term on the R.H.S. of Eqn.(4.11) and assuming $K_h \approx K_m$, Ri can be written solely in terms of grid mean variables as follows.

$$Ri \equiv -\mathcal{C}P_bP_s = \mathcal{C}K_h \cdot N^2K_m \cdot S^2 \approx \mathcal{C}N^2S^2 \quad (4.13)$$

$$N^2 \equiv c_h \cdot \mathcal{C}\partial\bar{s}_c\partial z + c_q \cdot \mathcal{C}\partial\bar{q}_t\partial z, \quad S^2 \equiv (\mathcal{C}\partial\bar{u}\partial z)^2 + (\mathcal{C}\partial\bar{v}\partial z)^2 \quad (4.14)$$

1707 In the code, $c_{h,s}, c_{h,u}, c_{q,s}, c_{q,u}$ and a are given at the layer mid-points. By averaging two
 1708 adjacent layers' mid-point values, these are converted into model interface values. However, if a
 1709 in the adjacent upper layer is smaller than the average value, we took the smaller value, which is
 1710 a necessary procedure to identify stably stratified interface at the top of stratocumulus-capped
 1711 PBL.

1712 4.2.2 Identification of Convective, Stably Turbulent, and Stable Lay- 1713 ers

1714
 1715 Using Ri defined at the interfaces, all model interfaces are grouped into *Convective Interface*
 1716 (CI with $Ri \leq 0$), *Stably Turbulent Interface* (STI with $0 \leq Ri \leq Ri_c$), and *Stable Interface*
 1717 (SI with $Ri > Ri_c$). Here, $Ri_c = 0.19$ is a critical Richardson number and turbulence can exist
 1718 only when $Ri < Ri_c$ (see Fig.4.1). If several CIs are adjacent (or even when one CI exists),
 1719 they form a single *Convective Layer*, CL. If several STIs are adjacent (or even when one STI
 1720 exists), they form a single *Stably Turbulent Layer*, STL. The remaining SIs form *Stable Layer*,
 1721 SL where no turbulence exists. After finishing CL extension-merging which will be explained
 1722 later, the external interfaces surrounding CL will be named as *Entrainment Interface* (EI with
 1723 $Ri > 0$) and the remaining CL interfaces as CL internal interfaces.

1724 In CL and STL, we neglect TKE storage. In STL, we further neglect TKE transport. In CL,
 1725 turbulence can exist from the base to the top interfaces of CL, but in the STL, turbulence can
 1726 exist from the layer mid-point just below the lowest STI to the layer mid-point just above the
 1727 highest STI. This defines turbulent layer thickness, h in a slightly different way between CL and
 1728 STL (see Fig.4.1). After CL extension-merging, a single stability function $\langle S \rangle^{int}$ is assigned to
 1729 all CL internal interfaces.

1730 We use Eqn.(4.9) to compute eddy diffusivity at all interfaces except the top entrainment
 1731 interface of CL where Eqn.(4.10) is used. If CL is elevated from the surface, Eqn.(4.10) is also
 1732 applied to the CL base entrainment interface. If any interface is a double entraining interface
 1733 from above and below, final eddy diffusivity is a simple sum of the two eddy diffusivities obtained
 1734 from above CL and below CL. If surface buoyancy flux is positive (negative), surface is
 1735 considered as a CL internal (external) interface and contributes (does not contribute) to
 1736 the computation of internal energetics of CL.

1737 Several CLs and STLs can exist in a single grid column. The same physical equation set is
 1738 used for all CLs and STLs regardless of whether they are based at the surface or elevated. Our
 1739 moist turbulence scheme, thus, is not a PBL scheme - it is operating in all layers above as well
 1740 as within the PBL. The conventional PBL is simply a surface-based CL or surface-based STL
 1741 in our scheme. PBL top height is defined as the top external interface of surface-based CL. If

1742 STL is based at the surface instead, PBL top height is defined as the layer mid-point height just
 1743 above the STL top interface. We don't impose any minimum value on the PBL height.

1744 We also define additional *Single Radiatively Driven Convective Layer* (SRCL) if any single
 1745 layer satisfies the following 5 conditions: it has (1) grid-mean LWC larger than $10^{-2} [g \cdot kg^{-1}]$ but
 1746 no LWC in the layer just above it, (2) LW radiative cooling, (3) $Ri > Ri_c$ at the top interface,
 1747 (4) positive buoyancy production in the upper half-layer, and (5) it is not within the previously
 1748 identified CLs. Similar to other CLs, entrainment parameterization is applied at the top and
 1749 base interfaces of SRCL. Several SRCLs can exist in a single column.

1750 4.2.3 Turbulent Length Scale

1751

Following Blackadar [1962] and Grenier and Bretherton [2001], turbulent length scale is computed as

$$(Cl)^\alpha = (C1k \cdot z)^\alpha + (C1l_\infty)^\alpha \quad (4.15)$$

$$l_\infty = \eta \cdot h \quad (4.16)$$

$$\eta = \begin{cases} 0.085 & \text{at STI} \\ 0.085 \cdot [2 - \exp(\min(0, \langle Ri \rangle^{int}))] & \text{at CI} \end{cases} \quad (4.17)$$

1752 where $k = 0.4$ is a von Karman constant, l_∞ is asymptotic length scale, h is turbulent layer
 1753 thickness, and $\langle Ri \rangle^{int} = \langle l^2 \cdot N^2 \rangle^{int} / \langle l^2 \cdot S^2 \rangle^{int}$ is the mean Ri averaged over CL internal interfaces
 1754 ($\langle \rangle^{int}$ denotes vertical average over the CL internal interfaces). We chose $\alpha = 3$.

1755 As explained in the previous section and Fig.4.1, h for CL is defined as the depth between
 1756 two external interfaces, while h for STL is defined as the distance between the two outmost
 1757 layers' mid-points. When CL is based at surface but surface buoyancy flux is negative, h is
 1758 defined down to the mid-point of the lowest model layer instead of down to the surface.

1759 Our formulation approximates l to l_∞ except near the ground, where it asymptotes $k \cdot z$ to
 1760 match surface layer similarity theory. As explained before, the actual turbulent *mixing* length
 1761 should be understood as the product of l and stability function S .

1762 4.2.4 Steady-State Turbulent Kinetic Energy

1763

We assume steady-state TKE, that is, at each model interface, $P_b + P_s + T_e - D = 0$ where
 dissipation (D) and TKE transport (T_e) are parameterized as

$$D = [C e^{3/2} b_1 \cdot l] \quad (4.18)$$

$$T_e = [a_e \cdot C \sqrt{e} \cdot (\langle e \rangle - e) l] \quad (4.19)$$

where $b_1 = 5.8$ and $\langle e \rangle$ denotes TKE averaged over the whole CL. In case of STL, $a_e = 0$ (no TKE transport) while in CL, $a_e = 1$. Ideally, $\langle T_e \rangle$ should be zero but Eqn.(4.19) only satisfies this condition approximately. Combining with P_b and P_s , steady-state TKE at any model interface becomes

$$e = b_1 \cdot [Cl \sqrt{e} \cdot (P_b + P_s) + a_e \cdot (\langle e \rangle - e)] \quad (4.20)$$

1764 At the internal interfaces of CL, $P_b = -K_h \cdot N^2$ and $P_s = K_m \cdot S^2$ with $K_h = l \cdot \sqrt{e} \cdot \langle S_h \rangle^{int}$
 1765 and $K_m = l \cdot \sqrt{e} \cdot \langle S_m \rangle^{int}$ where $\langle S_h \rangle^{int}$ and $\langle S_m \rangle^{int}$ are mean stability functions averaged over
 1766 internal interfaces of CL computed by using $\langle Ri \rangle^{int}$ and Eqn.(4.23) and (4.24).

At entrainment interfaces, $P_b = -K_e \cdot N^2 + f_R \cdot c_{h,s} \cdot \Delta \bar{F}_R / \rho$ and $P_s = K_e \cdot S^2$ with $K_e = w_e \cdot \Delta z_e$ where Δz_e is the thickness of entrainment interface. In computing P_b at the entrainment interfaces, N^2 is redefined using the cloud fraction in the half-layer just below (above) the CL top (base) entrainment interface. This redefinition of N^2 is necessary in order to correctly take into account of buoyancy production associated with the evaporative cooling of entrained airs. $\Delta \bar{F}_R$ is grid-mean radiative flux divergence across the CL top layer in unit of $[W \cdot m^{-2}]$ given from the radiation scheme and $0 \leq f_R \leq 1$ is the fraction of radiative flux divergence confined in the thin transition zone near the top entrainment interface of CL among $\Delta \bar{F}_R$. Following Bretherton and Park [2009a], f_R is parameterized as

$$f_R = [\mathcal{C}\tau \cdot (4 + \tau)24 + \tau \cdot (6 + \tau)] \quad (4.21)$$

$$\tau = 156 \cdot \bar{q}_l^{top} \cdot \Delta p^{top} / g \quad (4.22)$$

1767 where τ is the grid-mean cloud optical depth of CL top layer that has grid-mean LWC of \bar{q}_l^{top}
 1768 and a thickness of Δp^{top} . As PBL deepens, cloud can be formed in the layer just above the PBL
 1769 top (i.e., *ambiguous layer*). In this case, most of radiative flux divergence will be confined
 1770 at the top of the ambiguous layer. In order to take into account of this case, we simply added
 1771 $f_R \cdot \Delta \bar{F}_R / \rho$ both in the CL top and ambiguous layers.

1772 At the surface interface, $P_{b,sfc} = c_h \cdot (F_h^* / \rho) + c_m \cdot (F_q^* / \rho)$ where F_h^* is sensible heat flux
 1773 $[J \cdot s^{-1} \cdot m^{-2}]$ and F_q^* is water vapor flux $[kg \cdot s^{-1} \cdot m^{-2}]$ at surface given from the surface flux
 1774 computation scheme to the moist turbulence scheme, and $P_{s,sfc} = u_*^3 / (k \cdot z_0)$ where z_0 is the
 1775 mid-point height of the lowest model layer and u_* is frictional velocity at surface defined as
 1776 $u_*^2 = \sqrt{\tau_x^2 + \tau_y^2} / \rho$ where τ_x, τ_y is surface momentum flux $[kg \cdot m \cdot s^{-1} \cdot s^{-1} \cdot m^{-2}]$. Assuming no
 1777 TKE transport and turbulent length scale $l = k \cdot z_0$, we compute TKE at surface half-layer, e_{sfc}
 1778 using Eqn.(4.20). In order to prevent negative e_s , we impose a minimum positive value on e_{sfc} .

1779 By integrating Eqn.(4.20) over the whole CL with an approximation of $e \approx \langle e \rangle$ at the
 1780 entrainment interfaces, we can compute $\langle e \rangle$ by solving a cubic equation of $\langle e \rangle^{1/2}$. Once $\langle e \rangle$ is
 1781 computed, we can compute e at each internal interfaces of CL using Eqn.(4.20) again.

1782 Our moist turbulence scheme computes characteristic excesses (or standard deviations) of
 1783 turbulent updraft vertical velocity (σ_w), temperature (σ_T), and water vapor (σ_q) within
 1784 PBL or near surface. If PBL is CL (STL), we estimate $\sigma_w = \sqrt{\langle e \rangle}$ ($\sigma_w = u_* / 8.5$) and then
 1785 $\sigma_T = (F_h^* / \rho / C_p) / \sigma_w$ and $\sigma_q = (F_q^* / \rho) / \sigma_w$. These characteristic convective excesses when PBL
 1786 is CL are used to define cumulus source air properties within deep convection scheme.

1787 4.2.5 Stability Functions

1788 Following Galperin et al. [1988], stability functions are parameterized as

$$S_h = [\mathcal{C}\alpha_5 1 + \alpha_3 \cdot G_h] \quad (4.23)$$

$$S_m = [\mathcal{C}\alpha_1 + \alpha_2 \cdot G_h(1 + \alpha_3 \cdot G_h) \cdot (1 + \alpha_4 \cdot G_h)] \quad (4.24)$$

where $\alpha_1 = 0.5562$, $\alpha_2 = -4.3643$, $\alpha_3 = -34.6764$, $\alpha_4 = -6.1272$, $\alpha_5 = 0.6986$ and $G_h \equiv -N^2 \cdot l^2 / (2 \cdot e)$ is a nondimensional stability ratio restricted by $-3.5334 < G_h < 0.0233$. In case of STL, G_h is obtained by combining Eqn.(4.20),(4.23),(4.24) as follows.

$$Ri \cdot (1 + \alpha_3 \cdot G_h) \cdot (1 + \alpha_4 \cdot G_h) = 2 \cdot b_1 \cdot G_h \cdot [Ri \cdot \alpha_5 \cdot (1 + \alpha_4 \cdot G_h) - (\alpha_1 + \alpha_2 \cdot G_h)] \quad (4.25)$$

1789 For $Ri > Ri_c = 0.19$, there is no physically realizable solution G_h and the interface is
 1790 assumed to be non-turbulent. For $Ri < Ri_c$, this polynomial has two real roots, but only
 1791 the larger one is realizable. In case of internal CL, we use the same Eqn.(4.25) but with
 1792 $\langle Ri \rangle^{int} = \langle l^2 \cdot N^2 \rangle^{int} / \langle l^2 \cdot S^2 \rangle^{int}$ to compute $\langle G_h \rangle^{int}$, $\langle S_h \rangle^{int}$ and $\langle S_m \rangle^{int}$. For $\langle Ri \rangle^{int} < -44.5$,
 1793 the allowable upper bound $\langle G_h \rangle^{int} = 0.0233$ is exceeded and stability functions assume their
 1794 maximum values $S_h^{max} = 3.64$ and $S_m^{max} = 2.76$.

1795 4.2.6 CL Extension-Merging Procedure

1796

Several CLs can be identified in a single grid column. A contiguous set of interfaces with negative Ri is initially identified as a CL core. Starting from the lowest CL, each CL is extended first upward as far as possible, then downward as far as possible from the CL core into any adjacent layers of sufficiently weak stable stratification. Any external interface of CL is incorporated into the CL if the following criterion is satisfied.

$$(\Delta z \cdot l^2 \cdot N^2)^E < \left[Cr_{inc1} - r_{inc} \right] \cdot \int_{CL_{int}} l^2 \cdot N^2 \cdot dz \quad (4.26)$$

1797 where superscript E denotes CL external interface being tested for incorporation into CL, Δz
 1798 is the thickness of external interface, and the R.H.S. denotes vertical integration over the CL
 1799 internal interfaces. We chose $r_{inc} = -0.04$ to be consistent with a dry convective boundary layer
 1800 in which the entrainment buoyancy flux is -0.2 of the surface buoyancy flux. Strictly speaking,
 1801 Eqn.(4.26) compares buoyancy production during TKE dissipation time scale by assuming that
 1802 S_h of the external interface being tested for merging is the same as the $\langle S_h \rangle^{int}$. The first
 1803 interface above (below) CL that fails this criterion will be the top (bottom) entrainment
 1804 interface for that CL. No extension-merging is performed for SRCL since SRCL does not have
 1805 internal interfaces.

1806 Above criteria ensures that as long as the initial CL internal core (CL_{int}) has net positive
 1807 buoyancy production, the internal CL after incorporating external interface will also have posi-
 1808 tive buoyancy production. Our incorporation test also guarantees that if any external interface
 1809 is unstably stratified, it will be incorporated. Thus, if we incorporate any of the interior of a
 1810 CL, we will incorporate or merge all of it.

1811 If CL is based at surface and surface buoyancy flux is positive, the contribution of surface
 1812 half-layer is also incorporated into the above integration of CL_{int} . In the surface half-layer, we
 1813 use $G_h = (k \cdot z_0 \cdot P_{b,sfc}) / (2 \cdot S_h \cdot e_{sfc}^{3/2})$ and by combining with Eqn.(4.23), S_h can be computed.
 1814 Finally, $(l^2 \cdot N^2)_{sfc} = -k \cdot z_0 \cdot P_{b,sfc} / (S_h \cdot \sqrt{e_{sfc}})$.

1815 In computing turbulent length scale from Eqns.(4.15)-(4.17) during CL extension-merging
 1816 procedure, we simply assume $\eta = 0.5 \cdot (0.085 + 0.170) = 0.1275$ for all merging and merged

1817 interfaces and turbulent layer thickness h is fixed by the initial value before CL extension-
 1818 merging. After finishing all the extension-merging procedure, $\langle S_h \rangle^{int}$ and $\langle S_m \rangle^{int}$ are computed
 1819 using $\langle Ri \rangle^{int} = \langle l^2 \cdot N^2 \rangle^{int} / \langle l^2 \cdot S^2 \rangle^{int}$ and the updated h .

1820 4.2.7 Entrainment Rates at the CL Top and Base Interfaces

1821

At entrainment interfaces, eddy diffusivity is computed using Eqn.(4.10). Entrainment rate w_e is computed as

$$w_e = A \cdot (\mathcal{C} \bar{s}_{vl} g) \cdot [\mathcal{C} w_*^3 \Delta^E \bar{s}_{vl} \cdot h] \quad (4.27)$$

where $h = z_t - z_b$ is the thickness of CL, $\Delta^E \bar{s}_{vl}$ is the jump of mean liquid virtual static energy $s_{vl} \equiv s_l \cdot (1 + 0.61 \cdot q_t)$ across the entrainment interfaces at the top ($\Delta^E \bar{s}_{vl} = \bar{s}_{vl}(k_t - 1) - \bar{s}_{vl}(k_t)$) and base ($\Delta^E \bar{s}_{vl} = \bar{s}_{vl}(k_b - 1) - \bar{s}_{vl}(k_b)$) of the CL. w_* is convective velocity defined as

$$w_* = \left[2.5 \cdot \int_{z_b}^{z_t} P_b \cdot dz \right]^{1/3} \quad (4.28)$$

and A is an entrainment coefficient defined as

$$A = \begin{cases} 0.2 \cdot [1 + a_2 \cdot 0.8 \cdot (\mathcal{C} L_v \cdot \bar{q}_l^{top} \Delta^E \bar{s}_{vl})] & \text{at CL top} \\ 0.2 & \text{at CL base} \end{cases} \quad (4.29)$$

1822 where a_2 is a tuning parameter being allowed to be changed between 10 and 60, and we chose
 1823 $a_2 = 30$. As PBL deepens, cloud can be formed in the ambiguous layer. In order to fully take
 1824 into account of all possible mixtures between PBL air and free air above inversion, $\Delta^E \bar{s}_{vl}$ in
 1825 *computing* A in Eqn.(4.29) is obtained by using the layer-value just above the ambiguous layer,
 1826 not the value in the ambiguous layer (i.e., $\Delta^E \bar{s}_{vl} = \bar{s}_{vl}(k_t - 2) - \bar{s}_{vl}(k_t)$ in Eqn.(4.29)). In the
 1827 similar context, we take $\bar{q}_l^{top} = \max[\bar{q}_l(k_t), \bar{q}_l(k_t - 1)]$.

1828 Due to the way how the model is structured, we don't have information on K_h when en-
 1829 trainment rate is computed. Thus, in computing $P_b = -K_h \cdot N^2$ at CL internal interfaces for
 1830 entrainment parameterization, we use K_h of previous iteration or previous time step. Since
 1831 we are using a predictor-corrector iteration method, K_h is likely to converge as iteration is
 1832 proceeded.

1833 If eddy diffusivity at the entrainment interface is smaller than the value obtained by assuming
 1834 entrainment interface is STI, the final eddy diffusivity is set to be that of STI.

1835 4.2.8 Implicit Diffusion with Implicit Diffusivity

1836

1837 CAM5 is using process splitting. At each time step, successive parameterizations oper-
 1838 ate on the updated state resulting from the previous parameterizations. The parameter-
 1839 izations in CAM5 are called in the following order at each time step: **deep convection**
 1840 \rightarrow **shallow convection** (computes (1) cumulus fraction and condensate, (2) vertical
 1841 transport of heat, moisture, momentum, and tracers by asymmetric turbulences) \rightarrow
 1842 **stratiform macrophysics** (stratus fractions and stratiform net condensation-deposition rates
 1843) \rightarrow **stratiform microphysics** ((1) activation of cloud liquid droplets and ice crystals, (2)

1844 conversions among cloud liquid droplets, ice crystals, rain, and snow, (3) evaporations of pre-
1845 cipitation and sedimented cloud condensates) → **wet deposition of aerosols** → **radiation**
1846 → **surface fluxes** (upward fluxes of heat, water vapor, momentum, and tracers at surface) →
1847 **aerosol and chemical conversion processes** (conversions among various aerosol and chem-
1848 ical species) → **turbulent diffusion** (vertical transport of heat, moisture, momentum, and
1849 tracers by symmetric turbulences) → **gravity wave drag** → **dry deposition of aerosols** →
1850 **dynamics** (large scale advection of grid mean heat, moisture, momentum, and tracers).

Given a diffusivity profile $K(z)$ and an input state $\bar{\phi}^*(z)$ updated to include all physical and dynamic processes (including explicit deposition of surface fluxes into the lowest model layer except horizontal momentum), our moist turbulence scheme diffuses $\bar{\phi}^*$ using the following implicit backward Euler scheme.

$$[\mathcal{C}\bar{\phi}(t + \Delta t) - \bar{\phi}^* \Delta t] = \mathcal{C}\partial\partial z [K(z) \cdot \mathcal{C}\partial\partial z \bar{\phi}(t + \Delta t)] \quad (4.30)$$

1851 subject to specified upward surface fluxes of horizontal momentums ($\tau_{x,tot} = \tau_x^* - k_{tms} \cdot \bar{u}_{s,i}$,
1852 $\tau_{y,tot} = \tau_y^* - k_{tms} \cdot \bar{v}_{s,i}$ in unit of $[kg \cdot m \cdot s^{-1} \cdot s^{-1} \cdot m^{-2}]$ where the second term on the R.H.S.
1853 is turbulent mountain stress obtained by using updated surface wind $\bar{u}_{s,i}, \bar{v}_{s,i}$ after i^{th} iteration
1854), sensible heat (F_h^* in unit of $[J \cdot s^{-1} \cdot m^{-2}]$), and water vapor (F_q^* in unit of $[kg \cdot s^{-1} \cdot m^{-2}]$
1855) where superscript * denotes the input value given to the moist turbulence scheme. The eddy
1856 diffusivity profile $K(z)$ may be computed using the input state variable $\bar{\phi}^*$. However, when a
1857 long time step $\Delta t = 1800$ [s] is used as in CAM5, this is not a desirable approach since the
1858 physical processes proceeding turbulent diffusion scheme (e.g., radiation) can dramatically
1859 destabilize the input profile $\bar{\phi}^*(z)$, resulting in unreasonable $K(z)$. To address this problem, we
1860 use an iterative predictor-corrector approach to recalculate eddy diffusivities based on an better
1861 approximation to the post-diffusion state.

Let's assume that K_i is diffusivity profile obtained from $\bar{\phi}_i$. When $i = 0$, $\bar{\phi}_0 \equiv \bar{\phi}^*$ and $K_0 \equiv K^*$. Using $\bar{\phi}_0$, we compute K_0 and obtain the first diffused profile $\bar{\phi}_1$ by solving Eqn.(4.30) applied to the initial state $\bar{\phi}^*$. Using $\bar{\phi}_1$, we compute K_1 and the predictor-corrector averaged $K_{0:1} \equiv \lambda \cdot K_1 + (1 - \lambda) \cdot K_0$. Using this $K_{0:1}$, we diffuse the *input state* $\bar{\phi}^*$ again and obtain the second diffused profile $\bar{\phi}_2$ from which K_2 and $K_{0:2} \equiv \lambda \cdot K_2 + (1 - \lambda) \cdot K_{0:1}$ are computed. By repeating this process, the predictor-corrector averaged K profile after N iteration becomes

$$K_{0:N} \equiv \lambda \cdot K_N + (1 - \lambda) \cdot K_{0:N-1} \quad (4.31)$$

$$K_{0:0} \equiv K^* \quad (4.32)$$

1862 We chose $N = 4$ and $\lambda = 0.5$ to compute the final eddy diffusivity $K = K_{0:N}$ from the
1863 eddy diffusion scheme. During individual iterative diffusion processes of $\bar{\phi}^*$ by $K = K_{0:n}$ ($1 \leq$
1864 $n \leq N$), we diffused conservative scalars $\bar{\phi}^* = \bar{s}_l^*, \bar{q}_t^*, \bar{u}^*, \bar{v}^*$ and reconstructed the diffused non-
1865 conservative scalars $\bar{T}, \bar{q}_v, \bar{q}_l, \bar{q}_i$ profiles by assuming that (1) \bar{q}_i is not diffused and (2) the layer
1866 has homogeneous distribution of cloud condensate across the grid at saturation equilibrium
1867 state.

1868 Since the initial profiles $\bar{\phi}^*$ are continuously updated within each iteration, we should also
1869 update surface fluxes ($\tau_x^*, \tau_y^*, F_h^*, F_q^*$) and the profiles of stratus fraction and radiative heating
1870 rate within each iteration. However, this will hugely increase computation time and make the
1871 CAM5 structure much more complex. Thus, we simply ignore the variations of surface fluxes,
1872 stratus fraction and radiative heating rate during iteration. This simplification can inevitably

1873 cause K_i ($i \geq 1$) to be computed on the $\bar{\phi}_i$ that has inconsistency among various state variables.
 1874 Finally, because of the flipping of layer structures and corresponding eddy diffusivities between
 1875 the iterations, our predictor-corrector method may not produce fully convergent K regardless of
 1876 the iteration number. By choosing $\lambda = 0.5$, however, we address this issue to our best. Once the
 1877 final K is obtained from Eqn.(4.31), we diffuse the input grid mean scalars ($\bar{s}, \bar{q}_v, \bar{q}_l, \bar{q}_i, \bar{n}_i, \bar{u}, \bar{v}$
 1878).

1879 Vertical transport of horizontal momentum by symmetric turbulence conserves column-mean
 1880 horizontal momentum. However, it will change column-mean kinetic energy (KE) of the mean
 1881 wind. In reality, this KE change will be converted into TKE and eventually internal heat energy
 1882 (or potential energy, PE). In CAM5, however, we don't store TKE between time steps because
 1883 of steady-state TKE assumption and yet require conservation of column-mean total energy,
 1884 PE+KE. In order to conserve total energy in each column, we computed KE dissipation heating
 1885 rate in each layer following [Boville and Bretherton \[2003b\]](#) after diffusing horizontal momentum,
 1886 and explicitly added KE dissipation heating into \bar{s} before diffusing \bar{s} .

1887 Since air parcel temperature changes during vertical displacement due to adiabatic
 1888 compression-expansion, moist turbulence scheme should also handle associated condensation-
 1889 evaporation of cloud droplets during vertical transport. The same should be true for convection
 1890 and large-scale advection schemes. However, this evaporation-condensation associated with ver-
 1891 tical diapycnal displacement of air parcels will be treated in the following stratiform cloud macrophysics.
 1892 Thus, diffusing non-conservative scalars with a phase change ($\bar{s}, \bar{q}_v, \bar{q}_l, \bar{q}_i, \bar{n}_l, \bar{n}_i$) is not a problem
 1893 if we admit that reasonable profiles of cloud condensates can be restored only after stratiform
 1894 macro-microphysics.

1895 When turbulence transports non-saturated air into the overlying saturated air, new cloud
 1896 droplets can be formed without the change of cloud condensate mass (so called, cloud droplet
 1897 activation). In order to handle adiabatic turbulent vertical transport and concurrent diabatic
 1898 sources of cloud droplet number in a consistent way, turbulent diffusions of \bar{n}_l , aerosol mass and
 1899 numbers are separately treated by the cloud droplet activation routine within the stratiform
 1900 microphysics.

1901 4.2.9 Implicit Surface Stress

1902
 1903 In CAM5, surface fluxes of various scalars ($s, q_v, q_l, q_i, n_l, n_i$ and tracers) are explicitly
 1904 deposited into the lowest model layer (this forms the input $\bar{\phi}^*$ to Eqn.(4.30)) and then implicit
 1905 vertical diffusion is performed using Eqn.(4.30). In case of surface momentum fluxes (τ_x^*, τ_y^*
 1906), however, such explicit adding can flip the direction of the lowest model layer wind (\bar{u}_s^*, \bar{v}_s^*
 1907). This is not a physically realizable situation since as wind speed decreases by surface drag,
 1908 surface drag itself decreases too, preventing flipping of wind in nature. This flipping of the
 1909 wind in the model can be a source of numerical instability especially when the lowest model
 1910 layer is thin. Thus, τ_x^*, τ_y^* should be added into the lowest model layer in an implicit way.
 1911 This implicit adding, however, will cause discrepancy between the horizontal momentum that
 1912 the Earth surface lost (which are explicit surface momentum flux τ_x^*, τ_y^* given to the turbulent
 1913 diffusion scheme) and the momentum that the atmosphere receives (which are implicit surface
 1914 momentum flux). To conserve horizontal momentum of the whole coupled system, they should
 1915 be identical. In order to address both the numerical stability and momentum conservation

1916 issues, we partitioned the residual surface momentum flux (= explicit surface momentum flux
 1917 - implicit surface momentum flux) over a certain time interval, e.g., 2 hr. This process is called
 1918 implicit surface stress being detailed below.

First, in order to compute implicit surface stress, we compute total surface drag coefficient (k_{tot}) by summing the *normal* drag coefficient (k_{nor}) obtained from the lowest model layer wind and the *turbulent mountain stress* drag coefficient (k_{tms}) triggered by sub-grid distribution of surface topography. This k_{tms} is computed by separate turbulent mountain stress module.

$$k_{nor} = \max \left[\mathcal{C} \sqrt{(\tau_x^*)^2 + (\tau_y^*)^2} \max(\sqrt{(\bar{u}_s^*)^2 + (\bar{v}_s^*)^2}, 1), 10^{-4} \right] \quad (4.33)$$

$$k_{tot} = k_{nor} + k_{tms} \quad (4.34)$$

Second, a certain fraction of residual stress accumulated upto the current time step from the first time step is added into the lowest model layer. This changes the wind in the lowest model layer.

$$\bar{u}_s^+(t) = \bar{u}_s^*(t) + \tau_{x,res}(t) \cdot \Lambda (\mathcal{C}g\Delta p) \cdot \Delta t, \quad \bar{v}_s^+(t) = \bar{v}_s^*(t) + \tau_{y,res}(t) \cdot \Lambda (\mathcal{C}g\Delta p) \cdot \Delta t, \quad (4.35)$$

$$\Lambda = [\mathcal{C}\Delta t\Delta t_{res}], \quad \Delta t \leq \Delta t_{res} = 7200 [sec] \quad (4.36)$$

1919 where $\tau_{x,res}(t), \tau_{y,res}(t)$ are residual stress accumulated upto the current time step from the first
 1920 time step, and Δt_{res} is a time interval over which residual stress is deposited into the atmosphere.
 1921 With $K(z), k_{tot}$, and given input wind profiles of $\bar{u}_s^*(t)$ and $\bar{v}_s^*(t)$ but with the lowest model layer
 1922 winds of $\bar{u}_s^+(t)$ and $\bar{v}_s^+(t)$ instead of $\bar{u}_s^*(t)$ and $\bar{v}_s^*(t)$, we can solve Eqn.(4.30) to obtain implicitly
 1923 time-marched wind profiles, $\bar{u}(t + \Delta t)$ and $\bar{v}(t + \Delta t)$.

Finally, the net residual stress accumulated upto the end of current time step which will be used at the next time step becomes

$$\tau_{x,res}(t + \Delta t) = \tau_{x,res}(t) \cdot (1 - \Lambda) + \tau_x^* + k_{nor} \cdot \bar{u}_s(t + \Delta t) \quad (4.37)$$

$$\tau_{y,res}(t + \Delta t) = \tau_{y,res}(t) \cdot (1 - \Lambda) + \tau_y^* + k_{nor} \cdot \bar{v}_s(t + \Delta t) \quad (4.38)$$

1924 where $\bar{u}_s(t + \Delta t)$ and $\bar{v}_s(t + \Delta t)$ are implicitly marched winds of the lowest model layer at
 1925 the end of turbulent diffusion scheme at the current time step. At the first time step, it is
 1926 $\tau_{x,res}(t) = \tau_{y,res}(t) = 0$. Our formulation assumes that turbulent mountain stress is fully implic-
 1927 itly added into the atmosphere without generating any residual stress. This assumption causes
 1928 no conservation problem since turbulent mountain stress is used only within the atmospheric
 1929 model not in the ocean, sea ice, and land models.

1930 One complexity arises because $K(z)$ is iteratively computed at each time step. We assume
 1931 that all of $\tau_{x,res}(t), k_{tms}$ and k_{nor} are not changed within the iteration loop : k_{tms} and k_{nor}
 1932 are obtained from the initial wind profile $\bar{u}_s^*(t), \bar{v}_s^*(t)$ given to the moist turbulence scheme. In
 1933 computing eddy diffusivity K_i within each iteration loop, however, we used $\tau_{x,tot} = \tau_x^* - k_{tms} \cdot$
 1934 $\bar{u}_{s,i}(t), \tau_{y,tot} = \tau_y^* - k_{tms} \cdot \bar{v}_{s,i}(t)$ where $\bar{u}_{s,i}(t), \bar{v}_{s,i}(t)$ are iteratively updated wind in the lowest
 1935 model layer after i^{th} iteration at the current time step. Here, we included turbulent mountain
 1936 stress in computing eddy diffusivity since it is a source of shear production and TKE in the
 1937 lowest model layer, too.

4.3 Shallow Convection Scheme

Shallow convection scheme in CAM5 is from [Park and Bretherton \[2009\]](#) that is a replacement of [Hack \[1994b\]](#) shallow convection scheme in CAM3 and CAM4. Similar to its precedents, CAM5 performs shallow convection scheme just after deep convection scheme. In general, distinctions between deep and shallow convections are made by the differences in cloud top height, the existence of convective precipitation and convective downdraft. While named as shallow convection, CAM5's shallow convection scheme does not have any limitation on its cloud top height and convective precipitation. However, because the proceeding deep convection scheme consumes most of Convective Available Potential Energy (CAPE) and stabilizes the atmosphere, cloud top height simulated by shallow convection scheme is naturally limited in the tropical regions. In contrast to deep convection scheme, shallow convection scheme does not have a separate formulation for convective downdraft, but have an explicit parameterization of penetrative entrainment in the overshooting zone near cumulus top. Future implementation of convective downdraft as well as refinements of other aspects (e.g., updraft mixing rate and cloud microphysics) can make shallow convection scheme work for deep convective case, too.

The role of shallow convection scheme is to vertically transport heat, moisture, momentum, and tracers by asymmetric turbulences. On the other hands, vertical transport by symmetric turbulences are performed by separate moist turbulence scheme. CAM5's shallow convection scheme is carefully designed to optimally operate with CAM5's moist turbulence scheme without missing or double-counting processes. Similar to the other convection schemes, CAM5 shallow convection scheme assumes (1) steady state convective updraft plume, and (2) small updraft fractional area, so that compensating subsidence entirely exists within the same grid box as convective updraft. One of the unique aspects of CAM5 shallow convection scheme is its ability to compute convective updraft vertical velocity and updraft fractional area by using updraft vertical momentum equation. Computation of updraft vertical velocity enables to compute more refined fractional entrainment-detrainment rates, cloud top height, and penetrative entrainment. While not implemented in the current CAM5's shallow convection scheme, updraft vertical velocity will make it possible to compute activated fraction of aerosol masses and numbers at the cumulus base, more elegant cumulus microphysics, and aerosol-cumulus interactions.

CAM5's shallow convection scheme consists of 8 main processes: (1) Reconstruction of mean profiles and cloud condensate partitioning, (2) Computation of source air properties of a single ensemble-mean updraft plume at the PBL (Planetary Boundary Layer) top, (3) Cloud base mass flux and updraft vertical velocity closures using Convective Inhibition (CIN) and TKE (Turbulent Kinetic Energy), (4) Vertical evolution of a single entraining-detraining buoyancy sorting plume from the PBL top to the cumulus top, (5) Penetrative entrainment in the overshooting zone near cumulus top, (6) Computation of convective fluxes within the PBL, (7) Computation of grid-mean tendencies of conservative scalars, and (8) Computation of grid-mean tendencies of non-conservative scalars. The following sections describe each of these processes in detail.

4.3.1 Reconstruction of Mean Profiles and Cloud Condensate Partitioning

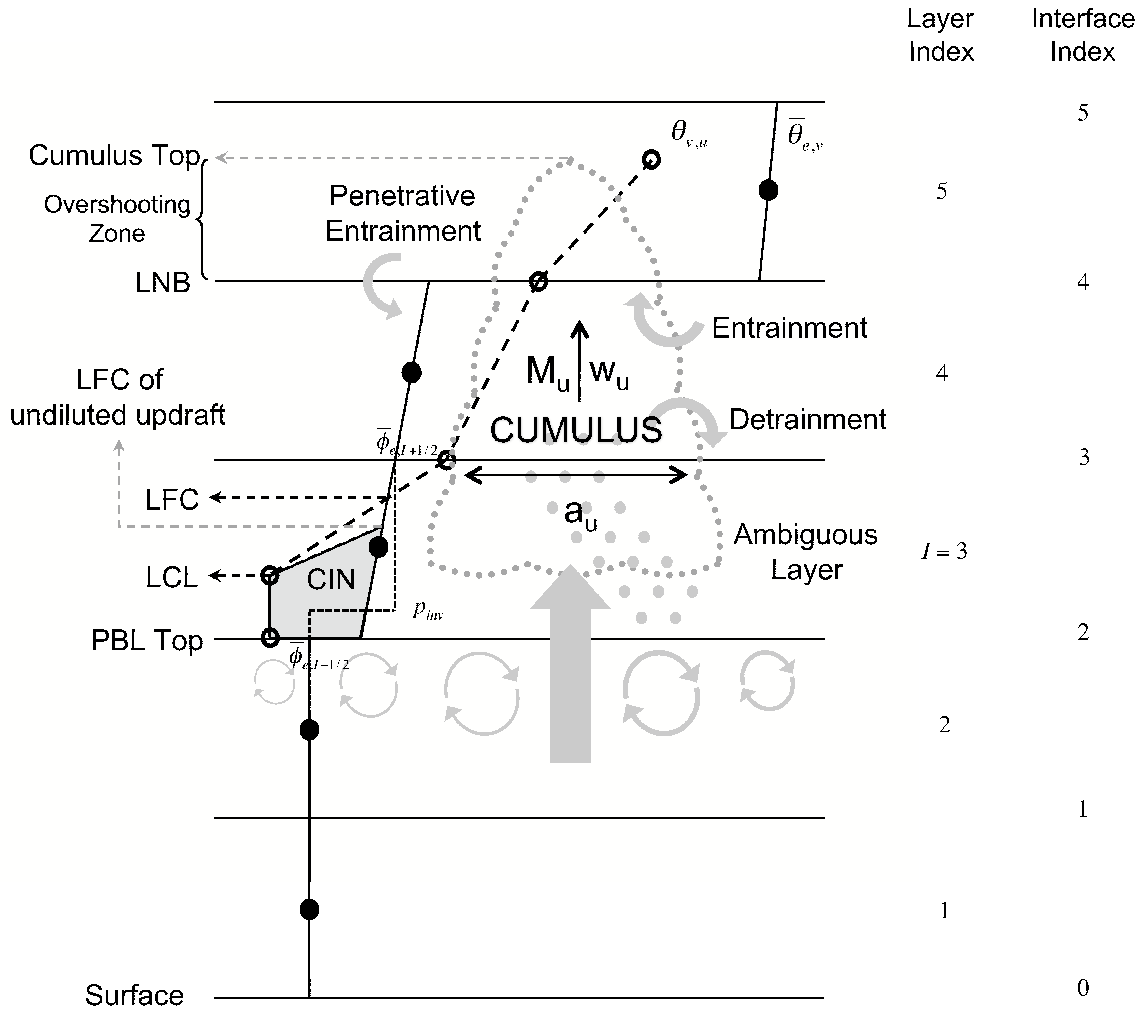


Figure 4.2: Schematic structure of shallow cumulus scheme describing vertical evolution of a bulk cumulus updraft and its interaction with environment and the subcloud layer. Black dots denote environmental mean virtual potential temperature $\bar{\theta}_{e,v}$, from which a $\bar{\theta}_{e,v}$ profile (solid line) is reconstructed. The horizontal solid lines are flux interfaces, where the updraft virtual potential temperature $\theta_{v,u}$ (open circles) is computed, from which a cumulus updraft $\theta_{v,u}$ profile (dashed) is reconstructed. The model layer and interface indices used in CAM5 are denoted on the right axis. The layer index I indicates the ambiguous layer, and p_{inv} is the reconstructed PBL capping inversion within this layer. Environmental conservative variables reconstructed just above and below the ambiguous layer are denoted by $\bar{\phi}_{e,I+1/2}$ and $\bar{\phi}_{e,I-1/2}$, respectively. See the text for details.

1980 The input state variables to shallow convection scheme are environmental mean
 1981 $\bar{q}_v, \bar{q}_l, \bar{q}_i, \bar{T}, \bar{u}, \bar{v}$, and mass and number of aerosols, $\bar{\zeta}$. While stratus condensate should reside
 1982 only within cloudy portion, shallow convection scheme assumes uniform distribution of stratus
 1983 condensate across the grid except when evaporation of precipitation is computed. From the
 1984 given inputs, we compute *condensate potential temperature* $\bar{\theta}_c = \bar{\theta} - (L_v/C_p/\pi) \cdot \bar{q}_l - (L_s/C_p/\pi) \cdot \bar{q}_i$
 1985 and *total specific humidity* $\bar{q}_t = \bar{q}_v + \bar{q}_l + \bar{q}_i$. With respect to vertical displacement involving
 1986 phase change but without precipitation formation and evaporation of precipitation, θ_c is nearly
 1987 conserved and q_t is completely conserved.

1988 Instead of assuming zero slope, we assign a certain slope of $\bar{\theta}_c$ and \bar{q}_t within each layer. In
 1989 each layer, upward [$(\bar{\theta}_c(k+1) - \bar{\theta}_c(k))/(p(k+1) - p(k))$] and downward [$(\bar{\theta}_c(k) - \bar{\theta}_c(k-1))/(p(k) - p(k-1))$]
 1990 slopes are computed. If they have different signs or either of two has zero
 1991 slope, internal slope is set to zero. If they have the same sign, we take the one with minimum
 1992 absolute slope. In the lowest model layer, internal slope is set to the upward slope, and in the
 1993 top model layer, it is set to the slope of the layer below. This profile reconstruction is performed
 1994 indepently to each of $\bar{\theta}_c, \bar{q}_t, \bar{u}, \bar{v}$ and $\bar{\zeta}$. The reconstructed profiles conserve mean quantity in
 1995 each layer but have discontinuity across the model interfaces. Similar profile reconstruction is
 1996 performed in the moist turbulence scheme.

1997 From the reconstructed $\bar{\theta}_c$ and \bar{q}_t , we compute *virtual potential temperature* $\bar{\theta}_v = \bar{\theta} \cdot (1 +$
 1998 $0.61 \cdot \bar{q}_v - \bar{q}_l - \bar{q}_i)$ at just below and above each model interface by assuming that ice fraction
 1999 among cloud condensate is a raming function of temperature between 248 K and 268 K, and
 2000 saturation specific humidity is a weighting average of two values defined over water and ice.
 2001 The same temperature partitioning is applied to cloud condensate within convective updraft.
 2002 In case of detrained convective condensate, we use 238.15 K and 268.15 K as the two end
 2003 points of temperature in the cloud condensate ramping function. For computation of radiative
 2004 properties of cumulus updraft, we repartition in-cumulus condensate into liquid and ice following
 2005 the partitioning of pre-existing of stratus clouds.

2006 4.3.2 Source Air Properties of Convective Updraft

2007 At the PBL top, we define source air properties of a single updraft plume. In CAM5, PBL
 top is located at the top most interface of convective boundary layer, which is diagnosed by
 the separate moist turbulence scheme. Here, we define $\hat{q}_{t,src}, \hat{\theta}_{c,src}, \hat{u}_{src}, \hat{v}_{src}, \hat{\zeta}_{src}$ where the
hat denotes convective updraft properties and the subscript *src* denotes the values of convective
 updraft source air at the PBL top interface. $\hat{q}_{t,src}$ is defined as the environmental-mean value in
 the lowest model layer (In the below equations, (1) denotes the lowest model layer value). $\hat{\zeta}_{src}$
 is defined in the same way as $\hat{q}_{t,src}$. We first define condensate virtual potential temperature of
 source air ($\theta_{vc} = \theta_c \cdot (1 + 0.61 \cdot q_t)$) using the profile-reconstructed minimum value within the
 PBL ($\bar{\theta}_{vc,min}$), and from $\hat{q}_{t,src}$ and $\bar{\theta}_{vc,min}$, $\hat{\theta}_{c,src}$ is computed. \hat{u}_{src} and \hat{v}_{src} are defined as the
 profile-reconstructed values just below the PBL top interface.

$$\hat{q}_{t,src} = \bar{q}_t(1) \quad (4.39)$$

$$\hat{\theta}_{c,src} = \left[\mathcal{C} \bar{\theta}_{vc,min} (1 + 0.61 \cdot \hat{q}_{t,src}) \right] \quad (4.40)$$

$$\hat{u}_{src} = \bar{u}_{top} \quad (4.41)$$

$$\hat{v}_{src} = \bar{v}_{top} \quad (4.42)$$

$$\hat{\zeta}_{src} = \bar{\zeta}(1) \quad (4.43)$$

2008 ζ includes the mass of individual aerosol species and aerosol numbers in each mode (Aitken,
 2009 Accumulation, Coarse). ζ also contains the numbers of cloud liquid droplets and ice crystals.
 2010 Since CAM5's cumulus microphysics is the first moment scheme and the size of in-cumulus
 2011 and detrained shallow convective condensate are independently specified, vertical convective
 2012 transport of cloud droplet numbers do not influence climate simulation in the current CAM5.
 2013 But we retain this functionality to transport cloud droplet number for future development of
 2014 higher order cumulus microphysics and aerosol-cumulus interactions.

2015 The only unknown source air properties at this stage are updraft mass flux (\hat{M}_{src}) and
 2016 updraft vertical velocity (\hat{w}_{src}) which are computed in the next section. \hat{M}_{src} and \hat{w}_{src} allows
 2017 us to compute updraft fractional area, A_{src} .

2018 4.3.3 Closures at the Cloud Base

2019

We assume that turbulent updraft vertical velocity w at the PBL top follows a symmetric Gaussian distribution. The width of the distribution σ_w is determined by the mean TKE within the PBL (\bar{e}_{PBL}) given from the moist turbulence scheme, $\sigma_w = \sqrt{k \cdot \bar{e}_{PBL} + e_m}$ where $k = 1$ and $e_m = 5 \cdot 10^{-4} [m^2 \cdot s^{-2}]$ is a background minimum TKE. $P(w)$, PDF of w at the PBL top is given as

$$P(w) = C1\sigma_w \cdot \sqrt{2 \cdot \pi} \cdot \exp \left[-Cw^2 2 \cdot \sigma_w^2 \right] \quad (4.44)$$

2020 Among these, only strong updrafts enough to reach to their undiluted Level of Free Convec-
 2021 tion (LFC) are assumed to form *a single ensemble mean convective updraft* being simulated
 2022 by shallow convection scheme. The effects of remaining weak updrafts that eventually sink back
 2023 to the PBL by negative buoyancy are implicitly simulated by the separate moist turbulence
 2024 scheme through entrainment parameterization. We define CIN as the strength of potential en-
 2025 ergy barrier of the undiluted ensemble-mean plume from the PBL top to the undiluted LFC
 2026 (see Fig.4.2). Then, the minimum vertical velocity of the deflatable convective updrafts, or
 2027 critical vertical velocity becomes $w_c = \sqrt{2 \cdot a \cdot CIN}$ where buoyancy coefficient $a = 1$. In order
 2028 to reduce the on-and-off behavior of convection between the long model time step $\Delta t = 1800 [s]$,
 2029 CIN is computed using thermodynamic profiles at the end of convection time step (so called,
 2030 implicit CIN) as described in [Park and Bretherton \[2009\]](#).

Then, mass flux (\hat{M}_{src}), updraft fractional area (\hat{A}_{src}), and area-weighted updraft vertical velocity (\hat{w}_{src}) of a single ensemble-mean convective updraft at the PBL top can be computed as follows by integrating all deflatable plumes with $w > w_c$.

$$\hat{M}_{src} = \rho \cdot \int_{w_c}^{\infty} w \cdot P(w) \cdot dw = \rho \cdot C\sigma_w \sqrt{2 \cdot \pi} \cdot \exp \left[-Ca \cdot CIN\sigma_w^2 \right] \quad (4.45)$$

$$\hat{A}_{src} = \int_{w_c}^{\infty} P(w) \cdot dw = C12 \cdot erf \left[C\sqrt{a \cdot CIN}\sigma_w \right] \quad (4.46)$$

$$\hat{w}_{src} = \left[\mathcal{C} \int_{w_c}^{\infty} w \cdot P(w) \cdot dw \int_{w_c}^{\infty} P(w) \cdot dw \right] = \left[\mathcal{C} \hat{M}_{src} \rho \cdot \hat{A}_{src} \right] \quad (4.47)$$

2031 Here, we impose additional constraints that (1) \hat{M}_{src} should be smaller than 0.9 of the mass
 2032 in the layer just below the PBL top, that is, $\hat{M}_{src} < 0.9 \cdot \Delta p(I-1)/g/\Delta t$ where $\Delta p(I-1)$ is the
 2033 pressure thickness of the layer just below the PBL top, and (2) \hat{A}_{src} and \hat{A}_{LCL} (updraft core
 2034 fractional area at the LCL) are smaller than 0.1, assuming no lateral mixing from the PBL top
 2035 to the LCL. From the constrained \hat{M}_{src} and \hat{A}_{src} , we compute the constrained \hat{w}_{src} . As of this,
 2036 we finished the convective closure at the PBL top.

2037 4.3.4 Vertical Evolution of A Single Updraft Plume

2038 Assuming steady-state updraft plume (or updraft plume with very small fractional area),
 vertical variations of updraft mass flux and conservative scalars can be written as

$$\mathcal{C}1\hat{M} \cdot \mathcal{C}\partial\hat{M}\partial p = \epsilon - \delta \quad (4.48)$$

$$\mathcal{C}\partial\hat{\phi}\partial p = -\epsilon \cdot (\hat{\phi} - \bar{\phi}_e) + \hat{S}_\phi + \hat{C}_\phi \quad (4.49)$$

2039 where pressure coordinate p is defined increasing upward, (ϵ, δ) are fractional entrainment and
 2040 detrainment rates, respectively, $\phi = q_t, \theta_c, u, v, \zeta$ is scalar being transported, $\hat{\phi}$ is updraft value,
 2041 $\bar{\phi}_e$ is environmental mean value (note that this is different from the grid-mean $\bar{\phi} = \hat{A} \cdot \hat{\phi} + (1 -$
 2042 $\hat{A}) \cdot \bar{\phi}_e$ unless $\hat{A} = 0$), \hat{S}_ϕ is net diabatic source within cumulus updraft, and \hat{C}_ϕ is a direct
 2043 conversion term from environmental to updraft without lateral mass exchange. In case of steady
 2044 state updraft plume, \hat{S}_ϕ changes the column mean total energy, while \hat{C}_ϕ conserves the column
 2045 mean total energy. \hat{S}_ϕ and \hat{C}_ϕ for each component are parameterized as follows. Otherwise,
 2046 they are set to zero.

$$\hat{S}_{q_t} \cdot \Delta p = -max(\hat{q}_t + \hat{q}_i - \hat{q}_{c,crit}, 0) \quad (4.50)$$

$$\hat{S}_{\theta_c} \cdot \Delta p = max \left[(\mathcal{C}L_v \cdot \hat{q}_t + L_s \cdot \hat{q}_i C_p \cdot \pi \cdot (\hat{q}_t + \hat{q}_i)) \cdot (\hat{q}_t + \hat{q}_i - \hat{q}_{c,crit}), 0 \right] \quad (4.51)$$

$$\hat{C}_u = PGFc \cdot (\mathcal{C}\partial\bar{u}_e\partial p), \quad \hat{C}_v = PGFc \cdot (\mathcal{C}\partial\bar{v}_e\partial p) \quad (4.52)$$

2047 where $\hat{q}_{c,crit} = 0.7 [g \cdot kg^{-1}]$ is maximum cloud condensate amount that cumulus updraft can hold,
 2048 and $PGFc = 0.7$ measures the degree to which cumulus updraft adjusts to environment by large-
 2049 scale horizontal pressure gradient force during vertical motion. Above \hat{S}_{q_t} and \hat{S}_{θ_c} assume that if
 2050 in-cumulus cloud condensate is larger than $\hat{q}_{c,crit}$, the excessive condensate is simply precipitated
 2051 out. This simple cumulus microphysics can be refined using updraft vertical velocity and cloud
 2052 drop size distribution in future. Following Gregory et al. [1997a], \hat{C}_u and \hat{C}_v assume that when
 2053 cumulus updraft rises across the layer with vertical shear of environmental horizontal wind,
 2054 updraft gains horizontal momentum increment directly from the environment without lateral
 2055 mass exchange. We neglect radiative effect and evaporation of convective precipitation within
 2056 convective updraft.

One unique aspect of our shallow convection scheme is to compute updraft vertical velocity
 for computing (1) updraft fractional area, (2) lateral entrainment and detrainment rates, and

(3) cumulus top height and penetrative entrainment rates. Steady state vertical momentum equation is

$$\mathcal{C}12 \cdot \mathcal{C} \partial \hat{w}^2 \partial p = a \cdot B - b \cdot \epsilon \cdot \hat{w}^2 \quad (4.53)$$

2057 where B is updraft buoyancy ($B = (g/\bar{\theta}_v) \cdot (\hat{\theta}_v - \bar{\theta}_v)$), and non-dimensional coefficients a, b
 2058 include the partition of perturbation vertical PGF into buoyancy and entrainment drag forces.
 2059 Without perturbation vertical PGF, $a = b = 1$ but we use $a = 1, b = 2$ assuming that
 2060 perturbation vertical PGF is entirely incorporated into entrainment drag force.

Instead of directly parameterizing (ϵ, δ) , we assume that a certain amount of updraft airs ($\epsilon_o \cdot \hat{M} \cdot \delta p$) is mixed with the same amount of environmental airs during incremental vertical displacement δp , producing a spectrum of mixtures with the same mixing probability $P(\chi) = 1$ where $0 \leq \chi \leq 1$ ($\chi = 0$ is cumulus updraft, $\chi = 1$ is environmental air). Among these mixtures, we entrain (1) positively buoyant mixtures and (2) negatively buoyant mixtures with vertical velocity strong enough to reach 0.1 of cumulus top height. This process is so called *inertial buoyancy sorting* (Kain and Fritsch [1990], Bretherton et al. [2004]). This allows us to compute a single critical mixing fraction χ_c : mixtures with $\chi \leq \chi_c$ are entrained while the others are detrained. Then, we can derive (ϵ, δ) as follows.

$$\epsilon = \epsilon_o \cdot \chi_c^2 \quad (4.54)$$

$$\delta = \epsilon_o \cdot (1 - \chi_c)^2 \quad (4.55)$$

where fractional mixing rate ϵ_o is parameterized as an inverse function of geometric height,

$$\epsilon_o = \left[\mathcal{C}c\rho \cdot g \cdot z \right] \quad (4.56)$$

2061 where non-dimensional coefficient $c = 8$ and z is geometric height above the surface. In order to
 2062 simulate deep convection, we can use a smaller value, e.g., $c = 4$. Cumulus top height necessary
 2063 to compute χ_c is initially set to the previous time step's value and then recomputed using an
 2064 iteration loop.

2065 Now, we can compute vertical evolution of $\hat{M}, \hat{\phi}, \hat{w}$. Instead of solving discrete numerical
 2066 equation, we used the explicit analytical solution by solving the first order differential equation
 2067 to obtain the cumulus updraft properties at the top interface of each layer from the value at
 2068 the base interface. In solving Eqn.(4.53), we assume a linear profile of B in each layer. At
 2069 the top interface, we computed updraft fractional area \hat{A} from \hat{M} and \hat{w} , and if $\hat{A} > 0.1$,
 2070 detrainment rate δ is enhanced such that \hat{A} is always less than 0.1. Note that this enhancement
 2071 of detrainment only changes \hat{M} not \hat{w} at the top interface.

2072 4.3.5 Penetrative Entrainment

2073 When convective updraft rises into the stably stratified layers (i.e., Overshooting Zone. See Fig.4.2) above the Level of Neutral Buoyancy (LNB), some air masses within the overshooting zone are entrained into the layers below. This process is so called *penetrative entrainment*. We assume that the amount of penetratively entrained airs (M_{pen}) is proportional to the mass involved in the lateral mixing in the overshooting zone and the properties of penetratively

entrained airs (ϕ_{pen}) are identical to the mean environmental values from LNB to LNB + Δp_{pen} :

$$M_{pen} = r_{pen} \cdot \hat{M} \cdot \epsilon_o \cdot \Delta p_{pen} \quad (4.57)$$

$$\phi_{pen} = \bar{\phi}_e \quad (4.58)$$

2074 where Δp_{pen} is vertical overshooting distance of cumulus updraft above LNB and $1 \leq r_{pen} \leq 10$
 2075 is a tunable non-dimensional penetrative entrainment coefficient. In CAM5, we chose $r_{pen} = 10$.
 2076 The thickness of overshooting zone above LNB, or the cumulus top height is diagnosed as the
 2077 level where convective updraft vertical velocity \hat{w} becomes zero.

2078 When convective updraft penetrates into several layers above LNB, Eqn.(4.57) and (4.58)
 2079 are computed for each layers within penetrative overshooting zone, and all the penetratively
 2080 entrained mass is deposited into a single layer just below LNB. We neglect convective updraft
 2081 fluxes at the interfaces at and above LNB since most of updraft mass fluxes crossing over the
 2082 LNB are likely to sink down below LNB due to negative updraft buoyancy in the overshooting
 2083 zone. The thickness of overshooting zone above LNB, or the cumulus top height is diagnosed as
 2084 the level where convective updraft vertical velocity \hat{w} becomes zero.

2085 4.3.6 Convective Fluxes at and below the PBL top interface

2086 We view the layer just above the PBL top (*ambiguous layer*, I . See Fig.4.2) as the
 accumulation of partial grid layer of PBL air and another partial grid layer of above-PBL
 air. The interface between these two partial layers, the reconstructed PBL top height p_{inv} , is
 computed using a simple conservation principle for individual scalar component $\phi = q_t, \theta_c, u, v, \zeta$
 as follows.

$$p_{inv} = pi_{I-1} - r \cdot |\Delta p_I|, \quad r = \left[\mathcal{C} \bar{\phi}_{e,I} - \bar{\phi}_{e,I+1/2} \bar{\phi}_{e,I-1/2} - \bar{\phi}_{e,I+1/2} \right] \quad (4.59)$$

2087 where $|p_I|$ is the pressure thickness of the ambiguous layer, pi is the pressure at the model
 2088 interface, $\bar{\phi}_{e,I-1/2}$ and $\bar{\phi}_{e,I+1/2}$ are the profile-reconstructed environmental values just below the
 2089 PBL top interface and just above the ambiguous layer, respectively (See Fig.4.2).

Convective updraft mass flux \hat{M}_{src} is assumed to be deflated from the p_{inv} with $\hat{\phi}_{src}$, which
 enables us to compute convective flux at the p_{inv} . To avoid over stabilizing or destabilizing
 the ambiguous layer and PBL through cumulus ventilation, this flux is uniformly extracted
 throughout the whole PBL, which results in the following linear profile of convective flux at
 model interfaces below p_{inv} .

$$(\overline{\omega' \phi'}) (k) = g \cdot \hat{M}_{src} \cdot (\hat{\phi}_{src} - \bar{\phi}_{e,I-1/2}) \cdot \left[\mathcal{C} pi_0 - pi_k pi_0 - p_{inv} \right], \quad for \quad 0 \leq k \leq I - 1 \quad (4.60)$$

2090 where ω is pressure vertical velocity, $k = 0$ is surface, $k = I - 1$ is PBL top interface index.

It is possible for compensating subsidence associated with cumulus updraft mass flux to
 lower the p_{inv} below the bottom of the ambiguous layer, in which case compensating subsidence
 will also warm and dry the grid layer below. To diagnose whether compensating subsidence
 would lower p_{inv} below pi_{I-1} during Δt , we compare the normalized cumulus updraft mass flux,
 $r_c = (g \cdot \hat{M}_{src} \cdot \Delta t) / |\Delta p_I|$ to r . If $r_c \geq r$, p_{inv} will be lowered down into the layer $I - 1$, replacing

PBL-top air with $\phi = \bar{\phi}_{e,I-1/2}$ with above-PBL air with $\phi = \bar{\phi}_{e,I+1/2}$. This effect is included by adding the below compensating subsidence flux

$$(\overline{\omega'\phi'}) (k = I - 1) = -g \cdot \hat{M}_{src} \cdot (\bar{\phi}_{e,I+1/2} - \bar{\phi}_{e,I-1/2}) \cdot \left[1 - \mathcal{C}rr_c \right], \quad \text{for } r_c > r \quad (4.61)$$

2091 where we assumed that cumulus mass flux is not strong enough to lower down p_{inv} below pi_{I-2} ,
 2092 that is, $g \cdot \hat{M}_{src} \cdot \Delta t < r \cdot |\Delta p_I| + |\Delta p_{I-1}|$. In order to ensure this condition, we impose an upper
 2093 bound on the convective base mass flux of $g \cdot \hat{M}_{src} \cdot \Delta t < 0.9 \cdot |\Delta p_{I-1}|$.

2094 4.3.7 Grid-Mean Tendency of Conservative Scalars

2095

In case of steady state updraft plume approximation with a finite updraft fractional area but compensating subsidence entirely within the same grid box as convective updraft, the budget equation of grid mean conservative scalar represented in flux convergence form becomes

$$\mathcal{C}\partial\bar{\phi}\partial t = \mathcal{C}\partial\partial t (A_e \cdot \bar{\phi}_e) = -g \cdot \mathcal{C}\partial\partial p \left[\hat{M} \cdot (\hat{\phi} - \bar{\phi}_e) + M_{pen} \cdot (\phi_{pen} - \bar{\phi}_e) \right] + g \cdot \hat{M} \cdot \hat{S}_\phi + \mathcal{C}\partial\partial t (A_e \cdot \bar{\phi}_e)_S \quad (4.62)$$

2096 where $A_e = 1 - \hat{A}$ is environmental fractional area and on the R.H.S. the first and second
 2097 terms are convergence of convective updraft and penetrative entrainment fluxes, respectively,
 2098 and the third and fourth terms are diabatic sources within convective updraft and environment,
 2099 respectively. We use the above flux convergence form to compute tendencies of conservative
 2100 scalars in order to ensure conservation of column-integrated energy during vertical redistribu-
 2101 tion of air masses by convective updraft. \hat{M} in the third term of the R.H.S. is obtained by
 2102 averaging updraft mass fluxes at the top and base interfaces of each layer. In contrast to $\hat{\phi}$, $\bar{\phi}_e$
 2103 is discontinuous across the model interface due to profile reconstruction. In order to take into
 2104 account of the effects of compensating subsidence (upwelling) in this flux form, $\bar{\phi}_e$ in the first
 2105 (second) term on the R.H.S is taken as the reconstructed environmental value just above the
 2106 top interface (below the base interface) of each layer. If downdraft is also considered in future,
 2107 we should add $-g \cdot \partial/\partial p [\hat{M}_d \cdot (\hat{\phi}_d - \bar{\phi}_e)] + g \cdot \hat{M}_d \cdot \hat{S}_{d,\phi}$ on the R.H.S.

If $\phi = u, v$, diabatic sources both within convective updraft (\hat{S}_ϕ) and environment are zero. Note that a direct conversion term from environment to updraft without lateral mass exchange (\hat{C}_ϕ) should not be included in this tendency equation in order to conserve column-integrated horizontal momentum. If $\phi = q_t, \theta_c$, these diabatic sources are precipitation production within convective updraft (Eqn.(4.50),(4.51)) and evaporation of precipitation within environment. Following the formulation in CAM3 and CAM4, we assume that whenever convective precipitation flux exists, it is spread all over the grid. The resulting formulation of evaporation of convective precipitation within environment is

$$\mathcal{C}\partial\partial t (A_e \cdot \bar{q}_{t,e})_S = A_e \cdot k_e \cdot (1 - \bar{U}_e) \cdot (\sqrt{\bar{F}_R} + \sqrt{\bar{F}_S}) \quad (4.63)$$

2108 where \bar{F}_R and \bar{F}_S are grid-mean rain and snow fluxes respectively in unit of $[kg \cdot m^{-2} \cdot s^{-1}]$ falling
 2109 into the model layer from the top interface, and \bar{U}_e is mean relative humidity within environment
 2110 obtained using a mean saturation specific humidity that is a weighting average over water and
 2111 ice, $k_e = 2 \cdot 10^{-6} [(kg \cdot m^{-2} \cdot s^{-1})^{-1/2} \cdot s^{-1}]$ is evaporation efficiency. We also consider snow

2112 melting during fall and corresponding changes of θ_c . This is a very simple formula bypassing
 2113 the detailed vertical overlap structure of cumulus and stratus clouds. More refined treatment
 2114 considering vertical cloud overlap will be done in future.

2115 Vertical transport of horizontal momentum by convective updraft does not change column-
 2116 mean horizontal momentum. However, it will change column-mean kinetic energy (KE) of the
 2117 mean wind. In reality, this KE change will be eventually converted into internal heat energy
 2118 (or potential energy, PE). In CAM5, we require conservation of column-mean total energy,
 2119 PE+KE. In order to satisfy this constraint, we add kinetic energy dissipation heating into $\bar{\theta}_c$
 2120 following [Boville and Bretherton \[2003b\]](#). Similar treatment was made in the moist turbulence
 2121 scheme.

2122 In CAM5, input state variables passed into individual physical schemes is *not* the grid-mean
 2123 value including cumulus updraft contribution ($\bar{\phi} = \hat{A} \cdot \hat{\phi} + (1 - \hat{A}) \cdot \bar{\phi}_e$) *but* the environmental
 2124 mean value without cumulus portion ($\bar{\phi}_e$). In order to conserve column-integrated grid-mean
 2125 energy, we print out $\partial (A_e \cdot \bar{\phi}_e) / \partial t$ instead of $\partial (\bar{\phi}_e) / \partial t$ from our shallow convection
 2126 scheme. Under the approximation of very small updraft fractional area ($\hat{A} \approx 0$ and $A_e \approx 1$), it is
 2127 $\partial (A_e \cdot \bar{\phi}_e) / \partial t \approx \partial (\bar{\phi}_e) / \partial t$. In Eqn.(4.63), we also approximate $A_e \approx 1$.

2128 4.3.8 Grid-Mean Tendency of Non-Conservative Scalars

2129
 2130 In contrast to the conservative scalars, we use the following explicit *detrainment* and
 2131 *compensating subsidence* tendency form to compute the tendency of non-conservative scalars.
 2132 We first compute the tendencies of cloud condensates, and then the tendencies of water vapor
 2133 (\bar{q}_v) and dry static energy (\bar{s}) are extracted from them.

$$\mathcal{C}\partial\partial t (A_e \cdot \bar{q}_{l,e}) = -g \cdot (\hat{M} - M_{pen}) \cdot \mathcal{C}\partial\bar{q}_{l,e}\partial p + g \cdot \hat{M} \cdot \delta \cdot (\hat{q}_l - \bar{q}_{l,e}) + g \cdot M_{pen} \cdot (q_{l,pen} - \bar{q}_{l,e}) \quad (4.64)$$

$$\mathcal{C}\partial\partial t (A_e \cdot \bar{q}_{i,e}) = -g \cdot (\hat{M} - M_{pen}) \cdot \mathcal{C}\partial\bar{q}_{i,e}\partial p + g \cdot \hat{M} \cdot \delta \cdot (\hat{q}_i - \bar{q}_{i,e}) + g \cdot M_{pen} \cdot (q_{i,pen} - \bar{q}_{i,e}) \quad (4.65)$$

$$\mathcal{C}\partial\partial t (A_e \cdot \bar{q}_{v,e}) = \mathcal{C}\partial\partial t (A_e \cdot \bar{q}_{t,e}) - \mathcal{C}\partial\partial t (A_e \cdot \bar{q}_{l,e}) - \mathcal{C}\partial\partial t (A_e \cdot \bar{q}_{i,e}) \quad (4.66)$$

$$\mathcal{C}\partial\partial t (A_e \cdot \bar{s}_e) = \mathcal{C}\partial\partial t (A_e \cdot \bar{s}_{c,e}) + L_v \cdot \mathcal{C}\partial\partial t (A_e \cdot \bar{q}_{l,e}) + L_s \cdot \mathcal{C}\partial\partial t (A_e \cdot \bar{q}_{i,e}) \quad (4.67)$$

2134 where *condensate static energy* $s_c = C_p \cdot \pi \cdot \theta_c + g \cdot z$ and the first term on the R.H.S in Eqn.(4.64)
 2135 and (4.65) is tendency associated with compensating subsidence and upwelling of environmental
 2136 condensate, and the second and third terms are tendencies due to condensate detrainment from
 2137 convective updraft and penetrative entrainment masses. If $\hat{M} - M_{pen} > 0$ ($\hat{M} - M_{pen} < 0$),
 2138 downward (upward) diffencing between upper (lower) and current layers is used in computing
 2139 compensating subsidence (upwelling) tendency. Any convective updraft condensate detrained
 2140 into the layers above the LNB are assumed to move down into the layer just below LNB by
 2141 negative buoyancy and be detrained there. That is, the second term on the R.H.S. in Eqn.(4.64)
 2142 and (4.65) is zero in the overshooting zone. Similarly, all the penetratively entrained condensate
 2143 are detrained into the layer just below LNB. That is, the third term on the R.H.S. in Eqn.(4.64)
 2144 and (4.65) is non-zero only in the layer just below LNB.

2145 If environmental condensate is displaced vertically by compensating subsidence/upwelling,
 2146 phase change should occur due to compression heating/expansion cooling. Ideally, this phase

2147 change should be treated within convection scheme but our current scheme does not. How-
2148 ever, this phase change of displaced condensate will be treated by separate stratiform macro-
2149 microphysics schemes later.

2150 The tendencies of cloud droplet number concentration ($\bar{n}_{l,e}, \bar{n}_{i,e}$) by compensating sub-
2151 sidence/upwelling are treated in a similar way as the tendencies of cloud condensate mass.
2152 However, because CAM5's cumulus microphysics is the 1st moment scheme, we don't have any
2153 information on the droplet number concentration within cumulus updraft (\hat{n}_l, \hat{n}_i). We assume
2154 that the effective droplet radius of detrained shallow (deep) convective condensate is 8 (10)
2155 and 25 (50) [μm] for liquid and ice respectively.

2156 4.4 Deep Convection

2157 The process of deep convection is treated with a parameterization scheme developed by
 2158 [Zhang and McFarlane \[1995\]](#) and modified with the addition of convective momentum
 2159 transports by [Richter and Rasch \[2008\]](#) and a modified dilute plume calculation following
 2160 [Raymond and Blyth \[1986, 1992\]](#). The scheme is based on a plume ensemble approach where it
 2161 is assumed that an ensemble of convective scale updrafts (and the associated saturated down-
 2162 drafts) may exist whenever the atmosphere is conditionally unstable in the lower troposphere.
 2163 The updraft ensemble is comprised of plumes sufficiently buoyant so as to penetrate the unstable
 2164 layer, where all plumes have the same upward mass flux at the bottom of the convective layer.
 2165 Moist convection occurs only when there is convective available potential energy (CAPE) for
 2166 which parcel ascent from the sub-cloud layer acts to destroy the CAPE at an exponential rate
 2167 using a specified adjustment time scale. For the convenience of the reader we will review some
 2168 aspects of the formulation, but refer the interested reader to [Zhang and McFarlane \[1995\]](#) for
 2169 additional detail, including behavioral characteristics of the parameterization scheme. Evap-
 2170 oration of convective precipitation is computed following the procedure described in section
 2171 [4.5](#).

The large-scale budget equations distinguish between a cloud and sub-cloud layer where temperature and moisture response to convection in the cloud layer is written in terms of bulk convective fluxes as

$$c_p \left(\frac{\partial T}{\partial t} \right)_{cu} = -\frac{1}{\rho} \frac{\partial}{\partial z} (M_u S_u + M_d S_d - M_c S) + L(C - E) \quad (4.68)$$

$$\left(\frac{\partial q}{\partial t} \right)_{cu} = -\frac{1}{\rho} \frac{\partial}{\partial z} (M_u q_u + M_d q_d - M_c q) + E - C, \quad (4.69)$$

for $z \geq z_b$, where z_b is the height of the cloud base. For $z_s < z < z_b$, where z_s is the surface height, the sub-cloud layer response is written as

$$c_p \left(\rho \frac{\partial T}{\partial t} \right)_m = -\frac{1}{z_b - z_s} (M_b [S(z_b) - S_u(z_b)] + M_d [S(z_b) - S_d(z_b)]) \quad (4.70)$$

$$\left(\rho \frac{\partial q}{\partial t} \right)_m = -\frac{1}{z_b - z_s} (M_b [q(z_b) - q_u(z_b)] + M_d [q(z_b) - q_d(z_b)]) , \quad (4.71)$$

2172 where the net vertical mass flux in the convective region, M_c , is comprised of upward, M_u , and
 2173 downward, M_d , components, C and E are the large-scale condensation and evaporation rates,
 2174 S , S_u , S_d , q , q_u , q_d , are the corresponding values of the dry static energy and specific humidity,
 2175 and M_b is the cloud base mass flux.

2176 4.4.1 Updraft Ensemble

The updraft ensemble is represented as a collection of entraining plumes, each with a characteristic fractional entrainment rate λ . The moist static energy in each plume h_c is given by

$$\frac{\partial h_c}{\partial z} = \lambda(h - h_c), \quad z_b < z < z_D . \quad (4.72)$$

Mass carried upward by the plumes is detrained into the environment in a thin layer at the top of the plume, z_D , where the detrained air is assumed to have the same thermal properties as in the environment ($S_c = S$). Plumes with smaller λ penetrate to larger z_D . The entrainment rate λ_D for the plume which detrains at height z is then determined by solving (4.72), with lower boundary condition $h_c(z_b) = h_b$:

$$\frac{\partial h_c}{\partial(z - z_b)} = \lambda_D(h - h_b) - \lambda_D(h_c - h_b) \quad (4.73)$$

$$\frac{\partial(h_c - h_b)}{\partial(z - z_b)} - \lambda_D(h_c - h_b) = \lambda_D(h - h_b) \quad (4.74)$$

$$\frac{\partial(h_c - h_b)e^{\lambda_D(z - z_b)}}{\partial(z - z_b)} = \lambda_D(h - h_b)e^{\lambda_D(z - z_b)} \quad (4.75)$$

$$(h_c - h_b)e^{\lambda_D(z - z_b)} = \int_{z_b}^z \lambda_D(h - h_b)e^{\lambda_D(z' - z_b)} dz' \quad (4.76)$$

$$(h_c - h_b) = \lambda_D \int_{z_b}^z (h - h_b)e^{\lambda_D(z' - z)} dz' . \quad (4.77)$$

Since the plume is saturated, the detraining air must have $h_c = h^*$, so that

$$(h_b - h^*) = \lambda_D \int_{z_b}^z (h_b - h)e^{\lambda_D(z' - z)} dz' . \quad (4.78)$$

2177 Then, λ_D is determined by solving (4.78) iteratively at each z .

The top of the shallowest of the convective plumes, z_0 is assumed to be no lower than the mid-tropospheric minimum in saturated moist static energy, h^* , ensuring that the cloud top detrainment is confined to the conditionally stable portion of the atmospheric column. All condensation is assumed to occur within the updraft plumes, so that $C = C_u$. Each plume is assumed to have the same value for the cloud base mass flux M_b , which is specified below. The vertical distribution of the cloud updraft mass flux is given by

$$M_u = M_b \int_0^{\lambda_D} \frac{1}{\lambda_0} e^{\lambda(z - z_b)} d\lambda = M_b \frac{e^{\lambda_D(z - z_b)} - 1}{\lambda_0(z - z_b)} , \quad (4.79)$$

where λ_0 is the maximum detrainment rate, which occurs for the plume detraining at height z_0 , and λ_D is the entrainment rate for the updraft that detrains at height z . Detrainment is confined to regions where λ_D decreases with height, so that the total detrainment $D_u = 0$ for $z < z_0$. Above z_0 ,

$$D_u = -\frac{M_b}{\lambda_0} \frac{\partial \lambda_D}{\partial z} . \quad (4.80)$$

The total entrainment rate is then just given by the change in mass flux and the total detrainment,

$$E_u = \frac{\partial M_u}{\partial z} - D_u . \quad (4.81)$$

The updraft budget equations for dry static energy, water vapor mixing ratio, moist static energy, and cloud liquid water, ℓ , are:

$$\frac{\partial}{\partial z}(M_u S_u) = (E_u - D_u) S + \rho L C_u \quad (4.82)$$

$$\frac{\partial}{\partial z}(M_u q_u) = E_u q - D_u q^* + \rho C_u \quad (4.83)$$

$$\frac{\partial}{\partial z}(M_u h_u) = E_u h - D_u h^* \quad (4.84)$$

$$\frac{\partial}{\partial z}(M_u \ell) = -D_u \ell_d + \rho C_u - \rho R_u, \quad (4.85)$$

where (4.84) is formed from (4.82) and (4.83) and detraining air has been assumed to be saturated ($q = q^*$ and $h = h^*$). It is also assumed that the liquid content of the detrained air is the same as the ensemble mean cloud water ($\ell_d = \ell$). The conversion from cloud water to rain water is given by

$$\rho R_u = c_0 M_u \ell, \quad (4.86)$$

2178 following Lord et al. [1982], with $c_0 = 2 \times 10^{-3} \text{ m}^{-1}$.

Since M_u , E_u and D_u are given by (4.79-4.81), and h and h^* are environmental profiles, (4.84) can be solved for h_u , given a lower boundary condition. The lower boundary condition is obtained by adding a 0.5 K temperature perturbation to the dry (and moist) static energy at cloud base, or $h_u = h + c_p \times 0.5$ at $z = z_b$. Below the lifting condensation level (LCL), S_u and q_u are given by (4.82) and (4.83). Above the LCL, q_u is reduced by condensation and S_u is increased by the latent heat of vaporization. In order to obtain a saturated updraft at the temperature implied by S_u , we define ΔT as the temperature perturbation in the updraft, then:

$$h_u = S_u + L q_u \quad (4.87)$$

$$S_u = S + c_p \Delta T \quad (4.88)$$

$$q_u = q^* + \frac{dq^*}{dT} \Delta T. \quad (4.89)$$

Substituting (4.88) and (4.89) into (4.87),

$$h_u = S + L q^* + c_p \left(1 + \frac{L}{c_p} \frac{dq^*}{dT} \right) \Delta T \quad (4.90)$$

$$= h^* + c_p (1 + \gamma) \Delta T \quad (4.91)$$

$$\gamma \equiv \frac{L}{c_p} \frac{dq^*}{dT} \quad (4.92)$$

$$\Delta T = \frac{1}{c_p} \frac{h_u - h^*}{1 + \gamma}. \quad (4.93)$$

The required updraft quantities are then

$$S_u = S + \frac{h_u - h^*}{1 + \gamma} \quad (4.94)$$

$$q_u = q^* + \frac{\gamma}{L} \frac{h_u - h^*}{1 + \gamma}. \quad (4.95)$$

2179 With S_u given by (4.94), (4.82) can be solved for C_u , then (4.85) and (4.86) can be solved for ℓ
 2180 and R_u .

The expressions above require both the saturation specific humidity to be

$$q^* = \frac{\epsilon e^*}{p - e^*}, \quad e^* < p, \quad (4.96)$$

where e^* is the saturation vapor pressure, and its dependence on temperature (in order to maintain saturation as the temperature varies) to be

$$\frac{dq^*}{dT} = \frac{\epsilon}{p - e^*} \frac{de^*}{dT} - \frac{\epsilon e^*}{(p - e^*)^2} \frac{d(p - e^*)}{dT} \quad (4.97)$$

$$= \frac{\epsilon}{p - e^*} \left(1 + \frac{1}{p - e^*} \right) \frac{de^*}{dT} \quad (4.98)$$

$$= \frac{\epsilon}{p - e^*} \left(1 + \frac{q^*}{\epsilon e^*} \right) \frac{de^*}{dT}. \quad (4.99)$$

The deep convection scheme does not use the same approximation for the saturation vapor pressure e^* as is used in the rest of the model. Instead,

$$e^* = c_1 \exp \left[\frac{c_2(T - T_f)}{(T - T_f + c_3)} \right], \quad (4.100)$$

where $c_1 = 6.112$, $c_2 = 17.67$, $c_3 = 243.5$ K and $T_f = 273.16$ K is the freezing point. For this approximation,

$$\frac{de^*}{dT} = e^* \frac{d}{dT} \left[\frac{c_2(T - T_f)}{(T - T_f + c_3)} \right] \quad (4.101)$$

$$= e^* \left[\frac{c_2}{(T - T_f + c_3)} - \frac{c_2(T - T_f)}{(T - T_f + c_3)^2} \right] \quad (4.102)$$

$$= e^* \frac{c_2 c_3}{(T - T_f + c_3)^2} \quad (4.103)$$

$$\frac{dq^*}{dT} = q^* \left(1 + \frac{q^*}{\epsilon e^*} \right) \frac{c_2 c_3}{(T - T_f + c_3)^2}. \quad (4.104)$$

We note that the expression for γ in the code gives

$$\frac{dq^*}{dT} = \frac{c_p}{L} \gamma = q^* \left(1 + \frac{q^*}{\epsilon} \right) \frac{\epsilon L}{RT^2}. \quad (4.105)$$

2181 The expressions for dq^*/dT in (4.104) and (4.105) are not identical. Also, $T - T_f + c_3 \neq T$ and
 2182 $c_2 c_3 \neq \epsilon L/R$.

2183 4.4.2 Downdraft Ensemble

Downdrafts are assumed to exist whenever there is precipitation production in the updraft ensemble where the downdrafts start at or below the bottom of the updraft detrainment layer.

Detrainment from the downdrafts is confined to the sub-cloud layer, where all downdrafts have the same mass flux at the top of the downdraft region. Accordingly, the ensemble downdraft mass flux takes a similar form to (4.79) but includes a “proportionality factor” to ensure that the downdraft strength is physically consistent with precipitation availability. This coefficient takes the form

$$\alpha = \mu \left[\frac{P}{P + E_d} \right] , \quad (4.106)$$

2184 where P is the total precipitation in the convective layer and E_d is the rain water evaporation
 2185 required to maintain the downdraft in a saturated state. This formalism ensures that the
 2186 downdraft mass flux vanishes in the absence of precipitation, and that evaporation cannot
 2187 exceed some fraction, μ , of the precipitation, where $\mu = 0.2$.

2188 4.4.3 Closure

The parameterization is closed, i.e., the cloud base mass fluxes are determined, as a function of the rate at which the cumulus consume convective available potential energy (CAPE). Since the large-scale temperature and moisture changes in both the cloud and sub-cloud layer are linearly proportional to the cloud base updraft mass flux (*e.g.* see eq. 4.68 – 4.71), the CAPE change due to convective activity can be written as

$$\left(\frac{\partial A}{\partial t} \right)_{cu} = -M_b F , \quad (4.107)$$

where F is the CAPE consumption rate per unit cloud base mass flux. The closure condition is that the CAPE is consumed at an exponential rate by cumulus convection with characteristic adjustment time scale $\tau = 7200$ s:

$$M_b = \frac{A}{\tau F} . \quad (4.108)$$

2189 4.4.4 Numerical Approximations

The quantities $M_{u,d}$, ℓ , $S_{u,d}$, $q_{u,d}$, $h_{u,d}$ are defined on layer interfaces, while D_u , C_u , R_u are defined on layer midpoints. S , q , h , γ are required on both midpoints and interfaces and the interface values $\psi^{k\pm}$ are determined from the midpoint values ψ^k as

$$\psi^{k-} = \log \left(\frac{\psi^{k-1}}{\psi^k} \right) \frac{\psi^{k-1}\psi^k}{\psi^{k-1} - \psi^k} . \quad (4.109)$$

All of the differencing within the deep convection is in height coordinates. The differences are naturally taken as

$$\frac{\partial \psi}{\partial z} = \frac{\psi^{k-} - \psi^{k+}}{z^{k-} - z^{k+}} , \quad (4.110)$$

where ψ^{k-} and ψ^{k+} represent values on the upper and lower interfaces, respectively for layer k . The convention elsewhere in this note (and elsewhere in the code) is $\delta^k \psi = \psi^{k+} - \psi^{k-}$. Therefore, we avoid using the compact δ^k notation, except for height, and define

$$d^k z \equiv z^{k-} - z^{k+} = -\delta^k z , \quad (4.111)$$

2190 so that $d^k z$ corresponds to the variable $dz(k)$ in the deep convection code.

2191 Although differences are in height coordinates, the equations are cast in flux form and the
 2192 tendencies are computed in units $\text{kg m}^{-3} \text{s}^{-1}$. The expected units are recovered at the end by
 2193 multiplying by $g\delta z/\delta p$.

The environmental profiles at midpoints are

$$S^k = c_p T^k + g z^k \quad (4.112)$$

$$h^k = S^k + L q^k \quad (4.113)$$

$$h^{*k} = S^k + L q^{*k} \quad (4.114)$$

$$q^{*k} = \epsilon e^{*k} / (p^k - e^{*k}) \quad (4.115)$$

$$e^{*k} = c_1 \exp \left[\frac{c_2 (T^k - T_f)}{(T^k - T_f + c_3)} \right] \quad (4.116)$$

$$\gamma^k = q^{*k} \left(1 + \frac{q^{*k}}{\epsilon} \right) \frac{\epsilon L^2}{c_p R T^{k2}} . \quad (4.117)$$

The environmental profiles at interfaces of S , q , q^* , and γ are determined using (4.109) if $|\psi^{k-1} - \psi^k|$ is large enough. **However, there are inconsistencies in what happens if $|\psi^{k-1} - \psi^k|$ is not large enough.** For S and q the condition is

$$\psi^{k-} = (\psi^{k-1} + \psi^k)/2, \quad \frac{|\psi^{k-1} - \psi^k|}{\max(\psi^{k-1} - \psi^k)} \leq 10^{-6} . \quad (4.118)$$

For q^* and γ the condition is

$$\psi^{k-} = \psi^k, \quad |\psi^{k-1} - \psi^k| \leq 10^{-6} . \quad (4.119)$$

Interface values of h are not needed and interface values of h^* are given by

$$h^{*k-} = S^{k-} + L q^{*k-} . \quad (4.120)$$

The unitless updraft mass flux (scaled by the inverse of the cloud base mass flux) is given by differencing (4.79) as

$$M_u^{k-} = \frac{1}{\lambda_0 (z^{k-} - z_b)} \left(e^{\lambda_D^k (z^{k-} - z_b)} - 1 \right) , \quad (4.121)$$

with the boundary condition that $M_u^{M+} = 1$. The entrainment and detrainment are calculated using

$$m_u^{k-} = \frac{1}{\lambda_0 (z^{k-} - z_b)} \left(e^{\lambda_D^{k+1} (z^{k-} - z_b)} - 1 \right) \quad (4.122)$$

$$E_u^k = \frac{m_u^{k-} - M_u^{k+}}{d^k z} \quad (4.123)$$

$$D_u^k = \frac{m_u^{k-} - M_u^{k-}}{d^k z} . \quad (4.124)$$

2194 Note that M_u^{k-} and m_u^{k-} differ only by the value of λ_D .

The updraft moist static energy is determined by differencing (4.84)

$$\frac{M_u^{k-} h_u^{k-} - M_u^{k+} h_u^{k+}}{d^k z} = E_u^k h^k - D_u^k h^{*k} \quad (4.125)$$

$$h_u^{k-} = \frac{1}{M_u^{k-}} [M_u^{k+} h_u^{k+} + d^k z (E_u^k h^k - D_u^k h^{*k})] , \quad (4.126)$$

2195 with $h_u^{M-} = h^M + c_p/2$, where M is the layer of maximum h .

Once h_u is determined, the lifting condensation level is found by differencing (4.82) and (4.83) similarly to (4.84):

$$S_u^{k-} = \frac{1}{M_u^{k-}} [M_u^{k+} S_u^{k+} + d^k z (E_u^k S^k - D_u^k S^k)] \quad (4.127)$$

$$q_u^{k-} = \frac{1}{M_u^{k-}} [M_u^{k+} q_u^{k+} + d^k z (E_u^k q^k - D_u^k q^{*k})] . \quad (4.128)$$

2196 The detrainment of S_u is given by $D_u^k S^k$ not by $D_u^k S_u^k$, since detrainment occurs at the environ-
2197 mental value of S . The detrainment of q_u is given by $D_u^k q^{*k}$, even though the updraft is not yet
2198 saturated. The LCL will usually occur below z_0 , the level at which detrainment begins, but this
2199 is not guaranteed.

The lower boundary conditions, $S_u^{M-} = S^M + c_p/2$ and $q_u^{M-} = q^M$, are determined from the first midpoint values in the plume, rather than from the interface values of S and q . The solution of (4.127) and (4.128) continues upward until the updraft is saturated according to the condition

$$q_u^{k-} > q^*(T_u^{k-}), \quad (4.129)$$

$$T_u^{k-} = \frac{1}{c_p} (S_u^{k-} - g z^{k-}) . \quad (4.130)$$

The condensation (in units of m^{-1}) is determined by a centered differencing of (4.82):

$$\frac{M_u^{k-} S_u^{k-} - M_u^{k+} S_u^{k+}}{d^k z} = (E_u^k - D_u^k) S^k + LC_u^k \quad (4.131)$$

$$C_u^k = \frac{1}{L} \left[\frac{M_u^{k-} S_u^{k-} - M_u^{k+} S_u^{k+}}{d^k z} - (E_u^k - D_u^k) S^k \right] . \quad (4.132)$$

The rain production (in units of m^{-1}) and condensed liquid are then determined by differencing (4.85) as

$$\frac{M_u^{k-} \ell^{k-} - M_u^{k+} \ell^{k+}}{d^k z} = -D_u^k \ell^{k+} + C_u^k - R_u^k , \quad (4.133)$$

and (4.86) as

$$R_u^k = c_0 M_u^{k-} \ell^{k-} . \quad (4.134)$$

Then

$$M_u^{k-} \ell^{k-} = M_u^{k+} \ell^{k+} - d^k z (D_u^k \ell^{k+} - C_u^k + c_0 M_u^{k-} \ell^{k-}) \quad (4.135)$$

$$M_u^{k-} \ell^{k-} (1 + c_0 d^k z) = M_u^{k+} \ell^{k+} + d^k z (D_u^k \ell^{k+} - C_u^k) \quad (4.136)$$

$$\ell^{k-} = \frac{1}{M_u^{k-} (1 + c_0 d^k z)} [M_u^{k+} \ell^{k+} - d^k z (D_u^k \ell^{k+} - C_u^k)] . \quad (4.137)$$

4.4.5 Deep Convective Momentum Transports

Sub-grid scale Convective Momentum Transports (CMT) have been added to the existing deep convection parameterization following [Richter and Rasch \[2008\]](#) and the methodology of [Gregory et al. \[1997b\]](#). The sub-grid scale transport of momentum can be cast in the same manner as (4.69). Expressing the grid mean horizontal velocity vector, \mathbf{V} , tendency due to deep convection transport following [Kershaw and Gregory \[1997\]](#) gives

$$\left(\frac{\partial \mathbf{V}}{\partial t}\right)_{cu} = -\frac{1}{\rho} \frac{\partial}{\partial z} (M_u \mathbf{V}_u + M_d \mathbf{V}_d - M_c \mathbf{V}) , \quad (4.138)$$

and neglecting the contribution from the environment the updraft and downdraft budget equation can similarly be written as

$$-\frac{\partial}{\partial z} (M_u \mathbf{V}_u) = E_u \mathbf{V} - D_u \mathbf{V}_u + \mathbf{P}_G^u \quad (4.139)$$

$$-\frac{\partial}{\partial z} (M_d \mathbf{V}_d) = E_d \mathbf{V} + \mathbf{P}_G^d , \quad (4.140)$$

where \mathbf{P}_G^u and \mathbf{P}_G^d the updraft and downdraft pressure gradient sink terms parameterized from [Gregory et al. \[1997b\]](#) as

$$\mathbf{P}_G^u = -C_u M_u \frac{\partial \mathbf{V}}{\partial z} \quad (4.141)$$

$$\mathbf{P}_G^d = -C_d M_d \frac{\partial \mathbf{V}}{\partial z} . \quad (4.142)$$

2201 C_u and C_d are tunable parameters. In the CAM 5.0 implementation we use $C_u = C_d = 0.4$. The
 2202 value of C_u and C_d control the strength of convective momentum transport. As these coefficients
 2203 increase so do the pressure gradient terms, and convective momentum transport decreases.

4.4.6 Deep Convective Tracer Transport

2205 The CAM 5.0 provides the ability to transport constituents via convection. The method used
 2206 for constituent transport by deep convection is a modification of the formulation described in
 2207 [Zhang and McFarlane \[1995\]](#).

2208 We assume the updrafts and downdrafts are described by a steady state mass continuity
 2209 equation for a ‘‘bulk’’ updraft or downdraft

$$\frac{\partial(M_x q_x)}{\partial p} = E_x q_e - D_x q_x . \quad (4.143)$$

2210 The subscript x is used to denote the updraft (u) or downdraft (d) quantity. M_x here is the
 2211 mass flux in units of Pa/s defined at the layer interfaces, q_x is the mixing ratio of the updraft or
 2212 downdraft. q_e is the mixing ratio of the quantity in the environment (that part of the grid volume
 2213 not occupied by the up and downdrafts). E_x and D_x are the entrainment and detrainment rates
 2214 (units of s^{-1}) for the up- and down-drafts. Updrafts are allowed to entrain or detrain in any
 2215 layer. Downdrafts are assumed to entrain only, and all of the mass is assumed to be deposited
 2216 into the surface layer.

2217 Equation 4.143 is first solved for up and downdraft mixing ratios q_u and q_d , assuming the
2218 environmental mixing ratio q_e is the same as the gridbox averaged mixing ratio \bar{q} .

Given the up- and down-draft mixing ratios, the mass continuity equation used to solve for the gridbox averaged mixing ratio \bar{q} is

$$\frac{\partial \bar{q}}{\partial t} = \frac{\partial}{\partial p} (M_u(q_u - \bar{q}) + M_d(q_d - \bar{q})) . \quad (4.144)$$

2219 These equations are solved for in subroutine CONVTRAN. There are a few numerical details
2220 employed in CONVTRAN that are worth mentioning here as well.

- 2221 • mixing quantities needed at interfaces are calculated using the geometric mean of the layer
2222 mean values.
- 2223 • simple first order upstream biased finite differences are used to solve 4.143 and 4.144.
- 2224 • fluxes calculated at the interfaces are constrained so that the resulting mixing ratios are
2225 positive definite. *This means that this parameterization is not suitable for moving mixing*
2226 *ratios of quantities meant to represent perturbations of a trace constituent about a mean*
2227 *value* (in which case the quantity can meaningfully take on positive and negative mix-
2228 ing ratios). The algorithm can be modified in a straightforward fashion to remove this
2229 constraint, and provide meaningful transport of perturbation quantities if necessary. *the*
2230 *reader is warned however that there are other places in the model code where similar mod-*
2231 *ifications are required because the model assumes that all mixing ratios should be positive*
2232 *definite quantities.*

4.5 Evaporation of convective precipitation

The CAM 5.0 employs a [Sundqvist \[1988\]](#) style evaporation of the convective precipitation as it makes its way to the surface. This scheme relates the rate at which raindrops evaporate to the local large-scale subsaturation, and the rate at which convective rainwater is made available to the subsaturated model layer

$$E_{r_k} = K_E (1 - \text{RH}_k) (\hat{R}_{r_k})^{1/2} . \quad (4.145)$$

where RH_k is the relative humidity at level k , \hat{R}_{r_k} denotes the total rainwater flux at level k (which can be different from the locally diagnosed rainwater flux from the convective parameterization, as will be shown below), the coefficient K_E takes the value $0.2 \cdot 10^{-5} \text{ (kg m}^{-2} \text{ s}^{-1})^{-1/2} \text{ s}^{-1}$, and the variable E_{r_k} has units of s^{-1} . The evaporation rate E_{r_k} is used to determine a local change in q_k and T_k , associated with an evaporative reduction of \hat{R}_{r_k} . Conceptually, the evaporation process is invoked after a vertical profile of R_{r_k} has been evaluated. An evaporation rate is then computed for the uppermost level of the model for which $R_{r_k} \neq 0$ using (4.145), where in this case $R_{r_k} \equiv \hat{R}_{r_k}$. This rate is used to evaluate an evaporative reduction in R_{r_k} which is then accumulated with the previously diagnosed rainwater flux in the layer below,

$$\hat{R}_{r_{k+1}} = \hat{R}_{r_k} - \left(\frac{\Delta p_k}{g} \right) E_{r_k} + R_{r_{k+1}} . \quad (4.146)$$

A local increase in the specific humidity q_k and a local reduction of T_k are also calculated in accordance with the net evaporation

$$q_k = q_k + E_{r_k} 2\Delta t , \quad (4.147)$$

and

$$T_k = T_k - \left(\frac{L}{c_p} \right) E_{r_k} 2\Delta t . \quad (4.148)$$

The procedure, (4.145)-(4.148), is then successively repeated for each model level in a downward direction where the final convective precipitation rate is that portion of the condensed rainwater in the column to survive the evaporation process

$$P_s = \left(\hat{R}_{r_K} - \left(\frac{\Delta p_K}{g} \right) E_{r_K} \right) / \rho_{H_2O} . \quad (4.149)$$

2234 In global annually averaged terms, this evaporation procedure produces a very small reduction
 2235 in the convective precipitation rate where the evaporated condensate acts to moisten the middle
 2236 and lower troposphere.

2237 4.6 Cloud Microphysics

2238 The base parameterization of stratiform cloud microphysics is described by Morrison and Gettelman
2239 [2008]. Details of the CAM implementation are described by Gettelman et al. [2008]. Mod-
2240 ifications to handle ice nucleation and ice supersaturation are described by Gettelman et al.
2241 [2010b].

2242 The scheme seeks the following:

- 2243 • A more flexible, self-consistent, physically-based treatment of cloud physics.
- 2244 • A reasonable level of simplicity and computational efficiency.
- 2245 • Treatment of both number concentration and mixing ratio of cloud particles to address
2246 indirect aerosol effects and cloud-aerosol interaction.
- 2247 • Representation of precipitation number concentration, mass, and phase to better treat wet
2248 deposition and scavenging of aerosol and chemical species.
- 2249 • The achievement of equivalent or better results relative to the CAM3 microphysics pa-
2250 rameterization when compared to observations.

2251 The novel aspects of the scheme are an explicit representation of sub-grid cloud water distri-
2252 bution for calculation of the various microphysical process rates, and the diagnostic two-moment
2253 treatment of rain and snow.

2254 4.6.1 Overview of the microphysics scheme

2255 The two-moment scheme is based loosely on the approach of Morrison et al. [2005]. This scheme
2256 predicts the number concentrations (N_c , N_i) and mixing ratios (q_c , q_i) of cloud droplets (sub-
2257 script c) and cloud ice (subscript i). Hereafter, unless stated otherwise, the cloud variables N_c ,
2258 N_i , q_c , and q_i represent grid-averaged values; prime variables represent mean in-cloud quantities
2259 (e.g., such that $N_c = F_{\text{cld}} N'_c$, where F_{cld} is cloud fraction); and double prime variables repre-
2260 sent local in-cloud quantities. The treatment of sub-grid cloud variability is detailed in section
2261 2.1.

The cloud droplet and ice size distributions ϕ are represented by gamma functions:

$$\phi(D) = N_0 D^\mu \exp^{-\lambda D} \quad (4.150)$$

2262 where D is diameter, N_0 is the intercept parameter, λ is the slope parameter, and $\mu =$
2263 $1/\eta^2 - 1$ is the spectra shape parameter; η is the relative radius dispersion of the size distribution.
2264 The parameter η for droplets is specified following Martin et al. [1994]. Their observations of
2265 maritime versus continental warm stratocumulus have been approximated by the following $\eta - N''_c$
2266 relationship:

$$\eta = 0.0005714 N''_c + 0.2714 \quad (4.151)$$

2267 where N''_c has units of cm^{-3} . The upper limit for η is 0.577, corresponding with a N''_c of 535
2268 cm^{-3} . Note that this expression is uncertain, especially when applied to cloud types other than
2269 those observed by Martin et al. [1994]. In the current version of the scheme, $\mu = 0$ for cloud ice.

The spectral parameters N_0 and λ are derived from the predicted N'' and q'' and specified μ :

$$\lambda = \left[\frac{\pi \rho N'' \Gamma(\mu + 4)}{6 q'' \Gamma(\mu + 1)} \right]^{(1/3)} \quad (4.152)$$

$$N_0 = \frac{N'' \lambda^{\mu+1}}{\Gamma(\mu + 1)} \quad (4.153)$$

where Γ is the Euler gamma function. Note that 4.152 and 4.153 assume spherical cloud particles with bulk density $\rho = 1000 \text{ kg m}^{-3}$ for droplets and $\rho = 500 \text{ kg m}^{-3}$ for cloud ice following Reisner et al. [1998].

The effective size for cloud ice needed by the radiative transfer scheme is obtained directly by dividing the third and second moments of the size distribution given by 4.150 and accounting for differences in cloud ice density and that of pure ice. After rearranging terms, this yields

$$d_{ei} = \frac{3\rho}{\lambda \rho_i} \quad (4.154)$$

where $\rho_i = 917 \text{ kg m}^{-3}$ is the bulk density of pure ice. Note that optical properties for cloud droplets are calculated using a lookup table from the N_0 and λ parameters. The droplet effective radius, which is used for output purposes only, is given by

$$r_{ec} = \frac{\Gamma(\mu + 4)}{2\lambda\Gamma(\mu + 3)} \quad (4.155)$$

The time evolution of q and N is determined by grid-scale advection, convective detrainment, turbulent diffusion, and several microphysical processes:

$$\frac{\partial N}{\partial t} + \frac{1}{\rho} \nabla \cdot [\rho \mathbf{u} N] = \left(\frac{\partial N}{\partial t} \right)_{nuc} + \left(\frac{\partial N}{\partial t} \right)_{evap} + \left(\frac{\partial N}{\partial t} \right)_{auto} + \left(\frac{\partial N}{\partial t} \right)_{acer} + \left(\frac{\partial N}{\partial t} \right)_{accs} + \left(\frac{\partial N}{\partial t} \right)_{het} + \left(\frac{\partial N}{\partial t} \right)_{hom} + \dots \quad (4.156)$$

$$\frac{\partial q}{\partial t} + \frac{1}{\rho} \nabla \cdot [\rho \mathbf{u} q] = \left(\frac{\partial q}{\partial t} \right)_{cond} + \left(\frac{\partial q}{\partial t} \right)_{evap} + \left(\frac{\partial q}{\partial t} \right)_{auto} + \left(\frac{\partial q}{\partial t} \right)_{acer} + \left(\frac{\partial q}{\partial t} \right)_{accs} + \left(\frac{\partial q}{\partial t} \right)_{het} + \left(\frac{\partial q}{\partial t} \right)_{hom} + \left(\frac{\partial q}{\partial t} \right)_{mt} + \dots \quad (4.157)$$

where t is time, \mathbf{u} is the 3D wind vector, ρ is the air density, and D is the turbulent diffusion operator. The symbolic terms on the right hand side of 4.156 and 4.157 represent the grid-average microphysical source/sink terms for N and q . Note that the source/sink terms for q and N are considered separately for cloud water and ice (giving a total of four rate equations), but are generalized here using 4.156 and 4.157 for conciseness. These terms include activation of cloud condensation nuclei or deposition/condensation-freezing nucleation on ice nuclei to form droplets or cloud ice (subscript *nuc*; N only); ice multiplication via rime-splintering on snow (subscript *mult*); condensation/deposition (subscript *cond*; q only), evaporation/sublimation (subscript *evap*), autoconversion of cloud droplets and ice to form rain and snow (subscript *auto*), accretion of cloud droplets and ice by rain (subscript *accr*), accretion of cloud droplets and ice by snow (subscript *accs*), heterogeneous freezing of droplets to form ice (subscript *het*),

2292 homogeneous freezing of cloud droplets (subscript hom), melting (subscript mlt), ice multipli-
 2293 cation (subscript mult), sedimentation (subscript sed), and convective detrainment (subscript
 2294 det). The formulations for these processes are detailed in section 3. Numerical aspects in solving
 2295 4.156 and 4.157 are detailed in section 4.

2296 Sub-grid cloud variability

2297 Sub-grid variability is considered for cloud water but neglected for cloud ice and precipitation
 2298 at present; furthermore, we neglect sub-grid variability of droplet number concentration for
 2299 simplicity. We assume that the PDF of in-cloud cloud water, $P(q_c'')$, follows a gamma distribution
 2300 function based on observations of optical depth in marine boundary layer clouds [Barker, 1996;
 2301 Barker et al., 1996; McFarlane and Klein, 1999]:

$$P(q_c'') = \frac{q_c''^{\nu-1} \alpha^\nu}{\Gamma(\nu)} \exp^{-\alpha q_c''} \quad (4.158)$$

2302 where $\nu = 1/\sigma^2$; σ^2 is the relative variance (i.e., variance divided by $q_c'^2$); and $\alpha = \nu/q_c'$ (q_c' is
 2303 the mean in-cloud cloud water mixing ratio). Note that this PDF is applied to all cloud types
 2304 treated by the stratiform cloud scheme; the appropriateness of such a PDF for stratiform cloud
 2305 types other than marine boundary layer clouds (e.g., deep frontal clouds) is uncertain given a
 2306 lack of observations.

2307 Satellite retrievals described by Barker et al. [1996] suggest that $\nu > 1$ in overcast conditions
 2308 and $\nu \sim 1$ (corresponding to an exponential distribution) in broken stratocumulus. The model
 2309 assumes a constant $\nu = 1$ for simplicity.

2310 A major advantage of using gamma functions to represent sub-grid variability of cloud water
 2311 is that the grid-average microphysical process rates can be derived in a straightforward manner
 2312 as follows. For any generic local microphysical process rate $M_p = x q_c''^y$, replacing q_c'' with $P(q_c'')$
 2313 from 4.158 and integrating over the PDF yields a mean in-cloud process rate

$$M_p' = x \frac{\Gamma(\nu + y)}{\Gamma(\nu) \nu^y} q_c'^y \quad (4.159)$$

2314 Thus, each cloud water microphysical process rate in 4.156 and 4.157 is multiplied by a factor

$$E = \frac{\Gamma(\nu + y)}{\Gamma(\nu) \nu^y} \quad (4.160)$$

2315 Diagnostic treatment of precipitation

2316 As described by Ghan and Easter [1992], diagnostic treatment of precipitation allows for a longer
 2317 time step, since prognostic precipitation is constrained by the Courant criterion for sedimenta-
 2318 tion. Furthermore, the neglect of horizontal advection of precipitation in the diagnostic approach
 2319 is reasonable given the large grid spacing (~ 100 km) and long time step (~ 15 -40 min) of GCMs.
 2320 A unique aspect of this scheme is the diagnostic treatment of both precipitation mixing ratio
 2321 q_p and number concentration N_p . Considering only the vertical dimension, the grid-scale time
 2322 rates of change of q_p and N_p are:

$$\frac{\partial q_p}{\partial t} = \frac{1}{\rho} \frac{\partial(V_q \rho q_p)}{\partial z} + S_q \quad (4.161)$$

$$\frac{\partial N_p}{\partial t} = \frac{1}{\rho} \frac{\partial(V_N \rho N_p)}{\partial z} + S_N \quad (4.162)$$

2323 where z is height, V_q and V_N are the mass- and number-weighted terminal fallspeeds, respec-
 2324 tively, and S_q and S_N are the grid-mean source/sink terms for q_p and N_p , respectively:

$$S_q = \left(\frac{\partial q_p}{\partial t}\right)_{auto} + \left(\frac{\partial q_p}{\partial t}\right)_{accw} + \left(\frac{\partial q_p}{\partial t}\right)_{acci} + \left(\frac{\partial q_p}{\partial t}\right)_{het} + \left(\frac{\partial q_p}{\partial t}\right)_{hom} + \left(\frac{\partial q_p}{\partial t}\right)_{mlt} + \left(\frac{\partial q_p}{\partial t}\right)_{mult} + \left(\frac{\partial q_p}{\partial t}\right)_{evap} + \left(\frac{\partial q_p}{\partial t}\right)_{coll} \quad (4.163)$$

$$S_N = \left(\frac{\partial N_p}{\partial t}\right)_{auto} + \left(\frac{\partial N_p}{\partial t}\right)_{het} + \left(\frac{\partial N_p}{\partial t}\right)_{hom} + \left(\frac{\partial N_p}{\partial t}\right)_{mlt} + \left(\frac{\partial N_p}{\partial t}\right)_{evap} + \left(\frac{\partial N_p}{\partial t}\right)_{self} + \left(\frac{\partial N_p}{\partial t}\right)_{coll} \quad (4.164)$$

2325 The symbolic terms on the right-hand sides of 4.163 and 4.164 are autoconversion (subscript
 2326 auto), accretion of cloud water (subscript accw), accretion of cloud ice (subscript acci), heteroge-
 2327 neous freezing (subscript het), homogeneous freezing (subscript hom), melting (subscript mlt),
 2328 ice multiplication via rime splintering (subscript mult; qp only), evaporation (subscript evap),
 2329 and self-collection (subscript self; collection of rain drops by other rain drops, or snow crystals
 2330 by other snow crystals; N_p only), and collection of rain by snow (subscript coll). Formulations
 2331 for these processes are described in section 3.

2332 In the diagnostic treatment, $(\partial q_p / \partial t) = 0$ and $(\partial N_p / \partial t) = 0$. This allows 4.161 and 4.162
 2333 to be expressed as a function of z only. The q_p and N_p are therefore determined by discretizing
 2334 and numerically integrating 4.161 and 4.162 downward from the top of the model atmosphere
 2335 following Ghan and Easter [1992]:

$$\rho_{a,k} V_{q,k} q_{p,k} = \rho_{a,k+1} V_{q,k+1} q_{p,k+1} + \frac{1}{2} [\rho_{a,k} S_{q,k} \delta Z_k + \rho_{a,k+1} S_{q,k+1} \delta Z_{k+1}] \quad (4.165)$$

$$\rho_{a,k} V_{N,k} N_{p,k} = \rho_{a,k+1} V_{N,k+1} N_{p,k+1} + \frac{1}{2} [\rho_{a,k} S_{N,k} \delta Z_k + \rho_{a,k+1} S_{N,k+1} \delta Z_{k+1}] \quad (4.166)$$

2336 where k is the vertical level (increasing with height, i.e., $k+1$ is the next vertical level above
 2337 k). Since $V_{q,k}$, $S_{q,k}$, $V_{N,k}$, and $S_{N,k}$ depend on $q_{p,k}$ and $N_{p,k}$, 4.165 and 4.166 must be solved by
 2338 iteration or some other method. The approach of Ghan and Easter [1992] uses values of $q_{p,k}$ and
 2339 $N_{p,k}$ from the previous time step as provisional estimates in order to calculate $V_{q,k}$, $V_{N,k}$, $S_{p,k}$,
 2340 and $S_{N,k}$. “Final” values of $q_{p,k}$ and $N_{p,k}$ are calculated from these values of $V_{q,k}$, $V_{N,k}$, $S_{q,k}$ and
 2341 $S_{N,k}$ using 4.165 and 4.166. Here we employ another method that obtains provisional values of
 2342 $q_{p,k}$ and $N_{p,k}$ from 4.165 and 4.166 assuming $V_{q,k} \sim V_{q,k+1}$ and $V_{N,k} \sim V_{N,k+1}$. It is also assumed
 2343 that all source/sink terms in $S_{q,k}$ and $S_{N,k}$ can be approximated by the values at $k+1$, except
 2344 for the autoconversion, which can be obtained directly at the k level since it does not depend
 2345 on $q_{p,k}$ or $N_{p,k}$. If there is no precipitation flux from the level above, then the provisional $q_{p,k}$
 2346 and $N_{p,k}$ are calculated using autoconversion at the k level in $S_{q,k}$ and $S_{N,k}$; $V_{q,k}$ and $V_{N,k}$ are

2347 estimated assuming newly-formed rain and snow particles have fallspeeds of 0.45 m/s for rain
 2348 and 0.36 m/s for snow.

2349 Rain and snow are considered separately, and both may occur simultaneously in supercooled
 2350 conditions (hereafter subscript p for precipitation is replaced by subscripts r for rain and s for
 2351 snow). The rain/snow particle size distributions are given by 4.150, with the shape parameter
 2352 $\mu = 0$, resulting in Marshall-Palmer (exponential) size distributions. The size distribution
 2353 parameters λ and N_0 are similarly given by 4.152 and 4.153 with $\mu = 0$. The bulk particle
 2354 density (parameter ρ in 4.152) is $\rho = 1000 \text{ kg m}^{-3}$ for rain and $\rho = 100 \text{ kg m}^{-3}$ for snow
 2355 following Reisner et al. [1998].

2356 Cloud and precipitation particle terminal fallspeeds

2357 The mass- and number-weighted terminal fallspeeds for all cloud and precipitation species are
 2358 obtained by integration over the particle size distributions with appropriate weighting by number
 2359 concentration or mixing ratio:

$$2360 \quad V_N = \frac{\int_0^\infty \left(\frac{\rho_a}{\rho_{a0}}\right)^{0.54} aD^b \phi(D) dD}{\int_0^\infty \phi(D) dD} = \frac{\left(\frac{\rho_a}{\rho_{a0}}\right)^{0.54} a\Gamma(1+b+\mu)}{\lambda^b \Gamma(\mu+1)} \quad (4.167)$$

$$2361 \quad V_q = \frac{\int_0^\infty \frac{\pi\rho}{6} \left(\frac{\rho_a}{\rho_{a0}}\right)^{0.54} aD^{b+3} \phi(D) dD}{\int_0^\infty \frac{\pi\rho}{6} D^3 \phi(D) dD} = \frac{\left(\frac{\rho_a}{\rho_{a0}}\right)^{0.54} a\Gamma(4+b+\mu)}{\lambda^b \Gamma(\mu+4)} \quad (4.168)$$

2360 where ρ^{a0} is the reference air density at 850 mb and 0 C, a and b are empirical coefficients
 2361 in the diameter-fallspeed relationship $V = aD^b$, where V is terminal fallspeed for an individual
 2362 particle with diameter D . The air density correction factor is from Heymsfield and Bansemer
 2363 (2007). V_N and V_q are limited to maximum values of 9.1 m/s for rain and 1.2 m/s for snow.
 2364 The a and b coefficients for each hydrometeor species are given in Table 2. Note that for cloud
 2365 water fallspeeds, sub-grid variability of q is considered by appropriately multiplying the V_N and
 2366 V_q by the factor E given by 4.160.

2367 Ice Cloud Fraction

2368 Several modifications have been made to the determination of diagnostic fractional cloudiness
 2369 in the simulations. The ice and liquid cloud fractions are now calculated separately. Ice and
 2370 liquid cloud can exist in the same grid box. Total cloud fraction, used for radiative transfer, is
 2371 determined assuming maximum overlap between the two.

2372 The diagnostic ice cloud fraction closure is constructed using a total water formulation of the
 2373 Slingo [1987a] scheme. There is an indirect dependence of prognostic cloud ice on the ice cloud
 2374 fraction since the in-cloud ice content is used for all microphysical processes involving ice. The
 2375 new formulation of ice cloud fraction (CF_i) is calculated using relative humidity (RH) based on
 2376 total ice water mixing ratio, including the ice mass mixing ratio (q_i) and the vapor mixing ratio
 2377 (q_v). The RH based on total ice water (RH_{ti}) is then $RH_{ti} = (q_v + q_i)/q_{sat}$ where q_{sat} is the
 2378 saturation vapor mixing ratio over ice. Because this is for ice clouds only, we do not include q_l
 2379 (liquid mixing ratio). We have tested that the inclusion of q_l does not substantially impact the
 2380 scheme (since there is little liquid present in this regime).

2381 Ice cloud fraction is then given by $CF_i = \min(1, RH_d^2)$ where

$$RH_d = \max\left(0, \frac{RH_{ti} - RH_{i_{min}}}{RH_{i_{max}} - RH_{i_{min}}}\right) \quad (4.169)$$

2382 $RH_{i_{max}}$ and $RH_{i_{min}}$ are prescribed maximum and minimum threshold humidities with re-
2383 spect to ice, set at $RH_{i_{max}}=1.1$ and $RH_{i_{min}}=0.8$. These are adjustable parameters that reflect
2384 assumptions about the variance of humidity in a grid box. The scheme is not very sensitive to
2385 $RH_{i_{min}}$. $RH_{i_{max}}$ affects the total ice supersaturation and ice cloud fraction.

2386 With $RH_{i_{max}} = 1$ and $q_i = 0$ the scheme reduces to the [Slingo \[1987a\]](#) scheme. RH_{ti} is
2387 preferred over RH in RH_d because when q_i increases due to vapor deposition, it reduces q_v , and
2388 without any precipitation or sedimentation the decrease in RH would change diagnostic cloud
2389 fraction, whereas RH_{ti} is constant.

2390 4.6.2 Radiative Treatment of Ice

2391 The simulations use a self consistent treatment of ice in the radiation code. The radiation code
2392 uses as input the prognostic effective diameter of ice from the cloud microphysics (give eq. #
2393 from above). Ice cloud optical properties are calculated based on the modified anomalous diffraction
2394 approximation (MADA), described in [Mitchell \[2000, 2002\]](#) and [Mitchell et al. \[2006a\]](#). The
2395 mass-weighted extinction (volume extinction coefficient/ice water content) and the single scattering
2396 albedo, ω_0 , are evaluated using a look-up table. For solar wavelengths, the asymmetry
2397 parameter g is determined as a function of wavelength and ice particle size and shape as de-
2398 scribed in [Mitchell et al. \[1996a\]](#) and [Nousiainen and McFarquhar \[2004\]](#) for quasi-spherical ice
2399 crystals. For terrestrial wavelengths, g was determined following [Yang et al. \[2005\]](#). An ice particle
2400 shape recipe was assumed when calculating these optical properties. The recipe is described
2401 in [Mitchell et al. \[2006b\]](#) based on mid-latitude cirrus cloud data from [Lawson et al. \[2006\]](#) and
2402 consists of 50% quasi-spherical and 30% irregular ice particles, and 20% bullet rosettes for the
2403 cloud ice (i.e. small crystal) component of the ice particle size distribution (PSD). Snow is also
2404 included in the radiation code, using the diagnosed mass and effective diameter of falling snow
2405 crystals (MG2008). For the snow component, the ice particle shape recipe was based on the
2406 crystal shape observations reported in [Lawson et al. \[2006\]](#) at -45°C : 7% hexagonal columns,
2407 50% bullet rosettes and 43% irregular ice particles.

2408 4.6.3 Formulations for the microphysical processes

2409 Activation of cloud droplets

2410 Activation of cloud droplets, occurs on a multi-modal lognormal aerosol size distribution
2411 based on the scheme of [Abdul-Razzak and Ghan \[2000a\]](#). Activation of cloud droplets oc-
2412 curs if N_c decreases below the number of active cloud condensation nuclei diagnosed as a
2413 function of aerosol chemical and physical parameters, temperature, and vertical velocity (see
2414 [Abdul-Razzak and Ghan \[2000a\]](#)), and if liquid condensate is present. We use the existing N_c
2415 as a proxy for the number of aerosols previously activated as droplets since the actual number
2416 of activated aerosols is not tracked as a prognostic variable from time step to time step (for

2417 coupling with prescribed aerosol scheme). This approach is similar to that of [Lohmann et al.](#)
2418 [\[1999\]](#).

2419 Since local rather than grid-scale vertical velocity is needed for calculating droplet activation,
2420 a sub-grid vertical velocity w_{sub} is derived from the square root of the Turbulent Kinetic Energy
2421 (TKE) following [Morrison and Pinto \[2005\]](#):

$$w_{sub} = \sqrt{\frac{2}{3}TKE} \quad (4.170)$$

2422 where TKE is defined using a steady state energy balance (eqn [17] and [28] in
2423 [Bretherton and Park \[2009b\]](#))

2424 In regions with weak turbulent diffusion, a minimum sub-grid vertical velocity of 10 cm/s
2425 is assumed. Some models use the value of w at cloud base to determine droplet activation in
2426 the cloud layer (e.g., [Lohmann et al. \[1999\]](#)); however, because of coarse vertical and horizontal
2427 resolution and difficulty in defining the cloud base height in GCMs, we apply the w_{sub} calculated
2428 for a given layer to the droplet activation for that layer. Note that the droplet number may
2429 locally exceed the number activated for a given level due to advection of Nc. Some models
2430 implicitly assume that the timescale for droplet activation over a cloud layer is equal to the
2431 model time step (e.g., [Lohmann et al. \[1999\]](#)), which could enhance sensitivity to the time step.
2432 This timescale can be thought of as the timescale for recirculation of air parcels to regions of
2433 droplet activation (i.e., cloud base), similar to the timescale for large eddy turnover; here, we
2434 assume an activation timescale of 20 min.

2435 Primary ice nucleation

2436 Ice crystal nucleation is based on [Liu et al. \[2007\]](#), which includes homogeneous freezing of
2437 sulfate competing with heterogeneous immersion freezing on mineral dust in ice clouds (with
2438 temperatures below -37°C) [[Liu and Penner, 2005](#)]. Because mineral dust at cirrus levels is very
2439 likely coated [[Wiacek and Peter, 2009](#)], deposition nucleation is not explicitly included in this
2440 work for pure ice clouds. Immersion freezing is treated for cirrus (pure ice), but not for mixed
2441 phase clouds. The relative efficiency of immersion versus deposition nucleation in mixed phase
2442 clouds is an unsettled problem, and the omission of immersion freezing in mixed phase clouds
2443 may not be appropriate (but is implicitly included in the deposition/condensation nucleation:
2444 see below). Deposition nucleation may act at temperatures lower than immersion nucleation
2445 (i.e. $T < -25^{\circ}\text{C}$) [[Field et al., 2006](#)], and immersion nucleation has been inferred to dominate
2446 in mixed phase clouds [[Ansmann et al., 2008, 2009](#); [Hoose and Kristjansson, 2010](#)]. We have
2447 not treated immersion freezing on soot because while [Liu and Penner \[2005\]](#) assumed it was an
2448 efficient mechanism for ice nucleation, more recent studies [[Kärcher et al., 2007](#)] indicate it is
2449 still highly uncertain.

2450 In the mixed phase cloud regime ($-37 < T < 0^{\circ}\text{C}$), deposition/condensation nucleation is con-
2451 sidered based on [Meyers et al. \[1992\]](#), with a constant nucleation rate for $T < -20^{\circ}\text{C}$. The
2452 [Meyers et al. \[1992\]](#) parameterization is assumed to treat deposition/condensation on dust in
2453 the mixed phase. Since it is based on observations taken at water saturation, it should include
2454 all important ice nucleation mechanisms (such as the immersion and deposition nucleation dis-
2455 cussed above) except contact nucleation, though we cannot distinguish all the specific processes.
2456 [Meyers et al. \[1992\]](#) has been shown to produce too many ice nuclei during the Mixed Phase

2457 Arctic Clouds Experiment (MPACE) by [Prenni et al. \[2007\]](#). Contact nucleation by mineral
 2458 dust is included based on [Young \[1974\]](#) and related to the coarse mode dust number. It acts in
 2459 the mixed phase where liquid droplets are present and includes Brownian diffusion as well
 2460 as phoretic forces. Hallet-Mossop secondary ice production due to accretion of drops by snow
 2461 is included following [Cotton et al. \[1986\]](#).

2462 In the [Liu and Penner \[2005\]](#) scheme, the number of ice crystals nucleated is a function of
 2463 temperature, humidity, sulfate, dust and updraft velocity, derived from fitting the results from
 2464 cloud parcel model experiments. A threshold RH_w for homogeneous nucleation was fitted as
 2465 a function of temperature and updraft velocity (see [Liu et al. \[2007\]](#), equation 6). For driving
 2466 the parameterization, the sub-grid velocity for ice (w_{sub}) is derived following equation 4.170. A
 2467 minimum of 0.2 m s^{-1} is set for ice nucleation.

2468 It is also implicitly assumed that there is some variation in humidity over the grid box. For
 2469 purposes of ice nucleation, nucleation rates for a grid box are estimated based on the ‘most
 2470 humid portion’ of the grid-box. This is assumed to be the grid box average humidity plus a
 2471 fixed value (20% RH). This implies that the ‘local’ threshold supersaturation for ice nucleation
 2472 will be reached at a grid box mean value 20% lower than the RH process threshold value. This
 2473 represents another gross assumption about the RH variability in a model grid box and is an
 2474 adjustable parameter in the scheme. In the baseline case, sulfate for homogeneous freezing is
 2475 taken as the portion of the Aitken mode particles with radii greater than 0.1 microns, and
 2476 was chosen to better reproduce observations (this too can be adjusted to alter the balance of
 2477 homogeneous freezing). The size represents the large tail of the Aitken mode. In the upper
 2478 troposphere there is little sulfate in the accumulation mode (it falls out), and almost all sulfate
 2479 is in the Aitken mode.

2480 Deposition/sublimation of ice

2481 Several cases are treated below that involve ice deposition in ice-only clouds or mixed-phase
 2482 clouds in which all liquid water is depleted within the time step. Case [1] Ice only clouds in
 2483 which $q_v > q_{vi}^*$ where q_v is the grid mean water vapor mixing ratio and q_{vi}^* is the local vapor
 2484 mixing ratio at ice saturation (q_{sat}). Case [2] is the same as case [1] ($q_v > q_{vi}^*$) but there is
 2485 existing liquid water depleted by the Bergeron-Findeisen process (*ber*). Case [3], liquid water is
 2486 depleted by the Bergeron-Findeisen process and the local liquid is less than local ice saturation
 2487 ($q_v^* \leq q_{vi}^*$). In Case [4] $q_v < q_{vi}^*$ so sublimation of ice occurs.

2488 Case [1]: If the ice cloud fraction is larger than the liquid cloud fraction (including grid
 2489 cells with ice but no liquid water), or if all new and existing liquid water in mixed-phase clouds
 2490 is depleted via the Bergeron-Findeisen process within the time step, then vapor depositional
 2491 ice growth occurs at the expense of water vapor. In the case of a grid cell where ice cloud
 2492 fraction exceeds liquid cloud fraction, vapor deposition in the pure ice cloud portion of the cell
 2493 is calculated similarly to eq. [21] in MG08:

$$\left(\frac{\partial q_i}{\partial t}\right)_{dep} = \frac{(q_v - q_{vi}^*)}{\Gamma_p \tau}, q_v > q_{vi}^* \quad (4.171)$$

2494 where $\Gamma_p = 1 + \frac{L_s}{c_p} \frac{dq_{vi}}{dT}$ is the psychrometric correction to account for the release of latent
 2495 heat, L_s is the latent heat of sublimation, c_p is the specific heat at constant pressure, $\frac{dq_{vi}}{dT}$ is the
 2496 change of ice saturation vapor pressure with temperature, and τ is the supersaturation relaxation

2497 timescale associated with ice deposition given by eq. [22] in MG08 (a function of ice crystal
 2498 surface area and the diffusivity of water vapor in air). The assumption for pure ice clouds is
 2499 that the in-cloud vapor mixing ratio for deposition is equal to the grid-mean value. The same
 2500 assumption is used in Liu et al. [2007], and while it is uncertain, it is the most straightforward.
 2501 Thus we do not consider sub-grid variability of water vapor for calculating vapor deposition in
 2502 pure ice-clouds.

2503 The form of the deposition rate in equation 4.171 differs from that used by Rotstayn et al.
 2504 [2000] and Liu et al. [2007] because they considered the increase in ice mixing ratio q_i due
 2505 to vapor deposition during the time step, and formulated an implicit solution based on this
 2506 consideration (see eq. [6] in Rotstayn et al. [2000]). However, these studies did not consider
 2507 sinks for the ice due to processes such as sedimentation and conversion to precipitation when
 2508 formulating their implicit solution; these sink terms may partially (or completely) balance the
 2509 source for the ice due to vapor deposition. Thus, we use a simple explicit forward-in-time
 2510 solution that does not consider changes of q_i within the microphysics time step.

Case [2]: When all new and existing liquid water is depleted via the Bergeron-Findeisen
 process (*ber*) within the time step, the vapor deposition rate is given by a weighted average of
 the values for growth in mixed phase conditions prior to the depletion of liquid water (first term
 on the right hand side) and in pure ice clouds after depletion (second term on the right hand
 side):

$$\left(\frac{\partial q_i}{\partial t}\right)_{dep} = \frac{q_c^*}{\Delta t} + \left(1 - \frac{q_c^*}{\Delta t} \left(\frac{\partial q_i}{\partial t}\right)_{ber}^{-1}\right) \left(\frac{(q_v^* - q_{vi}^*)}{\Gamma_p \tau}\right), q_v > q_{vi}^* \quad (4.172)$$

2511 where q_c^* is the sum of existing and new liquid condensate mixing ratio, Δt is the model
 2512 time step, $\left(\frac{\partial q_i}{\partial t}\right)_{ber}$ is the ice deposition rate in the presence of liquid water (i.e., assuming vapor
 2513 mixing ratio is equal to the value at liquid saturation) as described above, and q_v^* is an average
 2514 of the grid-mean vapor mixing ratio and the value at liquid saturation.

2515 Case [3]: If $q_v^* \leq q_{vi}^*$ then it is assumed that no additional ice deposition occurs after
 2516 depletion of the liquid water. The deposition rate in this instance is given by:

$$\left(\frac{\partial q_i}{\partial t}\right)_{dep} = \left(\frac{q_c^*}{\Delta t}\right), q_v^* \leq q_{vi}^* \quad (4.173)$$

2517 Case [4]: Sublimation of pure ice cloud occurs when the grid-mean water vapor mixing ratio
 2518 is less than value at ice saturation. In this case the sublimation rate of ice is given by:

$$\left(\frac{\partial q_i}{\partial t}\right)_{sub} = \frac{(q_v - q_{vi}^*)}{\Gamma_p \tau}, q_v < q_{vi}^* \quad (4.174)$$

2519 Again, the use of grid-mean vapor mixing ratio in equation 4.174 follows the assumption
 2520 of Liu et al. [2007] that the in-cloud q_v is equal to the grid box mean in pure ice clouds. Grid-
 2521 mean deposition and sublimation rates are given by the in-cloud values for pure ice or mixed-
 2522 phase clouds described above, multiplied by the appropriate ice or mixed-phase cloud fraction.
 2523 Finally, ice deposition and sublimation are limited to prevent the grid-mean mixing ratio from
 2524 falling below the value for ice saturation in the case of deposition and above this value in the
 2525 case of sublimation.

2526 Cloud water condensation and evaporation are given by the bulk closure scheme within the
 2527 cloud macrophysics scheme, and therefore not described here.

2528 Conversion of cloud water to rain

2529 Autoconversion of cloud droplets and accretion of cloud droplets by rain is given by a version
 2530 of the [Khairoutdinov and Kogan \[2000\]](#) scheme that is modified here to account for sub-grid
 2531 variability of cloud water within the cloudy part of the grid cell as described previously in section
 2532 2.1. Note that the Khairoutdinov and Kogan scheme was originally developed for boundary layer
 2533 stratocumulus, but is applied here to all stratiform cloud types.

2534 The grid-mean autoconversion and accretion rates are found by replacing the q_c in Eqs.
 2535 (29) and (33) of [Khairoutdinov and Kogan \[2000\]](#) with $P(q_c'')$ given by equation 4.158 here,
 2536 integrating the resulting expressions over the cloud water PDF, and multiplying by the cloud
 2537 fraction. This yields

$$\left(\frac{\partial q_c}{\partial t}\right)_{auto} = -F_{cld} \frac{\Gamma(\nu + 2.47)}{\Gamma(\nu)\nu^{2.47}} 1350 q_c'^{2.47} N_c'^{-1.79} \quad (4.175)$$

$$\left(\frac{\partial q_c}{\partial t}\right)_{accr} = -F_{cld} \frac{\Gamma(\nu + 1.15)}{\Gamma(\nu)\nu^{1.15}} 67 (q_c' q_r')^{1.15} \quad (4.176)$$

2538 The changes in q_r due to autoconversion and accretion are given by $(\partial q_r / \partial t)_{auto} =$
 2539 $-(\partial q_c / \partial t)_{auto}$ and $(\partial q_r / \partial t)_{accr} = -(\partial q_c / \partial t)_{accr}$. The changes in N_c and N_r due to autocon-
 2540 version and accretion $(\partial N_c / \partial t)_{auto}$, $(\partial N_r / \partial t)_{auto}$, $(\partial N_c / \partial t)_{accr}$, are derived from Eqs. (32) and
 2541 (35) in [Khairoutdinov and Kogan \[2000\]](#). Since accretion is nearly linear with respect to q_c , sub-
 2542 grid variability of cloud water is much less important for accretion than it is for autoconversion.

2543 Note that in the presence of a precipitation flux into the layer from above, new drizzle drops
 2544 formed by cloud droplet autoconversion would be accreted rapidly by existing precipitation
 2545 particles (rain or snow) given collection efficiencies near unity for collision of drizzle with rain
 2546 or snow (e.g., [Pruppacher and Klett \[1997\]](#)). This may be especially important in models with
 2547 low vertical resolution, since they cannot resolve the rapid growth of precipitation that occurs
 2548 over distances much less than the vertical grid spacing. Thus, if the rain or snow mixing ratio
 2549 in the next level above is greater than 10-6 g kg⁻¹, we assume that autoconversion produces an
 2550 increase in rain mixing ratio but not number concentration (since the newly-formed drops are
 2551 assumed to be rapidly accreted by the existing precipitation). Otherwise, autoconversion results
 2552 in a source of both rain mixing ratio and number concentration.

2553 Conversion of cloud ice to snow

2554 The autoconversion of cloud ice to form snow is calculated by integration of the cloud ice
 2555 mass- and number-weighted size distributions greater than some specified threshold size, and
 2556 transferring the resulting mixing ratio and number into the snow category over some specified
 2557 timescale, similar to [Ferrier \[1994\]](#). The grid-scale changes in q_i and N_i due to autoconversion
 2558 are

$$\left(\frac{\partial q_i}{\partial t}\right)_{auto} = -F \frac{\pi \rho_i N_{0i}}{6\tau_{auto}} \left[\frac{D_{cs}^3}{\lambda_i} + \frac{3D_{cs}^2}{\lambda_i^2} + \frac{6D_{cs}}{\lambda_i^3} + \frac{6D}{\lambda_i^4} \right] \exp^{-\lambda_i D_{cs}} \quad (4.177)$$

$$\left(\frac{\partial N_i}{\partial t}\right)_{auto} = -F \frac{N_{0i}}{\lambda_i \tau_{auto}} \exp^{-\lambda_i D_{cs}} \quad (4.178)$$

2559 where $D_{cs} = 200 \mu\text{m}$ is the threshold size separating cloud ice from snow, ρ_i is the bulk
 2560 density of cloud ice, and $\tau_{auto} = 3 \text{ min}$ is the assumed autoconversion timescale. Note that this
 2561 formulation assumes the shape parameter $\mu = 0$ for the cloud ice size distribution; different
 2562 formulation must be used for other values of μ . The changes in q_s and N_s due to autoconversion
 2563 are given by $(\partial q_s / \partial t)_{auto} = -(\partial q_i / \partial t)_{auto}$ and $(\partial N_s / \partial t)_{auto} = -(\partial N_i / \partial t)_{auto}$.

2564 Accretion of q_i and N_i by snow $(\partial q_i / \partial t)_{accs}$, $(\partial N_i / \partial t)_{accs}$, $(\partial q_s / \partial t)_{acci}$, and $(\partial q_s / \partial t)_{acci} =$
 2565 $-(\partial q_i / \partial t)_{accs}$, are given by the continuous collection equation following [Lin et al. \[1983\]](#), which
 2566 assumes that the fallspeed of snow \gg cloud ice fallspeed. The collection efficiency for collisions
 2567 between cloud ice and snow is 0.1 following [Reisner et al. \[1998\]](#). Newly- formed snow particles
 2568 formed by cloud ice autoconversion are not assumed to be rapidly accreted by existing snowflakes,
 2569 given aggregation efficiencies typically much less than unity (e.g., [Field et al. \[2007\]](#)).

2570 Other collection processes

2571 The accretion of q_c and N_c by snow $(\partial q_c / \partial t)_{accs}$, $(\partial N_c / \partial t)_{accs}$, and $(\partial q_s / \partial t)_{accw} = -(\partial q_c / \partial t)_{accs}$
 2572 are given by the continuous collection equation. The collection efficiency for droplet-snow col-
 2573 lisions is a function of the Stokes number following [Thompson et al. \[2004\]](#) and thus depends
 2574 on droplet size. Self-collection of snow, $(\partial N_s / \partial t)_{self}$ follows [Reisner et al. \[1998\]](#) using an as-
 2575 sumed collection efficiency of 0.1. Self-collection of rain $(\partial N_r / \partial t)_{self}$ follows [Beheng \[1994\]](#).
 2576 Collisions between rain and cloud ice, cloud droplets and cloud ice, and self-collection of cloud
 2577 ice are neglected for simplicity. Collection of q_r and N_r by snow in subfreezing conditions,
 2578 $(\partial q_r / \partial t)_{coll} = -(\partial q_s / \partial t)_{coll}$ and $(\partial N_r / \partial t)_{coll}$, is given by [Ikawa and Saito \[1990\]](#) assuming col-
 2579 lection efficiency of unity.

2580 Freezing of cloud droplets and rain and ice multiplication

2581 Heterogeneous freezing of cloud droplets and rain to form cloud ice and snow, respectively,
 2582 occurs by immersion freezing following [Bigg \[1953\]](#), which has been utilized in previous micro-
 2583 physics schemes (e.g., [Reisner et al. \[1998\]](#), see Eq. A.22, A.55, A.56; [Morrison et al. \[2005\]](#);
 2584 [Thompson et al. \[2008\]](#)). Here the freezing rates are integrated over the mass- and number-
 2585 weighted cloud droplet and rain size distributions and the impact of sub-grid cloud water vari-
 2586 ability is included as described previously. Homogeneous freezing of cloud droplets to form cloud
 2587 ice occurs instantaneously at -40°C . All rain is assumed to freeze instantaneously at -5°C .

2588 Contact freezing of cloud droplets by mineral dust is included based on [Young \[1974\]](#) and
 2589 related to the coarse mode dust number. It acts in the mixed phase where liquid droplets are
 2590 present and includes Brownian diffusion as well as phoretic forces. Hallet-Mossop ice multi-
 2591 plication (secondary ice production) due to accretion of drops by snow is included following
 2592 [Cotton et al. \[1986\]](#). This represents a sink term for snow mixing ratio and source term for
 2593 cloud ice mixing ratio and number concentration.

2594 Melting of cloud ice and snow

2595 For simplicity, detailed formulations for heat transfer during melting of ice and snow are not
 2596 included. Melting of cloud ice occurs instantaneously at 0°C . Melting of snow occurs instan-
 2597 taneously at $+2^\circ\text{C}$. We have tested the sensitivity of both single- column and global results

2598 to changing the specified snow melting temperature from +2° to 0°C and found no significant
 2599 changes.

2600 **Evaporation/sublimation of precipitation**

2601 Evaporation of rain and sublimation of snow, $(\partial q_s/\partial t)_{evap}$ and $(\partial q_r/\partial t)_{evap}$, are given by dif-
 2602 fusional mass balance in subsaturated conditions Lin et al. [1983], including ventilation effects.
 2603 Evaporation of precipitation occurs within the region of the grid cell containing precipitation
 2604 but outside of the cloudy region. The fraction of the grid cell with evaporation of precipitation
 2605 is therefore F_{pre} , where F_{pre} is the precipitation fraction. F_{pre} is calculated assuming maximum
 2606 cloud overlap between vertical levels, and neglecting tilting of precipitation shafts due to wind
 2607 shear ($F_{pre} = F_{cld}$ at cloud top). The out-of-cloud water vapor mixing ratio is given by

$$q_{clr} = \frac{q_v - F_{cld}q_s(T)}{1 - F_{cld}}, F_{cld} < 1 \quad (4.179)$$

2608 where $q_s(T)$ is the in-cloud water vapor mixing ratio after bulk condensation/evaporation of
 2609 cloud water and ice as described previously. As in the older CAM3 microphysics parameteri-
 2610 zation, condensation/deposition onto rain/snow is neglected. Following Morrison et al. [2005],
 2611 the evaporation/sublimation of N_r and N_s , $(\partial N_r/\partial t)_{evap}$ and $(\partial N_s/\partial t)_{evap}$, is proportional to
 2612 the reduction of q_r and q_s during evaporation/sublimation.

2613 **Sedimentation of cloud water and ice**

2614 The time rates of change of q and N for cloud water and cloud ice due to sedimentation,
 2615 $(\partial q_c/\partial t)_{sed}$, $(\partial q_i/\partial t)_{sed}$, $(\partial N_c/\partial t)_{sed}$, and $(\partial N_i/\partial t)_{sed}$, are calculated with a first-order forward-
 2616 in-time-backward-in-space scheme. Numerical stability for cloud water and ice sedimentation is
 2617 ensured by sub-stepping the time step, although these numerical stability issues are insignificant
 2618 for cloud water and ice because of the low terminal fallspeeds ($\ll 1$ m/s). We assume that the
 2619 sedimentation of cloud water and ice results in evaporation/sublimation when the cloud fraction
 2620 at the level above is larger than the cloud fraction at the given level (i.e., a sedimentation
 2621 flux from cloudy into clear regions), with the evaporation/condensate rate proportional to the
 2622 difference in cloud fraction between the levels.

2623 **Convective detrainment of cloud water and ice**

2624 The ratio of ice to total cloud condensate detrained from the convective parameterizations, F_{det} ,
 2625 is a linear function of temperature between -40° C and -10° C; $F_{det} = 1$ at $T < -40^\circ$ C, and F_{det}
 2626 = 0 at $T > -10^\circ$ C. Detrainment of number concentration is calculated by assuming a mean
 2627 volume radius of 8 and 32 micron for droplets and cloud ice, respectively.

2628 **Numerical considerations**

2629 To ensure conservation of both q and N for each species, the magnitudes of the various sink terms
 2630 are reduced if the provisional q and N are negative after stepping forward in time. This approach
 2631 ensures critical water and energy balances in the model, and is similar to the approach employed
 2632 in other bulk microphysics schemes (e.g., Reisner et al. [1998]). Inconsistencies are possible

2633 because of the separate treatments for N and q , potentially leading to unrealistic mean cloud and
2634 precipitation particle sizes. For consistency, N is adjusted if necessary so that mean (number-
2635 weighted) particle diameter () remains within a specified range of values for each species.
2636 Limiting to a maximum mean diameter can be thought of as an implicit parameterization of
2637 particle breakup.

2638 For the diagnostic precipitation, the source terms for q and N at a given vertical level are
2639 adjusted if necessary to ensure that the vertical integrals of the source terms (from that level to
2640 the model top) are positive. In other words, we ensure that at any given level, there isnt more
2641 precipitation removed (both in terms of mixing ratio and number concentration) than is available
2642 falling from above (this is also the case in the absence of any sources/sinks at that level). This
2643 check and possible adjustment of the precipitation and cloud water also ensures conservation
2644 of the total water and energy. Our simple adjustment procedure to ensure conservation could
2645 potentially result in sensitivity to time step, although as described in section 3, time truncation
2646 errors are minimized with appropriate sub-stepping.

2647 Melting rates of cloud ice and snow are limited so that the temperature of the layer does not
2648 decrease below the melting point (i.e., in this instance an amount of cloud ice or snow is melted
2649 so that the temperature after melting is equal to the melting point). A similar approach is
2650 applied to ensure that homogeneous freezing does increase the temperature above homogeneous
2651 freezing threshold.

2652 4.7 Cloud Macrophysics

2653 Cloud macrophysics is a suite of physical processes that computes (1) cloud fractions in each
2654 layer, (2) horizontal and vertical overlapping structures of clouds, (3) net conversion rates of
2655 water vapor into cloud condensates. Cloud macrophysics is a process unique for GCM that
2656 handles partial cloud fraction. In case of cloud resolving model, for example, cloud fraction in
2657 each layer is either 0 or 1, and so there is no need to use special treatment for cloud overlap
2658 and partial condensation. Along with convection scheme, correct setting of cloud macrophysics
2659 is essential for developing a seamless GCM across the various sizes of horizontal GCM grid.

2660 Cloud macrophysics sets a stage for cloud droplet activation and nucleation, cloud micro-
2661 physics (i.e., processes controlling conversion from sustained to falling hydrometeors), wet
2662 scavenging of aerosols, radiative transfer, and moist turbulent processes. Cloud macrophysics in
2663 CAM3/CAM4 (cloud macrophysics in CAM3 is nearly identical to the cloud macrophysics in
2664 CAM4) was constructed to be compatible with and to some degrees to compensate for the in-
2665 complete CAM3/CAM4 physics package. For example, (1) without a need to do explicit droplet
2666 nucleation and activation processes due to the prescribed cloud droplet radius, CAM3/CAM4
2667 simply assume zero supersaturation within ice stratus, (2) without the information of realistic
2668 in-cumulus condensate from shallow and deep convection schemes, CAM3/CAM4 assumes that
2669 in-cumulus condensate is identical to in-stratus condensate, and (3) without cloud-radiation-
2670 turbulence interaction in the dry PBL scheme, CAM3/CAM4 uses additional stability-based
2671 stratus fraction as well as RH-based stratus fraction to simulate marine stratocumulus over the
2672 subtropical, mid-latitude and Arctic oceans. With the new CAM5 physics addressing these lim-
2673 itations in the CAM3/CAM4 physics, cloud macrophysics should also be revised for consistency
2674 among various model physics. Here, we document the revised cloud macrophysics in CAM5.
2675 Additional details on CAM5's cloud macrophysics are discussed in [Park et al. \[2010\]](#).

2676 In the following sections, we will document how CAM5 computes (1) cloud fractions - deep
2677 cumulus fraction, shallow cumulus fraction, and stratus (liquid and ice separately) fractions,
2678 (2) horizontal and vertical overlapping structures of clouds, and (3) net condensation rates of
2679 water vapor into cloud liquid and ice.

2680 4.7.1 Cloud Fractions

2681
2682 Cloud fraction is a volume containing hydrometeors sustained in the atmosphere. In CAM5,
2683 two types of clouds exist: *stratus* and *cumulus*. In nature, these two clouds can be identified
2684 by their shapes and turbulent properties. Stratus is horizontally extended with symmetric
2685 turbulence properties: fractional area, strength of vertical velocity, vertical extent, and degree
2686 of saturation within updraft are similar to those within downdraft. On the other hand, cumulus
2687 is vertically stretched with asymmetric turbulence properties: updraft is narrow, strong, and
2688 usually saturated while compensating subsidence is broad, weak, and unsaturated. In CAM5,
2689 moist turbulence scheme is designed to simulate symmetric turbulences while convection schemes
2690 are for simulating asymmetric turbulences. While there is an attempt to treat these two distinct
2691 turbulences in a unified way, we stick to the more convective approach.

2692 **Deep Cumulus Fraction**

2693

Similar to CAM3/CAM4, CAM5 computes deep cumulus fraction $a_{dp,cu}$ using the following empirical formula.

$$a_{dp,cu} = k_{1,dp} \cdot \log_e(1 + \cdot k_2 M_{dp,cu}), \quad a_{dp,cu} = \max(0, \min(a_{dp,cu}, 0.6)) \quad (4.180)$$

2694 where $k_{1,dp}$ is an adjustable parameter given in Appendix C, $k_2 = 675$ and $M_{dp,cu}$ is convective
 2695 updraft mass flux [$kg \cdot m^{-2} \cdot s^{-1}$] from deep convection scheme. When identified to be active,
 2696 $M_{dp,cu}$ is non-zero from the lowest model layer to the cumulus top. With no further attempt to
 2697 separate dry and moist deep convection, Eqn.(4.180) can generate *empty* (without in-cumulus
 2698 condensate) deep convective cloud fraction in the layers below the Lifting Condensation Level
 2699 (LCL). In contrast to stratus fraction that will be discussed later, we compute a single deep
 2700 cumulus fraction not the separate liquid and ice deep cumulus fractions. We impose a constraint
 2701 that $a_{dp,cu}$ is always smaller than 0.6.

2702 Originally, this empirical formula was obtained by including not only cumulus but also
 2703 stratus generated by detrained cumulus condensate, which by construction results in overesti-
 2704 mated cumulus fraction. Thus, we are using a freedom to change the two coefficients 0.04 and
 2705 675 to simulate convective updraft fractional area only. Currently these coefficients are also
 2706 used as tuning parameters to obtain reasonable regional/global radiation budget and grid-mean
 2707 LWC/IWC.

2708 **Shallow Cumulus Fraction**

2709

In contrast to CAM3/CAM4, CAM5's new shallow convection scheme (Park and Bretherton,
 2009) computes vertical velocity as well as mass flux within cumulus updraft. Thus, shallow
 cumulus fraction $a_{sh,cu}$ in CAM5 is directly computed using the definition of convective updraft
 mass flux:

$$a_{sh,cu} = 2 \cdot \left[\mathcal{C} M_{sh,cu} \rho \cdot w_{u,cu} \right], \quad a_{sh,cu} = \max(0, \min(a_{sh,cu}, 0.2)) \quad (4.181)$$

2710 where $M_{sh,cu}$ is shallow convective mass flux within cumulus updraft [$kg \cdot m^{-2} \cdot s^{-1}$], ρ is density
 2711 [$kg \cdot m^{-3}$] and $w_{u,cu}$ is vertical velocity within cumulus updraft [$m \cdot s^{-1}$]. Note that a factor
 2712 2 is multiplied by considering the difference between *core* (e.g., positively buoyant saturated
 2713 portions) updraft fractional area and saturated updraft fractional area estimated from the LES.
 2714 The details on how to compute $M_{sh,cu}$ and $w_{u,cu}$ are described in Park and Bretherton [2009].
 2715 This $a_{sh,cu}$ is computed from the LCL of cumulus updraft (or PBL top if LCL is within the
 2716 PBL) to the cumulus top where updraft vertical velocity is zero. So, $a_{sh,cu}$ always contains
 2717 positive cumulus condensate, that is, there is no empty shallow cumulus clouds. Similar to deep
 2718 cumulus fraction, we compute a single shallow cumulus fraction not the separate liquid and ice
 2719 shallow cumulus fractions. We impose a constraint that $a_{sh,cu}$ is always smaller than 0.2.

2720 **Liquid Stratus Fraction**

2721

2722 In CAM3/CAM4, stratus fraction was parameterized as a sum of *RH – based* and
 2723 *Stability – based* cloud fractions. The latter was necessary because the dry PBL scheme in
 2724 CAM3/CAM4 cannot moisten upper portion of stratocumulus-topped PBL due to its inability
 2725 to simulate cloud-radiation-turbulence interactions.

The RH-based stratus fraction in CAM3/CAM4 is a quadratic function of grid-mean RH ([Slingo \[1987b\]](#), [Rasch and Kristjansson \[1998b\]](#)).

$$a_{st} = \left[\mathcal{C}U - U_c 1 - U_c \right]^2 \quad (4.182)$$

where U is grid-mean RH defined using saturation specific humidity over a mixture of cloud water and ice where mixing fraction is a function of temperature, and U_c is a critical RH. Stratus is formed only when U is larger than U_c . Note that CAM3/CAM4 diagnoses a single stratus fraction not the separate liquid and ice stratus fractions in contrast to CAM5. While simple to use, above Eqn.(4.182) has two shortcomings. First, at the limit of $a_{st} \rightarrow 1$, we expect that RH in the clear portion (U_r) approaches to 1 in nature. However, Eqn.(4.182) does not satisfy this condition unless $U_c \rightarrow 1$ as shown below:

$$\lim_{a_{st} \rightarrow 1} U_r = \lim_{a_{st} \rightarrow 1} \left[\mathcal{C}(1 - U_c) \sqrt{a_{st}} + U_c - a_{st} 1 - a_{st} \right] = 0.5 \cdot (1 + U_c) \quad (4.183)$$

Second, Eqn.(4.182) is not derived from the explicit subgrid scale distributions of total specific humidity, making it hard to impose internal consistency between stratus fraction and in-stratus condensate. Following [Smith \[1990\]](#), liquid stratus fraction in CAM5 is derived from the assumed triangular distribution of total relative humidity, $v = q_{t,l}/q_{s,w}$ where $q_{t,l}$ is total liquid specific humidity ($=q_v + q_l$) and $q_{s,w}$ is saturation specific humidity over water. Then liquid stratus fraction $a_{l,st}$ becomes a function of grid-mean RH over water, U_l ([Park et al. \[2010\]](#)).

$$a_{l,st} = \begin{cases} 1 & \text{if } U_l \geq \hat{U}_l, \\ 1 - \left[\mathcal{C}3\sqrt{2} \cdot \left(\mathcal{C}\hat{U}_l - U_l \hat{U}_l - U_{cl} \right) \right]^{2/3} & \text{if } \mathcal{C}16 \cdot (5 + U_{cl}) \leq U_l \leq \hat{U}_l, \\ 4 \cdot \cos \left[\mathcal{C}13 \cdot \left\{ \arccos \left(\mathcal{C}32 \cdot \sqrt{2} \cdot \left(\mathcal{C}U_l - U_{cl} \hat{U}_l - U_{cl} \right) \right) - 2 \cdot \pi \right\} \right] & \text{if } U_{cl} \leq U_l \leq \mathcal{C}16 \cdot (5 + U_{cl}), \\ 0 & \text{if } U_l \leq U_{cl}, \end{cases} \quad (4.184)$$

2726 where \hat{U}_l is RH within liquid stratus ($=1$) and U_{cl} is critical RH that liquid stratus is formed
 2727 when U_l is larger than U_{cl} . We can easily check $\lim_{a_{l,st} \rightarrow 1} RH_r = 1$. For a given $U_l \geq U_{cl}$, CAM5
 2728 (Eqn.(4.184)) produces less stratus fraction than CAM3/CAM4 (Eqn.(4.182)). In addition,
 2729 the sensitivity of liquid stratus fraction to the changes of grid-mean RH differs between the two
 2730 models.

2731 Note that $U_{cl} = 1 - \Delta v$ where Δv is the half-width of the triangular distribution. Ideally,
 2732 subgrid-scale variability Δv should be internally computed by considering all sources of subgrid-
 2733 scale motions from individual physical processes - moist turbulence, detrainment of convective
 2734 condensate, meso-scale organizations, gravity waves induced by convection or surface inhomogeneity,
 2735 and etc. In CAM5, however, U_{cl} is externally specified as a function of height and
 2736 surface properties and being used as a tuning parameter. We chose $U_{cl} = 0.89$ in the layers

below 700 hPa (Low-Level Stratus) but $U_{cl} = 0.79$ over lands when a water-equivalent snow depth is less than 10^{-6} [m], $U_{cl} = 0.80$ in the layers above 400 hPa (High-Level Stratus), and a linearly-interpolated U_{cl} between 700 hPa and 400 hPa (Mid-Level Stratus).

In principle, LWC within the liquid stratus can be diagnosed from the assumed triangular PDF (Smith [1990], Park et al. [2010]). However, CAM5 uses a separate prognostic condensation scheme for liquid stratus condensation similar to CAM3/CAM4. This (diagnostic cloud fraction but separate prognostic condensation for liquid stratus) can cause inconsistency between stratus fraction and in-stratus cloud condensate. We perform additional pseudo condensation-evaporation process to remove this inconsistency as will be discussed later.

Ice Stratus Fraction

2747

In CAM3/CAM4, a single stratus fraction a_{st} was diagnosed using a mean saturation specific humidity $q_s = \alpha \cdot q_{s,w} + (1 - \alpha) \cdot q_{s,i}$ where $q_{s,w}$ and $q_{s,i}$ are saturation specific humidities over water and ice, respectively, and $0 \leq \alpha \leq 1$ is a function of temperature. In CAM5, however, we separately diagnose ice stratus fraction $a_{i,st}$ using a modified Slingo's formula as below (Gettelman et al. [2010a]).

$$a_{i,st} = \left[\mathcal{C}U_i - U_{ci}\hat{U}_i - U_{ci} \right]^2 \quad (4.185)$$

$$U_i = \left[\mathcal{C}q_v + q_i q_{s,i} \right]$$

where U_i is grid-mean total RH *including ice condensate* defined over ice, and \hat{U}_i is RH within ice stratus. In contrast to liquid condensation that always occurs whenever $q_v > q_{s,w}$, ice nucleation and ice growth processes are not spontaneous and very slow. Thus, the linkage between ice saturation excess $s = q_v - q_{s,i}$ and the amount of ice condensate is weak. Eqn.(4.185) is an attempt to address these properties of ice processes: supersaturation within ice stratus is taken into account by using $\hat{U}_i > 1$, and by including ice condensate in the definition of U_i , ice condensate as well as ice saturation excess contributes to ice stratus fraction. In CAM5, we chose $\hat{U}_i = 1.1$ and $U_{ci} = 0.80$ regardless of heights and the properties of the Earth surface.

4.7.2 Cloud Overlaps

2757

We have computed 4 independent cloud fractions ($0 \leq a_{l,st}, a_{i,st} \leq 1$, $0 \leq a_{sh,cu} \leq 0.2$, $0 \leq a_{dp,cu} \leq 0.6$) in each layer. The performance of individual physical processes is sensitive how these clouds are distributed in the horizontal plane and vertical column. For example, if $a_{l,st}$ and $a_{i,st}$ are maximally-overlapped (non-overlapped) in the horizontal, Bergeron-Findeisen conversion process from cloud liquid droplet to ice crystal will be active (inactive). If cumulus preferentially grows into the pre-existing stratus (clear portions), cumulus will detrain convective condensate into the pre-existing stratus (clear portions) without (with) evaporation. We can also easily expect that the vertical profiles of grid-mean radiative flux, evaporation of precipitation, activation and wet deposition of aerosols are sensitive to the vertical overlapping structures of various clouds. Given the 2-moment stratiform microphysics in CAM5, correct simulations

2768 of activation and wet deposition of aerosols become even more important. So, parameterization
 2769 of cloud overlapping structures is as important as the parameterization of individual cloud frac-
 2770 tions. Ideally, all physics schemes should use a single consistent cloud overlapping structure. In
 2771 this section, we describe the horizontal and vertical overlapping structures of clouds in CAM5.

2772 Horizontal Overlap

2773

In CAM5, we assume that (1) shallow and deep cumulus fractions are non-overlapped with each other, (2) liquid and ice stratus fractions are maximally overlapped, i.e., $a_{st} = \max(a_{l,st}, a_{i,st})$, and (3) stratus only fills the non-cumulus areas, i.e., a higher occupancy priority is given to the cumulus over stratus in each layer. Stratiform microphysics in CAM5 assumes that stratus LWC/IWC is uniformly distributed over the single stratus fraction a_{st} even though further elaboration is possible. The third assumption above comes from distinct turbulent properties in each clouds: cumulus updraft is strong and grows vertically, and so, if there are any pre-existing stratus on its path, cumulus updraft will push out the pre-existing stratus and occupy the original portion. The assumed horizontal overlapping structure between cumulus and stratus determines the *physical* stratus fractions. If a is each of 4 cloud fractions computed in the previous section, the physical cloud fraction A of each cloud fraction a becomes

$$A_{sh,cu} = a_{sh,cu} \leq 0.2 \quad (4.186)$$

$$A_{dp,cu} = a_{dp,cu} \leq 0.6$$

$$A_{cu} = A_{sh,cu} + A_{dp,cu} \leq 0.8$$

$$A_{l,st} = (1 - A_{cu}) \cdot a_{l,st} \leq 1$$

$$A_{i,st} = (1 - A_{cu}) \cdot a_{i,st} \leq 1$$

$$A_{st} = \max(A_{l,st}, A_{i,st}) \leq 1$$

$$A_{net} = A_{st} + A_{cu} \leq 1$$

2774 where U_l and U_i in Eqs.(4.184) and (4.185) are now changed to the mean RH averaged over the
 2775 non-cumulus areas in each layer. In CAM5, state variables saved into the standard physical state
 2776 arrays are the mean values averaged over the non-cumulus areas, that is, environmental mean
 2777 not the grid mean. These physical cloud fractions A are passed into various physics schemes
 2778 following the cloud macrophysics.

2779 Vertical Overlap

2780

2781 In CAM5, the following physical processes make use of vertical overlap assumption of clouds:
 2782 (a) deep and shallow convection schemes to compute evaporation of convective precipitations,
 2783 (b) stratiform microphysics to compute production and evaporation of stratiform precipitation,
 2784 (c) activation and wet scavenging of aerosols by convective and stratiform precipitations, and
 2785 (d) radiation scheme. While computations of cloud fractions and horizontal cloud overlaps
 2786 are substantially revised, CAM5's vertical cloud overlap is similar to CAM3/CAM4, which is
 2787 summarized below.

2788 (a) CAM5's deep and shallow convection schemes assume that convective precipitation area
2789 is always 1 if convective precipitation flux is positive. In reality, however, if vertical shear
2790 of horizontal winds is neglected, most of the convective precipitation is likely to fall into the
2791 saturated cumulus updraft not into clear portions. Thus, CAM5's vertical cumulus overlap may
2792 overestimate evaporation of convective precipitation, leading to excessive water vapor in the
2793 atmosphere.

2794 (b) CAM5's stratiform microphysics assumes that stratus fraction a_{st} is maximally over-
2795 lapped in vertical regardless of vertical separation distance, and stratiform precipitation area is
2796 the same as maximum stratus fraction in the layers above the current layer as long as precipita-
2797 tion flux is positive. In reality, however, precipitation falling into clear portion can be completely
2798 evaporated, so that precipitation area can be smaller than the maximum stratus fraction in the
2799 layers above.

2800 (c) CAM5's cloud droplet activation routine assumes maximum overlap of stratus fraction
2801 between any adjacent layers. CAM5 computes wet scavenging of aerosols by two processes. The
2802 first is the scavenging of activated aerosols within cloud droplets by the production of precipita-
2803 tion. The second is the scavenging of the remaining non-activated aerosols by the precipitation
2804 flux. These two processes are separately applied for each convective and stratiform precipi-
2805 tations. For the purpose of wet scavenging of aerosols, CAM5 assumes that (1) convective (
2806 stratiform) precipitation area at any height is a sum of cumulus (stratus) fractions in the layers
2807 above weighted by the ratio of net production rate of convective (stratiform) precipitation in
2808 each layer to the vertically integrated net production rate of convective (stratiform) precipi-
2809 tation from the top layer to the layer just above the current layer, and (2) in computing wet
2810 scavenging of non-activated aerosols, precipitation flux area at the top interface of each layer is
2811 randomly overlapped with the cloud fraction. The second assumption allows CAM5 to bypass
2812 the computation of complex overlapping areas between precipitation flux and cloud fractions.

2813 (d) CAM5's radiation scheme computes one single cloud fraction and in-cloud LWC/IWC
2814 in each layer by combining deep and shallow cumulus and stratus cloud properties through a
2815 simple cloud area weighting. Then, it assumes a maximum vertical overlap in each of the 3
2816 regimes representing lower ($p > 700$ hPa), middle ($400 \text{ hPa} < p < 700 \text{ hPa}$), and upper ($p <$
2817 400 hPa) atmospheres, and a random vertical overlap between these 3 regimes. This generates
2818 a set of sub-columns in which cloud fraction is either 1 or 0 in each layer. By averaging each
2819 sub-column's radiative heating rate, it computes grid-mean radiative heating rate.

2820 In principle, all the above 4 processes should use the identical vertical cloud overlapping
2821 structure. Due to the contrasting natures of turbulences, cumulus and stratus are likely to
2822 have different vertical cloud overlap. If vertical shear of horizontal winds is neglected, cumulus
2823 fractions are likely to be maximally overlapped over the entire depth of convective updrafts. On
2824 the other hand, vertical distance over which stratus is maximally overlapped is likely to be much
2825 smaller than the cumulus. Simultaneous treatment of different vertical overlapping structures
2826 of cumulus and stratus and implementation of the single unified vertical cloud overlap into the
2827 CAM is one of the future development plans.

2828 4.7.3 Condensation Processes

2829
2830 This section describes how much water vapor is converted into cloud condensates. This

2831 process differs from the conversion of cloud droplet into precipitation, which is treated by the
 2832 cloud microphysics.

2833 Stratus Liquid

2834
 2835 Similar to CAM3/4 (Zhang et al. [2003a]), CAM5 uses prognostic condensation scheme
 2836 for liquid stratus condensate. The fundamental assumption used for computing grid-mean net
 2837 condensation rate of water vapor into liquid stratus droplet (Q) is that (1) RH over the water
 2838 within the liquid stratus is always 1, and (2) no liquid stratus droplet exists in the clear portion
 2839 outside of the liquid stratus fraction. These two conditions will be called *saturation equilibrium*
 2840 of liquid stratus. Whenever any GCM grid is perturbed by external forcings, the system always
 2841 tries to restore the saturation equilibrium state. This allows us to compute the grid-mean
 2842 net condensation rate of water vapor into liquid stratus condensate for a given set of external
 2843 forcings. The details of liquid stratus condensation is described in Park et al. [2010].

Let's assume that one GCM grid layer is in saturation equilibrium state at a certain moment.
 During the model time step Δt , the layer is perturbed by external forcings (e.g., stratiform
 microphysics, radiation, moist turbulence, large-scale advection, and convections). In order to
 restore saturation equilibrium, Q should be initiated within the layer. The changes of grid-mean
 liquid stratus condensate $\bar{q}_{l,st} = A_{l,st} \cdot \hat{q}_{l,st}$ during Δt is the sum of grid-mean net condensate
 rate Q and the grid-mean external forcings of liquid condensates \bar{F}_l :

$$Q = \dot{\bar{q}}_{l,st} - \bar{F}_l = A_{l,st} \cdot \dot{\hat{q}}_{l,st} + c \cdot \hat{q}_{l,st} \cdot \dot{A}_{l,st} - \bar{F}_l \quad (4.187)$$

2844 where $0 \leq c \leq 1$ is the ratio of in-cloud condensate of newly formed or dissipated stratus to the
 2845 in-cloud condensate of pre-existing stratus. The $\dot{\phi}$ denotes time-tendency of ϕ . If liquid stratus
 2846 has homogeneous condensate, it will be $c = 1$, but it is likely that $c < 1$ in nature since stratus
 2847 has non-homogeneous condensate in general. In CAM5, we use $c = 0.1$.

From the two assumptions for saturation equilibrium of liquid stratus, we can derive the
 following simultaneous linear equations (Park et al. [2010]).

$$a_{11} \cdot \dot{\bar{q}}_{l,st} + a_{12} \cdot \dot{A}_{l,st} = b_1 \quad (4.188)$$

$$a_{21} \cdot \dot{\bar{q}}_{l,st} + a_{22} \cdot \dot{A}_{l,st} = b_2$$

where individual coefficients a_{ij} and b_i are

$$a_{11} = \gamma \cdot A_{l,st} \quad (4.189)$$

$$a_{12} = G + \gamma \cdot c \cdot \hat{q}_{l,st}$$

$$a_{21} = \alpha + (CL_v C_p) \cdot \hat{\beta} \cdot A_{l,st}$$

$$a_{22} = (CL_v C_p) \cdot \hat{\beta} \cdot c \cdot \hat{q}_{l,st}$$

$$b_1 = \alpha \cdot \dot{\bar{q}}_{t,all} - \beta \cdot \dot{\bar{T}}_{l,all} - G \cdot a_{l,st} \cdot \dot{a}_{cu}$$

$$b_2 = \alpha \cdot \dot{\hat{q}}_{t,all} - \beta \cdot \dot{\bar{T}}_{l,all}$$

with

$$\begin{aligned}
\alpha &= [\mathcal{C}1q_{s,w}] & (4.190) \\
\beta &= \mathcal{C}\bar{q}_v q_{s,w}^2 \cdot (\mathcal{C}\partial q_{s,w}\partial T) \\
\hat{\beta} &= \alpha \cdot (\mathcal{C}\partial q_{s,w}\partial T) \\
\gamma &= \alpha + \mathcal{C}L_v C_p \cdot \beta \\
G &= \mathcal{C}11 - a_{cu} \cdot (\mathcal{C}\partial a_{l,st}\partial \bar{U}_e)^{-1}
\end{aligned}$$

and

$$\dot{\bar{q}}_{l,all} = \dot{\bar{q}}_{v,adv} + \dot{\bar{q}}_{l,adv} + \dot{\bar{q}}_{v,mic} + \dot{\bar{q}}_{l,mic} \quad (4.191)$$

$$\dot{\bar{T}}_{l,all} = \dot{\bar{T}}_{adv} + \dot{\bar{T}}_{mic} - \mathcal{C}L_v C_p \cdot (\dot{\bar{q}}_{l,adv} + \dot{\bar{q}}_{l,mic}) \quad (4.192)$$

$$\dot{\hat{q}}_{l,all} = \dot{\hat{q}}_{v,adv} + \dot{\hat{q}}_{l,adv} + \dot{\hat{q}}_{l,mic} \quad (4.193)$$

$$\dot{\hat{q}}_{l,mic} = [\mathcal{C}\dot{\hat{q}}_{l,mic} \max(A_{l,st}, A_{i,st})] \quad (4.194)$$

2848 where $\dot{\bar{\phi}}$ denotes local time-tendency, subscript *all* denotes all the processes except cloud macro-
2849 physics, which is the sum of cloud microphysics (subscript *mic*) and the other processes denoted
2850 by subscript *adv*. In Eqn.(4.194), we used $\max(A_{l,st}, A_{i,st})$ instead of $A_{l,st}$ since stratiform mi-
2851 crophysics is formulated based on a single stratus fraction, $\max(A_{l,st}, A_{i,st})$. Above formulation
2852 was derived assuming that temperature is uniform within the grid, and stratiform microphysics
2853 does not change water vapor within the liquid stratus, and all forcings except stratiform micro-
2854 physics are uniformly applied into the grid. Using $A_{l,st}$ from Eqn.(4.184) and (4.186), we can
2855 compute Q if \bar{F}_l is given.

2856 Although the computation of Q explicitly makes use of $A_{l,st}$, the updated $\bar{q}_{l,st}(t + \Delta t)$ is not
2857 necessarily consistent with the updated $A_{l,st}(t + \Delta t)$. For example, it can be $\bar{q}_{l,st}(t + \Delta t) = 0$
2858 but $A_{l,st}(t + \Delta t) > 0$ (so called *empty cloud*) or $\bar{q}_{l,st}(t + \Delta t) > 0$ but $A_{l,st}(t + \Delta t) = 0$ (
2859 so called *infinitely dense cloud*). This inconsistency between stratus fraction and in-stratus
2860 condensate comes from the combined use of prognostic stratiform condensation and diagnostic
2861 stratus fraction schemes with a finite model intergation time step Δt . In order to prevent
2862 these unreasonable situations, we additionally condensate water vapor or evaporate stratus
2863 liquid droplets until the *in-stratus LWC*, $\hat{q}_{l,st}(t + \Delta t)$ falls within the externally specified ranges,
2864 $0.02 \leq \hat{q}_{l,st}(t + \Delta t) [g \cdot kg^{-1}] \leq 3$. Note that this *pseudo condensation – evaporation* process
2865 does not change the grid-mean liquid stratus condensate and is not performed if $\bar{q}_{l,st}(t + \Delta t) = 0$
2866 and $A_{l,st}(t + \Delta t) = 0$ at the beginning.

2867 CAM5 is using two moment stratiform microphysics and so prognoses not only the mass
2868 but also the number concentration of cloud droplets. When net condensation occurs ($Q > 0$),
2869 cloud macrophysics does not change droplet number concentration, but when net evaporation
2870 occurs ($Q < 0$), droplet number concentration is reduced in proportion to the decrease of the
2871 mass of stratus liquid droplets. Regardless of the sign of Q , however, droplet activation process
2872 within stratus is additionally performed at the beginning of cloud microphysics at each time
2873 step. Thus, cloud droplet number is consistently generated when $Q > 0$ in the initially clear
2874 layer.

2875 Stratus Ice

2876

2877 In contrast to liquid stratus, we cannot assume a certain equilibrium state for ice stratus
2878 because ice process is much slower than the liquid process. Thus, deposition-sublimation rate
2879 between water vapor and ice crystals are computed using an explicit process algorithm.

2880

2881 In CAM5, deposition of water vapor into ice crystals (this is a separate process from the
2882 Bergeron-Findeisen conversion of cloud liquid droplets into ice crystals) only occurs when ice
2883 stratus exists at temperature lower than 273.15K. In case of pure ice stratus, in-cloud water vapor
2884 is set to the grid-mean water vapor. If in-cloud water vapor is larger than the saturation water
2885 vapor over ice, water vapor is deposited into ice crystals. In case of mixed-phase stratus, in-
2886 cloud water vapor is set to the equal weighting average of grid-mean water vapor and saturation
2887 water vapor over water. In this case, however, direct deposition of water vapor into ice crystals
2888 occurs only after pre-existing cloud liquid droplets are completely depleted into ice crystals by
2889 Bergeron-Findeisen process. That is, if Bergeron-Findeisen process is not strong enough to
2890 deplete pre-existing cloud liquid droplets, no direct deposition occurs from the water vapor into
2891 ice crystals. Sublimation of ice crystals into water vapor occurs regardless of temperature as
2892 long as water vapor within the ice stratus is smaller than the saturation water vapor over the
2893 pre-existing ice crystals.

2894

2895 A constraint is imposed such that direct deposition of water vapor into ice crystals does not
2896 reduce grid-mean RH over ice below 1. Additional constraint is imposed such that sublimation
2897 should not exceed the available ice crystals and not increase grid-mean RH over ice above 1.
2898 See [Gettelman et al. \[2010a\]](#) and the chapter for cloud microphysics for additional details.

2897 Condensation within Shallow Cumulus Updraft

2898

2899 Condensation within shallow cumulus updraft is described in [Park and Bretherton \[2009\]](#).
2900 Shallow convective updraft rises from the PBL top but condensation occurs from the LCL.
2901 If LCL is lower than PBL top, condensation is assumed to occur from the PBL top. During
2902 ascent, convective updraft experiences adiabatic cooling, mixing with environmental airs, and
2903 precipitation fallout. Vertical evolutions of two conservative scalars $q_t = q_v + q_l + q_i$, $\theta_c =$
2904 $\theta - (L_v/C_p/\pi) \cdot q_l - (L_s/C_p/\pi) \cdot q_i$ within convective updraft are explicitly computed using the
2905 parameterized entrainment mixing and precipitation processes. From the computed q_t, θ_c and
2906 saturation specific humidity q_s defined as a weighting average of the values over water $q_{s,w}$ and
2907 ice $q_{s,i}$ (the weighting factor is a function of temperature), we compute condensate amount
2908 within convective updraft. Since shallow convective cloud fraction $a_{sh,cu}$ is non-zero from the
2909 LCL (or PBL top if LCL is below the PBL) to the cumulus top, shallow cumulus does not
2910 have any empty clouds.

2911

2912 Within shallow convection scheme, condensate is partitioned into liquid and ice as a ramping
2913 function of temperature between 248K and 268K. However, a separate re-partitioning is per-
2914 formed for convective detrainment (as a ramping function of temperature between 238.15K and
2915 268.15K) and for radiative treatment of in-cumulus condensate (in this case, the repartitioning
2916 function is the same as that of stratiform condensate). When shallow convective condensate is

2916 detrained into the environment, we assume a fixed droplet radius of 8 and 25 $[\mu \cdot m]$ for liquid
2917 and ice condensates, respectively.

2918 **Condensation within Deep Cumulus Updraft**

2919
2920 Condensates within deep convective updraft is computed in a similar way as shallow convec-
2921 tive updraft. When deep convective condensate is detrained into the environment, we assume
2922 a fixed droplet radius of 10 and 50 $[\mu \cdot m]$ for liquid and ice condensates, respectively. See the
2923 chapter for deep convection for additional details.

4.8 Aerosols

Two different modal representations of the aerosol were implemented in CAM5. A 7-mode version of the modal aerosol model (MAM-7) serves as a benchmark for the further simplification. It includes Aitken, accumulation, primary carbon, fine dust and sea salt and coarse dust and sea salt modes (4.3). Within a single mode, for example the accumulation mode, the mass mixing ratios of internally-mixed sulfate, ammonium, secondary organic aerosol (SOA), primary organic matter (POM) aged from the primary carbon mode, black carbon (BC) aged from the primary carbon mode, sea salt, and the number mixing ratio of accumulation mode particles are predicted. Primary carbon (OM and BC) particles are emitted to the primary carbon mode and aged to the accumulation mode due to condensation of H_2SO_4 , NH_3 and SOA (gas) and coagulation with Aitken and accumulation mode (see section below).

Aerosol particles exist in different attachment states. We mostly think of aerosol particles that are suspended in air (either clear or cloudy air), and these are referred to as interstitial aerosol particles. Aerosol particles can also be attached to (or contained within) different hydrometeors, such as cloud droplets. In CAM5, the interstitial aerosol particles and the aerosol particles in stratiform cloud droplets¹ (referred to as cloud-borne aerosol particles) are both explicitly predicted, as in Easter et al. [2004]. The interstitial aerosol particle species are stored in the q array of the state variable and are transported in 3 dimensions. The cloud-borne aerosol particle species are stored in the $qqcw$ array of the physics buffer and are not transported (except for vertical turbulent mixing), which saves computer time but has little impact on their predicted values Ghan and Easter [2006].

Aerosol water mixing ratio associated with interstitial aerosol for each mode is diagnosed following Kohler theory (see water uptake below), assuming equilibrium with the ambient relative humidity. It also is not transported in 3 dimensions, and is held in the $qaerwat$ array of the physics buffer.

The size distributions of each mode are assumed to be log-normal, with the mode dry or wet radius varying as number and total dry or wet volume change, and standard deviation prescribed as given in 4.3. The total number of transported aerosol species is 31 for MAM-7. The transported gas species are SO_2 , H_2O_2 , DMS, H_2SO_4 , NH_3 , and SOA (gas).

For long-term (multiple century) climate simulations a 3-mode version of MAM (MAM-3) is also developed which has only Aitken, accumulation and coarse modes (4.4). For MAM-3 the following assumptions are made: (1) primary carbon is internally mixed with secondary aerosol by merging the primary carbon mode with the accumulation mode; (2) the coarse dust and sea salt modes are merged into a single coarse mode based on the assumption that the dust and sea salt are geographically separated. This assumption will impact dust loading over the central Atlantic transported from Sahara desert because the assumed internal mixing between dust and sea salt there will increase dust hygroscopicity and thus wet removal; (3) the fine dust and sea salt modes are similarly merged with the accumulation mode; and (4) sulfate is partially neutralized by ammonium in the form of NH_4HSO_4 , so ammonium is effectively prescribed and NH_3 is not simulated. We note that in MAM-3 we predict the mass mixing ratio of sulfate

¹Note that the explicitly-predicted cloud-borne aerosol particles are for stratiform clouds only, and thus are stratiform-cloud-borne aerosol particles. The convective-cloud-borne aerosol particles in deep and shallow convective clouds are not treated explicitly, and are prescribed as a fraction of the interstitial aerosol particles when calculating wet removal.

2964 aerosol in the form of NH_4HSO_4 while in MAM-7 it is in the form of SO_4 . The total number of
2965 transported aerosol tracers in MAM-3 is 15.

2966 4.8.1 Emissions

2967 Anthropogenic (defined here as originating from industrial, domestic and agriculture activity
2968 sectors) emissions are from the [Lamarque et al. \[2010a\]](#) IPCC AR5 emission data set. Emissions
2969 of black carbon (BC) and organic carbon (OC) represent an update of [Bond et al. \[2007\]](#) and
2970 [Junker and Lioussé \[2008\]](#). Emissions of sulfur dioxide are an update of [Smith et al. \[2001, 2004\]](#).

2971 The IPCC AR5 emission data set includes emissions for anthropogenic aerosols and precursor
2972 gases: SO_2 , primary OM (POM), and BC. However, it does not provide injection heights and
2973 size distributions of primary emitted particles and precursor gases for which we have followed
2974 the AEROCOM protocols [[Dentener et al., 2006a](#)]. We assumed that 2.5% by molar of sulfur
2975 emissions are emitted directly as primary sulfate aerosols and the rest as SO_2 [[Dentener et al.,](#)
2976 [2006a](#)]. Sulfur from agriculture, domestic, transportation, waste, and shipping sectors is emitted
2977 at the surface while sulfur from energy and industry sectors is emitted at 100-300 m above the
2978 surface, and sulfur from forest fire and grass fire is emitted at higher elevations (0-6 km). Sulfate
2979 particles from agriculture, waste, and shipping (surface sources), and from energy, industry,
2980 forest fire and grass fire (elevated sources) are put in the accumulation mode, and those from
2981 domestic and transportation are put in the Aitken mode. POM and BC from forest fire and
2982 grass fire are emitted at 0-6 km, while those from other sources (domestic, energy, industry,
2983 transportation, waste, and shipping) are emitted at surface. Injection height profiles for fire
2984 emissions are derived from the corresponding AEROCOM profiles, which vary spatially and
2985 temporally. Mass emission fluxes for sulfate, POM and BC are converted to number emission
2986 fluxes for Aitken and accumulation mode at surface or at higher elevations based on AEROCOM
2987 prescribed lognormal size distributions as summarized in Table 4.1.

2988 The IPCC AR5 data set also does not provide emissions of natural aerosols and precursor
2989 gases: volcanic sulfur, DMS, NH_3 , and biogenic volatile organic compounds (VOCs). Thus AE-
2990 ROCOM emission fluxes, injection heights and size distributions for volcanic SO_2 and sulfate and
2991 for DMS flux at surface are used. The emission flux for NH_3 is prescribed from the MOZART-4
2992 data set [[Emmons, 2010](#)]. Emission fluxes for isoprene, monoterpenes, toluene, big alkenes, and
2993 big alkanes, which are used to derive SOA (gas) emissions (see below), are prescribed from the
2994 MOZART-2 data set [[Horowitz, 2003](#)]. These emissions represent late 1990's conditions. For
2995 years prior to 2000, we use anthropogenic non-methane volatile organic compound (NMVOC)
2996 emissions from IPCC AR5 data set and scale the MOZART toluene, bigene, and big alkane
2997 emissions by the ratio of year-of-interest NMVOC emissions to year 2000 NMVOC emissions.

2998 The emission of sea salt aerosols from the ocean follows the parameterization by
2999 [Martensson et al. \[2003\]](#) for aerosols with geometric diameter $< 2.8 \mu\text{m}$. The total particle
3000 flux F_0 is described by

$$\frac{dF_0}{d\log D_p} = \Phi W = (A_k T_w + B_k) W \quad (4.195)$$

3001 where D_p is the particle diameter, T_w is the water temperature and A_k and B_k are coefficients
3002 dependent on the size interval. W is the white cap area:

$$W = 3.84 \times 10^{-4} U_{10}^{3.41} \quad (4.196)$$

3003 where U_{10} is the wind speed at 10 m. For aerosols with a geometric diameter $> 2.8 \mu\text{m}$, sea
3004 salt emissions follow the parameterization by [Monahan et al. \[1986\]](#)

$$\frac{dF_0}{d\log r} = 1.373 U_{10}^{3.41} r^{-3} (1 + 0.0057 r^{1.05}) \times 10^{1.19 e^{-B^2}} \quad (4.197)$$

3005 where r is the radius of the aerosol at a relative humidity of 80% and $B = (0.380 - \log r) / 0.650$.
3006 All sea salt emissions fluxes are calculated for a size interval of $d\log D_p = 0.1$ and then summed
3007 up for each modal size bin. The cut-off size range for sea salt emissions in MAM-7 is 0.02-0.08
3008 (Aitken), 0.08-0.3 (accumulation), 0.3-1.0 (fine sea salt), and 1.0-10 μm (coarse sea salt); for
3009 MAM-3 the range is 0.02-0.08 (Aitken), 0.08-1.0 (accumulation), and 1.0-10 μm (coarse).

3010 Dry, unvegetated soils, in regions of strong winds generate soil particles small enough to
3011 be entrained into the atmosphere, and these are referred to here at desert dust particles. The
3012 generation of desert dust particles is calculated based on the Dust Entrainment and Deposition
3013 Model, and the implementation in the Community Climate System Model has been described
3014 and compared to observations [[Mahowald et al., 2006a,b](#); [Yoshioka et al., 2007](#)]. The only change
3015 to the CAM5 source scheme from the previous studies is the increase in the threshold for leaf area
3016 index for the generation of dust from 0.1 to 0.3 m^2/m^2 , to be more consistent with observations
3017 of dust generation in more productive regions [[Okin, 2008](#)]. The cut-off size range for dust
3018 emissions is 0.1-2.0 μm (fine dust) and 2.0-10 μm (coarse dust) for MAM-7; and 0.1-1.0 μm
3019 (accumulation), and 1.0-10 μm (coarse) for MAM-3.

3020 4.8.2 Chemistry

3021 Simple gas-phase chemistry is included for sulfate aerosol. This includes (1) DMS oxidation with
3022 OH and NO_3 to form SO_2 ; (2) SO_2 oxidation with OH to form H_2SO_4 (gas); (3) H_2O_2 production
3023 ($\text{HO}_2 + \text{HO}_2$); and (4) H_2O_2 loss (H_2O_2 photolysis and $\text{H}_2\text{O}_2 + \text{OH}$). The rate coefficients for these
3024 reactions are provided from the MOZART model [[Emmons, 2010](#)]. Oxidant concentrations (O_3 ,
3025 OH, HO_2 , and NO_3) are temporally interpolated from monthly averages taken from MOZART
3026 simulations [[Lamarque et al., 2010a](#)].

3027 SO_2 oxidation in bulk cloud water by H_2O_2 and O_3 is based on the MOZART treatment
3028 [[Tie et al., 2001](#)]. The pH value in the bulk cloud water is calculated from the electroneutral-
3029 ity equation between the bulk cloud-borne SO_4 and NH_4 ion concentrations (summation over
3030 modes), and ion concentrations from the dissolution and dissociation of trace gases based on the
3031 Henry's law equilibrium. Irreversible uptake of H_2SO_4 (gas) to cloud droplets is also calculated
3032 [[Seinfeld and Pandis, 1998](#)]. The sulfate produced by SO_2 aqueous oxidation and H_2SO_4 (gas)
3033 uptake is partitioned to the cloud-borne sulfate mixing ratio in each mode in proportion to the
3034 cloud-borne aerosol number of the mode (i.e., the cloud droplet number associated with each
3035 aerosol mode), by assuming droplets associated with each mode have the same size. For MAM-7,
3036 changes to aqueous NH_4 ion from dissolution of NH_3 (g) are similarly partitioned among modes.
3037 SO_2 and H_2O_2 mixing ratios are at the same time reduced due to aqueous phase consumption.

4.8.3 Secondary Organic Aerosol

The simplest treatment of secondary organic aerosol (SOA), which is used in many global models, is to assume fixed mass yields for anthropogenic and biogenic precursor VOC's, then directly emit this mass as primary aerosol particles. MAM adds one additional step of complexity by simulating a single lumped gas-phase SOA (gas) species. Fixed mass yields for five VOC categories of the MOZART-4 gas-phase chemical mechanism are assumed, as shown in Table 4.2. These yields have been increased by an additional 50% for the purpose of reducing aerosol indirect forcing by increasing natural aerosols. The total yielded mass is emitted as the SOA (gas) species. MAM then calculates condensation/evaporation of the SOA (gas) to/from several aerosol modes. The condensation/evaporation is treated dynamically, as described later. The equilibrium partial pressure of SOA (gas), over each aerosol mode m is expressed in terms of Raoult's Law as:

$$P_m^* = \left(\frac{A_m^{SOA}}{A_m^{SOA} + 0.1A_m^{POA}} \right) P^0 \quad (4.198)$$

where A_m^{SOA} is SOA mass concentration in mode m , A_m^{POA} is the primary organic aerosol (POA) mass concentration in mode m (10% of which is assumed to be oxygenated), and P^0 is the mean saturation vapor pressure of SOA whose temperature dependence is expressed as:

$$P^0(T) = P^0(298K) \times \exp\left[-\frac{\Delta H_{vap}}{R} \left(\frac{1}{T} - \frac{1}{298}\right)\right] \quad (4.199)$$

where $P^0(298K)$ is assumed at 1×10^{-10} atm and the mean enthalpy of vaporization ΔH_{vap} is assumed at 156 kJ mol⁻¹.

Treatment of the gaseous SOA and explicit condensation/evaporation provides (1) a realistic method for calculating the distribution of SOA among different modes and (2) a minimal treatment of the temperature dependence of the gas/aerosol partitioning.

4.8.4 Nucleation

New particle formation is calculated using parameterizations of binary H₂SO₄-H₂O homogeneous nucleation, ternary H₂SO₄-NH₃-H₂O homogeneous nucleation, and boundary layer nucleation. A binary parameterization [Vehkamaki et al., 2002] is used in MAM-3, which does not predict NH₃, while a ternary parameterization [Merikanto et al., 2007] is used in MAM-7. The boundary layer parameterization, which is used in both versions, uses the empirical 1st order nucleation rate in H₂SO₄ from Sihto et al. [2006], with a first order rate coefficient of 1.0×10^{-6} s⁻¹ as in Wang et al. [2009]. The new particles are added to the Aitken mode, and we use the parameterization of Kerminen and Kulmala [2002] to account for loss of the new particles by coagulation as they grow from critical cluster size to Aitken mode size.

4.8.5 Condensation

Condensation of H₂SO₄ vapor, NH₃ (MAM-7 only), and the SOA (gas) to various modes is treated dynamically, using standard mass transfer expressions [Seinfeld and Pandis, 1998] that

3071 are integrated over the size distribution of each mode [Binkowski and Shankar, 1995]. An ac-
3072 commodation coefficient of 0.65 is used for H_2SO_4 [Poschl et al., 1998], and currently, for the
3073 other species too. H_2SO_4 and NH_3 condensation are treated as irreversible. NH_3 uptake stops
3074 when the NH_4/SO_4 molar ratio of a mode reaches 2. SOA (gas) condensation is reversible, with
3075 the equilibrium vapor pressure over particles given by Eq. (4.296).

3076 In MAM-7, condensation onto the primary carbon mode produces aging of the parti-
3077 cles in this mode. Various treatments of the aging process have been used in other models
3078 [Cooke and Wilson, 1996; Wilson et al., 2001; Liu et al., 2005; Riemer et al., 2003]. In CAM5
3079 a criterion of 3 mono-layers of sulfate is used to convert a fresh POM/BC particle to the aged
3080 accumulation mode. Using this criterion, the mass of sulfate required to age all the particles
3081 in the primary carbon mode, $M_{\text{SO}_4, \text{age-all}}$, is computed. If $M_{\text{SO}_4, \text{cond}}$ condenses on the mode
3082 during a time step, we assume that a fraction $f_{\text{age}} = M_{\text{SO}_4, \text{cond}} / M_{\text{SO}_4, \text{age-all}}$ has been aged.
3083 This fraction of the POM, BC, and number in the mode is transferred to the accumulation
3084 mode, along with the condensed soluble species. SOA is included in the aging process. The
3085 SOA that condenses in a time step is scaled by its lower hygroscopicity to give a condensed SO_4
3086 equivalent.

3087 The two continuous growth processes (condensation and aqueous chemistry) can result in
3088 Aitken mode particles growing to a size that is nominally within the accumulation mode size
3089 range. Most modal aerosol treatments thus transfer part of the Aitken mode number and mass
3090 (those particles on the upper tail of the distribution) to the accumulation mode after calculating
3091 continuous growth [Easter et al., 2004].

3092 4.8.6 Coagulation

3093 Coagulation of the Aitken, accumulation, and primary carbon modes is treated. Coagulation
3094 within each of these modes reduces number but leaves mass unchanged. For coagulation of
3095 Aitken with accumulation mode and of primary-carbon with accumulation mode, mass is trans-
3096 ferred from Aitken or primary-carbon mode to the accumulation mode. For coagulation of
3097 Aitken with primary-carbon mode in MAM-7, Aitken mass is first transferred to the primary-
3098 carbon mode. This ages some of the primary-carbon particles. An aging fraction is calculated as
3099 with condensation, then the Aitken mass and the aged fraction of the primary-carbon mass and
3100 number are transferred to the accumulation mode. Coagulation rates are calculated using the
3101 fast/approximate algorithms of the Community Multiscale Air Quality (CMAQ) model, version
3102 4.6.

3103 4.8.7 Water Uptake

3104 Water uptake is based on the equilibrium Kohler theory [Ghan and Zaveri, 2007] using the rel-
3105 ative humidity and the volume mean hygroscopicity for each mode to diagnose the wet volume
3106 mean radius of the mode from the dry volume mean radius. The hygroscopicity of each com-
3107 ponent is listed in Table 4.3. The hygroscopicities here are equivalent to the κ parameters of
3108 Petters and Kreidenweis [2007]. Note that the measured solubility of dust varies widely, from
3109 0.03 to 0.26 [Koehler et al., 2009a].

Table 4.1: Size distributions of primary emissions.

Emission Source	Geometric standard deviation, s_g	Number mode diameter, $D_{gn}(\mu\text{m})$	$D_{emit}(\mu\text{m})^1$
BC/OM			
Forest fire/grass fire	1.8	0.080	0.134
Domestic/energy/industry/transportation/shipping/waste	See note ²	See note ²	0.134
SO ₄			
Forest fire/grass fire/waste	1.8	0.080	0.134
Energy/industry/shipping	See note ³	See note ³	0.261
Domestic/transportation	1.8	0.030	0.0504
Continuous volcano, 50% in Aitken mode	1.8	0.030	0.0504
Continuous volcano, 50% in accum. mode	1.8	0.080	0.134

¹Demit is volume-mean diameter = $D_{gn} \exp(1.5 \times \ln(s_g)^2)$ used in number emissions as $E_{number} = E_{mass}/(\pi/6 \times \rho D_{emit}^3)$

²This value is intermediate between the [Dentener et al. \[2006a\]](#) $D_{emit} = 0.0504m$ and [Liu et al. \[2005\]](#) $D_{emit} = 0.206m$.

³Adapted from [Stier et al. \[2005\]](#) where 50% of mass goes to accumulation mode with $D_{emit} = 0.207m$, and 50% goes to coarse mode with $D_{emit} = 3.08m$. We put all mass in accumulation mode, and $D_{emit} = 0.261m$ gives same number emissions as [Stier et al. \[2005\]](#). [[Dentener et al. \[2006a\]](#) put all in coarse mode with $D_{emit} = 2.06m$]

Table 4.2: Assumed SOA (gas) yields

Species	Mass yield	Reference
Big Alkanes	5%	Lim and Ziemann [2005]
Big Alkenes	5%	assumed
Toluene	15%	Odum et al. [1997]
Isoprene	4%	Kroll et al. [2006]
Monoterpenes	25%	Ng et al. [2007]

Table 4.3: Hygroscopicity of aerosol components

Seasalt	sulfate	nitrate	ammonium	SOA	POM	BC	dust
1.16	0.507	0.507	0.507	0.14	0.10	10^{-10}	0.068

3110 4.8.8 Subgrid Vertical Transport and Activation/Resuspension

3111 The vertical transport of interstitial aerosols and trace gases by deep convective clouds, using
3112 updraft and downdraft mass fluxes from the Zhang-McFarlane parameterization, is described in
3113 [Collins et al. \[2004a\]](#). Currently this vertical transport is calculated separately from wet removal,
3114 but a more integrated treatment is planned. Cloud-borne aerosols, which are associated with
3115 large-scale stratiform cloud, are assumed to not interact with the convective clouds. Vertical
3116 transport by shallow convective clouds is treated similarly, using mass fluxes from the shallow
3117 convection parameterization. Turbulent transport of the aerosol is given a special treatment with
3118 respect to other tracers. To strengthen the coupling between turbulent transport and aerosol
3119 activation in stratiform clouds, the implicit time integration scheme used for turbulent transport
3120 of heat, energy, and momentum is replaced by an explicit scheme for droplets and aerosol. A
3121 sub-timestep is calculated for each column based on the minimum turbulent transport time in
3122 the column. Turbulent transport is integrated over the sub-time steps using a forward time
3123 integration scheme.

3124 Aerosol activation converts particles from the interstitial attachment state to the cloud-
3125 borne state. In stratiform cloud, activation is treated consistently with droplet nucleation, so
3126 that the total number of particles activated and transferred to the cloud-borne state equals to
3127 the number of droplets nucleated. Activation is parameterized in terms of updraft velocity and
3128 the properties of all of the aerosol modes [[Abdul-Razzak and Ghan, 2000b](#)], with both mass
3129 and number transferred to the cloud-borne state. The updraft velocity is approximated by the
3130 square root of the turbulence kinetic energy, with a minimum value of 0.2 m s^{-1} . Activation
3131 is assumed to occur as updrafts carry air into the base of the cloud [[Ghan et al., 1997](#)] and as
3132 cloud fraction increases [[Ovtchinnikov and Ghan, 2005](#)]. In addition, activation is assumed to
3133 occur as air is continuously cycled through clouds, assuming a cloud regeneration time scale of
3134 one hour. Consider a model time step of 20 minutes, so that 1/3 of the cloud is regenerated
3135 in a time step. We essentially dissipate then reform 1/3 of cloud each time step. During
3136 dissipation, grid-cell mean cloud droplet number is reduced by 1/3, and 1/3 of the cloud-borne
3137 aerosols are resuspended and converted to the interstitial state. During regeneration, interstitial
3138 aerosols are activated in the "new" cloud, and cloud droplet number is increased accordingly.
3139 The regeneration has small impact on shallow boundary layer clouds, but it noticeably increases
3140 droplet number in deeper free-tropospheric clouds where vertical turbulence mixing is slow.
3141 Particles are resuspended as aerosol when droplets evaporate. This process is assumed to occur
3142 as droplets are transferred below or above cloud and as clouds dissipate.

3143 4.8.9 Wet Deposition

3144 Aerosol wet removal is calculated using the CAM3.5 wet removal routine [[Rasch et al., 2000](#);
3145 [Barth et al., 2000](#)] with modifications for the consistency with cloud macro- and microphysics.
3146 The routine treats in-cloud scavenging (the removal of cloud-borne aerosol particles) and below-
3147 cloud scavenging (the removal of interstitial aerosol particles by precipitation particles through
3148 impaction and Brownian diffusion).

3149 For in-cloud scavenging, the stratiform and convective cloud fraction, cloud water, and pre-
3150 cipitation production profiles are used to calculate first-order loss rate profiles for cloud-water.
3151 These cloud-water first-order loss rates are multiplied by "solubility factors" to obtain aerosol

3152 first-order loss rates, which are applied to the aerosol profiles. The solubility factors can be
3153 interpreted as (the fraction of aerosols that are in cloud drops) \times (an additional tuning factor).
3154 In CAM3.5, where the cloud-borne aerosol is not explicitly calculated, a value of 0.3 is used
3155 for solubility factors for all aerosol types and sizes. Different values are used for the MAM.
3156 The stratiform in-cloud scavenging only affects the stratiform-cloud-borne aerosol particles, and
3157 these have solubility factors of 1.0. It does not affect the interstitial aerosol particles, and these
3158 have solubility factors of 0.0.

3159 For convective in-cloud scavenging of MAM aerosols, both a solubility factor and a within-
3160 convective-cloud activation fraction are passed to the wet removal routine. For the stratiform-
3161 cloud-borne aerosol particles, there is no wet removal by convective clouds, and these factors are
3162 zero. For interstitial (with respect to stratiform cloud) aerosol, the solubility factor is 0.5, and
3163 the activation fractions are 0.0 for the primary carbon mode, 0.4 for the fine and coarse dust
3164 modes, and 0.8 for other modes. The lower values reflect lower hygroscopicity. These factors are
3165 applied to both number and mass species within each mode, with one exception. In MAM-3,
3166 different activation fractions are applied to the dust and sea salt of the coarse mode (0.4 and
3167 0.8 respectively), and a weighted average is applied to the coarse mode sulfate and number.

3168 For below-cloud scavenging, the first-order removal rate is equal to [(solubility factor) \times
3169 (scavenging coefficient) \times (precipitation rate)]. Again, the solubility factor can be viewed as
3170 a tuning factor. In CAM3.5, a solubility factor of 0.3 and a scavenging coefficient of 0.1 mm^{-1}
3171 are used for all aerosols. In MAM, the scavenging coefficient for interstitial aerosol is explicitly
3172 calculated as in [Easter et al. \[2004\]](#) and thus varies strongly with particle size, with lowest values
3173 for the accumulation mode; and the solubility factor is 0.1. For stratiform-cloud-borne aerosol,
3174 there is no below-cloud scavenging, and the solubility factor is 0.0.

3175 Aerosol that is scavenged at one altitude can be resuspended at a lower altitude if precip-
3176 itation evaporates. In CAM5, as in CAM3.5, this process is treated for aerosol removed by
3177 stratiform in-cloud scavenging. A fraction of the in-cloud scavenged aerosol is resuspended, and
3178 the resuspended fraction is equal to the fraction of precipitation that evaporates below cloud.

3179 4.8.10 Dry Deposition

3180 Aerosol dry deposition velocities are calculated using the [[Zhang et al., 2001](#)] parameterization
3181 with the CAM5 land-use and surface layer information. Gravitational settling velocities are
3182 calculated at layers above the surface [[Seinfeld and Pandis, 1998](#)]. Both velocities depend on
3183 particle wet size and are different for mass and number and between modes. The velocities for
3184 cloud-borne aerosols are calculated based on droplet sizes. Aerosol mixing ratio changes and
3185 fluxes from dry deposition and sedimentation throughout a vertical column are then calculated
3186 using the CAM5 dust deposition/sedimentation routine.

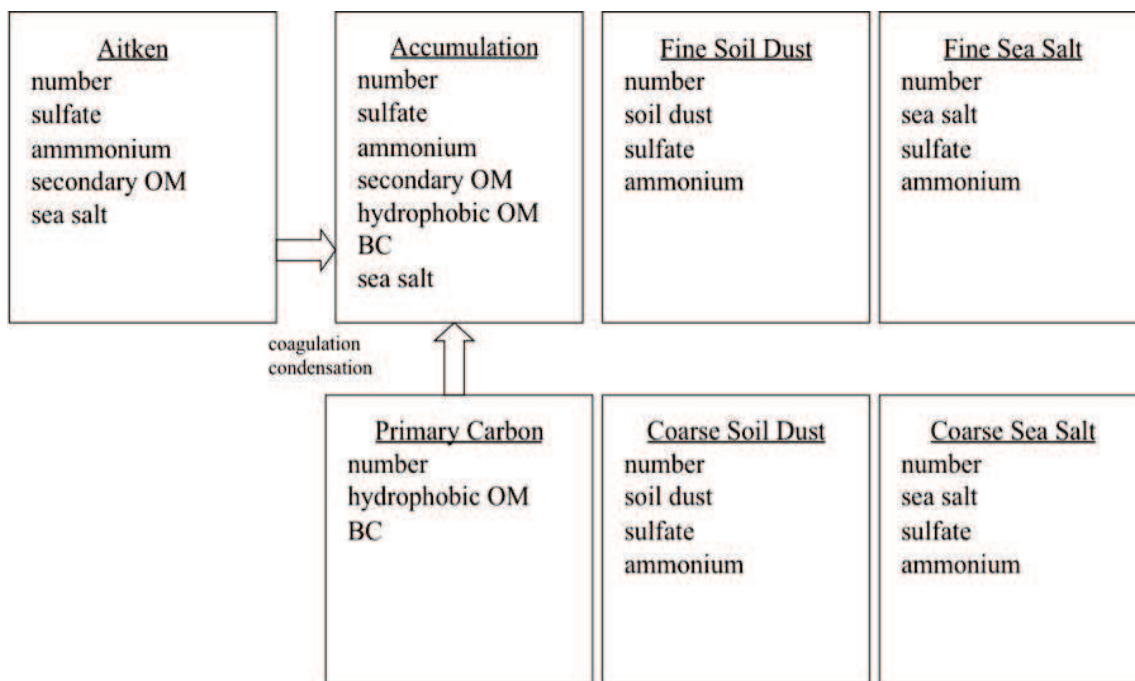


Figure 4.3: Predicted species for interstitial and cloud-borne component of each aerosol mode in MAM-7. Standard deviation for each mode is 1.6 (Aitken), 1.8 (accumulation), 1.6 (primary carbon), 1.8 (fine and coarse soil dust), and 2.0 (fine and coarse sea salt)

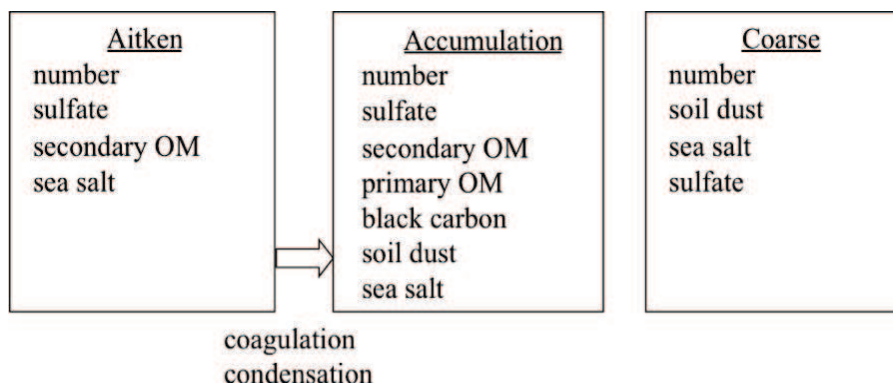


Figure 4.4: Predicted species for interstitial and cloud-borne component of each aerosol mode in MAM-3. Standard deviation for each mode is 1.6 (Aitken), 1.8 (accumulation) and 1.8 (coarse mode)

Table 4.4: Density (kg/m^3) of aerosol material.

Sea salt	Sulfate	Nitrate	Ammonium	SOA	POA	BC	Dust
1900	1770	1770	1770	1000	1000	1700	2600

Table 4.5: Hygroscopicity of aerosol components.

Sea salt	Sulfate	Nitrate	Ammonium	SOA	POA	BC	Dust
1.16	0.507	0.507	0.507	0.14	1.e-10	1.e-10	0.068

4.9 Condensed Phase Optics

Condensed phase (aerosols, liquid cloud droplets, hydrometeors, and ice crystal) optics are provided as a mass-specific quantities in m^2/kg . These optics are specified for each band of the shortwave and longwave radiation code. For the shortwave, unscaled extinction, single-scattering albedo, and asymmetry parameter are specified. For the longwave, the mass-specific absorption is specified. Vertical optical depths are computed by multiplying by the mass-specific quantities by the vertical mass path of the corresponding material.

For clouds, the in-cloud values of the mixing ratios are used to compute the in-cloud values of cloud optical depths. The radiation does not use grid-cell average optical depths of clouds.

4.9.1 Tropospheric Aerosol Optics

While the radiation code supports a range of possible aerosol packages, the modal aerosol package is the default configuration, and we will discuss the optics treatment used in that package. Aerosol optical properties for each mode are parameterized in terms of wet refractive index and wet surface mode radius of the mode, as described by [Ghan and Zaveri, 2007], except that volume mixing rather than the Maxwell-Garnett mixing rule is used to calculate the wet refractive index for mixtures of insoluble and soluble particles (We found little difference between the volume mixing treatment and the Maxwell-Garnett mixing rule.) Refractive indices for water and for most aerosol components are taken from OPAC [Koepke and Schult, 1998], but for black carbon the value (1.95,0.79i) from [Bond and Bergstrom, 2006] is used for solar wavelengths. Densities for each component are listed in Table 4.4.

The wet volume mean radius for each mode is calculated from the dry volume mean radius using equilibrium Kohler theory [Ghan and Zaveri, 2007], the relative humidity and the volume mean hygroscopicity. The hygroscopicity of each component is listed in Table 4.5. Note that the measured solubility of dust varies widely, from 0.03 to 0.26 [Koehler et al., 2009b]. The wet surface mode radius is calculated from the wet volume mean radius assuming a wet lognormal size distribution with the same geometric standard deviation as the dry size distribution. The geometric standard deviation is assumed to be constant for each mode.

4.9.2 Stratospheric Volcanic Aerosol Optics

CAM 5.0 specifies the volcanic aerosol as a mass mixing ratio q_V of wet volcanic aerosol to dry air as a function of height, latitude, longitude and time. CAM 5.0 also specifies a geometric

3217 mean radius r_g of the volcanic aerosol. The volcanic optics are stored as a lookup table as a
 3218 function of geometric mean radius.

The size distribution is defined by a log-normal size distribution with a geometric mean radius r_g and geometric standard deviation σ_g . For the standard version of the optics,

$$\sigma_g = 1.8 \quad (4.200)$$

$$\mu = \ln(r_g) \quad (4.201)$$

$$\mu \in [\mu_{\min}, \mu_{\max}] \quad (4.202)$$

$$\mu_{\min} = \ln(0.01 * 10^{-6} \exp(-5/2 * (\ln \sigma_g)^2)) \quad (4.203)$$

$$\mu_{\max} = \ln(2.00 * 10^{-6} \exp(-5/2 * (\ln \sigma_g)^2)) \quad (4.204)$$

In other words, r_{eff} spans the range $[0.01, 2.0] \mu\text{m}$. The density of the sulfuric acid / water mixture at 75% / 25% at 215K is

$$\rho = 1.75 * 10^3 \text{ kg/m}^3 \quad (4.205)$$

3219 The index of refraction is that specified by Biermann [Biermann et al., 2000] and is available
 3220 from the HITRAN [Rothman et al., 2009] database. The index at 75%/25% weight percent
 3221 (sulfuric acid to water) and at 215K is used.

The incomplete gamma weight,

$$L(r) = \int_0^r r^{*2} n(r^*) dr^* / \int_0^\infty r^{*2} n(r^*) dr^* \quad (4.206)$$

can be used to define the mass-specific aerosol extinction, scattering, and asymmetric scattering,

$$b_{\text{ext}} = \frac{3}{4\rho r_{\text{eff}}} \int_0^\infty q_{\text{ext}}(r) dL(r) \quad (4.207)$$

$$b_{\text{sca}} = \frac{3}{4\rho r_{\text{eff}}} \int_0^\infty q_{\text{sca}}(r) dL(r) \quad (4.208)$$

$$b_{\text{asm}} = \frac{3}{4\rho r_{\text{eff}}} \int_0^\infty q_{\text{gqsc}}(r) dL(r) \quad (4.209)$$

$$b_{\text{abs}} = \frac{3}{4\rho r_{\text{eff}}} \int_0^\infty (q_{\text{ext}}(r) - q_{\text{sca}}(r)) dL(r) \quad (4.210)$$

3222 where $q_{\text{ext}}(r)$, $q_{\text{sca}}(r)$, $q_{\text{gqsc}}(r)$ are efficiencies obtained from the MIEV0 program of Wiscombe
 3223 [Wiscombe, 1996].

3224 These mass-specific properties are averaged over each frequency band of RRTMG and pa-
 3225 rameterized in a lookup table with $\mu = \ln(r_g)$ as the dependent variable.

The vertical optical depths are derived as the product of vertical mass path with mass-specific aerosol properties at runtime.

$$\tau_{\text{ext}} = q_V * \frac{\Delta P_{\text{dry}}}{g} * b_{\text{ext}}(\mu) \quad (4.211)$$

3226 where q_V is the mixing ratio of volcanic aerosol. The corresponding scattering optical depth,
 3227 asymmetric scattering optical depth, and absorption optical depth are derived similarly.

3228 **4.9.3 Liquid Cloud Optics**

For liquid clouds CAM 5.0 specifies the fraction of each grid cell occupied by liquid cloud droplets C_{liq} , the ratio of mass of condensed water to wet air in the cloud q_{liq} , and the number-size distribution in terms of the 2 parameters, μ and λ of the gamma distribution,

$$n(D) = \frac{dN}{dD} = \frac{\lambda^{\mu+1}}{\Gamma(\mu+1)} D^\mu e^{-\lambda D} \quad (4.212)$$

3229 where D is the diameter of the droplets.

Both the parameters, μ and λ have limited ranges:

$$2. < \mu < 15. \quad (4.213)$$

$$\frac{\mu+1}{50 * 10^{-6}\text{m}} < \lambda < \frac{\mu+1}{2 * 10^{-6}\text{m}} \quad (4.214)$$

3230 The liquid cloud optics are specified in terms of a lookup table in μ and $1/\lambda$. These optics are
3231 computed as size-distribution and spectral-band averages of the quantities (e.g., Q_{ext}) computed
3232 by the MIEV0 program [Wiscombe, 1996].

The size-integrated mass-specific extinction coefficient, k_{ext} , (units m^2/kg) is given by:

$$k_{\text{ext}}(\nu) = \frac{\frac{\pi}{4} \int_0^\infty D^2 Q_{\text{ext}}(D; \nu, m) n(D) dD}{\frac{\pi}{6} \rho_w \int_0^\infty D^3 n(D) dD} \quad (4.215)$$

3233 The corresponding quantities are used to compute mass-specific absorption in the longwave as
3234 well as single-scattering albedo and asymmetry parameter.

The in-cloud optical depth is then given by:

$$\tau_{\text{liq}}(\nu) = k_{\text{ext}}(\nu) q_{\text{liq}} \frac{\Delta P}{g} \quad (4.216)$$

3235 where q_{liq} is the ratio of droplet mass to dry air mass.

3236 For RRTMG, the wavenumber average values of τ_{liq} , $\tau_{\text{liq}}\omega_{\text{liq}}$, $\tau_{\text{liq}}\omega_{\text{liq}}g_{\text{liq}}$ on each SW band, and
3237 the wavenumber average value of the absorption optical depth, $\tau_{\text{liq}}(1 - \omega_{\text{liq}})$, on each longwave
3238 band.

3239 In-cloud water path variability is not treated by the optics.

3240 **4.9.4 Ice Cloud Optics**

3241 CAM 5.0 specifies an in-cloud ice water path, an ice cloud fraction, and an effective diameter
3242 for ice particles in the cloud. The optics for ice clouds are constructed as a lookup table as a
3243 function of effective diameter for each of the shortwave and longwave bands in the radiation
3244 code.

3245 Ice cloud optical properties have been derived using two approaches: (1) calculations of
3246 single ice crystal scattering properties based on electrodynamic theory, followed by their appli-
3247 cation to assumed ice particle size distributions (PSD) and the representation of PSD optical
3248 properties through the effective diameter (D_e) of the PSD, and (2) parameterization of scatter-
3249 ing/absorption processes in terms of ice particle shape and size, and integrating these expressions

3250 over the PSD to produce analytical expressions of PSD optical properties in terms of ice crystal
3251 and PSD parameters. In the latter case, the PSD extinction and absorption coefficients can be
3252 expressed as explicit functions of the ice particle projected area- and mass-dimension power laws
3253 and the PSD parameters of the gamma form. The modified anomalous diffraction approximation
3254 (MADA) uses this second approach to calculate ice cloud optical properties. The development
3255 of MADA was motivated by a desire to explicitly represent ice optical properties in terms of the
3256 ice PSD and ice crystal shape parameters, given that the ice PSD optical properties cannot be
3257 uniquely defined by D_e [Mitchell, 2002].

3258 MADA was developed from van de Hulst's anomalous diffraction theory or ADT
3259 [van de Hulst, 1957] through a series of physical insights, which are:

- 3260 1. The effective photon path through a particle by which its scattering properties can be pre-
3261 dicted is given by the ratio of particle projected area/particle volume [Bryant and Latimer,
3262 1969; Mitchell and Arnott, 1994], where volume is defined as particle mass/bulk density
3263 of ice (0.917 g/cm^3).
- 3264 2. The processes of internal reflection and refraction can be viewed as extending the photon
3265 path and can be parameterized using a MADA framework [Mitchell et al., 1996b].
- 3266 3. The maximum contribution of wave resonance or photon tunneling to absorption and
3267 extinction can be estimated as a linear function of the real part of the refractive index for
3268 ice, n_r . Photon tunneling can then be parameterized in terms of n_r , size parameter x and
3269 the other MADA parameters described above [Mitchell, 2000].
- 3270 4. Edge effects as surface wave phenomena pertain only to extinction and can be represented
3271 in terms of the size parameter x as described by [Wu, 1956] and modified by [Mitchell,
3272 2000]. Based on a laboratory ice cloud study [Mitchell et al., 2001], edge effects for non-
3273 spherical ice crystals do not appear significant.

3274 The first insight greatly simplified van de Hulst's ADT, resulting in analytic and integrable
3275 expressions for the PSD extinction and absorption coefficients as shown in [Mitchell and Arnott,
3276 1994]. This simplified ADT may be more accurate than the original ADT [Mitchell et al., 2006a].
3277 This simplified ADT provided an analytical framework on which the other three insights or
3278 processes were expressed. These processes were represented analytically for a single ice particle,
3279 and then integrated over the PSD to produce extinction and absorption coefficients that account
3280 for these processes. These coefficients were formulated in terms of ice particle shape (i.e. the
3281 ice particle area- and mass-dimension power laws) and the three gamma PSD parameters. The
3282 basic MADA equations formulated for ice clouds are given in the appendix of [Mitchell, 2002].
3283 Details regarding their derivation and their physical basis are described in [Mitchell, 2000] and
3284 [Mitchell et al., 1996b].

3285 The asymmetry parameter g is not treated by MADA, but was parameterized for solar
3286 wavelengths as a function of wavelength and ice particle shape and size, based on ray-
3287 tracing calculations by Andreas Macke, as described in [Mitchell et al., 1996b]. The g pa-
3288 rameterization for quasi-spherical ice particles is based on the phase function calculations of
3289 [Nousiainen and McFarquhar, 2004]. These parameterizations relate g for a PSD to the ice par-
3290 ticle size that divides the PSD into equal projected areas (since scattering depends on projected

3291 area). For terrestrial radiation, CAM 5.0 g values for ice are based on the g parameterization
3292 described in [Yang et al., 2005].

3293 Tests of MADA

3294 While this treatment of ice optical properties began and evolved through van de Hulst’s orig-
3295 inal insights formulated in ADT, optical properties predicted by MADA closely agree with
3296 those predicted by other ice optics schemes based on electrodynamic theory. As described in
3297 [Mitchell et al., 2001, 2006a], MADA has been tested in a laboratory ice cloud experiment where
3298 the MADA extinction error was 3% on average relative to the FTIR measured extinction effi-
3299 ciency over the 2-14 μm wavelength range. These same laboratory PSD were used to calculate
3300 the absorption efficiencies using MADA and T-matrix, which differed by 6% on average over
3301 the wavelength range 2-18 μm (size parameter range 2-22). In corresponding T-matrix cal-
3302 culations of the single-scattering albedo, the mean MADA error was 2.5%. In another test,
3303 MADA absorption errors relative to the Finite Difference Time Domain (FDTD) method (i.e.
3304 [Yang et al., 2005] over the wavelength range 3-100 μm were no greater than 15% for six ice
3305 particle shapes. Finally, the absorption coefficients predicted by MADA and the [Fu et al., 1998]
3306 and the [Yang et al., 2005] ice optics schemes generally agreed within 5%.

3307 Application to CAM 5.0

3308 The MADA-based ice optics scheme described above is not used explicitly in CAM 5.0, but was
3309 used to generate a look-up table of optical properties as a function of effective diameter, D_e . The
3310 PSD optical properties consist of the mass-normalized extinction coefficient (volume extinction
3311 coefficient / ice water content), the single-scattering albedo and the asymmetry parameter for
3312 bands covering all solar and terrestrial wavelengths. The radiation bands coincide with those
3313 used in RRTMG. The ice refractive index values used are from [Warren and Brandt, 2008]. Since
3314 MADA is formulated to accept any ice particle shape recipe, a shape recipe corresponding to
3315 that observed for mid-latitude cirrus clouds at -45°C (see [Lawson et al., 2006]) was assumed
3316 for ice particles larger than 60 μm : 7% hexagonal columns, 50% bullet rosettes and 43% irregular
3317 ice particles. At smaller sizes, the shape recipe consists of 50% quasi-spherical, 30% irregular
3318 and 20% bullet rosette ice crystals, based on in-situ measurements in tropical cirrus [P. Lawson,
3319 2005, personal communication].

The effective diameter is defined in a way that is universal for both ice and water clouds,
which is essentially the photon path characterizing the PSD [Mitchell, 2002]:

$$De = \frac{3 \text{IWC}}{2 \rho_i A} \quad (4.217)$$

3320 where IWC is the ice water content (g/cm^3), ρ_i is the bulk ice density ($0.917 \text{ g}/\text{cm}^3$) and A is
3321 the total projected area of the PSD (cm^2/cm^3).

3322 4.9.5 Snow Cloud Optics

3323 CAM 5.0 specifies snow as a cloud fraction of snow, an effective diameter of snow, and an
3324 in-cloud mass mixing ratio of snow. The snow optics are identical to the optics for ice clouds.

3325 4.10 Radiative Transfer

3326 Radiative transfer calculations in the longwave and shortwave are provided by the radiation code
 3327 RRTMG [Iacono et al., 2008; Mlawer et al., 1997]. This is an accelerated and modified version
 3328 of the correlated k -distribution model, RRTM. The condensed phase radiative parameterizations
 3329 are external to the radiation package, however the gas optics and radiative transfer solver are
 3330 provided within RRTMG.

3331 4.10.1 Combination of Aerosol Radiative Properties

The number N_a of aerosol species is arbitrary; however in the standard configuration there are 3 modes. The radiative properties are combined before being passed to the radiative transfer solver. If the extinction optical depth of species i in band b is τ_{ib} and the single-scattering albedo is ω_{ib} and the asymmetry parameter is g_{ib} then the aerosol optics are combined as follows:

$$\tau_b = \sum_{i=1}^{N_a} \tau_{ib} \quad (4.218)$$

$$\omega_b = \sum_{i=1}^{N_a} \tau_{ib} \omega_{ib} / \tau_b \quad (4.219)$$

$$g_b = \sum_{i=1}^{N_a} \tau_{ib} \omega_{ib} g_{ib} / (\tau_b \omega_b) \quad (4.220)$$

3332 where τ_b is the total aerosol extinction optical depth in band b , ω_b is the total single-scattering
 3333 albedo in band b , and g_b is the asymmetry parameter in band b .

3334 4.10.2 Combination of Cloud Optics

CAM 5.0 specifies three different types of clouds: ice clouds, liquid clouds, and snow clouds. Each of these clouds has a separate cloud fraction C_{liq} , C_{ice} , C_{snow} , as well as an in-cloud radiative characterization in terms of optical depths τ_i , single-scattering albedo ω_i and asymmetry parameter g_i . The optics are smeared together into a total cloud fraction C as follows:

$$C = \max\{C_{\text{liq}}, C_{\text{ice}}, C_{\text{snow}}\} \quad (4.221)$$

$$\tau_c = \sum_{t \in \text{type}} \tau_t * C_t / C \quad (4.222)$$

$$\omega_c = \sum_{t \in \text{type}} \tau_{tb} \omega_{tb} C_t / (\tau_c C) \quad (4.223)$$

$$g_c = \sum_{t \in \text{type}} \tau_{tb} \omega_{tb} g_{tb} C_t / (\tau_c \omega_c C) \quad (4.224)$$

3335 where C , τ_c , ω_c , g_c are the combined cloud radiative parameters.

4.10.3 Radiative Fluxes and Heating Rates

Radiative fluxes and heating rates in CAM 5.0 are calculated using RRTMG [Iacono et al., 2008].

This model utilizes the correlated k -distribution technique to calculate irradiance and heating rate efficiently in broad spectral intervals, while realizing the objective of retaining a high level of accuracy relative to measurements and high-resolution line-by-line models. Sub-grid cloud characterization in RRTMG is treated in both the longwave and shortwave spectral regions with McICA, the Monte-Carlo Independent Column Approximation [Pincus and Morcrette, 2003], using the maximum-random cloud overlap assumption.

The thermodynamic state, gas concentrations, cloud fraction, condensed phase optics, and aerosol properties are specified elsewhere. The CAM 5.0 surface model provides both the surface albedo, area-averaged for each atmospheric column, and the upward longwave surface flux, which incorporates the surface emissivity, for input to the radiation. The bulk aerosol package of CAM4 continues to be supported by this radiation code as an option, however a description of this optional configuration is not provided in this document.

To provide fluxes at the top of the atmosphere, RRTMG uses with an additional layer above the CAM 5.0 model top in both the longwave and shortwave. This extra layer is specified by replicating the composition of the highest CAM 5.0 layer into a layer that extends from the top of the model to 10^{-4} hPa. RRTMG does not treat non-LTE (local thermodynamic equilibrium) effects in the upper atmosphere. It provides accurate fluxes and heating rates up to about 0.1 hPa, above which non-LTE effects become more significant.

Shortwave Radiative Transfer

RRTMG divides the solar spectrum into 14 shortwave bands that extend over the spectral range from $0.2 \mu\text{m}$ to $12.2 \mu\text{m}$ (820 to 50000 cm^{-1}). Modeled sources of extinction (absorption and scattering) are H₂O, O₃, CO₂, O₂, CH₄, N₂, clouds, aerosols, and Rayleigh scattering. The model uses a two-stream δ -Eddington approximation assuming homogeneously mixed layers, while accounting for both absorption and scattering in the calculation of reflectance and transmittance. The model distinguishes the direct solar beam from scattered (diffuse) radiation. The scattering phase function is parameterized using the Henyey-Greenstein approximation to represent the forward scattering fraction as a function of the asymmetry parameter. This delta-scaling is applied to the total irradiance as well as to the direct and diffuse components. The latter are consistent with the direct and diffuse components of the surface albedo, which are applied to the calculation of surface reflectance.

The shortwave version of RRTMG used in CAM5 is derived from RRTM_SW [Clough et al., 2005]. It utilizes a reduced complement of 112 quadrature points (g-points) to calculate radiative transfer across the 14 spectral bands, which is half of the 224 g-points used in RRTM_SW, to enhance computational performance with little impact on accuracy. The number of g-points needed within each band varies depending on the strength and complexity of the absorption in each spectral interval. Total fluxes are accurate to within 1-2 W/m² relative to the standard RRTM_SW (using DISORT with 16 streams) in clear sky and in the presence of aerosols and within 6 W/m² in overcast sky. RRTM_SW with DISORT is itself accurate to within 2 W/m² of the data-validated multiple scattering model, CHARTS [Moncet and Clough, 1997]. Input absorption coefficient data for the k -distributions used by RRTMG are obtained directly from the line-by-line radiation model LBLRTM [Clough et al., 2005].

Table 4.6: RRTMG_SW spectral band boundaries and the solar irradiance in each band.

Band Index	Band Min (μm)	Band Max (μm)	Band Min (cm^{-1})	Band Max (cm^{-1})	Solar Irradiance (W/m^2)
1	3.077	3.846	2600	3250	12.11
2	2.500	3.077	3250	4000	20.36
3	2.150	2.500	4000	4650	23.73
4	1.942	2.150	4650	5150	22.43
5	1.626	1.942	5150	6150	55.63
6	1.299	1.626	6150	7700	102.93
7	1.242	1.299	7700	8050	24.29
8	0.778	1.242	8050	12850	345.74
9	0.625	0.778	12850	16000	218.19
10	0.442	0.625	16000	22650	347.20
11	0.345	0.442	22650	29000	129.49
12	0.263	0.345	29000	38000	50.15
13	0.200	0.263	38000	50000	3.08
14	3.846	12.195	820	2600	12.89

3379 RRTMG shortwave utilizes McICA, the Monte-Carlo Independent Column Approximation,
 3380 to represent sub-grid scale cloud variability such as cloud fraction and cloud overlap. An external
 3381 sub-column generator is used to define the stochastic cloud arrays used by the McICA technique.

3382 The Kurucz solar source function is used in the shortwave model, which assumes a total
 3383 solar irradiance (TSI) at the top of the atmosphere of $1368.22 \text{ W}/\text{m}^2$. However, this value is
 3384 scaled in each spectral band through the specification of a time-varying solar spectral irradiance
 3385 as discussed below. The TSI assumed in each RRTMG shortwave band is listed in the table
 3386 below, along with the spectral band boundaries in μm and wavenumbers.

3387 Shortwave radiation is only calculated by RRTMG when the cosine of the zenith angle is
 3388 larger than zero, that is, when the sun is above the horizon.

3389 Longwave Radiative Transfer

3390 The infrared spectrum in RRTMG is divided into 16 longwave bands that extend over the
 3391 spectral range from $3.1 \mu\text{m}$ to $1000.0 \mu\text{m}$ (10 to 3250 cm^{-1}). The band boundaries are listed
 3392 in the table below. The model calculates molecular, cloud and aerosol absorption and emission.
 3393 Scattering effects are not presently included. Molecular sources of absorption are H_2O , CO_2 ,
 3394 O_3 , N_2O , CH_4 , O_2 , N_2 and the halocarbons CFC-11 and CFC-12. CFC-11 is specified by
 3395 CAM5 as a weighed sum of multiple CFCs (other than CFC-12). The water vapor continuum
 3396 is treated with the CKD_v2.4 continuum model. For completeness, band 16 includes a small
 3397 adjustment to add the infrared contribution from the spectral interval below $3.1 \mu\text{m}$.

3398 The longwave version of RRTMG [Iacono et al., 2008, 2003, 2000] used in CAM5 has been
 3399 modified from RRTM_LW [Mlawer et al., 1997] to enhance its computational efficiency with
 3400 minimal effect on the accuracy. This includes a reduction in the total number of g-points from
 3401 256 to 140. The number of g-points used within each band varies depending on the strength

Table 4.7: RRTMG_LW spectral band boundaries.

Band Index	Band Min (μm)	Band Max (μm)	Band Min (cm^{-1})	Band Max (cm^{-1})
1	28.57	1000.0	10	350
2	20.00	28.57	350	500
3	15.87	20.00	500	630
4	14.29	15.87	630	700
5	12.20	14.29	700	820
6	10.20	12.20	820	980
7	9.26	10.20	980	1080
8	8.47	9.26	1080	1180
9	7.19	8.47	1180	1390
10	6.76	7.19	1390	1480
11	5.56	6.76	1480	1800
12	4.81	5.56	1800	2080
13	4.44	4.81	2080	2250
14	4.20	4.44	2250	2380
15	3.85	4.20	2380	2600
16	3.08	3.85	2600	3250

3402 and complexity of the absorption in each band. Fluxes are accurate to within 1.0 W/m^2 at all
3403 levels, and cooling rate generally agrees within 0.1 K/day in the troposphere and 0.3 K/day
3404 the stratosphere relative to the line-by-line radiative transfer model, LBLRTM [Clough et al.,
3405 2005; Clough and Iacono, 1995]. Input absorption coefficient data for the k -distributions used
3406 by RRTMG are obtained directly from LBLRTM.

3407 This model also utilizes McICA, the Monte-Carlo Independent Column Approximation
3408 [Pincus and Morcrette, 2003], to represent sub-grid scale cloud variability such as cloud fraction
3409 and cloud overlap. An external sub-column generator is used to define the stochastic cloud
3410 arrays needed by the McICA technique.

3411 Within the longwave radiation model, the surface emissivity is assumed to be 1.0. However,
3412 the radiative surface temperature used in the longwave calculation is derived with the Stefan-
3413 Boltzmann relation from the upward longwave surface flux that is input from the land model.
3414 Therefore, this value may include some representation of surface emissivity less than 1.0 if this
3415 condition exists in the land model. RRTMG longwave also provides the capability of varying
3416 the surface emissivity within each spectral band, though this feature is not presently utilized.

3417 Longwave radiative transfer is performed over a single (diffusivity) angle (secant =1.66) for
3418 one upward and one downward calculation. RRTMG includes an accuracy adjustment in profiles
3419 with very high water vapor that slightly varies the diffusivity angle in some bands as a function
3420 of total column water vapor.

3421 4.10.4 Surface Radiative Properties

3422 For the shortwave, the surface albedoes are specified at every grid point at every time step. The
3423 albedoes are partitioned for the spectral ranges $[2.0, 0.7]\mu\text{m}$ and $[0.7, 12.0]\mu\text{m}$. In addition they
3424 are partitioned between the direct and diffuse beam.

3425 In the longwave, the surface is assumed to have an emissivity of 1.0 within the radiation
3426 model. However, the radiative surface temperature used in the longwave calculation is derived
3427 with the Stefan-Boltzmann relation from the upward longwave surface flux that is input from
3428 the surface models. Therefore, this value may include some representation of surface emissivity
3429 less than 1.0, if this condition exists in surface models (e.g. the land model).

3430 4.10.5 Time Sampling

3431 Both the shortwave and longwave radiation is computed at hourly intervals by default. The
3432 heating rates and fluxes are assumed to be constant between time steps.

3433 4.10.6 Diurnal Cycle and Earth Orbit

In CAM 5.0, the diurnal cycle and earth orbit is computed using the method of [Berger, 1978].
Using this formulation, the insolation can be determined for any time within 10^6 years of
1950 AD. The insolation at the top of the model atmosphere is given by

$$S_I = S_0 \rho^{-2} \cos \mu, \quad (4.225)$$

3434 where S_0 is the solar constant, μ is the solar zenith angle, and ρ^{-2} is the distance factor (square
3435 of the ratio of mean to actual distance that depends on the time of year). A time series of the
3436 solar spectral irradiance at 1 a.u. for 1870-2100 based upon [Wang et al., 2005] is included with
3437 the standard model and is in section 4.10.7.

We represent the annual and diurnal cycle of solar insolation with a repeatable solar year of
exactly 365 days and with a mean solar day of exactly 24 hours, respectively. The repeatable
solar year does not allow for leap years. The expressions defining the annual and diurnal variation
of solar insolation are:

$$\cos \mu = \sin \phi \sin \delta - \cos \phi \cos \delta \cos(H) \quad (4.226)$$

$$\delta = \arcsin(\sin \epsilon \sin \lambda) \quad (4.227)$$

$$\rho = \frac{1 - e^2}{1 + e \cos(\lambda - \tilde{\omega})} \quad (4.228)$$

$$\tilde{\omega} = \Pi + \psi \quad (4.229)$$

where

$$\begin{aligned}
\phi &= \text{latitude in radians} \\
\delta &= \text{solar declination in radians} \\
H &= \text{hour angle of sun during the day} \\
\epsilon &= \text{obliquity} \\
\lambda &= \text{true longitude of the earth relative to vernal equinox} \\
e &= \text{eccentricity factor} \\
\tilde{\omega} &= \text{longitude of the perihelion} + 180^\circ \\
\Pi &= \text{longitude of perihelion based on the fixed equinox} \\
\psi &= \text{general precession}
\end{aligned} \tag{4.230}$$

The hour angle H in the expression for $\cos \mu$ depends on the calendar day d as well as model longitude:

$$H = 2\pi \left(d + \frac{\theta}{360^\circ} \right), \tag{4.231}$$

where θ = model longitude in degrees starting from Greenwich running eastward. Note that the calendar day d varies continuously throughout the repeatable year and is updated every model time step. The values of d at 0 GMT for January 1 and December 31 are 0 and 364, respectively. This would mean, for example, that a model calendar day d having no fraction (such as 182.00) would refer to local midnight at Greenwich, and to local noon at the date line (180° longitude).

The obliquity ϵ may be approximated by an empirical series expansion of solutions for the Earth's orbit

$$\epsilon = \epsilon^* + \sum_{j=1}^{47} A_j \cos(f_j t + \delta_j) \tag{4.232}$$

where A_j , f_j , and δ_j are determined by numerical fitting. The term $\epsilon^* = 23.320556^\circ$, and t is the time (in years) relative to 1950 AD.

Since the series expansion for the eccentricity e is slowly convergent, it is computed using

$$e = \sqrt{(e \cos \Pi)^2 + (e \sin \Pi)^2} \tag{4.233}$$

The terms on the right-hand side may also be written as empirical series expansions:

$$e \begin{Bmatrix} \cos \\ \sin \end{Bmatrix} \Pi = \sum_{j=1}^{19} M_j \begin{Bmatrix} \cos \\ \sin \end{Bmatrix} (g_j t + \beta_j) \tag{4.234}$$

where M_j , g_j , and β_j are estimated from numerical fitting. Once these series have been computed, the longitude of perihelion Π is calculated using

$$\Pi = \arctan \left(\frac{e \sin \Pi}{e \cos \Pi} \right) \tag{4.235}$$

The general precession is given by another empirical series expansion

$$\psi = \tilde{\psi} t + \zeta + \sum_{j=1}^{78} F_j \sin(f'_j t + \delta'_j) \quad (4.236)$$

3445 where $\tilde{\psi} = 50.439273''$, $\zeta = 3.392506^\circ$, and F_j , f'_j , and δ'_j are estimated from the numerical
3446 solution for the Earth's orbit.

The calculation of λ requires first determining two mean longitudes for the orbit. The mean longitude λ_{m0} at the time of the vernal equinox is :

$$\begin{aligned} \lambda_{m0} = 2 \left\{ \left(\frac{e}{2} + \frac{e^3}{8} \right) (1 + \beta) \sin(\tilde{\omega}) \right. \\ \left. - \frac{e^2}{4} \left(\frac{1}{2} + \beta \right) \sin(2\tilde{\omega}) \right. \\ \left. + \frac{e^3}{8} \left(\frac{1}{3} + \beta \right) \sin(3\tilde{\omega}) \right\} \end{aligned} \quad (4.237)$$

where $\beta = \sqrt{1 - e^2}$. The mean longitude is

$$\lambda_m = \lambda_{m0} + \frac{2\pi(d - d_{ve})}{365} \quad (4.238)$$

where $d_{ve} = 80.5$ is the calendar day for the vernal equinox at noon on March 21. The true longitude λ is then given by:

$$\begin{aligned} \lambda = \lambda_m + \left(2e - \frac{e^3}{4} \right) \sin(\lambda_m - \tilde{\omega}) \\ + \frac{5e^2}{4} \sin[2(\lambda_m - \tilde{\omega})] \\ + \frac{13e^3}{12} \sin[3(\lambda_m - \tilde{\omega})] \end{aligned} \quad (4.239)$$

3447 The orbital state used to calculate the insolation is held fixed over the length of the model
3448 integration. This state may be specified in one of two ways. The first method is to specify
3449 a year for computing t . The value of the year is held constant for the entire length of the
3450 integration. The year must fall within the range of 1950 ± 10^6 . The second method is to specify
3451 the eccentricity factor e , longitude of perihelion $\tilde{\omega} - 180^\circ$, and obliquity ϵ . This set of values
3452 is sufficient to specify the complete orbital state. Settings for AMIP II style integrations under
3453 1995 AD conditions are $\epsilon = 23.4441$, $e = 0.016715$, and $\tilde{\omega} - 180 = 102.7$.

3454 4.10.7 Solar Spectral Irradiance

3455 The reference spectrum assumed by RRTMG is the Kurucz spectrum. CAM 5.0 specifies the
3456 solar spectral irradiance in a file, based on the work of Lean [Wang et al., 2005]. The Kurucz
3457 spectrum can be seen in figure 4.5. The Lean data seen in figure 4.6 is time-varying and the
3458 graphed values are an average over one solar cycle. These two spectra postulate different values
3459 of the total solar irradiance. A graph of the relative difference between them can be seen in
3460 figure 4.7.

Solar Irradiance	Kurucz	Lean
Total	1368.60	1366.96
In RRTMG bands	1368.14	1366.39
> 12195 nm	0.46	0.46
[120, 200] nm	0	0.11
EUV	0	0.0047

RRTMG Band Index	λ_{high} , nm	λ_{low} , nm	Kurucz W/m ²	Lean W/m ²	Lean - Kurucz	Relative %	Lean(<i>t</i>) Max % Variation	Lean(<i>t</i>) Max Δ Flux
14	12195	3846	12.79	12.78	-0.01	-0.08	0.16	0.020
1	3846	3077	12.11	11.99	-0.12	-1.00	0.02	0.003
2	3077	2500	20.36	20.22	-0.14	-0.69	0.03	0.007
3	2500	2151	23.73	23.49	-0.24	-1.02	0.02	0.005
4	2151	1942	22.43	22.17	-0.26	-1.17	0.01	0.003
5	1942	1626	55.63	55.61	-0.02	-0.04	0.02	0.011
6	1626	1299	102.9	102.9	0.0	0.	0.02	0.019
7	1299	1242	24.29	24.79	0.50	2.06	0.04	0.011
8	1242	778	345.7	348.9	3.2	0.93	0.06	0.226
9	778	625	218.1	218.2	0.1	0.05	0.11	0.238
10	625	441	347.2	344.9	-2.3	-0.67	0.13	0.463
11	441	345	129.5	130.0	0.5	0.39	0.26	0.340
12	345	263	50.15	47.41	-2.74	-5.78	0.45	0.226
13	263	200	3.120	3.129	0.009	0.29	4.51	0.141

Table 4.8: Band-level ratio of Solar Irradiances, based on average of one solar cycle

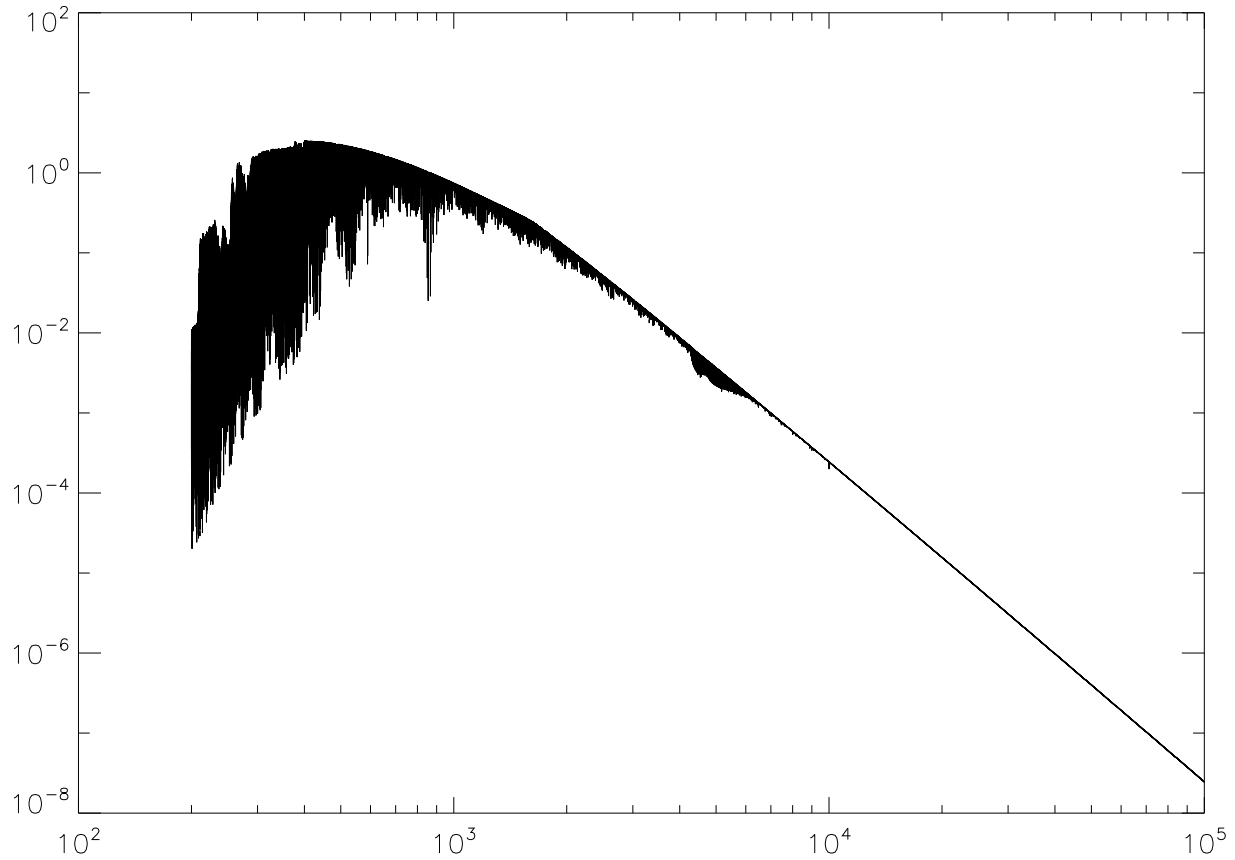


Figure 4.5: Kurucz spectrum. sf in $\text{W}/\text{m}^2/\text{nm}$. Source Data: AER. Range from [20, 20000] nm.

3461 The heating in each band b is scaled by the ratio, $\frac{\text{Lean}(t)_b}{\text{Kurucz}_b}$, where Kurucz_b is assumed by
 3462 RRTMG as specified in table 4.8, and $\text{Lean}(t)_b$ is the solar irradiance specified by the time-
 3463 dependent solar spectral irradiance file. $\text{Lean}(t)_{14}$ includes the Lean irradiance longward of
 3464 12195 nm to capture irradiance in the very far infrared.

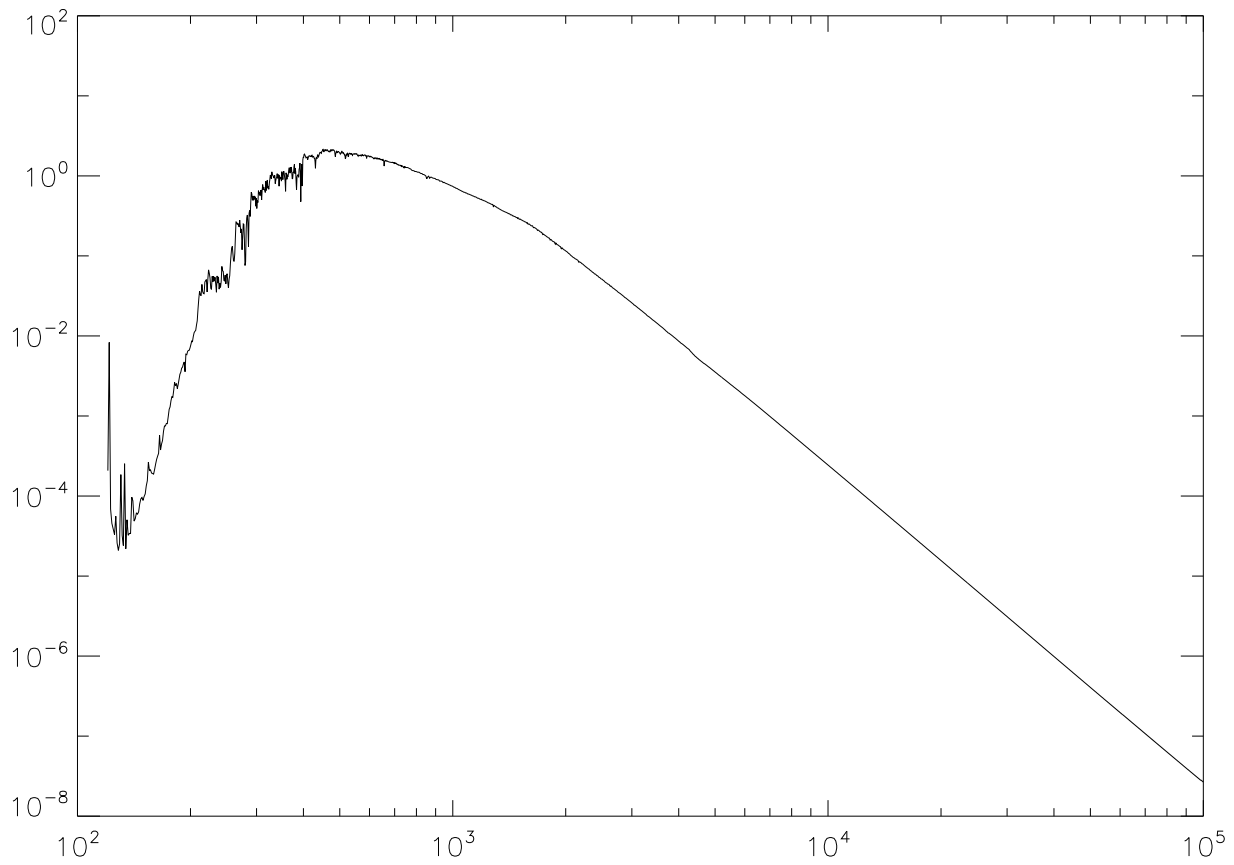


Figure 4.6: Lean spectrum. Average over 1 solar cycle, May 1, 1996 to Dec 31, 2006. Source Data: Marsh. ssf in $\text{W}/\text{m}^2/\text{nm}$. Range from [120, 99975] nm.

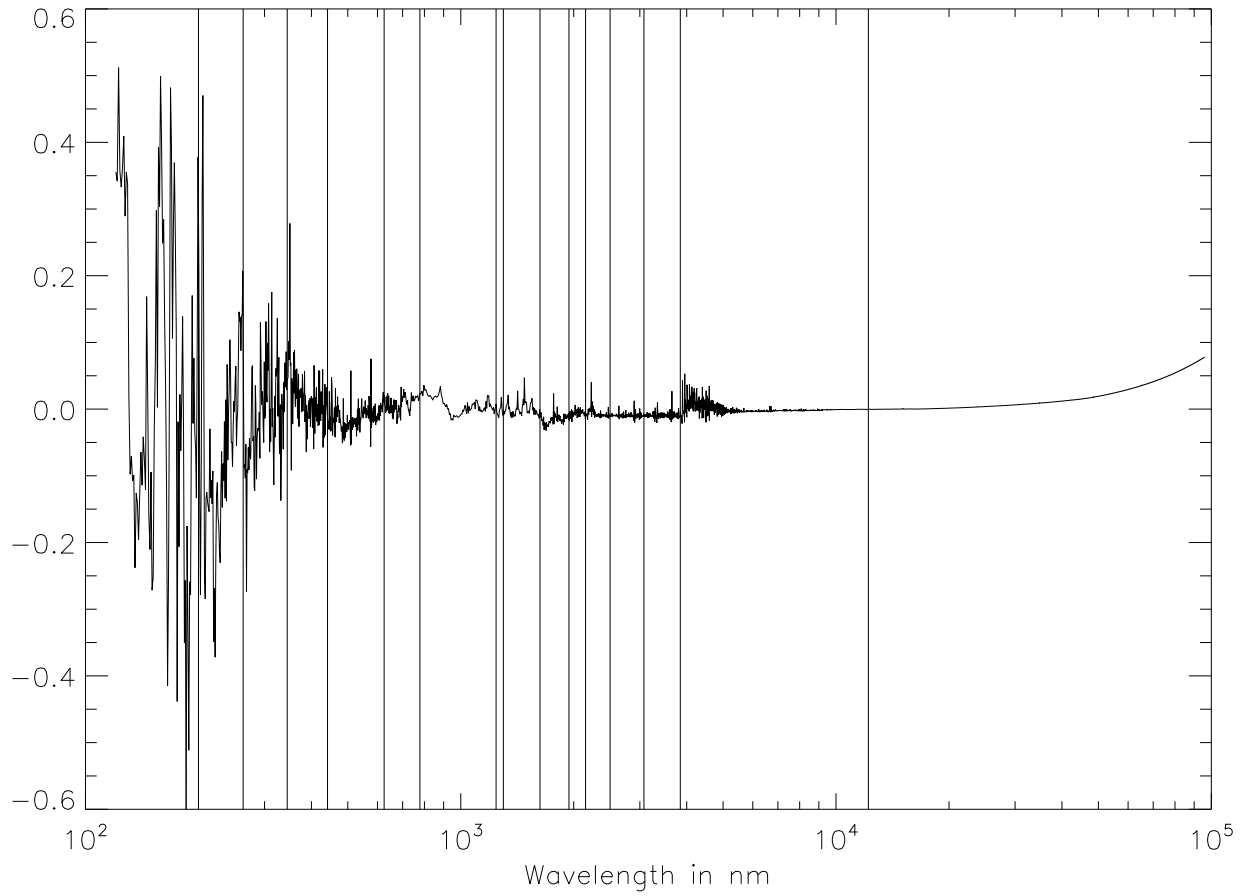


Figure 4.7: Relative difference, $\frac{Lean-Kurucz}{.5(Lean+Kurucz)}$ between spectra. RRTMG band boundaries are marked with vertical lines.

3465 4.11 Surface Exchange Formulations

3466 The surface exchange of heat, moisture and momentum between the atmosphere and land,
 3467 ocean or ice surfaces are treated with a bulk exchange formulation. We present a description of
 3468 each surface exchange separately. Although the functional forms of the exchange relations are
 3469 identical, we present the descriptions of these components as developed and represented in the
 3470 various subroutines in CAM 5.0. The differences in the exchange expressions are predominantly
 3471 in the definition of roughness lengths and exchange coefficients. The description of surface
 3472 exchange over ocean follows from Bryan et al. [1996], and the surface exchange over sea ice is
 3473 discussed in the sea-ice model documentation. Over lakes, exchanges are computed by a lake
 3474 model embedded in the land surface model described in the following section.

3475 4.11.1 Land

3476 In CAM 5.0, the NCAR Land Surface Model (LSM) [Bonan, 1996] has been replaced by the
 3477 Community Land Model CLM2 [Bonan et al., 2002]. This new model includes components
 3478 treating hydrological and biogeochemical processes, dynamic vegetation, and biogeophysics.
 3479 Because of the increased complexity of this new model and since a complete description is
 3480 available online, users of CAM 5.0 interested in CLM should consult this documentation at
 3481 <http://www.cgd.ucar.edu/tss/clm/>. A discussion is provided here only of the component of
 3482 CLM which controls surface exchange processes.

Land surface fluxes of momentum, sensible heat, and latent heat are calculated from Monin-Obukhov similarity theory applied to the surface (i.e. constant flux) layer. The zonal τ_x and meridional τ_y momentum fluxes ($\text{kg m}^{-1}\text{s}^{-2}$), sensible heat H (W m^{-2}) and water vapor E ($\text{kg m}^{-2}\text{s}^{-1}$) fluxes between the surface and the lowest model level z_1 are:

$$\tau_x = -\rho_1 \overline{(u'w')} = -\rho_1 u_*^2 (u_1/V_a) = \rho_1 \frac{u_s - u_1}{r_{am}} \quad (4.240)$$

$$\tau_y = -\rho_1 \overline{(v'w')} = -\rho_1 u_*^2 (v_1/V_a) = \rho_1 \frac{v_s - v_1}{r_{am}} \quad (4.241)$$

$$H = \rho_1 c_p \overline{(w'\theta')} = -\rho_1 c_p u_* \theta_* = \rho_1 c_p \frac{\theta_s - \theta_1}{r_{ah}} \quad (4.242)$$

$$E = \rho_1 \overline{(w'q')} = -\rho_1 u_* q_* = \rho_1 \frac{q_s - q_1}{r_{aw}} \quad (4.243)$$

$$r_{am} = V_a/u_*^2 \quad (4.244)$$

$$r_{ah} = (\theta_1 - \theta_s)/u_* \theta_* \quad (4.245)$$

$$r_{aw} = (q_1 - q_s)/u_* q_* \quad (4.246)$$

3483 where ρ_1 , u_1 , v_1 , θ_1 and q_1 are the density (kg m^{-3}), zonal wind (m s^{-1}), meridional wind (m s^{-1}),
 3484 air potential temperature (K), and specific humidity (kg kg^{-1}) at the lowest model level. By
 3485 definition, the surface winds u_s and v_s equal zero. The symbol θ_1 represents temperature, and
 3486 q_1 is specific humidity at surface. The terms r_{am} , r_{ah} , and r_{aw} are the aerodynamic resistances
 3487 (s m^{-1}) for momentum, sensible heat, and water vapor between the lowest model level at height

3488 z_1 and the surface at height $z_{0m} + d$ [$z_{0h} + d$]. Here z_{0m} [z_{0h}] is the roughness length (m) for
 3489 momentum [scalar] fluxes, and d is the displacement height (m).

3490 For the vegetated fraction of the grid, $\theta_s = T_{af}$ and $q_s = q_{af}$, where T_{af} and q_{af} are the air
 3491 temperature and specific humidity within canopy space. For the non-vegetated fraction, $\theta_s = T_g$
 3492 and $q_s = q_g$, where T_g and q_g are the air temperature and specific humidity at ground surface.
 3493 These terms are described by Dai et al. [2001].

3494 Roughness lengths and zero-plane displacement

The aerodynamic roughness z_{0m} is used for wind, while the thermal roughness z_{0h} is used for
 heat and water vapor. In general, z_{0m} is different from z_{0h} , because the transfer of momen-
 tum is affected by pressure fluctuations in the turbulent waves behind the roughness elements,
 while for heat and water vapor transfer no such dynamical mechanism exists. Rather, heat and
 water vapor must ultimately be transferred by molecular diffusion across the interfacial sub-
 layer. Over bare soil and snow cover, the simple relation from Zilitinkevich [1970] can be used
 [Zeng and Dickinson, 1998]:

$$\ln \frac{z_{0m}}{z_{0h}} = a \left(\frac{u_* z_{0m}}{\nu} \right)^{0.45} \quad (4.247)$$

$$a = 0.13 \quad (4.248)$$

$$\nu = 1.5 \times 10^{-5} \text{m}^2 \text{s}^{-1} \quad (4.249)$$

Over canopy, the application of energy balance

$$R_n - H - L_v E = 0 \quad (4.250)$$

3495 (where R_n is the net radiation absorbed by the canopy) is equivalent to the use of different z_{0m}
 3496 versus z_{0h} over bare soil, and hence thermal roughness is not needed over canopy [Zeng et al.,
 3497 1998].

3498 The roughness z_{0m} is proportional to canopy height, and is also affected by fractional vegeta-
 3499 tion cover, leaf area index, and leaf shapes. The roughness is derived from the simple relationship
 3500 $z_{0m} = 0.07 h_c$, where h_c is the canopy height. Similarly, the zero-plane displacement height d
 3501 is proportional to canopy height, and is also affected by fractional vegetation cover, leaf area
 3502 index, and leaf shapes. The simple relationship $d/h_c = 2/3$ is used to obtain the height.

3503 Monin-Obukhov similarity theory

3504 (1) Turbulence scaling parameters

A length scale (the Monin-Obukhov length) L is defined by

$$L = \frac{\theta_v u_*^2}{kg\theta_{v*}} \quad (4.251)$$

where k is the von Kàrman constant, and g is the gravitational acceleration. $L > 0$ indicates
 stable conditions, $L < 0$ indicates unstable conditions, and $L = \infty$ applies to neutral conditions.
 The virtual potential temperature θ_v is defined by

$$\theta_v = \theta_1 (1 + 0.61q_1) = T_a \left(\frac{p_s}{p_l} \right)^{R/c_p} (1 + 0.61q_1) \quad (4.252)$$

where T_1 and q_1 are the air temperature and specific humidity at height z_1 respectively, θ_1 is the atmospheric potential temperature, p_l is the atmospheric pressure, and p_s is the surface pressure. The surface friction velocity u_* is defined by

$$u_*^2 = [\overline{u'w'^2} + \overline{v'w'^2}]^{1/2} \quad (4.253)$$

The temperature scale θ_* and θ_{*v} and a humidity scale q_* are defined by

$$\theta_* = -\overline{w'\theta'}/u_* \quad (4.254)$$

$$q_* = -\overline{w'q'}/u_* \quad (4.255)$$

$$\begin{aligned} \theta_{v*} &= -\overline{w'\theta'_v}/u_* \\ &\approx -(\overline{w'\theta'} + 0.61\overline{\theta w'q'})/u_* \\ &= \theta_* + 0.61\overline{\theta}q_* \end{aligned} \quad (4.256)$$

3505 (where the mean temperature $\overline{\theta}$ serves as a reference temperature in this linearized form of θ_v).

The stability parameter is defined as

$$\zeta = \frac{z_1 - d}{L}, \quad (4.257)$$

with the restriction that $-100 \leq \zeta \leq 2$. The scalar wind speed is defined as

$$V_a^2 = u_1^2 + v_1^2 + U_c^2 \quad (4.258)$$

$$U_c = \begin{cases} 0.1 \text{ ms}^{-1} & , \text{ if } \zeta \geq 0 \text{ (stable)} \\ \beta w_* = \beta \left(z_i \frac{g}{\theta_v} \theta_{v*} u_* \right)^{1/3} & , \text{ if } \zeta < 0 \text{ (unstable)}. \end{cases} \quad (4.259)$$

3506 Here w_* is the convective velocity scale, z_i is the convective boundary layer height, and $\beta = 1$.

3507 The value of z_i is taken as 1000 m

3508 **(2) Flux-gradient relations [Zeng et al., 1998]**

3509 The flux-gradient relations are given by:

$$\frac{k(z_1 - d)}{\theta_*} \frac{\partial \theta}{\partial z} = \phi_h(\zeta) \quad (4.260)$$

$$\frac{k(z_1 - d)}{q_*} \frac{\partial q}{\partial z} = \phi_q(\zeta) \quad (4.261)$$

$$\phi_h = \phi_q \quad (4.262)$$

$$\phi_m(\zeta) = \begin{cases} (1 - 16\zeta)^{-1/4} & \text{for } \zeta < 0 \\ 1 + 5\zeta & \text{for } 0 < \zeta < 1 \end{cases} \quad (4.263)$$

$$\phi_h(\zeta) = \begin{cases} (1 - 16\zeta)^{-1/2} & \text{for } \zeta < 0 \\ 1 + 5\zeta & \text{for } 0 < \zeta < 1 \end{cases} \quad (4.264)$$

Under very unstable conditions, the flux-gradient relations are taken from [Kader and Yaglom \[1990\]](#):

$$\phi_m = 0.7k^{2/3}(-\zeta)^{1/3} \quad (4.265)$$

$$\phi_h = 0.9k^{4/3}(-\zeta)^{-1/3} \quad (4.266)$$

3510 To ensure the functions $\phi_m(\varsigma)$ and $\phi_h(\varsigma)$ are continuous, the simplest approach (i.e., without
 3511 considering any transition regions) is to match the above equations at $\varsigma_m = -1.574$ for $\phi_m(\varsigma)$
 3512 and $\varsigma_h = -0.465$ for $\phi_h(\varsigma)$.

Under very stable conditions (i.e., $\varsigma > 1$), the relations are taken from [Holtslag et al. \[1990\]](#):

$$\phi_m = \phi_h = 5 + \varsigma \quad (4.267)$$

3513 (3) Integral forms of the flux-gradient relations

Integration of the wind profile yields:

$$V_a = \frac{u_*}{k} f_M(\varsigma) \quad (4.268)$$

$$f_M(\varsigma) = \left\{ \left[\ln \left(\frac{\varsigma_m L}{z_{0m}} \right) - \psi_m(\varsigma_m) \right] + 1.14 [(-\varsigma)^{1/3} - (-\varsigma_m)^{1/3}] \right\}, \quad \varsigma < \varsigma_m = -1.574 \quad (4.268a)$$

$$f_M(\varsigma) = \left[\ln \left(\frac{z_1 - d}{z_{0m}} \right) - \psi_m(\varsigma) + \psi_m \left(\frac{z_{0m}}{L} \right) \right], \quad \varsigma_m < \varsigma < 0 \quad (4.268b)$$

$$f_M(\varsigma) = \left[\ln \left(\frac{z_1 - d}{z_{0m}} \right) + 5\varsigma \right], \quad 0 < \varsigma < 1 \quad (4.268c)$$

$$f_M(\varsigma) = \left\{ \left[\ln \left(\frac{L}{z_{0m}} \right) + 5 \right] + [5 \ln(\varsigma) + \varsigma - 1] \right\}, \quad \varsigma > 1 \quad (4.268d)$$

Integration of the potential temperature profile yields:

$$\theta_1 - \theta_s = \frac{\theta_*}{k} f_T(\varsigma) \quad (4.269)$$

$$f_T(\varsigma) = \left\{ \left[\ln \left(\frac{\varsigma_h L}{z_{0h}} \right) - \psi_h(\varsigma_h) \right] + 0.8 [(-\varsigma_h)^{-1/3} - (-\varsigma)^{-1/3}] \right\}, \quad \varsigma < \varsigma_h = -0.465 \quad (4.269a)$$

$$f_T(\varsigma) = \left[\ln \left(\frac{z_1 - d}{z_{0h}} \right) - \psi_h(\varsigma) + \psi_h \left(\frac{z_{0h}}{L} \right) \right], \quad \varsigma_h < \varsigma < 0 \quad (4.269b)$$

$$f_T(\varsigma) = \left[\ln \left(\frac{z_1 - d}{z_{0h}} \right) + 5\varsigma \right], \quad 0 < \varsigma < 1 \quad (4.269c)$$

$$f_T(\varsigma) = \left\{ \left[\ln \left(\frac{L}{z_{0h}} \right) + 5 \right] + [5 \ln(\varsigma) + \varsigma - 1] \right\}, \quad \varsigma > 1 \quad (4.269d)$$

The expressions for the specific humidity profiles are the same as those for potential temperature except that $(\theta_1 - \theta_s)$, θ_* and z_{0h} are replaced by $(q_1 - q_s)$, q_* and z_{0q} respectively. The stability functions for $\varsigma < 0$ are

$$\psi_m = 2 \ln \left(\frac{1 + \chi}{2} \right) + \ln \left(\frac{1 + \chi^2}{2} \right) - 2 \tan^{-1} \chi + \frac{\pi}{2} \quad (4.270)$$

$$\psi_h = \psi_q = 2 \ln \left(\frac{1 + \chi^2}{2} \right) \quad (4.271)$$

where

$$\chi = (1 - 16\varsigma)^{1/4} \quad (4.272)$$

3514 Note that the CLM code contains extra terms involving z_{0m}/ζ , z_{0h}/ζ , and z_{0q}/ζ for com-
 3515 pleteness. These terms are very small most of the time and hence are omitted in Eqs. 4.268 and
 3516 4.269.

3517 In addition to the momentum, sensible heat, and latent heat fluxes, land surface albedos
 3518 and upward longwave radiation are needed for the atmospheric radiation calculations. Surface
 3519 albedos depend on the solar zenith angle, the amount of leaf and stem material present, their
 3520 optical properties, and the optical properties of snow and soil. The upward longwave radiation
 3521 is the difference between the incident and absorbed fluxes. These and other aspects of the land
 3522 surface fluxes have been described by Dai et al. [2001].

3523 4.11.2 Ocean

The bulk formulas used to determine the turbulent fluxes of momentum (stress), water (evap-
 oration, or latent heat), and sensible heat into the atmosphere over ocean surfaces are

$$(\boldsymbol{\tau}, E, H) = \rho_A |\Delta \mathbf{v}| (C_D \Delta \mathbf{v}, C_E \Delta q, C_p C_H \Delta \theta), \quad (4.273)$$

3524 where ρ_A is atmospheric surface density and C_p is the specific heat. Since CAM 5.0 does not
 3525 allow for motion of the ocean surface, the velocity difference between surface and atmosphere
 3526 is $\Delta \mathbf{v} = \mathbf{v}_A$, the velocity of the lowest model level. The potential temperature difference
 3527 is $\Delta \theta = \theta_A - T_s$, where T_s is the surface temperature. The specific humidity difference is
 3528 $\Delta q = q_A - q_s(T_s)$, where $q_s(T_s)$ is the saturation specific humidity at the sea-surface temperature.

In (4.273), the transfer coefficients between the ocean surface and the atmosphere are com-
 puted at a height Z_A and are functions of the stability, ζ :

$$C_{(D,E,H)} = \kappa^2 \left[\ln \left(\frac{Z_A}{Z_{0m}} \right) - \psi_m \right]^{-1} \left[\ln \left(\frac{Z_A}{Z_{0(m,e,h)}} \right) - \psi_{(m,s,s)} \right]^{-1} \quad (4.274)$$

where $\kappa = 0.4$ is von Kármán's constant and $Z_{0(m,e,h)}$ is the roughness length for momentum,
 evaporation, or heat, respectively. The integrated flux profiles, ψ_m for momentum and ψ_s for
 scalars, under stable conditions ($\zeta > 0$) are

$$\psi_m(\zeta) = \psi_s(\zeta) = -5\zeta. \quad (4.275)$$

For unstable conditions ($\zeta < 0$), the flux profiles are

$$\begin{aligned} \psi_m(\zeta) = & 2 \ln[0.5(1 + X)] + \ln[0.5(1 + X^2)] \\ & - 2 \tan^{-1} X + 0.5\pi, \end{aligned} \quad (4.276)$$

$$\psi_s(\zeta) = 2 \ln[0.5(1 + X^2)], \quad (4.277)$$

$$X = (1 - 16\zeta)^{1/4}. \quad (4.278)$$

The stability parameter used in (4.275)–(4.278) is

$$\zeta = \frac{\kappa g Z_A}{u^{*2}} \left(\frac{\theta^*}{\theta_v} + \frac{Q^*}{(\epsilon^{-1} + q_A)} \right), \quad (4.279)$$

where the virtual potential temperature is $\theta_v = \theta_A(1 + \epsilon q_A)$; q_A and θ_A are the lowest level atmospheric humidity and potential temperature, respectively; and $\epsilon = 0.606$. The turbulent velocity scales in (4.279) are

$$\begin{aligned} u^* &= C_D^{1/2} |\Delta \mathbf{v}|, \\ (Q^*, \theta^*) &= C_{(E,H)} \frac{|\Delta \mathbf{v}|}{u^*} (\Delta q, \Delta \theta). \end{aligned} \quad (4.280)$$

Over oceans, $Z_{0e} = 9.5 \times 10^{-5}$ m under all conditions and $Z_{0h} = 2.2 \times 10^{-9}$ m for $\zeta > 0$, $Z_{0h} = 4.9 \times 10^{-5}$ m for $\zeta \leq 0$, which are given in Large and Pond [1982]. The momentum roughness length depends on the wind speed evaluated at 10 m as

$$\begin{aligned} Z_{om} &= 10 \exp \left[-\kappa \left(\frac{c_4}{U_{10}} + c_5 + c_6 U_{10} \right)^{-1} \right], \\ U_{10} &= U_A \left[1 + \frac{\sqrt{C_{10}^N}}{\kappa} \ln \left(\frac{Z_A}{10} - \psi_m \right) \right]^{-1}, \end{aligned} \quad (4.281)$$

3529 where $c_4 = 0.0027 \text{ m s}^{-1}$, $c_5 = 0.000142$, $c_6 = 0.0000764 \text{ m}^{-1} \text{ s}$, and the required drag coefficient
 3530 at 10-m height and neutral stability is $C_{10}^N = c_4 U_{10}^{-1} + c_5 + c_6 U_{10}$ as given by Large et al. [1994].

3531 The transfer coefficients in (4.273) and (4.274) depend on the stability following (4.275)–
 3532 (4.278), which itself depends on the surface fluxes (4.279) and (4.280). The transfer coefficients
 3533 also depend on the momentum roughness, which itself varies with the surface fluxes over oceans
 3534 (4.281). The above system of equations is solved by iteration.

3535 4.11.3 Sea Ice

3536 The fluxes between the atmosphere and sea ice are described in detail in the sea-ice model
 3537 documentation.

4.12 Dry Adiabatic Adjustment

If a layer is unstable with respect to the dry adiabatic lapse rate, dry adiabatic adjustment is performed. The layer is stable if

$$\frac{\partial T}{\partial p} < \frac{\kappa T}{p}. \quad (4.282)$$

In finite-difference form, this becomes

$$T_{k+1} - T_k < C1_{k+1}(T_{k+1} + T_k) + \delta, \quad (4.283)$$

where

$$C1_{k+1} = \frac{\kappa(p_{k+1} - p_k)}{2p_{k+1/2}}. \quad (4.284)$$

If there are any unstable layers in the top three model layers, the temperature is adjusted so that (4.283) is satisfied everywhere in the column. The variable δ represents a convergence criterion. The adjustment is done so that sensible heat is conserved,

$$c_p(\hat{T}_k \Delta p_k + \hat{T}_{k+1} \Delta p_{k+1}) = c_p(T_k \Delta p_k + T_{k+1} \Delta p_{k+1}), \quad (4.285)$$

and so that the layer has neutral stability:

$$\hat{T}_{k+1} - \hat{T}_k = C1_{k+1}(\hat{T}_{k+1} + \hat{T}_k). \quad (4.286)$$

As mentioned above, the hats denote the variables after adjustment. Thus, the adjusted temperatures are given by

$$\hat{T}_{k+1} = \frac{\Delta p_k}{\Delta p_{k+1} + \Delta p_k C2_{k+1}} T_k + \frac{\Delta p_{k+1}}{\Delta p_{k+1} + \Delta p_k C2_{k+1}} T_{k+1}, \quad (4.287)$$

and

$$\hat{T}_k = C2_{k+1} \hat{T}_{k+1}, \quad (4.288)$$

where

$$C2_{k+1} = \frac{1 - C1_{k+1}}{1 + C1_{k+1}}. \quad (4.289)$$

Whenever the two layers undergo dry adjustment, the moisture is assumed to be completely mixed by the process as well. Thus, the specific humidity is changed in the two layers in a conserving manner to be the average value of the original values,

$$\hat{q}_{k+1} = \hat{q}_k = (q_{k+1} \Delta p_{k+1} + q_k \Delta p_k) / (\Delta p_{k+1} + \Delta p_k). \quad (4.290)$$

3539 The layers are adjusted iteratively. Initially, $\delta = 0.01$ in the stability check (4.283). The column
 3540 is passed through from $k = 1$ to a user-specifiable lower level (set to 3 in the standard model
 3541 configuration) up to 15 times; each time unstable layers are adjusted until the entire column is
 3542 stable. If convergence is not reached by the 15th pass, the convergence criterion is doubled, a
 3543 message is printed, and the entire process is repeated. If δ exceeds 0.1 and the column is still
 3544 not stable, the model stops.

3545 As indicated above, the dry convective adjustment is only applied to the top three levels
 3546 of the standard model. The vertical diffusion provides the stabilizing vertical mixing at other
 3547 levels. Thus, in practice, momentum is mixed as well as moisture and potential temperature in
 3548 the unstable case.

3549

4.13 Prognostic Greenhouse Gases

3550

3551

3552

3553

3554

3555

The principal greenhouse gases whose longwave radiative effects are included in CAM 5.0 are H₂O, CO₂, O₃, CH₄, N₂O, CFC11, and CFC12. The prediction of water vapor is described elsewhere in this chapter, and CO₂ is assumed to be well mixed. Monthly O₃ fields are specified as input, as described in chapter 6. The radiative effects of the other four greenhouse gases (CH₄, N₂O, CFC11, and CFC12) may be included in CAM 5.0 through specified concentration distributions [Kiehl et al., 1998] or prognostic concentrations [Boville et al., 2001].

3556

3557

3558

The specified distributions are globally uniform in the troposphere. Above a latitudinally and seasonally specified tropopause height, the distributions are zonally symmetric and decrease upward, with a separate latitude-dependent scale height for each gas.

3559

3560

3561

3562

Prognostic distributions are computed following Boville et al. [2001]. Transport equations for the four gases are included, and losses have been parameterized by specified zonally symmetric loss frequencies: $\partial q/\partial t = -\alpha(y, z, t)q$. Monthly averaged loss frequencies, α , are obtained from the two-dimensional model of Garcia and Solomon [1994].

3563

3564

3565

3566

3567

3568

3569

3570

3571

3572

3573

We have chosen to specify globally uniform surface concentrations of the four gases, rather than their surface fluxes. The surface sources are imperfectly known, particularly for CH₄ and N₂O in preindustrial times. Even given constant sources and reasonable initial conditions, obtaining equilibrium values for the loading of these gases in the atmosphere can take many years. CAM 5.0 was designed for tropospheric simulation with relatively coarse vertical resolution in the upper troposphere and lower stratosphere. It is likely that the rate of transport into the stratosphere will be misrepresented, leading to erroneous loading and radiative forcing if surface fluxes are specified. Specifying surface concentrations has the advantage that we do not need to worry much about the atmospheric lifetime. However, we cannot examine observed features such as the interhemispheric gradient of the trace gases. For climate change experiments, the specified surface concentrations are varied but the stratospheric loss frequencies are not.

3574

3575

3576

3577

3578

3579

3580

3581

3582

3583

3584

Oxidation of CH₄ is an important source of water vapor in the stratosphere, contributing about half of the ambient mixing ratio over much of the stratosphere. Although CH₄ is not generally oxidized directly into water vapor, this is not a bad approximation, as shown by Le Texier et al. [1988]. In CAM 5.0, it is assumed that the water vapor (volume mixing ratio) source is twice the CH₄ sink. This approach was also taken by Mote et al. [1993] for middle atmosphere studies with an earlier version of the CCM. This part of the water budget is of some importance in climate change studies, because the atmospheric CH₄ concentrations have increased rapidly with time and this increase is projected to continue into the next century (e.g., Alcamo et al. [1995]) The representation of stratospheric water vapor in CAM 5.0 is necessarily crude, since there are few levels above the tropopause. However, the model is capable of capturing the main features of the CH₄ and water distributions.

3585 **Chapter 5**

3586 **Extensions to CAM**

3587 5.1 Chemistry

3588 5.1.1 Introduction

3589 In this Section, we provide a description of the neutral constituent chemical processes adopted
3590 in CAM-chem and WACCM4.0. This section will contain a description of constituent: 1) surface
3591 boundary conditions; 2) numerical algorithms used to solve the corresponding set of ordinary
3592 differential equations. 3) gas-phase and heterogeneous reactions; and 4) wet and dry deposition
3593 removal processes;

3594 5.1.2 Emissions

3595 Surface emissions are used in as a flux boundary condition for the diffusion equation of all
3596 applicable tracers in the planetary boundary-layer scheme. The surface flux files used in the
3597 released version are discussed in Lamarque et al. [2010b] and conservatively remapped from their
3598 original resolution (monthly data available every decade at 0.5x0.5) to (monthly data every year
3599 at 1.9x2.5). In addition, natural emissions from MOZART-4 were added to all relevant species.
3600 Finally, isoprene emissions are calculated interactively (within CLM (point 2) above), leading
3601 to approximately (emissions depend on light and temperature) 500 Tg/year.

	Anthro.	Natural	Interactive
CH ₂ O	x	x	
CO	x	x	
DMS		x	
ISOP			x
NO	x		
SO ₂	x		

Table 5.1: Surface fluxes for CAM4 superfast chemistry.

3602 Additional emissions (volcanoes and aircraft) are included as three-dimension arrays,
3603 conservatively-remapped to the CAM-chem grid. The volcanic emission are from Dentener et al.
3604 [2006b] and the aircraft (NO₂) emissions are from Lamarque et al. [2010b]. In the case of vol-
3605 canic emissions (SO₂ and SO₂), an assumed 2% of the total sulfur mass is directly released as
3606 SO₂.

3607 5.1.3 Lower boundary conditions

3608 The concentration of specific long-lived chemical tracers (methane and longer lifetimes, in addi-
3609 tion to hydrogen and methyl bromide) are fixed in the lowest model layer using the reconstructed
3610 concentrations (CMIP5 recommended data) available from
3611 <http://www.iiasa.ac.at/web-apps/tnt/RcpDb/dsd?Action=htmlpage&page=download>. As this
3612 dataset only provides annual average values, a specified seasonal cycle (based on present-day
3613 observations) is added to methane and carbon dioxide.

3614 5.1.4 Lightning

3615 The lightning parameterization differs slightly from that used in MOZART-2 [Horowitz et al.,
3616 2003]. The lightning strength still depends on cloud top height, with a stronger dependence
3617 over land than ocean [Price et al., 1997a]. The definition of ocean grid boxes has been refined
3618 to include only boxes surrounded by ocean, so that the land parameterization is extended one
3619 grid box beyond the continents Price and Rind [1992]. Flash frequency is determined by area,
3620 not grid box. The vertical distribution of NO emissions has been modified from that given by
3621 Pickering et al. [1998], to have a reduced proportion of the emissions emitted near the surface,
3622 similar to that used by DeCaria et al. [2006]. In addition, the strength of intra-cloud (IC) light-
3623 ning strikes is assumed to be equal to cloud-to-ground strikes, as recommended by Ridley et al.
3624 [2005].

3625 Because the lightning NO source is very resolution-dependent, it can be scaled under non-
3626 standard resolutions to a produce 5-7 Tg(N)/year globally.

3627 5.1.5 Dry deposition

3628 The list of species affected by dry deposition is subject to user selection. Dry deposition ve-
3629 locities are computed interactively (i.e. are influenced by variations in temperature, solar in-
3630 solation and precipitation), based on the resistance-based parameterization of Wesely [1989],
3631 Walmsley and Wesely [1996], and Wesely and Hicks [2000]. The calculation of surface resis-
3632 tances over land uses the vegetation distribution as defined in CLM. In addition, as the pa-
3633 rameters in the Wesely [1989] parameterization are season-dependent (to take into account the
3634 specific role of changes in vegetation cover), a season index is computed from the monthly-
3635 averaged leaf-area index input file to CLM. In the case of CLM-CN or DGVM (where the LAI
3636 is prognostic), this file is still read and seasonality is still defined accordingly. Deposition over
3637 the ocean is computed separately in CAM (but using the same formulation), with the overall
3638 deposition velocity computed as the weighted (by the land/ocean fraction) mean between the
3639 land and ocean values.

3640 The deposition velocity calculation has been extended from the aforementioned references
3641 to take into account special cases for CO, H₂ and PAN. In the case of CO and H₂, surface
3642 uptake is caused by the oxidation by soil bacteria or enzymes [Yonemura et al., 2000]. This has
3643 been parameterized using the approach of Sanderson et al. [2003], which defines the deposition
3644 velocity by a linear or quadratic function in soil moisture content (or its logarithm), depending
3645 on the land cover type. In the case of PAN, new laboratory experiments have indicated a strong
3646 uptake of PAN by leaves [Teklemariam and Sparks, 2004]. Using the results from that study,
3647 we have included a leaf uptake of PAN that is vegetation-dependent, based on Sparks et al.
3648 (2003). Results from this parameterization agreed with observations during a field experiment
3649 [Turnipseed et al., 2006].

3650 5.1.6 Wet removal

3651 Wet deposition for gas-phase species is represented as a first-order loss process within the chem-
3652 istry operator, with loss rates computed based on the large-scale and convective precip- ita-
3653 tion rates in CAM. Soluble species (H₂O₂, HNO₃, CH₂O, SO₂) undergo wet removal by in-

3654 cloud scavenging, using the parameterization of [Giorgi and Chameides \[1985\]](#) based on their
3655 temperature-dependent effective Henry’s law constants. In addition, highly soluble species
3656 (HNO_3 , H_2O_2) are also removed by below-cloud washout, using the formulation described in
3657 detail by [Brasseur et al. \[1998\]](#).

3658 5.1.7 Photolytic Approach (Neutral Species)

3659 The calculation of the photolysis coefficients is divided into two regions: (1) 120 nm to 200 nm
3660 (33 wavelength intervals); (2) 200 nm to 750 nm (67 wavelength intervals). The total photolytic
3661 rate constant (J) for each absorbing species is derived during model execution by integrating the
3662 product of the wavelength dependent exo-atmospheric flux (F_{exo}); the atmospheric transmission
3663 function (or normalized actinic flux) (N_A), which is unity at the top of atmosphere in most wave-
3664 length regions; the molecular absorption cross-section (σ); and the quantum yield (ϕ). The exo-
3665 atmospheric flux over these wavelength intervals can be specified from observations and varied
3666 over the 11-year solar sunspot cycle (see section 5.3.6). The wavelength-dependent transmission
3667 function is derived as a function of the model abundance of ozone and molecular oxygen. For
3668 wavelengths greater than 200 nm a normalized flux lookup table (LUT) approach is used, based
3669 on the 4-stream version of the Stratosphere, Troposphere, Ultraviolet (STUV) radiative transfer
3670 model (S. Madronich, personal communication). The transmission function is interpolated from
3671 the LUT as a function of altitude, column ozone, surface albedo, and zenith angle. The tem-
3672 perature and pressure dependences of the molecular cross sections and quantum yields for each
3673 photolytic process are also represented by a LUT in this wavelength region. At wavelengths
3674 less than 200 nm, the wavelength-dependent cross section and quantum yields for each species
3675 are specified and the transmission function is calculated explicitly for each wavelength interval.
3676 There are two exceptions to this approach. In the case of $J(\text{NO})$ and $J(\text{O}_2)$, detailed photolysis
3677 parameterizations are included inline. In the Schumann-Runge Band region (SRBs), the param-
3678 eterization of NO photolysis in the δ -bands is based on [Minschwaner and Siskind \[1993\]](#). This
3679 parameterization includes the effect of self-absorption and subsequent attenuation of atmospheric
3680 transmission by the model-derived NO concentration. For $J(\text{O}_2)$, the SRB and Lyman-alpha pa-
3681 rameterizations are based on [Koppers and Murtagh \[1996\]](#) and [Chabrillat and Kockarts \[1997\]](#),
3682 respectively.

3683 The photolytic reactions included in WACCM4.0 are listed in Table 4. In most all cases the
3684 photolytic rate constants are taken from JPL02-25 [[Sander, S. P., et al., 2003](#)]. Exceptions to
3685 this condition are described in the comment section for any given reaction.

3686 In addition, tropospheric photolysis rates can be computed interactively following [Tie et al.](#)
3687 [[1992](#)]. Users interested in using this capability have to contact the Chemistry-CLimate Working
3688 Group Liaison as this is an unsupported option.

3689 5.1.8 Numerical Solution Approach

Chemical and photochemical processes are expressed by a system of time-dependent ordinary differential equations at each point in the spatial grid, of the following form:

$$\frac{d\vec{y}}{dt} = \vec{P}(\vec{y}, t) - \vec{L}(\vec{y}, t) \cdot \vec{y} \quad (5.1)$$

$$\vec{y}(t) = \{y_i(t)\} \quad i = 1, 2, \dots, N$$

where \vec{y} is the vector of all solution variables (chemical species), N is the number of variables in the system, and y_i represents the i^{th} variable. \vec{P} and \vec{L} represent the production and loss rates, which are, in general, non-linear functions of the y_i . This system of equations is solved via two algorithms: an explicit forward Euler method:

$$y_i^{n+1} = y_i^n + \Delta t \cdot f_i(t_n, y^n) \quad (5.2)$$

in the case of species with long lifetimes and weak forcing terms (e.g., N_2O), and a more robust implicit backward Euler method:

$$y_i^{n+1} = y_i^n + \Delta t \cdot f_i(t_{n+1}, y^{n+1}) \quad (5.3)$$

for species that comprise a “stiff system” with short lifetimes and strong forcings (e.g., OH). Here n represents the time step index. Each method is first order accurate in time and conservative. The overall chemistry time step, $\Delta t = t_{n+1} - t_n$, is fixed at 30 minutes. Preprocessing software requires the user to assign each solution variable, y_i , to one of the solution schemes. The discrete analogue for methods (5.2) and (5.3) above results in two systems of algebraic equations at each grid point. The solution to these algebraic systems for equation (5.2) is straightforward (i.e., explicit). The algebraic system from the implicit method (5.3) is quadratically non-linear. This system can be written as:

$$\vec{G}(\vec{y}^{n+1}) = \vec{y}^{n+1} - \vec{y}^n - \Delta t \cdot \vec{f}(t_{n+1}, \vec{y}^{n+1}) = 0 \quad (5.4)$$

Here G is an N -valued, non-linear vector function, where N equals the number of species solved via the implicit method. The solution to equation (5.4) is solved with a Newton- Raphson iteration approach as shown below:

$$\vec{y}_{m+1}^{n+1} = \vec{y}_m^{n+1} - \vec{J} \cdot \vec{G}(\vec{y}_m^{n+1}); \quad m = 0, 1, \dots, M \quad (5.5)$$

Where m is the iteration index and has a maximum value of ten. The elements of the Jacobian matrix \vec{J} are given by:

$$J_{ij} = \frac{\partial G_i}{\partial y_j}$$

3690 The iteration and solution of equation (5.5) is carried out with a sparse matrix solution al-
 3691 gorithm. This process is terminated when the given solution variable changes in a relative
 3692 measure by less than a prescribed fractional amount. This relative error criterion is set on a
 3693 species by species basis, and is typically 0.001; however, for some species (e.g., O_3), where a
 3694 tighter error criterion is desired, it is set to 0.0001. If the iteration maximum is reached (for
 3695 any species) before the error criterion is met, the time step is cut in half and the solution to
 3696 equation (5.5) is iterated again. The time step can be reduced five times before the solution is
 3697 accepted. This approach is based on the work of Sandu et al. [1996] and Sandu et al. [1997]; see
 3698 also Brasseur et al. [1999].

3699

5.2 Superfast Chemistry

3700

5.2.1 Chemical mechanism

3701

3702

3703

3704

3705

3706

3707

3708

3709

3710

3711

3712

3713

The super-fast mechanism was developed for coupled climate model usage, and is based on an updated version of the full non-methane hydrocarbon effects (NMHC) chemical mechanism for the troposphere and stratosphere used in the Lawrence Livermore National Laboratory off-line 3D global chemistry-transport model (IMPACT) [Rotman et al., 2004]. The super-fast mechanism includes 15 photochemically active trace species (O_3 , OH, HO_2 , H_2O_2 , NO, NO_2 , HNO_3 , CO, CH_2O , CH_3O_2 , CH_3OOH , DMS, SO_2 , SO_4 , and C_5H_8) that allow us to calculate the major terms by which global change operates in tropospheric ozone and sulfate photochemistry. The families selected are Ox, HOx, NOy, the CH_4 oxidation suite plus isoprene (to capture the main NMHC effects), and a group of sulfur species to simulate natural and anthropogenic sources leading to sulfate aerosol. Sulfate aerosols is handled following Tie et al. [2005]. In this scheme, CH_4 concentrations are read in from a file and uses CAM3.5 simulations Lamarque et al. [2010b]. The super-fast mechanism was validated by comparing the super-fast and full mechanisms in side-by-side simulations.

3714

5.2.2 LINOZ

3715

3716

3717

3718

3719

3720

3721

3722

3723

3724

Linoz is linearized ozone chemistry for stratospheric modeling [McLinden et al., 2000]. It calculates the net production of ozone (i.e., production minus loss) as a function of only three independent variables: local ozone concentration, temperature, and overhead column ozone). A zonal mean climatology for these three variables as well as the other key chemical variables such a total odd-nitrogen methane abundance is developed from satellite and other in situ observations. A relatively complete photochemical box model Prather [1992] is used to integrate the radicals to a steady state balance and then compute the net production of ozone. Small perturbations about the chemical climatology are used to calculate the coefficients of the first-order Taylor series expansion of the net production in terms of local ozone mixing ratio (f), temperature (T), and overhead column ozone (c).

$$\begin{aligned} \frac{df}{df} = & (P - L)^o + \left. \frac{\delta(P - L)}{\delta f} \right|_o (f - f^o) + \left. \frac{\delta(P - L)}{\delta T} \right|_o (T - T^o) \\ & + \left. \frac{\delta(P - L)}{\delta c} \right|_o (c - c^o) \end{aligned} \quad (5.6)$$

3725

3726

3727

3728

3729

3730

3731

3732

The photochemical tendency for the climatology is denoted by $(P - L)_o$, and the climatology values for the independent variables are denoted by f_o , c_o , and T_o , respectively. Including these four climatology values and the three partial derivatives, Linoz is defined by seven tables. Each table is specified by 216 atmospheric profiles: 12 months by 18 latitudes (85°S to 85°N). For each profile, quantities are evaluated at every 2 km in pressure altitude from $z^* = 10$ to 58 km ($z^* = 16 \text{ km log}_{10}(1000/p)$). These tables (calculated for each decade, 1850-2000 to take into account changes in CH_4 and N_2O) are automatically remapped onto the CAM-chem grid with the mean vertical properties for each CAM-chem level calculated as the mass-weighted average

3733 of the interpolated Linoz profiles. Equation (1) is implemented for the chemical tendency of
3734 ozone in CAM-chem.

3735 **5.2.3 PSC ozone loss**

3736 In the superfast chemistry, we incorporate the PSCs parameterization scheme of [Cariolle et al.](#)
3737 [\[1990\]](#) when the temperature falls below 195 K and the sun is above the horizon at stratospheric
3738 altitudes. The O₃ loss scales as the squared stratospheric chlorine loading (normalized by the
3739 1980 level threshold). In this formulation PSC activation invokes a rapid e-fold of O₃ based
3740 on a photochemical model, but only when the temperature stays below the PSC threshold.
3741 The stratospheric chlorine loading (1850-2005) is input in the model using equivalent effective
3742 stratospheric chlorine (EESC) [\[Newman et al., 2007\]](#) table based on observed mixing ratios at
3743 the surface.

3744 **5.2.4 Upper boundary condition**

3745 The model top is considered a rigid lid (no flux across that boundary) for all chemical species.

5.3 WACCM4.0 Physical Parameterizations

In WACCM4.0, we extend the physical parameterizations used in CAM4 by adding constituent separation velocities to the molecular (vertical) diffusion and modifying the gravity spectrum parameterization. Both of these parameterizations are present, but not used, in CAM4. In addition, we replace the CAM4 parameterizations for both solar and longwave radiation above ~ 65 km, and add neutral and ion chemistry models.

5.3.1 WACCM4.0 Domain and Resolution

WACCM4.0 has 66 vertical levels from the ground to 5.1×10^{-6} hPa, as in the previous WACCM versions. As in CAM4, the vertical coordinate is purely isobaric above 100 hPa, but is terrain following below that level. At any model grid point, the local pressure p is determined by

$$p(i, j, k) = A(k) p_0 + B(k) p_s(i, j) \quad (5.7)$$

where A and B are functions of model level, k , only; $p_0 = 10^3$ hPa is a reference surface pressure; and p_s is the predicted surface pressure, which is a function of model longitude and latitude (indexed by i and j). The finite volume dynamical core uses locally material surfaces for its internal vertical coordinate and remaps (conservatively interpolates) to the hybrid surfaces after each time step.

Within the physical and chemical parameterizations, a local pressure coordinate is used, as described by (5.7). However, in the remainder of this note we refer to the vertical coordinate in terms of log-pressure altitude

$$Z = H \log \left(\frac{p_0}{p} \right). \quad (5.8)$$

The value adopted for the scale height, $H = 7$ km, is representative of the real atmosphere up to ~ 100 km, above that altitude temperature increases very rapidly and the typical scale height becomes correspondingly larger. It is important to distinguish Z from the *geopotential* height z , which is obtained from integration of the hydrostatic equation.

In terms of log-pressure altitude, the model top level is found at $Z = 140$ km ($z \simeq 150$ km). It should be noted that the solution in the top 15-20 km of the model is undoubtedly affected by the presence of the top boundary. However, it should not be thought of as a *sponge layer*, since molecular diffusion is a real process and is the primary damping on upward propagating waves near the model top. Indeed, this was a major consideration in moving the model top well above the turbopause. Considerable effort has been expended in formulating the upper boundary conditions to obtain realistic solutions near the model top and all of the important physical and chemical processes for that region have been included.

The standard vertical resolution is variable; it is 3.5 km above about 65 km, 1.75 km around the stratopause (50 km), 1.1-1.4 km in the lower stratosphere (below 30 km), and 1.1 km in the troposphere (except near the ground where much higher vertical resolution is used in the planetary boundary layer).

Two standard horizontal resolutions are supported in WACCM4.0: the $4 \times 5^\circ$ (latitude \times longitude) low resolution version has 72 longitude and 46 latitude points; the $1.9 \times 2.5^\circ$ medium resolution version has 96 longitude and 144 latitude points. A $0.9 \times 1.25^\circ$ high resolution

3777 version of WACCM4.0 has had limited testing, and is not yet supported, due to computational
 3778 cost constraints. The $4 \times 5^\circ$ version has been used extensively for MLT studies, where it gives
 3779 very similar results to the $1.9 \times 2.5^\circ$ version. However, caution should be exercised in using
 3780 $4 \times 5^\circ$ results below the stratopause, since the meridional resolution may not be sufficient to
 3781 represent adequately the dynamics of either the polar vortex or synoptic and planetary waves.

3782 At all resolutions, the time step is 1800 s for the physical parameterizations. Within the finite
 3783 volume dynamical core, this time step is subdivided as necessary for computational stability.

3784 5.3.2 Molecular Diffusion and Constituent Separation

3785 The vertical diffusion parameterization in CAM4 provides the interface to the turbulence pa-
 3786 rameterization, computes the molecular diffusivities (if necessary) and finally computes the ten-
 3787 dencies of the input variables. The diffusion equations are actually solved implicitly, so the ten-
 3788 dencies are computed from the difference between the final and initial profiles. In WACCM4.0,
 3789 we extend this parameterization to include the terms required for the gravitational separation
 3790 of constituents of differing molecular weights. The formulation for molecular diffusion follows
 3791 [Banks and Kockarts \[1973\]](#)

A general vertical diffusion parameterization can be written in terms of the divergence of diffusive fluxes:

$$\frac{\partial}{\partial t}(u, v, q) = -\frac{1}{\rho} \frac{\partial}{\partial z}(F_u, F_v, F_q) \quad (5.9)$$

$$\frac{\partial}{\partial t}s = -\frac{1}{\rho} \frac{\partial}{\partial z}F_H + D \quad (5.10)$$

where $s = c_p T + gz$ is the dry static energy, z is the geopotential height above the local surface (does not include the surface elevation) and D is the heating rate due to the dissipation of resolved kinetic energy in the diffusion process. The diffusive fluxes are defined as:

$$F_{u,v} = -\rho K_m \frac{\partial}{\partial z}(u, v), \quad (5.11)$$

$$F_H = -\rho K_H \frac{\partial s}{\partial z} + \rho K_H^t \gamma_H, \quad (5.12)$$

$$F_q = -\rho K_q \frac{\partial q}{\partial z} + \rho K_q^t \gamma_q + \text{sep} - \text{flux}. \quad (5.13)$$

The viscosity K_m and diffusivities $K_{q,H}$ are the sums of: turbulent components $K_{m,q,H}^t$, which dominate below the mesopause; and molecular components $K_{m,q,H}^m$, which dominate above 120 km. The non-local transport terms $\gamma_{q,H}$ are given by the ABL parameterization and the kinetic energy dissipation is

$$D \equiv -\frac{1}{\rho} \left(F_u \frac{\partial u}{\partial z} + F_v \frac{\partial v}{\partial z} \right). \quad (5.14)$$

3792 The treatment of the turbulent diffusivities $K_{m,q,H}^t$, the energy dissipation D and the nonlocal
 3793 transport terms $\gamma_{H,q}$ is described in the CAM 5.0 Technical Description and will be omitted
 3794 here.

3795 **Molecular viscosity and diffusivity**

The empirical formula for the molecular kinematic viscosity is

$$K_m^m = 3.55 \times 10^{-7} T^{2/3} / \rho, \quad (5.15)$$

and the molecular diffusivity for heat is

$$K_H^m = P_r K_m^m, \quad (5.16)$$

where P_r is the Prandtl number and we assume $P_r = 1$ in WACCM4.0. The constituent diffusivities are

$$K_q^m = T^{1/2} M_w / \rho, \quad (5.17)$$

3796 where M_w is the molecular weight.

3797 **Diffusive separation velocities**

3798 As the mean free path increases, constituents of different molecular weights begin to separate
 3799 in the vertical. In WACCM4.0, this separation is represented by a separation velocity for each
 3800 constituent with respect mean air. Since WACCM4.0 extends only into the lower thermosphere,
 3801 we avoid the full complexity of the separation problem and represent mean air by the usual dry
 3802 air mixture used in the lower atmosphere ($M_w = 28.966$) [Banks and Kockarts \[1973\]](#).

3803 **Discretization of the vertical diffusion equations**

In CAM4, as in previous version of the CCM, (5.9–5.12) are cast in pressure coordinates, using

$$dp = -\rho g dz, \quad (5.18)$$

and discretized in a time-split form using an Euler backward time step. Before describing the numerical solution of the diffusion equations, we define a compact notation for the discrete equations. For an arbitrary variable ψ , let a subscript denote a discrete time level, with current step ψ_n and next step ψ_{n+1} . The model has L layers in the vertical, with indexes running from top to bottom. Let ψ^k denote a layer midpoint quantity and let $\psi^{k\pm}$ denote the value at the interface above (below) k . The relevant quantities, used below, are then:

$$\begin{aligned} \psi^{k+} &= (\psi^k + \psi^{k+1})/2, & k \in (1, 2, 3, \dots, L-1) \\ \psi^{k-} &= (\psi^{k-1} + \psi^k)/2, & k \in (2, 3, 4, \dots, L) \\ \delta^k \psi &= \psi^{k+} - \psi^{k-}, \\ \delta^{k+} \psi &= \psi^{k+1} - \psi^k, \\ \delta^{k-} \psi &= \psi^k - \psi^{k-1}, \\ \psi_{n+} &= (\psi_n + \psi_{n+1})/2, \\ \delta_n \psi &= \psi_{n+1} - \psi_n, \\ \delta t &= t_{n+1} - t_n, \\ \Delta^{k,l} &= 1, & k = l, \\ &= 0, & k \neq l. \end{aligned}$$

Like the continuous equations, the discrete equations are required to conserve momentum, total energy and constituents. Neglecting the nonlocal transport terms, the discrete forms of (5.9–5.10) are:

$$\frac{\delta_n(u, v, q)^k}{\delta t} = g \frac{\delta^k F_{u,v,q}}{\delta^k p} \quad (5.19)$$

$$\frac{\delta_n s^k}{\delta t} = g \frac{\delta^k F_H}{\delta^k p} + D^k. \quad (5.20)$$

For interior interfaces, $1 \leq k \leq L - 1$,

$$F_{u,v}^{k+} = (g\rho^2 K_m)_n^{k+} \frac{\delta^{k+}(u, v)_{n+1}}{\delta^{k+p}} \quad (5.21)$$

$$F_{q,H}^{k+} = (g\rho^2 K_{q,H})_n^{k+} \frac{\delta^{k+}(u, v)_{n+1}}{\delta^{k+p}}. \quad (5.22)$$

3804 Surface fluxes $F_{u,v,q,H}^{L+}$ are provided explicitly at time n by separate surface models for land,
 3805 ocean, and sea ice while the top boundary fluxes are usually $F_{u,v,q,H}^{1-} = 0$. The turbulent
 3806 diffusion coefficients $K_{m,q,H}^t$ and non-local transport terms $\gamma_{q,H}$ are calculated for time n by the
 3807 turbulence model (identical to CAM4). The molecular diffusion coefficients, given by (5.15–5.17)
 3808 are also evaluated at time n .

3809 Solution of the vertical diffusion equations

3810 Neglecting the discretization of $K_{m,q,H}^t$, D and $\gamma_{q,H}$, a series of time-split operators is defined by
 3811 (5.19–5.22). Once the diffusivities ($K_{m,q,H}$) and the non-local transport terms ($\gamma_{q,H}$) have been
 3812 determined, the solution of (5.19–5.22), proceeds in several steps.

- 3813 1. update the bottom level values of u , v , q and s using the surface fluxes;
- 3814 2. invert (5.19) and (5.21) for u , v_{n+1} ;
- 3815 3. compute D and use to update the s profile;
- 3816 4. invert (5.19,5.20) and (5.22) for s_{n+1} and q_{n+1}

3817 Note that since all parameterizations in CAM4 return tendencies rather modified profiles,
 3818 the actual quantities returned by the vertical diffusion are $\delta_n(u, v, s, q)/\delta t$.

Equations (5.19–5.22) constitute a set of four tridiagonal systems of the form

$$-A^k \psi_{n+1}^{k+1} + B^k \psi_{n+1}^k - C^k \psi_{n+1}^{k-1} = \psi_{n+1}^k, \quad (5.23)$$

where ψ_{n+1} indicates u , v , q , or s after updating from time n values with the nonlocal and boundary fluxes. The super-diagonal (A^k), diagonal (B^k) and sub-diagonal (C^k) elements of (5.23) are:

$$A^k = \frac{1}{\delta^k p} \frac{\delta t}{\delta^{k+p}} (g^2 \rho^2 K)_n^{k+}, \quad (5.24)$$

$$B^k = 1 + A^k + C^k, \quad (5.25)$$

$$C^k = \frac{1}{\delta^k p} \frac{\delta t}{\delta^{k-p}} (g^2 \rho^2 K)_n^{k-}. \quad (5.26)$$

The solution of (5.23) has the form

$$\psi_{n+1}^k = E^k \psi_{n+1}^{k-1} + F^k, \quad (5.27)$$

or,

$$\psi_{n+1}^{k+1} = E^{k+1} \psi_{n+1}^k + F^{k+1}. \quad (5.28)$$

Substituting (5.28) into (5.23),

$$\psi_{n+1}^k = \frac{C^k}{B^k - A^k E^{k+1}} \psi_{n+1}^{k-1} + \frac{\psi_{n+1}^k + A^k F^{k+1}}{B^k - A^k E^{k+1}}. \quad (5.29)$$

Comparing (5.27) and (5.29), we find

$$E^k = \frac{C^k}{B^k - A^k E^{k+1}}, \quad L > k > 1, \quad (5.30)$$

$$F^k = \frac{\psi_{n+1}^k + A^k F^{k+1}}{B^k - A^k E^{k+1}}, \quad L > k > 1. \quad (5.31)$$

The terms E^k and F^k can be determined upward from $k = L$, using the boundary conditions

$$E^{L+1} = F^{L+1} = A^L = 0. \quad (5.32)$$

Finally, (5.29) can be solved downward for ψ_{n+1}^k , using the boundary condition

$$C^1 = 0 \Rightarrow E^1 = 0. \quad (5.33)$$

3819 CCM1-3 used the same solution method, but with the order of the solution reversed, which
 3820 merely requires writing (5.28) for ψ_{n+1}^{k-1} instead of ψ_{n+1}^{k+1} . The order used here is particularly
 3821 convenient because the turbulent diffusivities for heat and all constituents are the same but
 3822 their molecular diffusivities are not. Since the terms in (5.30-5.31) are determined from the
 3823 bottom upward, it is only necessary to recalculate A^k , C^k , E^k and $1/(B^k - A^k E^{k+1})$ for each
 3824 constituent within the region where molecular diffusion is important.

3825 5.3.3 Gravity Wave Drag

3826 Vertically propagating gravity waves can be excited in the atmosphere where stably stratified
 3827 air flows over an irregular lower boundary and by internal heating and shear. These waves
 3828 are capable of transporting significant quantities of horizontal momentum between their source
 3829 regions and regions where they are absorbed or dissipated. Previous GCM results have shown
 3830 that the large-scale momentum sinks resulting from breaking gravity waves play an important
 3831 role in determining the structure of the large-scale flow. CAM4 incorporates a parameterization
 3832 for a spectrum of vertically propagating internal gravity waves based on the work of Lindzen
 3833 [1981], Holton [1982], Garcia and Solomon [1985] and McFarlane [1987]. The parameterization
 3834 solves separately for a general spectrum of monochromatic waves and for a single stationary wave
 3835 generated by flow over orography, following McFarlane [1987]. The spectrum is omitted in the
 3836 standard tropospheric version of CAM4, as in previous versions of the CCM. Here we describe
 3837 the modified version of the gravity wave spectrum parameterization used in WACCM4.0.

Adiabatic inviscid formulation

Following Lindzen [1981], the continuous equations for the gravity wave parameterization are obtained from the two-dimensional hydrostatic momentum, continuity and thermodynamic equations in a vertical plane:

$$\left(\frac{\partial}{\partial t} + u\frac{\partial}{\partial x}\right)u = -\frac{\partial\Phi}{\partial x}, \quad (5.34)$$

$$\frac{\partial u}{\partial x} + \frac{\partial W}{\partial Z} = 0, \quad (5.35)$$

$$\left(\frac{\partial}{\partial t} + u\frac{\partial}{\partial x}\right)\frac{\partial\Phi}{\partial Z} + N^2w = 0. \quad (5.36)$$

Where N is the local Brunt-Väisälä frequency, and W is the vertical velocity in log pressure height (Z) coordinates. Eqs. (5.34)–(5.36) are linearized about a large scale background wind \bar{u} , with perturbations u', w' , and combined to obtain:

$$\left(\frac{\partial}{\partial t} + \bar{u}\frac{\partial}{\partial x}\right)^2\frac{\partial^2 w'}{\partial Z^2} + N^2\frac{\partial^2 w'}{\partial x^2} = 0. \quad (5.37)$$

Solutions to (5.37) are assumed to be of the form:

$$w' = \hat{w} e^{ik(x-ct)} e^{Z/2H}, \quad (5.38)$$

where H is the scale height, k is the horizontal wavenumber and c is the phase speed of the wave. Substituting (5.38) into (5.37), one obtains:

$$-k^2(\bar{u} - c)^2 \left(\frac{\partial}{\partial Z} + \frac{1}{2H}\right)^2 \hat{w} - k^2 N^2 \hat{w} = 0. \quad (5.39)$$

Neglecting $\frac{1}{2H}$ compared to $\frac{\partial}{\partial Z}$ in (5.39), one obtains the final form of the two dimensional wave equation:

$$\frac{d^2 \hat{w}}{dZ^2} + \lambda^2 \hat{w} = 0, \quad (5.40)$$

with the coefficient defined as:

$$\lambda = \frac{N}{(\bar{u} - c)}. \quad (5.41)$$

The WKB solution of (5.40) is:

$$\hat{w} = A\lambda^{-1/2} \exp\left(i \int_0^Z \lambda dz'\right), \quad (5.42)$$

and the full solution, from (5.38), is:

$$w'(Z, t) = A\lambda^{-1/2} \exp\left(i \int_0^Z \lambda dz'\right) e^{ik(x-ct)} e^{Z/2H}. \quad (5.43)$$

The constant A is determined from the wave amplitude at the source ($z = 0$), The Reynolds stress associated with (5.43) is:

$$\tau(Z) = \tau(0) = \overline{\rho u' w'} = -\frac{2}{k} |A|^2 \rho_0 \text{sgn}(\lambda), \quad (5.44)$$

and is conserved, while the momentum flux $\overline{u' w'} = -(m/k) \overline{w' w'}$ grows exponentially with altitude as $\exp(Z/H)$, per (5.43). We note that the vertical flux of wave energy is $c_{gz} E' = (U - c) \tau$ (Andrews et al. [1987]), where c_{gz} is the vertical group velocity, so that deposition of wave momentum into the mean flow will be accompanied by a transfer of energy to the background state.

3844 Saturation condition

The wave amplitude in (5.43) grows as $e^{Z/2H}$ until the wave becomes unstable to convective overturning, Kelvin-Helmholtz instability, or other nonlinear processes. At that point, the wave amplitude is assumed to be limited to the amplitude that would trigger the instability and the wave is “saturated”. The saturation condition used in CAM4 is from McFarlane [1987], based on a maximum Froude number (F_c), or streamline slope.

$$|\overline{\rho u' w'}| \leq \tau^* = F_c^2 \frac{k}{2} \rho \frac{|\bar{u} - c|^3}{N}, \quad (5.45)$$

where τ^* is the saturation stress and $F_c^2 = 0.5$. In WACCM4.0, $F_c^2 = 1$ and is omitted hereafter. Following Lindzen [1981], within a saturated region the momentum tendency can be determined analytically from the divergence of τ^* :

$$\begin{aligned} \frac{\partial \bar{u}}{\partial t} &= -\frac{e}{\rho} \frac{\partial}{\partial Z} \overline{\rho u' w'}, \\ &\simeq -e \frac{k (\bar{u} - c)^3}{2} \frac{1}{N} \frac{\partial \rho}{\rho \partial Z}, \\ &\simeq -e \frac{k (\bar{u} - c)^3}{2} \frac{1}{NH}, \end{aligned} \quad (5.46)$$

where e is an “efficiency” factor. For a background wave spectrum, e represents the temporal and spatial intermittency in the wave sources. The analytic solution (5.46) is not used in WACCM4.0; it is shown here to illustrate how the acceleration due to breaking gravity waves depends on the intrinsic phase speed. In the model, the stress profile is computed at interfaces and differenced to get the specific force at layer midpoints.

3850 Diffusive damping

In addition to breaking as a result of instability, vertically propagating waves can also be damped by molecular diffusion (both thermal and momentum) or by radiative cooling. Because the intrinsic periods of mesoscale gravity waves are short compared to IR relaxation time scales throughout the atmosphere, we ignore radiative damping. We take into account the molecular viscosity, K_m^m , such that the stress profile is given by:

$$\tau(Z) = \tau(Z_t) \exp\left(-\frac{2}{H} \int_0^Z \lambda_i dz'\right), \quad (5.47)$$

where Z_t denotes the top of the region, below Z , not affected by thermal dissipation or molecular diffusion. The imaginary part of the local vertical wavenumber, λ_i is then:

$$\lambda_i = \frac{N^3 K_m^m}{2k(\bar{u} - c)^4}. \quad (5.48)$$

3851 In WACCM4.0, (5.47–5.48) are only used within the domain where molecular diffusion is im-
 3852 portant (above ~ 75 km). At lower altitudes, molecular diffusion is negligible, $\lambda_i \rightarrow 0$, and τ is
 3853 conserved outside of saturation regions.

3854 Transport due to dissipating waves

When the wave is dissipated, either through saturation or diffusive damping, there is a transfer of wave momentum and energy to the background state. In addition, a phase shift is introduced between the wave's vertical velocity field and its temperature and constituent perturbations so that fluxes of heat and constituents are nonzero within the dissipation region. The nature of the phase shift and the resulting transport depends on the dissipation mechanism; in WACCM4.0, we assume that the dissipation can be represented by a linear damping on the potential temperature and constituent perturbations. For potential temperature, θ , this leads to:

$$\left(\frac{\partial}{\partial t} + \bar{u} \frac{\partial}{\partial x} \right) \theta' + w' \frac{\partial \bar{\theta}}{\partial z} = -\delta \theta', \quad (5.49)$$

where δ is the dissipation rate implied by wave breaking, which depends on the wave's group velocity, c_{gz} (see Garcia [2001]):

$$\delta = \frac{c_{gz}}{2H} = k \frac{(\bar{u} - c)^2}{2HN}. \quad (5.50)$$

Substitution of (5.50) into (5.49) then yields the eddy heat flux:

$$\overline{w'\theta'} = - \left[\frac{\delta \overline{w'w'}}{k^2(\bar{u} - c)^2 + \delta^2} \right] \frac{\partial \bar{\theta}}{\partial z}. \quad (5.51)$$

3855 Similar expressions can be derived for the flux of chemical constituents, with mixing ratio sub-
 3856 stituted in place of potential temperature in (5.51). We note that these wave fluxes are al-
 3857 ways downgradient and that, for convenience of solution, they may be represented as vertical
 3858 diffusion, with coefficient K_{zz} equal to the term in brackets in (5.51), but they do not repre-
 3859 sent turbulent diffusive fluxes but rather eddy fluxes. Any additional turbulent fluxes due to
 3860 wave breaking are ignored. To take into account the effect of localization of turbulence (e.g.,
 3861 Fritts and Dunkerton [1985]; McIntyre [1989]), (5.51) is multiplied times an inverse Prandtl
 3862 number, Pr^{-1} ; in WACCM4.0 we use $Pr^{-1} = 0.25$.

3863 Heating due to wave dissipation

The vertical flux of wave energy density, E' , is related to the stress according to:

$$c_{gz} E' = (\bar{u} - c) \tau, \quad (5.52)$$

where c_{gz} is the vertical group velocity [Andrews et al., 1987]. Therefore, the stress divergence $\partial\tau/\partial Z$ that accompanies wave breaking implies a loss of wave energy. The rate of dissipation of wave energy density is:

$$\frac{\partial E'}{\partial t} \simeq (\bar{u} - c) \frac{1}{c_{gz}} \frac{\partial \tau}{\partial t} = (\bar{u} - c) \frac{\partial \tau}{\partial Z}. \quad (5.53)$$

For a saturated wave, the stress divergence is given by (5.46), so that:

$$\frac{\partial E'}{\partial t} = (\bar{u} - c) \frac{\partial \tau^*}{\partial Z} = -e \cdot \rho \frac{k(U - c)^4}{2NH}. \quad (5.54)$$

This energy loss by the wave represents a heat source for the background state, as does the change in the background kinetic energy density implied by wave drag on the background flow:

$$\frac{\partial \bar{K}}{\partial t} \equiv \frac{\rho}{2} \frac{\partial \bar{u}^2}{\partial t} = \bar{u} \frac{\partial \tau^*}{\partial Z} = -e \cdot \rho \frac{k \bar{u} (\bar{u} - c)^3}{2NH}, \quad (5.55)$$

which follows directly from (5.46). The background heating rate, in K sec^{-1} , is then:

$$Q_{gw} = -\frac{1}{\rho c_p} \left[\frac{\partial \bar{K}}{\partial t} + \frac{\partial E'}{\partial t} \right]. \quad (5.56)$$

Using (5.54) – (5.55), this heating rate may be expressed as:

$$Q_{gw} = \frac{1}{\rho c_p} c \frac{\partial \tau^*}{\partial Z} = \frac{1}{c_p} \left[e \cdot \frac{k c (c - \bar{u})^3}{2NH} \right], \quad (5.57)$$

3864 where c_p is the specific heat at constant pressure. In WACCM4.0, Q_{gw} is calculated for each
 3865 component of the gravity wave spectrum using the first equality in (5.57), i.e., the product of
 3866 the phase velocity times the stress divergence.

3867 Orographic source function

For orographically generated waves, the source is taken from McFarlane [1987]:

$$\tau_g = |\overline{\rho u' w'}|_0 = \frac{k}{2} h_0^2 \rho_0 N_0 \bar{u}_0, \quad (5.58)$$

where h_0 is the streamline displacement at the source level, and ρ_0 , N_0 , and \bar{u}_0 are also defined at the source level. For orographic waves, the subgrid-scale standard deviation of the orography σ is used to estimate the average mountain height, determining the typical streamline displacement. An upper bound is used on the displacement (equivalent to defining a “separation streamline”) which corresponds to requiring that the wave not be supersaturated at the source level:

$$h_0 = \min(2\sigma, \frac{\bar{u}_0}{N_0}). \quad (5.59)$$

The source level quantities ρ_0 , N_0 , and \bar{u}_0 are defined by vertical averages over the source region, taken to be 2σ , the depth to which the average mountain penetrates into the domain:

$$\psi_0 = \int_0^{2\sigma} \psi \rho dz, \quad \psi \in \{\rho, N, u, v\}. \quad (5.60)$$

3868 The source level wind vector (u_0, v_0) determines the orientation of the coordinate system in
 3869 (5.34)–(5.36) and the magnitude of the source wind \bar{u}_0 .

3870 **Non-orographic source functions**

3871 The source spectrum for non-orographic gravity waves is no longer assumed to be a specified
 3872 function of location and season, as was the case with the earlier version of the model described
 3873 by Garcia et al. [2007]. Instead, gravity waves are launched according to trigger functions that
 3874 depend on the atmospheric state computed in WACCM4 at any given time and location, as
 3875 discussed by Richter et al. [2010]. Two trigger functions are used: convective heat release (which
 3876 is a calculated model field) and a “frontogenesis function”, Hoskins [1982], which diagnoses
 3877 regions of strong wind field deformation and temperature gradient using the horizontal wind
 3878 components and potential temperature field calculated by the model.

3879 In the case of convective excitation, the method of Beres et al. [2005] is used to determine a
 3880 phase speed spectrum based upon the properties of the convective heating field. A spectrum is
 3881 launched whenever the deep convection parameterization in WACCM4 is active, and the vertical
 3882 profile of the convective heating, together with the mean wind field in the heating region, are
 3883 used to determine the phase speed spectrum of the momentum flux. Convectively generated
 3884 waves are launched at the top of the convective region (which varies according to the depth of
 3885 the convective heating calculated in the model).

Waves excited by frontal systems are launched whenever the frontogenesis trigger function exceeds a critical value (see Richter et al. [2010]). The waves are launched from a constant source level, which is specified to be 600 mb. The momentum flux phase speed spectrum is given by a Gaussian function in phase speed:

$$\tau_s(c) = \tau_b \exp \left[- \left(\frac{c - V_s}{c_w} \right)^2 \right], \quad (5.61)$$

centered on the source wind, $V_s = |\mathbf{V}_s|$, with width $c_w = 30$ m/s. A range of phase speeds with specified width and resolution is used:

$$c \in V_s + [\pm d_c, \pm 2d_c, \dots \pm c_{max}], \quad (5.62)$$

3886 with $d_c = 2.5$ m s⁻¹ and $c_{max} = 80$ m s⁻¹, giving 64 phase speeds. Note that $c = V_s$ is retained
 3887 in the code for simplicity, but has a critical level at the source and, therefore, $\tau_s(c = V_s) = 0$.
 3888 Note also that τ_b is a tunable parameter; in practice this is set such that the height of the polar
 3889 mesopause, which is very sensitive to gravity wave driving, is consistent with observations. In
 3890 WACCM4, $\tau_b = 1.5 \times 10^{-3}$ Pa.

Above the source region, the saturation condition is enforced separately for each phase speed, c_i , in the momentum flux spectrum:

$$\tau(c_i) \leq \tau_i^* = F_c^2 \frac{k}{2} \rho \frac{|\bar{u} - c_i|^3}{N}. \quad (5.63)$$

3891 **Numerical approximations**

The gravity wave drag parameterization is applied immediately after the nonlinear vertical diffusion. The interface Brunt-Väisällä frequency is

$$(N^{k+})^2 = \frac{g^2}{T^{k+}} \left(\frac{1}{c_p} - \rho^{k+} \frac{\delta^{k+T}}{\delta^{k+p}} \right), \quad (5.64)$$

Where the interface density is:

$$\rho^{k+} = \frac{RT^{k+}}{p^{k+}}. \quad (5.65)$$

3892 The midpoint Brunt-Väisällä frequencies are $N^k = (N^{k+} + N^{k-})/2$.

3893 The level for the orographic source is an interface determined from an estimate of the vertical
 3894 penetration of the subgrid mountains within the grid box. The subgrid scale standard deviation
 3895 of the orography, σ_h , gives the variation of the mountains about the mean elevation, which
 3896 defines the Earth's surface in the model. Therefore the source level is defined as the interface,
 3897 $k_s - 1/2$, for which $z^{k_s+} < 2\sigma_h < z^{k_s-}$, where the interface heights are defined from the midpoint
 3898 heights by $z^{k+} = \sqrt{(z^k z^{k+1})}$.

The source level wind vector, density and Brunt-Väisällä frequency are determined by vertical integration over the region from the surface to interface $k_s + 1/2$:

$$\psi_0 = \sum_{k=k_s}^K \psi^k \delta^k p, \quad \psi \in \{\rho, N, u, v\}. \quad (5.66)$$

The source level background wind is $\bar{u}_0 = \sqrt{(u_0^2 + v_0^2)}$, the unit vector for the source wind is

$$(x_0, y_0) = (u_0, v_0)/\bar{u}_0, \quad (5.67)$$

and the projection of the midpoint winds onto the source wind is

$$\bar{u}^k = u^k x_0 + v^k y_0. \quad (5.68)$$

3899 Assuming that $\bar{u}_0 > 2 \text{ m s}^{-1}$ and $2\sigma^h > 10 \text{ m}$, then the orographic source term, τ_g is given
 3900 by (5.58) and (5.59), with $F_c^2 = 1$ and $k = 2\pi/10^5 \text{ m}^{-1}$. Although the code contains a provision
 3901 for a linear stress profile within a “low level deposition region”, this part of the code is not used
 3902 in the standard model.

3903 The stress profiles are determined by scanning up from the bottom of the model to the top.
 3904 The stress at the source level is determined by (5.58). The saturation stress, τ_ℓ^* at each interface
 3905 is determined by (5.63), and $\tau_\ell^* = 0$ if a critical level is passed. A critical level is contained
 3906 within a layer if $(\bar{u}^{k+} - c_\ell)/(\bar{u}^{k-} - c_\ell) < 0$.

Within the molecular diffusion domain, the imaginary part of the vertical wavenumber is given by (5.48). The interface stress is then determined from the stress on the interface below by:

$$\tau^{k-} = \min \left[(\tau^*)^{k-}, \tau^{k+} \exp \left(-2\lambda_i \frac{R}{g} T^k \delta^k \ln p \right) \right]. \quad (5.69)$$

3907 Below the molecular diffusion domain, the exponential term in (5.69) is omitted.

Once the complete stress profile has been obtained, the forcing of the background wind is determined by differentiating the profile during a downward scan:

$$\frac{\partial \bar{u}_\ell^k}{\partial t} = g \frac{\delta^k \tau_\ell}{\delta^k p} < \left(\frac{\partial \bar{u}_\ell^k}{\partial t} \right)^{\max}. \quad (5.70)$$

$$\left(\frac{\partial \bar{u}_\ell^k}{\partial t} \right)^{\max} = \min \left[\frac{|c_\ell - \bar{u}_\ell^k|}{2\delta t}, 500 \text{ m s}^{-1} \text{ day}^{-1} \right]. \quad (5.71)$$

3908 The first bound on the forcing comes from requiring that the forcing not be large enough to
 3909 push the wind more than half way towards a critical level within a time step and takes the place
 3910 of an implicit solution. This bound is present for numerical stability, it comes into play when
 3911 the time step is too large for the forcing. It is not feasible to change the time step, or to write
 3912 an implicit solver, so an *a priori* bound is used instead. The second bound is used to constrain
 3913 the forcing to lie within a physically plausible range (although the value used is extremely large)
 3914 and is rarely invoked.

When any of the bounds in (5.70) are invoked, conservation of stress is violated. In this case, stress conservation is ensured by decreasing the stress on the lower interface to match the actual stress divergence in the layer:

$$\tau_\ell^{k+} = \tau_\ell^{k-} + \frac{\partial \bar{u}^k}{\partial t} \frac{\delta^k p}{g}. \quad (5.72)$$

3915 This has the effect of pushing some of the stress divergence into the layer below, a reasonable
 3916 choice since the waves are propagating up from below.

Finally, the vector momentum forcing by the gravity waves is determined by projecting the background wind forcing with the unit vectors of the source wind:

$$\frac{\partial \mathbf{V}^k}{\partial t} = (x_0, y_0) \times E \sum_\ell \frac{\partial \bar{u}_\ell^k}{\partial t}. \quad (5.73)$$

3917 In addition, the frictional heating implied by the momentum tendencies, $\frac{1}{c_p} \mathbf{V}^k \cdot \partial \mathbf{V}^k / \partial t$, is
 3918 added to the thermodynamic equation. This is the correct heating for orographic ($c_\ell = 0$)
 3919 waves, but not for waves with $c_\ell \neq 0$, since it does not account for the wave energy flux. This
 3920 flux is accounted for in some middle and upper atmosphere versions of CAM4, but also requires
 3921 accounting for the energy flux at the source.

3922 5.3.4 Turbulent Mountain Stress

3923 An important difference between WACCM4 and earlier versions is the addition of surface stress
 3924 due to unresolved orography. A numerical model can compute explicitly only surface stresses
 3925 due to resolved orography. At the standard $1.9^\circ \times 2.5^\circ$ (longitude x latitude) resolution used
 3926 by WACCM4 only the gross outlines of major mountain ranges are resolved. To address this
 3927 problem, unresolved orography is parameterized as turbulent surface drag, using the concept
 3928 of effective roughness length developed by Fiedler and Panofsky [1972]. Fiedler and Panofsky
 3929 defined the roughness length for heterogeneous terrain as the roughness length that homogenous
 3930 terrain would have to give the correct surface stress over a given area. The concept of effective
 3931 roughness has been used in several Numerical Weather Prediction models (e.g., Wilson [2002];
 3932 Webster et al. [2003]).

In WACCM4 the effective roughness stress is expressed as:

$$\tau = \rho C_d |\mathbf{V}| \mathbf{V}, \quad (5.74)$$

where ρ is the density and C_d is a turbulent drag coefficient,

$$C_d = \frac{f(R_i) k^2}{\ln^2 \left[\frac{z+z_0}{z_0} \right]}, \quad (5.75)$$

3933 k is von Kármán's constant; z is the height above the surface; z_0 is an effective roughness length,
3934 defined in terms of the standard deviation of unresolved orography; and $f(R_i)$ is a function of
3935 the Richardson number (see Richter et al. [2010] for details).

3936 The stress calculated by (5.74) is used the model's nonlocal PBL scheme to evaluate the
3937 PBL height and nonlocal transport, per Eqs. (3.10)(3.12) of Holstlag and Boville [1993]. This
3938 calculation is carried out only over land, and only in grid cells where the height of topography
3939 above sea level, z , is nonzero.

3940 5.3.5 QBO Forcing

3941 WACCM4 has several options for forcing a quasi-biennial oscillation (QBO) by applying a
3942 momentum forcing in the tropical stratosphere. The parameterization relaxes the simulated
3943 winds to a specified wind field that is either fixed or varies with time. The parameterization can
3944 also be turned off completely. The namelist variables and input files can be selected to choose
3945 one of the following options:

- 3946 • Idealized QBO East winds, used for perpetual fixed-phase of the QBO, as described by
3947 [Matthes et al. \[2010\]](#).
- 3948 • Idealized QBO West winds, as above but for the west phase.
- 3949 • Repeating idealized 28-month QBO, also described by [Matthes et al. \[2010\]](#).
- 3950 • QBO for the years 1953-2004 based on the climatology of Giorgetta [see:
3951 http://www.pa.op.dlr.de/CCMVal/Forcings/qbo_data_ccmval/u_profile_195301-200412.html,
3952 2004].
- 3953 • QBO with a 51-year repetition, based on the 1953-2004 climatology of Giorgetta, which
3954 can be used for any calendar year, past or future.

3955 The relaxation of the zonal wind is based on [Balachandran and Rind \[1995\]](#) and is described
3956 in [Matthes et al. \[2010\]](#). The input winds are specified at the equator and the parameterization
3957 extends latitudinally from 22°N to 22°S, as a Gaussian function with a half width of 10° centered
3958 at the equator. Full vertical relaxation extends from 86 to 4 hPa with a time constant of 10
3959 days. One model level below and above this altitude range, the relaxation is half as strong and is
3960 zero for all other levels. This procedure constrains the equatorial winds to more realistic values
3961 while allowing resolved and parameterized waves to continue to propagate.

3962 The fixed or idealized QBO winds (first 3 options) can be applied for any calendar period.
3963 The observed input (Giorgetta climatology) can be used only for the model years 1953-2004.
3964 The winds in the final option were determined from the Giorgetta climatology for 1954-2004 via
3965 filtered spectral decomposition of that climatology. This gives a set of Fourier coefficients that
3966 can be expanded for any day and year. The expanded wind fields match the climatology during
3967 the years 1954-2004.

5.3.6 Radiation

The radiation parameterizations in CAM4 are quite accurate up to ~ 65 km, but deteriorate rapidly above that altitude. Because 65 km is near a local minimum in both shortwave heating and longwave cooling, it is a particularly convenient height to merge the heating rates from parameterizations for the lower and upper atmosphere. Therefore, we retain the CAM4 parameterizations below ~ 65 km and use new parameterizations above.

The merged shortwave and longwave radiative heatings are determined from

$$Q = w_1 Q_{CAM3} + w_2 Q_{MLT}, \quad (5.76)$$

where $w_1(z^* < z_b^*) = 1$, $w_2(z^* > z_t^*) = 1$ and $z^* = \log(10^5/p)$ is the pressure scale height. The CAM4 radiation parameterizations are used below z_b^* and the MLT parameterizations are used above z_t^* . For $z_b^* < z < z_t^*$, $w_2 = 1 - w_1$ and

$$w_1 = 1 - \tanh\left(\frac{z^* - z_b^*}{z_w^*}\right), \quad (5.77)$$

where z_w^* is the transition width.

The merging was developed and tested separately for shortwave and longwave radiation and the constants are slightly different. For longwave radiation, the constants are $z_b^* = 8.57$, $z_t^* = 10$ and $z_w^* = 0.71$. For shortwave radiation, the constants are $z_b^* = 9$, $z_t^* = 10$ and $z_w^* = 0.75$. These constants give smooth heating profiles. Note that a typical atmospheric scale height of $H = 7$ km places the transition zones between 60 and 70 km.

Longwave radiation

WACCM4.0 retains the longwave (LW) formulation used in CAM4 [Kiehl and Briegleb, 1991]. However, in the MLT longwave radiation uses the parameterization of Fomichev et al. [1998] for CO₂ and O₃ cooling and the parameterization of Kockarts [1980] for NO cooling at 5.3 μm . As noted above, the LW heating/cooling rates produced by these parameterizations are merged smoothly at 65 km with those produced by the standard CAM4 LW code, as recently revised by Collins et al. [2002]. In the interactive chemistry case all of the gases (O, O₂, O₃, N₂, NO, and CO₂) that are required by these parameterizations, are predicted within WACCM4.0.

Shortwave radiation

WACCM4.0 uses a combination of solar parameterizations to specify spectral irradiances over two spectral intervals. The first spectral interval covers soft x-ray and extreme ultraviolet irradiances (wavelengths between 0.05 nm to Lyman- α (121.6 nm)) and is calculated using the parameterization of Solomon and Qiang [2005]. The parameterizations take as input the 10.7 cm solar radio flux ($f_{10.7}$) and its 81-day average ($f_{10.7a}$). Daily values of $f_{10.7}$ are obtained from NOAA's Space Environment Center (www.sec.noaa.gov).

The irradiance of the j th spectral interval is:

$$F_j = F_j^0 * \left\{ 1 + R_j * \left[\frac{(f_{10.7} + f_{10.7a})}{2} - F_{min} \right] \right\} \quad (5.78)$$

3995 where $F_{min} = 80$. F_j^0 and R_j are taken from Table A1 of [Solomon and Qiang \[2005\]](#).

3996 Fluxes for the second interval between Lyman- α (121.6 nm) and 100 μm . are specified using
 3997 an empirical model of the wavelength-dependent sunspot and facular influences [[Lean, 2000](#);
 3998 [Wang et al., 2005](#)]. Spectral resolution is 1 nm between 121.6 nm and 750nm, 5 nm between
 3999 750nm and 5 μm , 10 nm between 5 μm and 10 μm , and 50 nm between 10 μm and 100 μm .

In the troposphere, stratosphere and lower mesosphere ($z < 65\text{km}$) WACCM4.0 retains the CAM4 shortwave heating (200 nm to 4.55 μm) which is calculated from the net shortwave spectral flux into each layer [Collins et al. \[2004b\]](#). The solar spectrum for the CAM4 heating calculation is divided into 19 intervals [[Collins, 1998](#)]. The heating in these intervals must be adjusted to match the irradiances calculated for the upper part of the model, and those used in the photolysis calculations. This is achieved by applying a scaling (S_j) to the solar heating in the j th CAM4 spectral interval using the spectrum from [Lean \[2000\]](#) and [Wang et al. \[2005\]](#):

$$S_j = \frac{F_j}{F_j^{ref}}, \quad (5.79)$$

4000 where F_j is the spectral irradiance ($\text{W}/\text{m}^2/\text{nm}$) integrated over the j th band, and F_j^{ref} is the
 4001 same integral taken over a reference spectrum calculated from annual mean fluxes over a 3-solar-
 4002 cycle period from XX to YY.

4003 In the MLT region, shortwave heating is the sum of the heating due to absorption of photons
 4004 and subsequent exothermic chemical reactions that are initiated by photolysis. The majority
 4005 of energy deposited by an absorbed photon goes into breaking molecular bonds, rather than
 4006 into translational energy of the absorbing molecule (heat). Chemical heating results when con-
 4007 stituents react to form products of lower total chemical potential energy. This heating can take
 4008 place months after the original photon absorption and thousands of kilometers away. Heating
 4009 rates range from 1 K/day near 75 km to 100-300 K/day near the top of the model domain. It
 4010 is clear that quenching of $O(^1D)$ is a large source of heating throughout the MLT. Above 100
 4011 km ion reactions and reactions involving atomic nitrogen are significant sources of heat, while
 4012 below that level O_X ($= O + O_3$) and HO_X ($= H + OH + HO_2$) reactions are the dominant
 4013 producers of chemical heating.

Heating within the MLT from the absorption of radiation that *is* directly thermalized is calculated over the wavelength range of 0.05 nm to 350 nm. For wavelengths less than Lyman- α , it is assumed that 5% of the energy of each absorbed photon is directly thermalized:

$$Q_{EUV} = (\rho c_p)^{-1} \sum_k n_k \sum_j \epsilon J_k(\lambda_j) \frac{hc}{\lambda_j}, \quad (5.80)$$

4014 where $\epsilon = 0.05$. Here ρ is mass density, c_p is the specific heat of dry air, n is the number density
 4015 of the absorbing species, and J is the photolysis/photoionization rate. The total heating is the
 4016 sum of k photolysis reactions and j wavelengths intervals. At these wavelengths absorption of
 4017 a photon typically leads to photoionization, with the resulting photoelectron having sufficient
 4018 energy to ionize further molecules. Calculation of J_{ij} and ionization rates from photoelectrons
 4019 is calculated based on the parameterization of [Solomon and Qiang \[2005\]](#). In a similar manner,
 4020 the heating rate within the aurora (Q_{AUR}) is calculated as the product of the total ionization
 4021 rate, 35 eV per ion pair, and the same heating efficiency of 5%.

Between Lyman- α and 350 nm the energy required to break molecular bonds is explicitly accounted for. The heating rate is thus defined as:

$$Q_{UV} = (\rho c_p)^{-1} \sum_k n_k \sum_j J_k(\lambda_j) \left\{ \frac{hc}{\lambda_j} - BDE_k \right\}, \quad (5.81)$$

4022 where BDE is the bond dissociation energy.

4023 In addition to these sources of heat, WACCM4.0 calculates heating by absorption in the near-
 4024 infrared by CO₂ (between 1.05 to 4.3 μm), which has its largest contribution near 70km and
 4025 can exceed 1 K/day [Fomichev et al., 2004]. Heating from this process is calculated using the
 4026 parameterization of Ogibalov and Fomichev [2003]. Finally, the heating produced by collisions
 4027 of electrons and neutrals (Joule heating) is also calculated using the predicted ion and electron
 4028 concentrations. This is described in section 5.3.8. Local heating rates from joule heating can be
 4029 very large in the auroral regions, reaching over 10³K/day in the upper levels of the model.

4030 Airglow, radiation produced when excited atoms or molecules spontaneously emit, is ac-
 4031 counted for in WACCM4.0 for emissions of O₂(¹ Δ), O₂(¹ Σ), and vibrationally excited OH.
 4032 Airglow from the excited molecular oxygen species are handled explicitly; radiative lifetimes for
 4033 O₂(¹ Δ) and O₂(¹ Σ) are 2.58 \times 10⁻⁴ s⁻¹ and 0.085 s⁻¹ respectively. However, modeling of the
 4034 many possible vibrational transitions of OH is impractical in a model as large as WACCM4.0.
 4035 Energy losses from the emission of vibrationally excited OH are therefore accounted for by
 4036 applying an efficiency factor to the exothermicity of the reaction that produces vibrationally
 4037 excited OH; the reaction of hydrogen and ozone. In other words, the reaction H + O₃ produces
 4038 ground state OH only, but the chemical heating from the reaction has been reduced to take
 4039 into consideration that some of the chemical potential energy has been lost in airglow. This
 4040 approach is the same one used by Mlynczak and Solomon [1993] and we use their recommended
 4041 efficiency factor of 60%. Any energy lost through airglow is assumed to be lost to space, and so
 4042 represents an energy pathway that does not generate heat.

4043 Volcanic Heating

4044 The sulfate aerosol heating is a function of a prescribed aerosol distribution varying in space
 4045 and time that has a size distribution similar to that seen after a volcanic eruption [Tilmes et al.,
 4046 2009]. The H₂SO₄ mass distribution is calculated from the prescribed sulfate surface area density
 4047 (SAD) assuming a lognormal size distribution, number of particles per cm⁻³, and distribution
 4048 width (see section 3.6.2). The H₂SO₄ mass distribution is then passed to the radiative transfer
 4049 code (CAMRT), which in turn calculates heating and cooling rates.

4050 5.3.7 WACCM4.0 chemistry

4051 Chemical Mechanism (Neutral Species)

4052 WACCM4.0 includes a detailed neutral chemistry model for the middle atmosphere based on
 4053 the Model for Ozone and Related Chemical Tracers, Version 3 [Kinnison et al., 2006]. The
 4054 mechanism represents chemical and physical processes in the troposphere through the lower
 4055 thermosphere. The species included within this mechanism are contained within the O_X, NO_X,
 4056 HO_X, ClO_X, and BrO_X chemical families, along with CH₄ and its degradation products. This

4057 mechanism contains 52 neutral species, one invariant (N_2), 127 neutral gas-phase reactions, 48
 4058 neutral photolytic reactions, and 17 heterogeneous reactions on three aerosol types (see below).
 4059 Lists of the chemical species are given in Table 1. The first column lists the symbolic name
 4060 (as used in the mechanism); the second column lists the species atomic composition; the third
 4061 column designates which numerical solution approach is used (i.e., explicit or implicit); the
 4062 fourth column lists any deposition processes (wet or dry) for that species; and the fifth column
 4063 indicates whether the surface (or upper) boundary condition is fixed vmr or flux, or if a species
 4064 has an in-situ flux (from lightning or aircraft emissions).

4065 The gas-phase reactions included in the WACCM4.0 middle atmosphere chemical mechanism
 4066 are listed in Table 2. In most all cases the chemical rate constants are taken from JPL06-2
 4067 [Sander, S. P., et al., 2006]. Exceptions to this condition are described in the comment section
 4068 for any given reaction.

Heterogeneous reactions on four different aerosols types are also represented in the WACCM4.0 chemical mechanism (see Table 3): 1) liquid binary sulfate (LBS); 2) Supercooled ternary solution (STS); 3) Nitric acid trihydrate (NAT); and 4) water-ice. There are 17 reactions, six reactions on liquid sulfate aerosols (LBS or STS), five reactions on solid NAT aerosols, and six reactions on solid water-ice aerosols. The rate constants for these 17 heterogeneous reactions can be divided up into two types: 1) first order; and 2) pseudo second order. For first order hydrolysis reactions (Table 3, reactions 1-3, 7-8, 11, and 12-14), the heterogeneous rate constant is derived in the following manner:

$$k = \frac{1}{4}V \cdot SAD \cdot \gamma \quad (5.82)$$

4069 Where V = mean velocity; SAD = surface area density of LBS, STS, NAT, or water-ice, and γ
 4070 = reaction probability for each reaction. The units for this rate constant are s^{-1} . Here the H_2O
 4071 abundance is in excess and assumed not change relative to the other reactant trace constituents.
 4072 The mean velocity is dependent on the molecular weight of the non- H_2O reactant (i.e., N_2O_5 ,
 4073 $ClONO_2$, or $BrONO_2$). The SAD for each aerosol type is described in section 7. The reaction
 4074 probability is dependent on both composition and temperature for sulfate aerosol (see JPL06-2).
 4075 The reaction probability is a fixed quantity for NAT and water-ice aerosols and is listed in Table
 4076 3. Multiplying the rate constant times the concentration gives a loss rate in units of molecules
 4077 $cm^{-3} sec^{-1}$ for the reactants and is used in the implicit solution approach. The non-hydrolysis
 4078 reaction (Table 3, reactions 4-6, 9-10, and 15-17) are second order reactions. Here, the first order
 4079 rate constant (equation 6) is divided by the HCl concentration, giving it the typical bimolecular
 4080 rate constant unit value of $cm^3 molecule^{-1} sec^{-1}$. This approach assumes that all the HCl is in
 4081 the aerosol particle.

4082 Stratospheric Aerosols

Heterogeneous processes on liquid sulfate aerosols and solid polar stratospheric clouds (Type 1a, 1b, and 2) are included following the approach of Considine et al. [2000]. This approach assumes that the condensed phase mass follows a lognormal size distribution taken from Considine et al. [2000],

$$N(r) = \frac{N_0}{r\sigma\sqrt{2\pi}} \exp\left[\frac{-\ln(r/r_0)^2}{2\sigma^2}\right] \quad (5.83)$$

4083 where N is the aerosol number density (particles cm^{-3}); r and r_0 are the particle radius and
4084 median radius respectively; and σ is the standard deviation of the lognormal distribution. N_0
4085 and r_0 are supplied for each aerosol type. The aerosol surface area density (SAD) is the second
4086 moment of this distribution.

4087 At model temperatures (T_{model}) greater than 200 K, liquid binary sulfate (LBS) is the
4088 only aerosol present. The surface area density (SAD) for LBS is derived from observa-
4089 tions from SAGE, SAGE-II and SAMS [Thomason et al., 1997] as updated by Considine
4090 [World Meteorological Organization, 2003]. As the model atmosphere cools, the LBS aerosol
4091 swells, taking up both HNO_3 and H_2O to give STS aerosol. The Aerosol Physical Chemistry
4092 Model (ACPM) is used to derive STS composition Tabazadeh et al. [1994]. The STS aerosol me-
4093 dian radius and surface area density is derived following the approach of Considine et al. [2000].
4094 The width of the STS size distribution ($\sigma = 1.6$) and number density ($10 \text{ particles cm}^{-3}$) are
4095 prescribed according to measurements from Dye et al. [1992]. The STS aerosol median radius
4096 can swell from approximately $0.1 \mu\text{m}$ to approximately $0.5 \mu\text{m}$. There is no aerosol settling
4097 assumed for this type of aerosol. The median radius is used in derivation of sulfate aerosol
4098 reaction probability coefficients. Both the LBS and STS surface area densities are used for the
4099 calculation of the rate constants as listed in Table 3; reactions (1)-(6).

4100 Solid nitric acid containing aerosol formation is allowed when the model temperature reaches
4101 a prescribed super saturation ratio of HNO_3 over NAT [Hansen and Mauersberger, 1988]. This
4102 ratio is set to 10 in WACCM4.0 [Peter et al., 1991]. There are three methods available to
4103 handle the HNO_3 uptake on solid aerosol. The first method directly follows Considine et al.
4104 [2000, 2004]. Here, after the supersaturation ratio assumption is met, the available condensed
4105 phase HNO_3 is assumed to reside in the solid NAT aerosol. The derivation of the NAT median
4106 radius and surface area density follows the same approach as the STS aerosol, by assuming: a
4107 lognormal size distribution, a width of a distribution ($\sigma = 1.6$; Dye et al. [1992]), and a number
4108 density ($0.01 \text{ particles cm}^{-3}$; Tabazadeh et al. [2000]). The NAT radius settles with a value of
4109 r_0 ranging between 2 and $5 \mu\text{m}$; this value depends on the model temperature and subsequent
4110 amount of condensed phase HNO_3 formed. This NAT median radius r_0 is also used to derive
4111 the terminal velocity for settling of NAT (section 8) and the eventual irreversible denitrification.
4112 The NAT surface area density is used to calculate the rate constants for heterogeneous reactions
4113 7-11 (Table 3). Since the available HNO_3 is included inside the NAT aerosol, there is no STS
4114 aerosol present. However, there are still heterogeneous reactions occurring on the surface of LBS
4115 aerosols.

4116 If the calculated atmospheric temperature, T , becomes less than or equal to the saturation
4117 temperature (T_{sat}) for water vapor over ice (e.g., Marti and Mauersberger [1993]), water-ice
4118 aerosols can form. In WACCM4.0 the condensed phase H_2O is derived in the prognostic water
4119 routines of CAM and passed into the chemistry module. Using this condensed phase H_2O , the
4120 median radius and the surface area density for water-ice are again derived following the approach
4121 of Considine et al. [2000]. The water-ice median radius and surface area density assumes a
4122 lognormal size distribution, a width of a distribution = 1.6 [Dye et al., 1992], and a number
4123 density of $0.001 \text{ particles cm}^{-3}$ [Dye et al., 1992]. The value of r_0 is typically $10 \mu\text{m}$. The water-
4124 ice surface area density is used for the calculation of the rate constants for reactions 12-17 (Table
4125 3).

4126 Sedimentation of Stratospheric Aerosols

The sedimentation of HNO_3 in stratospheric aerosols follows the approach described in [Considine et al. \[2000\]](#). The following equation is used to derive the flux (F) of HNO_3 , as NAT aerosol, across model levels in units of molecules $\text{cm}^{-2} \text{sec}^{-1}$.

$$F_i = V_i \cdot C_i \exp(8 \ln^2 \sigma_i), \quad (5.84)$$

4127 where $i = 1$ for NAT; V_i is the terminal velocity of the aerosol particles (cm s^{-1}); C is the
4128 condensed-phase concentration of HNO_3 (molecules cm^{-3}); σ is the width of the lognormal size
4129 distribution for NAT (see discussion above). The terminal velocity is dependent on the given
4130 aerosol: 1) mass density; 2) median radius; 3) shape; 4) dynamic viscosity; and 5) Cunning-
4131 ham correction factor for spherical particles (see [Fuch \[1964\]](#) and [Kasten \[1968\]](#) for the theory
4132 behind the derivation of terminal velocity). For each aerosol type the terminal velocity could
4133 be calculated, however, in WACCM4.0 this quantity is only derived for NAT. Settling of HNO_3
4134 contain in STS is not derived based on the assumption that the median radius is too small
4135 to cause any significant denitrification and settling of condensed phase H_2O is handled in the
4136 CAM4 prognostic water routines.

4137 Ion Chemistry

4138 WACCM4.0 includes a six constituent ion chemistry model (O^+ , O_2^+ , N^+ , N_2^+ , NO^+ , and elec-
4139 trons) that represents the the E-region ionosphere. The global mean ion and electron distribu-
4140 tions simulated by WACCM4.0 for solar minimum conditions are shown in [Figure 5.1](#), which
4141 clearly shows that the dominant ions in this region are NO^+ and O_2^+ . Ion-neutral and recomb-
4142 ination reactions included in WACCM4.0 are listed in [Table 5.3.7](#). The reaction rate constants
4143 for these reactions are taken from [R.G.Roble \[1995\]](#).

4144 Ionization sources include not only the aforementioned absorption of extreme ultraviolet and
4145 soft x-ray photons, and photoelectron impact, but also energetic particles precipitation in the
4146 auroral regions. The latter is calculated by a parameterization based on code from the NCAR
4147 TIME-GCM model [[Roble and Ridley, 1987](#)] that rapidly calculates ion-pair production rates,
4148 including production in the polar cusp and polar cap. The parameterization takes as input
4149 hemispheric power (HP), the estimated power in gigawatts deposited in the polar regions by
4150 energetic particles.

Currently WACCM4.0 uses a parameterization of HP (in GW) based on an empirical rela-
tionships between HP and the K_p planetary geomagnetic index. For $K_p \leq 7$, WACCM4.0 uses
the relationship obtained by [Zhang and Paxton \[2008\]](#) from TIMED/GUVI observations:

$$\text{HP} = 16.82 * K_p * \exp(0.32) - 4.86 \quad (5.85)$$

For $K_p > 7$, WACCM4.0 linearly interpolates HP, assuming HP equals to 300 when K_p is 9,
based on NOAA satellite measurements:

$$\text{HP} = 153.13 + \frac{K_p - 7}{9 - 7} * (300 - 153.13) \quad (5.86)$$

4151 K_p is also available from NOAA's Space Environment Center and covers the period from 1933
4152 to the present, making it ideal for long-term retrospective simulations.

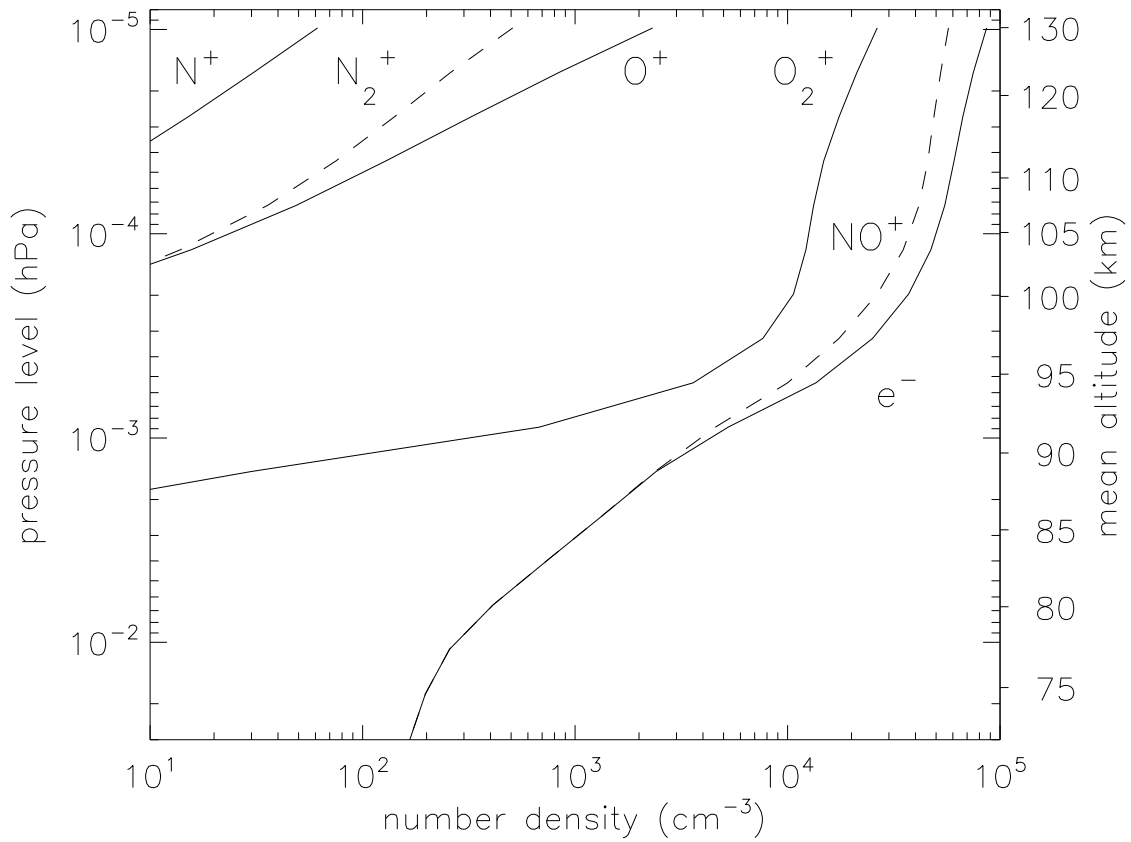


Figure 5.1: Global mean distribution of charged constituents during July solar minimum conditions.

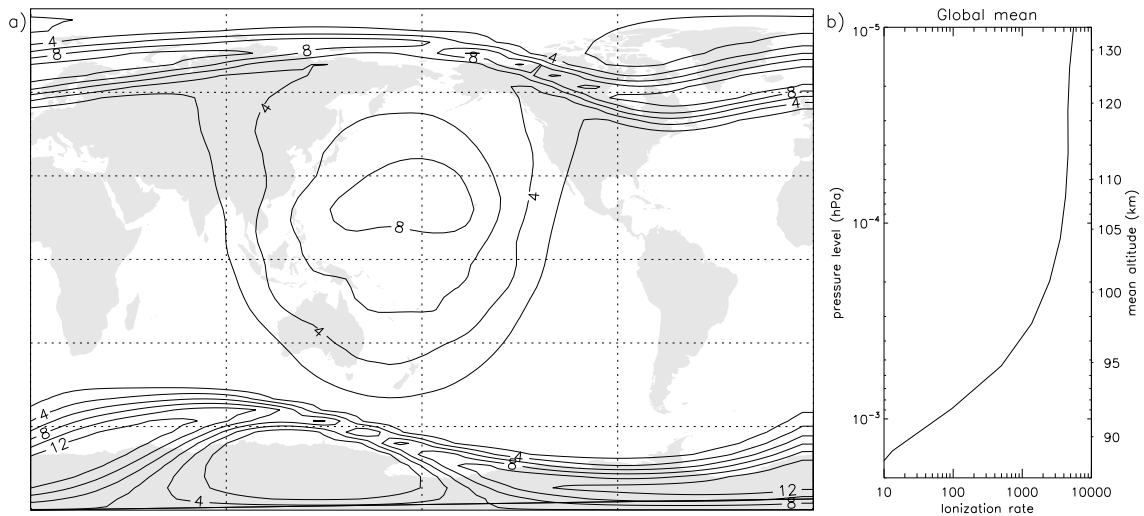
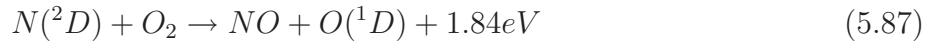


Figure 5.2: a) Global distribution of ionization rates at 7.3×10^{-5} hPa, July 1, UT0100 HRS. Contour interval is $2 \times 10^3 \text{ cm}^{-3} \text{ s}^{-1}$. b) Simultaneous global mean ionization rates ($\text{cm}^{-3} \text{ s}^{-1}$) versus pressure.

4153 Total ionization rates at 110km during July for solar maximum conditions are shown in
4154 Figure 5.2a. The broad region of ionization centered in the tropics is a result of EUV ionization,
4155 and has a peak value of almost 10^3 at 22°N . Ionization rates from particle precipitation can
4156 exceed this rate by 40% but are limited to the high-latitudes, as can be seen by the two bands
4157 that are approximately aligned around the magnetic poles. The global mean ionization rate
4158 (Figure 5.2b)

An important aspect of including ionization processes (both in the aurora and by energetic photons and photoelectrons), is that it leads to a more accurate representation of thermospheric nitric oxide. Not only does nitric oxide play an important role in the energy balance of the lower thermosphere through emission at $5.3\ \mu\text{m}$, it might also be transported to the upper stratosphere, where it can affect ozone concentrations. Nitric oxide is produced through quenching of $\text{N}(^2D)$:



4159 $\text{N}(^2D)$ is produced either via recombination of NO^+ (see Table 5.3.7) or directly by ionization
4160 of molecular nitrogen. The branching ratio between $\text{N}(^2D)$ and ground-state atomic nitrogen
4161 for the photoionization process is critical in determining the effectiveness of NO production.
4162 If ground-state atomic nitrogen is produced then it can react with NO to produce molecular
4163 nitrogen and effectively remove to members of the NOx family. In WACCM4.0 60% of the
4164 atomic nitrogen produced is in the excited state, which implies absorption of EUV results
4165 in a net source of NO. Also shown are maxima at high latitudes due to auroral ionization.
4166 WACCM4.0 reproduces many of the features of the Nitric Oxide Empirical Model (NOEM)
4167 distribution [Marsh et al., 2004], which is based on data from the Student Nitric Oxide Explorer
4168 satellite [Barth et al., 2003] In particular, larger NO in the winter hemisphere (a result of less
4169 photolytic loss), and a more localized NO maximum in the Northern Hemisphere (related to the
4170 lesser offset of geographic and magnetic poles, and so less spread when viewed as a geographic
4171 zonal mean).

Table 5.2: WACCM4.0 Neutral Chemical Species (51 computed species + N₂)

no.	Symbolic Name	Chemical Formula	Numerics	Deposition	Boundary Condition
1	O	O(³ P)	Implicit		ubvmr
2	O1D	O(¹ D)	Implicit		
3	O3	O ₃	Implicit	dry	
4	O2	O ₂	Implicit		ubvmr
5	O2_1S	O ₂ (¹ Σ)	Implicit		
6	O2_1D	O ₂ (¹ Δ)	Implicit		
7	H	H	Implicit		ubvmr
8	OH	OH	Implicit		
9	HO2	HO ₂	Implicit		
10	H2	H ₂	Implicit		vmr, ubvmr
11	H2O2	H ₂ O ₂	Implicit	dry, wet	
12	N	N	Implicit		ubvmr
13	N2D	N(² D)	Implicit		from TIME-GCM
14	N2	N ₂	Invariant		
15	NO	NO	Implicit		flux, ubvmr, lflux, airflux
16	NO2	NO ₂	Implicit	dry	
17	NO3	NO ₃	Implicit		
18	N2O5	N ₂ O ₅	Implicit		
19	HNO3	HNO ₃	Implicit	dry, wet	
20	HO2NO2	HO ₂ NO ₂	Implicit	dry, wet	
21	CL	Cl	Implicit		
22	CLO	ClO	Implicit		
23	CL2	Cl ₂	Implicit		
24	OCLO	OClO	Implicit		
25	CL2O2	Cl ₂ O ₂	Implicit		
26	HCL	HCl	Implicit	wet	
27	HOCL	HOCl	Implicit	wet	
28	ClONO2	ClONO ₂	Implicit	wet	
29	BR	Br	Implicit		
30	BRO	BrO	Implicit		
31	HOBR	HOBr	Implicit	wet	
32	HBR	HBr	Implicit	wet	
33	BrONO 2	BrONO ₂	Implicit	wet	
34	BRCL	BrCl	Implicit		

Table 5.1: (continued) WACCM4.0 Neutral Chemical Species (51 computed species + N₂)

no.	Symbolic Name	Chemical Formula	Numerics	Deposition	Boundary Condition
35	CH4	CH ₄	Implicit		vmr, airflux
36	CH3O2	CH ₃ O ₂	Implicit		
37	CH3OOH	CH ₃ OOH	Implicit	dry, wet	
38	CH2O	CH ₂ O	Implicit	dry, wet	flux
39	CO	CO	Explicit	dry	flux, ubvmr, airflux
40	CH3CL	CH ₃ Cl	Explicit		vmr
41	CH3BR	CH ₃ Br	Explicit		vmr
42	CFC11	CFCl ₃	Explicit		vmr
43	CFC12	CF ₂ Cl ₂	Explicit		vmr
44	CFC113	CCl ₂ FCClF ₂	Explicit		vmr
45	HCFC22	CHClF ₂	Explicit		vmr
46	CCL4	CCl ₄	Explicit		vmr
47	CH3CCL3	CH ₃ CCl ₃	Explicit		vmr
48	CF2CLBR	CBr ₂ F ₂ (Halon-1211)	Explicit		vmr
49	CF3BR	CBrF ₃ (Halon-1301)	Explicit		vmr
50	H2O	H ₂ O	Explicit		flux
51	N2O	N ₂ O	Explicit		vmr
52	CO2	CO ₂	Explicit		vmr, ubvmr

Deposition:

wet = wet deposition included

dry = surface dry deposition included

If there is no designation in the deposition column, this species is not operated on by wet or dry deposition algorithms.

Boundary Condition:

flux = flux lower boundary conditions

vmr = fixed volume mixing ratio (vmr) lower boundary condition

ubvmr = fixed vmr upper boundary condition

lflux = lightning emission included for this species

airflux= aircraft emissions included for this species

If there is no designation in the Boundary Conditions column, this species has a zero flux boundary condition for the top and bottom of the model domain.

Table 5.2: WACCM4.0 Gas-phase Reactions.

no.	Reactions	Comments
	Oxygen Reactions	
1	$O + O_2 + M \rightarrow O_3 + M$	JPL-06
2	$O + O_3 \rightarrow 2 O_2$	JPL-06
3	$O + O + M \rightarrow O_2 + M$	Smith and Robertson (2008)
4	$O_2(^1\Sigma) + O \rightarrow O_2(^1\Delta) + O$	JPL-06
5	$O_2\ 1S + O_2 \rightarrow O_2(^1\Delta) + O_2$	JPL-06
6	$O_2(^1\Sigma) + N_2 \rightarrow O_2(^1\Delta) + N_2$	JPL-06
7	$O_2(^1\Sigma) + O_3 \rightarrow O_2(^1\Delta) + O_3$	JPL-06
8	$O_2(^1\Sigma) + CO_2 \rightarrow O_2(^1\Delta) + CO_2$	JPL-06
9	$O_2(^1\Sigma) \rightarrow O_2$	JPL-06
10	$O_2(^1\Delta) + O \rightarrow O_2 + O$	JPL-06
11	$O_2(^1\Delta) + O_2 \rightarrow 2 O_2$	JPL-06
12	$O_2(^1\Delta) + N_2 \rightarrow O_2 + N_2$	JPL-06
13	$O_2(^1\Delta) \rightarrow O_2$	JPL-06
14	$O(^1D) + N_2 \rightarrow O + N_2$	JPL-06
15	$O(^1D) + O_2 \rightarrow O + O_2(^1\Sigma)$	JPL-06
16	$O(^1D) + O_2 \rightarrow O + O_2$	JPL-06
17	$O(^1D) + H_2O \rightarrow 2 OH$	JPL-06
18	$O(^1D) + N_2O \rightarrow 2 NO$	JPL-06
19	$O(^1D) + N_2O \rightarrow N_2 + O_2$	JPL-06
20	$O(^1D) + O_3 \rightarrow 2 O_2$	JPL-06
21	$O(^1D) + CFC11 \rightarrow 3 Cl$	JPL-06; Bloomfield [1994] for quenching of $O(^1D)$
22	$O(^1D) + CFC12 \rightarrow 2 Cl$	JPL-06; Bloomfield [1994]
23	$O(^1D) + CFC113 \rightarrow 3 Cl$	JPL-06; Bloomfield [1994]
24	$O(^1D) + HCFC22 \rightarrow Cl$	JPL-06; Bloomfield [1994]
25	$O(^1D) + CCl_4 \rightarrow 4 Cl$	JPL-06
26	$O(^1D) + CH_3Br \rightarrow Br$	JPL-06
27	$O(^1D) + CF_2ClBr \rightarrow Cl + Br$	JPL-06
28	$O(^1D) + CF_3Br \rightarrow Br$	JPL-06
29	$O(^1D) + CH_4 \rightarrow CH_3O_2 + OH$	JPL-06
30	$O(^1D) + CH_4 \rightarrow CH_2O + H + HO_2$	JPL-06
31	$O(^1D) + CH_4 \rightarrow CH_2O + H_2$	JPL-06
32	$O(^1D) + H_2 \rightarrow H + OH$	JPL-06
33	$O(^1D) + HCl \rightarrow Cl + OH$	JPL-06
34	$O(^1D) + HBr \rightarrow Br + OH$	JPL-06

Table 5.2: (continued) WACCM4.0 Gas-phase Reactions.

no.	Reactions	Comments
	Nitrogen Radicals	
35	$N(^2D) + O_2 \rightarrow NO + O(^1D)$	JPL-06
36	$N(^2D) + O \rightarrow N + O$	JPL-06
37	$N + O_2 \rightarrow NO + O$	JPL-06
38	$N + NO \rightarrow N_2 + O$	JPL-06
39	$N + NO_2 \rightarrow N_2O + O$	JPL-06
40	$NO + O + M \rightarrow NO_2 + M$	JPL-06
41	$NO + HO_2 \rightarrow NO_2 + OH$	JPL-06
42	$NO + O_3 \rightarrow NO_2 + O_2$	JPL-06
43	$NO_2 + O \rightarrow NO + O_2$	JPL-06
44	$NO_2 + O + M \rightarrow NO_3 + M$	JPL-06
45	$NO_2 + O_3 \rightarrow NO_3 + O_2$	JPL-06
46	$NO_2 + NO_3 + M \rightarrow N_2O_5 + M$	JPL-06
47	$N_2O_5 + M \rightarrow NO_2 + NO_3 + M$	JPL-06
48	$NO_2 + OH + M \rightarrow HNO_3 + M$	JPL-06
49	$HNO_3 + OH \rightarrow NO_3 + H_2O$	JPL-06
50	$NO_2 + HO_2 + M \rightarrow HO_2NO_2 + M$	JPL-06
51	$NO_3 + NO \rightarrow 2 NO_2$	JPL-06
52	$NO_3 + O \rightarrow NO_2 + O_2$	JPL-06
53	$NO_3 + OH \rightarrow NO_2 + HO_2$	JPL-06
54	$NO_3 + HO_2 \rightarrow NO_2 + OH + O_2$	JPL-06
55	$HO_2NO_2 + OH \rightarrow NO_2 + H_2O + O_2$	JPL-06
56	$HO_2NO_2 + M \rightarrow HO_2 + NO_2 + M$	JPL-06

Table 5.2: (continued) WACCM4.0 Gas-phase Reactions.

no.	Reactions	Comments
	Hydrogen Radicals	
57	$\text{H} + \text{O}_2 + \text{M} \rightarrow \text{HO}_2 + \text{M}$	JPL-06
58	$\text{H} + \text{O}_3 + \text{M} \rightarrow \text{OH} + \text{O}_2$	JPL-06
59	$\text{H} + \text{HO}_2 \rightarrow 2 \text{OH}$	JPL-06
60	$\text{H} + \text{HO}_2 \rightarrow \text{H}_2 + \text{O}_2$	JPL-06
61	$\text{H} + \text{HO}_2 \rightarrow \text{H}_2\text{O} + \text{O}$	JPL-06
62	$\text{OH} + \text{O} \rightarrow \text{H} + \text{O}_2$	JPL-06
63	$\text{OH} + \text{O}_3 \rightarrow \text{HO}_2 + \text{O}_2$	JPL-06
64	$\text{OH} + \text{HO}_2 \rightarrow \text{H}_2\text{O} + \text{O}_2$	JPL-06
65	$\text{OH} + \text{OH} \rightarrow \text{H}_2\text{O} + \text{O}$	JPL-06
66	$\text{OH} + \text{OH} + \text{M} \rightarrow \text{H}_2\text{O}_2 + \text{M}$	JPL-06
67	$\text{OH} + \text{H}_2 \rightarrow \text{H}_2\text{O} + \text{H}$	JPL-06
68	$\text{OH} + \text{H}_2\text{O}_2 \rightarrow \text{H}_2\text{O} + \text{HO}_2$	JPL-06
69	$\text{HO}_2 + \text{O} \rightarrow \text{OH} + \text{O}_2$	JPL-06
70	$\text{HO}_2 + \text{O}_3 \rightarrow \text{OH} + 2\text{O}_2$	JPL-06
71	$\text{HO}_2 + \text{HO}_2 \rightarrow \text{H}_2\text{O}_2 + \text{O}_2$	JPL-06
72	$\text{H}_2\text{O}_2 + \text{O} \rightarrow \text{OH} + \text{HO}_2$	JPL-06
	Chlorine Radicals	
73	$\text{Cl} + \text{O}_3 \rightarrow \text{ClO} + \text{O}_2$	JPL-06
74	$\text{Cl} + \text{H}_2 \rightarrow \text{HCl} + \text{H}$	JPL-06
75	$\text{Cl} + \text{H}_2\text{O}_2 \rightarrow \text{HCl} + \text{HO}_2$	JPL-06
76	$\text{Cl} + \text{HO}_2 \rightarrow \text{HCl} + \text{O}_2$	JPL-06
77	$\text{Cl} + \text{HO}_2 \rightarrow \text{ClO} + \text{OH}$	JPL-06
78	$\text{Cl} + \text{CH}_2\text{O} \rightarrow \text{HCl} + \text{HO}_2 + \text{CO}$	JPL-06
79	$\text{Cl} + \text{CH}_4 \rightarrow \text{CH}_3\text{O}_2 + \text{HCl}$	JPL-06
80	$\text{ClO} + \text{O} \rightarrow \text{Cl} + \text{O}_2$	JPL-06
81	$\text{ClO} + \text{OH} \rightarrow \text{Cl} + \text{HO}_2$	JPL-06
82	$\text{ClO} + \text{OH} \rightarrow \text{HCl} + \text{O}_2$	JPL-06
83	$\text{ClO} + \text{HO}_2 \rightarrow \text{HOCl} + \text{O}_2$	JPL-06
84	$\text{ClO} + \text{NO} \rightarrow \text{NO}_2 + \text{Cl}$	JPL-06
85	$\text{ClO} + \text{NO}_2 + \text{M} \rightarrow \text{ClONO}_2 + \text{M}$	JPL-06

Table 5.2: (continued) WACCM4.0 Gas-phase Reactions.

no.	Reactions	Comments
	Chlorine Radicals Continued	
86	$\text{ClO} + \text{ClO} \rightarrow 2 \text{Cl} + \text{O}_2$	JPL-06
87	$\text{ClO} + \text{ClO} \rightarrow \text{Cl}_2 + \text{O}_2$	JPL-06
88	$\text{ClO} + \text{ClO} \rightarrow \text{Cl} + \text{OClO}$	JPL-06
89	$\text{ClO} + \text{ClO} + \text{M} \rightarrow \text{Cl}_2\text{O}_2 + \text{M}$	JPL-06
90	$\text{Cl}_2\text{O}_2 + \text{M} \rightarrow 2 \text{ClO} + \text{M}$	JPL-06
91	$\text{HCl} + \text{OH} \rightarrow \text{H}_2\text{O} + \text{Cl}$	JPL-06
92	$\text{HCl} + \text{O} \rightarrow \text{Cl} + \text{OH}$	JPL-06
93	$\text{HOCl} + \text{O} \rightarrow \text{ClO} + \text{OH}$	JPL-06
94	$\text{HOCl} + \text{Cl} \rightarrow \text{HCl} + \text{ClO}$	JPL-06
95	$\text{HOCl} + \text{OH} \rightarrow \text{ClO} + \text{H}_2\text{O}$	JPL-06
96	$\text{ClONO}_2 + \text{O} \rightarrow \text{ClO} + \text{NO}_3$	JPL-06
97	$\text{ClONO}_2 + \text{OH} \rightarrow \text{HOCl} + \text{NO}_3$	JPL-06
98	$\text{ClONO}_2 + \text{Cl} \rightarrow \text{Cl}_2 + \text{NO}_3$	JPL-06
	Reactions	Comments
	Bromine Radicals	
99	$\text{Br} + \text{O}_3 \rightarrow \text{BrO} + \text{O}_2$	JPL-06
100	$\text{Br} + \text{HO}_2 \rightarrow \text{HBr} + \text{O}_2$	JPL-06
101	$\text{Br} + \text{CH}_2\text{O} \rightarrow \text{HBr} + \text{HO}_2 + \text{CO}$	JPL-06
102	$\text{BrO} + \text{O} \rightarrow \text{Br} + \text{O}_2$	JPL-06
103	$\text{BrO} + \text{OH} \rightarrow \text{Br} + \text{HO}_2$	JPL-06
104	$\text{BrO} + \text{HO}_2 \rightarrow \text{HOBr} + \text{O}_2$	JPL-06
105	$\text{BrO} + \text{NO} \rightarrow \text{Br} + \text{NO}_2$	JPL-06
106	$\text{BrO} + \text{NO}_2 + \text{M} \rightarrow \text{BrONO}_2 + \text{M}$	JPL-06
107	$\text{BrO} + \text{ClO} \rightarrow \text{Br} + \text{OClO}$	JPL-06
108	$\text{BrO} + \text{ClO} \rightarrow \text{Br} + \text{Cl} + \text{O}_2$	JPL-06
109	$\text{BrO} + \text{ClO} \rightarrow \text{BrCl} + \text{O}_2$	JPL-06
110	$\text{BrO} + \text{BrO} \rightarrow 2 \text{Br} + \text{O}_2$	JPL-06
111	$\text{HBr} + \text{OH} \rightarrow \text{Br} + \text{H}_2\text{O}$	JPL-06
112	$\text{HBr} + \text{O} \rightarrow \text{Br} + \text{OH}$	JPL-06
113	$\text{HOBr} + \text{O} \rightarrow \text{BrO} + \text{OH}$	JPL-06
114	$\text{BrONO}_2 + \text{O} \rightarrow \text{BrO} + \text{NO}_3$	JPL-06

Table 5.2: (continued) WACCM4.0 Gas-phase Reactions.

no.	Reactions	Comments
	Halogen Radicals	
115	$\text{CH}_3\text{Cl} + \text{Cl} \rightarrow \text{HO}_2 + \text{CO} + 2\text{HCl}$	JPL-06
116	$\text{CH}_3\text{Cl} + \text{OH} \rightarrow \text{Cl} + \text{H}_2\text{O} + \text{HO}_2$	JPL-06
117	$\text{CH}_3\text{CCl}_3 + \text{OH} \rightarrow 3 \text{Cl} + \text{H}_2\text{O}$	JPL-06
118	$\text{HCFC22} + \text{OH} \rightarrow \text{Cl} + \text{H}_2\text{O} + \text{HO}_2$	JPL-06
119	$\text{CH}_3\text{Br} + \text{OH} \rightarrow \text{Br} + \text{H}_2\text{O} + \text{HO}_2$	JPL-06
	CH_4 and Derivatives	
120	$\text{CH}_4 + \text{OH} \rightarrow \text{CH}_3\text{O}_2 + \text{H}_2\text{O}$	JPL-06
121	$\text{CH}_3\text{O}_2 + \text{NO} \rightarrow \text{CH}_2\text{O} + \text{NO}_2 + \text{HO}_2$	JPL-06
122	$\text{CH}_3\text{O}_2 + \text{HO}_2 \rightarrow \text{CH}_3\text{OOH} + \text{O}_2$	JPL-06
123	$\text{CH}_3\text{OOH} + \text{OH} \rightarrow 0.7 \text{CH}_3\text{O}_2 + 0.3 \text{OH} + 0.3 \text{CH}_2\text{O} + \text{H}_2\text{O}$	JPL-06
124	$\text{CH}_2\text{O} + \text{NO}_3 \rightarrow \text{CO} + \text{HO}_2 + \text{HNO}_3$	JPL-06
125	$\text{CH}_2\text{O} + \text{OH} \rightarrow \text{CO} + \text{H}_2\text{O} + \text{H}$	JPL-06
126	$\text{CH}_2\text{O} + \text{O} \rightarrow \text{OH} + \text{HO}_2 + \text{CO}$	JPL-06
127	$\text{CO} + \text{OH} \rightarrow \text{H} + \text{CO}_2$	JPL-06

Table 5.3: WACCM4.0 Heterogeneous Reactions on liquid and solid aerosols.

no.	Reaction	Comments
	Sulfate Aerosol	
1	$\text{N}_2\text{O}_5 + \text{H}_2\text{O} \rightarrow 2 \text{HNO}_3$	JPL-06; f (sulfuric acid wt %)
2	$\text{ClONO}_2 + \text{H}_2\text{O} \rightarrow \text{HOCl} + \text{HNO}_3$	JPL-06; f (T, P, HCl, H ₂ O, r)
3	$\text{BrONO}_2 + \text{H}_2\text{O} \rightarrow \text{HOBr} + \text{HNO}_3$	JPL-06; f (T, P, H ₂ O, r)
4	$\text{ClONO}_2 + \text{HCl} \rightarrow \text{Cl}_2 + \text{HNO}_3$	JPL-06; f (T, P, HCl, H ₂ O, r)
5	$\text{HOCl} + \text{HCl} \rightarrow \text{Cl}_2 + \text{H}_2\text{O}$	JPL-06; f (T, P, HCl, HCl, H ₂ O, r)
6	$\text{HOBr} + \text{HCl} \rightarrow \text{BrCl} + \text{H}_2\text{O}$	JPL-06; f (T, P, HCl, HOBr, H ₂ O, r)
	NAT Aerosol	
7	$\text{N}_2\text{O}_5 + \text{H}_2\text{O} \rightarrow 2 \text{HNO}_3$	JPL-06; $\gamma = 4 \times 10^{-4}$
8	$\text{ClONO}_2 + \text{H}_2\text{O} \rightarrow \text{HOCl} + \text{HNO}_3$	JPL-06; $\gamma = 4 \times 10^{-3}$
9	$\text{ClONO}_2 + \text{HCl} \rightarrow \text{Cl}_2 + \text{HNO}_3$	JPL-06; $\gamma = 0.2$
10	$\text{HCl} + \text{HCl} \rightarrow \text{Cl}_2 + \text{H}_2\text{O}$	JPL-06; $\gamma = 0.1$
11	$\text{BrONO}_2 + \text{H}_2\text{O} \rightarrow \text{HOBr} + \text{HNO}_3$	JPL-06; $\gamma = 0.3$
	Water-Ice Aerosol	
12	$\text{N}_2\text{O}_5 + \text{H}_2\text{O} \rightarrow 2 \text{HNO}_3$	JPL-06; $\gamma = 0.02$
13	$\text{ClONO}_2 + \text{H}_2\text{O} \rightarrow \text{HOCl} + \text{HNO}_3$	JPL-06; $\gamma = 0.3$
14	$\text{BrONO}_2 + \text{H}_2\text{O} \rightarrow \text{HOBr} + \text{HNO}_3$	JPL-06; $\gamma = 0.3$
15	$\text{ClONO}_2 + \text{HCl} \rightarrow \text{Cl}_2 + \text{HNO}_3$	JPL-06; $\gamma = 0.3$
16	$\text{HOCl} + \text{HCl} \rightarrow \text{Cl}_2 + \text{H}_2\text{O}$	JPL-06; $\gamma = 0.2$
17	$\text{HOBr} + \text{HCl} \rightarrow \text{BrCl} + \text{H}_2\text{O}$	JPL-06; $\gamma = 0.3$

Table 5.4: WACCM4.0 Photolytic Reactions.

no.	Reactants	Products	Comments
1	$O_2 + h\nu$	$O + O(^1D)$	Ly- α : Chabrilat and Kockarts (1997, 1998) ϕ (Ly- α): Lacoursiere et al. (1999) SRB: Koppers and Murtaugh (1996) For wavelength ν regions not Ly- α or SRB, σ (120-205nm): Brasseur and Solomon (1986); σ (205-240 nm): Yoshino et al. (1988)
2	$O_2 + h\nu$	2 O	see above
3	$O_3 + h\nu$	$O(^1D) + O_2$	σ (120-136.5nm): Tanaka et al. (1953); σ (136.5-175nm): Ackerman (1971); σ (175-847nm): WMO (1985); except for σ (185-350nm): Molina and Molina (1986) ϕ (<280nm): Marsh (1999) ϕ (>280nm): JPL-06.
4	$O_3 + h\nu$	$O + O_2$	see above
5	$N_2O + h\nu$	$O(^1D) + N_2$	JPL-06
6	$NO + h\nu$	$N + O$	Minschwaner et al. (1993)
7	$NO + h\nu$	$NO^+ + e$	
8	$NO_2 + h\nu$	$NO + O$	JPL-06
9	$N_2O_5 + h\nu$	$NO_2 + NO_3$	JPL-06
10	$N_2O_5 + h\nu$	$NO + O + NO_3$	JPL-06
11	$HNO_3 + h\nu$	$OH + NO_2$	JPL-06
12	$NO_3 + h\nu$	$NO_2 + O$	JPL-06
13	$NO_3 + h\nu$	$NO + O_2$	JPL-06
14	$HO_2NO_2 + h\nu$	$OH + NO_3$	JPL-06
15	$HO_2NO_2 + h\nu$	$NO_2 + HO_2$	JPL-06
16	$CH_3OOH + h\nu$	$CH_2O + H + OH$	JPL-06
17	$CH_2O + h\nu$	$CO + 2 H$	JPL-06
18	$CH_2O + h\nu$	$CO + H_2$	JPL-06
19	$H_2O + h\nu$	$H + OH$	ϕ (Ly- α): Slinger et al. (1982); ϕ (105-145nm): Stief et al. (1975); ϕ (>145): JPL-06 ϕ (120-182nm): Yoshino et al. (1996); ϕ (183-194nm): Cantrell et al. (1997)

Table 5.4: (continued) WACCM4.0 Photolytic Reactions.

no.	Reactants	Products	Comments
20	H ₂ O + hν	H ₂ + O(¹ D)	(see above)
21	H ₂ O + hν	H + 2 O	(see above)
22	H ₂ O ₂ + hν	2 OH	JPL-06
23	Cl ₂ + hν	2 Cl	JPL-06
24	ClO + hν	Cl + O	JPL-06
25	OCIO + hν	O + ClO	JPL-06
26	Cl ₂ O ₂ + hν	Cl + ClOO	Burkholder et al. (1990); Stimpfle et al. (2004)
27	HOCl + hν	Cl + OH	JPL-06
28	HCl + hν	Cl + H	JPL-06
29	ClONO ₂ + hν	Cl + NO ₃	JPL-06
30	ClONO ₂ + hν	ClO + NO ₂	JPL-06
31	BrCl + hν	Br + Cl	JPL-06
32	BrO + hν	Br + O	JPL-06
33	HOBr + hν	Br + OH	JPL-06
34	BrONO ₂ + hν	Br + NO ₃	JPL-06
35	BrONO ₂ + hν	BrO + NO ₂	JPL-06
36	CH ₃ Cl + hν	Cl + CH ₃ O ₂	JPL-06
37	CCl ₄ + hν	4 Cl	JPL-06
38	CH ₃ CCl ₃ + hν	3 Cl	JPL-06
39	CFC11 + hν	3 Cl	JPL-06
40	CFC12 + hν	2 Cl	JPL-06
41	CFC113 + hν	3 Cl	JPL-06
42	HCFC22 + hν	Cl	JPL-06
43	CH ₃ Br + hν	Br + CH ₃ O ₂	JPL-06
44	CF ₃ Br + hν	Br	JPL-06
45	CF ₂ ClBr + hν	Br + Cl	JPL-06
46	CO ₂ + hν	CO + O	σ (120-167): Nakata, et al. (1965); σ (167-199): Huffman (1971)
47	CH ₄ + hν	H + CH ₃ O ₂	σ: JPL-06; based on Brownsword et al. (1997)
48	CH ₄ + hν	H ₂ + 0.18 CH ₂ O + 0.18 O + 0.44 CO ₂ + 0.44 H ₂ + 0.38 CO + 0.05 H ₂ O	see above

Table 5.5: Ion-neutral and recombination reactions and exothermicities.

Reaction	ΔH (kJ mol ⁻¹)
$O^+ + O_2 \rightarrow O_2^+ + O$	150.11
$O^+ + N_2 \rightarrow NO^+ + N$	105.04
$N_2^+ + O \rightarrow NO^+ + N(^2D)$	67.53
$O_2^+ + N \rightarrow NO^+ + O$	406.16
$O_2^+ + NO \rightarrow NO^+ + O_2$	271.38
$N^+ + O_2 \rightarrow O_2^+ + N$	239.84
$N^+ + O_2 \rightarrow NO^+ + O$	646.28
$N^+ + O \rightarrow O^+ + N$	95.55
$N_2^+ + O_2 \rightarrow O_2^+ + N_2$	339.59
$O_2^+ + N_2 \rightarrow NO^+ + NO$	–
$N_2^+ + O \rightarrow O^+ + N_2$	–
$NO^+ + e \rightarrow 0.2N + 0.8N(^2D) + O$	82.389
$O_2^+ + e \rightarrow 1.15O + 0.85O(^1D)$	508.95
$N_2^+ + e \rightarrow 1.1N + 0.9N(^2D)$	354.83

4172 5.3.8 Electric Field

4173 The global electric field is based on a composite of two empirical models for the different latitude
 4174 regions: at high latitude the Weimer95 model [Weimer, 1995], and at low- and midlatitude the
 4175 Scherliess model [Scherliess et al., 2002]. In the following the different models are described
 4176 since the model is not published to date.

4177 Low- and midlatitude electric potential model

The low- and mid latitude electric field model was developed by Lüdger Scherliess [Scherliess et al., 2002]. It's based on Incoherent Scatter Radar data (ISR) from Jicamarca, Arecibo, Saint Santin, Millstone Hill, and the MU radar in Shigaraki. The electric field is calculated for a given year, season, UT, S_a , local time, and with longitudinal/latitudinal variation. The empirical model is constructed from a model for low solar flux ($S_a = 90$) and a high solar flux model ($S_a = 180$). The global electric potential is expressed according to Richmond et al. [1980] by

$$\Phi(d, T, t, \lambda) = \sum_{k=0}^2 \sum_{l=-2}^2 \sum_{m=-n}^n \sum_{n=1}^{12} A_{klmn} P_n^m(\sin\lambda) f_m\left(\frac{2\Pi t}{24}\right) f_l\left(\frac{2\Pi T}{24}\right) f_{-k}\left(\frac{2\Pi(d+9)}{365.24}\right) \quad (5.88)$$

Table 5.6: Ionization reactions.

$O + h\nu \rightarrow O^+ + e$
$O + e^* \rightarrow O^+ + e + e^*$
$N + h\nu \rightarrow N^+ + e$
$O_2 + h\nu \rightarrow O_2^+ + e$
$O_2 + e^* \rightarrow O_2^+ + e + e^*$
$O_2 + h\nu \rightarrow O + O^+ + e$
$O_2 + e^* \rightarrow O + O^+ + e + e^*$
$N_2 + h\nu \rightarrow N_2^+ + e$
$N_2 + e^* \rightarrow N_2^+ + e + e^*$
$N_2 + h\nu \rightarrow N + N^+ + e$
$N_2 + e^* \rightarrow N + N^+ + e + e^*$
$N_2 + h\nu \rightarrow N(^2D) + N^+ + e$
$N_2 + e^* \rightarrow N(^2D) + N^+ + e + e^*$

Table 5.7: EUVAC model parameters.

wavelength interval nm	F_i^0 ph cm ⁻² s ⁻¹	R_i
0.05 - 0.4	5.010e+01	6.240e-01
0.4 - 0.8	1.000e+04	3.710e-01
0.8 - 1.8	2.000e+06	2.000e-01
1.8 - 3.2	2.850e+07	6.247e-02
3.2 - 7.0	5.326e+08	1.343e-02
7.0 - 15.5	1.270e+09	9.182e-03
15.5 - 22.4	5.612e+09	1.433e-02
22.4 - 29.0	4.342e+09	2.575e-02
29.0 - 32.0	8.380e+09	7.059e-03
32.0 - 54.0	2.861e+09	1.458e-02
54.0 - 65.0	4.830e+09	5.857e-03
65.0 - 79.8	1.459e+09	5.719e-03
65.0 - 79.8	1.142e+09	3.680e-03
79.8 - 91.3	2.364e+09	5.310e-03
79.8 - 91.3	3.655e+09	5.261e-03
79.8 - 91.3	8.448e+08	5.437e-03
91.3 - 97.5	3.818e+08	4.915e-03
91.3 - 97.5	1.028e+09	4.955e-03
91.3 - 97.5	7.156e+08	4.422e-03
97.5 - 98.7	4.482e+09	3.950e-03
98.7 - 102.7	4.419e+09	5.021e-03
102.7 - 105.0	4.235e+09	4.825e-03
105.0 - 121.0	2.273e+10	3.383e-03

with

$$f_m(\phi) = \sqrt{2} \sin(m\phi) \quad m > 0 \quad (5.89)$$

$$f_m(\phi) = 1 \quad m = 0 \quad (5.90)$$

$$f_m(\phi) = \sqrt{2} \cos(m\phi) \quad m < 0 \quad (5.91)$$

the day of the year is denoted by d , universal time by T , magnetic local time by t , and geomagnetic latitude λ . The values of d , T , and t are expressed as angles between 0 and 2π . P_n^m are fully normalized Legendre polynomials. Due to the assumption that the geomagnetic field lines are highly conducting, the $n + m$ odd coefficients are set to zero to get a symmetrical electric potential about the magnetic equator. The coefficients A_{klmn} are found by a least-square fit for low and high solar flux. The solar cycle dependence is introduced by inter- and extrapolation of the sets of coefficients A_{klmn}^{low} for $S_a = 90$ and A_{klmn}^{high} for $S_a = 180$.

$$A_{klmn} = A_{klmn}^{low} + S_{aM} [A_{klmn}^{high} - A_{klmn}^{low}] \quad (5.92)$$

with

$$S_{aM} = \frac{\arctan[(S_a - 65)^2/90^2] - a_{90}}{a_{180} - a_{90}} \quad (5.93)$$

$$a_{90} = \arctan[(90 - 65)^2/90^2] \quad (5.94)$$

$$a_{180} = \arctan[(180 - 65)^2/90^2] \quad (5.95)$$

4178 We are using the daily $F_{10.7}$ number for S_a . S_{aM} levels off at high and low solar flux numbers,
4179 and therefore the model does not predict unrealistic high or low electric potential values.

4180

The geomagnetic field is described by modified apex coordinates [Richmond, 1995] which already take into account the distortion of the magnetic field. Modified apex coordinates have a reference height associated with them, which in our case is set to 130 km. The electric field \mathbf{E} and the electromagnetic drift velocity \mathbf{v}_E can be expressed by quantities mapped to the reference height, e.g. by E_{d1} , E_{d2} and v_{e1} , v_{e2} . These quantities are not actual electric field or electromagnetic drift velocity components, but rather the representation of the electric field or electromagnetic drift velocities by being constant along the geomagnetic field line. The fields in an arbitrary direction \mathbf{I} can be expressed by

$$\mathbf{I} \cdot \mathbf{E} = \mathbf{I} \cdot \mathbf{d}_1 E_{d1} + \mathbf{I} \cdot \mathbf{d}_2 E_{d2} \quad (5.96)$$

$$\mathbf{I} \cdot \mathbf{v}_E = \mathbf{I} \cdot \mathbf{e}_1 v_{e1} + \mathbf{I} \cdot \mathbf{e}_2 v_{e2} \quad (5.97)$$

4181 The basis vector \mathbf{d}_1 and \mathbf{e}_1 are in more-or-less magnetic eastward direction and \mathbf{d}_2 and \mathbf{e}_2 in
4182 downward/ equatorward direction. The base vectors vary with height, \mathbf{d}_i is decreasing and \mathbf{e}_i
4183 increasing with altitude. Therefore when the base vectors are applied to the mapped field at
4184 the reference height, e.g. E_{d1} , E_{d2} and v_{e1} , v_{e2} , they already take into account the height and
4185 directional variation of the corresponding quantity. Note that the modified apex coordinates
4186 are using the International Geomagnetic Reference Field (IGRF), and in the WACCM4 code
4187 the IGRF is only defined between the years 1900 and 2000. The description of the IGRF can
4188 be updated every 5 years to be extended in time.

4189 High-latitude electric potential model

The high-latitude electric potential model from Weimer [Weimer, 1995] is used. The model is based on spherical harmonic coefficients that were derived by least square fitting of measurements from the Dynamics Explorer 2 (DE2) satellite. The variation of the spherical harmonic coefficients with the interplanetary magnetic field (IMF) clock angle, IMF strength, solar wind velocity and season can be reproduced by a combination of Fourier series and multiple linear regression formula. The final model varies with magnetic latitude, magnetic local time, season, IMF strength and direction, and solar wind velocity. For our purpose we have set the solar wind speed to a constant value of 400 km/s and only consider the effects of IMF B_z ($B_y = 0$). Since the IMF conditions are not known all the time, we developed an empirical relation between B_z and the K_p index and the solar flux number S_a . Both, the K_p index and the daily solar flux number $F_{10.7}$, are known in the WACCM4 model.

$$B_z(K_p, F_{10.7}) = -0.085K_p^2 - 0.08104K_p + 0.4337 + 0.00794F_{10.7} - 0.00219K_pF_{10.7} \quad (5.98)$$

4190 Note that the Weimer model uses an average year of 365.24 days/year and an average month
4191 of 30.6001 days/month. The boundary of the Weimer model is at 46° magnetic latitude. The
4192 model was developed for an averaged northern and southern hemisphere. The B_y value and the
4193 season are reversed to get the values for the other hemisphere.

4194 Combing low-/ mid-latitude with the high latitude electric potential

After the low/mid-latitude electric potential Φ_{mid} and the high latitude potential Φ_{hgh} are calculated, both patterns are combined to be smooth at the boundary. The boundary between high and mid latitude λ_{bnd} is defined to lie where the electric field magnitude E from Φ_{hgh} equals 15 mV/m. After finding the longitudinal variation of the high latitude boundary λ_{bnd} , it's shifted halfway towards 54° magnetic latitude. The width of the transition zone $2\Delta\lambda_{trs}$ from high to mid latitude varies with magnetic local time. First, the high and mid latitude electric potential are adjusted by a constant factor such that the average for the high and mid latitude electric potential along the boundary λ_{bnd} are the same. The combined electric potential Φ is defined by

$$\Phi = \begin{cases} \Phi_{mid} & |\lambda| < \lambda_{bnd} - \Delta\lambda_{trs} \\ \Phi_{hgh} & |\lambda| > \lambda_{bnd} + \Delta\lambda_{trs} \\ F_{int}(\Phi_{mid}, \Phi_{hgh}) & \lambda_{bnd} - \Delta\lambda_{trs} \leq |\lambda| \leq \lambda_{bnd} + \Delta\lambda_{trs} \end{cases} \quad (5.99)$$

with

$$F_{int}(\Phi_{mid}, \Phi_{hgh}) = \frac{1}{3} \frac{1}{2\Delta\lambda_{trs}} [\{\Phi_{mid}(\phi, \lambda_{bnd} - \Delta\lambda_{trs}) + 2\Phi_{mid}(\phi, \lambda)\} \{\lambda_{bnd} - |\lambda| + \Delta\lambda_{trs}\} + (\Phi_{hgh}(\phi, \lambda_{bnd} + \Delta\lambda_{trs}) + 2\Phi_{hgh}(\phi, \lambda)) \{-\lambda_{bnd} + |\lambda| + \Delta\lambda_{trs}\}] \quad (5.100)$$

4195 **Calculation of electric field**

The electric field can be derived from the electric potential by

$$\mathbf{E} = -\nabla\Phi \quad (5.101)$$

The more-or-less magnetic eastward electric field component E_{d1} and the in general downward/equatorward E_{d2} component are calculated. These components are constant along the magnetic field line. They are calculated at a reference height $h_r = 130$ km with $R = R_{earth} + h_r$. The electric field does not vary much with altitude, and therefore we assume in the code that the electric field is constant in height.

$$E_{d1} = -\frac{1}{R\cos\lambda} \frac{\partial\Phi}{\partial\phi} \quad (5.102)$$

$$E_{d2} = \frac{1}{R\sin I} \frac{\partial\Phi}{\partial\lambda} \quad (5.103)$$

4196 with $\sin I = 2 \sin \lambda [4 - 3 \cos^2 \lambda]^{0.5}$.

4197 **Calculation of electrodynamic drift velocity**

The electric field is calculated on a $2^\circ \times 2^\circ$ degree geomagnetic grid with the magnetic longitude represented by the magnetic local time (MLT) from 0 MLT to 24 MLT. Therefore, the magnetic local time of the geographic longitudes of the WACCM4 grid has to be determined first to map from the geomagnetic to the geographic WACCM4 grid. The magnetic local time is calculated by using the location of the geomagnetic dipole North pole, the location of the subsolar point, and the apex longitude of the geographic WACCM4 grid point. A bilinear interpolation is used for the mapping. Note that every processor calculates the global electric field, which is computationally inexpensive. Otherwise, to calculate the electric field some communication between the different processors would be necessary to get the spatial derivatives.

The mapped electric field is rotated into the geographic direction by

$$\mathbf{E} = \mathbf{d}_1 E_{d1} + \mathbf{d}_2 E_{d2} \quad (5.104)$$

with the components of \mathbf{E} being the geographic eastward, westward and upward electric field. At high altitudes the ion-neutral collision frequency ν_{in} is small in relation to the angular gyrofrequency of the ions Ω_i ($\nu_{in} \ll \Omega_i$), and the electron-neutral collision frequency ν_{en} is much smaller than the angular gyrofrequency of the electrons Ω_e ($\nu_{en} \ll \Omega_e$), due to the decrease in neutral density with increasing altitude. Therefore, the ion drift $\mathbf{v}_{i\perp}$ perpendicular to the geomagnetic field can be simplified by the electrodynamic drift velocity \mathbf{v}_E

$$\mathbf{v}_{i\perp} \approx \mathbf{v}_E = \frac{\mathbf{E} \times \mathbf{B}_o}{B_o^2} \quad (5.105)$$

4198 with \mathbf{B}_o the geomagnetic main field from IGRF.

The following is written according to the source code. Two subroutines `iondrag_calc` exist in the code, one uses the calculated ion drag coefficients if `WACCM_MOZART` is used, and the other one uses look-up tables for the ion drag coefficients λ_1 and λ_2 .

It is assumed that the electron T_e and ion T_i temperature is equal to the neutral temperature T_n .

$$T_i = T_e = T_n \quad (5.106)$$

The dip angle I of the geomagnetic field is calculated by

$$I = \arctan \frac{B_z}{\sqrt{B_{north}^2 + B_{east}^2}} \quad (5.107)$$

with a minimum dip angle $|I| \geq 0.17$. The declination is

$$D = \arctan \frac{B_{east}}{B_{north}} \quad (5.108)$$

The magnetic field component B_z, B_{east}, B_{north} are determined from the International Geomagnetic Reference Field (IGRF).

The collision frequencies ν in units of s^{-1} are determined by, e.g. [Schunk and Nagy \[2000\]](#)

$$\frac{1}{N_{O_2}} \nu_{O_2^+ - O_2} = 2.59 \times 10^{-11} \sqrt{\frac{T_i + T_e}{2}} \left[1 - 0.73 \log_{10} \sqrt{\frac{T_i + T_e}{2}} \right]^2 \quad (5.109)$$

$$\frac{1}{N_{O_2}} \nu_{O^+ - O_2} = 6.64 \times 10^{-10} \quad (5.110)$$

$$\frac{1}{N_{O_2}} \nu_{NO^+ - O_2} = 4.27 \times 10^{-10} \quad (5.111)$$

$$\frac{1}{N_O} \nu_{O^+ - O} = 3.67 \times 10^{-11} \sqrt{\frac{T_i + T_e}{2}} \left[1 - 0.064 \log_{10} \sqrt{\frac{T_i + T_e}{2}} \right]^2 f_{cor} \quad (5.112)$$

$$\frac{1}{N_O} \nu_{NO^+ - O} = 2.44 \times 10^{-10} \quad (5.113)$$

$$\frac{1}{N_O} \nu_{O_2^+ - O} = 2.31 \times 10^{-10} \quad (5.114)$$

$$\frac{1}{N_{N_2}} \nu_{O_2^+ - N_2} = 4.13 \times 10^{-10} \quad (5.115)$$

$$\frac{1}{N_{N_2}} \nu_{NO^+ - N_2} = 4.34 \times 10^{-10} \quad (5.116)$$

$$\frac{1}{N_{N_2}} \nu_{O^+ - N_2} = 6.82 \times 10^{-10} \quad (5.117)$$

with N_n the number density for the neutral n in units of $1/cm^3$, and the temperature in Kelvins. The collisions frequencies for $\nu_{O_2^+ - O_2}$ and $\nu_{O^+ - O}$ are resonant, all other are nonresonant. The

arbitrary correction factor f_{cor} multiplies the ν_{O+O} collision frequency and is set to $f_{cor} = 1.5$ which has been found to improve agreement between calculated and observed winds and electron densities in the upper thermosphere in other models. The mean mass \bar{m}_{mid} [g/mole] at the midpoints of the height level is calculated in the Mozart module. The number densities [$1/cm^3$] are

$$N_{O_2} = \frac{N\bar{m}_{mid}mmr_{O_2}}{m_{O_2}} \quad (5.118)$$

$$N_O = \frac{N\bar{m}_{mid}mmr_O}{m_O} \quad (5.119)$$

$$N_{N_2} = \frac{N\bar{m}_{mid}mmr_{N_2}}{m_{N_2}} \quad (5.120)$$

$$N_{O_2^+} = \frac{N\bar{m}_{mid}mmr_{O_2^+}}{m_{O_2^+}} \quad (5.121)$$

$$N_{O^+} = \frac{N\bar{m}_{mid}mmr_{O^+}}{m_{O^+}} \quad (5.122)$$

$$N_e = \frac{N\bar{m}_{mid}mmr_e}{m_e} \quad (5.123)$$

with mmr the mass mixing ratio, and N the total number density in units of $1/cm^3$. The pressure [$dyne/cm^2$] and the mean mass at the midpoint \bar{m}_{mid} in units of $g/mole$ are

$$p = 10 p_{mid} \quad (5.124)$$

$$N\bar{m}_{mid} = \frac{p \bar{m}}{k_B T_n} \quad (5.125)$$

with the factor 10 to convert from [Pa] to [$dyne/cm^2$], and k_B the Boltzmann constant. The collision frequencies are

$$\nu_{O_2^+} = \nu_{O_2^+-O_2} + \nu_{O_2^+-O} + \nu_{O_2^+-N_2} \quad (5.126)$$

$$\nu_{O^+} = \nu_{O^+-O_2} + \nu_{O^+-O} + \nu_{O^+-N_2} \quad (5.127)$$

$$\nu_{NO^+} = \nu_{NO^+-O_2} + \nu_{NO^+-O} + \nu_{NO^+-N_2} \quad (5.128)$$

$$\begin{aligned} \nu_{en} = & 2.33 \times 10^{-11} N_{N_2} T_e (1 - 1.21 \times 10^{-4} T_e) + \\ & 1.82 \times 10^{-10} N_{O_2} \sqrt{T_e} (1 + 3.6 \times 10^{-2} \sqrt{T_e}) + \\ & 8.9 \times 10^{-11} N_O \sqrt{T_e} (1 + 5.7 \times 10^{-4} T_e) \end{aligned} \quad (5.129)$$

The ratios r between collision frequency ν and gyro frequency Ω are

$$r_{O_2^+} = \frac{\nu_{O_2^+}}{\Omega_{O_2^+}} \quad (5.130)$$

$$r_{O^+} = \frac{\nu_{O^+}}{\Omega_{O^+}} \quad (5.131)$$

$$r_{NO^+} = \frac{\nu_{NO^+}}{\Omega_{NO^+}} \quad (5.132)$$

$$r_e = \frac{\nu_{en}}{\Omega_e} \quad (5.133)$$

with the gyro frequency for ions $\Omega_i = eB/m_i$ and for electrons $\Omega_e = eB/m_e$. The Pedersen conductivity [S/m] is

$$\sigma_P = \frac{e}{B} \left[N_{O^+} \frac{r_{O^+}}{1 + r_{O^+}^2} + N_{O_2^+} \frac{r_{O_2^+}}{1 + r_{O_2^+}^2} + N_{NO^+} \frac{r_{NO^+}}{1 + r_{NO^+}^2} + N_e \frac{r_e}{1 + r_e^2} \right] \quad (5.134)$$

The Hall conductivity [S/m] is

$$\sigma_H = \frac{e}{B} \left[-N_{O^+} \frac{1}{1 + r_{O^+}^2} - N_{O_2^+} \frac{1}{1 + r_{O_2^+}^2} - N_{NO^+} \frac{1}{1 + r_{NO^+}^2} + N_e \frac{1}{1 + r_e^2} \right] \quad (5.135)$$

The ion drag coefficients are

$$\lambda_1 = \frac{\sigma_P B^2}{\rho} \quad (5.136)$$

$$\lambda_2 = \frac{\sigma_H B^2}{\rho} \quad (5.137)$$

with $\rho = N \frac{\bar{m}}{N_A}$, and N_A the Avagadro number. The ion drag tensor in magnetic direction $\underline{\lambda}^{mag}$ is

$$\underline{\lambda}^{mag} = \begin{pmatrix} \lambda_{xx}^{mag} & \lambda_{xy}^{mag} \\ \lambda_{yx}^{mag} & \lambda_{yy}^{mag} \end{pmatrix} = \begin{pmatrix} \lambda_1 & \lambda_2 \sin I \\ -\lambda_2 \sin I & \lambda_1 \sin^2 I \end{pmatrix} \quad (5.138)$$

with the x–direction in magnetic east, and y–direction magnetic north in the both hemispheres. The ion drag tensor can be rotated in geographic direction by using the rotation matrix \mathbf{R}

$$\mathbf{R} = \begin{pmatrix} \cos D & \sin D \\ -\sin D & \cos D \end{pmatrix} \quad (5.139)$$

Applying the rotation to the ion drag tensor $\mathbf{R} \underline{\lambda}^{mag} \mathbf{R}^{-1}$ leads to

$$\Lambda = \begin{pmatrix} \lambda_{xx} & \lambda_{xy} \\ \lambda_{yx} & \lambda_{yy} \end{pmatrix} = \quad (5.140)$$

$$\begin{pmatrix} \lambda_{xx}^{mag} \cos^2 D + \lambda_{yy}^{mag} \sin^2 D & \lambda_{xy}^{mag} + (\lambda_{yy}^{mag} - \lambda_{xx}^{mag}) \sin D \cos D \\ \lambda_{yx}^{mag} + (\lambda_{yy}^{mag} - \lambda_{xx}^{mag}) \sin D \cos D & \lambda_{yy}^{mag} \cos^2 D + \lambda_{xx}^{mag} \sin^2 D \end{pmatrix} \quad (5.141)$$

The ion drag acceleration \mathbf{a}_i due to the Ampère force is

$$\mathbf{a}_i = \frac{\mathbf{J} \times \mathbf{B}}{\rho} = \lambda_1 (\mathbf{v}_E - \mathbf{u}_{n\perp}) + \lambda_2 \hat{\mathbf{b}} \times (\mathbf{v}_E - \mathbf{u}_{n\perp}) \quad (5.142)$$

with $\mathbf{u}_{n\perp}$ the neutral wind velocity perpendicular to the geomagnetic field and $\hat{\mathbf{b}}$ the unit vector of the geomagnetic field. The tendencies on the neutral wind are calculated by

$$\frac{\partial \mathbf{v}_{En}}{\partial t} = -\Lambda \mathbf{v}_{En} \quad (5.143)$$

For stability an implicit scheme is used with

$$\frac{\mathbf{v}_{En}(t + \Delta t) - \mathbf{v}_{En}(t)}{\Delta t} = -\Lambda \mathbf{v}_{En}(t + \Delta t) \quad (5.144)$$

which leads to

$$\left(\frac{1}{\Delta t}I + \Lambda\right)\mathbf{v}_{En}(t + \Delta t) = \frac{1}{\Delta t}\mathbf{v}_{En}(t) \quad (5.145)$$

with I the unit matrix. Solving for $\mathbf{v}_{En}(t + \Delta t)$ gives

$$\mathbf{v}_{En}(t + \Delta t) = \frac{1}{\Delta t} \left(\frac{1}{\Delta t}I + \Lambda\right)^{-1} \mathbf{v}_{En}(t) \quad (5.146)$$

The tendencies are determined by

$$\frac{\partial \mathbf{v}_{En}}{\partial t} = \frac{\mathbf{v}_{En}(t + \Delta t) - \mathbf{v}_{En}(t)}{\Delta t} = \frac{1}{\Delta t} \left[\frac{1}{\Delta t} \left(\frac{1}{\Delta t}I + \Lambda\right)^{-1} - 1 \right] \mathbf{v}_{En}(t) \quad (5.147)$$

The tensor $\frac{1}{\Delta t}I + \Lambda$ is

$$\begin{pmatrix} \lambda_{11}^* & \lambda_{12}^* \\ \lambda_{21}^* & \lambda_{22}^* \end{pmatrix} = \begin{pmatrix} \frac{1}{\Delta t} + \lambda_{xx} & \lambda_{xy} \\ \lambda_{yx} & \frac{1}{\Delta t} + \lambda_{yy} \end{pmatrix} \quad (5.148)$$

$$\frac{Det}{\Delta t} = \frac{1}{\Delta t} \frac{1}{\lambda_{11}^* \lambda_{22}^* - \lambda_{12}^* \lambda_{21}^*} \quad (5.149)$$

The tendencies applied to the neutral winds with $\mathbf{v}_{En} = (u_E - u_n, v_E - v_n)$ gives

$$d_t u_i = \frac{1}{\Delta t} \left[\frac{Det}{\Delta t} (\lambda_{12}^* (v_E - v_n) - \lambda_{22}^* (u_E - u_n)) + u_E - u_n \right] \quad (5.150)$$

$$d_t v_i = \frac{1}{\Delta t} \left[\frac{Det}{\Delta t} (\lambda_{21}^* (u_E - u_n) - \lambda_{11}^* (v_E - v_n)) + v_E - v_n \right] \quad (5.151)$$

4200

4201

The electromagnetic energy transfer to the ionosphere is

$$\mathbf{J} \cdot \mathbf{E} = \mathbf{J} \cdot \mathbf{E}' + \mathbf{u}_n \cdot \mathbf{J} \times \mathbf{B} \quad (5.152)$$

The first term on the right hand side denotes the Joule heating, which is the electromagnetic energy transfer rate in the frame of reference of the neutral wind. The second term represents the generation of kinetic energy due to the Ampère force. Since the electric field is small along the magnetic field line, we consider only the perpendicular component to the magnetic field of the Joule heating $\mathbf{J}_\perp \cdot \mathbf{E}'$. The electric field in the frame of the neutral wind \mathbf{u} can be written as

$$\mathbf{E}' = \mathbf{E} + \mathbf{u} \times \mathbf{B} \quad (5.153)$$

The Joule heating can be expressed by

$$\mathbf{J}_\perp \cdot \mathbf{E}' = \sigma_P \mathbf{E}'^2 \quad (5.154)$$

with

$$\mathbf{E}'^2 = B^2 \left(\frac{\mathbf{E} \times \mathbf{B}}{B^2} - \mathbf{u}_\perp \right)^2 \quad (5.155)$$

and $\frac{\mathbf{E} \times \mathbf{B}}{B^2}$ the electromagnetic drift velocity \mathbf{v}_E with the components u_E and v_E . The Joule heating Q_J is

$$Q_J = (u_E - u_n)^2 \lambda_{xx} + (u_E - u_n)(v_E - v_n)(\lambda_{xy} - \lambda_{yx}) + (v_E - v_n)^2 \lambda_{yy} \quad (5.156)$$

4202 Note, that the vertical velocity components are not taken into account here.

4203 5.3.9 Boundary Conditions

4204 The upper boundary conditions for momentum and for most constituents are the usual zero
 4205 flux conditions used in CAM4. However, in the energy budget of the thermosphere, much
 4206 of the SW radiation at wavelengths <120 nm is absorbed above 145 km (the upper bound-
 4207 ary of the model), where LW radiation is very inefficient. This energy is transported down-
 4208 ward by molecular diffusion to below 120 km, where it can be dissipated more efficiently by
 4209 LW emission. Imposing a zero flux upper boundary condition on heat omits a major term
 4210 in the heat budget and causes the lower thermosphere to be much too cold. Instead, we
 4211 use the Mass Spectrometer-Incoherent Scatter (MSIS) model [Hedin, 1987, 1991] to specify
 4212 the temperature at the top boundary as a function of season and phase of the solar cy-
 4213 cle. The version of the MSIS model used in WACCM4.0 is NRLMSISE-00 [see [http://uap-
 www.nrl.navy.mil/models_web/msis/msis_home.htm](http://uap-

 4214 www.nrl.navy.mil/models_web/msis/msis_home.htm)].

4215 For chemical constituents, surface mixing ratios of CH_4 , N_2O , CO_2 , H_2 , CFC-11, CFC-12,
 4216 CFC-113, HCFC-22, H-1211, H-1301, CCl_4 , CH_3CCH_3 , CH_3Cl , and CH_3Br are specified from
 4217 observations. The model accounts for surface emissions of NO_x and CO based on the emission
 4218 inventories described in Horowitz et al. [2003]. The NO_x source from lightning is distributed
 4219 according to the location of convective clouds based on Price et al. [1997a] and Price et al.
 4220 [1997b], with a vertical profile following Pickering et al. [1998]. Aircraft emissions of NO_x and
 4221 CO are included in the model and based on Friedl [1997].

4222 At the upper boundary, a zero-flux upper boundary condition is used for most species whose
 4223 mixing ratio is negligible in the lower thermosphere, while mixing ratios of other species are
 4224 specified from a variety of sources. The MSIS model is used to specify the mixing ratios of O,
 4225 O_2 , H, and N; as in the case of temperature, the MSIS model returns values of these constituents
 4226 as functions of season and phase of the solar cycle. CO and CO_2 are specified at the upper
 4227 boundary using output from the TIME-GCM [Roble and Ridley, 1994]. NO is specified using
 4228 data from the Student Nitric Oxide Explorer (SNOE) satellite [Barth et al., 2003], which has
 4229 been parameterized as a function of latitude, season, and phase of the solar cycle in the Nitric
 4230 Oxide Empirical Model (NOEM) of Marsh et al. [2004]. Finally, a global-mean value (typical of
 4231 the sunlit lower thermosphere) is specified for species such as H_2O , whose abundance near the top
 4232 of the model is very small under sunlit conditions, but which can be rapidly transported upward

4233 by diffusive separation in polar night (since they are lighter than the background atmosphere).
4234 In these cases, a zero-flux boundary condition leads to unrealistically large mixing ratios at the
4235 model top in polar night.

4236

Chapter 6

4237

Initial and Boundary Data

4238

6.1 Initial Data

In this section, we describe how the time integration is started from data consistent with the spectral truncation. The land surface model requires its own initial data, as described by Bonan [1996]. The basic initial data for the model consist of values of u, v, T, q, Π , and Φ_s on the Gaussian grid at time $t = 0$. From these, U, V, T' , and Π are computed on the grid using (3.139), and (3.177). The Fourier coefficients of these variables U^m, V^m, T'^m, Π^m , and Φ_s^m are determined via an FFT subroutine (3.277), and the spherical harmonic coefficients T_n^m, Π_n^m , and $(\Phi_s)_n^m$ are determined by Gaussian quadrature (3.278). The relative vorticity ζ and divergence δ spherical harmonic coefficients are determined directly from the Fourier coefficients U^m and V^m using the relations,

$$\zeta = \frac{1}{a(1-\mu^2)} \frac{\partial V}{\partial \lambda} - \frac{1}{a} \frac{\partial U}{\partial \mu}, \quad (6.1)$$

$$\delta = \frac{1}{a(1-\mu^2)} \frac{\partial U}{\partial \lambda} + \frac{1}{a} \frac{\partial V}{\partial \mu}. \quad (6.2)$$

4239

The relative vorticity and divergence coefficients are obtained by Gaussian quadrature directly, using (3.282) for the λ -derivative terms and (3.285) for the μ -derivatives.

4241

Once the spectral coefficients of the prognostic variables are available, the grid-point values of ζ, δ, T', Π , and Φ_s may be calculated from (3.308), the gradient $\nabla \Pi$ from (3.311) and (3.312), and U and V from (3.317) and (3.318). The absolute vorticity η is determined from the relative vorticity ζ by adding the appropriate associated Legendre function for f (3.245). This process gives grid-point fields for all variables, including the surface geopotential, that are consistent with the spectral truncation even if the original grid-point data were not. These grid-point values are then convectively adjusted (including the mass and negative moisture corrections).

4248

The first time step of the model is forward semi-implicit rather than centered semi-implicit, so only variables at $t = 0$ are needed. The model performs this forward step by setting the variables at time $t = -\Delta t$ equal to those at $t = 0$ and by temporarily dividing $2\Delta t$ by 2 for this time step only. This is done so that formally the code and the centered prognostic equations of chapter 3 also describe this first forward step and no additional code is needed for this special step. The model loops through as indicated sequentially in chapter 3. The time step $2\Delta t$ is set to its original value before beginning the second time step.

4254

6.2 Boundary Data

In addition to the initial grid-point values described in the previous section, the model also requires lower boundary conditions. The required data are surface temperature (T_s) at each ocean point, the surface geopotential at each point, and a flag at each point to indicate whether the point is land, ocean, or sea ice. The land surface model requires its own boundary data, as described by Bonan [1996]. A surface temperature and three subsurface temperatures must also be provided at non-ocean points.

For the uncoupled configuration of the model, a seasonally varying sea-surface temperature, and sea-ice concentration dataset is used to prescribe the time evolution of these surface quantities. This dataset prescribes analyzed monthly mid-point mean values of SST and ice concentration for the period 1950 through 2001. The dataset is a blended product, using the global HadISST OI dataset prior to 1981 and the Smith/Reynolds EOF dataset post-1981 (see Hurrell, 2002). In addition to the analyzed time series, a composite of the annual cycle for the period 1981-2001 is also available in the form of a mean “climatological” dataset. The sea-surface temperature and sea ice concentrations are updated every time step by the model at each grid point using linear interpolation in time. The mid-month values have been evaluated in such a way that this linear time interpolation reproduces the mid-month values.

Earlier versions of the global atmospheric model (the CCM series) included a simple land-ocean-sea ice mask to define the underlying surface of the model. It is well known that fluxes of fresh water, heat, and momentum between the atmosphere and underlying surface are strongly affected by surface type. The CAM 5.0 provides a much more accurate representation of flux exchanges from coastal boundaries, island regions, and ice edges by including a fractional specification for land, ice, and ocean. That is, the area occupied by these surface types is described as a fractional portion of the atmospheric grid box. This fractional specification provides a mechanism to account for flux differences due to sub-grid inhomogeneity of surface types.

In CAM 5.0 each atmospheric grid box is partitioned into three surface types: land, sea ice, and ocean. Land fraction is assigned at model initialization and is considered fixed throughout the model run. Ice concentration data is provided by the external time varying dataset described above, with new values determined by linear interpolation at the beginning of every time-step. Any remaining fraction of a grid box not already partitioned into land or ice is regarded as ocean.

Surface fluxes are then calculated separately for each surface type, weighted by the appropriate fractional area, and then summed to provide a mean value for a grid box:

$$F_{\psi_T} = a_i F_{\psi_i} + a_o F_{\psi_o} + a_l F_{\psi_l} , \quad (6.3)$$

where F denotes the surface flux of the arbitrary scalar quantity ψ , a denotes fractional area, and the subscripts T, i, o , and l respectively denote the total, ice, ocean, and land components of the fluxes. For each time-step the aggregated grid box fluxes are passed to the atmosphere and all flux arrays which have been used for the accumulations are reset to zero in preparation for the next time-step. The fractional land values for CAM 5.0 were calculated from Navy 10-Min Global Elevation Data. An area preserving binning algorithm was used to interpolate from the high-resolution Navy dataset to standard model resolutions.

The radiation parameterization requires monthly mean ozone volume mixing ratios to be specified as a function of the latitude grid, 23 vertical pressure levels, and time. The ozone path

4295 lengths are evaluated from the mixing-ratio data. The path lengths are interpolated to the model
4296 η -layer interfaces for use in the radiation calculation. As with the sea-surface temperatures, the
4297 seasonal version assigns the monthly averages to the mid-month date and updates them every
4298 12 hours via linear interpolation. The actual mixing ratios used in the standard version were
4299 derived by Chervin [1986] from analysis of Dütsch [1986].

4300 The sub-grid scale standard deviation of surface orography is specified in the following man-
4301 ner. The variance is first evaluated from the global Navy 10' topographic height data over an
4302 intermediate grid (*e.g.* $2^\circ \times 2^\circ$ grid for T42 and lower resolutions, $1.67^\circ \times 1.67^\circ$ for T63, and
4303 $1.0^\circ \times 1.0^\circ$ for T106 resolution) and is assumed to be isotropic. Once computed on the appropri-
4304 ate grid, the standard deviations are binned to the CAM 5.0 grid (*i.e.*, all values whose latitude
4305 and longitude centers fall within each grid box are averaged together). Finally, the standard
4306 deviation is smoothed twice with a 1-2-1 spatial filter. Values over ocean are set to zero.

4307

Appendix A

4308

Physical Constants

Following the American Meteorological Society convention, the model uses the International System of Units (SI) (see August 1974 *Bulletin of the American Meteorological Society*, **Vol. 55**, No. 8, pp. 926-930).

a	$= 6.37122 \times 10^6 \text{ m}$	Radius of earth
g	$= 9.80616 \text{ m s}^{-2}$	Acceleration due to gravity
π	$= 3.14159265358979323846$	Pi
t_s	$= 86164.0 \text{ s}$	Earth's sidereal day
Ω	$= 2 * \pi / t_s \text{ [s}^{-1}\text{]}$	Earth's angular velocity
σ_B	$= 5.67 \times 10^{-8} \text{ W m}^{-2} \text{ K}^{-4}$	Stefan – Boltzmann constant
k	$= 1.38065 \times 10^{-23} \text{ JK}^{-1}$	Boltzmann constant
N	$= 6.02214 \times 10^{26}$	Avogadro's number
R^*	$= k N \text{ [JK}^{-1}\text{]}$	Universal gas constant
m_{air}	$= 28.966 \text{ kg}$	Molecular weight of dry air
R	$= R^* / m_{air} \text{ [J kg}^{-1} \text{ K}^{-1}\text{]}$	Gas constant for dry air
m_v	$= 18.016 \text{ kg}$	Molecular weight of water vapor
R_v	$= R^* / m_v \text{ [J kg}^{-1} \text{ K}^{-1}\text{]}$	Gas constant for water vapor
c_p	$= 1.00464 \times 10^3 \text{ J kg}^{-1} \text{ K}^{-1}$	Specific heat of dry air at constant pressure
κ	$= 2/5$	Von Karman constant
z_{vir}	$= R_v / R - 1$	Ratio of gas constants for water vapor and dry air
L_v	$= 2.501 \times 10^6 \text{ J kg}^{-1}$	Latent heat of vaporization
L_i	$= 3.337 \times 10^5 \text{ J kg}^{-1}$	Latent heat of fusion
ρ_{H_2O}	$= 1.0 \times 10^3 \text{ kg m}^{-3}$	Density of liquid water
c_{pv}	$= 1.81 \times 10^3 \text{ J kg}^{-1} \text{ K}^{-1}$	Specific heat of water vapor at constant pressure
T_{melt}	$= 273.16 \text{ }^\circ\text{K}$	Melting point of ice
p_{std}	$= 1.01325 \times 10^5 \text{ Pa}$	Standard pressure
ρ_{air}	$= p_{std} / (R T_{melt}) \text{ [kgm}^{-3}\text{]}$	Density of dry air at standard pressure/temperature

4309

The model code defines these constants to the stated accuracy. We do not mean to imply that

4310

these constants are known to this accuracy nor that the low-order digits are significant to the

4311

physical approximations employed.

4312 Appendix B

4313 Acronyms

4314	ABL	Atmospheric Boundary Layer
	AMIP	Atmospheric Model Intercomparison Project
	AMWG	Atmospheric Model Working Group
	BATS	Biosphere-Atmosphere Transfer Scheme
	CAM	Community Atmosphere Model
	CAPE	Convectively Available Potential Energy
	CCM	Community Climate Model
	CCN	Cloud Condensation Nucleus
	CCSM	Community Climate System Model
	CFC	Chloro-Fluoro Carbon
	CFL	Courant-Friedrichs-Levy Condition
	CGD	NCAR Climate and Global Dynamics Division
	CGS	Centimeters/grams/seconds
	CKD	Clough-Kneizys-Davies
	CLM	Community Land Model
	CMS	(NCAR) Climate Modeling Section
	CSIM	Community Sea-Ice Model
	CWP	Condensed Water Path
	DAO	(NASA Goddard) Data Assimilation Office
	DAS	Data Assimilation System
	DISORT	DIScrete-Ordinate method Radiative Transfer
	ECMWF	European Centre for Medium Range Forecasts
	EOF	Empirical Orthogonal Function
	FASCODE	FASt atmosphere Signature Code
	FFSL	Flux-Form Semi-Lagrangian Transport
	FFT	Fast Fourier Transform
	FV/fv	Finite Volume
	GCM	General Circulation Model
	GENLN	General Line-by-line Atmospheric Transmittance and Radiance Model
	GEOS	Goddard Earth Observing System
	GFDL	Geophysical Fluid Dynamics Laboratory
	GSFC	Goddard Space Flight Center
	GMT	Greenwich Mean Time

HadISST	Hadley Centre for Climate Prediction and Research SST
HITRAN	High-resolution Transmission Molecular Absorption Database
ICA	Independent Column Approximation
IPCC	International Panel on Climate Change
KNMI	Royal Netherlands Meteorological Institute
LBL	Line by line
LCL	Lifting condensation level
LSM	Land Surface Model
MATCH	Model for Atmospheric Transport and Chemistry
M/R	Maximum/Random overlap
NASA	National Space Administration
NCAR	National Center for Atmospheric Research
NCEP	National Center for Environmental Prediction
NOAA	National Oceanographic and Atmospheric Administration
NWP	Numerical Weather Prediction
OI	Optimal Interpolation
OPAC	Optical Properties of Aerosols and Clouds
PBL	Planetary Boundary Layer
PCMDI	Program for Climate Model Diagnosis and Intercomparison
PPM	Piece-wise Parabolic Method
RHS	Right Hand Side
RMS	Root-mean Square
SCMO	Sufficient Condition for Monotonicity
SI	International System of Units
SOM	Slab Ocean Model
SST	Sea-surface temperature
TOA	Top Of Atmosphere
TOM	Top Of Model
UCAR	University Corporation for Atmospheric Research
WKB	Wentzel-Kramer-Brillouin approximation

4316 **Appendix C**

4317 **Resolution and dycore-dependent**
 4318 **parameters**

4319 The following adjustable parameters differ between various finite volume resolutions in the CAM
 4320 5.0. Refer to the model code for parameters relevant to alternative dynamical cores.

Table C.1: Resolution-dependent parameters

Parameter	FV 1 deg	FV 2 deg	Description
$q_{ic,warm}$	2.e-4	2.e-4	threshold for autoconversion of warm ice
$q_{ic,cold}$	18.e-6	9.5e-6	threshold for autoconversion of cold ice
$k_{e, strat}$	5.e-6	5.e-6	stratiform precipitation evaporation efficiency parameter
RH_{min}^{low}	.92	.91	minimum RH threshold for low stable clouds
RH_{min}^{high}	.77	.80	minimum RH threshold for high stable clouds
$k_{1, deep}$	0.10	0.10	parameter for deep convection cloud fraction
p_{mid}	750.e2	750.e2	top of area defined to be mid-level cloud
$c_{0, shallow}$	1.0e-4	1.0e-4	shallow convection precip production efficiency parameter
$c_{0, deep}$	3.5E-3	3.5E-3	deep convection precipitation production efficiency parameter
$k_{e, conv}$	1.0E-6	1.0E-6	convective precipitation evaporation efficiency parameter
v_i	1.0	0.5	Stokes ice sedimentation fall speed (m/s)

Bibliography

- 4321
- 4322 Abdul-Razzak, H., and S. J. Ghan, A parameterization of aerosol activation 2. multiple aerosol
4323 types, *J. Geophys. Res.*, *105* (D5), 6837–6844, 2000a.
- 4324 Abdul-Razzak, H., and S. J. Ghan, A parameterization of aerosol activation 2. multiple aerosol
4325 types, *Journal of Geophysical Research-Atmospheres*, *105* (D5), 6837–6844, 2000b, 294KT
4326 Times Cited:82 Cited References Count:27.
- 4327 Alcamo, J., A. Bouwman, J. Edmonds, A. Grubler, T. Morita, and A. Sugandhy, An evaluation
4328 of the ipcc is92 emission scenarios, in *Climate Change 1994: Radiative Forcing of Climate*
4329 *Change and an Evaluation of the IPCC IS92 Emission Scenarios*, edited by J. Houghton,
4330 247–304, Cambridge University Press, 1995.
- 4331 Andrews, D. G., J. R. Holton, and C. B. Leovy, *Middle Atmosphere Dynamics*. Academic Press,
4332 1987.
- 4333 Ansmann, A. et al., Influence of Saharan dust on cloud glaciation in southern Morocco during
4334 the Saharan Mineral Dust Experiment, *J. Geophys. Res.*, *113* (D04210), 2008.
- 4335 Ansmann, A., M. Tesche, P. Seifert, D. Althausen, R. Engelmann, J. Furrntke, U. Wandinger,
4336 I. Mattis, and D. Müller, Evolution of the ice phase in tropical altocumulus: SAMUM lidar
4337 observations over Cape Verde, *J. Geophys. Res.*, *114* (D17208), 2009.
- 4338 Anthes, R. A., Summary of workshop on the NCAR Community Climate/forecast Models 14–26
4339 July 1985, Boulder, Colorado, *Bull. Am. Meteorol. Soc.*, *67*, 94–198, 1986.
- 4340 Arakawa, A., and V. R. Lamb, A potential enstrophy and energy conserving scheme for the
4341 shallow-water equations, *Mon. Wea. Rev.*, *109*, 18–36, 1981.
- 4342 Asselin, R., Frequency filter for time integrations, *Mon. Wea. Rev.*, *100*, 487–490, 1972.
- 4343 Baede, A. P. M., M. Jarraud, and U. Cubasch, Adiabatic formulation and organization of
4344 ECMWF’s model, Technical Report 15, ECMWF, Reading, U.K., 1979.
- 4345 Balachandran, N., and D. Rind, Modeling the effects of uv variability and the qbo on the
4346 troposphere-stratosphere system. part i: The middle atmosphere, *J. Climate*, *8*, 2058–2079,
4347 1995.
- 4348 Banks, P. M., and G. Kockarts, *Aeronomy, Part B*. Academic Press, San Diego, Calif., 1973,
4349 355 pp.

- 4350 Barker, H., A parameterization for computing grid-averaged solar fluxes for inhomogenous ma-
4351 rine boundary layer clouds. part I: Methodology and homogenous biases, *J. Atmos. Sci.*, *53*,
4352 2289–2303, 1996.
- 4353 Barker, H., B. A. Weilicki, and L. Parker, A parameterization for computing grid-averaged solar
4354 fluxes for inhomogenous marine boundary layer clouds. part II: Validation using satellite data,
4355 *J. Atmos. Sci.*, *53*, 2304–2316, 1996.
- 4356 Barth, C. A., K. D. Mankoff, S. M. Bailey, and S. Solomon, Global observations of nitric oxide
4357 in the thermosphere, *J. Geophys. Res.*, *108*, doi:10.1029/2002JA009458, 2003.
- 4358 Barth, M. C., P. J. Rasch, J. T. Kiehl, C. M. Benkovitz, and S. E. Schwartz, Sulfur chemistry
4359 in the National Center for Atmospheric Research Community Climate Model: Description,
4360 evaluation, features and sensitivity to aqueous chemistry, *J. Geophys. Res.*, *105*, 1387–1415,
4361 2000.
- 4362 Bates, J. R., F. H. M. Semazzi, R. W. Higgins, and S. R. Barros, Integration of the shallow
4363 water equations on the sphere using a vector semi-Lagrangian scheme with a multigrid solver,
4364 *Mon. Wea. Rev.*, *118*, 1615–1627, 1990.
- 4365 Bath, L., J. Rosinski, and J. Olson, User’s Guide to NCAR CCM2, Technical Report NCAR/TN-
4366 379+IA, National Center for Atmospheric Research, Boulder, CO, 156 pp., 1992.
- 4367 Bath, L. M., M. A. Dias, D. L. Williamson, G. S. Williamson, and R. J. Wolski, User’s Guide
4368 to NCAR CCM1, Technical Report NCAR/TN-286+IA, National Center for Atmospheric
4369 Research, Boulder, CO, 173 pp., 1987.
- 4370 Beheng, K. D., A parameterization of warm cloud microphysical conversion processes, *Atmos.*
4371 *Res.*, *33*, 193–206, 1994.
- 4372 Beres, J. H., R. R. Garcia, B. A. Boville, and F. Sassi, Implementation of a gravity wave source
4373 spectrum parameterization dependent on the properties of convection in the whole atmosphere
4374 community climate model (waccm), *J. Geophys. Res.*, *110*, doi:10.1029/2004JD005504, 2005.
- 4375 Berger, A. L., Long-term variations of daily insolation and quaternary climatic changes, *J. At-*
4376 *mos. Sci.*, *35*, 2362–2367, 1978.
- 4377 Biermann, U. M., B. P. Luo, and T. Peter, Absorption spectra and optical constants of binary
4378 and ternary solutions of h₂so₄, hno₃, and h₂o in the mid infrared at atmospheric temperatures,
4379 *The Journal of Physical Chemistry A*, *104* (4), 783–793, 01, 2000.
- 4380 Bigg, E. K., The supercooling of water, *Proc. Phys. Soc. B*, *66*, 688–694, 1953.
- 4381 Binkowski, F. S., and U. Shankar, The regional particulate matter model .1. model description
4382 and preliminary results, *Journal of Geophysical Research-Atmospheres*, *100*, 26191–26209,
4383 1995.
- 4384 Blackadar, A. K., The vertical distribution of wind and turbulent exchange in a neutral atmo-
4385 sphere, *J. Geophys. Res.*, *67*, 3095–3102, 1962.

- 4386 Bloomfield, P., Inferred lifetimes, in *NASA Report on Concentrations, Lifetimes and Trends of*
4387 *CFCs, Halons and Related Species*, edited by J. Kaye, S. Penkett,, and F. Osmond, NASA,
4388 Washington, D.C., 1994.
- 4389 Bonan, G. B., A land surface model (LSM version 1.0) for ecological, hydrological, and at-
4390 mospheric studies: Technical description and user's guide, Technical Report NCAR/TN-
4391 417+STR, National Center for Atmospheric Research, Boulder, CO, 150 pp., 1996.
- 4392 Bonan, G. B., K. W. Oleson, M. Vertenstein, S. Levis, X. Zeng, Y. Dai, R. E. Dickinson, ,
4393 and Z.-L. Yang, The land surface climatology of the Community Land Model coupled to the
4394 NCAR Community Climate Model, *J. Climate*, *15*, 3123–3149, 2002.
- 4395 Bond, T. C., and R. W. Bergstrom, Light absorption by carbonaceous particles: An investigative
4396 review, *Aerosol. Sci. Technol.*, *40*, 27–67, 2006.
- 4397 Bond, T. C., E. Bhardwaj, R. Dong, R. Jogani, S. K. Jung, C. Roden, D. G. Streets, and
4398 N. M. Trautmann, Historical emissions of black and organic carbon aerosol from energy-
4399 related combustion, 1850-2000, *Global Biogeochemical Cycles*, *21* (**2**), –, 2007, 174KO Times
4400 Cited:24 Cited References Count:98.
- 4401 Bourke, W., B. McAvaney, K. Puri, and R. Thurling, Global modeling of atmospheric flow by
4402 spectral methods, in *Methods in Computational Physics*, Vol. 17, 267–324, Academic Press,
4403 New York, 1977.
- 4404 Boville, B. A., and C. S. Bretherton, Heating and dissipation in the NCAR community atmo-
4405 sphere model, *J. Climate*, *16*, 3877–3887, 2003a.
- 4406 Boville, B. A., and C. S. Bretherton, Heating and kinetic energy dissipation in the near com-
4407 munity atmosphere model, *J. Climate*, *16*, 3877–3887, 2003b.
- 4408 Boville, B. A., J. T. Kiehl, P. J. Rasch, and F. O. Bryan, Improvements to the near csm-1 for
4409 transient climate simulations, *J. Climate*, *14*, 164–179, 2001.
- 4410 Brasseur, G. P., D. A. Hauglustaine, S. Walters, P. J. Rasch, J.-F. Muller, C. Granier, and X.-X.
4411 Tie, Mozart: A global chemical transport model for ozone and related chemical tracers, part
4412 1: Model description, *J. Geophys. Res.*, *103*, 28,265–28,289, 1998.
- 4413 Brasseur, G. P., J. J. Orlando, and G. S. Tyndall, *Atmospheric Chemistry and Global Change*.
4414 Oxford University Press, 1999.
- 4415 Bretherton, C. S., J. R. McCaa, and H. Grenier, A new parameterization for shallow cumulus
4416 convection and its application to marine subtropical cloud-topped boundary layer. part i:
4417 Description and 1d results, *Mon. Wea. Rev.*, *132*, 864–882, 2004.
- 4418 Bretherton, C. S., and S. Park, A new moist turbulence parameterization in the community
4419 atmosphere model, *J. Climate*, *22*, 3422–3448, 2009a.
- 4420 Bretherton, C. S., and S. Park, A new moist turbulence parameterization in the Community
4421 Atmosphere Model, *J. Clim.*, *22*, 3422–3448, 2009b.

- 4422 Briegleb, B. P., Delta-Eddington approximation for solar radiation in the NCAR Community
4423 Climate Model, *J. Geophys. Res.*, *97*, 7603–7612, 1992.
- 4424 Bryan, F. O., B. G. Kauffman, W. G. Large, and P. R. Gent, The NCAR CSM Flux Coupler,
4425 Technical Report NCAR/TN-424+STR, National Center for Atmospheric Research, Boulder,
4426 Colorado, 58 pp., 1996.
- 4427 Bryant, F. D., and P. Latimer, Optical efficiencies of large particles of arbitrary shape and
4428 orientation, *J. Colloid Interface Sci.*, *30*, 291–304, 1969.
- 4429 Cariolle, D., A. Lasserre-Bigorry, J.-F. Royer, and J.-F. Geleyn, A general circulation model
4430 simulation of the springtime antarctic ozone decrease and its impact on mid-latitudes., *J.*
4431 *Geophys. Res.*, *95*, 1883–1898, 1990.
- 4432 Chabrillat, S., and G. Kockarts, Simple parameterization of the absorption of the solar lyman-
4433 alpha line, *Geophys. Res. Lett.*, *24*, 2659–2662, 1997.
- 4434 Chervin, R. M., Interannual variability and seasonal climate predictability, *J. Atmos. Sci.*, *43*,
4435 233–251, 1986.
- 4436 Clough, S. A., M. W. Shephard, E. H. Mlawer, J. S. Delamere, M. J. Iacono, K. Cady-Pereira,
4437 S. Boukabara, and P. D. Brown, Atmospheric radiative transfer modeling: a summary of the
4438 aer codes, *J. Quant. Spectrosc. Radiat. Transfer*, *91*, 233–244, 2005.
- 4439 Clough, S., and M. Iacono, Line-by-line calculation of atmospheric fluxes and cooling rates 2.
4440 application to carbon dioxide, ozone, methane, nitrous oxide and the halocarbons., *J. Geophys.*
4441 *Res.*, *100*, 16519–16535, 1995.
- 4442 Colella, P., and P. R. Woodward, The piecewise parabolic method (ppm) for gas-dynamical
4443 simulations, *J. Comp. Phys.*, *54*, 174–201, 1984.
- 4444 Collins, W. D., A global signature of enhanced shortwave absorption by clouds, *J. Geophys.*
4445 *Res.*, *103(D24)*, 31,669–31,680, 1998.
- 4446 Collins, W. D., P. J. Rasch, B. A. Boville, J. J. Hack, J. R. McCaa, D. L. Williamson, J. T.
4447 Kiehl, B. P. Briegleb, C. Bitz, S. J. Lin, M. Zhang, and Y. Dai, Description of the near
4448 community atmosphere model (cam 3.0), Technical report, National Center for Atmospheric
4449 Research, 2004a.
- 4450 Collins, W. D., P. J. Rasch, B. A. Boville, J. J. Hack, J. R. McCaa, D. L. Williamson, J. T.
4451 Kiehl, B. P. Briegleb, C. Bitz, S.-J. Lin, M. Zhang, and Y. Dai, *Description of the NCAR*
4452 *Community Atmosphere Model (CAM3)*. Nat. Cent. for Atmos. Res., Boulder, Colo., 2004b.
- 4453 Collins, W., J. Hackney, and D. Edwards, A new parameterization for infrared emission and
4454 absorption of water vapor in the national center for atmospheric research community atmo-
4455 spheric model, *J. Geophys. Res.*, *107*, doi: 10.1029/2001JD001365, 2002.

- 4456 Considine, D. B., A. R. Douglass, D. E. Kinnison, P. S. Connell, and D. A. Rotman, A polar
4457 stratospheric cloud parameterization for the three dimensional model of the global modeling
4458 initiative and its response to stratospheric aircraft emissions, *J. Geophys. Res.*, *105*, 3955–
4459 3975, 2000.
- 4460 Considine, D. B., P. S. Connell, D. Bergmann, D. A. Rotman, and S. Strahan, Sensitivity of
4461 Global Modeling Initiative CTM predictions of Antarctic ozone recovery to GCM and DAS
4462 generated meteorological fields, *J. Geophys. Res.*, *109*, doi:10.1029/20003JD004487, 2004.
- 4463 Cooke, W. F., and J. J. N. Wilson, A global black carbon aerosol model, *J. Geophys. Res.*, *101*,
4464 19395–19409, 1996.
- 4465 Côté, J., and A. Staniforth, A two-time-level semi-Lagrangian semi-implicit scheme for spectral
4466 models, *Mon. Wea. Rev.*, *116*, 2003–2012, 1988.
- 4467 Cotton, W. R., G. J. Tripoli, R. M. Rauber, and E. A. Mulvihill, Numerical simulation of the
4468 effects of varying ice crystal nucleation rates and aggregation processes on orographic snowfall,
4469 *J. Appl. Meteor.*, *25*, 1658–1680, 1986.
- 4470 Dai, Y., X. Zeng, R. E. Dickinson, and coauthors, The Common Land Model: Documentation
4471 and User’s Guide, <http://climate.eas.gatech.edu/dai/clmdoc.pdf>, 2001.
- 4472 Daley, R., C. Girard, J. Henderson, and I. Simmonds, Short-term forecasting with a multi-level
4473 spectral primitive equation model. Part I—model formulation, *Atmosphere*, *14*, 98–116, 1976.
- 4474 DeCaria, A. J., K. E. Pickering, G. L. Stenchikov, and L. E. Ott, Lightning-generated nox
4475 and its impact on tropospheric ozone production: A three-dimensional modeling study of a
4476 stratosphere-troposphere experiment: Radiation, aerosols and ozone (sterao-a) thunderstorm,
4477 *J. Geophys. Res.*, *110*, D14303, 2006.
- 4478 Dennis, J., A. Fournier, W. F. Spitz, A. St.-Cyr, M. A. Taylor, S. J. Thomas, and H. Tufo,
4479 High resolution mesh convergence properties and parallel efficiency of a spectral element
4480 atmospheric dynamical core, *Int. J. High Perf. Comput. Appl.*, *19*, 225–235, 2005.
- 4481 Dentener, F., S. Kinne, T. Bond, O. Boucher, J. Cofala, S. Generoso, P. Ginoux, S. Gong,
4482 J. J. Hoelzemann, A. Ito, L. Marelli, J. E. Penner, J. P. Putaud, C. Textor, M. Schulz,
4483 G. R. van derWerf, and J. Wilson, Emissions of primary aerosol and precursor gases in the
4484 years 2000 and 1750 prescribed data-sets for aerocom, *Atmospheric Chemistry and Physics*,
4485 *6*, 4321–4344, 2006a, 087YG Times Cited:81 Cited References Count:52.
- 4486 Dentener, F., D. Stevenson, K. Ellingsen et al., Global atmospheric environment for the next
4487 generation, *Environmental Science and Technology*, *40*, 3586–3594, 2006b.
- 4488 Deville, M. O., P. F. Fischer, and E. H. Mund, *High Order Methods for Incompressible Fluid*
4489 *Flow*. Cambridge University Press, 1 edition, 8, 2002.
- 4490 Dickinson, R. E., A. Henderson-Sellers, P. J. Kennedy, and M. F. Wilson, Biosphere-atmosphere
4491 transfer scheme (BATS) for the NCAR Community Climate Model, Technical Report
4492 NCAR/TN-275+STR, National Center for Atmospheric Research, Boulder, Colorado, 69 pp.,
4493 1987.

- 4494 Dütsch, H. U., Vertical ozone distribution on a global scale, *Pure Appl. Geophys.*, *116*, 511–529,
4495 1986.
- 4496 Dye, J. E., D. Baumgardner, B. W. Gandrun, S. R. Kawa, K. K. Kelly, M. Loewenstein, G. V.
4497 Ferry, K. R. Chan, and B. L. Gary, Particle size distributions in arctic polar stratospheric
4498 clouds, growth and freezing of sulfuring acid droplets, and implications for cloud formation,
4499 *J. Geophys. Res.*, *97*, 8015–8034, 1992.
- 4500 Easter, R. C., S. J. Ghan, Y. Zhang, R. D. Saylor, E. G. Chapman, N. S. Laulainen, H. Abdul-
4501 Razzak, L. R. Leung, X. D. Bian, and R. A. Zaveri, Mirage: Model description and evaluation
4502 of aerosols and trace gases, *Journal of Geophysical Research-Atmospheres*, *109* (D20), –, 2004,
4503 867ZR Times Cited:37 Cited References Count:280.
- 4504 Eaton, B. E., User’s Guide to the Community Atmosphere Model AM4.0, Tech-
4505 nical report, National Center for Atmospheric Research, Boulder, Colorado,
4506 http://www.cesm.ucar.edu/models/ccsm4.0/cam/docs/users_guide/book1.html, 2010.
- 4507 Emmons, e. a., L. K., Description and evaluation of the model for ozone and related chemical
4508 tracers, version 4 (mozart-4), *Geosci. Model Dev*, *3*, 43–67, 2010.
- 4509 Ferrier, B., A double-moment multiple-phase four-class bulk ice scheme. part I: Description, *J.*
4510 *Atmos. Sci.*, *51*, 249–280, 1994.
- 4511 Fiedler, F., and H. A. Panofsky, The geostrophic drag coefficient and the “effective roughness
4512 length, *Quart. J. Roy. Meteor. Soc.*, *98*, 213–220, 1972.
- 4513 Field, P. R., O. Möhler, P. Connolly, M. Krmer, R. Cotton, A. J. Heymsfield, H. Saathoff,
4514 and M. Schnaiter, Some ice nucleation characteristics of Asian and Saharan desert dust,
4515 *Atmospheric Chemistry and Physics*, *6* (10), 2991–3006, 2006.
- 4516 Field, P. R., A. J. Heymsfield, and A. Bansemer, Shattering and particle inter-arrival times
4517 measured by optical array probes in ice clouds, *J. Atmos. Oceanic Technol.*, *23*, 1357–1371,
4518 2007.
- 4519 Fomichev, V. I., J. P. Blanchet, and D. S. Turner, Matrix parameterization of the 15 μm CO_2
4520 band cooling in the middle and upper atmosphere for variable CO_2 concentration, *J. Geophys.*
4521 *Res.*, *103*, 11505–11528, 1998.
- 4522 Fomichev, V. I., V. P. Ogibalov, and S. R. Beagley, Solar heating by the near-IR CO_2 bands in
4523 the mesosphere, *Geophys. Res. Lett.*, *31*, L21102, 2004.
- 4524 Fournier, A., M. A. Taylor, and J. Tribbia, The spectral element atmosphere model (SEAM):
4525 High-resolution parallel computation and localized resolution of regional dynamics, *Mon. Wea.*
4526 *Rev.*, *132*, 726–748, 2004.
- 4527 Friedl, R., editor, *Atmospheric effects of subsonic aircraft: Interim assessment report of the*
4528 *advanced subsonic technology program*. 1997.

- 4529 Fritts, D. C., and T. J. Dunkerton, Fluxes of heat and constituents due to convectively unstable
4530 gravity waves, *jas*, *42*, 549–556, 1985.
- 4531 Fu, Q., P. Yang, and W. B. Sun, An accurate parameterization of the infrared radiative prop-
4532 erties of cirrus clouds for climate models, *J. Climate*, *11*, 2223–2237, 1998.
- 4533 Fuch, N. A., *The Mechanics of Aerosols*. Pergamon, Oxford, 1964.
- 4534 Galperin, B., L. H. Kanta, S. Hassid, and A. Rosati, A quasi-equilibrium turbulent energy model
4535 for geophysical flows, *J. Atmos. Sci.*, *45*, 55–62, 1988.
- 4536 Garcia, R. R., Parameterization of planetary wave breaking in the middle atmosphere, *jas*, 2001.
- 4537 Garcia, R. R., D. R. Marsh, D. E. Kinnison, B. A. Boville, and F. Sassi, Simula-
4538 tion of secular trends in the middle atmosphere, 1950–2003, *J. Geophys. Res.*, *112*,
4539 doi:10.1029/2006JD007485, 2007.
- 4540 Garcia, R. R., and S. Solomon, The effect of breaking gravity waves on the dynamical and
4541 chemical composition of the mesosphere and lower thermosphere, *J. Geophys. Res.*, *90*, 3850–
4542 3868, 1985.
- 4543 Garcia, R. R., and S. Solomon, A new numerical model of the middle atmosphere. part ii: Ozone
4544 and related species, *J. Geophys. Res.*, *99*, 12937–12951, 1994.
- 4545 Gent, P. R., S. Yeager, R. B. Neale, S. Levis, and D. Bailey, Improvements in a half degree
4546 atmopshere/land version of the CCSM., *Climate Dynamics*, *79*, 25–58, 2009.
- 4547 Gettelman, A., H. Morrison, and S. J. Ghan, A new two-moment bulk stratiform cloud micro-
4548 physics scheme in the NCAR Community Atmosphere Model (CAM3), Part II: Single-column
4549 and global results, *J. Clim.*, *21* (15), 3660–3679, 2008.
- 4550 Gettelman, A., A. X. Liu, S. J. Ghan, H. Morrison, S. Park, A. J. Conley, S. A. Klein, J. Boyle,
4551 D. L. Mitchell, and J. L. F. Li, Global simulations of ice nucleation and ice supersaturation
4552 with an improved cloud scheme in the community atmosphere model, *J. Geophys. Res.*, *108*,
4553 ???–???, 2010a.
- 4554 Gettelman, A. et al., Multi-model assessment of the upper troposphere and lower stratosphere:
4555 Tropics and trends, *in press J. Geophys. Res.*, 2010b.
- 4556 Ghan, S. J., and R. C. Easter, Computationally efficient approximations to stratiform cloud
4557 microphysics parameterization, *Mon. Weather Rev.*, *120* (1572–1582), 1992.
- 4558 Ghan, S. J., and R. C. Easter, Impact of cloud-borne aerosol representation on aerosol direct
4559 and indirect effects, *Atmospheric Chemistry and Physics*, *6*, 4163–4174, 2006, 086FO Times
4560 Cited:5 Cited References Count:47.
- 4561 Ghan, S. J., L. R. Leung, R. C. EasterEaster, and K. AbdulRazzak, Prediction of cloud droplet
4562 number in a general circulation model, *J. Geophys Res-Atmos*, *102*, 21777–21794, 1997.

- 4563 Ghan, S. J., and R. A. Zaveri, Parameterization of optical properties for hydrated internally-
4564 mixed aerosol, *J. Geophys. Res.*, *112*, DOI 10.1029/2006JD007927, 2007.
- 4565 Giorgi, F., and W. Chameides, The rainout parameterization in a photochemical model, *J.*
4566 *Geophys. Res.*, *90*, 7872–7880, 1985.
- 4567 Giraldo, F. X., Trajectory calculations for spherical geodesic grids in cartesian space, *Mon. Wea.*
4568 *Rev.*, *127*, 1651–1662, 1999.
- 4569 Gregory, D., R. Kershaw, and P. M. Inness, Parameterization of momentum transport by con-
4570 vection. ii: Tests in single column and general circulation models, *Q. J. R. Meteorol. Soc.*,
4571 *123*, 1153–1184, 1997*a*.
- 4572 Gregory, D., R. Kershaw, and P. M. Inness, Parametrization of momentum transport by con-
4573 vection. II: Tests in single-column and general circulation models, *Q. J. R. Meteorol. Soc.*,
4574 *123*, 1153–1183, 1997*b*.
- 4575 Grenier, H., and C. S. Bretherton, A moist pbl parameterization for large-scale models and
4576 its application to subtropical cloud-topped marine boundary layer, *Mon. Wea. Rev.*, *129*,
4577 357–377, 2001.
- 4578 Hack, J. J., Parameterization of moist convection in the National Center for Atmospheric Re-
4579 search Community Climate Model (CCM2), *J. Geophys. Res.*, *99*, 5551–5568, 1994*a*.
- 4580 Hack, J. J., Parameterization of moist convection in the national center for atmospheric research
4581 community climate model (ccm2), *J. Geophys. Res.*, *99*, 5551–5568, 1994*b*.
- 4582 Hack, J. J., L. M. Bath, G. W. Williamson, and B. A. Boville, Modifications and enhancements
4583 to the NCAR Community Climate Model (CCM1), Technical Report NCAR/TN-336+STR,
4584 National Center for Atmospheric Research, Boulder, Colorado, 97 pp., 1989.
- 4585 Hack, J. J., B. A. Boville, B. P. Briegleb, J. T. Kiehl, P. J. Rasch, and D. L. Williamson,
4586 Description of the NCAR Community Climate Model (CCM2), Technical Report NCAR/TN-
4587 382+STR, National Center for Atmospheric Research, 120 pp., 1993.
- 4588 Hedin, A. E., Extension of the MSIS thermosphere model into the middle and lower atmosphere,
4589 *J. Geophys. Res.*, *96*, 1159, 1991.
- 4590 Hedin, A., MSIS-86 thermospheric model, *J. Geophys. Res.*, *92*, 4649, 1987.
- 4591 Heinbockel, J. H., *Introduction to Tensor Calculus and Continuum Mechanics*. Trafford Pub-
4592 lishing, Victoria, B.C., 12, 2001.
- 4593 Held, I. M., and M. J. Suarez, A proposal for the intercomparison of the dynamical cores of
4594 atmospheric general circulation models, *Bull. Am. Meteorol. Soc.*, *75*, 1825–1830, 1994.
- 4595 Hildebrand, F. B., *Introduction to Numerical Analysis*. McGraw-Hill, New York, New York,
4596 1956, 511 pp.

- 4597 Holstlag, A. M., and B. A. Boville, Local versus nonlocal boundary layer diffusion in a global
4598 climate model, *J. Climate*, 6, 1825–1842, 1993.
- 4599 Holton, J. R., The role of gravity wave induced drag and diffusion in the momentum budget of
4600 the mesosphere, *J. Atmos. Sci.*, 39, 791–799, 1982.
- 4601 Holstlag, A. A. M., and B. A. Boville, Local versus nonlocal boundary-layer diffusion in a global
4602 climate model, *J. Climate*, 6, 1825–1842, 1993a.
- 4603 Holstlag, A. A. M., and B. A. Boville, Local versus nonlocal boundary layer diffusion in a global
4604 model, *J. Climate*, 6, 1825–1842, 1993b.
- 4605 Holstlag, A. A. M., E. I. F. deBruijn, and H.-L. Pan, A high resolution air mass transformation
4606 model for short-range weather forecasting, *Mon. Wea. Rev.*, 118, 1561–1575, 1990.
- 4607 Hoose, C., and J. E. Kristjansson, A classical-theory-based parameterization of heterogeneous
4608 ice nucleation by mineral dust, soot and biological particles in a global climate model, *in*
4609 *press*, *J. Atmos. Sci.*, 2010.
- 4610 Horowitz, e. a., L., A global simulation of tropospheric ozone and related tracers: Description
4611 and evaluation of moztart, version 2, *Journal of Geophysical Research-Atmospheres*, 108, 4784,,
4612 2003.
- 4613 Horowitz, L., S. Walters, D. Mauzerall, L. Emmons, P. Rasch, C. Granier, X. Tie, J.-F. Lamar-
4614 que, M. Schultz, G. Tyndall, J. Orlando, and G. Brasseur, A global simulation of tropospheric
4615 ozone and related tracers: Description and evaluation of moztart, version 2, *J. Geophys. Res.*,
4616 108, 4784, 2003.
- 4617 Hortal, M. 1999. Aspects of the numerics of the ECMWF model. in *Proceedings of ECMWF*
4618 *Seminar: Recent developments in numerical methods for atmospheric modelling, 7–11 Septem-*
4619 *ber 1998*, 127–143, .
- 4620 Hoskins, B. J., The mathematical theory of frontogenesis, *Ann. Rev. Fluid Mech.*, 14, 131–151,
4621 1982.
- 4622 Hsu, Y.-J. G., and A. Arakawa, Numerical modeling of the atmosphere with an isentropic vertical
4623 coordinate, *Mon. Wea. Rev.*, 118, 1933–1959, 1990.
- 4624 Iacono, M., E. Mlawer, S. Clough, and J.-J. Morcrette, Impact of an improved longwave radiation
4625 model, rrtm, on the energy budget and thermodynamic properties of the near community
4626 climate model, ccm3, *J. Geophys. Res.*, 105, 14873–14890, 2000.
- 4627 Iacono, M., J. Delamere, E. Mlawer, and S. Clough, Evaluation of upper tropospheric water
4628 vapor in the near community climate model (ccm3) using modeled and observed hirs radiances,
4629 *J. Geophys. Res.*, 108(D2), 4037, 2003.
- 4630 Iacono, M., J. Delamere, E. Mlawer, M. Shephard, S. Clough, and W. Collins, Radiative forcing
4631 by long-lived greenhouse gases: Calculations with the aer radiative transfer models, *J. Geo-*
4632 *phys. Res.*, 2008.

- 4633 Ikawa, M., and K. Saito, description of the nonhydrostatic model developed at the forecast
4634 research department of the mri, Technical Report 28, Meteorological Institute MRI, 1990.
- 4635 Jablonowski, C., and D. L. Williamson, A baroclinic instability test case for atmospheric model
4636 dynamical cores, *Q. J. R. Meteorol. Soc.*, *132*, 2943–2975, 2006.
- 4637 Junker, C., and C. Liouise, A global emission inventory of carbonaceous aerosol from historic
4638 records of fossil fuel and biofuel consumption for the period 1860-1997, *Atmospheric Chemistry
4639 and Physics*, *8* (5), 1195–1207, 2008, 273CS Times Cited:8 Cited References Count:52.
- 4640 Kader, B. A., and A. M. Yaglom, Mean fields and fluctuation moments in unstably stratified
4641 turbulent boundary layers, *J. Fluid Mech.*, *212*, 637–662, 1990.
- 4642 Kain, J. S., and J. M. Fritsch, A one-dimensional entraining/detraining plume model and its
4643 application in convective parameterization, *J. Atmos. Sci.*, *47*, 2784–2802, 1990.
- 4644 Kärcher, B., O. Möhler, P. J. DeMott, S. Pechtl, and F. Yu, Insights into the role of soot aerosols
4645 in cirrus cloud formation, *Atmos. Chem. Phys.*, *7*, 4203–4227, 2007.
- 4646 Karniadakis, G. E., and S. J. Sherwin, *Spectral/hp Element Methods for Computational Fluid
4647 Dynamics (Numerical Mathematics and Scientific Computation)*. Oxford University Press,
4648 USA, 2 edition, 8, 2005.
- 4649 Kasahara, A., Various vertical coordinate systems used for numerical weather prediction, *Mon.
4650 Wea. Rev.*, *102*, 509–522, 1974.
- 4651 Kasten, F., Falling speed of aerosol particles, *J. Appl. Meteorol.*, *7*, 944–947, 1968.
- 4652 Kerminen, V. M., and M. Kulmala, Analytical formulae connecting the "real" and the "apparent"
4653 nucleation rate and the nuclei number concentration for atmospheric nucleation events,
4654 *Journal of Aerosol Science*, *33* (4), 609–622, 2002, 535VC Times Cited:67 Cited References
4655 Count:26.
- 4656 Kershaw, R., and D. Gregory, Parametrization of momentum transport by convection. I: Theory
4657 and cloud modelling results, *Q. J. R. Meteorol. Soc.*, *123*, 1133–1151, 1997.
- 4658 Khairoutdinov, M. F., and Y. Kogan, A new cloud physics parameterization in a large-eddy
4659 simulation model of marine stratocumulus, *Mon. Weather Rev.*, *128*, 229–243, 2000.
- 4660 Kiehl, J. T., and B. P. Briegleb, A new parameterization of the absorbance due to the 15 micron
4661 band system of carbon dioxide, *J. Geophys. Res.*, , 9013–9019, 1991.
- 4662 Kiehl, J. T., J. J. Hack, and B. P. Briegleb, The simulated Earth radiation budget of the National
4663 Center for Atmospheric Research Community Climate Model CCM2 and comparisons with
4664 the Earth Radiation Budget Experiment (ERBE), *J. Geophys. Res.*, *99*, 20815–20827, 1994.
- 4665 Kiehl, J. T., J. Hack, G. Bonan, B. Boville, B. Briegleb, D. Williamson, and P. Rasch, De-
4666 scription of the NCAR Community Climate Model (CCM3), Technical Report NCAR/TN-
4667 420+STR, National Center for Atmospheric Research, Boulder, Colorado, 152 pp., 1996.

- 4668 Kiehl, J. T., J. J. Hack, G. B. Bonan, B. B. Boville, D. L. Williamson, and P. J. Rasch, The
4669 National Center for Atmospheric Research Community Climate Model: CCM3, *J. Climate*,
4670 *11*, 1131–1149, 1998.
- 4671 Kinnison, D. E., G. P. Brasseur, S. Walters, R. R. Garcia, F. Sassi, B. A. Boville, D. Marsh,
4672 L. Harvey, C. Randall, W. Randel, J. F. Lamarque, L. K. Emmons, P. Hess, J. Orlando,
4673 J. Tyndall, and L. Pan, Sensitivity of chemical tracers to meteorological parameters in the
4674 mozart-3 chemical transport model, *J. Geophys. Res.*, *in press*, 2006.
- 4675 Kockarts, G., Nitric oxide cooling in the terrestrial thermosphere, *Geophys. Res. Lett.*, *7*, 137–
4676 140, 1980.
- 4677 Koehler, K. A., S. M. Kreidenweis, P. J. DeMott, M. D. Petters, A. J. Prenni, and C. M.
4678 Carrico, Hygroscopicity and cloud droplet activation of mineral dust aerosol, *Geophysical*
4679 *Research Letters*, *36*, –, 2009a, 435FB Times Cited:4 Cited References Count:25.
- 4680 Koehler, K. A., S. M. Kreidenweis, P. J. DeMott, M. D. Petters, A. J. Prenni, and C. M. Carrico,
4681 Hygroscopicity and cloud droplet activation of mineral dust aerosol., *Geophys. Res. Lett.*, *36*,
4682 2009b.
- 4683 Koepke, M. H. P., and I. Schult, Optical properties of aerosols and clouds: The software package
4684 opac, *Bull. Am. Meteorol. Soc.*, *79*, 831–844, 1998.
- 4685 Koppers, G. A. A., and D. P. Murtagh, Model studies of the influence of O₂ photodissociation
4686 parameterizations in the schumann-runge bands on ozone related photolysis in the upper
4687 atmosphere, *Ann. Geophys.*, *14*, 68–79, 1996.
- 4688 Kroll, J. H., N. L. Ng, S. M. Murphy, R. C. Flagan, and J. H. Seinfeld, Secondary organic aerosol
4689 formation from isoprene photooxidation, *Environmental Science and Technology*, *40* (**6**),
4690 1869–1877, 2006, 024RN Times Cited:121 Cited References Count:62.
- 4691 Lamarque, J. F., T. C. Bond, V. Eyring, C. Granier, A. Heil, Z. Klimont, D. Lee, C. Liousse,
4692 A. Mieville, B. Owen, M. G. Schultz, D. Shindell, S. J. Smith, E. Stehfest, J. vanAardenne,
4693 O. R. Cooper, M. Kainuma, N. Mahowald, J. R. McConnell, V. Naik, K. Riahi, and D. P.
4694 vanVuuren, Historical (18502000) gridded anthropogenic and biomass burning emissions of
4695 reactive gases and aerosols: methodology and application, *Atmospheric Chemistry and Physics*
4696 *Discussion*, *10*, 49635019, 2010a.
- 4697 Lamarque, J., T. C. Bond, V. Eyring, C. Granier, A. Heil, Z. Klimont, D. Lee, C. Liousse,
4698 A. Mieville, B. Owen, M. G. Schultz, D. Shindell, S. J. Smith, E. Stehfest, J. van Aardenne,
4699 O. R. Cooper, M. Kainuma, N. Mahowald, J. R. McConnell, V. Naik, K. Riahi, and D. P.
4700 van Vuuren, Historical (1850-2000) gridded anthropogenic and biomass burning emissions of
4701 reactive gases and aerosols: methodology and application, *Atmospheric Chemistry & Physics*
4702 *Discussions*, *10*, 4963–5019, Feb., 2010b.
- 4703 Large, W. G., J. C. McWilliams, and S. C. Doney, Oceanic vertical mixing: A review and a
4704 model with a nonlocal boundary layer parameterization, *Rev. Geophys.*, *32*, 363–403, 1994.

- 4705 Large, W. G., and S. Pond, Sensible and latent heat flux measurements over the ocean, *J. Phys.*
4706 *Oceanogr.*, *12*, 464–482, 1982.
- 4707 Lauritzen, P., C. Jablonowski, M. Taylor, and R. Nair, Rotated versions of the jablonowski
4708 steady-state and baroclinic wave test cases: A dynamical core intercomparison, *Journal of*
4709 *Advances in Modeling Earth Systems*, *In Press*, 2010.
- 4710 Lauritzen, P. H., A stability analysis of finite-volume advection schemes permitting long time
4711 steps, *Mon. Wea. Rev.*, *135*, 2658–2673, 2007.
- 4712 Lauritzen, P. H., P. A. Ullrich, and R. D. Nair, Atmospheric transport schemes: Desirable
4713 properties and a semi-lagrangian view on finite-volume discretizations, in: P.H. Lauritzen,
4714 R.D. nair, C. Jablonowski, M. Taylor (Eds.), Numerical techniques for global atmospheric
4715 models, *Lecture Notes in Computational Science and Engineering*, Springer, 2010, to appear.
- 4716 Lawson, R. P., B. Barker, B. Pilson, and Q. Mo, In situ observations of the microphysical
4717 properties of wave, cirrus and anvil clouds. Part 2: Cirrus cloud, *J. Atmos. Sci.*, *63*, 3186–
4718 3203, 2006.
- 4719 Le Texier, H., S. Solomon, and R. R. Garcia, Role of molecular hydrogen and methane oxidation
4720 in the water vapor budget of the stratosphere, *Q. J. R. Meteorol. Soc.*, *114*, 281–295, 1988.
- 4721 Lean, J., Evolution of the sun’s spectral irradiance since the maunder minimum, *Geophys. Res.*
4722 *Lett.*, *27* (**16**), 2425–2428, 2000.
- 4723 Lim, Y. B., and P. J. Ziemann, Products and mechanism of secondary organic aerosol formation
4724 from reactions of n-alkanes with oh radicals in the presence of nox, *Environmental Science*
4725 *and Technology*, *39* (**23**), 9229–9236, 2005, 989ZK Times Cited:53 Cited References Count:48.
- 4726 Lin, S.-J., W. C. Chao, Y. C. Sud, and G. K. Walker, A class of the van leer-type transport
4727 schemes and its applications to the moisture transport in a general circulation model, *Mon.*
4728 *Wea. Rev.*, *122*, 1575–1593, 1994.
- 4729 Lin, S.-J., and R. B. Rood, Multidimensional flux form semi-lagrangian transport schemes, *Mon.*
4730 *Wea. Rev.*, *124*, 2046–2070, 1996.
- 4731 Lin, S.-J., and R. B. Rood, An explicit flux-form semi-lagrangian shallow water model on the
4732 sphere, *Q. J. R. Meteorol. Soc.*, *123*, 2531–2533, 1997.
- 4733 Lin, S.-J., A vertically lagrangian finite-volume dynamical core for global models, *Mon. Wea.*
4734 *Rev.*, *132*, 2293–2397, 2004.
- 4735 Lin, Y.-L., R. R. Farley, and H. D. Orville, Bulk parameterization of the snow field in a cloud
4736 model, *J. Clim. Appl. Meteorol.*, *22*, 1065–1092, 1983.
- 4737 Lindzen, R. S., Turbulence and stress due to gravity wave and tidal breakdown, *J. Geophys.*
4738 *Res.*, *86*, 9701–9714, 1981.
- 4739 Liu, X., J. E. Penner, S. J. Ghan, and M. Wang, Inclusion of ice microphysics in the NCAR
4740 Community Atmosphere Model version 3 (CAM3), *J. Clim.*, *20*, 4526–4547, 2007.

- 4741 Liu, X., and S. Ghan, A modal aerosol model implementation in the Community Atmosphere
4742 Model, version 5 (CAM5), *J. Atmos. Sci.*, 2010.
- 4743 Liu, X., and J. E. Penner, Ice nucleation parameterization for global models, *Meteor. Z.*,
4744 *14* (**499-514**), 2005.
- 4745 Liu, X. H., J. E. Penner, and M. Herzog, Global modeling of aerosol dynamics: Model de-
4746 scription, evaluation, and interactions between sulfate and nonsulfate aerosols, *Journal of*
4747 *Geophysical Research-Atmospheres*, *110* (**D18**), –, 2005, 968RL Times Cited:39 Cited Refer-
4748 ences Count:207.
- 4749 Lohmann, U., J. Feichter, C. C. Chuang, and J. Penner, Prediction of the number of cloud
4750 droplets in the echam gcm, *J. Geophys. Res.*, *104* (**D8**), 9169–9198, 1999.
- 4751 Lord, S. J., W. C. Chao, and A. Arakawa, Interaction of a cumulus cloud ensemble with the
4752 large-scale environment. part iv: The discrete model, *J. Atmos. Sci.*, *39*, 104–113, 1982.
- 4753 Machenhauer, B., The spectral method, in *Numerical Methods Used in Atmospheric Models*,
4754 World Meteorological Organization, Geneva, Switzerland, 1979.
- 4755 Machenhauer, B. 1998. MPI workshop on conservative transport schemes. in *Report No. 265*, .
4756 Max-planck-Institute for Meteorology.
- 4757 Machenhauer, B., E. Kaas, and P. H. Lauritzen, Finite volume methods in meteorology, in: R.
4758 Temam, J. Tribbia, P. Ciarlet (Eds.), *Computational methods for the atmosphere and the*
4759 *oceans, Handbook of Numerical Analysis*, *14*, 2009, Elsevier, 2009, pp.3-120.
- 4760 Maday, Y., and A. T. Patera, Spectral element methods for the incompressible Navier Stokes
4761 equations, in *State of the Art Surveys on Computational Mechanics*, edited by A. K. Noor,
4762 and J. T. Oden, 71–143, ASME, New York, 1987.
- 4763 Mahowald, N. M., D. R. Muhs, S. Levis, P. J. Rasch, M. Yoshioka, C. S. Zender, and C. Luo,
4764 Change in atmospheric mineral aerosols in response to climate: Last glacial period, prein-
4765 dustrial, modern, and doubled carbon dioxide climates, *Journal of Geophysical Research-*
4766 *Atmospheres*, *111* (**D10**), –, 2006a, 050EP Times Cited:68 Cited References Count:123.
- 4767 Mahowald, N. M., M. Yoshioka, W. D. Collins, A. J. Conley, D. W. Fillmore, and D. B. Coleman,
4768 Climate response and radiative forcing from mineral aerosols during the last glacial maximum,
4769 pre-industrial, current and doubled-carbon dioxide climates, *Geophysical Research Letters*,
4770 *33* (**20**), –, 2006b, 100WD Times Cited:16 Cited References Count:21.
- 4771 Manabe, S., Climate and the ocean circulation: 1. The atmospheric circulation and the hydrology
4772 of the earth’s surface, *Mon. Wea. Rev.*, *97*, 739–774, 1969.
- 4773 Marsh, D., S. Solomon, and A. Reynolds, Empirical model of nitric oxide in the lower thermo-
4774 sphere, *J. Geophys. Res.*, *109*, doi:10.1029/2003JA010199, 2004.

- 4775 Martensson, E. M., E. D. Nilsson, G. deLeeuw, L. H. Cohen, and H. C. Hansson, Laboratory
4776 simulations and parameterization of the primary marine aerosol production, *Journal of Geo-*
4777 *physical Research-Atmospheres*, 108 (D9), –, 2003, 682QU Times Cited:51 Cited References
4778 Count:32.
- 4779 Marti, J., and K. Mauersberger, A survey and new measurements of ice vapor pressure at
4780 temperatures between 170 and 250 K, *Geophys. Res. Lett.*, 20, 363–366, 1993.
- 4781 Martin, G. M., D. W. Johnson, and A. Spice, The measurement and parameterization of effective
4782 radius of droplets in warm stratocumulus clouds, *J. Atmos. Sci.*, 51, 1823–1842, 1994.
- 4783 Matthes, K., D. R. Marsh, R. R. Garcia, D. E. Kinnison, F. Sassi, and S. Walters, The role
4784 of the qbo in modulating the influence of the 11-year solar cycle on the atmosphere using
4785 constant forcings, *J. Geophys. Res.*, ??, doi:10.1029/2009JD013020, 2010.
- 4786 McAvaney, B. J., W. Bourke, and K. Puri, A global spectral model for simulation of the general
4787 circulation, *J. Atmos. Sci.*, 35, 1557–1583, 1978.
- 4788 McFarlane, N. A., The effect of orographically excited gravity wave drag on the general circula-
4789 tion of the lower stratosphere and troposphere, *J. Atmos. Sci.*, 44, 1775–1800, 1987.
- 4790 McFarlane, R. P. S. A., and S. A. Klein, Albedo bias and the horizontal variability of clouds in
4791 subtropical marine boundary layers: Observations from ships and satellite, *J. Geophys. Res.*,
4792 104, 6138–6191, 1999.
- 4793 McIntyre, M. E., On dynamics and transport near the polar mesopause in summer, *J. Geophys.*
4794 *Res.*, 94, 14,617–14,628, 1989.
- 4795 McLinden, C., S. Olsen, B. Hannegan, O. Wild, and M. Prather, Stratospheric ozone in 3-d
4796 models: A simple chemistry and the cross-tropopause flux, *J. Geophys. Res.*, 105, 14,653–
4797 14,665, 2000.
- 4798 Merikanto, J., I. Napari, H. Vehkamäki, T. Anttila, and M. Kulmala, New parameterization
4799 of sulfuric acid-ammonia-water ternary nucleation rates at tropospheric conditions, *Journal*
4800 *of Geophysical Research-Atmospheres*, 112 (D15), –, 2007, 202AA Times Cited:16 Cited
4801 References Count:39.
- 4802 Meyers, M. P., P. J. DeMott, and W. R. Cotton, New primary ice-nucleation parameterizations
4803 in an explicit cloud model, *J. Applied Met.*, 31, 708–721, 1992.
- 4804 Minschwaner, K., and D. E. Siskind, A new calculation of nitric oxide photolysis in the strato-
4805 sphere, mesosphere, and lower thermosphere, *J. Geophys. Res.*, 98, 20401–20412, 1993.
- 4806 Mitchell, D. L., Parameterization of the Mie extinction and absorption coefficients for water
4807 clouds, *J. Atmos. Sci.*, 57, 1311–1326, 2000.
- 4808 Mitchell, D. L., Effective diameter in radiation transfer: General definition, applications and
4809 limitations, *J. Atmos. Sci.*, 59, 2330–2346, 2002.

- 4810 Mitchell, D. L., and W. P. Arnott, A model predicting the evolution of ice particle size spectra
4811 and radiative properties of cirrus clouds. part ii: Dependence of absorption and extinction on
4812 ice crystal morphology, *J. Atmos. Sci.*, , 817–832, 1994.
- 4813 Mitchell, D. L., A. Macke, and Y. Liu, Modeling cirrus clouds. Part II: Treatment of radiative
4814 properties, *J. Atmos. Sci.*, *53*, 2697–2988, 1996*a*.
- 4815 Mitchell, D. L., A. Macke, and Y. Liu, Modeling cirrus clouds. part ii: Treatment of radiative
4816 properties, *J. Atmos. Sci.*, *53*, 2967–2988, 1996*b*.
- 4817 Mitchell, D. L., W. P. Arnott, C. Schmitt, A. J. Baran, S. Havemann, and Q. Fu, Contributions of
4818 photon tunneling to extinction in laboratory grown hexagonal columns, *J. Quant. Spectrosc.*
4819 *Radiat. Transfer*, *70*, 761–776, 2001.
- 4820 Mitchell, D. L., A. J. Baran, W. P. Arnott, and C. Schmitt, Testing and comparing the modified
4821 anomalous diffraction approximation, *J. Atmos. Sci.*, *59*, 2330–2346, 2006*a*.
- 4822 Mitchell, D. L., R. P. d’Entremont, and R. P. Lawson, Passive thermal retrievals of ice and
4823 liquid water path, effective size and optical depth and their dependence on particle and size
4824 distribution shape, 12th AMS Conference on Atmospheric Radiation, July, 2006*b*.
- 4825 Mlawer, E., S. Taubman, P. Brown, M. Iacono, and S. Clough, Radiative transfer for inhomoge-
4826 neous atmospheres: Rrtm, a validated correlated-k model for the longwave, *J. Geophys. Res.*,
4827 *102*, 16663–16682, 1997.
- 4828 Mlynczak, M. G., and S. Solomon, A detailed evaluation of the heating efficiency in the middle
4829 atmosphere, *J. Geophys. Res.*, *98*, 10,517–10,541, 1993.
- 4830 Monahan, E. C., D. E. Spiel, and K. L. Davidson, A model of marine aerosol generation via
4831 whitecaps and wave disruption, in *Oceanic Whitecaps*, edited by E. C. Monahan, G. M.
4832 Niocaill, and D. Reidel, Norwell, Mass., 1986.
- 4833 Moncet, J.-L., and S. Clough, Accelerated monochromatic radiative transfer for scattering at-
4834 mospheres: Application of a new model to spectral radiance observations, *J. Geophys. Res.*,
4835 *102* (**21**), 853–866, 1997.
- 4836 Morrison, H., J. A. Curry, and V. I. Khvorostyanov, A new double-moment microphysics pa-
4837 rameterization for application in cloud and climate models. part i: Description, *J. Atmos.*
4838 *Sci.*, *62*, 1665–1677, 2005.
- 4839 Morrison, H., and A. Gettelman, A new two-moment bulk stratiform cloud microphysics scheme
4840 in the NCAR Community Atmosphere Model (CAM3), Part I: Description and numerical
4841 tests, *J. Clim.*, *21* (**15**), 3642–3659, 2008.
- 4842 Morrison, H., and J. O. Pinto, Mesoscale modeling of springtime arctic mixed-phase stratiform
4843 clouds using a new two-moment bulk microphysics scheme, *J. Atmos. Sci.*, *62*, 3683–3704,
4844 2005.

- 4845 Mote, P. W., J. R. Holton, J. M. Russell, and B. A. Boville, A comparison of observed (haloe)
4846 and modeled (ccm2) methane and stratospheric water vapor, *gri*, *20*, 1419–1422, 1993.
- 4847 Neale, R. B., J. H. Richter, and M. Jochum, The impact of convection on ENSO: From a delayed
4848 oscillator to a series of events, *J. Climate*, *21*, 5904–5924, 2008.
- 4849 Neale, R. B., and B. J. Hoskins, A standard test case for AGCMs including their physical
4850 parametrizations: I: The proposal, *Atmos. Sci. Lett.*, *1*, 101–107, 2001a.
- 4851 Neale, R. B., and B. J. Hoskins, A standard test case for AGCMs including their physical
4852 parametrizations: II: Results for the Met Office Model, *Atmos. Sci. Lett.*, *1*, 108–114, 2001b.
- 4853 Newman, P. A., J. S. Daniel, D. W. Waugh, and E. R. Nash, A new formulation of equivalent
4854 effective stratospheric chlorine (EESC), *Atmos. Chem. Phys.*, *7* (**17**), 4537–4552, 2007.
- 4855 Ng, N. L., P. S. Chhabra, A. W. H. Chan, J. D. Surratt, J. H. Kroll, A. J. Kwan, D. C.
4856 McCabe, P. O. Wennberg, A. Sorooshian, S. M. Murphy, N. F. Dalleska, R. C. Flagan, and
4857 J. H. Seinfeld, Effect of nox level on secondary organic aerosol (soa) formation from the
4858 photooxidation of terpenes, *Atmospheric Chemistry and Physics*, *7* (**19**), 5159–5174, 2007,
4859 235MS Times Cited:42 Cited References Count:63.
- 4860 Nousiainen, T., and G. M. McFarquhar, Light scattering by quasi-spherical ice crystals, *J. At-*
4861 *mos. Sci.*, *61*, 2229–2248, 2004.
- 4862 Odum, J. R., T. P. W. Jungkamp, R. J. Griffin, H. J. L. Forstner, R. C. Flagan, and J. H.
4863 Seinfeld, Aromatics, reformulated gasoline, and atmospheric organic aerosol formation, *En-*
4864 *vironmental Science and Technology*, *31* (**7**), 1890–1897, 1997, Xh483 Times Cited:168 Cited
4865 References Count:29.
- 4866 Ogibalov, V. P., and V. I. Fomichev, Parameterization of solar heating by the near IR co₂ bands
4867 in the mesosphere, *Adv. Space Res.*, *32*, 759–764, 2003.
- 4868 Okin, G. S., A new model of wind erosion in the presence of vegetation, *Journal of Geophysical*
4869 *Research-Earth Surface*, *113* (**F2**), –, 2008, 276QS Times Cited:5 Cited References Count:41.
- 4870 Orszag, S. A., Fourier series on spheres, *Mon. Wea. Rev.*, *102*, 56–75, 1974.
- 4871 Ovtchinnikov, M., and S. J. Ghan, Parallel simulations of aerosol influence on clouds us-
4872 ing cloud-resolving and single-column models, *Journal of Geophysical Research-Atmospheres*,
4873 *110* (**D15**), –, 2005, 916EG Times Cited:9 Cited References Count:45.
- 4874 Park, S., and C. S. Bretherton, The university of washington shallow convection and moist
4875 turbulence schemes and their impact on climate simulations with the community atmosphere
4876 model, *J. Climate*, *22*, 3449–3469, 2009.
- 4877 Park, S., C. S. Bretherton, and P. J. Rasch, The revised cloud macrophysics in the community
4878 atmosphere model, *J. Climate*, *000*, 0000–0000, 2010.
- 4879 Peter, T., C. Bruhl, and P. J. Crutzen, Increase in the PSC formation probability caused by
4880 high-flying aircraft, *J. Geophys. Res.*, *18*, 1465–1468, 1991.

- 4881 Petters, M., and S. Kreidenweis, A single parameter representation of hygroscopic growth and
4882 ccn activity, *Atmos. Chem. Phys.*, *7*, 1961–1971, 2007.
- 4883 Pickering, K., Y. Wang, W.-K. Tao, C. Price, and J. Mueller, Vertical distributions of lightning
4884 NO_x for use in regional and global chemical transport models, *J. Geophys. Res.*, *103*, 31,203–
4885 31,216, 1998.
- 4886 Pincus, R. H. W. B., and J.-J. Morcrette, A fast, flexible, approximation technique for computing
4887 radiative transfer in inhomogeneous cloud fields, *J. Geophys. Res.*, *108(D13)*, 4376, 2003.
- 4888 Poschl, U., M. Canagaratna, J. T. Jayne, L. T. Molina, D. R. Worsnop, C. E. Kolb, and M. J.
4889 Molina, Mass accommodation coefficient of h₂so₄ vapor on aqueous sulfuric acid surfaces and
4890 gaseous diffusion coefficient of h₂so₄ in n-2/h₂o, *Journal of Physical Chemistry A*, *102* (**49**),
4891 10082–10089, 1998, 146ZX Times Cited:40 Cited References Count:41.
- 4892 Prather, M., Catastrophic loss of stratospheric ozone in dense volcanic clouds, *J. Geophys. Res.*,
4893 *97*, 187–10,191, 1992.
- 4894 Prenni, A. J., J. Y. Harrington, M. Tjernstrom, P. J. DeMott, A. Avramov, C. N. Long, S. M.
4895 Kreidenweis, P. Q. Olsson, and J. Verlinde, Can ice-nucleating aerosols effect Arctic seasonal
4896 climate?, *Bull. Am. Meteorol. Soc.*, *88*, 541–550, 2007.
- 4897 Price, C., J. Penner, and M. Prather, NO_x from lightning. Part 1: Global distribution based on
4898 lightning physics, *J. Geophys. Res.*, *102*, 5929–5941, 1997a.
- 4899 Price, C., J. Penner, and M. Prather, NO_x from lightning. Part 2: Constraints from the global
4900 atmospheric electric circuit, *J. Geophys. Res.*, *102*, 5943–5952, 1997b.
- 4901 Price, C., and D. Rind, A simple lightning parameterization for calculating global lightning
4902 distributions, *J. Geophys. Res.*, *97*, 9919–9933, 1992.
- 4903 Pruppacher, H. R., and J. D. Klett, *Microphysics of Clouds and Precipitation*. Kluwer Academic,
4904 1997.
- 4905 Rančić, M., R. Purser, and F. Mesinger, A global shallow-water model using an expanded
4906 spherical cube: Gnomonic versus conformal coordinates, *Q. J. R. Meteorol. Soc.*, *122*, 959–
4907 982, 1996.
- 4908 Rasch, P. J., B. A. Boville, and G. P. Brasseur, A three-dimensional general circulation model
4909 with coupled chemistry for the middle atmosphere, *J. Geophys. Res.*, *100*, 9041–9071, 1995.
- 4910 Rasch, P. J., M. C. Barth, J. T. Kiehl, S. E. Schwartz, and C. M. Benkovitz, A description of
4911 the global sulfur cycle and its controlling processes in the National Center for Atmospheric
4912 Research Community Climate Model, Version 3, *J. Geophys. Res.*, *105*, 1367–1385, 2000.
- 4913 Rasch, P. J., and J. E. Kristjánsson, A comparison of the CCM3 model climate using diagnosed
4914 and predicted condensate parameterizations, *J. Climate*, *11*, 1587–1614, 1998a.
- 4915 Rasch, P. J., and J. E. Kristjansson, A comparison of the ccm3 model climate using diagnosed
4916 and predicted condensate parameterizations, *J. Climate*, *11*, 1587–1614, 1998b.

- 4917 Rasch, P. J., and D. L. Williamson, On shape-preserving interpolation and semi-Lagrangian
4918 transport, *SIAM J. Sci. Stat. Comput.*, *11*, 656–687, 1990.
- 4919 Raymond, D. J., and A. M. Blyth, A stochastic mixing model for non-precipitating cumulus
4920 clouds, *J. Atmos. Sci.*, *43*, 2708–2718, 1986.
- 4921 Raymond, D. J., and A. M. Blyth, Extension of the stochastic mixing model to cumulonimbus
4922 clouds, *J. Atmos. Sci.*, *49*, 1968–1983, 1992.
- 4923 Reisner, J., R. Rasmussen, and R. T. Bruintjes, Explicit forecasting of supercooled liquid water
4924 in winter storms using the mm5 forecast model, *Q. J. R. Meteorol. Soc.*, *124*, 1071–1107,
4925 1998.
- 4926 R.G.Roble, Energetics of the mesosphere and thermosphere, in *The upper mesosphere and lower*
4927 *thermosphere : a review of experiment and theory*, edited by R. Johnson, and T. Killeen,
4928 *Geophys. Monogr.*, *87*, 1–21, 1995.
- 4929 Richmond, A., Ionospheric electrodynamics using magnetic apex coordinates, *J. Geomag. Geo-*
4930 *electric.*, *47*, 191, 1995.
- 4931 Richmond, A., M. Blanc, B. Emery, R. Wand, B. Fejer, R. Woodman, S. Ganguly, P. Amayenc,
4932 R. Behnke, C. Calderon, and J. Evans, An empirical model of quiet-day ionospheric electric
4933 fields at middle and low latitudes, *J. Geophys. Res.*, *85*, 4658, 1980.
- 4934 Richter, J. H., F. Sassi, and R. R. Garcia, Towards a physically-based wave source parameteri-
4935 zation in a general circulation model, *J. Atmos. Sci.*, *67*, 136–156, 2010.
- 4936 Richter, J. H., and P. J. Rasch, Effects of convective momentum transport on the atmospheric
4937 circulation in the community atmosphere model, version 3, *J. Climate*, *21*, 1487–1499, 2008.
- 4938 Ridley, B., K. Pickering, and J. Dye, Comments on the parameterization of lightning-produced
4939 no in global chemistry-transport models, *Atmos. Environ.*, *39*, 6184–6187, 2005.
- 4940 Riemer, N., H. Vogel, B. Vogel, and F. Fiedler, Modeling aerosols on the mesoscale-gamma:
4941 Treatment of soot aerosol and its radiative effects, *Journal of Geophysical Research-*
4942 *Atmospheres*, *108 (D19)*, –, 2003, 732EM Times Cited:17 Cited References Count:90.
- 4943 Ringler, T. D., R. P. Heikes, , and D. A. Randall, Modeling the atmospheric general circulation
4944 using a spherical geodesic grid: A new class of dynamical cores, *Mon. Wea. Rev.*, *128*, 2471–
4945 2490, 2000.
- 4946 Ritchie, H., and M. Tanguay, A comparison of spatially averaged Eulerian and semi-Lagrangian
4947 treatments of mountains, *Mon. Wea. Rev.*, *124*, 167–181, 1996.
- 4948 Robert, A. J., The integration of a low order spectral form of the primitive meteorological
4949 equations, *J. Meteorol. Soc. Japan*, *44*, 237–245, 1966.
- 4950 Roble, R., and E. Ridley, An auroral model for the near thermospheric general circulation model
4951 (TGCM), *Ann. Geophys.*, *87*, 369, 1987.

- 4952 Roble, R., and E. Ridley, A thermosphere-ionosphere-mesosphere-electrodynamics general circu-
4953 lation model (TIME-GCM): Equinox solar cycle minimum simulations (30-500 km), *Geophys.*
4954 *Res. Lett.*, *21*, 417–420, 1994.
- 4955 Rothman, L. S., A. Barbe, D. C. Benner, L. R. Brown, C. Camy-Peyret, M. R. Carleer,
4956 K. Chance, C. Clerbaux, V. Dana, V. M. Devi, A. Fayt, J.-M. Flaud, R. R. Gamache, A. Gold-
4957 man, D. Jacquemart, K. W. Jucks, W. J. Lafferty, J.-Y. Mandin, S. T. Massie, V. Nemtchi-
4958 nov, D. A. Newnham, A. Perrin, C. P. Rinsland, J. Schroeder, K. M. Smith, M. A. H. Smith,
4959 K. Tang, R. A. Toth, J. V. Auwera, P. Varanasi, and K. Yoshino, The HITRAN molecu-
4960 lar spectroscopic database: Edition of 2000 including updates of 2001, *J. Quant. Spectrosc.*
4961 *Radiat. Transfer*, *82*, 2003.
- 4962 Rothman, L., I. Gordon, A. Barbe, D. Benner, P. Bernath, M. Birk, V. Boudon, L. Brown,
4963 A. Campargue, J.-P. Champion, K. Chance, L. Coudert, V. Dana, V. Devi, S. Fally, J.-M.
4964 Flaud, R. Gamache, A. Goldman, D. Jacquemart, I. Kleiner, N. Lacome, W. Lafferty, J.-Y.
4965 Mandin, S. Massie, S. Mikhailenko, C. Miller, N. Moazzen-Ahmadi, O. Naumenko, A. Nikitin,
4966 J. Orphal, V. Perevalov, A. Perrin, A. Predoi-Cross, C. Rinsland, M. Rotger, M. Simeckov,
4967 M. Smith, K. Sung, S. Tashkun, J. Tennyson, R. Toth, A. Vandaele, and J. V. Auwera,
4968 The hitran 2008 molecular spectroscopic database, *Journal of Quantitative Spectroscopy and*
4969 *Radiative Transfer*, *110 (9-10)*, 533 – 572, 2009, HITRAN.
- 4970 Rotstayn, L. D., B. F. Ryan, and J. J. Katzfey, A scheme for calculation of the liquid fraction in
4971 mixed-phase stratiform clouds in large-scale models, *Mon. Weather Rev.*, *128 (4)*, 1070–1088,
4972 2000.
- 4973 Sadourny, R., Conservative finite-difference approximations of the primitive equations on quasi-
4974 uniform spherical grids, *Mon. Wea. Rev.*, *100 (2)*, 136–144, 1972.
- 4975 Sander, S. P., et al., Chemical kinetics and photochemical data for use in atmospheric stud-
4976 ies. Evaluation number 14, Technical Report Publication 02-25, Jet Propulsion Laboratory,
4977 Pasadena, CA, 2003.
- 4978 Sander, S. P., et al., Chemical kinetics and photochemical data for use in atmospheric stud-
4979 ies. Evaluation number 15, Technical Report Publication 06-02, Jet Propulsion Laboratory,
4980 Pasadena, CA, 2006.
- 4981 Sanderson, M., W. Collins, R. Derwent, and C. Johnson, Simulation of global hydrogen levels
4982 using a lagrangian three-dimensional model, *J. Atmos. Chem.*, *46 (1)*, 15–28, SEP, 2003.
- 4983 Sandu, A., F. A. Potra, V. Damian-Iordache, and G. R. Carmichael, Efficient implementation
4984 of fully implicit methods for atmospheric chemistry, *J. Comp. Phys.*, *129*, 101–110, 1996.
- 4985 Sandu, A., J. Verwer, M. vanLoon, G. Carmichael, F. Potra, D. Dabdub, and J. Seinfeld,
4986 Benchmarking stiff ODE solvers for atmospheric chemistry problems I: Implicit versus explicit,
4987 *Atmospheric Environment*, *31*, 3151–3166, 1997.
- 4988 Sangster, W. E., A meteorological coordinate system in which the Earth’s surface is a coordinate
4989 surface, Ph.D. thesis, University of Chicago, Department of Geophysical Sciences, 1960.

- 4990 Sato, R. K., L. M. Bath, D. L. Williamson, and G. S. Williamson, User's guide to NCAR
4991 CCMOB, Technical Report NCAR/TN-211+IA, National Center for Atmospheric Research,
4992 Boulder, Colorado, 133 pp., 1983.
- 4993 Satoh, M., *Atmospheric Circulation Dynamics and Circulation Models (Springer Praxis Books*
4994 */ Environmental Sciences)*. Springer, 1 edition, 6, 2004.
- 4995 Scherliess, L., A. Richmond, and B. Fejer. 2002. Global empirical ionospheric electric field
4996 model. draft, Center for Atmospheric and Space Science, Utah State University, Logan.
- 4997 Schubert, W. H., J. S. Wakefield, E. J. Steiner, and S. K. Cox, Marine stratocumulus convection.
4998 part i: Governing equations and horizontally homogeneous solutions, *J. Atmos. Sci.*, *36*, 1286–
4999 1307, 1979.
- 5000 Schunk, R., and A. Nagy, *Ionospheres: Physics, Plasma Physics, and Chemistry*. Cambridge,
5001 University Press, 2000.
- 5002 Seinfeld, J. H., and S. N. Pandis, *Atmospheric Chemistry and Physics: From Air Pollution to*
5003 *Climate Change*. John Wiley, Hoboken, N. J, 1998.
- 5004 Sihto, S. L., M. Kulmala, V. M. Kerminen, M. D. Maso, T. Petaja, I. Riipinen, H. Korhonen,
5005 F. Arnold, R. Janson, M. Boy, A. Laaksonen, and K. E. J. Lehtinen, Atmospheric sulphuric
5006 acid and aerosol formation: implications from atmospheric measurements for nucleation and
5007 early growth mechanisms, *Atmospheric Chemistry and Physics*, *6*, 4079–4091, 2006.
- 5008 Simmons, A. J., and D. M. Burridge, An energy and angular momentum conserving vertical
5009 finite-difference scheme and hybrid vertical coordinates, *Mon. Wea. Rev.*, *109*, 758–766, 1981.
- 5010 Simmons, A. J., and R. Strüfing, An energy and angular-momentum conserving finite-difference
5011 scheme, hybrid coordinates and medium-range weather prediction, Technical Report ECMWF
5012 Report No. 28, European Centre for Medium-Range Weather Forecasts, Reading, U.K.,
5013 68 pp., 1981.
- 5014 Simmons, A. J., and R. Strüfing, Numerical forecasts of stratospheric warming events using a
5015 model with hybrid vertical coordinate, *Q. J. R. Meteorol. Soc.*, *109*, 81–111, 1983.
- 5016 Skamarock, W., Kinetic energy spectra and model filters, in: P.H. Lauritzen, R.D. nair, C.
5017 Jablonowski, M. Taylor (Eds.), Numerical techniques for global atmospheric models, *Lecture*
5018 *Notes in Computational Science and Engineering, Springer, 2010*, 2010, to appear.
- 5019 Slingo, J. M., The development and verification of a cloud prediction scheme for the ECMWF
5020 model, *Q. J. R. Meteorol. Soc.*, *113*, 899–927, 1987a.
- 5021 Slingo, J. M., The development and verification of a cloud prediction scheme for the ecmwf
5022 model, *Q. J. R. Meteorol. Soc.*, *113*, 899–927, 1987b.
- 5023 Smith, R. N. B., A scheme for predicting layer clouds and their water content in a general
5024 circulation model, *Q. J. R. Meteorol. Soc.*, *116*, 435–460, 1990.

- 5025 Smith, S. J., H. Pitcher, and T. M. L. Wigley, Global and regional anthropogenic sulfur dioxide
5026 emissions, *Glob. Biogeochem. Cycles*, *29*, 99–119, 2001.
- 5027 Smith, S. J., R. Andres, E. Conception, and J. Lurz, Historical sulfur dioxide emissions 18502000:
5028 Methods and results, Technical report, Pacific Northwest National Laboratory, Joint Global
5029 Change Research Institute, 2004.
- 5030 Solomon, S., and L. Qiang, Solar extreme-ultraviolet irradiance for general circulation models,
5031 *J. Geophys. Res.*, *110*, A10306, doi:10.1029/2005JA011160, 2005.
- 5032 Spiteri, R. J., and S. J. Ruuth, A new class of optimal high-order strong-stability-preserving
5033 time discretization methods, *SIAM J. Numer. Anal.*, *40* (2), 469–491, 2002.
- 5034 Staniforth, A., N. Wood, and C. Girard, Energy and energy-like invariants for deep non-
5035 hydrostatic atmospheres, *Q. J. R. Meteorol. Soc.*, *129*, 3495–3499, 2003.
- 5036 Starr, V. P., A quasi-lagrangian system of hydrodynamical equations, *J. Meteor.*, *2*, 227–237,
5037 1945.
- 5038 Stier, P., J. Feichter, S. Kinne, S. Kloster, E. Vignati, J. Wilson, L. Ganzeveld, I. Tegen,
5039 M. Werner, Y. Balkanski, M. Schulz, O. Boucher, A. Minikin, and A. Petzold, The aerosol-
5040 climate model echem5-ham, *Atmospheric Chemistry and Physics*, *5*, 1125–1156, 2005, 912EM
5041 Times Cited:156 Cited References Count:125.
- 5042 Suarez, M. J., and L. L. Takacs, Documentation of the aries/geos dynamical core: Version 2,
5043 Technical Report Technical Memorandum 104 606 Vol. 5, NASA, 1995.
- 5044 Sundqvist, H., Parameterization of condensation and associated clouds in models for weather
5045 prediction and general circulation simulation, in *Physically-based Modeling and Simulation of
5046 Climate and Climate Change*, Vol. 1, edited by M. E. Schlesinger, 433–461, Kluwer Academic,
5047 1988.
- 5048 Tabazadeh, A., R. P. Turco, and M. Z. Jacobson, A model for studying the composition and
5049 chemical effects of stratospheric aerosols, *J. Geophys. Res.*, *99*, 12,897–12,914, 1994.
- 5050 Tabazadeh, A., M. L. Santee, M. Y. Danilin, H. C. Pumphrey, P. A. Newman, P. J. Hamill, and
5051 J. L. Mergenthaler, Quantifying denitrification and its effect on ozone recovery, *Science*, *288*,
5052 1407–1411, 2000.
- 5053 Taylor, M. A., J. Edwards, and A. St.Cyr, Petascale atmospheric models for the community
5054 climate system model: New developments and evaluation of scalable dynamical cores, *J.
5055 Phys. Conf. Ser.*, *125* (012023), 2008.
- 5056 Taylor, M. 2010. Conservation of mass and energy for the moist atmospheric primitive equations
5057 on unstructured grids. in *Numerical Techniques for Global Atmospheric Models, Springer
5058 Lecture Notes in Computational Science and Engineering*, . Springer.
- 5059 Taylor, M., J. Tribbia, and M. Iskandarani, The spectral element method for the shallow water
5060 equations on the sphere, *J. Comp. Phys.*, *130*, 92–108, 1997.

- 5061 Taylor, M. A., A. St.Cyr, and A. Fournier. 2009. A non-oscillatory advection operator for the
5062 compatible spectral element method. in *Computational Science ICCS 2009 Part II, Lecture*
5063 *Notes in Computer Science 5545*, 273–282, , Berlin / Heidelberg. Springer.
- 5064 Taylor, M. A., and A. Fournier, A compatible and conservative spectral element method on
5065 unstructured grids, *J. Comp. Phys., In Press*, –, 2010.
- 5066 Teklemariam, T., and J. Sparks, Gaseous fluxes of peroxyacetyl nitrate (PAN) into plant leaves,
5067 *PLANT CELL AND ENVIRONMENT*, 27 (9), 1149–1158, SEP, 2004.
- 5068 Temperton, C., Treatment of the Coriolis terms in semi-Lagrangian spectral models, in *At-*
5069 *mospheric and Ocean Modelling. The André J. Robert Memorial Volume*, edited by C. Lin,
5070 R. Laprise,, and H. Ritchie, 293–302, Canadian Meteorological and Oceanographic Society,
5071 Ottawa, Canada, 1997.
- 5072 Temperton, C., M. Hortal, and A. Simmons, A two-time-level semi-Lagrangian global spectral
5073 model, *Q. J. R. Meteorol. Soc.*, 127, 111–127, 2001.
- 5074 Thomas, S., and R. Loft, Parallel semi-implicit spectral element methods for atmospheric general
5075 circulation models, *J. Sci. Comput.*, 15, 499–518, 2000.
- 5076 Thomas, S., and R. Loft, The NCAR spectral element climate dynamical core: Semi-implicit
5077 Eulerian formulation, *J. Sci. Comput.*, 25, 307–322, 2005.
- 5078 Thomason, L. W., L. R. Poole, and T. Deshler, A global climatology of stratospheric aerosol
5079 surface area density measurements: 1984-1994, *J. Geophys. Res.*, 102, 8967–8976, 1997.
- 5080 Thompson, G. M., R. M. Rasmussen, and K. Manning, Explicit forecasts of winter precipitation
5081 using and improved bulk microphysics scheme. part I: Description and sensitivity analysis,
5082 *Mon. Weather Rev.*, 132, 519–542, 2004.
- 5083 Thompson, G., P. R. Field, R. M. Rasmussen, and W. D. Hall, Explicit forecasts of winter
5084 precipitation using an improved bulk microphysics scheme. part ii: Implementation of a new
5085 snow parameterization, *Monthly Weather Review*, 136 (12), 5095–5115, 2008.
- 5086 Tie, X., S. Madronich, S. Walters, D. P. Edwards, P. Ginoux, N. Mahowald, R. Zhang, C. Lou,
5087 and G. Brasseur, Assessment of the global impact of aerosols on tropospheric oxidants, *J.*
5088 *Geophys. Res.*, 110, D03204, 1992.
- 5089 Tie, X., G. Brasseur, L. Emmons, L. Horowitz, and D. Kinnison, Effects of aerosols on tro-
5090 pospheric oxidants: A global model study, *Journal of Geophysical Research-Atmospheres*,
5091 106 (D19), 22931–22964, 2001, 481UJ Times Cited:64 Cited References Count:92.
- 5092 Tie, X. X., S. Madronich, S. Walters, D. P. Edwards, P. Ginoux, N. Mahowald, R. Y. Zhang,
5093 C. Lou, and G. Brasseur, Assessment of the global impact of aerosols on troposphic oxidants,
5094 *J. Geophys. Res.*, 110 (D03204), 2005.
- 5095 Tilmes, S., R. Garcia, D. Kinnisen, A. Gettelman, and P. J. Rasch, Impact of geoengineered
5096 aerosols on the troposphere and stratosphere, *J. Geophys. Res.*, 114, 2009.

- 5097 Turnipseed, A., G. Huey, E. Nemitz, R. Stickel, J. Higgs, D. Tanner D. and Slusher, J. Sparks,
5098 F. Flocke, and A. Guenther, Eddy covariance fluxes of peroxyacyl nitrates (PANs) and NO₂ to
5099 a coniferous forest, *J. Geophys. Res.*, *111*, D09304, 2006.
- 5100 van de Hulst, H. C., *Light Scattering by Small Particles*. Dover, 1957.
- 5101 Vavrus, S., and D. Waliser, An improved parameterization for simulating arctic cloud amount
5102 in the CCSM3 climate model, *J. Climate*, *21*, 5673–5687, 2008.
- 5103 Vehkamäki, H., M. Kulmala, I. Napari, K. E. J. Lehtinen, T. T. N. Noppel, and A. Laaksonen,
5104 an improved parameterization for sulfuric acid-water nucleation rates for tropospheric and
5105 stratospheric conditions, *Journal of Geophysical Research-Atmospheres*, *107*, 4622, 2002.
- 5106 Walmsley, J., and M. Wesely, Modification of coded parametrizations of surface resistances to
5107 gaseous dry deposition, *Atmos. Environ.*, *30* (7), 1181–1188, APR, 1996.
- 5108 Wang, H., J. J. Tribbia, F. Baer, A. Fournier, and M. A. Taylor, A spectral element version of
5109 CAM2, *Mon. Wea. Rev.*, *135*, 38253840, 2007.
- 5110 Wang, M. H., J. E. Penner, and X. H. Liu, Coupled impact aerosol and NCAR CAM3 model:
5111 Evaluation of predicted aerosol number and size distribution, *Journal of Geophysical Research-*
5112 *Atmospheres*, *114*, D06302, 2009.
- 5113 Wang, Y.-M., J. Lean, and N. Sheeley, Modeling the sun's magnetic field and irradiance since
5114 1713, *The Astrophysical Journal*, *625* (1), 2005.
- 5115 Warren, S., and R. E. Brandt, Optical constants of ice from the ultraviolet to the microwave:
5116 A revised compilation, *J. Geophys. Res.*, *113*, 2008.
- 5117 Washington, W. M., Documentation for the Community Climate Model (CCM), Version 0,
5118 Technical Report NTIS No. PB82 194192, National Center for Atmospheric Research, Boulder,
5119 Colorado, 1982.
- 5120 Webster, S., A. R. Brown, D. R. Cameron, and P. Jones, Improvements to the representation of
5121 orography in the met office unified model, *Quart. J. Roy. Meteor. Soc.*, *129*, 1989–2010, 2003.
- 5122 Weimer, D., Models of high-latitude electric potentials derived with the least error fit of spherical
5123 harmonic coefficients, *J. Geophys. Res.*, *100*, 19,595, 1995.
- 5124 Wesely, M., Parameterization of surface resistances to gaseous dry deposition in regional-scale
5125 numerical models, *Atmos. Environ.*, *23*, 1293–1304, 1989.
- 5126 Wesely, M., and B. Hicks, A review of the current status of knowledge on dry deposition, *Atmos.*
5127 *Environ.*, *34* (12-14), 2261–2282, 2000.
- 5128 Wiacek, A., and T. Peter, On the availability of uncoated mineral dust ice nuclei in cold cloud
5129 regions, *Geophys. Res. Lett.*, *36* (L17801), 2009.

- 5130 Williamson, D. L., Description of NCAR Community Climate Model (CCM0B), Technical Re-
5131 port NCAR/TN-210+STR, National Center for Atmospheric Research, Boulder, Colorado,
5132 NTIS No. PB83 23106888, 88 pp., 1983.
- 5133 Williamson, D. L., Time-split versus process-split coupling of parameterizations and dynamical
5134 core, *Mon. Wea. Rev.*, 130, 2024–2041, 2002.
- 5135 Williamson, D. L., L. M. Bath, R. K. Sato, T. A. Mayer, and M. L. Kuhn, Documentation of
5136 NCAR CCM0B program modules, Technical Report NCAR/TN-212+IA, National Center for
5137 Atmospheric Research, Boulder, Colorado, NTIS No. PB83 263996, 198 pp., 1983.
- 5138 Williamson, D. L., J. T. Kiehl, V. Ramanathan, R. E. Dickinson, and J. J. Hack, Descrip-
5139 tion of NCAR Community Climate Model (CCM1), Technical Report NCAR/TN-285+STR,
5140 National Center for Atmospheric Research, Boulder, Colorado, 112 pp., 1987.
- 5141 Williamson, D. L., and J. G. Olson, Climate simulations with a semi-Lagrangian version of the
5142 NCAR Community Climate Model, *Mon. Wea. Rev.*, 122, 1594–1610, 1994a.
- 5143 Williamson, D. L., and J. G. Olson, Climate simulations with a semi-lagrangian version of the
5144 NCAR community climate model, *Mon. Wea. Rev.*, 122, 1594–1610, 1994b.
- 5145 Williamson, D. L., and P. J. Rasch, Two-dimensional semi-Lagrangian transport with shape-
5146 preserving interpolation, *Mon. Wea. Rev.*, 117, 102–129, 1989.
- 5147 Williamson, D. L., and J. M. Rosinski, Accuracy of reduced grid calculations, *Q. J. R. Meteorol.*
5148 *Soc.*, 126, 1619–1640, 2000.
- 5149 Williamson, D. L., and G. S. Williamson, Circulation statistics from January and July simula-
5150 tions with the NCAR Community Climate Model (CCM0B), Technical Report NCAR/TN-
5151 224+STR,, National Center for Atmospheric Research, Boulder, Colorado, NTIS No. PB85
5152 165637/AS, 112 pp., 1984.
- 5153 Williamson, G. S., CCM2 datasets and circulation statistics, Technical Report NCAR/TN-
5154 391+STR, National Center for Atmospheric Research, Boulder, Colorado, 85 pp., 1993.
- 5155 Williamson, G. S., and D. L. Williamson, Circulation statistics from seasonal and perpetual
5156 January and July simulations with the NCAR Community Climate Model (CCM1): R15,
5157 Technical Report NCAR/TN-302+STR, National Center for Atmospheric Research, Boulder,
5158 Colorado, 199 pp., 1987.
- 5159 Wilson, J., C. Cuvelier, and F. Raes, A modeling study of global mixed aerosol fields, *Journal*
5160 *of Geophysical Research-Atmospheres*, 106 (D24), 34,08134,108, 2001.
- 5161 Wilson, J. D., Representing drag on unresolved terrain as a distributed momentum sink, *J.*
5162 *Atmos. Sci.*, 59, 1629–1637, 2002.
- 5163 Wiscombe, W. J., Mie scattering calculations: Advances in technique and fast, vector-speed
5164 computer codes., Technical Report Tech. Note. NCAR/TN-140+STR, NCAR, 1996.

- 5165 World Meteorological Organization, Scientific Assessment of Ozone Depletion: 2002 Global
5166 Ozone Research and Monitoring Project, Report no. 47, 498 pp., Geneva, 2003.
- 5167 Wu, T. T., High frequency scattering, *Phys. Rev.*, *104*, 1201–1212, 1956.
- 5168 Yang, P., H. Wei, H. L. Huang, B. A. Baum, Y. X. Hu, G. W. Kattawar, M. I. Mishchenko, and
5169 Q. Fu, Scattering and absorption property database for nonspherical ice particles in the near-
5170 through far-infrared spectral region, *Appl. Opt.*, *44*, 5512–5523, 2005.
- 5171 Yonemura, S., S. Kawashima, and H. Tsuruta, Carbon monoxide, hydrogen, and methane uptake
5172 by soils in a temperate arable field and a forest, *J. Geophys. Res.*, *105* (D11), 14,347–14,362,
5173 JUN 16, 2000.
- 5174 Yoshioka, M., N. M. Mahowald, A. J. Conley, W. D. Collins, D. W. Fillmore, C. S. Zender,
5175 and D. B. Coleman, Impact of desert dust radiative forcing on sahel precipitation: Relative
5176 importance of dust compared to sea surface temperature variations, vegetation changes, and
5177 greenhouse gas warming, *Journal of Climate*, *20* (8), 1445–1467, 2007, 157SY Times Cited:33
5178 Cited References Count:80.
- 5179 Young, K. C., The role of contact nucleation in ice phase initiation of clouds, *J. Atmos. Sci.*,
5180 *31*, 768–776, 1974.
- 5181 Zeng, X., and R. E. Dickinson, Effect of surface sublayer on surface skin temperature and fluxes,
5182 *J. Climate*, *11*, 537–550, 1998.
- 5183 Zeng, X., M. Zhao, and R. E. Dickinson, Intercomparison of bulk aerodynamic algorithms for
5184 the computation of sea surface fluxes using TOGA COARE and TAO data, *J. Climate*, *11*,
5185 2628–2644, 1998.
- 5186 Zerroukat, M., N. Wood, and A. Staniforth, A monotonic and positive-definite filter for a
5187 semi-lagrangian inherently conserving and efficient (slice) scheme, *Q. J. R. Meteorol. Soc.*,
5188 *131* (611), 2923–2936, 2005.
- 5189 Zhang, G. J., and N. A. McFarlane, Sensitivity of climate simulations to the parameterization of
5190 cumulus convection in the Canadian Climate Centre general circulation model, *Atmosphere-
5191 Ocean*, *33*, 407–446, 1995.
- 5192 Zhang, L. M., S. L. Gong, J. Padro, and L. Barrie, A size-segregated particle dry deposition
5193 scheme for an atmospheric aerosol module, *Atmospheric Environment*, *35* (3), 549–560, 2001,
5194 395TK Times Cited:136 Cited References Count:49.
- 5195 Zhang, M., W. Lyn, C. S. Bretherton, J. J. Hack, and P. J. Rasch, A modified formulation
5196 of fractional stratiform condensation rate in the near community atmosphere model (cam2),
5197 *J. Geophys. Res.*, *000*, 1000–0000, 2003a.
- 5198 Zhang, M., W. Lin, C. S. Bretherton, J. J. Hack, and P. J. Rasch, A modified formulation of
5199 fractional stratiform condensation rate in the NCAR community atmospheric model CAM2,
5200 *J. Geophys. Res.*, *108* (D1), 2003b.

- 5201 Zhang, Y., and L. Paxton, An empirical kp-dependent global auroral model based on timed/guvi
5202 fuv data, *Journal of Atmospheric and Solar-Terrestrial Physics*, 70 (8-9), 1231 – 1242, 2008.
- 5203 Zilitinkevich, S. S., *Dynamics of the Atmospheric Boundary Layer*. Gidrometeoizdat, Leningrad,
5204 1970, 292 pp.